

**Metallo-Supramolecular Assemblies With Photoresponsive
Functionality**

Samuel Oldknow

Submitted in accordance with the requirements for the degree of
Doctor of Philosophy

The University of Leeds
School of Chemistry

February 2018

The candidate confirms that the work submitted is his/her own except where work which has formed part of or jointly-authored publications has been included. The contribution of the candidate and other authors to this work has been indicated below. The candidate confirms that appropriate credit has been given where reference has been made to the work of others.

References for the jointly authored publications include:

1. V.E. Pritchard, D.R. Martir, S. Oldknow, S. Kei, S. Hiraoka, N.J. Cookson, E. Zysman-Colman and M.J. Hardie ‘Homochiral self-sorted and emissive Ir(III) metallocryptophanes’ *Chemistry – A European Journal*, 2017, **23**, 6290-6294.

Work reported within this publication is described in chapter 3 of this thesis. V. E. Pritchard synthesised and characterised the ligands and complexes and elucidated the solid state structure. D.R Martir and E. Zysman-Colman performed photophysical studies, S. Kei and S. Hiraoka performed chiral resolution NMR studies, N.J. Cookson performed 2D NMR experiments and M.J Hardie designed the study and wrote the paper. *Candidate’s contribution*: Resynthesis of materials, kinetic experiments of cage formation and chiral self-sorting studies with guest molecules.

2. S. Oldknow, D.R. Martir, V.E. Pritchard, M.A.Blitz, C.W.G. Fishwick, and M. J Hardie ‘Photo-induced structure-switching isomerisation of M₃L₂ Ir(III) coordination cages bearing host ligands with multiple azoaromatic groups’ *Journal of the American Chemical Society*, 2018, **Submitted**.

Work reported within this publication is described in chapters 2, 3 and 4 of this thesis. D.R Martir and E. Zysman-Colman performed photophysical studies, V.E. Pritchard provided materials and synthetic strategies, M.A. Blitz performed photoisomerisation studies in conjunction with the candidate, C.W.G. Fishwick performed molecular modelling studies and M.J Hardie designed the study and wrote the paper. *Candidate’s contribution*: Design, synthesis and characterisation of all new ligands and complexes; performing all photoisomerisation studies (in conjunction with M.A. Blitz).

This copy has been supplied on the understanding that it is copyright material and that no quotation from the thesis may be published without proper acknowledgement.

The right of Samuel Oldknow to be identified as Author of this work has been asserted by him in accordance with the Copyright, Designs and Patents Act 1988.

© 2018 The University of Leeds and Samuel Oldknow

Acknowledgements

I would like to begin by thanking my supervisor, Professor Michael Hardie for giving me the opportunity to work on what has been a highly engaging and rewarding PhD project and for all of her help and advice throughout the past three years. It has been a fantastic experience for me and I've learned more than I could ever have expected in my time here. Subsidized lunches, Christmas meals and barbeques have also been a great perk!

I must offer sincere thanks to a number of people without whom the work discussed herein would not have been possible. Foremost is Vikki – for all your support at a crucial point of my project, your contribution cannot be understated. I still hope to go for a sail on your boat someday. Sincere thanks are also due to Mark who went way beyond any minor obligations accorded to him in helping me with optics and lasers and a bunch of other stuff I knew nothing about. I would also like to thank Dr Chris Pask for all his tireless efforts to transform some truly shocking X-ray data into workable results. I probably won't miss the sound of the klaxon going off at 3am at Diamond preparing another failed crystal but never say never. To Diego, Eli, Simon, Nikki and Ben for all of your contributions to various aspects of this work, thank you.

I'd like to take a moment to thank the former members of office 1.32, Mike, Jordan and Heba for creating a bizarrely unique working environment. To Mike, the 'hullish thug/baby': thank you for reminding me that life need not be too serious and that rain is really really loud. I know that I have a great contact should I wish to pursue a life of crime. To Heba, thank you for all the spontaneous Wagamama's trips and for being a lone voice of calm in an otherwise insane office. As for 'Chief Baby' Jordan – the office (and most of the department) has seemed far quieter without you. Thank you for teaching me that anything sounds funny when said in a voice several octaves above normal human hearing. It feels good that even though I made mistakes during my time here I at least avoided writing off my fume cupboard.

Thank you also to the current occupants of the finest office at Leeds. Firstly Team Willans – Bank and Frances. Bank, I remain confident you will forever hold the title for mixing the strongest 'cocktails' I will ever drink. For me to be that inebriated by 8pm is an achievement you deserve all the credit for. And to Frances – the founder of carborane corner. I will miss our discussions on some incredibly specific topics - NHC's, climbing, hot drinks and bananas. I know you'll have a great finish to your project. I now also have the details of a great actor's guild for hire. Total commitment to the bit.

Sincere thanks are due to my fellow members of Team Hardie, Jonny, Hayder, Flo and Ed who have shared the occasional highs and copious lows of supramolecular

chemistry with me. To Jonny, thank you for a lifetime's supply of some of the worst puns I think I'm ever likely to come across and for founding the MPD (skree!) which was a high point of my time here. Hayder – thank you for introducing me to Iraqi cuisine as my palate is surprisingly described as 'boring'. Everything will be fine in the end. To Flo – thank you for helping me navigate the early perilous waters of CTG chemistry. I know you will also enjoy success in the equally perilous stages of early parenthood. Finally thank you to Ed, our resident technician/janitor/clever girl. I'll miss some of the highlights of our evenings out – high stakes fruity chess matches, pelting strangers with an inflatable beachball, the scarily accurate Anne Robinson impersonation and your attempting to conduct a conversation with a statue are just a few of the clownish exploits I can think of. Where you'll end up only the finger of true randomness knows.

Thanks are also due to the Halcrow, McGowan and assorted other groups and people with whom I've shared three years of great (if hazy) memories with. From office 1.29 - to Kay, Sam G (spooof bros), Raf (king of Poland) Iurii (The weatherman), Pablo (the fabulous Spaniard), Izar (the volatile Spaniard) Cecilia and Matt. And from elsewhere to Emma, Clara, Sarah, Jack, Oowis, Sophia and Becky *nickname omitted* Stones. You've all played an invaluable part in ensuring I come away from Leeds with much more than just a PhD. Within Leeds my final acknowledgement is for Laura. Thank you for three years of shenanigans and general mockery of everything from my diet to my wardrobe. I still rate our high street rendition of mamma mia as a highlight of my time here. More importantly thank you for always making me laugh throughout my three years at Leeds.

Finally my biggest thanks are to my parents, for giving me the courage to apply for my PhD to begin with and for your constant support throughout my time here in Leeds. It's fair to say this wouldn't have been possible without you.

Abstract

This thesis concerns the design of metallosupramolecular architectures incorporating a specific function, namely light-responsive properties, for potential applications in molecular recognition, molecular electronics and as stimuli-responsive materials. This is achieved by employing established geometrically directing metallotectons in combination with novel light-responsive tripodal hosts based on the cyclotrimeratrylene scaffold.

A novel library of light-responsive molecular hosts have been prepared *via* novel asymmetrical azobenzene precursors. These light-responsive ligands undergo self-assembly with a variety of Ir(III) metallotectons to give a family of M_3L_2 metallocryptophanes, thus implanting the light-responsive functionality into these systems. Solution-state analysis indicates these metallocages contain a significant internal space for potential applications in molecular recognition.

The photoresponsive properties of both the novel ligands and metallocryptophanes has been explored utilising light of UV and visible wavelengths to toggle between the *trans/cis* conformations of the embedded azobenzene units, resulting in dramatic structural perturbations in solution, pointing the way to sophisticated applications in molecular recognition. Photophysical analysis of these metallocryptophanes reveals deep blue emission properties, characteristically uncommon for Ir(III) complexes.

A series of non-discrete coordination polymers have also been prepared and crystallographically elucidated from the combination of a light-responsive ligand with various Cu(II) and Ag(I) salts. Although light-responsive behaviour is yet to be demonstrated in these systems, a solvent-induced structural rearrangement is observed in one example, potentially promising further sophisticated host-guest properties.

Table of Contents

Acknowledgements	iii
Abstract	v
Table of Contents	vi
List of Figures	ix
List of Schemes	xvii
List of Tables	xviii
List of Abbreviations	ix
Chapter 1 Introduction	1
1.1 Overview	1
1.2 Introduction to supramolecular chemistry	1
1.3 Metallo-supramolecular chemistry.....	4
1.4 Coordination Cages – Properties and applications.....	8
1.5 Stimuli-responsive metallo-supramolecular assemblies	13
1.6 Light responsive molecular motions	16
1.7 Cyclotrimeratrylene.....	22
1.8 Project Outline	28
1.9 References	29
Chapter 2 Synthesis of photoresponsive cyclotriguaiacylene derived ligands	41
2.1 Introduction	41
2.2 Cyclotriguaiacylene synthesis	45
2.3 Azobenzene precursors	47
2.4 Azobenzene (AZB) appended CTG ligands	58
2.5 Stilbene (SBN) appended CTG ligands	66
2.6 Conclusions and further direction	71
2.7 Experimental	73
2.7.1 Instrumentation	73
2.7.2 Chemical Syntheses	73
2.7.3 X-ray crystallography	91
2.8 References	93
Chapter 3 Synthesis and characterisation of Ir(III) metallocryptophanes with photoresponsive functionality	96
3.1 Introduction	96

3.2 Cis-protected Ir(III) metallotectons.....	101
3.3 Self-assembly of M_3L_2 metallocryptophanes bearing azobenzene units.....	102
3.4 Spectroscopic analysis of metallocryptophanes.....	105
3.5 Chiral self-sorting of metallocryptophanes in solution.....	117
3.6 Self-assembly of a M_3L_2 metallocryptophane bearing stilbene units	125
3.7 Computational modelling of cage 3.8	129
3.8 Other azobenzene containing metallocryptophanes.....	133
3.9 Conclusions and further direction	134
3.10 Experimental	136
3.10.1 Instrumentation	136
3.10.2 Chemical Syntheses	137
3.10.3 Chiral guest experiments with metallocryptophane 3.14.....	151
3.10.4 Chiral guest experiments with metallocryptophane 3.8.....	151
3.11 References	152

Chapter 4 Photoisomerisation and photophysical studies of CTG-based Ir(III) metallocryptophanes	156
4.1 Introduction.....	156
4.2 General considerations – photoisomerisation of azobenzene	158
4.3 Photoisomerisation of free ligands.....	161
4.4 UV studies of M_3L_2 ester cage isomerisation	170
4.5 UV studies of M_3L_2 ether cage isomerisation.....	176
4.6 Stilbene analogue	179
4.7 Conversion limits and photochemical fatigue.....	180
4.8 1H NMR study of cage 3.12 photoisomerisation	185
4.9 Photophysics of Metallocryptophanes	189
4.10 Conclusions and further direction	194
4.11 Experimental	197
4.11.1 General considerations	197
4.11.2 UV studies of free ligands.....	198
4.11.3 1H NMR studies of free ligands	198
4.11.4 UV studies of metallocryptophanes	199
4.11.5 1H NMR study of metallocryptophane 3.12.....	199
4.11.6 Photophysical studies	199

4.12 References	201
-----------------------	-----

Chapter 5 Coordination polymers featuring azobenzene functionalised

molecular hosts	207
------------------------------	------------

5.1 Introduction.....	207
-----------------------	-----

5.2 General Remarks.....	212
--------------------------	-----

5.3 {[Cu ₃ (H ₂ O) ₆ (2.12) ₄].6BF ₄ .9NMP.4H ₂ O} _n 2D Network.....	213
--	-----

5.4 [Cu(2.12) ₂ (OAc) ₂] discrete complex.....	218
---	-----

5.5 [Ag(2.12)] _n .X 1D coordination polymer (X = BF ₄ ⁻ , PF ₆ ⁻ , OTf).....	222
---	-----

5.6 {[Cu ₅ (2.12) ₄ (H ₂ O) ₁₂].2H ₂ O.4NMP.10OTf} _n 2D polymer	225
--	-----

5.7 {[Cu ₂ (2.12) ₂ (CF ₃ CO ₂) ₂ (NMP) ₂].7(o-C ₆ H ₄ Cl ₂) _n 2D coordination polymer	230
---	-----

5.8 Additional Coordination Complexes	237
---	-----

5.9 Conclusions and further direction.....	240
--	-----

5.10 Experimental	241
-------------------------	-----

5.10.1 Instrumentation	241
------------------------------	-----

5.10.2 Chemical Synthesis	242
---------------------------------	-----

5.10.3 X-ray crystallography.....	244
-----------------------------------	-----

5.11 References.....	248
----------------------	-----

Ligand and Complex roadmap.....	252
--	------------

List of Figures

Figure 1.1: Some examples of supramolecular interactions found in nature.....	2
Figure 1.2: Some examples of crown ethers prepared by Pedersen.....	3
Figure 1.3: Single crystal X-ray diffraction (SCXRD) structures of cryptates prepared by Lehn..	4
Figure 1.4: a. Chemical representation of Lehn's helicate assembled from polypyridyl ligands and copper(I) salts with metal centres represented as hard spheres; b. SCXRD structure of the asymmetric metallohelix prepared by Scott and coworkers which has anticancer properties..	5
Figure 1.5: SCXRD structure of a tetrafoil metal-templated molecular knot prepared by Leigh and coworkers.....	6
Figure 1.6: SCXRD structures of topologically complex assemblies accessed via supramolecular chemistry showing a. Sauvage's [2] catenane; b. Puddephatt's Solomon link; c. Stoddart's Borromean rings.....	7
Figure 1.7: SCXRD structures illustrating the structural transformation of Raymond's M_2L_3 helicate upon addition of NMe_4 to the tetrahedral M_4L_6 assembly.....	9
Figure 1.8: SCXRD structures of some tetrahedral cages prepared by Nitschke and coworkers showing: a. Encapsulation and stabilisation of white phosphorus within a $[Fe_4L_6]$ coordination cage; b. $[Fe_4L_6]$ cage with anthracene ligands capable of sequestering fullerene (C_{60}) as a guest.	10
Figure 1.9: SCXRD structures of some of the octahedral cages prepared by Fujita, showing a. Stabilisation of photoactive ruthenium dimer within Fujita's $[Pd_6L_4]$ octahedra; b. Binding of the ruthenium dimer guest is shown in spacefilling mode.....	11
Figure 1.10: SCXRD structure of Fujita's $Pd_{12}L_{24}$ assemblies showing: a. View down the crystallographic a axis; b. Cuboctahedral geometry.....	12
Figure 1.11a: Light driven shuttling of Sauvage's catenane.....	14
Figure 1.11b: Stoddart's rotaxane molecular shuttle..	15
Figure 1.11c: Leigh's molecular machine for stereoselective synthesis.....	15
Figure 1.12: Isomerisation of 11-cis retinal in the visual cascade	16
Figure 1.13: The main classes of light-responsive photoswitches showing: a. Cis-trans isomerisation of the azobenzene group; b. Dithienylethene; c. Spiropyran; d. Stilbene; e. Acylhydrazone.	17
Figure 1.14: Photoisomerisation of Rebek's azo-appended cavitand.	18
Figure 1.15: Photoisomerisation of Rebek's cavitand receptor for the binding of adamantane guests	19
Figure 1.16: Clever's dithienylethene ligand with different self assembly products.....	20
Figure 1.17: Solid state photocyclisation of Jin's M_4L_2 metallacycle..	21

- Figure 1.18:** SCXRD structures of Pd₂L₄ metallocages prepared by Clever and coworkers (open conformation) incorporating the photoresponsive dithienylethene unit showing: (a) side view; (b) top view..... 22
- Figure 1.19:** The cyclotrimeratrylene family of cavitands showing: a. Crown and saddle forms of CTV; b. Crown P and M enantiomers of the chiral tris hydroxy derivative CTG; c. The hexa hydroxyl derivative CTC (left) and the tris amino derivative aCTG (right). 23
- Figure 1.20:** Guest encapsulation by organic CTV derivatives showing a. SCXRD structure of the host-guest interaction between CTV and fullerene C₆₀; b. Chemical representation of the cryptophane prepared by Dutasta and coworkers for the encapsulation of xenon gas. 24
- Figure 1.21:** SCXRD structure of Ku's hemicarceplex for the binding of metallofullerenes 24
- Figure 1.22:** From the SCXRD structure of Robson's metallocages utilising cyclotricatechylene derived ligands showing a. Individual cage moiety; b. Packed display as viewed down the crystallographic c axis..... 25
- Figure 1.23:** SCXRD structures showing the diversity of CTG-derived metallosupramolecular assemblies: From the crystal structure of a. M₆L₆ Borromean rings; b. M₆L₈ stella octangula structure; c. Organic cryptophane bridged by disulphide bonds; d. Pd₃L₂ metallocryptophane. 26
- Figure 1.24:** SCXRD structure of the M₁₂L₈ metallocube prepared by Hardie, showing a. Individual tripodal CTG ligand; b. Silver metallocube. 27
- Figure 2.1:** SCXRD structure of the trinuclear rhenium (I) complex prepared by Hardie and coworkers; Inset: Chemical representation of the coordination environment about the metal centre..... 42
- Figure 2.2:** Isomerisation of azobenzene using UV light and heat. 43
- Figure 2.3:** The molecular host prepared by Clever and coworkers showing a. Chemical structure of the ligand; b. SCXRD structure of the M₂L₄ complex..... 43
- Figure 2.4:** Molecular hosts prepared by Rebek showing a. Photoswitchable deep cavitand capable of regulating binding of adamantane; b. Organic capsule capable of squalene binding. 44
- Figure 2.5:** Interpreted ¹H NMR spectrum of CTG (compound 2.3) in CDCl₃. 46
- Figure 2.6:** Enantiomeric interconversion of CTG via the saddle conformation. 46
- Figure 2.7:** Adapted azo coupling using nitroso intermediate 2.4. 51
- Figure 2.8:** 300MHz ¹H NMR spectrum of compound 2.5 in d⁶-DMSO..... 52
- Figure 2.9:** From the SCXRD structure of compound 2.5 showing a. Individual sodium bridged dimer; b. Chemical representation of the sodium bridged dimer; c. Extended hydrogen bonded network. 53
- Figure 2.10:** Changes to the ¹H NMR spectrum of compound 2.6 in D₂O over time. 55

Figure 2.11: From the SCXRD structure of compound 2.6 showing a. Bridging sodium dimer connecting two units of compound 2.6; b. Chemical representation of the sodium bridged dimer c. Part of the extended hydrogen bonding network.....	56
Figure 2.12: Formation of azopyridine 2.7 before acid catalysed cyclisation to triazine 2.8.....	57
Figure 2.13: Interpreted ^1H NMR spectrum of compound 2.12 in CDCl_3	59
Figure 2.14: Interpreted HR ESI-MS of ligand 2.11.....	60
Figure 2.15: From the SCXRD structure of ligand 2.12.....	61
Figure 2.16: Interpreted ^1H NMR spectrum of compound 2.17 in CDCl_3	63
Figure 2.17: Interpreted HRMS of ligand 2.17.....	64
Figure 2.18: From the X-ray structure of compound 2.17 showing a. Asymmetric unit of 2.17; b. Interpenetrating bowl-in-bowl stacks of 2.17.....	65
Figure 2.19: Interpreted ^1H NMR spectrum of compound 2.22 in CDCl_3	68
Figure 2.20: Interpreted HRMS of ligand 2.22.....	68
Figure 2.21: Interpreted ^1H NMR spectrum of ligand 2.24 in d^2 -DCM.....	70
Figure 2.22: Interpreted HRMS of ligand 2.24.....	70
Figure 2.23: Potential DTE appended CTG ligand.....	71
Figure 2.24: Potential solubilised analogue of ligand 2.11 utilising propylated CTG.....	72
Figure 3.1: SCXRD structures of a. Tetrahedral cage prepared by Nitschke with anionic triflate guest; b. Octahedral cage prepared by Fujita with tetrafulvalene guest.....	96
Figure 3.2: a. Palladium M_3L_2 metallocryptophane prepared by Shinkai and coworkers; b. Syn and anti forms of cryptophanes.....	97
Figure 3.3: SCXRD structure of the metallocryptophane prepared by Chambron.....	98
Figure 3.4: CTG-based M_3L_2 assemblies from the Hardie group favoured by geometrically directing metallotectons: a. $[\text{Pd}(\text{NHC})]_3\text{L}_2$ cage prepared by Henkelis; b. $[\text{Ir}(\text{ppy})_2]_3\text{L}_2$ cage prepared by Hardie containing luminescent functionality.....	99
Figure 3.5: Clever's photoswitchable ligand that can be incorporated into $[\text{Pd}_2\text{L}_4]$ coordination cages.....	100
Figure 3.6: Structure of substituted $[\{\text{Ir}(\text{ppy})_2\}_3(\text{L})_2]^{3+} \cdot 3\text{PF}_6^-$ metallocryptophanes 3.11 and 3.12.....	105
Figure 3.7: Interpreted high resolution mass spectrum of complex 3.8.....	106
Figure 3.8: Interpreted high resolution mass spectrum of complex 3.9.....	106
Figure 3.9: Interpreted high resolution mass spectrum of complex 3.10.....	107
Figure 3.10: Interpreted high resolution mass spectrum of complex 3.11.....	107

Figure 3.11: Interpreted high resolution mass spectrum of complex 3.12.....	108
Figure 3.12: Interpreted timecourse ¹ H NMR following the formation of complex 3.8.....	109
Figure 3.13: Interpreted ¹ H NMR spectrum of complex 3.9 in d-MeNO ₂	110
Figure 3.14: Interpreted ¹ H NMR spectrum of complex 3.10 in d-MeNO ₂	111
Figure 3.15: Interpreted ¹ H NMR spectrum of complex 3.11 in d-MeNO ₂	111
Figure 3.16: Interpreted ¹ H NMR spectrum of complex 3.12 in d-MeNO ₂	112
Figure 3.17: ¹ H- ¹ H COSY NMR of metallocryptophane 3.8 in d-MeNO ₂	113
Figure 3.18: The DOSY spectrum of cage 3.8 in d-MeNO ₂ showing the aromatic cage peaks diffusing with a D of 1.86x10 ⁻¹⁰ m ² s ⁻¹	114
Figure 3.19: The DOSY spectrum of cage 3.9 in d-MeNO ₂ showing a single large species in solution.	115
Figure 3.20: The DOSY spectrum of cage 3.10 in d-MeNO ₂ showing a single large species in solution.	116
Figure 3.21: The DOSY spectrum of cage 3.11 in d-MeNO ₂ showing a single large species in solution.	116
Figure 3.22: The DOSY spectrum of cage 3.12 in d-MeNO ₂ showing a single large species in solution.	117
Figure 3.23: SCXRD structure of the enantiopure M ₆ L ₄ ΔΔΔ metallocage prepared by Lusby.....	118
Figure 3.24: Interpreted timecourse ¹ H NMR showing the formation of 3.14 over time in d-MeNO ₂	120
Figure 3.25: Comparison of ¹ H NMR spectra of the self-sorted solution against self-sorted single crystals of complex 3.15.....	121
Figure 3.26: Timecourse ¹ H NMR spectra of complex 3.15 after 24 hours containing.....	122
Figure 3.27: ¹ H NMR spectra of the formation of cage 3.8 after 60 minutes in d-MeNO ₂ in the presence of guests.....	123
Figure 3.28: Stability of complex 3.8 in d-MeNO ₂ solution over time.....	124
Figure 3.29: Variable temperature (VT) NMR spectrum of cage 3.11 in d-MeNO ₂	124
Figure 3.30: Comparison of 4-pyridyl and 3-pyridyl bond vectors.	125
Figure 3.31: Timecourse ¹ H NMR spectra following the formation of metallocryptophane 3.15 in d-MeNO ₂ ;	127
Figure 3.32: Interpreted high resolution mass spectrum of cage 3.15 taken after 120 hours in solution.	128
Figure 3.33: The DOSY spectrum of cage 3.15 in d-MeNO ₂ showing a single large species in solution.	128
Figure 3.34: Energy-minimised (MMFF) molecular structure of all trans cage 3.8.....	130

Figure 3.35: Interpreted ROESY spectrum of complex 3.8.....	131
Figure 3.36: From the model of the all cis cage.....	133
Figure 3.37: ¹ H NMR spectrum evidencing the formation of the rhodium(III) analogue of complex 3.8	134
Figure 3.38: Model of a substituted fullerene derivative encapsulated in the azobenzene metallocryptophane 3.8.	136
Figure 4.1: Light controlled interconversion between tetranuclear and dinuclear squares as prepared by Lees.....	156
Figure 4.2: Representation of uptake and release of guest molecules in Ballester's hydrogen bonded capsules..	158
Figure 4.3: Simplified Jablonski diagram showing the excitation of azobenzene	159
Figure 4.4: Changes in the UV spectrum of ligand 2.12 upon irradiation at 330 nm (λ_1) for 45 minutes in DMSO solvent.	161
Figure 4.5: Changes in the UV spectrum of ligand 2.12 upon irradiation at 450 nm (λ_2) for 15 minutes in DMSO solvent.	162
Figure 4.6: Changes in the UV spectrum of ligand 2.17 upon irradiation at 350 nm (λ_1) for 45 minutes in DMSO solvent.	163
Figure 4.7: Changes in the UV spectrum of ligand 2.17 upon irradiation at 450 nm (λ_2) for 15 minutes in DMSO solvent.	163
Figure 4.8: Changes in the UV spectrum of ligand 2.18 upon irradiation at 330 nm (λ_1) for 45 minutes in DMSO solvent.	164
Figure 4.9: Changes in the UV spectrum of the photostationary state of ligand 2.18 upon irradiation at 450 nm (λ_2) for 15 minutes in DMSO solvent.	164
Figure 4.10: Shielding of aromatic protons in the cis isomer of azobenzene leading to pronounced chemical shift differences between isomers.....	166
Figure 4.11: Timecourse ¹ H NMR spectra of ligand 2.12 in CD ₂ Cl ₂ showing spectrum after irradiating with 355 nm laser	166
Figure 4.12: UV spectrum of the photostationary state compared to the initial trans isomer of ligand 2.12;.	167
Figure 4.13: Electronic classification and characteristics of azo derivatives.....	168
Figure 4.14: Stability of cis-rich photostationary state of ligand 2.12 in CD ₂ Cl ₂	168
Fig 4.15: Thermal relaxation of ligand 2.18 in CD ₂ Cl ₂	169
Figure 4.16: UV spectra of [Ir(ppy) ₂ (MeCN) ₂] ⁺ .PF ₆ ⁻ in CH ₂ Cl ₂ solvent showing the lack of spectral changes after irradiating at 355 nm.....	170
Figure 4.17: Interpreted UV spectrum of complex 3.8 in DCM solvent	171
Figure 4.18: changes to the UV spectrum of cage 3.8 upon irradiating at 355 nm.	172
Figure 4.19: changes to the UV spectrum of cage 3.11 upon irradiating at 355 nm	173

Figure 4.20: changes to the UV spectrum of cage 3.12 upon irradiating at 355 nm.	173
Figure 4.21: Regeneration of starting cage 3.8 configuration using irradiation with blue light	174
Figure 4.22: Regeneration of starting cage 3.11 configuration using irradiation with blue light	175
Figure 4.23: Regeneration of starting cage 3.12 configuration using irradiation with blue light.	175
Figure 4.24: changes to the UV spectrum of cage 3.9 upon irradiating at 355 nm.	176
Figure 4.25: changes to the UV spectrum of cage 3.10 upon irradiating at 355 nm.	177
Figure 4.26: Regeneration of starting cage 3.9 configuration using irradiation with blue light	178
Figure 4.27: Regeneration of starting cage 3.10 configuration using irradiation with blue light	178
Figure 4.28: Timecourse UV experiment showing photoisomerisation to the cis form of ligand 2.22 upon irradiation at 320 nm.	179
Figure 4.29: Cyclotrisazobenzene prepared by Wegner and coworkers incapable of photoisomerisation.	180
Figure 4.30: The M_4L_2 macrocycle prepared by Yam and coworkers that can modulate the efficiency of its photoisomerisation using Ag^+ ions	181
Figure 4.31: Trans \rightarrow cis conversion of cage 3.8 over time.	181
Figure 4.32: Schematic representation of the energy levels involved in the photoisomerisation of a. isolated azobenzene; b. A model azobenzene-iridium (III) complex, showing the competing pathway provided by excitation of the Ir (III) centre.....	183
Figure 4.33: Cycles of trans-cis irradiation of compound 3.9 showing the changes to the absorbance at 320 nm.....	185
Figure 4.34: Photoisomerisation of metallocage 3.12 in d_2 -DCM; a. Initial spectrum of cage 3.12; b. After irradiation for 200 seconds at 355 nm.....	186
Figure 4.35: ESI-Mass spectrum of cage 3.12 taken after 200 seconds of irradiation with 355nm in CH_2Cl_2	186
Figure 4.36: Dendrimeric species prepared by McGrath containing six azobenzene units.	188
Figure 4.37: Macrocycle prepared by Norikane containing multiple azo units showing a. Chemical structure; b. SCXRD structure.	189
Figure 4.38: Emission profile of ester complex 3.8 in DCM solvent and doped film.	191
Figure 4.39: Emission profile of ether complex 3.9 in DCM solvent and doped film.	191

Figure 4.40: Emission profile of ether complex 3.10 in DCM solvent and doped film.	192
Figure 4.41: Emission profile of ester complex 3.11 in DCM solvent and doped film.	192
Figure 4.42: Dark-room images of cages 3.8, 3.9, 3.10 and 3.11 showing the blue emission after irradiation with 360 nm light.	193
Figure 4.43: Solution phase emission of cage 3.9 in CD ₃ NO ₂ upon excitation with a 405 nm laser pen.	194
Figure 4.44: Metal coordinated dithienylethene photoswitches prepared by Lehn	197
Figure 5.1: SCXRD structure of the 3D network prepared by Robson and coworkers	207
Figure 5.2: SCXRD structures of MOF-5 as prepared by Yaghi and coworkers.	208
Figure 5.3: SCXRD structures of some coordination polymers prepared by Hardie and coworkers.	209
Figure 5.4: From the SCXRD structure of the coordination polymer prepared by Holman and coworkers ²⁰	210
Figure 5.5: SCXRD structures of the metal-organic frameworks prepared by Schroder and coworkers	210
Figure 5.6: SCXRD structure of Zhao's zinc(II) metal-organic framework containing both azo and stilbene units	211
Figure 5.7: Structure of ligand 2.12 employed in this chapter.	212
Figure 5.8: The asymmetric unit of complex 5.1	213
Figure 5.9: The star shaped M ₆ L ₆ macrocyclic moiety in the crystal structure of complex 5.1	215
Figure 5.10: From the SCXRD structure of complex 5.1 showing a coordination environment around Cu(I).	216
Figure 5.11: From the crystal structure of complex 5.1 showing interpenetration modes of the crystal lattice	217
Figure 5.12: Spacefilling view of the pores in complex 5.1 showing one of each of the star-shaped pores and one of the M ₄ L ₄ macrocycles.	218
Figure 5.13: The asymmetric unit of complex 5.2	219
Figure 5.14: The columnar bowl-in-bowl stacks of ligand 2.12 in the crystal structure of complex 5.2.	219
Figure 5.15: From the crystal structure of complex 5.2 as viewed down different crystallographic axes.	221
Figure 5.16: The asymmetric unit of complex 5.3 showing the disorder of the azobenzene arm and the silver ion	223
Figure 5.17: From the SCXRD structure of complex 5.3 showing structural motifs present in complex 5.3.	224

Figure 5.18: The asymmetric unit of complex 5.4	226
Figure 5.19: Motifs from the symmetry expansion of complex 5.4.....	228
Figure 5.20: Topological depiction of the connectivity in complex 5.4	229
Figure 5.21: The asymmetric unit of complex 5.5.	231
Figure 5.22: From the SCXRD structure of complex 5.5	232
Figure 5.23: Symmetry expanded view of complex 5.5 as viewed down the crystallographic a-axis	233
Figure 5.24: SCXRD structure showing the encapsulation of iodine guest that has been achieved in a SCTSC fashion by Hardie's M_3L_2 metallocryptophanes.	234
Figure 5.25: From the SCXRD structure of the CTV inclusion complex prepared by Payne.....	234
Figure 5.26: Optical microscope images of crystals of complexes 5.4 and 5.5	235
Figure 5.27 : SEM images of complex 5.4 (a-c)and complex 5.5 (d-f)	236
Figure 5.28: The asymmetric unit of complex 5.6.	238
Figure 5.29: From the SCXRD structure of complex 5.6 illustrating views down different crystallographic axes.	239
Figure 5.30: TGA spectrum of complex 5.1.	242
Figure 5.31: TGA spectrum of complex 5.3.	243

List of Schemes

Scheme 2.1: Three-step literature procedure of CTG (compound 2.3).	45
Scheme 2.2: Proposed theoretical route to AZB appended CTG ligands bearing pyridyl coordinating moieties.	48
Scheme 2.3: Diazo coupling reaction.	48
Scheme 2.4: Attempted coupling reactions using NaOCl.	49
Scheme 2.5: Attempted Mills reaction to form desired asymmetrical azopyridine.	50
Scheme 2.6: Mechanism of base catalysed azobenzene synthesis as reported by Zhao and coworkers.	50
Scheme 2.7: Formation of AZB appended ligands 2.11 and 2.12.	58
Scheme 2.8: Formation of AZB appended ligands 2.17 and 2.18.	62
Scheme 2.9: Photoisomerisation of stilbene.	66
Scheme 2.10: Synthetic route to stilbene appended ligand 2.22.	67
Scheme 2.11: Synthesis of ether linked stilbene 2.24.	69
Scheme 3.1: Synthesis of cis-protected metallotecton 3.2.	101
Scheme 3.2: Synthesis of substituted metallotectons 3.6 and 3.7.	102
Scheme 3.3: Preparation of [$\{\text{Ir}(\text{ppy})_2\}_3(\text{L})_2\]^{3+} \cdot 3\text{PF}_6^-$ metallocryptophanes 3.8, 3.9 and 3.10.	103
Scheme 3.4: Self-assembly of the metallocryptophane 3.14.	119
Scheme 3.5: Self-assembly of metallocryptophane 3.15 bearing stilbene units. ...	126
Scheme 4.1: Proposed synthetic route to ligands incorporating a spacer unit between the AZB unit and the Ir(III) centre.	196

List of Tables

Table 2.1: Selected bond lengths (Å) and angles (°) from the crystal structure of [Na ₂ (2.5) ₂ (H ₂ O) ₈] _n	54
Table 2.2: Selected bond lengths (Å) and angles (°) from the crystal structure of [Na ₂ (2.5) ₂ (H ₂ O) ₈] _n	57
Table 2.3: Details of crystal collection and analyses for X-ray datasets of compounds 2.5, 2.6, 2.8, 2.12 and 2.17.	92
Table 3.1: Assignments of through space coupling interactions observed in the ROESY NMR spectrum of cage 3.8.	132
Table 4.1: Conversion efficiency between isomers of free ligands.....	165
Table 4.2: Conversion efficiency between isomers of metallocages	184
Table 4.3: Photophysical properties of metallocryptophanes.	190
Table 5.1: Selected bond lengths (Å) and angles (°) from the crystal structure of complex 5.1.	214
Table 5.2: Selected bond lengths (Å) and angles (°) from the crystal structure of complex 5.2.	220
Table 5.3: Selected bond lengths (Å) and angles (°) from the crystal structure of complex 5.3.	223
Table 5.4: Selected bond lengths (Å) and angles (°) from the crystal structure of complex 5.4.	227
Table 5.5: Selected bond lengths (Å) and angles (°) from the crystal structure of complex 5.4.	231
Table 5.6: Details of crystal collection and analyses for X-ray datasets of compounds 5.1, 5.2, 5.3, 5.4 and 5.5.	247

List of Abbreviations

Å – Angstrom

Ar – Aryl

Asu – Asymmetric Unit

AZB - Azobenzene

COSY – Correlation Spectroscopy

CTC - Cyclotricatechylene

CTG - Cyclotriguaiacylene

CTV – Cyclotrimeratrylene

δ – lower case delta, chemical shift (NMR)

Δ – Upper case delta, helical chirality

DCM – Dichloromethane

DFT – Density Functional Theory

DMAC - Dimethylacetamide

DMAP – Dimethylaminopyridine

DMF – N-N' Dimethylformamide

DMSO – Dimethyl Sulfoxide

DOSY – Diffusion Ordered Spectroscopy

dppe – bis(diphenylphosphino)ethane

dppp - bis(diphenylphosphino)propane

DTE – Dithienylethene

EDTA – Ethylenediaminetetraacetic acid

EDX – Energy Dispersive X-ray

en – 1,2-ethylenediamine

et al – *et alia* (and others)

HPLC – High Performance Liquid Chromatography

HR ESI-MS – High Resolution Electrospray Ionisation Mass Spectrometry

Hz – Hertz

IR – Infrared Spectroscopy

J – Coupling Constant (NMR)

K – Kelvin

Λ – Upper case lambda, helical chirality

λ – Lower case lambda, wavelength

λ_{em} – emission wavelength

λ_{ex} – excitation wavelength

λ_{max} – wavelength with maximum of emission band

L – Ligand

LLCT – Ligand to Ligand Charge Transfer

LMCT – Ligand to Metal Charge Transfer

MeNO₂ - Nitromethane

MHz – Megahertz

MLCT – Metal to Ligand Charge Transfer

MMFF – Molecular Mechanics Force Field

MOF – Metal Organic Framework

MOP – Metal Organic Polyhedron

Nd:YAG – Neodymium: Yttrium Aluminium Garnet (laser class)

NHC – N-Heterocyclic carbene

nm – nanometres

NMP – N-Methyl Pyrollidone

NMR – Nuclear Magnetic Resonance

NOESY – Nuclear Overhauser Effect Spectroscopy

Φ – Quantum yield

PMMA – Polymethylmethacrylate

ppm – parts per million

ppy – 2-phenylpyridine

ROESY – Rotating Frame Overhauser Effect Spectroscopy

SBN – Stilbene

SCTSC – Single Crystal to Single Crystal (transformation)

SCXRD – Single Crystal X-ray Diffraction

SEM – Scanning Electron Microscope

τ – Emission Lifetime (luminescence)

tcb – 1,3,5 tricyanobenzene

TGA – Thermogravimetric Analysis

THF - Tetrahydrofuran

UV - Ultraviolet/Visible Spectroscopy

VT NMR – Variable Temperature Nuclear Magnetic Resonance

W - Watt

Chapter 1

Introduction

1.1 Overview

The body of work discussed in this thesis draws its origins from the field of supramolecular chemistry with elements of photophysics and general inorganic and organic chemistry. The principle objective of this work is the synthesis and design of metallocsupramolecular architectures that are able to respond to an external stimulus, in this case light. The purpose of this chapter is to provide an overview of the research area of supramolecular chemistry in general before an introductory discussion of the more specific elements that will form an underlying focus in later chapters. A brief, more focussed introduction is also given at the commencement of each chapter.

1.2 Introduction to supramolecular chemistry

Supramolecular chemistry is the study of chemical systems that are based on interactions other than covalent bonds. The existence of forces between molecules was recognised as early as 1880 by van der Waals.¹ The study of the field was pioneered by Jean-Marie Lehn who defined it as ‘chemistry beyond the molecule, the science of non-covalent interactions’.² These interactions – sub-classified as hydrogen bonding, van der Waals interactions and the hydrophobic effect (figure 1.1) – are found abundantly in both natural and synthetic systems. Whilst these interactions are relatively weak compared to the organic covalent bond, (approximate energies range from 1-2kJ/mol for van der Waals forces and are highly variable for hydrogen bonds, between 15-60kJ/mol)³ they are highly cooperative, with numerous interactions coming together to form the thermodynamic product.

The starkest example of such interactions is the double helix of DNA which are formed from hydrogen bonding between two sets of complementary base pairs, adenine/thymine and guanine/cytosine (figure 1.1). The resulting helix is exceptionally stable due to the millions of base pairs that can make up a single structure⁴ leading to countless hydrogen bonds, along with other stabilising contributions such as π - π stacking between nucleobases. As such, DNA requires either specific nuclease enzymes or strong heating (approximately 95°C in the polymerase chain reaction⁵) in order to break the hydrogen bonds and denature.

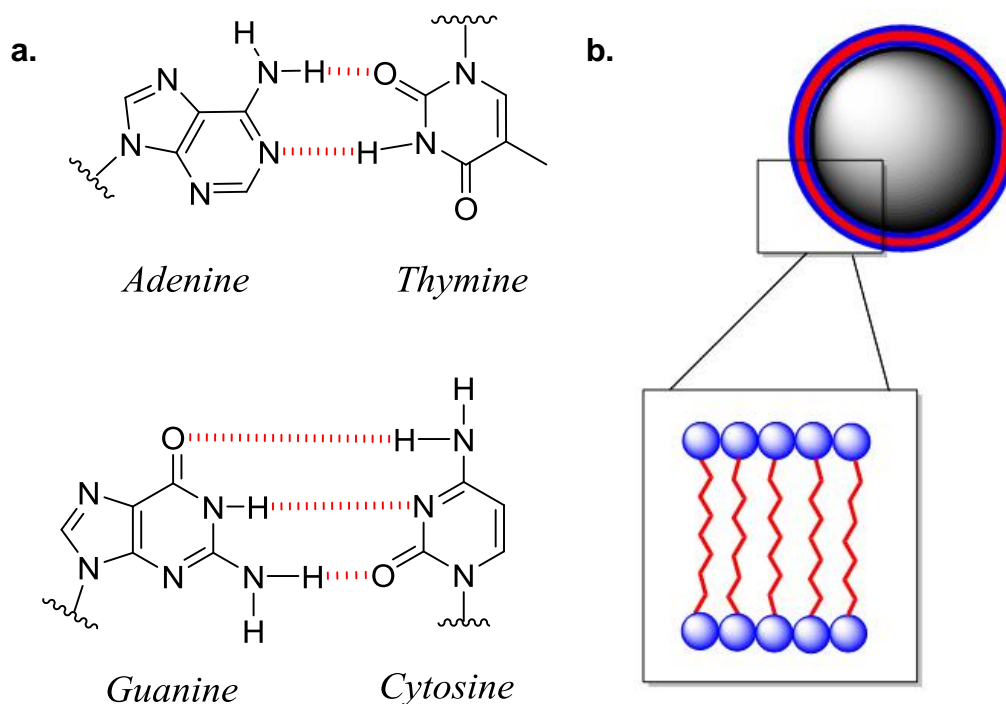


Figure 1.1: Some examples of supramolecular interactions in nature: **a.** Hydrogen bonding in DNA base-pairs; **b.** Cartoon representation of hydrophobic interactions in a cell membrane with the hydrophobic tails (red) shielded from interactions with water by the hydrophilic phosphate head groups (blue).

The stability of DNA and its structural elucidation in 1953 by Watson and Crick⁶ sparked interest in synthetic supramolecular systems. The pioneering early work of Pedersen in 1967 led to the development of the first crown ethers which are able to bind metal cations *via* electrostatic interactions (figure 1.2).⁷ Building on this work, Donald Cram recognised that many of the important enzymatic processes in the human body were based on a concept he termed ‘host-guest’ recognition in which a host (the enzyme) binds a molecular guest (the enzyme substrate) selectively and with high affinity *via* non-covalent interactions. He undertook the first efforts to replicate this phenomena synthetically in the design of novel macrocycles⁸ for applications in both enzyme modelling⁹ and chemical separation.¹⁰

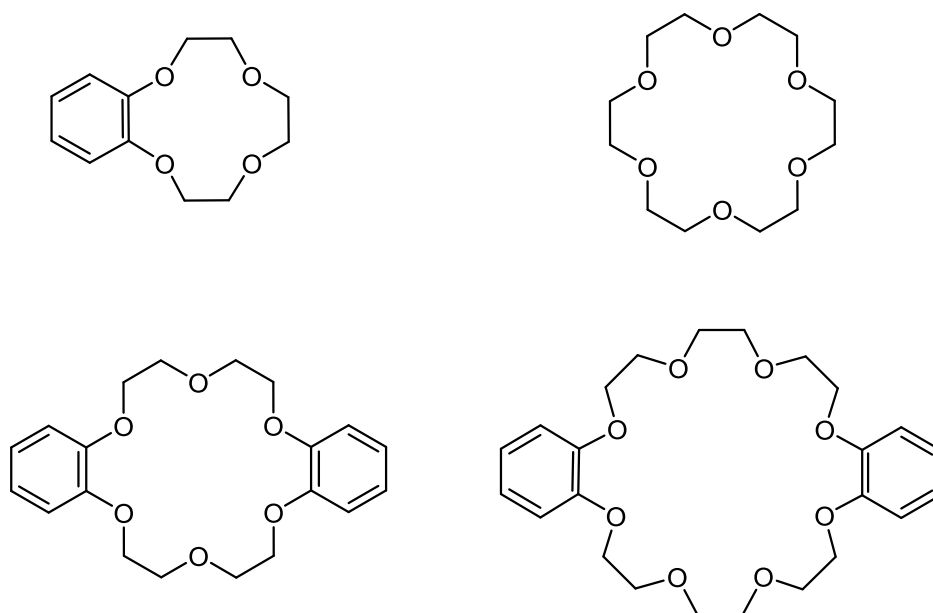


Figure 1.2: Some examples of crown ethers prepared by Pedersen.⁷ The electron-rich cavities are ideal for the sequestration of cationic metal ions such as sodium and potassium.

Lehn developed a series of ‘cryptates’ based on this principle – where the cryptand host binds its guest molecule selectively (figure 1.3). The systems became increasingly sophisticated; Lehn developed cryptands capable of encapsulating multiple molecular guests.¹¹⁻¹⁴ A range of applications began to become feasible such as the selective encapsulation of toxic heavy metals¹³ and the range of molecular guests expanded to include anions.¹⁵⁻¹⁷ More supramolecular architectures and applications continued to emerge and in 1987 the Nobel prize in Chemistry was awarded to Lehn, Cram and Pedersen for their development of the field, sparking widespread interest in the field and contributing to its emergence as an active focus of research.^{18, 19}

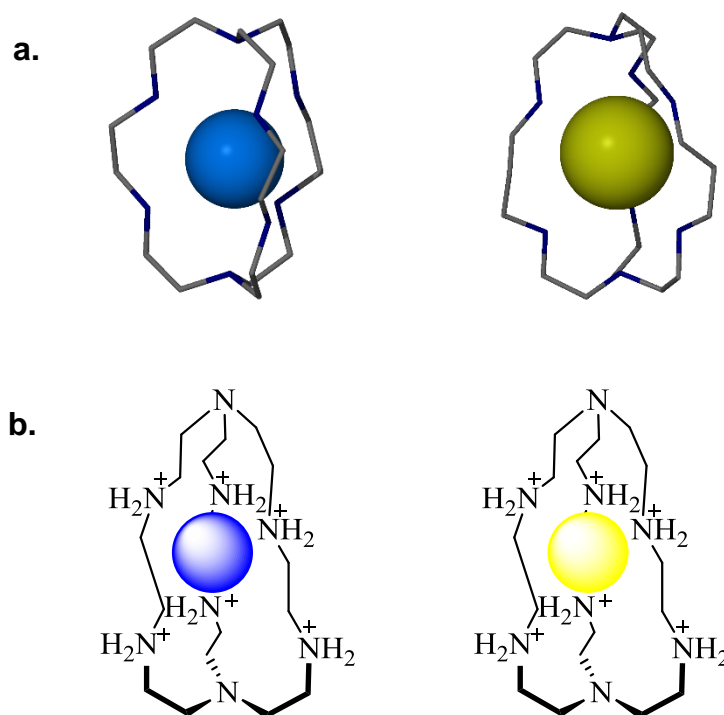


Figure 1.3: **a.** Single crystal X-ray diffraction (SCXRD) structures of cryptates prepared by Lehn.¹⁷ The encapsulation of F^- (blue sphere) and Cl^- (yellow sphere) is illustrated. Anionic guests are shown in spacefilling mode and hydrogen atoms have been omitted for clarity; **b.** Chemical representation of cryptates.

The systems discussed in this work are products of self-assembly. Self-assembly processes exploit the labile, often non-covalent interactions of supramolecular chemistry to form the individual, most thermodynamically stable product.²⁰ The most elegant aspect of this is that this product is by no means necessarily formed first. Often a series of kinetic products form but through synergy and cooperative effects, the system rearranges to the most thermodynamic product over time.^{2, 21} Careful design of the components can lead to a promotion of a particular assembly product, which remains a fundamental strategy of modern supramolecular chemistry. Much of the inspiration for the area is taken from nature which employs elegant tenets of supramolecular chemistry in the assembly of exceedingly complex biomolecules.^{2, 19, 21}

1.3 Metallo-supramolecular chemistry

Metallo-supramolecular chemistry is an important sub-genre of supramolecular chemistry and forms the focus of research presented in this thesis. This area deals exclusively with supramolecular assemblies containing metal units. The energy of a

metal-ligand bond coordination bond is energetically worth between 15-50 kJ/mol.²² This lies as an intermediate between weak intramolecular interactions (1-10 kJ/mol) and organic covalent bonds (60-120 kJ/mol).²² The self-assembly process is typically kinetically reversible with many association/dissociation steps with the final products(s) representing a thermodynamic minimum for the system. The key advantage of this approach is that tuning of reaction parameters can shift the reaction equilibria to favour a particular product, enabling a high level of control.²²

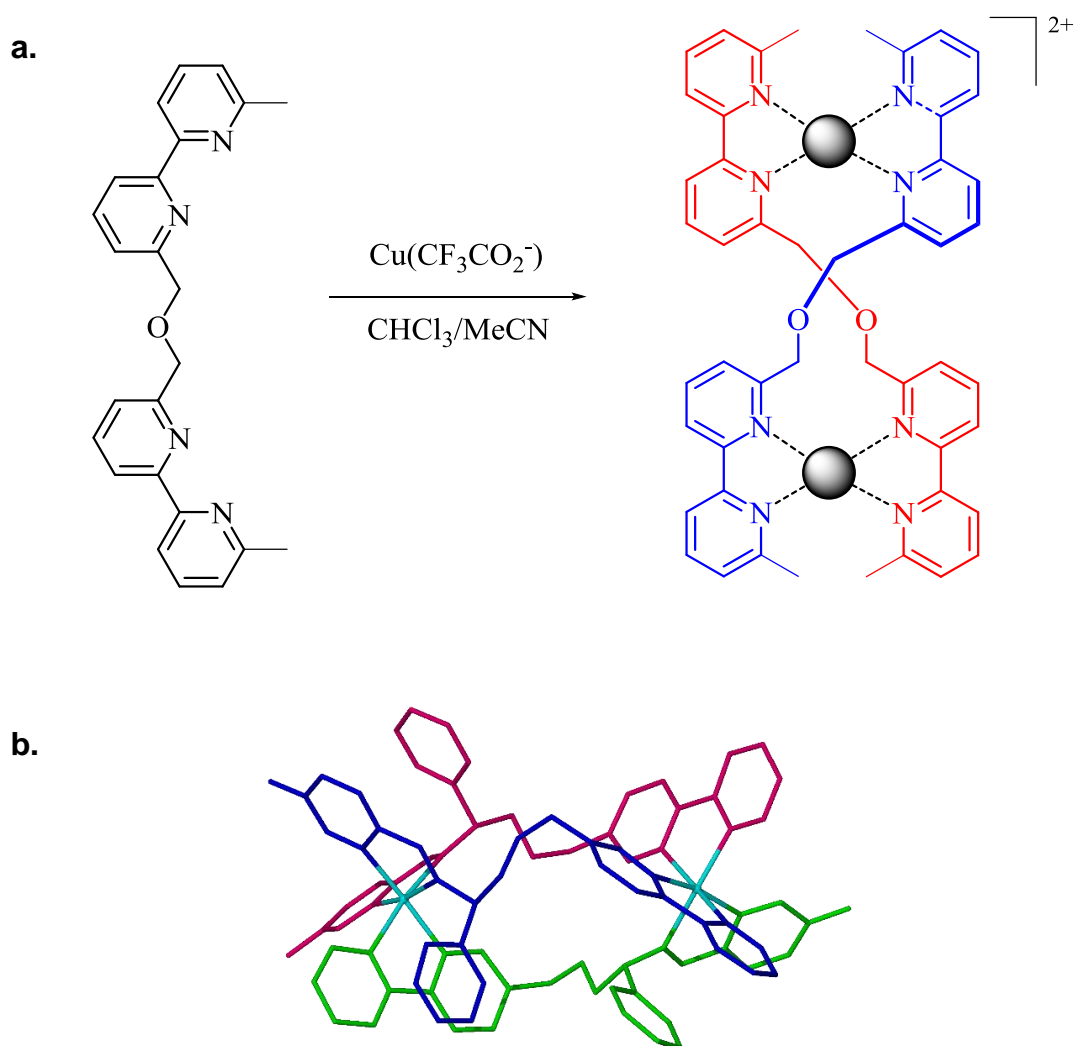


Figure 1.4: a. Chemical representation of Lehn's helicate assembled from polypyridyl ligands and copper(I) salts²³ with metal centres represented as hard spheres; b. SCXRD structure of the asymmetric metallohelix prepared by Scott and coworkers which has anticancer properties.²⁴ Hydrogen atoms and counterions have been removed and each ligand has been colour coded for clarity.

Jean-Marie Lehn was once again highly influential in the development of this area. In 1987 he reported the first metallo-supramolecular architecture, a double stranded 'helicite' molecule formed from the self-assembly of copper(I) trifluoroacetate with oligopyridine ligands (figure 1.4a).²³ The helical structure sparked comparisons with the structure of double stranded DNA; they remain of interest due to potential interactions with DNA.²⁵ Lehn went on to prepare higher order helicites including tetra and hexanuclear circular helicites.²⁶ Several recent examples of helicites from Scott^{24, 27} (figure 1.4b) and Hannon²⁸ have shown promising DNA binding, antimicrobial and anticancer properties.

An important dogma of this area is that the rational design of metal and ligand sets can be tuned to favour a particular desired product or function. The huge attraction of this strategy lies in the formation of extremely complex systems that are difficult or impossible to achieve with traditional organic synthesis. A recent striking example of this is Leigh's trefoil knot which is the smallest knot produced synthetically.²⁹ The preparation of this knot employed (after extensive organic synthesis) metal-templated threading of two organic macrocycles. The knot can then be completed by metal-catalysed coupling of the two organic components and removal of the metal templates using the chelating agent ethylenediamine tetraacetic acid (EDTA). The Leigh group, have gone on to prepare a range of molecular knots of different sizes³⁰⁻³⁵ using similar methodology, such as the tetrafoil knot illustrated in figure 1.5.

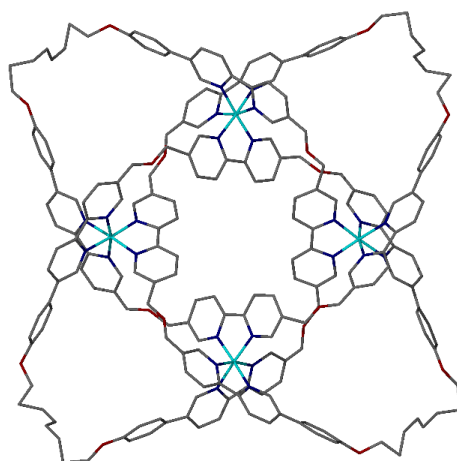


Figure 1.5: SCXRD structure of a tetrafoil metal-templated molecular knot prepared by Leigh and coworkers.³⁰ This example still contains the templating iron(II) ions which are ultimately removed in the final product. Hydrogen atoms and counterions have been omitted for clarity.

A diverse array of other topologically complex architectures have been prepared by exploiting simple principles of self-assembly and templating effects.³⁶ These range

from the simpler catenanes, as first prepared by Sauvage in 1985, consisting of two mechanically interlocked rings, figure 1.6a;³⁷ to infinitely more complicated Borromean rings³⁸⁻⁴³ consisting of three interlocking rings where the removal of any one of the rings results in all three being unlinked, figure 1.6c; with some of the more striking examples shown in figure 1.6. The synthesis of these materials often relies heavily on templating or directing a desired structure *via* addition of a templating agent or the use of geometrically directing metal and ligand combinations. Supramolecular chemists have grown skilled at utilising a diverse toolbox of chemical building blocks to effectively assemble complex architectures.

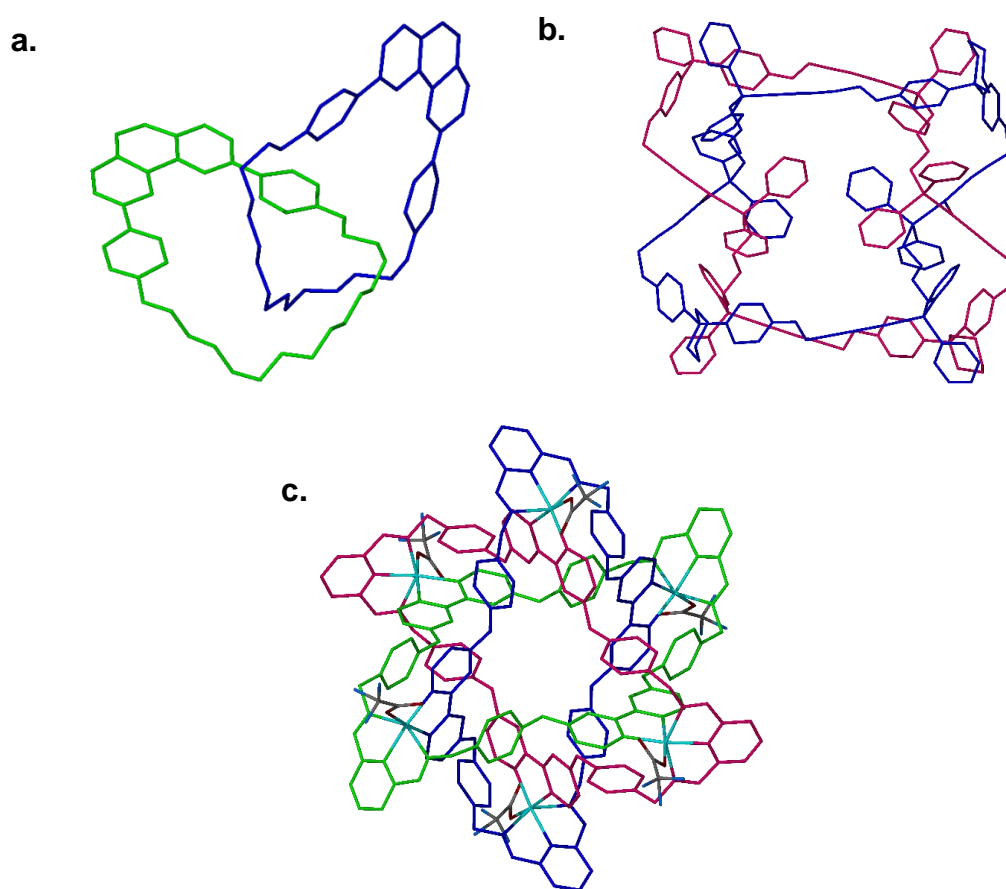


Figure 1.6: SCXRD structures of topologically complex assemblies accessed via supramolecular chemistry showing a. Sauvage's [2] catenane³⁷ with each different rings shown in green and blue for clarity; b. Puddephatt's Solomon link^{44, 45} with four crossing points of the two rings with each ring shown in pink and blue for clarity; c. Stoddart's Borromean rings³⁸ with each of the interlocked rings shown in a different colour for clarity. All hydrogen atoms have been omitted for clarity in each case.

The potential applications of these topologically complex systems have begun to emerge^{31, 46-49} with the 2016 Nobel prize in chemistry being awarded to Fraser Stoddart, Jean-Pierre Sauvage and Ben Feringa for their contributions to the development of molecular machines. For a system to be of use in host-guest chemistry and molecular recognition as outlined by Cram, requires the presence of a defined internal chemical space for the binding of guest molecules.⁵⁰ The discussion will now focus on an area of metallosupramolecular chemistry where the applications are widespread and well-established: the coordination cage.

1.4 Coordination Cages – Properties and applications

Coordination cages have been a subject of great interest in supramolecular chemistry for a number of years owing to their structural variability, tunability and host-guest chemistry. These systems are formed from the self-assembly of metal and ligand components and are thus under thermodynamic control.²² This allows for correction mechanisms in the event of the formation of kinetic products, to ensure that upon completion of the reaction, a single thermodynamic product is isolated. This often requires a labile metal-ligand bond as inert systems can become trapped in kinetic wells resulting in metastable intermediate products.⁵¹ This lability can offer advantages over purely organic cage compounds which often give poor yields due to significant levels of formation of irreversible side-products⁵² (although several examples of purely organic cages using labile organic bonds have been demonstrated⁵³⁻⁵⁸ with many examples utilising imine chemistry). Coordination cages can also be employed in templating strategies in the construction of organic systems to circumvent this issue.⁵⁹

A significant body of work has been undertaken on the preparation and applications of tetrahedral coordination cages. Although the first example was prepared in 1988 by Saalfrank,⁶⁰ Raymond was the first to develop this area fully in the self-assembly of catecholamide ligands with iron(III) and gallium (III) salts.⁶¹ These systems were found to be sensitive to cations⁶² with some systems initially forming a mixture of triple-stranded M_2L_3 helicates and the desired M_4L_6 tetrahedra. Upon addition of tetramethylammonium salts (NMe_4) the position of the equilibria was altered to favour the tetrahedral assembly, presumably *via* a templating effect.⁶³ Raymond's group has gone on to develop applications for some of these systems including catalytic^{64, 65} and host-guest⁶⁶ applications.

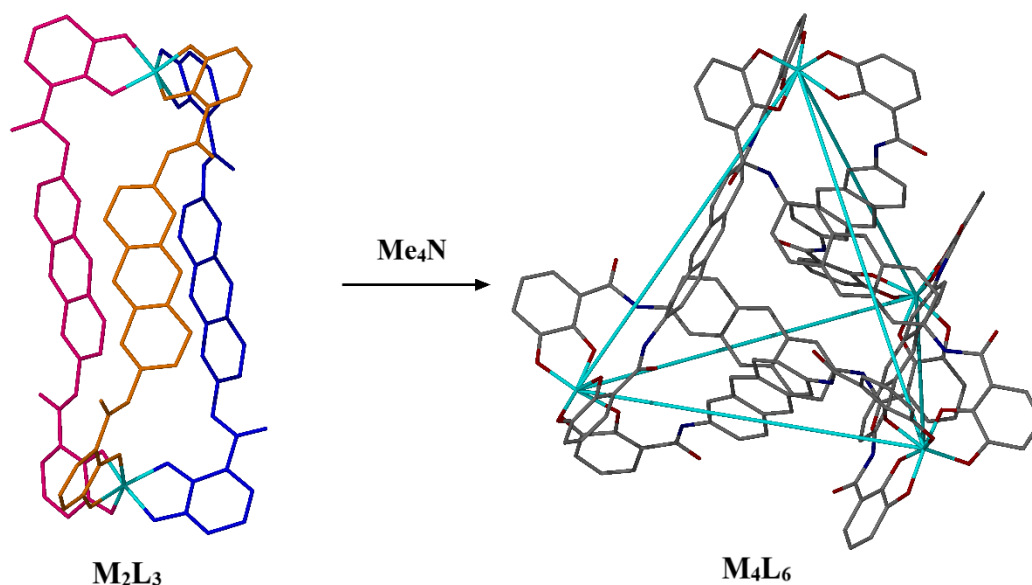


Figure 1.7: SCXRD structures illustrating the structural transformation of Raymond's M_2L_3 helicate upon addition of NMe_4 to the tetrahedral M_4L_6 assembly.⁶³ Hydrogen atoms have been omitted for clarity.

The synthesis and properties of tetrahedral coordination cages has been developed in extensive depth by the Nitschke group.⁶⁷⁻⁷² A series of water soluble tetrahedra based on imine ligands have been prepared with relatively simple synthetic methods. The size of the cage cavities can be controlled by the alternation of the ligand design and a whole library of cages can be prepared with differing host-guest properties.⁷³⁻⁷⁵ Larger cubic assemblies are also possible^{76,77} capable of encapsulating peptides⁷⁸ and undergoing spin crossover.⁷⁹ These systems have displayed sophisticated host-guest chemistry, binding a variety of small polar guests in a controllable manner for a variety of potential applications; perhaps the most significant of these examples is the stabilisation of white phosphorus (P_4), an explosive allotrope of elemental phosphorus (figure 1.8a).⁶⁸ The explosive properties originate from the oxidation of white phosphorus to form the stable oxide in a violently exothermic reaction. When sequestered within the cage however, oxidation is prevented which computational studies show is due to oxidation requiring a transition state that cannot fit inside the tetrahedral cavity. Yang has since replicated this feat along with the storage of yellow arsenic (As_4) within an anion bonded tetrahedral cage.⁸⁰

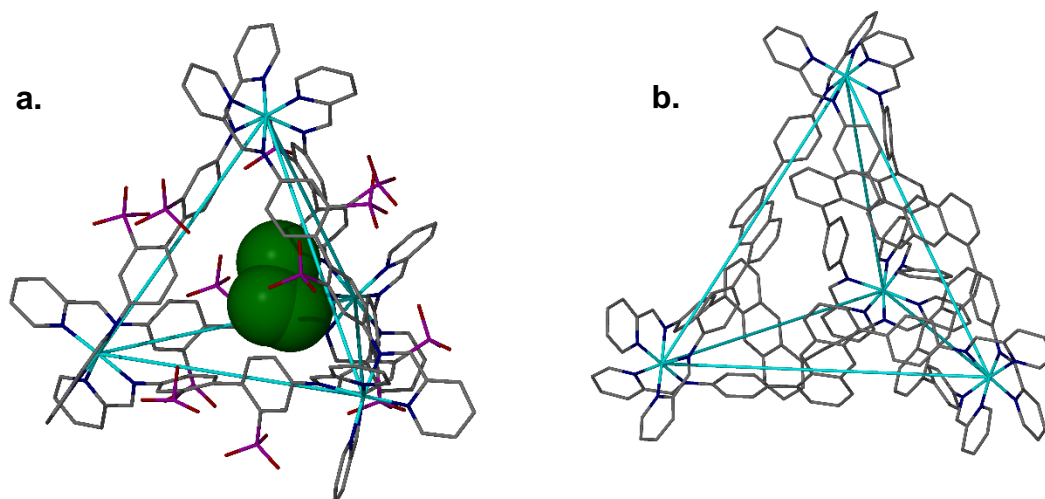
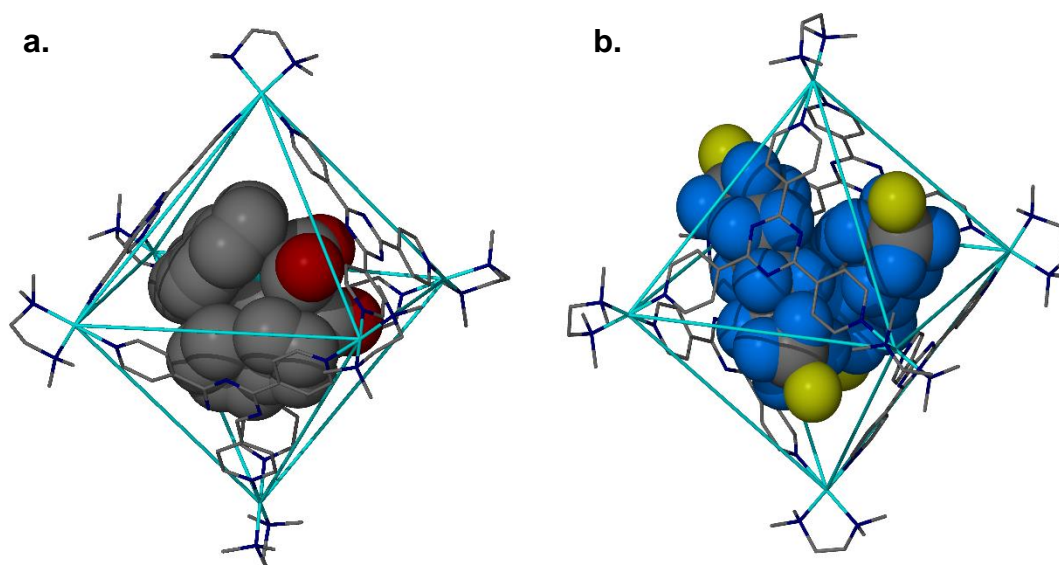


Figure 1.8: SCXRD structures of some tetrahedral cages prepared by Nitschke and coworkers showing: **a.** Encapsulation and stabilisation of white phosphorus within a $[Fe_4L_6]$ coordination cage⁶⁸; **b.** $[Fe_4L_6]$ cage with anthracene ligands capable of sequestering fullerene (C_{60}) as a guest.⁷⁵ Phosphorus guest is shown in spacefilling mode and all hydrogen atoms and counterions have been omitted for clarity.

The Fujita group has also contributed heavily to the field of coordination cages. Much of their focus has been on the preparation of octahedral coordination cages with the first example prepared in 1995. This cage was formed by the assembly of a rigid tridentate ligand, (1,3,5-tris(4 pyridyl)triazene with a *cis*-protected square planar palladium species, $[Pd(en)(NO_3)_2]$ where ‘en’ is 1,2-ethylenediamine to give a $[Pd_6L_4]$ metallocage.⁸¹ The ingenuity of this strategy lies in that the bidentate en ligand serves as the equivalent of an organic protecting group, preventing any coordination of the triazene ligand to these sites; the triazene is forced to replace the more labile nitrate ligands and is directed towards formation of the $[Pd_6L_4]$ architecture. This *cis*-protection strategy has become common in targeted synthesis of metallo-supramolecular architectures, particularly for square planar metals such as palladium, and is revisited in more detail in chapter 3 of this thesis.

Fujita has shown that this prototypical coordination cage, despite its simple design strategy, partakes in sophisticated interactions with guest molecules. Various guests have been shown to bind in the inner cavity.⁸²⁻⁸⁵ Similar to the stabilisation of phosphorus by Nitschke’s coordination cages, these octahedral assemblies can affect reactivity and stabilisation. Highly unstable ruthenium dimers which normally photolyse rapidly in solution have been stabilised within the confinements of the cage cavity (figure 1.9a)⁸⁶ which also have found numerous catalytic applications.^{87, 88} This phenomena of the stabilisation of reactive species indicates the potential of

coordination cages for a number of applications; other examples include the stabilisation of species such as imines (in water),⁸⁹ tropylium ions,⁹⁰ phosphonium ions⁹¹ as well as cycloheptatetraene,⁹² methyl iodide⁹³ and silver carbide.⁹⁴ A comprehensive review on the stabilising properties of coordination cages and capsules has also been published by Ballester.⁹⁵



*Figure 1.9: SCXRD structures of some of the octahedral cages prepared by Fujita, showing **a.** Stabilisation of photoactive ruthenium dimer within Fujita's $[Pd_6L_4]$ octahedra;⁸⁶ **b.** Binding of the ruthenium dimer guest is shown in spacefilling mode and all hydrogen atoms and counterions have been removed for clarity.*

In addition to the smaller assemblies, self-assembly principles have been utilised to prepare a range of far larger cage structures. Fujita has demonstrated the self-assembly of giant $[Pd_{12}L_{24}]$ coordination nanospheres from rigid polypyridal ligands with palladium (II) ions of approximately that are approximately 4.6nm in diameter (figure 1.10).⁹⁶ These systems have also shown a remarkable array of properties. The cages can be endrohedrally functionalised with coronene,⁹⁷ (enabling the solubilisation of fullerene (C_{60})) azobenzene⁹⁸ (enabling photoregulation of guest binding), saccharides⁹⁹ (enabling the formation of protein aggregates), polyethylene glycol¹⁰⁰ and perhaps most impressively of all, biotin¹⁰¹ (enabling the recognition and encapsulation of the small protein ubiquitin). Fujita went on to prepare even higher order $[Pd_{24}L_{48}]$ metallocages using a bis-pyridyl functionalised thiophene ligand, thus beginning to approach the scale of biological self-assembly.¹⁰² The varied chemistry, properties and modifications of these coordination cages was reviewed in 2013 by Fujita.¹⁰³

Whilst the area has been heavily influenced by Nitschke and Fujita who have prepared the most well characterised tetrahedral and octahedral assemblies respectively, other examples exist of large assemblies with a variety of metals such as de Mendoza's $[U_{20}L_{12}]^{20-}$ dodecahedra (L=carboxylate functionalised calix[5]arene),¹⁰⁴ Du's $[Co(L^1)_6(L^2)_8]^{6-}$ octahedra (L¹ = p-tertbutylsulfonylcalix[4]arene; L² = 4,4',4''-(benzene-1,3,5, triyltris-(ethyne 2,1 diyl) tribenzoate)¹⁰⁵ and Wang's $[Zn_{12}L_8]$ metallocubes (L = adamantane derived terpyridal ligand).¹⁰⁶

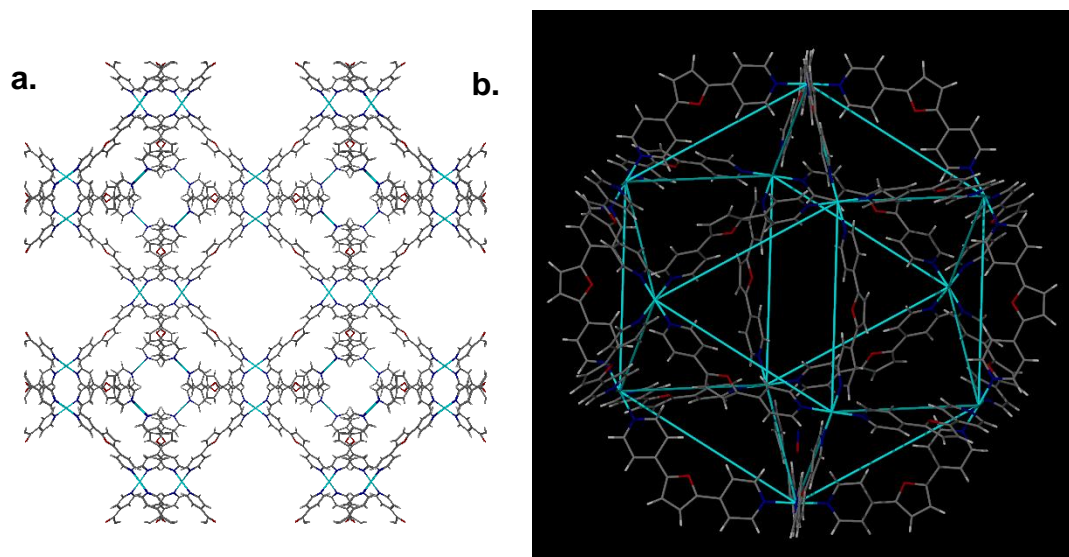


Figure 1.10: SCXRD structure of Fujita's $Pd_{12}L_{24}$ assemblies showing: a. View down the crystallographic a-axis;⁹⁶ b. Cubooctahedral geometry. These systems can be appended with a variety of functional groups via the ligand design for a number of applications.

Molecular recognition also remains but one potential application of coordination cages. As has been demonstrated extensively by a variety of research groups, by far the most popular choice of metal-ligand combination for the self-assembly of coordination cages are pyridyl appended ligands with Pd(II) ions¹⁰⁷ due to easy control of geometry *via* the square planar metal centres and rigid pyridyl ligands. A number of recent reports however have focussed on the incorporation of luminescent Ir(III) moieties to confer desirable photophysical properties into coordination cages, a somewhat unusual metal source for self-assembly as low spin d^6 metals of this ilk are typically inert complexes.

Lusby and coworkers demonstrated the formation of luminescent enantiopure M_6L_4 coordination cages based on the self-assembly of a rigid 1,3,5 tricyanobenzene ligand with $[Ir(ppy)_2(OTf)_2]$ (where ppy = 2-phenylpyridine and OTf = trifluoromethanesulfonate).¹⁰⁸ This is another example of *cis*-protection, with the

tricyanobenzene ligand directed to replace the more labile triflate ligands. The resulting complexes give luminescent orange emission that is over ten times more intense than analogous mononuclear complex. A similar assembly containing ruthenium (II) prepared by the Fujita group was found to show photochromic properties upon binding of adamantane guests.¹⁰⁹ Several other examples of metallo-supramolecular assemblies incorporating ruthenium (II),¹¹⁰⁻¹¹² and iridium (III)¹¹³⁻¹¹⁶ units have been reported.

More recently, Zysman-Colman and coworkers have reported the synthesis of red-emitting [Ir₈Pd₄] metallocages utilising a 4-4' bipyridine unit as the connecting ligand.¹¹⁷ The red-emitting cage compounds were found to be able to encapsulate mononuclear blue-emitting anionic guests such as [Ir(dFppy)₂(CN)₂]⁻ (where dFppy is 2,4 difluorophenyl pyridine). Efficient energy transfer was observed in these systems between the strongly blue-emitting guest and the red-emitting host. The use of [Ir(ppy)] as a geometrically directing metallotecton has been demonstrated recently in the Hardie group^{118, 119} and forms an important component of concepts that are discussed further in chapters 3 and 4 of this work.

1.5 Stimuli-responsive metallo-supramolecular assemblies

Response to external stimuli is a key mechanism by which nature coordinates a number of processes within living organisms. The range of functions that nature can achieve using this mechanism is staggering – spanning electrochemical signalling (nerve impulses), mechanical movement (muscle contraction), cell signalling, mammalian vision, temperature and pH control within the blood, all require a sophisticated detection and response to stimuli. The elegant way in which this is achieved in nature has been a source of inspiration for chemists from a variety of backgrounds seeking to develop new functional materials based on nature's ingenuity. Comprehensive reviews on the subject have been published by Nitschke¹²⁰ and more recently by Wang.¹²¹

Many biological assemblies can be viewed as supramolecular in nature – such as hydrogen-bonded double stranded DNA. Supramolecular chemistry has found many ingenious ways of mimicking some of these strategies in the design of functional materials. The power of enzymes in biological catalysis has inspired a wealth of research into 'molecular machines' which can rationalise an external stimulus and devise a response to it.^{122, 123} The development of elements of these machines led to the award of the 2016 Nobel prize in chemistry to Sauvage, Stoddart and Feringa.

Sauvage first developed catenanes – mechanically interlocked macrocycles with no formal covalent interaction between the rings – in 1985.³⁷ This first example was shown to undergo structural reorganisation upon complexation with copper ions; more recent examples have light-responsive¹²⁴ (figure 1.11a) and electrochemically-responsive¹²⁵⁻¹²⁹ ranges of motion. Many more examples have been developed since the original report.^{32, 130-134} Sauvage has also heavily contributed to the development of rotaxanes – these systems consist of two mechanically interlocked components, a ‘thread’ or ‘axle’ like component which is threaded through a macrocyclic component; typically upon association, the thread is capped with bulky stopper groups which prevent disassociation (figure 1.11b).¹³⁵ These molecules formed a focus of Stoddart’s research and he demonstrated that rotaxanes can be designed to implement simple movements such as mechanical shuttling and contraction with a variety of examples developed for a multitude of applications including molecular electronics.¹³⁶⁻¹⁴⁵ Other sophisticated examples exploit many of these simple molecular motions in a complex system such as Leigh’s molecular machines capable of catalysing peptide formation¹⁴⁶ and stereodivergent synthesis (figure 1.11c).¹⁴⁷ Interest in these systems for applications in molecular nanotechnology has grown rapidly; a full discussion of molecular machines is beyond the scope of this work but comprehensive reviews on the subject have been published by Stoddart¹²³ and Leigh.¹²²

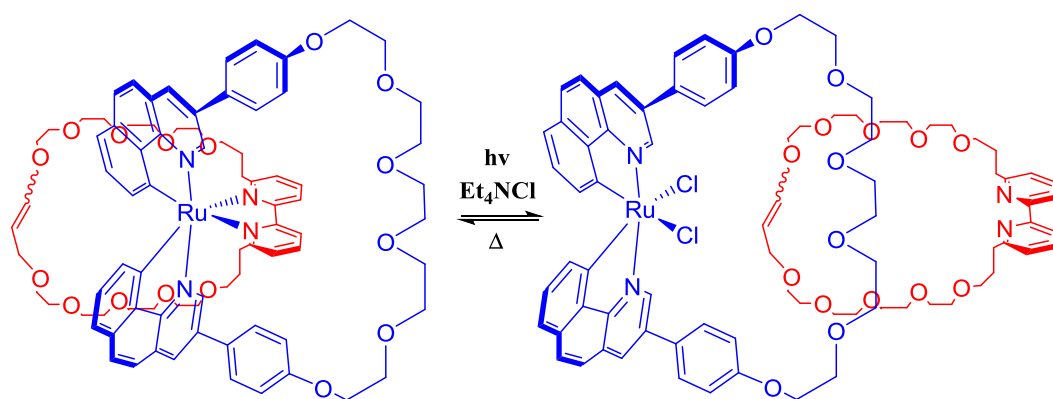


Figure 1.11a: Light driven shuttling of Sauvage’s catenane.¹²⁴ In the absence of light, the bipyridyl unit of the red ring coordinates to the ruthenium cation. Upon irradiation with light in the presence of NEt_4Cl , the red ring shuttles to the other side of the blue ring and the coordination sphere of the ruthenium cation is filled by chloride ions. Heating the system shuttles the red ring back to its original position with displacement of the bound chloride ions.

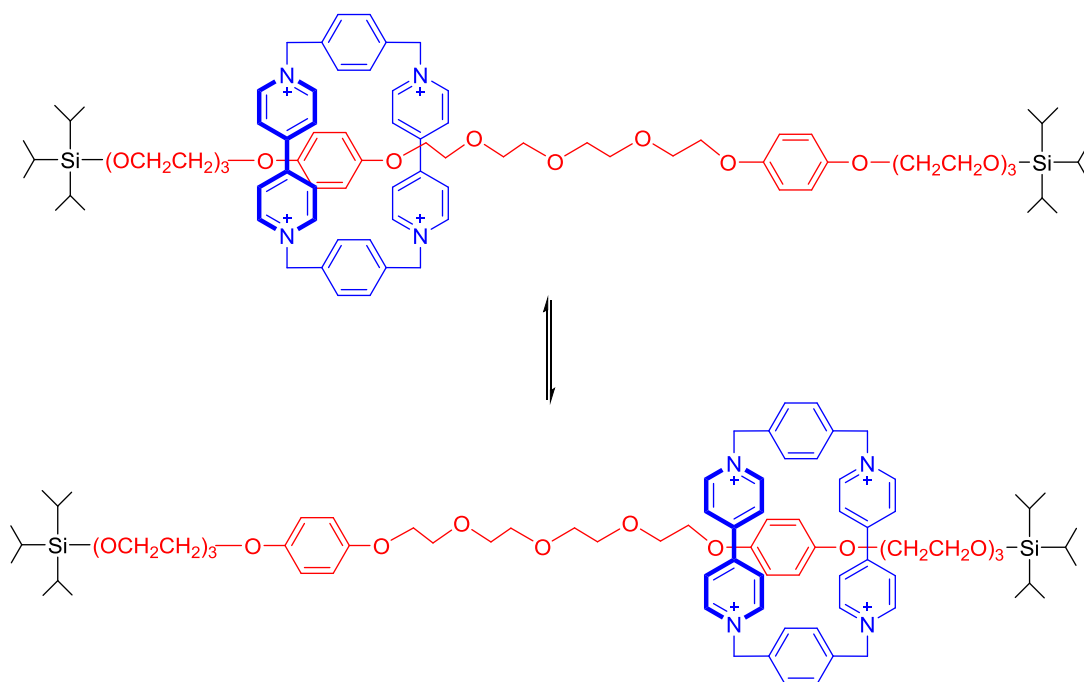


Figure 1.11b: Stoddart's rotaxane molecular shuttle.¹³⁵ The electron-poor paraquat moiety (blue) readily shuttles between the two electron rich aromatic rings on the axle (red). Bulky trimethylsilyl units (black) prevent the dissociation of the two rotaxane components.

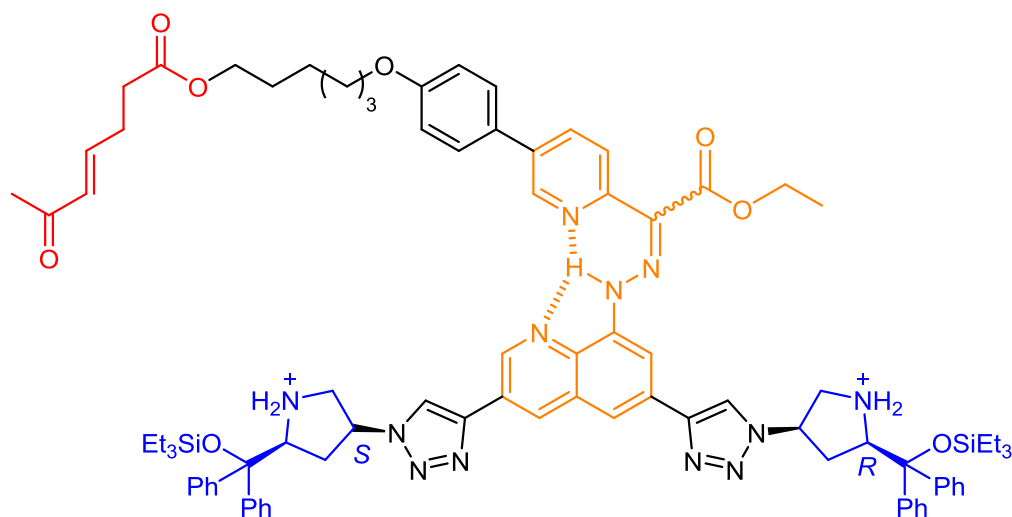


Figure 1.11c: Leigh's molecular machine for stereoselective synthesis.¹⁴⁷ Substrate loading (red) is followed by the E/Z isomerisation of the hydrazine unit (orange) to bring the substrate to the different R and S sites (blue) before further processing to give stereoisomers of the product depending on the configuration of the machine.

A wealth of materials have been developed that are responsive to other stimuli including electrochemical input,^{128, 148-151} pH,¹⁵²⁻¹⁵⁴ and chemical stimuli.¹⁵⁵⁻¹⁶² Of

particular interest to the supramolecular chemist is the ability to alter the shape or conformation of a molecule as this can dramatically impact upon its function and properties. Many of these stimuli-responsive systems are becoming key components of molecular nanotechnology which remains an exciting new focus of current research.

1.6 Light responsive molecular motions

A particularly attractive stimulus to invoke molecular motion is light. This strategy is fully external – no chemical additives need to be added or removed from the system. Light is also an efficient targeting stimulus with only the target area of the molecule likely to be affected and is often a reversible process, leading to much interest in the use of light in the development of molecular switches which can switch between two or more forms of a molecule.¹⁶³ Nature employs this strategy in mammalian vision pathways *via* the light induced photoisomerisation of 11-*cis* retinal to its all *trans* state. The resulting change in molecular structure allows 11-*trans* retinal to bind to opsin proteins, triggering the visual cascade.¹⁶⁴

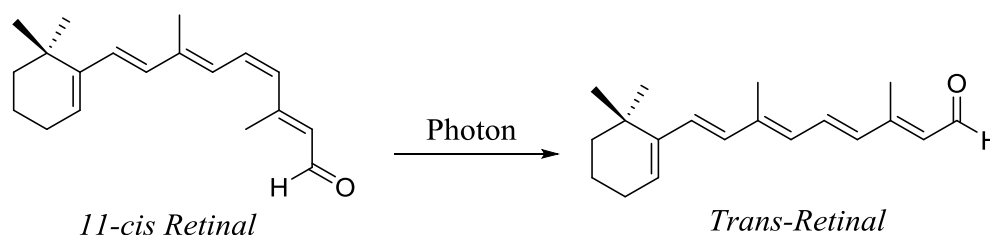


Figure 1.12: Isomerisation of the 11-*cis* retinal via absorption of a photon in the first step of the visual cascade.

A molecular switch must possess several properties in accordance with the criteria proposed by Irie.¹⁶⁵ These include thermal stability, low fatigue (ie can be cycled between different states many times without a loss of efficiency), high sensitivity and a rapid response to stimuli. Several light-responsive molecular switches exist – stilbenes, dithienylethenes, spiropyrans, acylhydrazones (figure 1.13) - but by far the most widely studied (and the main focus of this work) is the azobenzene unit. Azobenzene is a diazene (HN=NH) derivative where both of the hydrogen atoms have been replaced by phenyl rings (figure 1.13a). Upon irradiation with light, azobenzene can reversibly isomerise between the *cis* and *trans* forms depending on the irradiating wavelength.¹⁶⁶ The *trans* form is more thermodynamically stable by approximately 50 kJ/mol¹⁶⁷ such that (in most derivatives) the *trans* isomer dominates in the

absence of light stimulus. This process has also been demonstrated in a variety of other azo derivatives.¹⁶⁶ Lees was the first to employ these units in metallo-supramolecular assemblies in the preparation of interconvertible dinuclear and tetranuclear metallocsquares containing the azobenzene unit.¹⁶⁸

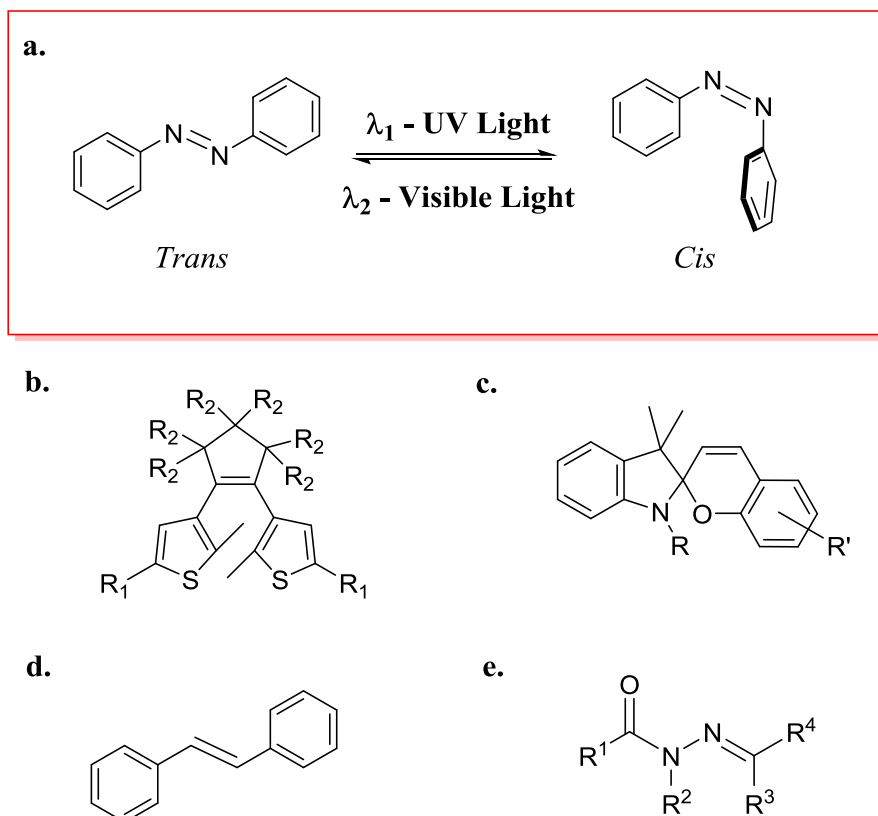


Figure 1.13: The main classes of light-responsive photoswitches showing: **a.** *Cis-trans* isomerisation of the azobenzene group; **b.** *Dithienylethene*; **c.** *Spiropyran*; **d.** *Stilbene*; **e.** *Acylhydrazone*.

The idea of introducing light-responsive functionality into supramolecular systems is by no means a new one.¹⁶⁹ Rebek has demonstrated the effectiveness of the azobenzene group at controlling guest uptake and release in supramolecular systems.¹⁷⁰⁻¹⁷⁴ Incorporation of the azobenzene unit onto the periphery of molecular cavitands allows the regulation of the binding of small adamantane guests.¹⁷¹ When the azo unit is in the *trans* conformation, the binding pocket of the cavitand is freely accessed by the guest molecules. Upon photoisomerisation to the *cis* isomer, the azo unit inserts into the cavity causing ejection of any bound guests into solution. Upon relaxation to the *trans* isomer, the cavitand is free to take up guests once more (figure 1.14). The same system can also be used as a photoresponsive catalyst for the Knoevenagel condensation between malononitrile and aromatic aldehydes.¹⁷⁵ Work

from the same group has also yielded other photoresponsive catalytic systems based on the azobenzene unit.^{172, 176}

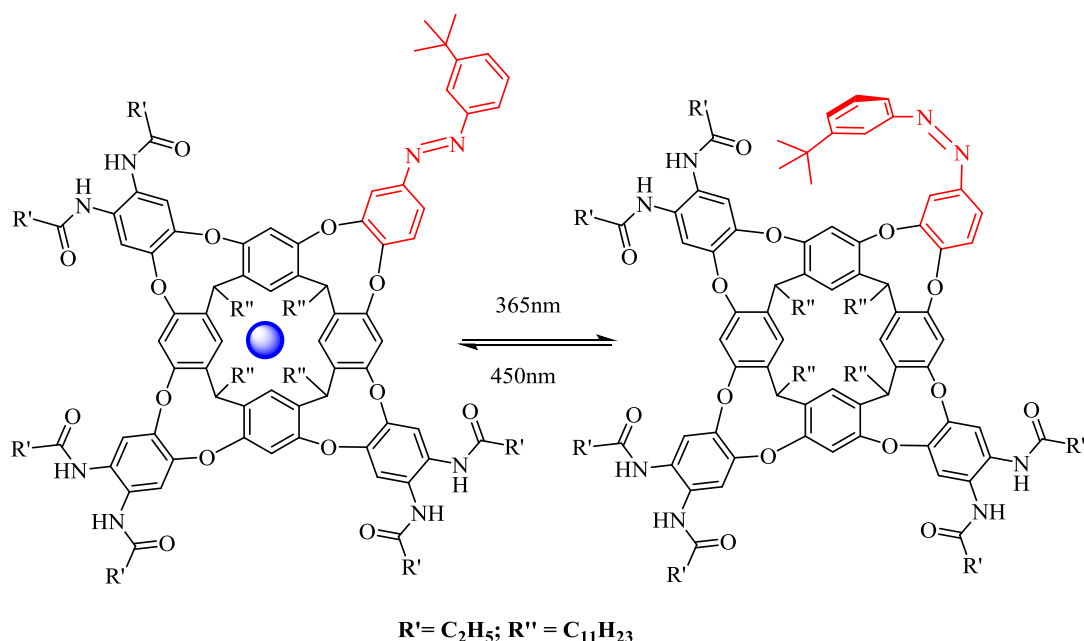


Figure 1.14: Photoisomerisation of Rebek's azo-appended cavitand¹⁷¹ showing: left. *Trans* configuration; right. *Cis* configuration. The adamantane guest is represented by a blue sphere and the photoswitchable azo moiety is shown in red for clarity.

Rebek has applied a similar strategy in the preparation of a ditopic cavitand bearing azobenzene units (figure 1.15).¹⁷⁴ Both *cis* and *trans* isomers of the cavitand can be accessed and once again display differing binding affinities for adamantyl guests. The *trans* configuration only forms stable host-guest complexes with guests with a long spacer. The opposite approach can also be employed, using the azobenzene unit as the guest molecule for a coordination capsule.¹⁷⁷ When in its *trans* conformation, the azobenzene is a good fit for the binding pocket of the capsule and excludes other guest molecules. Upon photoisomerisation, the *cis* form is released from the binding pocket, allowing the binding of other guests. Rebek has also reported organic capsules containing the azobenzene unit but has not remarked on their photoresponsive properties.¹⁷⁰

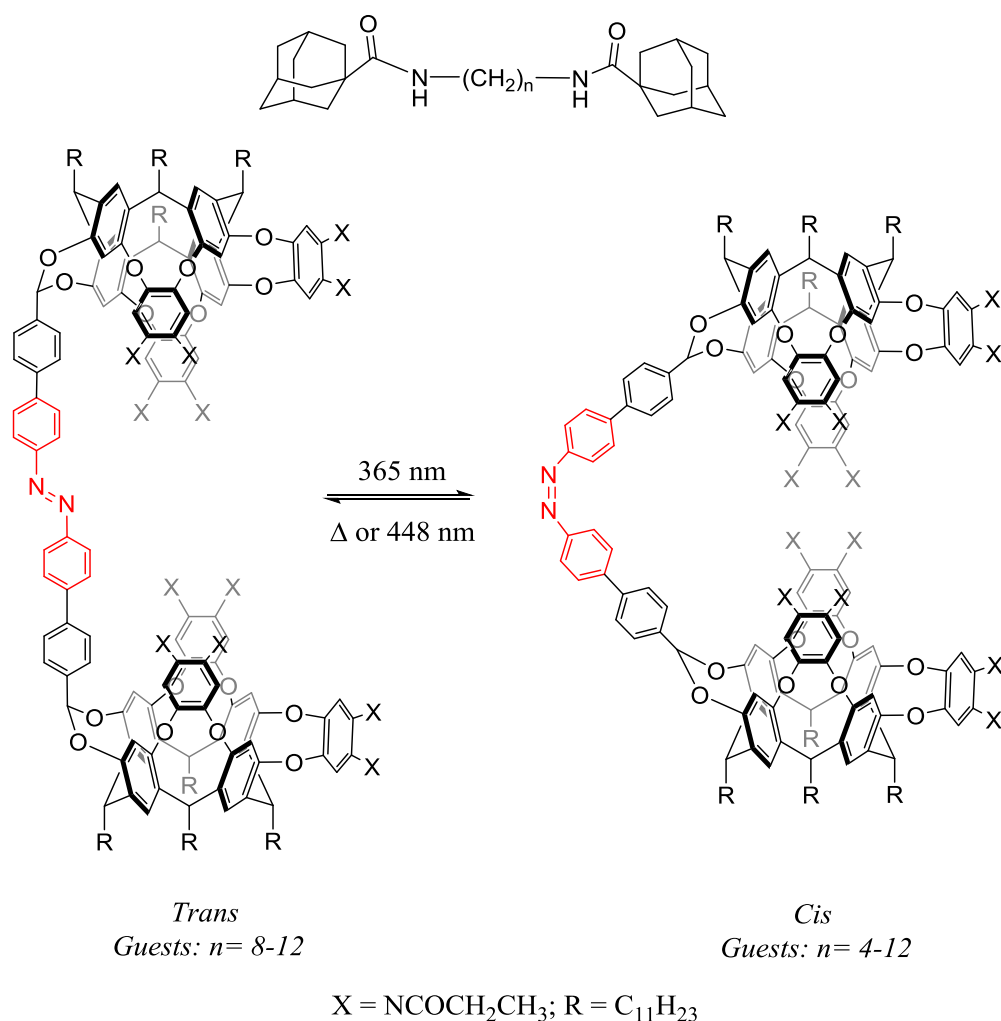


Figure 1.15: Photoisomerisation of Rebek's cavitand receptor¹⁷⁴ for the binding of adamantane guests showing: left. *Trans* receptor; right. *Cis* receptor.

A number of examples of dithienylethene moieties in supramolecular systems have also been developed. This molecular switch is a more subtle conformational change than azobenzene which often leads to high efficiency and fatigue resistance.^{165, 178} This subtlety has not prevented the unit being responsible for some interesting structural transformations however. Clever has reported a highly dramatic structural rearrangement between a M_3L_6 ring and a $\text{M}_{24}\text{L}_{48}$ sphere induced by light-triggered photoisomerisation.¹⁷⁹ Depending on the starting configuration of the ligand, self-assembly with Pd(II) ions gives either a Pd_3L_6 ring or a larger $\text{Pd}_{24}\text{L}_{48}$ coordination cage. Irradiation of one of these two products with light of the appropriate wavelength leads to the slow (approx. 15 hours) dismantling and reassembly of the components into the alternate structure (figure 1.16).

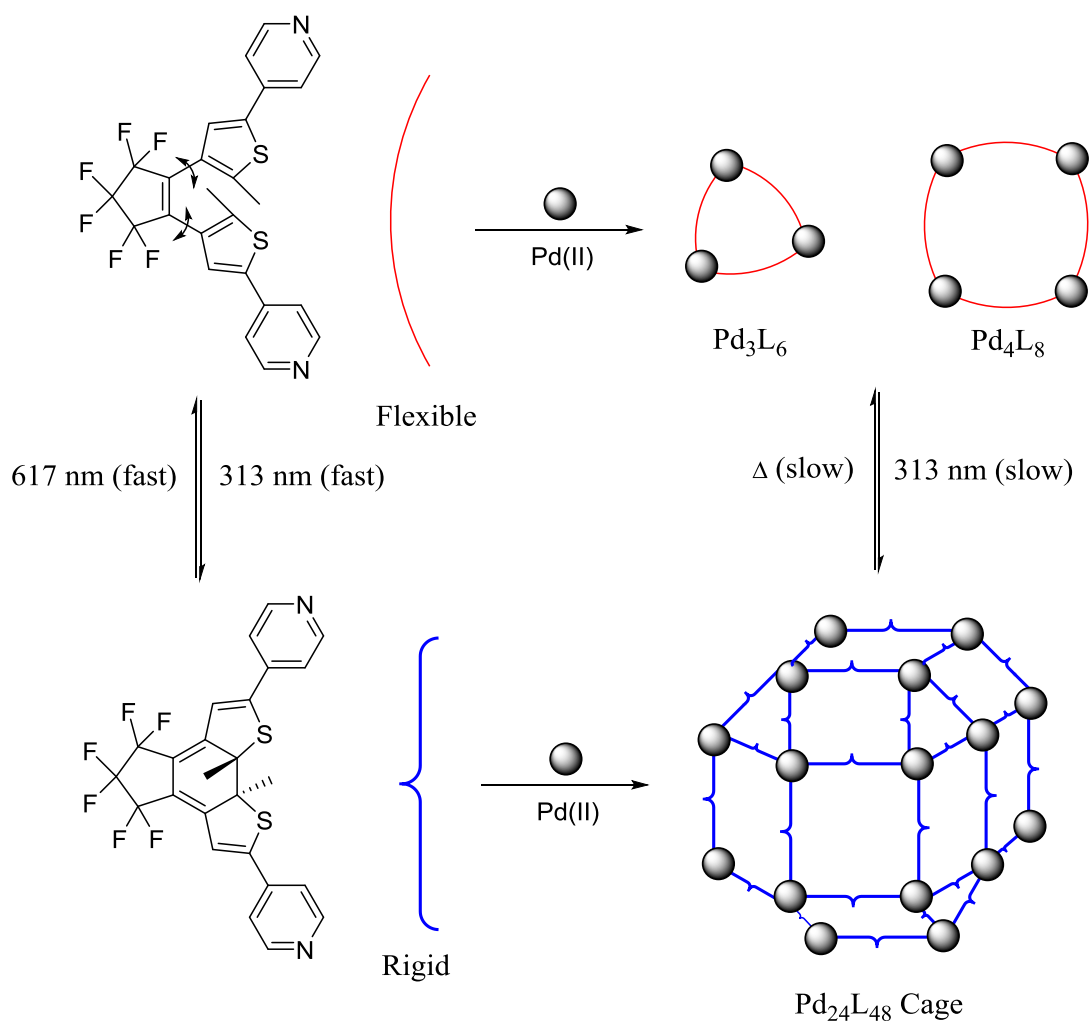


Figure 1.16: Clever's dithienylethene ligand which assembles into different supramolecular assemblies depending on the configuration and flexibility of the dithienylethene unit.¹⁷⁹

Chen has reported the precise control of the reversible transformation of supramolecular hexagons.¹⁸⁰ Several examples of stilbene¹⁸¹⁻¹⁸⁵ and spiropyran¹⁸⁶⁻¹⁸⁹ derivatives in supramolecular architectures and participating in supramolecular transformations have also been reported; perhaps most noteworthy are Jin's M₄L₂ metallacycles (figure 1.17).¹⁸² The stilbene units are able to undergo a light induced [2+2] cyclisation to give the cyclobutane product. Remarkably, this reaction can be induced in the solid state with none of the photoisomerisation to the *cis* stilbene observed.

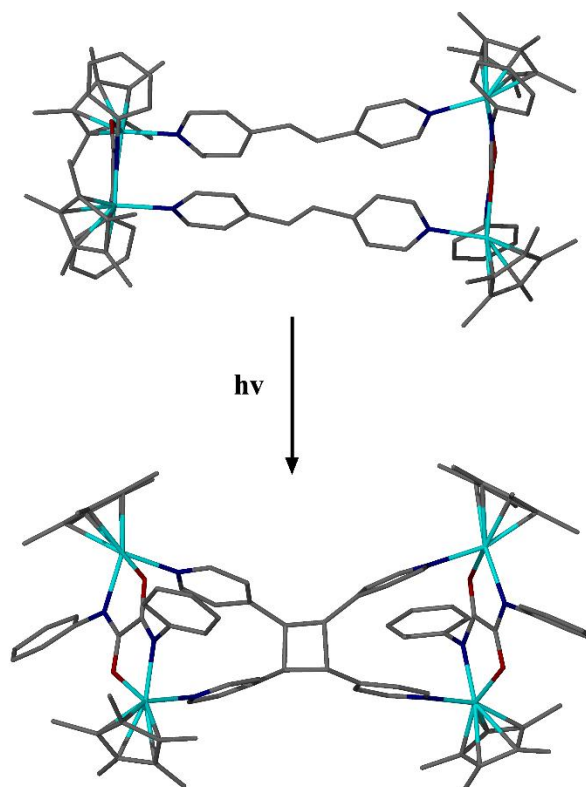
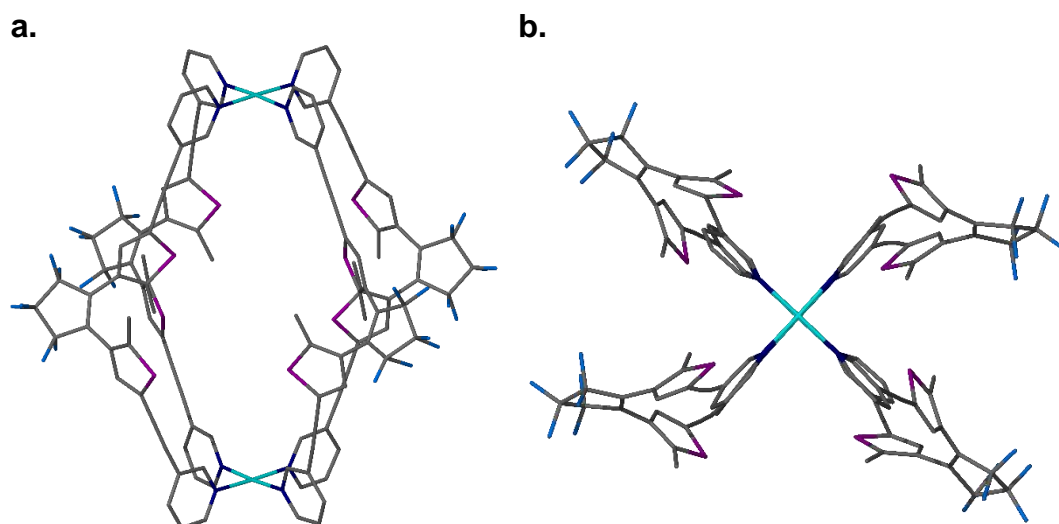


Figure 1.17: Solid state photocyclisation of Jin's M_4L_2 metallacycle.¹⁸² All hydrogen atoms and counterions have been omitted for clarity.

Perhaps the most relevant example to this discussion however also comes from the Clever group. Clever and coworkers have demonstrated the effectiveness of light-induced stimuli by incorporating the photoresponsive dithienylethene moiety into the ligand design of a series of palladium (II) cages (figure 1.18).¹⁹⁰ Upon irradiation with light at 365nm, the 'open' form of the dithienylethene unit cyclises to the 'closed' form. The induced conformational change was sufficient to significantly alter the binding constant K of a spherical $[B_{12}F_{12}]^{2-}$ guest molecule from 10^4 (open form) to 10^2 (closed form). The open form can be regenerated by the application of white light, thus enabling the modulation of binding of the guest molecules simply *via* the application of light. The smooth interconversion between isomers along with the relatively simple synthesis makes this arguably the most efficient photoswitchable coordination complex prepared to date. However, the lack of complete exclusion of the guest from the cavity upon isomerisation is likely due to the subtle nature of the conformational change of the dithienylethene subunit which makes it a double-edged sword: highly efficient interconversion is achieved but a weaker effect on the binding of guest molecules than, say, an azobenzene unit.



*Figure 1.18: SCXRD structures of Pd₂L₄ metallocages prepared by Clever and coworkers (open conformation) incorporating the photoresponsive dithienylethene unit¹⁹⁰ showing: **a.** Side view; **b.** Top view. All hydrogen atoms, counterions and solvents of crystallisation have been omitted for clarity.*

1.7 Cyclotrimeratrylene

Cyclotrimeratrylene (CTV) and its derivatives are a class of bowl-shaped molecular hosts with C_3 -symmetry.¹⁹¹ The system consists of a hydrophobic tribenzo[a,d,g]cyclononatriene core and a periphery to which various functional groups may be appended. The hydrophobic core and bowl-shaped conformation lends the system interesting properties as a molecular host.¹⁹² The CTV unit exists as a conformational equilibrium in solution of stable ‘crown’ and unstable ‘saddle’ forms (figure 1.19a).¹⁹³ The system is able to interconvert between the crown and saddle conformations in solution,¹⁹⁴ although the saddle conformation is not typically observed by spectroscopic techniques. The replacement of three of the methoxy groups with hydroxyl units gives the chiral analogue cyclotriguaiacylene (CTG, figure 1.19b), the principal cavitand employed in the Hardie research group. Removal of all six of the methoxy groups generates the achiral cyclotricatechylene (CTC, figure 1.19c). Other specialised derivatives have also been synthesised bearing amino¹⁹⁵ and sulphur¹⁹⁶ moieties.

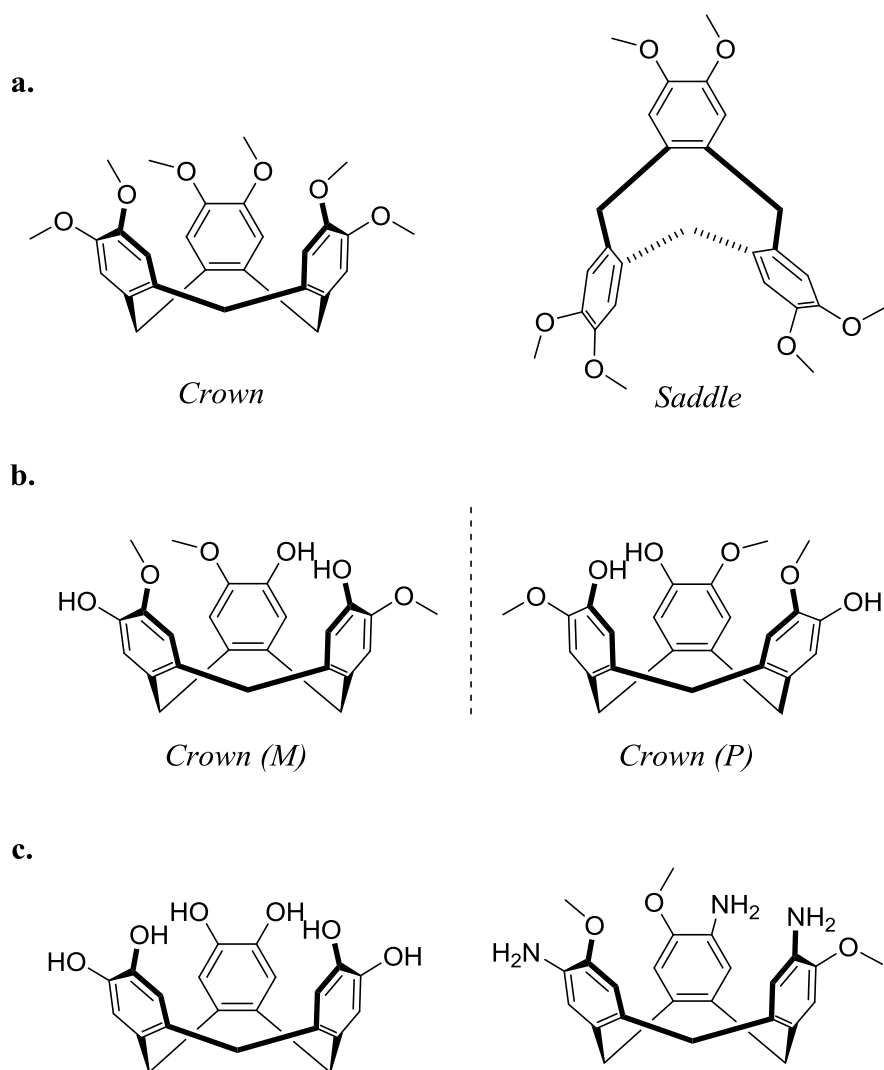


Figure 1.19: The cyclotrimeratrylene family of cavitands showing: a. Crown and saddle forms of CTV; b. Crown P and M enantiomers of the chiral tris hydroxy derivative CTG; c. The hexa hydroxyl derivative CTC (left) and the tris amino derivative aCTG (right).

The possibility for isomerisation *via* the saddle conformation of CTV means that the chiral derivative CTG exists as a mixture of *P* and *M* isomers (figure 1.19b) in solution. The CTV framework has well defined host-guest properties with particular research interest into the binding of globular guests such as fullerenes¹⁹⁷ (figure 1.20a). CTV derivatives are also of interest for the preparation of cryptophanes as reviewed by Collet and coworkers¹⁹³ or more recently, Brotin.¹⁹⁸ These are cage-like compounds which consist of two CTV derivatives linked in a head-to-head fashion to give an internal space capable of binding neutral guest molecules,^{193, 199-201} cations²⁰² and anions.²⁰³ Dutasta has shown that the core of these cryptophanes can be adapted for the binding of Xenon gas^{204, 205} and for electronic applications.²⁰⁶ Hardie and coworkers have subsequently prepared a sulphur-linked cryptophane capable of

binding methane gas.¹⁹⁶ A variety of studies have also focussed on the hemicryptophanes^{207, 208} which are asymmetric derivatives of CTV with promise in a variety of applications including catalysis²⁰⁹⁻²¹³ and molecular recognition.²¹⁴⁻²¹⁶

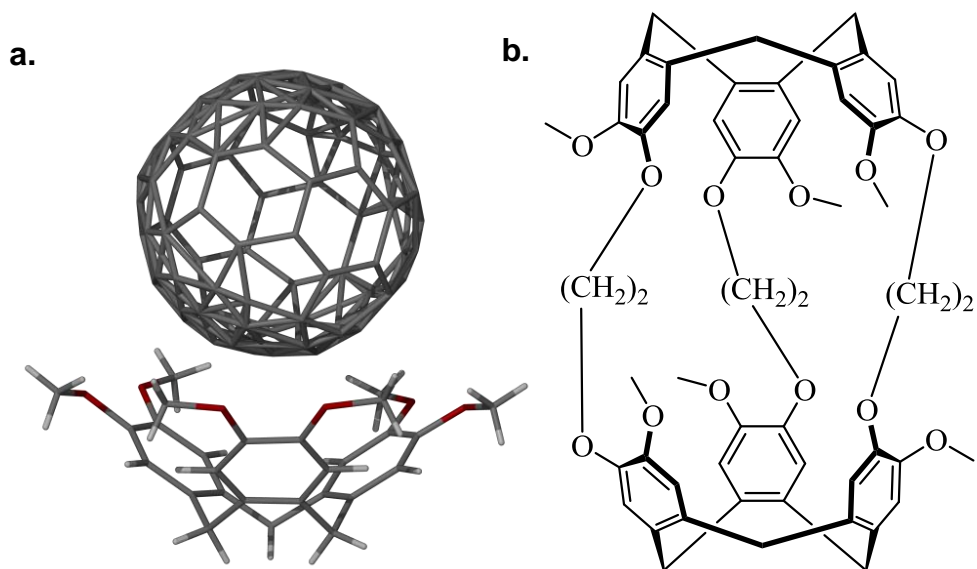


Figure 1.20: Guest encapsulation by organic CTV derivatives showing a. SCXRD structure of the host-guest interaction between CTV and fullerene¹⁹⁷ C₆₀; b. Chemical representation of the cryptophane prepared by Dutasta and coworkers for the encapsulation of xenon gas.²⁰⁴

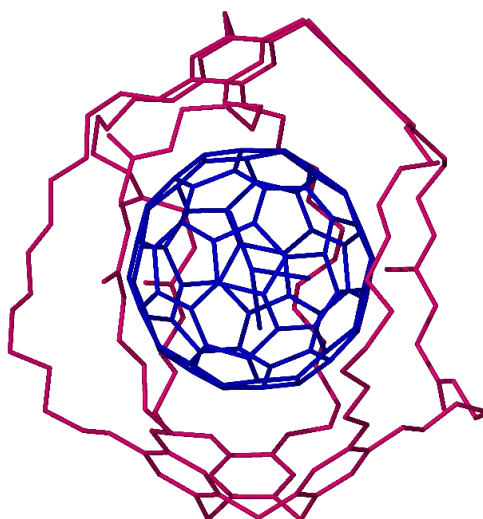
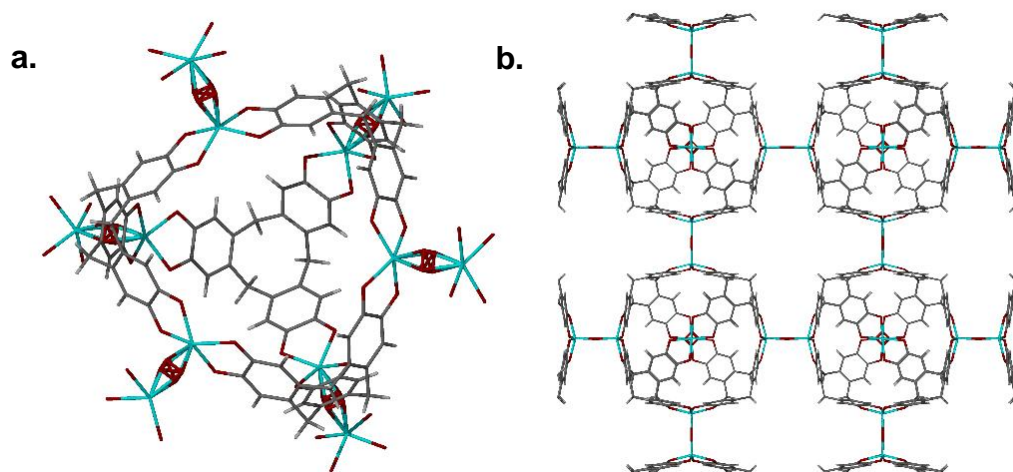


Figure 1.21: SCXRD structure of Ku's hemicarceplex (pink) for the binding of metallofullerenes (blue).²¹⁷

Ku and coworkers have recently shown that CTV can be linked into hemicarpiques which are able to selectively recognise and bind isomers of metallofullerenes (figure 1.21).^{217,218} These systems also help solubilise fullerenes which are notoriously poorly soluble in the majority of organic solvents.²¹⁹ These systems can be readily prepared in four synthetic steps and were found to be capable of selectively incarcerating either C₆₀ or C₈₀ complexed with scandium.

By far the most versatile congener of CTV is the tris hydroxyl analogue, CTG which has been thoroughly investigated in the Hardie group as a scaffold for the formation of metallosupramolecular assemblies. The three hydroxyl groups can be readily functionalised by appending a variety of metal-coordinating groups including carboxylate,^{220, 221} N-oxides,²²² bipyridines,²²³ thiazolyl,²²⁴ quinolyl,²²⁵ and terpyridyl.²²⁶ The majority of reports however, focus on the more accessible pyridyl^{191, 227-235} ligand. Depending on the metal-binding unit, a vast array of possible architectures can be formed using these ligands, ranging from small, discrete cage structures such as M₃L₂ metallocryptophanes^{230, 231} (with the first example prepared in 2001 by Shinkai and coworkers) to much larger assemblies such as coordination polymers.^{221, 222} Work from Holman²³⁶ has led to the preparation of cryptophanes which are linked into a polymeric network which has implications in amplifying the host-guest properties of the CTV core. Robson has reported the preparation of M₆L₄ coordination cages formed from the combination of the hexahydroxy CTV derivative cyclotricatechylene (CTC) with vanadium(II) sulfate²³⁷ or with copper(II) chloride.²³⁸



*Figure 1.22: From the SCXRD structure of Robson's metallocages utilising cyclotricatechylene derived ligands²³⁸ showing **a.** Individual cage moiety; **b.** Packed display as viewed down the crystallographic c axis. Counterions of crystallisation have been omitted for clarity.*

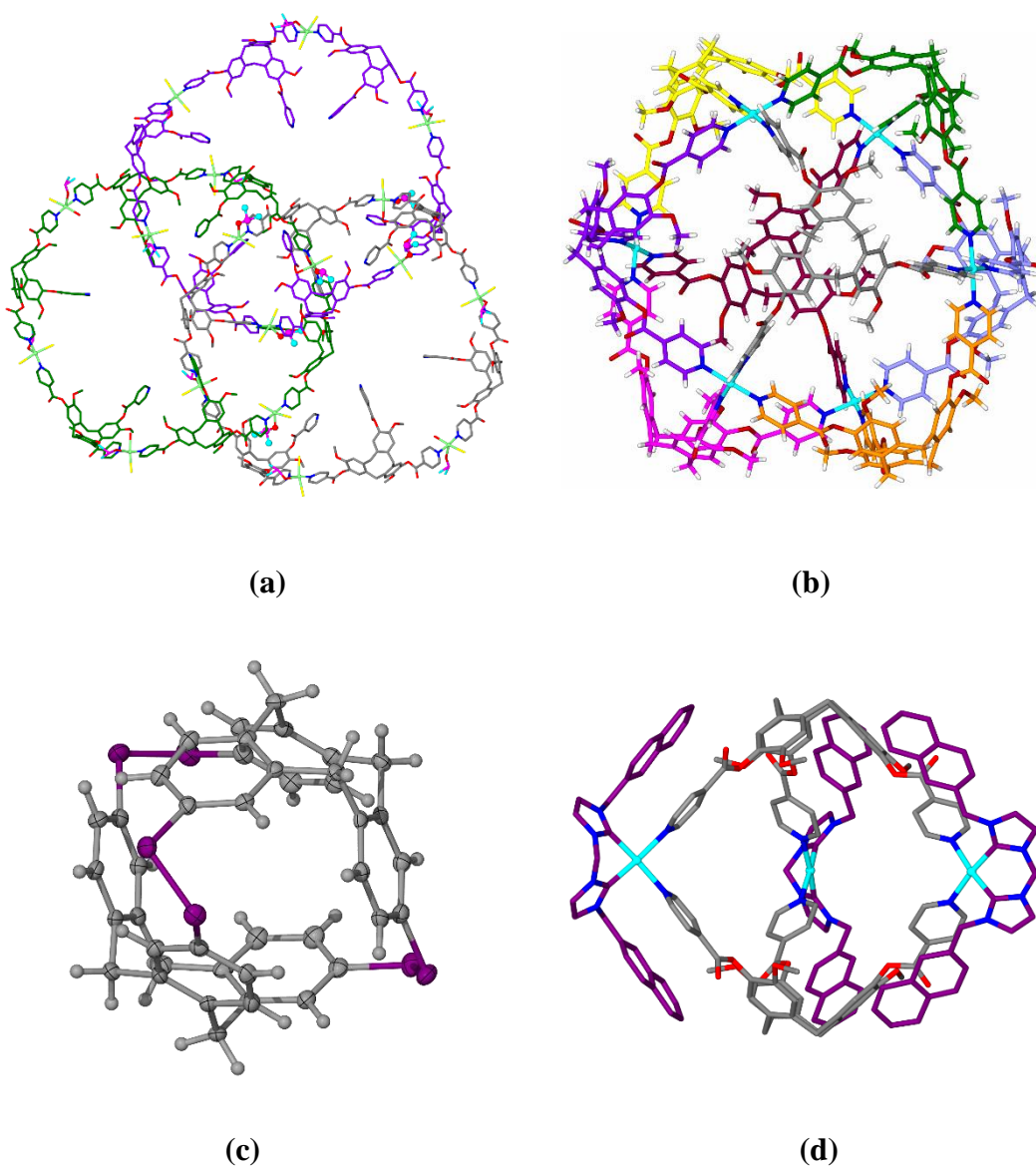


*Figure 1.23: SCXRD structures showing the diversity of CTG-derived metallosupramolecular assemblies: From the crystal structure of **a.** M_6L_6 Borromean rings;²³⁹ **b.** M_6L_8 stella octangula structure;²³⁴ **c.** Organic cryptophane bridged by disulphide bonds;¹⁹⁶ **d.** Pd_3L_2 metallocryptophane.²³¹ Examples **a**, **b** and **d** All utilise the same pyridyl-appended CTG ligand, indicating a remarkable diversity of structures.*

Several examples of coordination polymers with CTV derived ligands have also been reported by the Hardie group.^{221, 222, 240-244} Discrete metallocryptophanes and coordination polymers are revisited in chapters 3 and 5 of this thesis respectively. Systems with unusual topologies and properties such as the interwoven Pd_4L_4

‘Solomon’s Cube’²⁴⁵ and the ‘infinite chainmail’ Borromean rings formed from a M_6L_6 arrangement from the reaction of a pyridyl-appended CTG ligand with $CuBr_2$ have also been prepared (Figure 1.23a).²³⁹ Here again, the diversity is highlighted; the reaction of this same pyridyl ligand with $Pd(NO_3)_2$ gives rise to a completely different structure in the M_6L_8 stella octangula system (Figure 1.23b).²³⁴

The systems formed from this library of ligands have displayed a versatile array of host-guest chemistry. This guest binding ability can range from very small guest molecules, such as the CH_4 binding properties of the sulphur linked organic cages prepared by Hardie and coworkers,¹⁹⁶ figure 1.23c, to much larger guests such as sodium dodecyl sulphates that were encapsulated by the M_6L_8 stella octangula cages²²⁸ (figure 1.22b). The use palladium tectons that bear cis-protecting N-heterocyclic carbene (NHC) ligands in place of $Pd(NO_3)_2$ in a stoichiometric ratio leads to the controlled assembly of $[Pd_3L_2]$ metallocryptophanes (figure 1.23d).²³¹

Warmuth has demonstrated the edge-directed synthesis of an organic nanocube from the combination of an aldehyde appended CTG derivative with an organic linker, *p*-phenylenediamine.²⁴⁶ The tritopic CTG bowls form the cube corners, typically a challenging component of synthesising cubic architectures and the use of dynamic imine linkers help facilitate the formation of a cubic assembly. More recently, a $[M_{12}L_8]$ metallocube has been prepared by Hardie where ‘M’ is a variety of silver (I) salts and ‘L’ is a thiazole-appended CTG ligand. Once again, this exploits the tritopic nature of the ligand to form the cube vertices, again illustrating the versatility of this class of ligands.

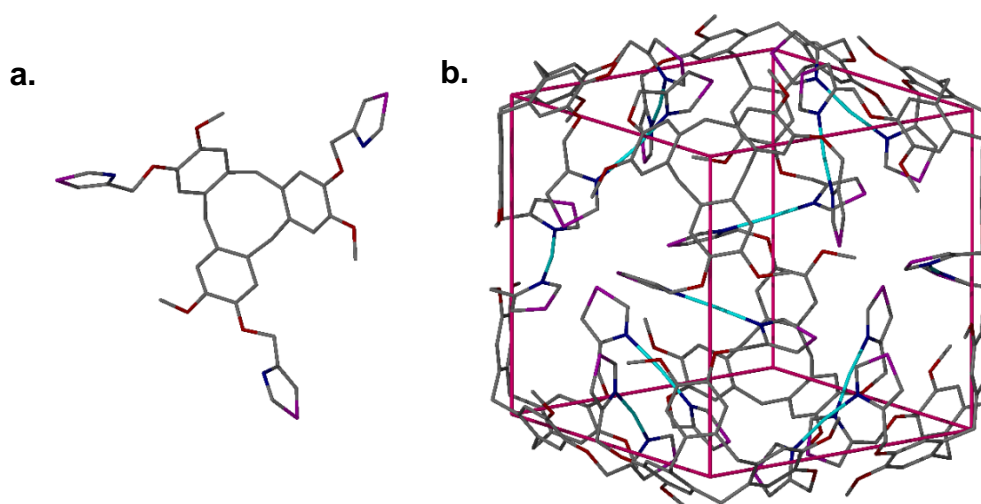


*Figure 1.24: SCXRD structure of the $M_{12}L_8$ metallocube prepared by Hardie,²²⁴ showing **a.** Individual tripodal CTG ligand; **b.** Silver metallocube showing the tripodal ligand acting as the cube vertices. All hydrogen atoms have been omitted for clarity.*

In terms of dynamic behaviour, reports of structural rearrangements in CTV based systems are rare. Henkelis and coworkers have reported a Pd₃L₂ metallocryptophane formed from the reaction of a pyridyl appended CTG ligand with [Pd(en)₂(NO₃)₂].²³¹ This system is metastable in solution and over time rearranges to the larger Pd₆L₈ stella octangula assembly. Henkelis went on to show that the stella octangula assembly can be reversibly degraded upon the addition of 24 equivalents of 4,4'-dimethylaminopyridine (DMAP) due to DMAP being a stronger base than the pyridyl ligand.²³³ Upon addition of 24 equivalents of tosyl alcohol (TsOH) the cage reassembles in a quantitative yield. This chemical-induced response is the most relevant example of a stimuli-responsive CTV system.

1.8 Project Outline

Current research within the Hardie group is directed towards the preparation of functional supramolecular architectures based on the CTV scaffold. Recent reports from our laboratories have demonstrated the introduction of luminescence^{118, 119, 247} via the incorporation of iridium (III)^{118, 119} and rhenium (I)²⁴⁷ moieties into the complex design and the use of *cis*-protecting strategies in the targeting of specific supramolecular architectures.²³¹

The aim of this work is the incorporation of the photoresponsive azobenzene unit into the ligand design on the CTG scaffold and subsequent incorporation of these ligands into the diverse array of structures that have been prepared using these cavitands. Photoisomerisation of the azo moiety constitutes a dramatic conformational change compared to other photoresponsive molecular switches such as the dithienylethenes. This in turn will confer dynamic behaviour upon a ligand class already renowned for its synthetic diversity, with the ultimate goal to prepare systems for sophisticated applications in molecular recognition and host guest chemistry.

Chapter 2 discusses the synthetic strategies to prepare the ligands containing the azo moiety and their characterisation. Chapters 3 and 4 discuss the assembly of these ligands into discrete coordination complexes, their characterisation and photophysical properties. Finally, chapter 5 discusses non-discrete coordination polymers of these ligands and their solid state structures, implications for further work and potential applications.

1.9 References

1. K.-T. Tang and J. P. Toennies, *Angewandte Chemie International Edition*, 2010, **49**, 9574-9579.
2. J.-M. Lehn, *Angewandte Chemie International Edition in English*, 1988, **27**, 89-112.
3. T. Steiner, *Angewandte Chemie International Edition*, 2002, **41**, 48-76.
4. P. Yakovchuk, E. Protozanova and M. D. Frank-Kamenetskii, *Nucleic Acids Research*, 2006, **34**, 564-574.
5. J. M. S. Bartlett and D. Stirling, in *PCR Protocols*, eds. J. M. S. Bartlett and D. Stirling, Humana Press, Totowa, NJ, 2003, pp. 3-6.
6. J. D. Watson and F. H. C. Crick, *Nature*, 1953, **171**, 737.
7. C. J. Pedersen, *Journal of the American Chemical Society*, 1967, **89**, 7017-7036.
8. E. P. Kyba, M. G. Siegel, L. R. Sousa, G. D. Y. Sogah and D. J. Cram, *Journal of the American Chemical Society*, 1973, **95**, 2691-2692.
9. D. J. Cram and J. M. Cram, *Science*, 1974, **183**, 803-809.
10. S. C. Peacock and D. J. Cram, *Journal of the Chemical Society, Chemical Communications*, 1976, **0**, 282-284.
11. J. M. Lehn, S. H. Pine, E. Watanabe and A. K. Willard, *Journal of the American Chemical Society*, 1977, **99**, 6766-6768.
12. A. H. Alberts, R. Annunziata and J. M. Lehn, *Journal of the American Chemical Society*, 1977, **99**, 8502-8504.
13. J.-M. Lehn and F. Montavon, *Helvetica Chimica Acta*, 1978, **61**, 67-82.
14. J. M. Lehn, *Accounts of Chemical Research*, 1978, **11**, 49-57.
15. J. M. Lehn, E. Sonveaux and A. K. Willard, *Journal of the American Chemical Society*, 1978, **100**, 4914-4916.
16. B. Dietrich, T. M. Fyles, J.-M. Lehn, L. G. Pease and D. L. Fyles, *Journal of the Chemical Society, Chemical Communications*, 1978, **0**, 934-936.
17. B. Dietrich, B. Dilworth, J.-M. Lehn, J.-P. Souchez, M. Cesario, J. Guilhem and C. Pascard, *Helvetica Chimica Acta*, 1996, **79**, 569-587.
18. J.-M. Lehn, *Science*, 2002, **295**, 2400-2403.
19. J.-M. Lehn, *Angewandte Chemie International Edition*, 2013, **52**, 2836-2850.
20. G. M. Whitesides and M. Boncheva, *Proceedings of the National Academy of Sciences USA*, 2002, **99**, 4769-4774.
21. J.-M. Lehn, *Angewandte Chemie International Edition in English*, 1990, **29**, 1304-1319.
22. R. Chakrabarty, P. S. Mukherjee and P. J. Stang, *Chemical Reviews*, 2011, **111**, 6810-6918.
23. J. M. Lehn, A. Rigault, J. Siegel, J. Harrowfield, B. Chevrier and D. Moras, *Proceedings of the National Academy of Sciences USA*, 1987, **84**, 2565-2569.

24. A. D. Faulkner, R. A. Kaner, Q. M. A. Abdallah, G. Clarkson, D. J. Fox, P. Gurnani, S. E. Howson, R. M. Phillips, D. I. Roper, D. H. Simpson and P. Scott, *Nature Chemistry*, 2014, **6**, 797-803.
25. M. Albrecht, *Nature Chemistry*, 2014, **6**, 761-762.
26. B. Hasenknopf, J.-M. Lehn, B. O. Kneisel, G. Baum and D. Fenske, *Angewandte Chemie International Edition in English*, 1996, **35**, 1838-1840.
27. S. E. Howson, A. Bolhuis, V. Brabec, G. J. Clarkson, J. Malina, A. Rodger and P. Scott, *Nature Chemistry*, 2011, **4**, 31-36.
28. M. J. Hannon, V. Moreno, M. J. Prieto, E. Moldrheim, E. Sletten, I. Meistermann, C. J. Isaac, K. J. Sanders and A. Rodger, *Angewandte Chemie International Edition*, 2001, **40**, 879-884.
29. P. E. Barran, H. L. Cole, S. M. Goldup, D. A. Leigh, P. R. McGonigal, M. D. Symes, J. Wu and M. Zengerle, *Angewandte Chemie International Edition*, 2011, **50**, 12280-12284.
30. J. J. Danon, A. Krüger, D. A. Leigh, J.-F. Lemonnier, A. J. Stephens, I. J. Vitorica-Yrezabal and S. L. Woltering, *Science*, 2017, **355**, 159-162.
31. V. Marcos, A. J. Stephens, J. Jaramillo-Garcia, A. L. Nussbaumer, S. L. Woltering, A. Valero, J.-F. Lemonnier, I. J. Vitorica-Yrezabal and D. A. Leigh, *Science*, 2016, **352**, 1555-1559.
32. D. A. Leigh, R. G. Pritchard and A. J. Stephens, *Nature Chemistry*, 2014, **6**, 978-982.
33. J.-F. Ayme, G. Gil-Ramírez, D. A. Leigh, J.-F. Lemonnier, A. Markevicius, C. A. Muryn and G. Zhang, *Journal of the American Chemical Society*, 2014, **136**, 13142-13145.
34. J.-F. Ayme, J. E. Beves, D. A. Leigh, R. T. McBurney, K. Rissanen and D. Schultz, *Journal of the American Chemical Society*, 2012, **134**, 9488-9497.
35. J.-F. Ayme, J. E. Beves, D. A. Leigh, R. T. McBurney, K. Rissanen and D. Schultz, *Nature Chemistry*, 2011, **4**, 15-20.
36. R. S. Forgan, J.-P. Sauvage and J. F. Stoddart, *Chemical Reviews*, 2011, **111**, 5434-5464.
37. M. Cesario, C. O. Dietrich-Buchecker, J. Guilhem, C. Pascard and J. P. Sauvage, *Journal of the Chemical Society, Chemical Communications*, 1985, **0**, 244-247.
38. K. S. Chichak, S. J. Cantrill, A. R. Pease, S.-H. Chiu, G. W. V. Cave, J. L. Atwood and J. F. Stoddart, *Science*, 2004, **304**, 1308-1312.
39. S.-L. Huang, Y.-J. Lin, Z.-H. Li and G.-X. Jin, *Angewandte Chemie International Edition*, 2014, **53**, 11218-11222.
40. S.-L. Huang, Y.-J. Lin, T. S. A. Hor and G.-X. Jin, *Journal of the American Chemical Society*, 2013, **135**, 8125-8128.
41. V. Kumar, T. Pilati, G. Terraneo, F. Meyer, P. Metrangolo and G. Resnati, *Chemical Science*, 2017, **8**, 1801-1810.
42. N. Singh, D. Kim, D. H. Kim, E.-H. Kim, H. Kim, M. S. Lah and K.-W. Chi, *Dalton Transactions*, 2017, **46**, 571-577.

43. M. Pan and C.-Y. Su, *CrystEngComm*, 2014, **16**, 7847-7859.
44. C. P. McArdle, J. J. Vittal and R. J. Puddephatt, *Angewandte Chemie International Edition*, 2000, **39**, 3819-3822.
45. C. P. McArdle, M. C. Jennings, J. J. Vittal and R. J. Puddephatt, *Chemistry – A European Journal*, 2001, **7**, 3572-3583.
46. A. M. Saitta, P. D. Soper, E. Wasserman and M. L. Klein, *Nature*, 1999, **399**, 46-48.
47. J.-F. Ayme, J. E. Beves, C. J. Campbell, G. Gil-Ramírez, D. A. Leigh and A. J. Stephens, *Journal of the American Chemical Society*, 2015, **137**, 9812-9815.
48. R. A. Bilbeisi, T. Prakasam, M. Lusi, R. El Khoury, C. Platas-Iglesias, L. J. Charbonniere, J.-C. Olsen, M. Elhabiri and A. Trabolsi, *Chemical Science*, 2016, **7**, 2524-2531.
49. Y. Liu, Y. Ma, Y. Zhao, X. Sun, F. Gándara, H. Furukawa, Z. Liu, H. Zhu, C. Zhu, K. Suenaga, P. Oleynikov, A. S. Alshammari, X. Zhang, O. Terasaki and O. M. Yaghi, *Science*, 2016, **351**, 365-369.
50. D. J. Cram, *Nature*, 1992, **356**, 29-36.
51. S. A. P. van Rossum, M. Tena-Solsona, J. H. van Esch, R. Eelkema and J. Boekhoven, *Chemical Society Reviews*, 2017, **46**, 5519-5535.
52. G. Zhang and M. Mastalerz, *Chemical Society Reviews*, 2014, **43**, 1934-1947.
53. M. Mastalerz, *Chemical Communications*, 2008, **0**, 4756-4758.
54. M. Mastalerz, M. W. Schneider, I. M. Oppel and O. Presly, *Angewandte Chemie International Edition*, 2011, **50**, 1046-1051.
55. M. W. Schneider, I. M. Oppel, A. Griffin and M. Mastalerz, *Angewandte Chemie International Edition*, 2013, **52**, 3611-3615.
56. A. G. Slater, M. A. Little, M. E. Briggs, K. E. Jelfs and A. I. Cooper, *Molecular Systems Design & Engineering*, 2018, Advance article.
57. M. E. Briggs, A. G. Slater, N. Lunt, S. Jiang, M. A. Little, R. L. Greenaway, T. Hasell, C. Battilocchio, S. V. Ley and A. I. Cooper, *Chemical Communications*, 2015, **51**, 17390-17393.
58. Z. Lin, J. Sun, B. Efremovska and R. Warmuth, *Chemistry – A European Journal*, 2012, **18**, 12864-12872.
59. S. Hiraoka, Y. Yamauchi, R. Arakane and M. Shionoya, *Journal of the American Chemical Society*, 2009, **131**, 11646-11647.
60. R. W. Saalfrank, A. Stark, K. Peters and H. G. von Schnering, *Angewandte Chemie International Edition in English*, 1988, **27**, 851-853.
61. T. Beissel, R. E. Powers and K. N. Raymond, *Angewandte Chemie International Edition in English*, 1996, **35**, 1084-1086.
62. T. Beissel, R. E. Powers, T. N. Parac and K. N. Raymond, *Journal of the American Chemical Society*, 1999, **121**, 4200-4206.
63. M. Scherer, D. L. Caulder, D. W. Johnson and K. N. Raymond, *Angewandte Chemie International Edition*, 1999, **38**, 1587-1592.

64. C. J. Hastings, M. D. Pluth, R. G. Bergman and K. N. Raymond, *Journal of the American Chemical Society*, 2010, **132**, 6938-6940.
65. D. Fiedler, H. van Halbeek, R. G. Bergman and K. N. Raymond, *Journal of the American Chemical Society*, 2006, **128**, 10240-10252.
66. T. N. Parac, D. L. Caulder and K. N. Raymond, *Journal of the American Chemical Society*, 1998, **120**, 8003-8004.
67. P. Mal, D. Schultz, K. Beyeh, K. Rissanen and J. R. Nitschke, *Angewandte Chemie International Edition*, 2008, **47**, 8297-8301.
68. P. Mal, B. Breiner, K. Rissanen and J. R. Nitschke, *Science*, 2009, **324**, 1697-1699.
69. I. A. Riddell, M. M. J. Smulders, J. K. Clegg and J. R. Nitschke, *Chemical Communications*, 2011, **47**, 457-459.
70. B. Breiner, J. K. Clegg and J. R. Nitschke, *Chemical Science*, 2011, **2**, 51-56.
71. J. K. Clegg, J. Cremers, A. J. Hogben, B. Breiner, M. M. J. Smulders, J. D. Thoburn and J. R. Nitschke, *Chemical Science*, 2013, **4**, 68-76.
72. J. L. Bolliger, A. M. Belenguer and J. R. Nitschke, *Angewandte Chemie International Edition*, 2013, **52**, 7958-7962.
73. R. A. Bilbeisi, J. K. Clegg, N. Elgrishi, X. d. Hatten, M. Devillard, B. Breiner, P. Mal and J. R. Nitschke, *Journal of the American Chemical Society*, 2012, **134**, 5110-5119.
74. A. Jiménez, R. A. Bilbeisi, T. K. Ronson, S. Zarra, C. Woodhead and J. R. Nitschke, *Angewandte Chemie International Edition*, 2014, **53**, 4556-4560.
75. T. K. Ronson, W. Meng and J. R. Nitschke, *Journal of the American Chemical Society*, 2017, **139**, 9698-9707.
76. W. Meng, B. Breiner, K. Rissanen, J. D. Thoburn, J. K. Clegg and J. R. Nitschke, *Angewandte Chemie International Edition*, 2011, **50**, 3479-3483.
77. W. J. Ramsay, F. J. Rizzuto, T. K. Ronson, K. Caprice and J. R. Nitschke, *Journal of the American Chemical Society*, 2016, **138**, 7264-7267.
78. J. Mosquera, B. Szyszko, S. K. Y. Ho and J. R. Nitschke, *Nature Communications*, 2017, **8**, 14882.
79. N. Struch, C. Bannwarth, T. K. Ronson, Y. Lorenz, B. Mienert, N. Wagner, M. Engeser, E. Bill, R. Puttreddy, K. Rissanen, J. Beck, S. Grimme, J. R. Nitschke and A. Lützen, *Angewandte Chemie International Edition*, 2017, **56**, 4930-4935.
80. D. Yang, J. Zhao, L. Yu, X. Lin, W. Zhang, H. Ma, A. Gogoll, Z. Zhang, Y. Wang, X.-J. Yang and B. Wu, *Journal of the American Chemical Society*, 2017, **139**, 5946-5951.
81. M. Fujita, D. Oguro, M. Miyazawa, H. Oka, K. Yamaguchi and K. Ogura, *Nature*, 1995, **378**, 469-471.
82. M. Yoshizawa, J. K. Klosterman and M. Fujita, *Angewandte Chemie International Edition*, 2009, **48**, 3418-3438.

83. Y. Inokuma, M. Kawano and M. Fujita, *Nature Chemistry*, 2011, **3**, 349-358.
84. H. Takezawa, T. Murase, G. Resnati, P. Metrangolo and M. Fujita, *Journal of the American Chemical Society*, 2014, **136**, 1786-1788.
85. H. Takezawa, T. Murase, G. Resnati, P. Metrangolo and M. Fujita, *Angewandte Chemie International Edition*, 2015, **54**, 8411-8414.
86. S. Horiuchi, T. Murase and M. Fujita, *Journal of the American Chemical Society*, 2011, **133**, 12445-12447.
87. T. Murase, S. Horiuchi and M. Fujita, *Journal of the American Chemical Society*, 2010, **132**, 2866-2867.
88. Y. Kohyama, T. Murase and M. Fujita, *Journal of the American Chemical Society*, 2014, **136**, 2966-2969.
89. V. M. Dong, D. Fiedler, B. Carl, R. G. Bergman and K. N. Raymond, *Journal of the American Chemical Society*, 2006, **128**, 14464-14465.
90. Julia L. Brumaghim, M. Michels, D. Pagliero and Kenneth N. Raymond, *European Journal of Organic Chemistry*, 2004, **2004**, 5115-5118.
91. M. Ziegler, J. L. Brumaghim and K. N. Raymond, *Angewandte Chemie International Edition*, 2000, **39**, 4119-4121.
92. R. Warmuth and M. A. Marvel, *Angewandte Chemie International Edition*, 2000, **39**, 1117-1119.
93. Y.-C. Horng, P.-S. Huang, C.-C. Hsieh, C.-H. Kuo and T.-S. Kuo, *Chemical Communications*, 2012, **48**, 8844-8846.
94. C.-Y. Gao, L. Zhao and M.-X. Wang, *Journal of the American Chemical Society*, 2012, **134**, 824-827.
95. A. Galan and P. Ballester, *Chemical Society Reviews*, 2016, **45**, 1720-1737.
96. M. Tominaga, K. Suzuki, M. Kawano, T. Kusukawa, T. Ozeki, S. Sakamoto, K. Yamaguchi and M. Fujita, *Angewandte Chemie International Edition*, 2004, **43**, 5621-5625.
97. K. Suzuki, K. Takao, S. Sato and M. Fujita, *Journal of the American Chemical Society*, 2010, **132**, 2544-2545.
98. T. Murase, S. Sato and M. Fujita, *Angewandte Chemie International Edition* 2007, **46**, 5133-5136.
99. N. Kamiya, M. Tominaga, S. Sato and M. Fujita, *Journal of the American Chemical Society*, 2007, **129**, 3816-3817.
100. H. Li, J. Luo and T. Liu, *Chemistry – A European Journal*, 2016, **22**, 17949-17952.
101. D. Fujita, K. Suzuki, S. Sato, M. Yagi-Utsumi, Y. Yamaguchi, N. Mizuno, T. Kumasaka, M. Takata, M. Noda, S. Uchiyama, K. Kato and M. Fujita, *Nature Communications*, 2012, **3**, 1093.
102. Q.-F. Sun, J. Iwasa, D. Ogawa, Y. Ishido, S. Sato, T. Ozeki, Y. Sei, K. Yamaguchi and M. Fujita, *Science*, 2010, **328**, 1144-1147.
103. K. Harris, D. Fujita and M. Fujita, *Chemical Communications*, 2013, **49**, 6703-6712.

104. S. Pasquale, S. Sattin, E. C. Escudero-Adán, M. Martínez-Belmonte and J. de Mendoza, *Nature Communications*, 2012, **3**, 785.
105. S. Du, C. Hu, J.-C. Xiao, H. Tan and W. Liao, *Chemical Communications*, 2012, **48**, 9177-9179.
106. C. Wang, X.-Q. Hao, M. Wang, C. Guo, B. Xu, E. N. Tan, Y.-Y. Zhang, Y. Yu, Z.-Y. Li, H.-B. Yang, M.-P. Song and X. Li, *Chemical Science*, 2014, **5**, 1221-1226.
107. M. Han, D. M. Engelhard and G. H. Clever, *Chemical Society Reviews*, 2014, **43**, 1848-1860.
108. O. Chepelin, J. Ujma, X. Wu, A. M. Z. Slawin, M. B. Pitak, S. J. Coles, J. Michel, A. C. Jones, P. E. Barran and P. J. Lusby, *Journal of the American Chemical Society*, 2012, **134**, 19334-19337.
109. K.I. Yamashita, M. Kawano and M. Fujita, *Chemical Communications*, 2007, 4102-4103.
110. C. Shen, A. D. W. Kennedy, W. A. Donald, A. M. Torres, W. S. Price and J. E. Beves, *Inorganica Chimica Acta*, 2017, **458**, 122-128.
111. S. Chen, K. Li, F. Zhao, L. Zhang, M. Pan, Y.-Z. Fan, J. Guo, J. Shi and C.-Y. Su, *Nature Communications*, 2016, **7**, 13169.
112. D. Liu, R. C. Huxford and W. Lin, *Angewandte Chemie International Edition*, 2011, **50**, 3696-3700.
113. X. Li, J. Wu, L. Chen, X. Zhong, C. He, R. Zhang and C. Duan, *Chemical Communications*, 2016, **52**, 9628-9631.
114. S. Horiuchi, H. Tanaka, E. Sakuda, Y. Arikawa and K. Umakoshi, *Chemistry – A European Journal*, 2016, **22**, 17533-17537.
115. P. Govindaswamy, D. Linder, J. Lacour, G. Suss-Fink and B. Therrien, *Dalton Transactions*, 2007, **0**, 4457-4463.
116. Z. Xie, L. Ma, K. E. deKrafft, A. Jin and W. Lin, *Journal of the American Chemical Society*, 2010, **132**, 922-923.
117. D. Rota Martir, D. Escudero, D. Jacquemin, D. Cordes, A. Slawin, H. Fruchtl, S. Warriner and E. Zysman-Colman, *Chemistry – A European Journal*, 2017, **23**, 14358-14366.
118. V. E. Pritchard, D. Rota Martir, S. Oldknow, S. Kai, S. Hiraoka, N. J. Cookson, E. Zysman-Colman and M. J. Hardie, *Chemistry – A European Journal*, 2017, **23**, 6290-6294.
119. V. E. Pritchard, D. Rota Martir, E. Zysman-Colman and M. J. Hardie, *Chemistry – A European Journal*, 2017, **23**, 8839-8849.
120. A. J. McConnell, C. S. Wood, P. P. Neelakandan and J. R. Nitschke, *Chemical Reviews*, 2015, **115**, 7729-7793.
121. W. Wang, Y.-X. Wang and H.-B. Yang, *Chemical Society Reviews*, 2016, **45**, 2656-2693.
122. E. R. Kay, D. A. Leigh and F. Zerbetto, *Angewandte Chemie International Edition*, 2007, **46**, 72-191.
123. A. Coskun, M. Banaszak, R. D. Astumian, J. F. Stoddart and B. A. Grzybowski, *Chemical Society Reviews*, 2012, **41**, 19-30.

124. P. Mobian, J.-M. Kern and J.-P. Sauvage, *Angewandte Chemie International Edition*, 2004, **43**, 2392-2395.
125. S. Durot, F. Reviriego and J.-P. Sauvage, *Dalton Transactions*, 2010, **39**, 10557-10570.
126. N. Weber, C. Hamann, J.-M. Kern and J.-P. Sauvage, *Inorganic Chemistry*, 2003, **42**, 6780-6792.
127. I. Poleschak, J.-M. Kern and J.-P. Sauvage, *Chemical Communications*, 2004, **0**, 474-476.
128. G. Periyasamy, J.-P. Collin, J.-P. Sauvage, R. D. Levine and F. Remacle, *Chemistry – A European Journal*, 2009, **15**, 1310-1313.
129. U. Létinois-Halbes, D. Hanss, J. M. Beierle, J.-P. Collin and J.-P. Sauvage, *Organic Letters*, 2005, **7**, 5753-5756.
130. C. Lincheneau, B. Jean-Denis and T. Gunnlaugsson, *Chemical Communications*, 2014, **50**, 2857-2860.
131. I. C. Gibbs-Hall, N. A. Vermeulen, E. J. Dale, J. J. Henkelis, A. K. Blackburn, J. C. Barnes and J. F. Stoddart, *Journal of the American Chemical Society*, 2015, **137**, 15640-15643.
132. O. Gidron, M. Jirásek, N. Trapp, M.-O. Ebert, X. Zhang and F. Diederich, *Journal of the American Chemical Society*, 2015, **137**, 12502-12505.
133. C. S. Wood, T. K. Ronson, A. M. Belenguer, J. J. Holstein and J. R. Nitschke, *Nature Chemistry*, 2015, **7**, 354.
134. E. M. López-Vidal, M. D. García, C. Peinador and J. M. Quintela, *Chemistry – A European Journal*, 2015, **21**, 2259-2267.
135. P. L. Anelli, N. Spencer and J. F. Stoddart, *Journal of the American Chemical Society*, 1991, **113**, 5131-5133.
136. B. Brough, B. H. Northrop, J. J. Schmidt, H.-R. Tseng, K. N. Houk, J. F. Stoddart and C.-M. Ho, *Proceedings of the National Academy of Sciences*, 2006, **103**, 8583-8588.
137. J. Berná, D. A. Leigh, M. Lubomska, S. M. Mendoza, E. M. Pérez, P. Rudolf, G. Teobaldi and F. Zerbetto, *Nature Materials*, 2005, **4**, 704.
138. M. C. Jiménez, C. Dietrich-Buchecker and J.-P. Sauvage, *Angewandte Chemie International Edition*, 2000, **39**, 3284-3287.
139. P. G. Clark, M. W. Day and R. H. Grubbs, *Journal of the American Chemical Society*, 2009, **131**, 13631-13633.
140. S. M. Goldup, D. A. Leigh, P. J. Lusby, R. T. McBurney and A. M. Z. Slawin, *Angewandte Chemie International Edition*, 2008, **47**, 3381-3384.
141. A. Altieri, F. G. Gatti, E. R. Kay, D. A. Leigh, D. Martel, F. Paolucci, A. M. Z. Slawin and J. K. Y. Wong, *Journal of the American Chemical Society*, 2003, **125**, 8644-8654.
142. V. Balzani, M. Clemente-León, A. Credi, B. Ferrer, M. Venturi, A. H. Flood and J. F. Stoddart, *Proceedings of the National Academy of Sciences*, 2006, **103**, 1178-1183.

143. D.-H. Qu, Q.-C. Wang and H. Tian, *Angewandte Chemie International Edition*, 2005, **44**, 5296-5299.
144. J. E. Green, J. Wook Choi, A. Boukai, Y. Bunimovich, E. Johnston-Halperin, E. DeIonno, Y. Luo, B. A. Sheriff, K. Xu, Y. Shik Shin, H.-R. Tseng, J. F. Stoddart and J. R. Heath, *Nature*, 2007, **445**, 414-417.
145. H. Kim, W. A. Goddard, S. S. Jang, W. R. Dichtel, J. R. Heath and J. F. Stoddart, *The Journal of Physical Chemistry A*, 2009, **113**, 2136-2143.
146. G. De Bo, M. A. Y. Gall, M. O. Kitching, S. Kuschel, D. A. Leigh, D. J. Tetlow and J. W. Ward, *Journal of the American Chemical Society*, 2017, **139**, 10875-10879.
147. S. Kassem, A. T. L. Lee, D. A. Leigh, V. Marcos, L. I. Palmer and S. Pisano, *Nature*, 2017, **549**, 374-378.
148. M. Boiocchi and L. Fabbrizzi, *Chemical Society Reviews*, 2014, **43**, 1835-1847.
149. R. Martinez, I. Ratera, A. Tarraga, P. Molina and J. Veciana, *Chemical Communications*, 2006, **0**, 3809-3811.
150. S. Kume, K. Nomoto, T. Kusamoto and H. Nishihara, *Journal of the American Chemical Society*, 2009, **131**, 14198-14199.
151. S. Kume and H. Nishihara, *Chemical Communications*, 2011, **47**, 415-417.
152. S. Ogi, T. Ikeda, R. Wakabayashi, S. Shinkai and M. Takeuchi, *Chemistry – A European Journal*, 2010, **16**, 8285-8290.
153. Y. Yamada, M. Okamoto, K. Furukawa, T. Kato and K. Tanaka, *Angewandte Chemie International Edition*, 2012, **51**, 709-713.
154. H. Li, X. Li, Y. Wu, H. Ågren and D.-H. Qu, *The Journal of Organic Chemistry*, 2014, **79**, 6996-7004.
155. S. O. Scottwell, J. E. Barnsley, C. J. McAdam, K. C. Gordon and J. D. Crowley, *Chemical Communications*, 2017, **53**, 7628-7631.
156. S.-S. Sun, C. L. Stern, S. T. Nguyen and J. T. Hupp, *Journal of the American Chemical Society*, 2004, **126**, 6314-6326.
157. Y.-R. Zheng, Z. Zhao, M. Wang, K. Ghosh, J. B. Pollock, T. R. Cook and P. J. Stang, *Journal of the American Chemical Society*, 2010, **132**, 16873-16882.
158. J. Heo, Y.-M. Jeon and C. A. Mirkin, *Journal of the American Chemical Society*, 2007, **129**, 7712-7713.
159. A.-M. Stadler and J.-M. P. Lehn, *Journal of the American Chemical Society*, 2014, **136**, 3400-3409.
160. M. Linke, J.-C. Chambron, V. Heitz, J.-P. Sauvage and V. Semetey, *Chemical Communications*, 1998, **0**, 2469-2470.
161. E. Coronado, P. Gaviña, J. Ponce and S. Tatay, *Chemistry – A European Journal*, 2014, **20**, 6939-6950.
162. F. Durola, V. Heitz, F. Reviriego, C. Roche, J.-P. Sauvage, A. Sour and Y. Trolez, *Accounts of Chemical Research*, 2014, **47**, 633-645.
163. J. L. Zhang, J. Q. Zhong, J. D. Lin, W. P. Hu, K. Wu, G. Q. Xu, A. T. S. Wee and W. Chen, *Chemical Society Reviews*, 2015, **44**, 2998-3022.

164. J. Buczyłko, J. C. Saari, R. K. Crouch and K. Palczewski, *Journal of Biological Chemistry*, 1996, **271**, 20621-20630.
165. M. Irie, *Chemical Reviews*, 2000, **100**, 1685-1716.
166. E. Merino and M. Ribagorda, *Beilstein Journal of Organic Chemistry*, 2012, **8**, 1071-1090.
167. H. Rau, *Angewandte Chemie International Edition in English*, 1973, **12**, 224-235.
168. S.-S. Sun, J. A. Anspach and A. J. Lees, *Inorganic Chemistry*, 2002, **41**, 1862-1869.
169. S. Yagai and A. Kitamura, *Chemical Society Reviews*, 2008, **37**, 1520-1529.
170. A. Asadi, D. Ajami and J. Rebek, *Chemical Communications*, 2014, **50**, 533-535.
171. O. B. Berryman, A. C. Sather and J. Rebek Jr, *Chemical Communications*, 2011, **47**, 656-658.
172. F. Würthner and J. Rebek, *Angewandte Chemie International Edition in English*, 1995, **34**, 446-448.
173. F. Durola and J. Rebek, *Angewandte Chemie International Edition*, 2010, **49**, 3189-3191.
174. E. Busseron, J. Lux, M. Degardin and J. Rebek, *Chemical Communications*, 2013, **49**, 4842-4844.
175. O. B. Berryman, A. C. Sather, A. Lledó and J. Rebek, *Angewandte Chemie International Edition*, 2011, **50**, 9400-9403.
176. F. Würthner and J. Rebek, *Journal of the Chemical Society, Perkin Transactions 2*, 1995, **0**, 1727-1734.
177. H. Dube, D. Ajami and J. Rebek, *Angewandte Chemie International Edition*, 2010, **49**, 3192-3195.
178. M. Irie, T. Fukaminato, K. Matsuda and S. Kobatake, *Chemical Reviews*, 2014, **114**, 12174-12277.
179. M. Han, Y. Luo, B. Damaschke, L. Gómez, X. Ribas, A. Jose, P. Peretzki, M. Seibt and G. H. Clever, *Angewandte Chemie International Edition*, 2016, **55**, 445-449.
180. S. Chen, L.-J. Chen, H.-B. Yang, H. Tian and W. Zhu, *Journal of the American Chemical Society*, 2012, **134**, 13596-13599.
181. X. Yan, J.-F. Xu, T. R. Cook, F. Huang, Q.-Z. Yang, C.-H. Tung and P. J. Stang, *Proceedings of the National Academy of Sciences*, 2014, **111**, 8717-8722.
182. W.-Z. Zhang, Y.-F. Han, Y.-J. Lin and G.-X. Jin, *Organometallics*, 2010, **29**, 2842-2849.
183. W.-B. Yu, Y.-F. Han, Y.-J. Lin and G.-X. Jin, *Chemistry – A European Journal*, 2011, **17**, 1863-1871.
184. T. Wu, L.-H. Weng and G.-X. Jin, *Chemical Communications*, 2012, **48**, 4435-4437.
185. T. Yan, L.-Y. Sun, Y.-X. Deng, Y.-F. Han and G.-X. Jin, *Chemistry – A European Journal*, 2015, **21**, 17610-17613.

186. R. Klajn, *Chemical Society Reviews*, 2014, **43**, 148-184.
187. T. Suzuki, T. Kato and H. Shinozaki, *Chemical Communications*, 2004, **0**, 2036-2037.
188. T. Suzuki, Y. Kawata, S. Kahata and T. Kato, *Chemical Communications*, 2003, **0**, 2004-2005.
189. T. Suzuki, Y. Hirahara, K. Bunya and H. Shinozaki, *Journal of Materials Chemistry*, 2010, **20**, 2773-2779.
190. M. Han, R. Michel, B. He, Y.-S. Chen, D. Stalke, M. John and G. H. Clever, *Angewandte Chemie International Edition*, 2013, **52**, 1319-1323.
191. M. J. Hardie, *Chemical Society Reviews*, 2010, **39**, 516-527.
192. R. Ahmad and M. J. Hardie, *CrystEngComm*, 2002, **4**, 227-231.
193. A. Collet, *Tetrahedron*, 1987, **43**, 5725-5759.
194. H. Zimmermann, P. Tolstoy, H.-H. Limbach, R. Poupko and Z. Luz, *The Journal of Physical Chemistry B*, 2004, **108**, 18772-18778.
195. D. S. Bohle and D. J. Stasko, *Inorganic Chemistry*, 2000, **39**, 5768-5770.
196. M. A. Little, J. Donkin, J. Fisher, M. A. Halcrow, J. Loder and M. J. Hardie, *Angewandte Chemie International Edition*, 2012, **51**, 764-766.
197. J. L. Atwood, M. J. Barnes, M. G. Gardiner and C. L. Raston, *Chemical Communications*, 1996, **0**, 1449-1450.
198. T. Brotin and J.-P. Dutasta, *Chemical Reviews*, 2008, **109**, 88-130.
199. C. E. O. Roesky, E. Weber, T. Rambusch, H. Stephan, K. Gloe and M. Czugler, *Chemistry – A European Journal*, 2003, **9**, 1104-1112.
200. L. Garel, J.-P. Dutasta and A. Collet, *Angewandte Chemie International Edition in English*, 1993, **32**, 1169-1171.
201. L. Garel, H. Vezin, J.-P. Dutasta and A. Collet, *Chemical Communications*, 1996, **0**, 719-720.
202. D. J. Cram, T. Kaneda, R. C. Helgeson, S. B. Brown, C. B. Knobler, E. Maverick and K. N. Trueblood, *Journal of the American Chemical Society*, 1985, **107**, 3645-3657.
203. R. M. Fairchild and K. T. Holman, *Journal of the American Chemical Society*, 2005, **127**, 16364-16365.
204. K. Bartik, M. Luhmer, J.-P. Dutasta, A. Collet and J. Reisse, *Journal of the American Chemical Society*, 1998, **120**, 784-791.
205. H. A. Fogarty, P. Berthault, T. Brotin, G. Huber, H. Desvaux and J.-P. Dutasta, *Journal of the American Chemical Society*, 2007, **129**, 10332-10333.
206. O. Perraud, J.-B. Tommasino, V. Robert, B. Albela, L. Khrouz, L. Bonneviot, J.-P. Dutasta and A. Martinez, *Dalton Transactions*, 2013, **42**, 1530-1535.
207. T. Brotin, V. Roy and J.-P. Dutasta, *The Journal of Organic Chemistry*, 2005, **70**, 6187-6195.
208. B. Chatelet, E. Payet, O. Perraud, P. Dimitrov-Raytchev, L.-L. Chapellet, V. r. Dufaud, A. Martinez and J.-P. Dutasta, *Organic Letters*, 2011, **13**, 3706-3709.

209. D. Zhang, K. Jamieson, L. Guy, G. Gao, J.-P. Dutasta and A. Martinez, *Chemical Science*, 2017, **8**, 789-794.
210. Y. Makita, K. Sugimoto, K. Furuyoshi, K. Ikeda, S.-i. Fujiwara, T. Shin-ike and A. Ogawa, *Inorganic Chemistry*, 2010, **49**, 7220-7222.
211. Y. Makita, K. Ikeda, K. Sugimoto, T. Fujita, T. Danno, K. Bobuatong, M. Ehara, S.-i. Fujiwara and A. Ogawa, *Journal of Organometallic Chemistry*, 2012, **706–707**, 26-29.
212. A. Martinez, V. Robert, H. Gornitzka and J.-P. Dutasta, *Chemistry – A European Journal*, 2010, **16**, 520-527.
213. A. Martinez, L. Guy and J.-P. Dutasta, *Journal of the American Chemical Society*, 2010, **132**, 16733-16734.
214. A. Schmitt, O. Perraud, E. Payet, B. Chatelet, B. Bousquet, M. Valls, D. Padula, L. Di Bari, J.-P. Dutasta and A. Martinez, *Organic & Biomolecular Chemistry*, 2014, **12**, 4211-4217.
215. D. Zhang, G. Gao, L. Guy, V. Robert, J.-P. Dutasta and A. Martinez, *Chemical Communications*, 2015, **51**, 2679-2682.
216. J. R. Cochrane, A. Schmitt, U. Wille and C. A. Hutton, *Chemical Communications*, 2013, **49**, 8504-8506.
217. M.-Y. Ku, S.-J. Huang, S.-L. Huang, Y.-H. Liu, C.-C. Lai, S.-M. Peng and S.-H. Chiu, *Chemical Communications*, 2014, **50**, 11709-11712.
218. C. Garcia-Simon, M. Costas and X. Ribas, *Chemical Society Reviews*, 2016, **45**, 40-62.
219. T.-H. Wong, J.-C. Chang, C.-C. Lai, Y.-H. Liu, S.-M. Peng and S.-H. Chiu, *The Journal of Organic Chemistry*, 2014, **79**, 3581-3586.
220. C. Carruthers, T. K. Ronson, C. J. Sumby, A. Westcott, L. P. Harding, T. J. Prior, P. Rizkallah and M. J. Hardie, *Chemistry – A European Journal*, 2008, **14**, 10286-10296.
221. J. J. Henkelis, T. K. Ronson and M. J. Hardie, *CrystEngComm*, 2014, **16**, 3688-3693.
222. J. J. Henkelis, S. A. Barnett, L. P. Harding and M. J. Hardie, *Inorganic Chemistry*, 2012, **51**, 10657-10674.
223. A. Westcott, J. Fisher, L. P. Harding, P. Rizkallah and M. J. Hardie, *Journal of the American Chemical Society*, 2008, **130**, 2950-2951.
224. J. M. Fowler, F. L. Thorp-Greenwood, S. L. Warriner, C. E. Willans and M. J. Hardie, *Chemical Communications*, 2016, **52**, 8699-8702.
225. M. J. Hardie, R. M. Mills and C. J. Sumby, *Organic & Biomolecular Chemistry*, 2004, **2**, 2958-2964.
226. C. J. Sumby, K. C. Gordon, T. J. Walsh and M. J. Hardie, *Chemistry – A European Journal*, 2008, **14**, 4415-4425.
227. C. J. Sumby and M. J. Hardie, *Angewandte Chemie International Edition*, 2005, **44**, 6395-6399.
228. N. J. Cookson, J. J. Henkelis, R. J. Ansell, C. W. G. Fishwick, M. J. Hardie and J. Fisher, *Dalton Transactions*, 2014, **43**, 5657-5661.
229. C. Carruthers, J. Fisher, L. P. Harding and M. J. Hardie, *Dalton Transactions*, 2010, **39**, 355-357.

230. J. J. Henkelis, T. K. Ronson, L. P. Harding and M. J. Hardie, *Chemical Communications*, 2011, **47**, 6560-6562.
231. J. J. Henkelis, C. J. Carruthers, S. E. Chambers, R. Clowes, A. I. Cooper, J. Fisher and M. J. Hardie, *Journal of the American Chemical Society*, 2014, **136**, 14393-14396.
232. M. J. Hardie, *Israel Journal of Chemistry*, 2011, **51**, 807-816.
233. J. J. Henkelis, J. Fisher, S. L. Warriner and M. J. Hardie, *Chemistry – A European Journal*, 2014, **20**, 4117-4125.
234. T. K. Ronson, J. Fisher, L. P. Harding and M. J. Hardie, *Angewandte Chemie International Edition*, 2007, **46**, 9086-9088.
235. T. K. Ronson, C. Carruthers, J. Fisher, T. Brotin, L. P. Harding, P. J. Rizkallah and M. J. Hardie, *Inorganic Chemistry*, 2009, **49**, 675-685.
236. S. T. Mough and K. T. Holman, *Chemical Communications*, 2008, **0**, 1407-1409.
237. B. F. Abrahams, N. J. FitzGerald and R. Robson, *Angewandte Chemie International Edition*, 2010, **49**, 2896-2899.
238. B. F. Abrahams, B. A. Boughton, N. J. FitzGerald, J. L. Holmes and R. Robson, *Chemical Communications*, 2011, **47**, 7404-7406.
239. F. L. Thorp-Greenwood, A. N. Kulak and M. J. Hardie, *Nature Chemistry*, 2015, **7**, 526-531.
240. C. J. Sumby and M. J. Hardie, *Crystal Growth & Design*, 2005, **5**, 1321-1324.
241. T. K. Ronson and M. J. Hardie, *CrystEngComm*, 2008, **10**, 1731-1734.
242. M. J. Hardie and C. J. Sumby, *Inorganic Chemistry*, 2004, **43**, 6872-6874.
243. M. J. Hardie, R. Ahmad and C. J. Sumby, *New Journal of Chemistry*, 2005, **29**, 1231-1240.
244. M. A. Little, T. K. Ronson and M. J. Hardie, *Dalton Transactions*, 2011, **40**, 12217-12227.
245. T. K. Ronson, J. Fisher, L. P. Harding, P. J. Rizkallah, J. E. Warren and M. J. Hardie, *Nature Chemistry*, 2009, **1**, 212-216.
246. D. Xu and R. Warmuth, *Journal of the American Chemical Society*, 2008, **130**, 7520-7521.
247. F. L. Thorp-Greenwood, V. E. Pritchard, M. P. Coogan and M. J. Hardie, *Organometallics*, 2016, **35**, 1632-1642.

Chapter 2

Synthesis of photoresponsive cyclotriguaiacylene derived ligands

2.1 Introduction

The cyclotriguaiacylene cavitand is the principal component to ligands prepared in the Hardie group. As introduced in chapter 1, the three hydroxyl groups can be readily functionalised by appending a variety of metal-coordinating groups including carboxylate,^{1, 2} N-oxides,³ bipyridines,⁴ thiazolyl,⁵ quinolyl,⁶ and terpyridal.⁷ The majority of reports however, focus on the more accessible pyridyl⁸⁻¹⁷ ligand. Depending on the metal-binding unit, a vast array of possible architectures can be formed using these ligands, ranging from small, discrete cage structures such as M_3L_2 metallocryptophanes^{11, 12} to much larger assemblies and coordination polymers.^{2, 3}

Despite a vast library of potential systems, there has been little focus on incorporation of functionality into the ligand design. Such an approach may allow the tuning of these host-guest properties. Recent work by Hardie has described the complexation of a bipyridyl-appended or terpyridal-appended CTG ligands with $[Re(CO)_5Br]$ to form discrete trinuclear rhenium (I) complexes (figure 2.1).¹⁸ These systems displayed rich red-shifted emissive properties compared to the monometallic $[Re(CO)_5Br]$ precursor. Subsequently Hardie has also prepared $[{Ir(ppy)}_2]_3L_2$ metallocryptophanes from the assembly of the same pyridyl ligand with $[Ir(ppy)_2(MeCN)_2]$ (where ppy is 2-phenylpyridine) which also display luminescent properties.¹⁹ These systems represent the most recent efforts to introduce functionality (in this case luminescence) into the metallosupramolecular assemblies formed by CTV derivatives.

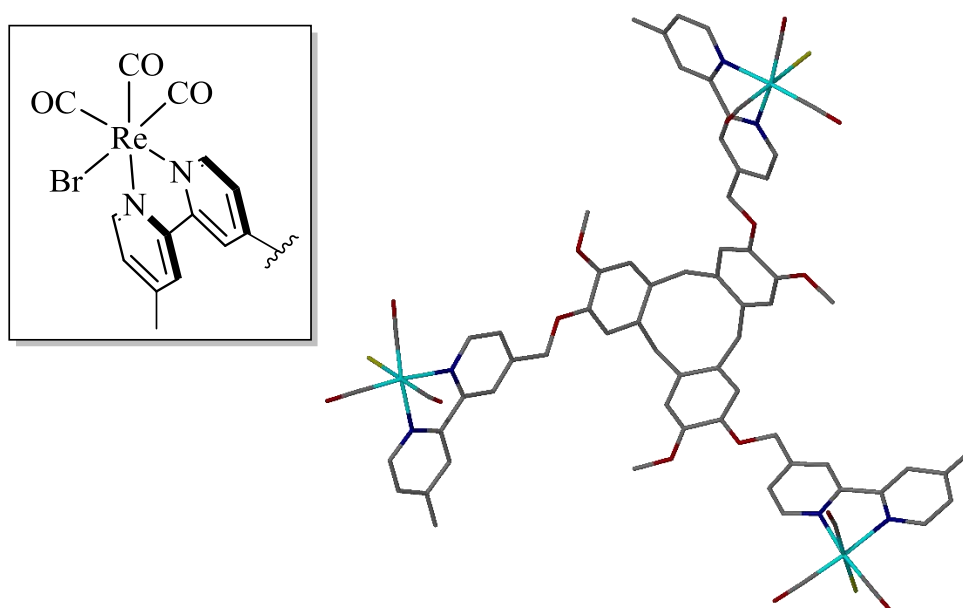


Figure 2.1: SCXRD structure of the trinuclear rhenium (I) complex prepared by Hardie and coworkers.¹⁸ Hydrogen atoms and counterions have been removed for clarity. Inset: Chemical representation of the coordination environment about the metal centre.

The focus of this work is the incorporation of photoresponsive units into the ligand design and thus into the resulting supramolecular systems with an aim to introducing dynamic functionality into these architectures. The azobenzene (AZB) group is a commonly employed photoresponsive moiety. Under ambient conditions, AZB exists in a mixture of two isomers at the N=N double bond, *cis* and *trans* with the *trans* isomer being the predominant isomer due to steric effects. (figure 2.2).²⁰

The thermodynamic barrier to interconversion is small (with the *trans* isomer approximately 12 kcal/mol more stable at room temperature). Upon irradiation with UV light of the appropriate wavelength, the *trans* isomer may convert to the *cis*; the reverse reaction is possible *via* irradiation with visible light or by heating. This process can be repeated multiple times without significant decline in efficiency. Thus AZB has proven to be a valuable photoswitch for a number of applications. The isomerisation is accompanied by a significant conformational change as the phenyl rings transform from a planar arrangement to being perpendicular to one another. The mechanism for this transformation remains heavily debated.²¹

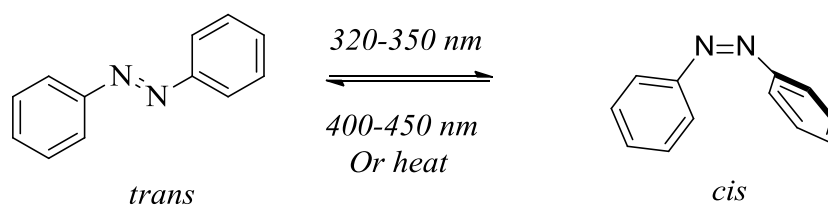


Figure 2.2: Isomerisation of azobenzene using UV light and heat.

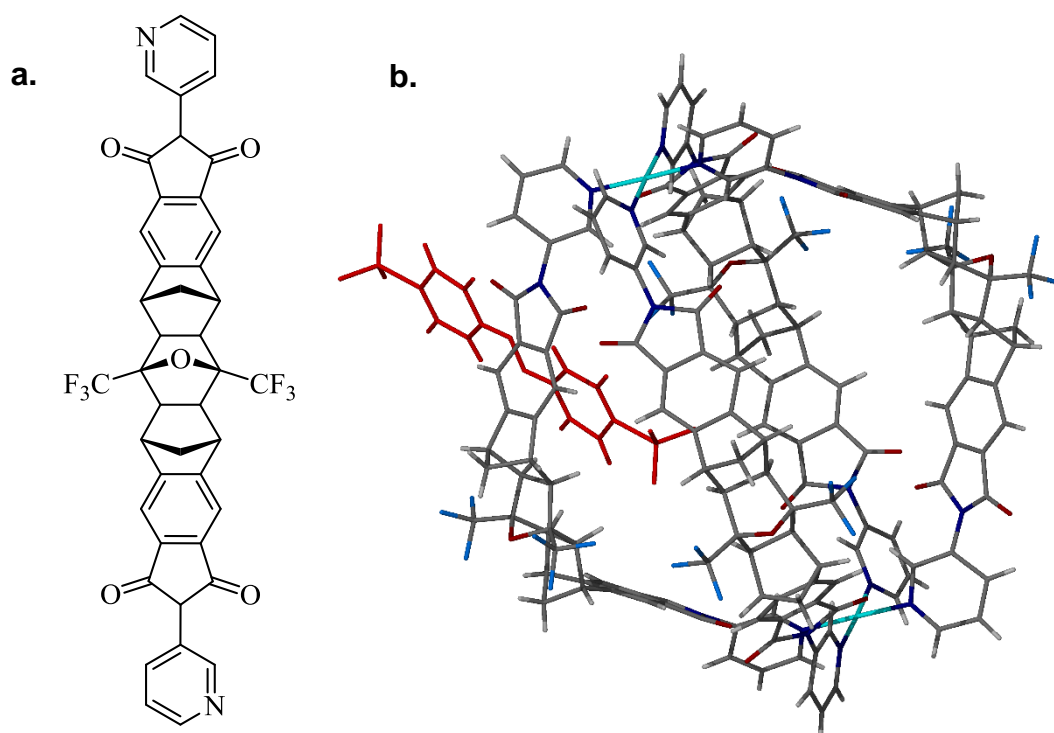


Figure 2.3: The molecular host prepared by Clever²² showing **a.** Chemical structure of the ligand employed; **b.** SCXRD structure of the full M_2L_4 host. *Trans*-4,4'-azobenzene bis-sulfonate guest (necessary for crystallisation) is shown in red and all solvents of crystallisation have been removed for clarity.

Clever and coworkers have recently described a Pd based M_2L_4 molecular host that can be crystallised under the influence of light. When the host encapsulates the *cis*-form of AZB, the compound does not crystallize; conversion to the *trans* isomer using visible light leads to the immediate crystallisation of the complex (figure 2.3).²² In terms of CTV based azo switches, an example from Verboom has been reported where the azo unit has been appended to the CTV scaffold.²³ The resulting cavitaⁿd was able to act as a sensor for Hg^{2+} ions *via* the azo nitrogen which upon the binding of mercury

leads to a colour change from yellow to red. This coordination of the azo nitrogen atoms precludes their ability to undergo photoswitching. Furthermore, no coordination is possible at any site other than the azo nitrogen atoms. However there are examples of other cavitands bearing AZB fragments, though these are predominantly organic based.

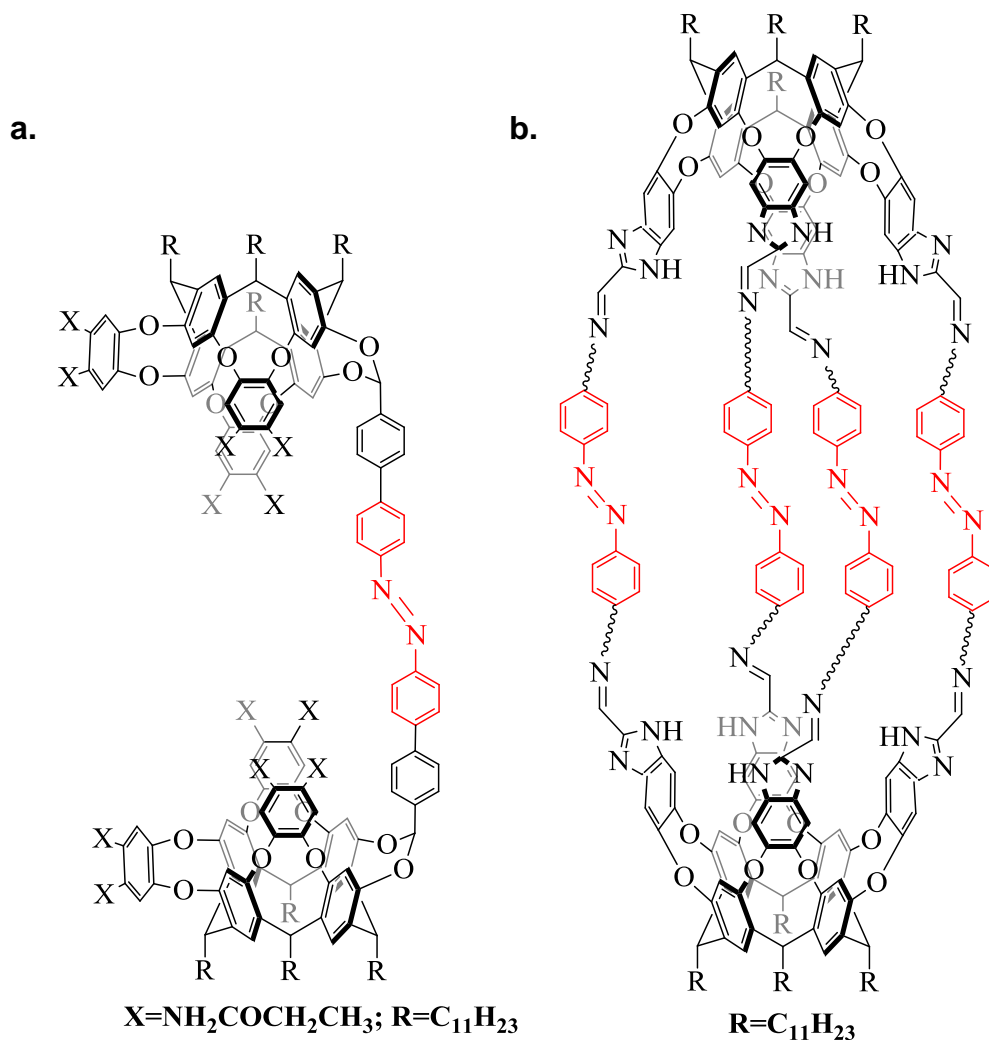


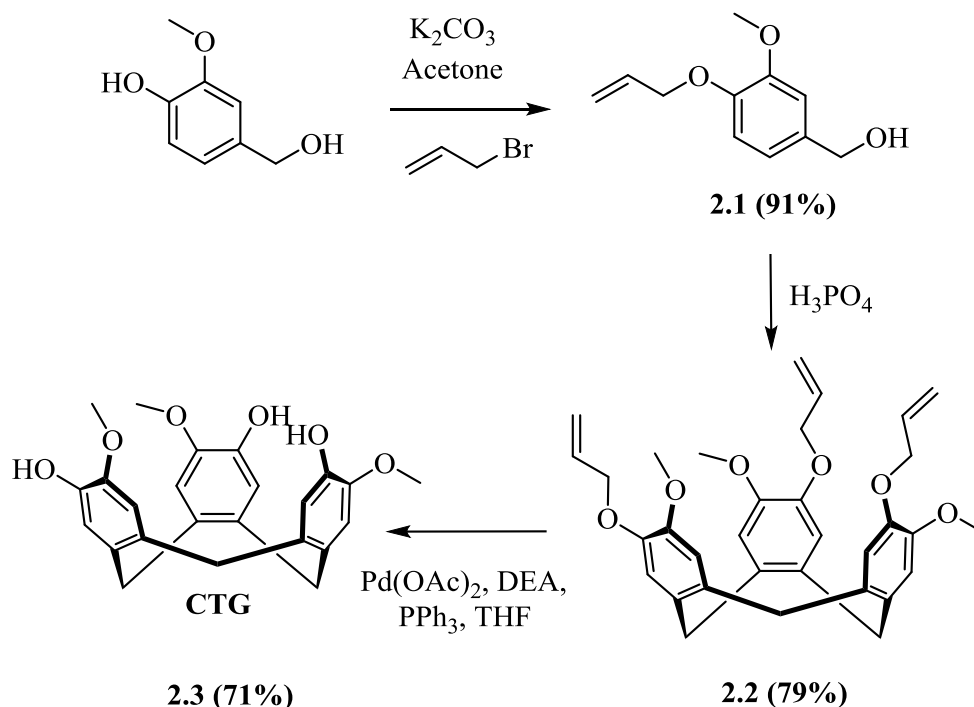
Figure 2.4: Molecular hosts prepared by Rebek showing **a.** Photoswitchable deep cavitand capable of regulating binding of adamantane;²⁴ **b.** Organic capsule capable of squalene binding.²⁵

Rebek has reported a ditopic photoswitchable cavitand²⁴ that was able to undergo efficient *cis-trans* isomerisation (figure 2.4a). This structure was able to regulate the binding affinity of adamantane guests depending on its configuration. Rebek has also reported an organic based capsule (figure 2.4b) where the bridging units are AZB units. Although this system was shown to be able to encapsulate long chain organic guests such as squalene, no photoisomerization data for the system was reported.²⁵

This chapter concerns the synthesis and characterisation of cyclotriguaiacylene derived ligands that bear azobenzene (AZB) and stilbene (SBN) groups in the ligand design. This introduces photoresponsive elements into the ligand design itself, a phenomena which has been hitherto unexplored in CTG chemistry. In turn, the design of such ligands may lead to photoresponsive self-assembled coordination compounds which can offer control over the uptake of guest molecules. When combined with the large array of structures possible with CTG derivatives, this strategy has great potential in host-guest chemistry.

2.2 Cyclotriguaiacylene synthesis

The synthesis of the CTG framework itself is well established and occurs in a three step procedure as illustrated in Scheme 2.1. Protection of the starting isovanillyl alcohol is achieved using allyl bromide and potassium carbonate in acetone to give the protected analogue **2.1** in excellent yields (>90%). This compound is then treated with superphosphoric acid in a solvent-free reaction to give the protected cyclised product **2.2**. Deprotection of **2.2** is achieved with palladium acetate and triphenylphosphine in dry THF to give the *tris*-hydroxy cavitand, CTG (**2.3**) as an off-white solid in a respectable yield (71%).²⁶



Scheme 2.1: Three-step literature procedure of CTG (compound 2.3).

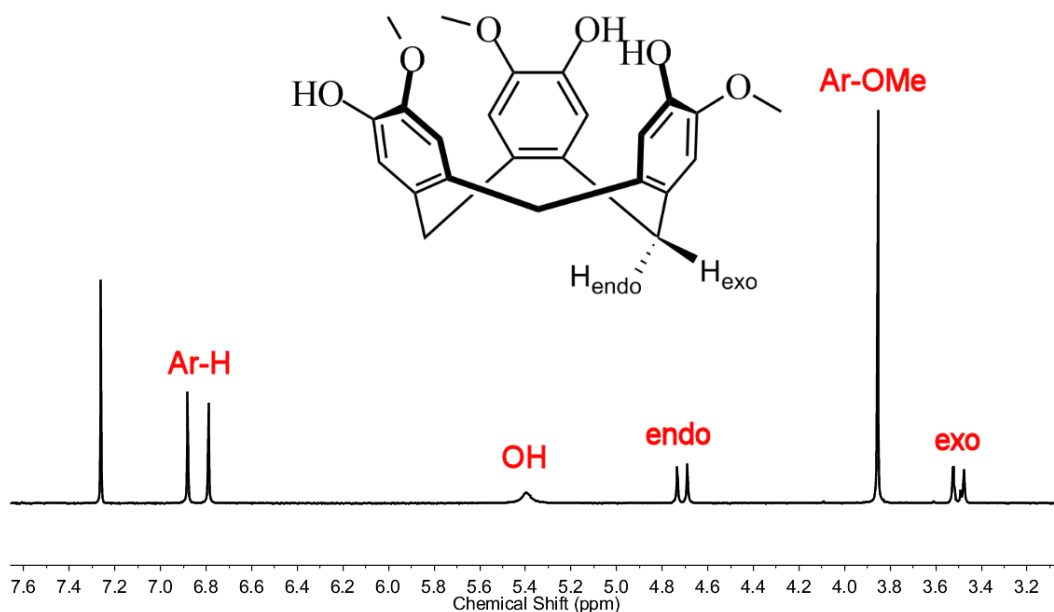


Figure 2.5: Interpreted ¹H NMR spectrum of CTG (compound 2.3) in CDCl₃.

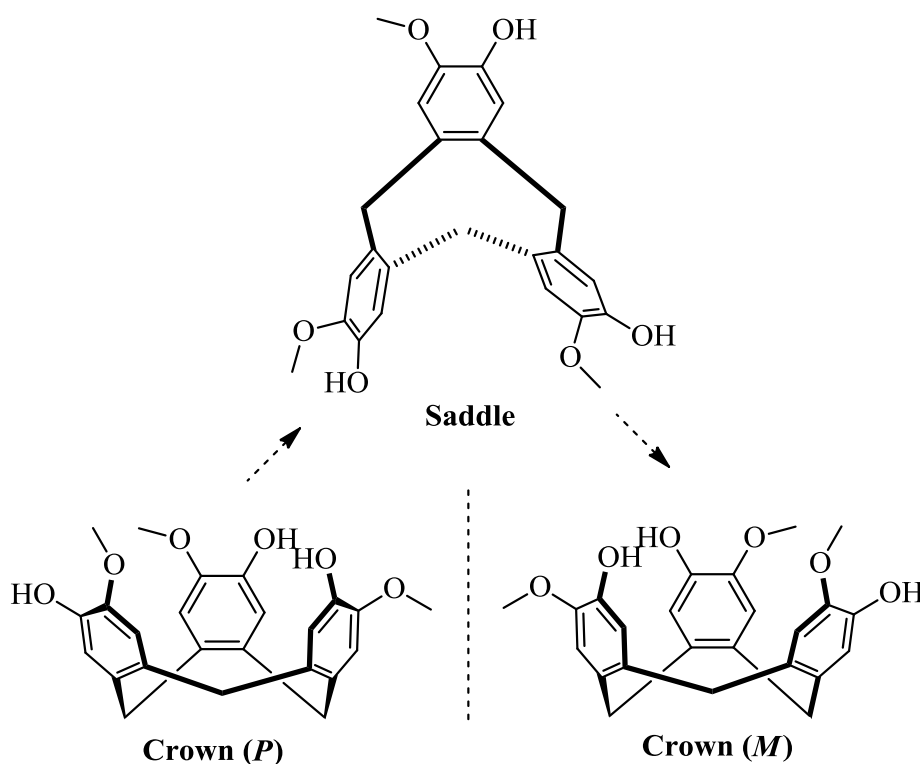


Figure 2.6: Enantiomeric interconversion of CTG via the saddle conformation.

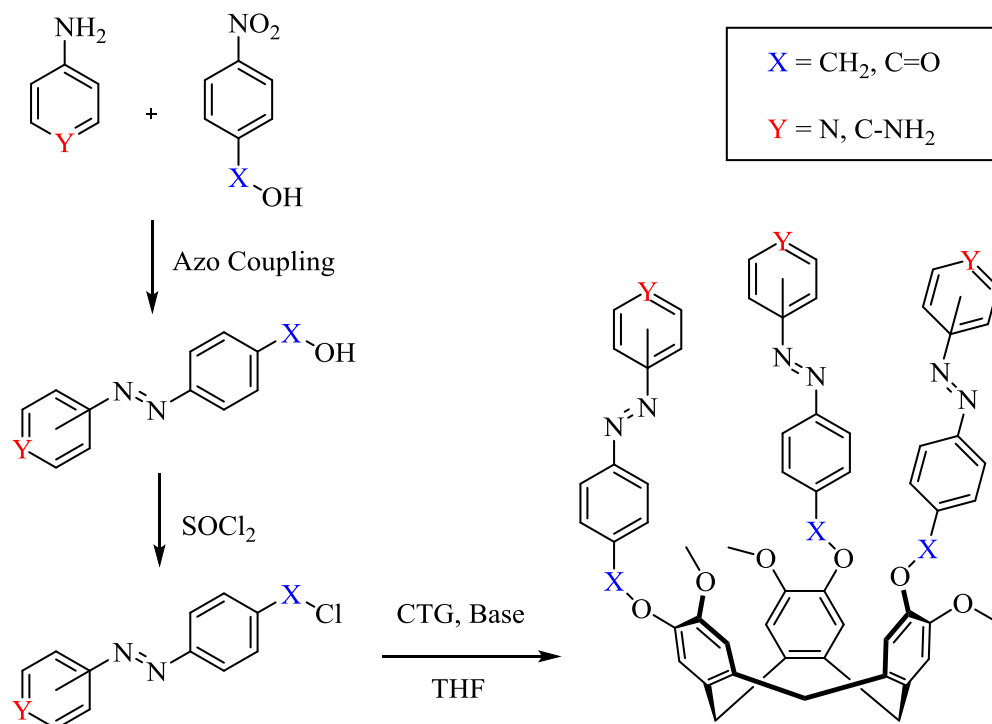
The ¹H NMR spectrum of compound 2.3 is illustrated in figure 2.5 and displays the diagnostic *endo* and *exo* diastereotopic protons at 4.71 and 3.46 ppm respectively which are characteristic of crown conformation CTV derivatives. The CTG unit is formed as a racemic mixture of *P* and *M* isomers; while these isomers are resolvable

using chiral HPLC facilities, the presence of the saddle conformation (figure 2.6) ensures there is always a route to interconversion in solution, despite this saddle being higher in energy than both crown conformations.²⁷

The isomerisation is slow with Steed and more recently Mendoza determining the half-life to inversion to be approximately one month under ambient conditions;²⁸ more recently Mendoza has found racemisation of CTV based hydrogen bonded capsules requires several hours in solution.²⁹ As this isomerisation does not impede ligand and complex synthesis, no attempt has been made to resolve these isomers and all ligands discussed in this chapter have been synthesised using racemic mixtures of CTG and are thus racemic themselves.

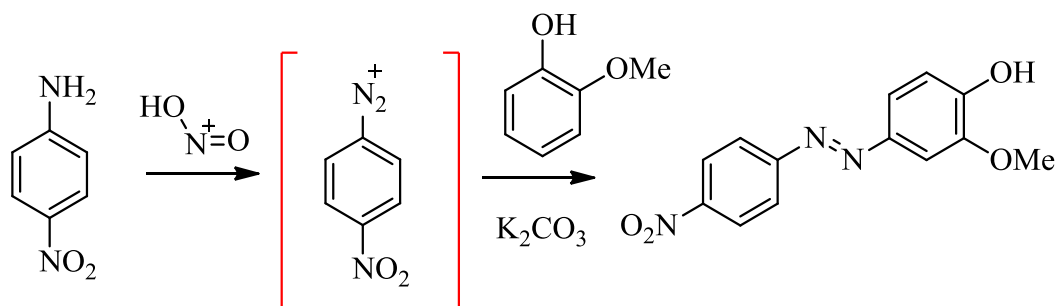
2.3 Azobenzene precursors

To synthesise ligands bearing the photoresponsive AZB unit, the AZB fragment must be linked to CTG via the hydroxyl group whilst maintaining a metal coordinating group on the other side of the azo bond. The general design of such a ligand is shown in scheme 2.2. The addition of a carboxylic acid or benzylic alcohol to one of the rings would allow conversion to the acid or alkyl chlorides; the connection of these functional groups to CTG is already well established. Of particular interest would be ligands where Y is a pyridyl group; pyridyl appended CTG ligands have displayed interesting self-assembly properties in previous publications.^{9, 11, 12, 30}



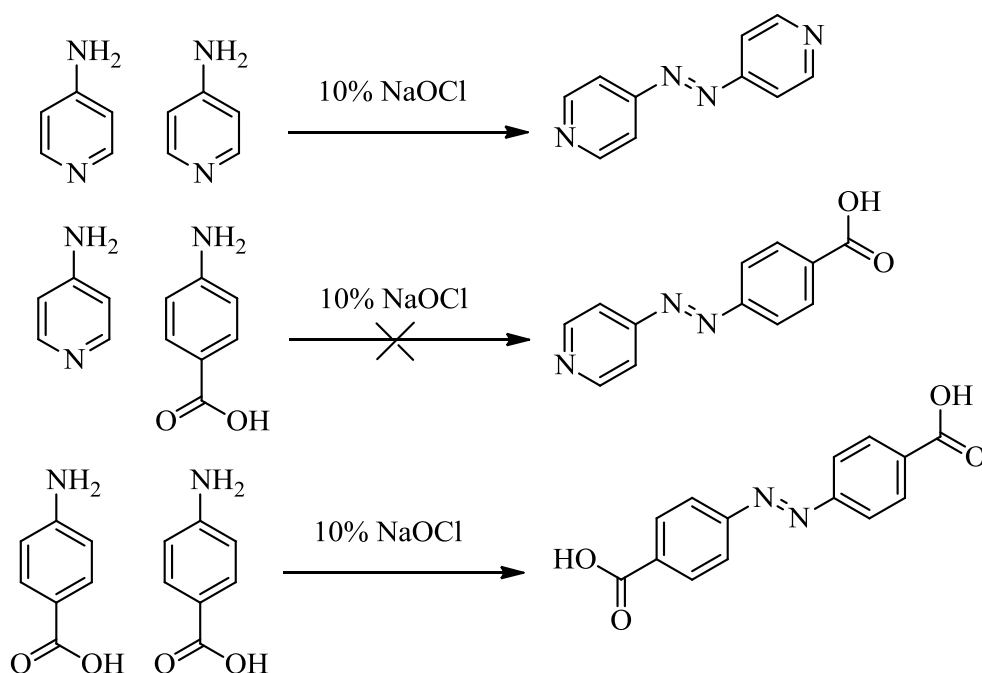
Scheme 2.2: Proposed route to AZB appended CTG ligands bearing pyridyl coordinating moieties.

Many different methods exist for the synthesis of aromatic azobenzenes with a comprehensive review published in 2011 by Merino and coworkers;³¹ however very few focus on the production of asymmetric azopyridines of the type shown in scheme 2.2 making the design of synthetic methodology challenging. The majority of azo compounds are produced *via* diazo coupling reactions using nitrous acid generated *in situ* (scheme 2.3) but this method is typically very sensitive to both pH and electron-withdrawing substituents on the phenolic reaction partner.³¹ Whilst highly effective in the preparation of a variety of azobenzenes, the strongly electron-withdrawing pyridyl unit renders this method infeasible for the preparation of the target compounds:



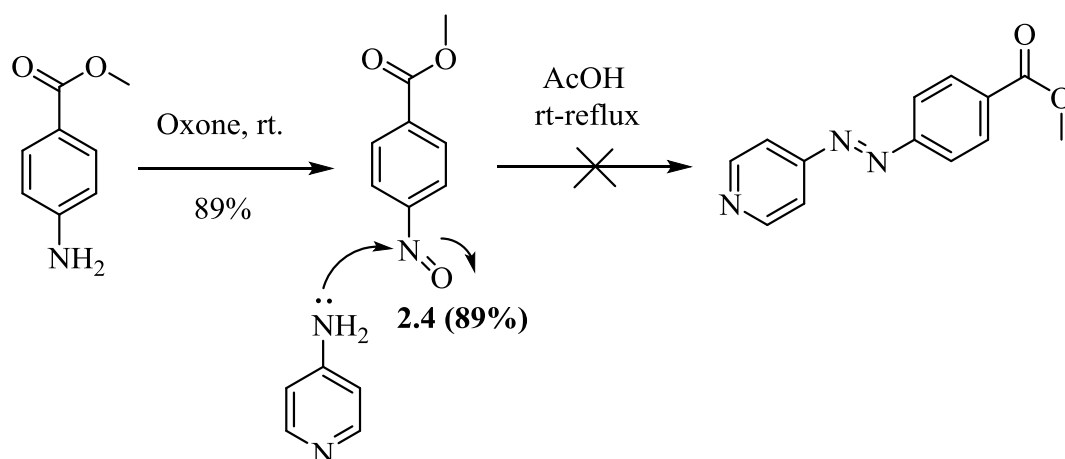
Scheme 2.3: Diazo coupling reaction.

A more promising synthesis was reported by Takumi and co-workers using 10% sodium hypochlorite as an oxidant in the reaction between 4-aminopyridine and 4-aminobenzoic acid to produce an asymmetrical pyridyl based azo compound.³² However no detailed experimental procedures or characterising data were reported and all attempts to reproduce these findings in our laboratory were unsuccessful despite intensive investigation into reaction conditions. It was found that the two reaction partners tended to homocouple preferentially to form symmetrical products even when working under dilute conditions (scheme 2.4).



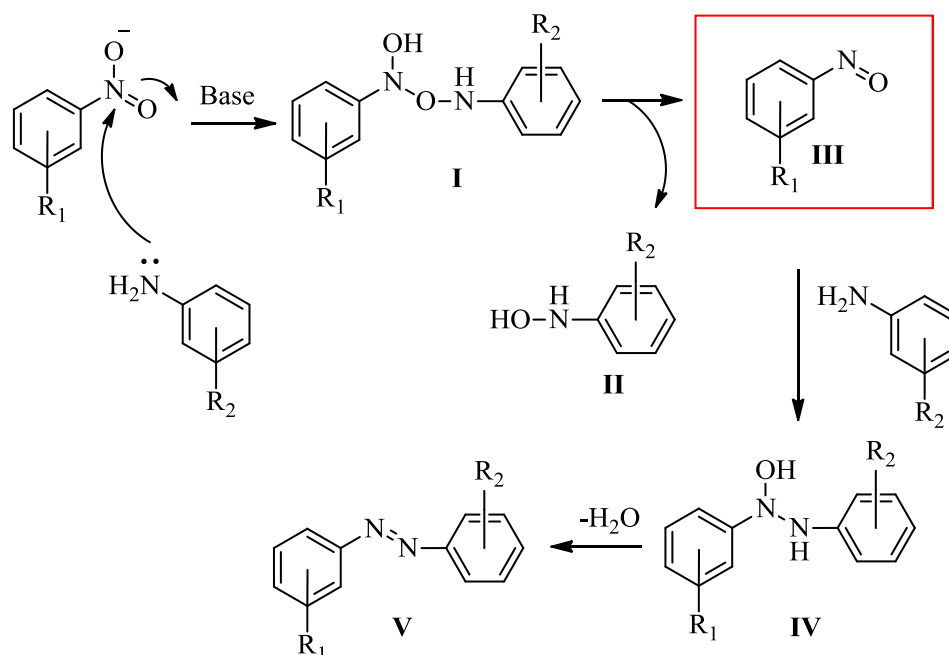
Scheme 2.4: Attempted coupling reactions using NaOCl; only homocoupled products were isolated.

With direct diazo and oxidative coupling unsuitable, a different strategy was implemented. The Mills reaction is used to couple aromatic nitroso compounds with aryl amines in the presence of acetic acid to form azobenzenes (scheme 2.5).³¹ A suitable nitroso arene, 4-nitroso methyl benzoate (**2.4**) was readily prepared in good yields from 4-amino methyl benzoate using potassium peroxydisulfate (Oxone)³³ with the biphasic solvent system of DCM/H₂O preventing over-oxidation to the nitro derivative. However the subsequent condensation reaction with aminopyridines to form the desired azo compounds was unsuccessful despite a variety of reaction conditions with only starting materials isolated after prolonged reaction times. Presumably this is once again due to low electron density present on the amine which hampers initial attack on the nitrosoarene.



Scheme 2.5: Attempted Mills reaction to form desired asymmetrical azopyridine.

With the failure of ‘traditional’ methods of synthesising the target azopyridines, a report from Zhao and co-workers³⁴ was investigated. Their method employed a base catalysed synthesis to form a library of asymmetrical azobenzenes from the condensation of the corresponding nitrobenzenes and anilines. As illustrated in scheme 2.6, their postulated mechanism involved the initial attack of the aniline on the nitroarene to form intermediate **I**. This unstable intermediate then eliminates a substituted phenylhydroxylamine **II** to give the key reactive intermediate, nitroso **III** (red box). This can then react with another molecule of amine before elimination of water to give the product azobenzene, **V**.



Scheme 2.6: Proposed mechanism of base catalysed azobenzene synthesis as reported by Zhao and coworkers.³⁴

The direct application of this method to the synthesis of the target azopyridines using 4-aminopyridine and 4-nitrobenzoic acid was unsuccessful as the initial step still requires an electron-rich amine (such as aniline) to attack the nitro group; despite harsh reaction conditions (150°C in refluxing DMF for several days), only starting materials were obtained. It was postulated that a more reactive reaction partner for the aminopyridine would help overcome this problem. Therefore the reaction was conducted using the more reactive nitrosoarene **2.4**³⁵ in place of 4-nitrobenzoic acid. An excess of 4-aminopyridine and high temperatures was used to attempt to drive the reaction towards the target azopyridine. This strategy ensured only one of the challenging nucleophilic steps was required and that a more reactive electrophile was present:

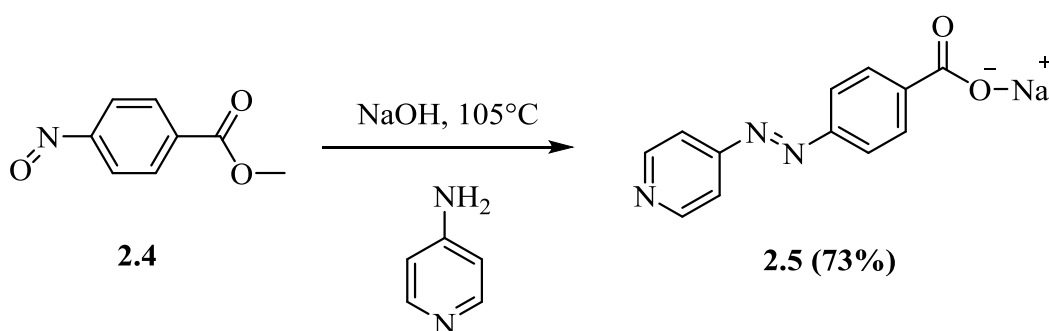


Figure 2.7: Adapted azo coupling using nitroso intermediate **2.4**.

Use of the nitroso intermediate resulted in successful conversion to the desired azopyridine **2.5** which was isolated as an orange solid in excellent yield. The basic environment also hydrolyses the ester group to a carboxylate as noted by the absence of ester peaks (ca. 4.0 ppm) in the ¹H NMR spectrum of **2.5** (figure 2.8). A simple aromatic region is observed with four resonances of equal integration corresponding to the expected four environments in the compound. A significant amount of residual water (3.3ppm) was also present. No acidic workup was necessary as upon cooling of the reaction vessel to ambient temperature, **2.5** rapidly crystallises from solution as the sodium salt, facilitating an easy isolation of product. Compound **2.5** gave excellent ESI mass spectrometry data with a single peak at [226.06]⁻ in negative ion mode which was assigned as the [M]⁻ species observed without the associated sodium ion.

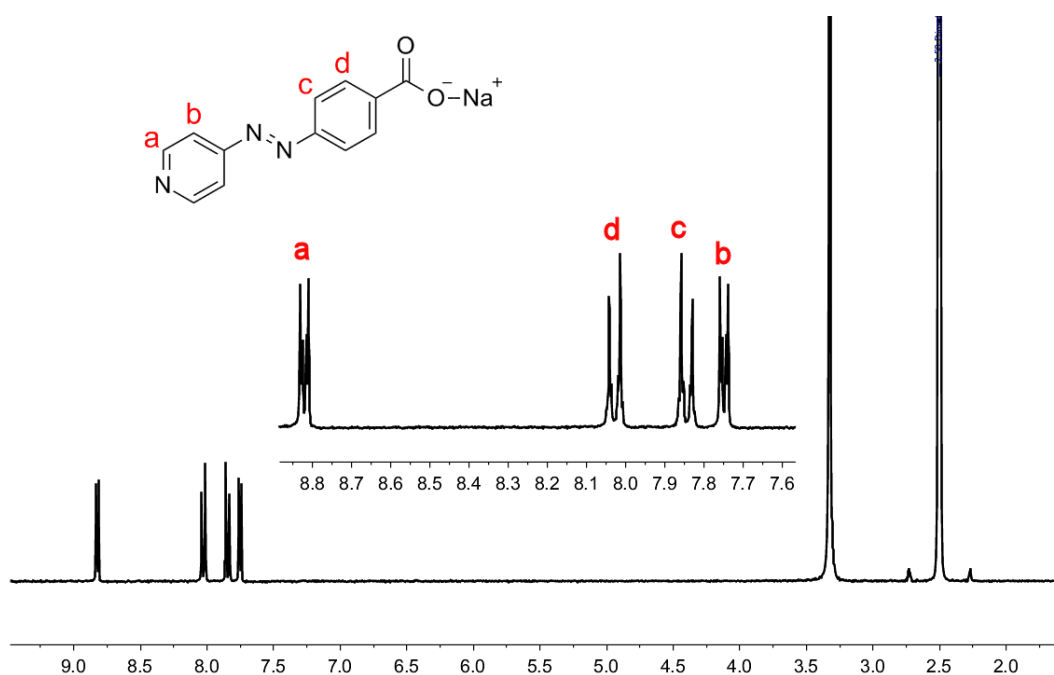


Figure 2.8: 300MHz ^1H NMR spectrum of compound **2.5** in d^6 -DMSO; inset: interpretation of aromatic region.

Confirmation of the structure of **2.5** was obtained from X-ray diffraction. Orange needles of **2.5** were obtained from the slow evaporation of solvent from a saturated solution in water. The structure solved in the $P\bar{1}$ space group with a triclinic unit cell. In the solid state, the compound exists as a hydrated sodium dimer with the formula $[\text{Na}_2(2.5)_2(\text{H}_2\text{O})_8]_n$, figure 2.9. Combustion analysis of **2.5** is also consistent with this structure. Despite being a relatively simple motif to envision, such adducts are surprisingly uncommon in the literature with only a few examples noticeably similar to the one found in **2.5**.³⁶⁻³⁸ All of the azobenzene units are observed in their more thermodynamically favourable *trans* isomer.

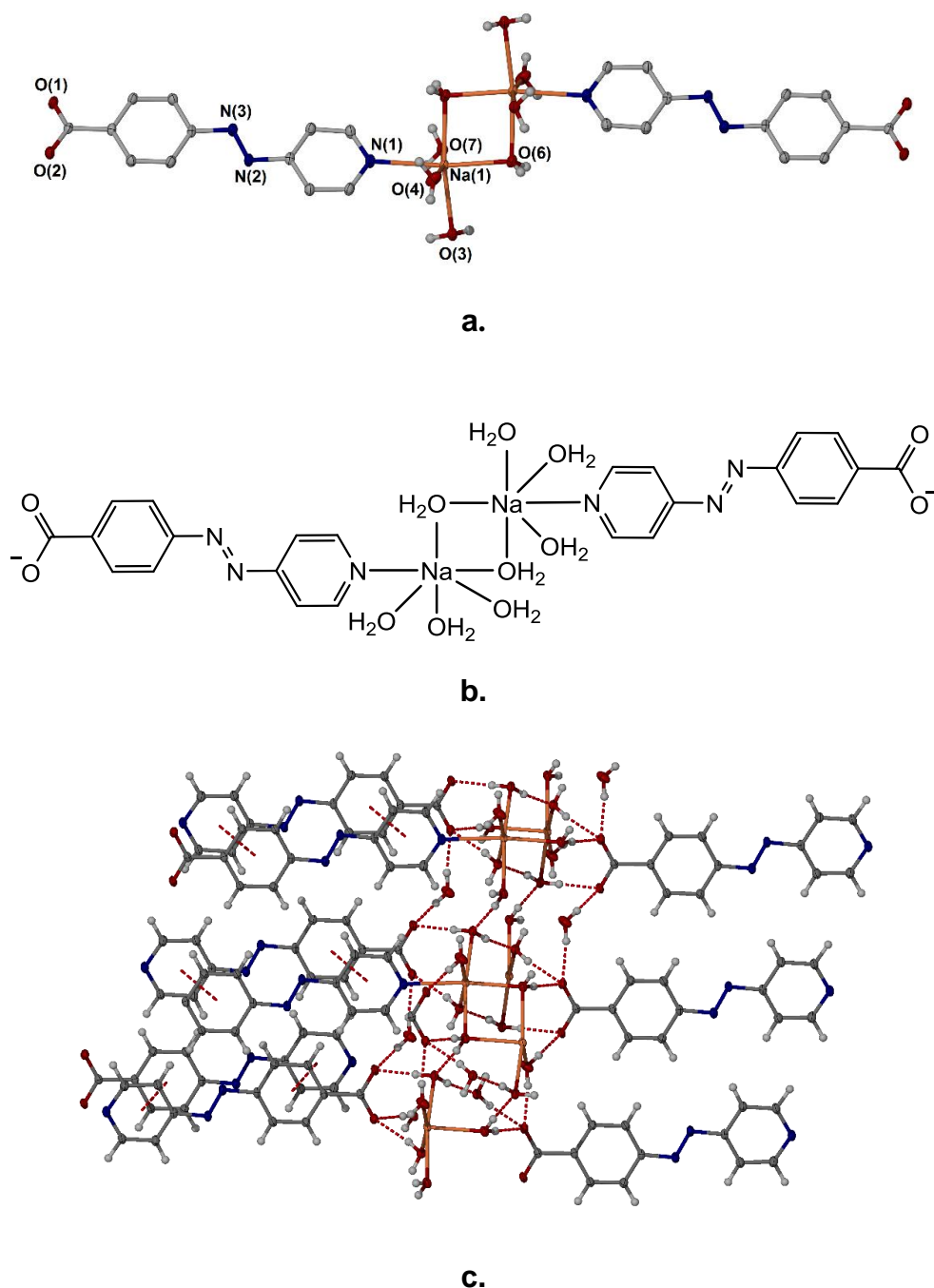


Figure 2.9: From the SCXRD structure of compound **2.5** showing **a.** Individual sodium bridged dimer; **b.** Chemical representation of the sodium bridged dimer; **c.** Extended hydrogen bonded network showing aromatic π - π stacking between adjacent layers; ellipsoids are displayed at 50% probability level.

Selected bond lengths and angles from the dimer are given in table 2.1. The pyridyl units coordinate to bridging sodium dimers of formula $[\text{Na}(\mu\text{-OH}_2)(\text{OH}_2)_3]_2$, thus bridging between two ligands (figure 2.9a). The carboxylate units do not coordinate, instead forming a hydrogen bonded network with further hydrated sodium dimers

(figure 2.9b); each carboxylate unit forms up to five hydrogen bonds with neighbouring water molecules with typical O---H-O distances of 1.948(10) Å. The aromatic units in different layers are slightly offset but are at an ideal distance (3.800 Å) for aromatic π - π stacking. The preference of the system to coordinate *via* the pyridyl units rather than the carboxylates is somewhat surprising given the hard nature of the sodium cation; it would be expected to prefer hard coordinating atoms such as the carboxylate oxygens.

Table 2.1: Selected bond lengths (Å) and angles (°) from the crystal structure of $[Na_2(2.5)_2(H_2O)_8]_n$.

N (1) – Na(1)	2.573(12)	N (1)-Na(1)-O(3)	40.84(3)
Na (1) – O(6)	2.381(12)	O (1)---H-O	172.87(6)
O (1)---H-O	1.940(14), 1.948(10), 1.951(1)	O (2)---H-O	175.14(4)
O (2)---H-O	1.841(11), 1.926(10)		

The investigation of this synthetic route was then extended to the synthesis of the 2-pyridyl and 3-pyridyl analogues of **2.5**. The reaction of 3-aminopyridine with 4-nitroso methyl benzoate **2.4** under the same conditions furnished the novel azopyridine **2.6** as an orange solid. Once again, ^1H NMR and ESI mass spectrometry confirmed successful product formation and hydrolysis of the ester group in **2.4**. The ^1H NMR spectrum (figure 2.10) displays the expected four environments for the desymmetrised pyridyl ring along with the usual two doublets from the arene ring. ESI mass spectrometry also showed good evidence for product formation with a single peak at m/z [227.9684] corresponding to the $\{M + H\}^+$ ion. Combustion analysis was also consistent with product formation.

The melting points of both **2.5** and **2.6** were found to be significantly higher ($>300^\circ\text{C}$) than commercially available *p*-phenylazobenzoic acid (mp $248\text{-}250^\circ\text{C}$).³⁹ This is likely to be a consequence of the extensive hydrogen bonded network. The infrared spectra of these salts contain a broad band between $3500\text{-}3000\text{cm}^{-1}$ indicating hydrogen bonded OH stretching. The C=O stretch is also affected, appearing at $1590\text{-}1600\text{cm}^{-1}$ which is consistent with a carboxylate salt rather than a carboxylic acid. The azobenzene N=N bond is inactive in IR spectroscopy and thus not observed.⁴⁰

Over time in solution, new peaks were observed to appear which were identified as spontaneous isomerisation to the *cis* isomer of **2.6** (red stars, figure 2.10). This isomerisation to the *cis* form without any form of irradiation was unexpected and is highly irregular owing to the traditional instability of *cis*-azobenzenes compared to their *trans* counterparts. Few reports of thermodynamically stable *cis*-azobenzenes are present, with the majority being cyclised variants that are locked into the *cis*-conformation.⁴¹⁻⁴³

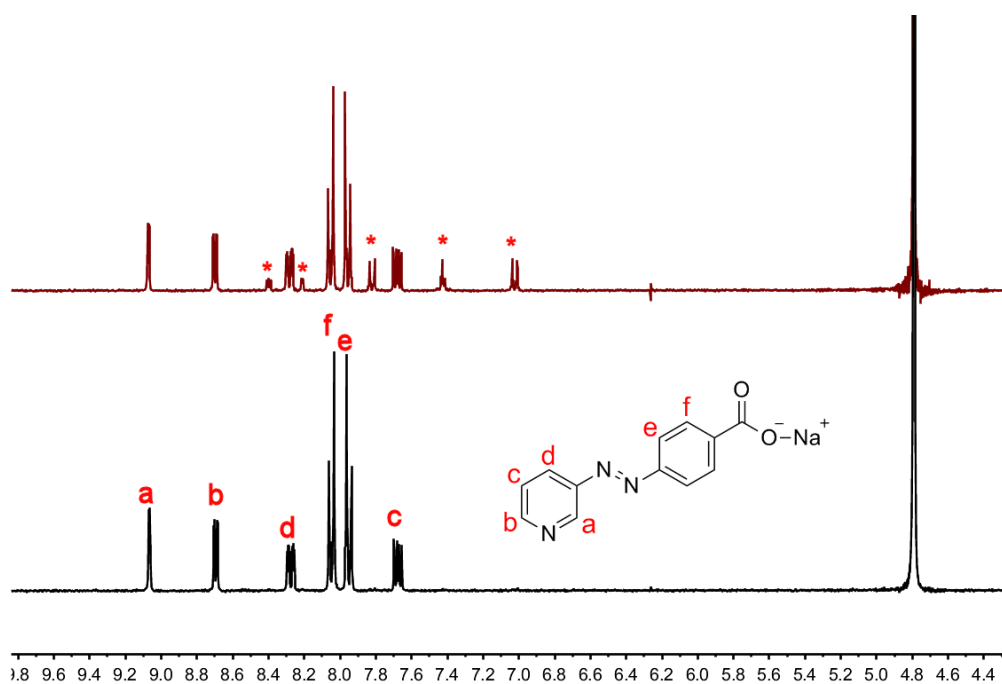


Figure 2.10: Changes to the ¹H NMR spectrum of compound **2.6** in D₂O over time; initial spectrum (black trace) and after 12 hours in solution (red trace).

The structure of **2.6** was again confirmed by X-ray diffraction. Orange needles of compound **2.6** were once again obtained from the slow evaporation of solvent from a saturated solution in water. The structure solves in the monoclinic *P2₁/n* space group. Interestingly, the pyridyl units no longer coordinate, instead forming a hydrogen bonded network with neighbouring water molecules in the same fashion as the carboxylate units; each carboxylate can form up to six hydrogen bonds to neighbouring water with each pyridyl unit forming one. The resulting structure should therefore be regarded as a hydrogen bonded assembly rather than a sodium salt. The offset π - π stacking between layers is maintained in this isomer with distances between aromatic rings in neighbouring layers at 3.854 Å. No evidence for the *cis* isomer is seen in the solid state, with all of the azobenzene units found in the *trans* orientation.

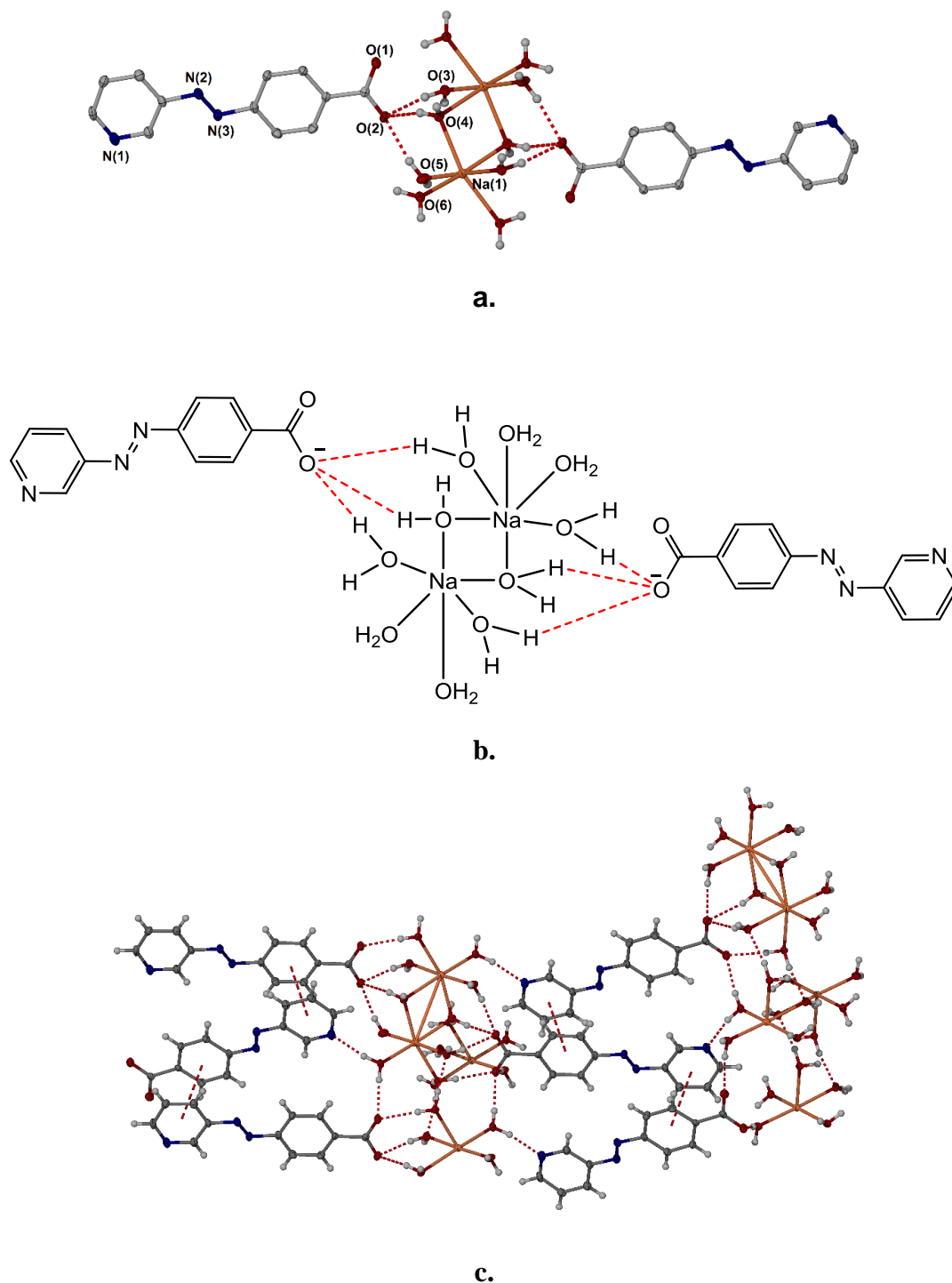


Figure 2.11: From the SCXRD structure of compound 2.6 showing a. Bridging sodium dimer connecting two units of compound 2.6; b. Chemical representation of the sodium bridged dimer, with hydrogen bonds shown in red for clarity; c. Part of the extended hydrogen bonding network, showing hydrogen bonds to the pyridyl units as well as the offset alignment resulting in aromatic π - π stacking. Ellipsoids are displayed at 50% probability level.

Table 2.2: Selected bond lengths (Å) and angles (°) from the crystal structure of $[Na_2(2.5)_2(H_2O)_8]_n$.

N (1)---H-O	1.94(4)	N (1)-Na(1)-O(3)	117.95(11)
Na (1) – O(6)	2.319(3)	O (1)---H-O	174.02(4)
O (1)---H-O	2.022(4), 1.942(4)	O (2)---H-O	171.59(4)
O (2)---H-O	1.953(5), 1.904(5), 2.13(4)		

Attempts to furnish the 2-pyridyl analogue **2.7** under the same conditions resulted in no product precipitation upon cooling of the reaction vessel. Upon acidifying to pH 6 with dilute hydrochloric acid resulted in the precipitation of a yellow solid which was initially unidentifiable by ^1H NMR. Single crystals of this material were grown once again from the slow evaporation of a saturated solution of the compound in water and the resulting compound was found to be the cyclised triazine **2.8** shown in figure 2.12. Examination of the literature found that 2-azopyridines can be prone to such cyclisation reactions in the presence of acid:⁴⁴ as connecting these arms to the CTG scaffold is conducted in the presence of acid, the 2-azopyridines were not investigated further.

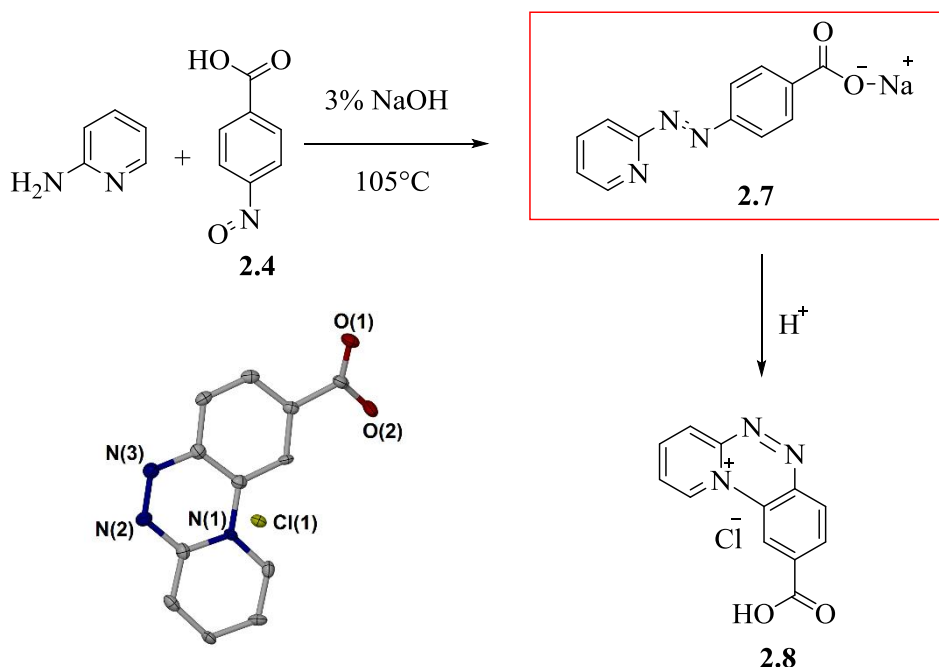
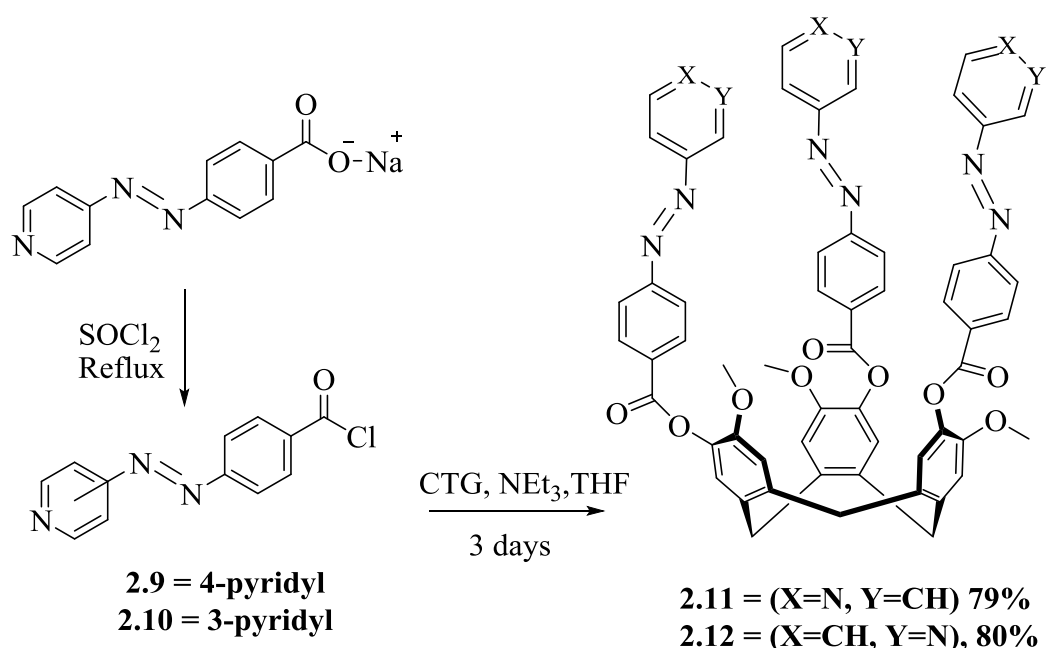


Figure 2.12: Formation of azopyridine **2.7** (red box) before acid catalysed cyclisation to triazine **2.8**.

2.4 Azobenzene (AZB) appended CTG ligands

With the successful preparation of azobenzene ‘arms’ **2.5** and **2.6**, the formation of novel CTG ligands bearing azobenzene groups was investigated. The reaction of **2.5** or **2.6** in refluxing thionyl chloride led to the formation of the acid chlorides **2.9** and **2.10** respectively as pale red solids after removal of the solvent. These were then reacted immediately with CTG in the presence of triethylamine in dry THF and after three days furnished the novel azobenzene appended CTG ligands **2.11** and **2.12** respectively as orange solids in respectable yields (scheme 2.7).



Scheme 2.7: Formation of AZB appended ligands 2.11 and 2.12.

The formation of these ligands was confirmed by ^1H NMR spectroscopy (figure 2.16) and ESI mass spectrometry. The ^1H NMR spectrum shows the characteristic endo and exo diastereotopic protons (j and k) as doublets at 4.86 and 3.72 ppm respectively. The symmetry of these peaks indicates full conversion to a trimeric ligand as incomplete substitution of the CTG arms leads to broad multiplets in this region. The overall symmetry of the spectrum also indicates an all *trans* arrangement of azobenzene units as the presence of any *cis* units would result in inequivalent protons on the azobenzene side-arms and the spectrum would likely be far more complex. Integrating the side-arm peaks against those arising from CTG confirms a trimeric structure. No evidence of any changes to the ^1H NMR spectrum were observed over time in contrast to observations of the free arm **2.6**.

The composition of ligands **2.11** and **2.12** were also ascertained with ^{13}C NMR, combustion analysis and infrared spectroscopy, all of which were consistent with the proposed structure. The infrared spectra of these compounds contain the expected strong C=O stretch at $1733\text{-}1740\text{cm}^{-1}$. As expected this is higher than in the free salts due to the C=O environment of an ester rather than a carboxylate salt. Combustion analysis confirms the structure of the desired products with each giving consistent data for the **2.11** + H_2O + CHCl_3 and **2.12** + H_2O . The observation of individual solvent units during combustion analysis is relatively common for CTG derivatives and is therefore unsurprising here.

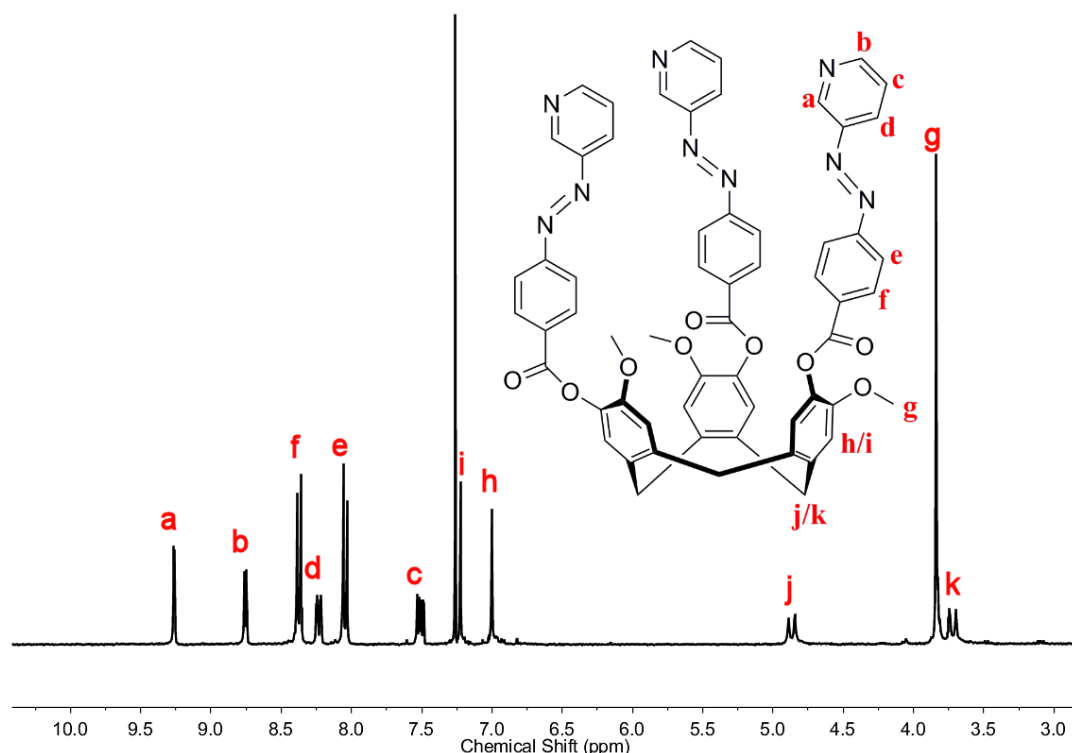


Figure 2.13: Interpreted ^1H NMR spectrum of compound **2.12** in CDCl_3 .

Ligand **2.11** gave excellent mass spectrometry data with peaks at m/z $[1036.34]^+$, $[1053.39]^+$, $[1555.01]^+$ and $[2072.68]^+$ which were assigned as the $\{\text{M} + \text{H}\}^+$, $\{\text{M} + \text{H}_2\text{O}\}^+$, $\{3\text{M} + 2\text{H}\}^{2+}$ and $\{2\text{M} + \text{H}\}^+$ ions respectively (figure 2.14). Ligand **2.12** also gave consistent mass data with peaks observed at $[1036.33]^+$, $[1554.95]^{2+}$ and $[2072.54]^{2+}$ which were assigned as the $\{\text{M} + \text{H}\}^+$, $\{3\text{M} + 2\text{H}\}^{2+}$ and $\{2\text{M} + 2\text{H}\}^{2+}$ peaks with the observation of two ligands flying together not uncommon for ligands of this type.

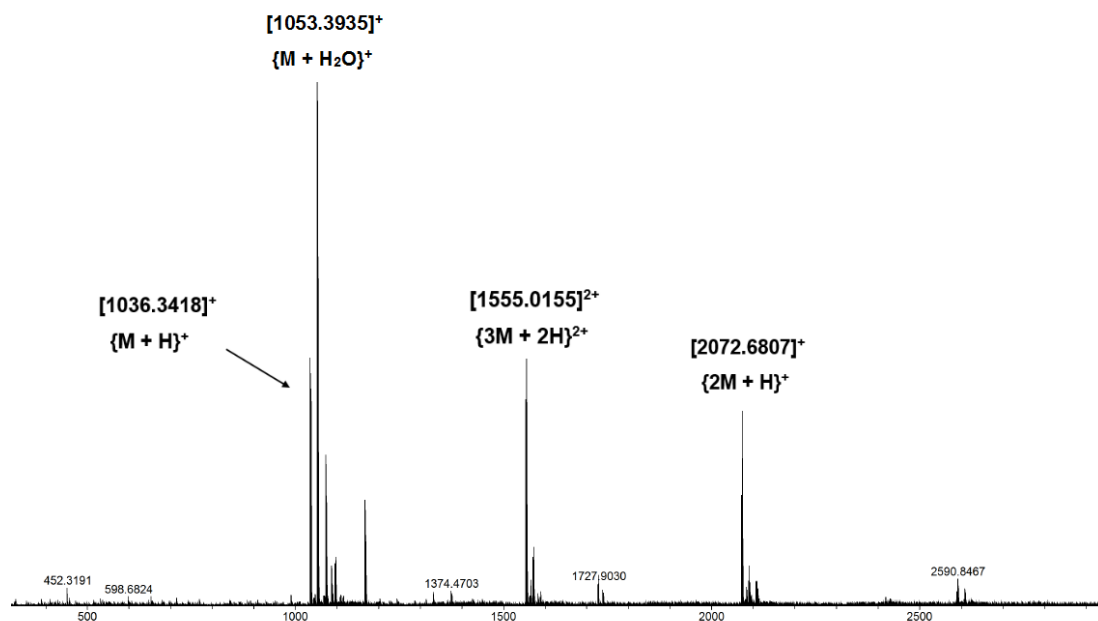


Figure 2.14: Interpreted HR ESI-MS of ligand **2.11**.

The structure of ligand **2.12** was also confirmed by X-ray diffraction. Single crystals of the compound grow readily from the slow evaporation of a saturated solution of the ligand in acetonitrile. These were very poorly diffracting and data was collected using synchrotron radiation at Diamond Light Source. The structure was solved in the $P\bar{1}$ space group and contained significant internal void space (with internal channels 2 nm in diameter) which may be a possible reason for the difficulty experienced in obtaining good diffraction. Multiple crystal sets of ligand **2.12** were screened, but all were found to give poor quality diffraction and resolution.

Two molecules of compound **2.12** were present in the asymmetric unit, one of each of *P* and *M* enantiomers (figure 2.15a). These display bowl-in-bowl stacking that is not uncommon for CTG derivatives. The structure contained residual electron density that could not be meaningfully refined as solvent, hence the SQUEEZE routine of PLATON was applied⁴⁵ (additional details given in the experimental section). Although the void space present is challenging from a crystallographic perspective, it offers an interesting scope for potential guest binding. Despite the large amount of disorder present, it becomes clear upon symmetry expansion of the asymmetric unit that the formation of these channels is likely to be caused by significant aromatic π - π stacking between adjacent azobenzene side chains (figure 2.15b) with typical distances of 3.699 Å between stacks. For ligand **2.12**, the calculated void space was found to be 48% of the crystal volume, going some way to explain the poorly diffracting nature of the system (somewhat unsurprisingly, these crystals lose their crystallinity upon the loss of solvent).

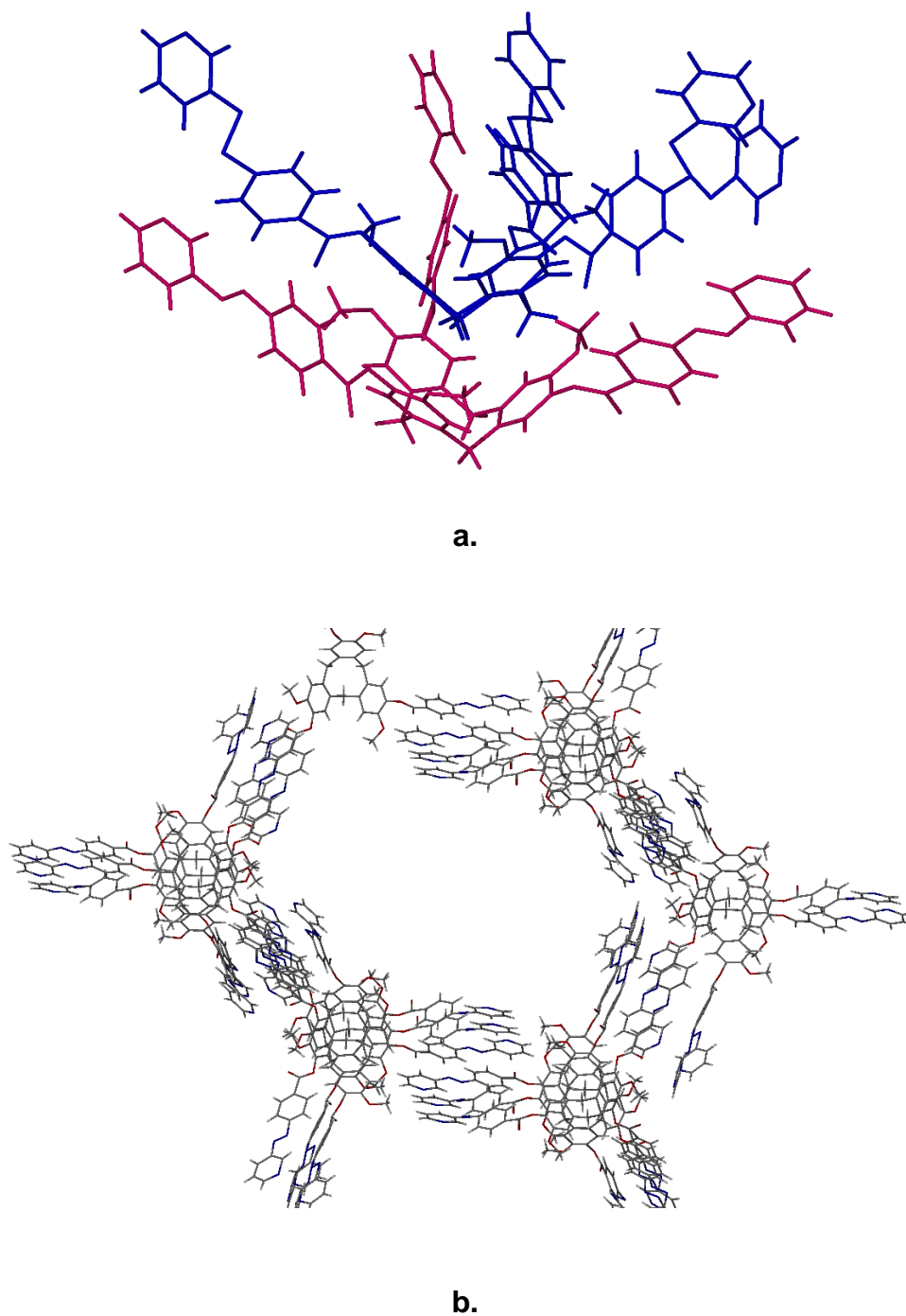
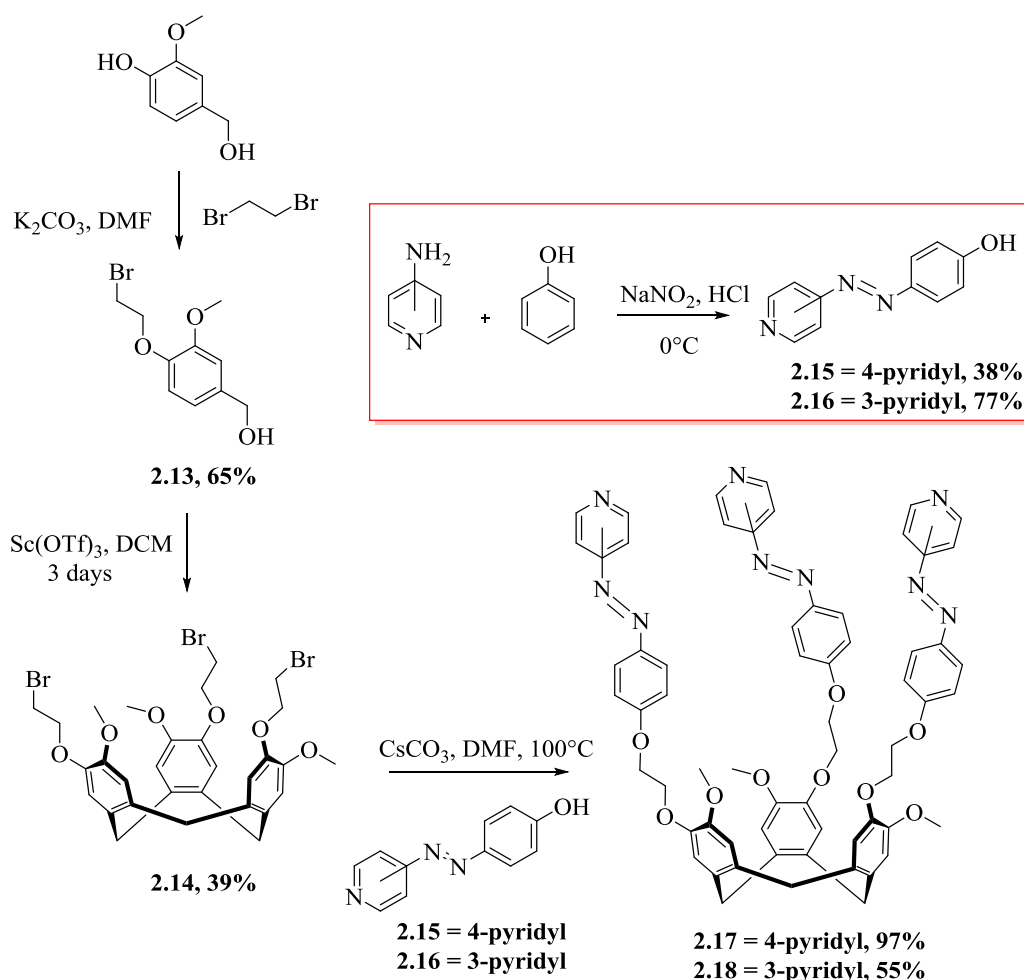


Figure 2.15: From the crystal structure of compound 2.12 showing a. Asymmetric unit of compound 2.12 with individual ligand enantiomers shown in pink and blue respectively – disorder of the azobenzene sidearm is observed ; b. Symmetry expanded 2 nm pore formed as a consequence of aromatic π - π stacking between azobenzene subunits.

Ligand **2.11** was found to be insoluble in practically all organic solvents and so its coordination chemistry in solution could not be meaningfully investigated. A strategy was therefore sought to overcome this. This involved the preparation of the bromoethyl appended analogue of CTG to introduce a solubilising CH₂CH₂ group into the ligand framework. The requisite [4-(2-bromoethoxy)-3-methoxyphenyl] methanol **2.13** was prepared in good yield using a literature procedure.⁴⁶ The subsequent cyclisation reaction to give **2.14** using Sc(OTf)₃ was consistently poor yielding due to the presence of a number of side products which then had to be removed with column chromatography. Suitable azobenzene units were prepared *via* a diazo coupling reaction as reported in the literature^{47, 48} to yield the hydroxylated azopyridines **2.15** and **2.16**. The reaction of **2.14** with each of these azopyridines in DMF along with Cs₂CO₃ led to the isolation of two new ligands **2.17** and **2.18**, both of which were appreciably soluble in organic solvents (scheme 2.8):



Scheme 2.8: Formation of AZB appended ligands **2.17** and **2.18**.

Ligands **2.17** and **2.18** were characterised by a variety of techniques including ^1H and ^{13}C NMR, mass spectrometry, combustion analyses and infrared spectroscopy. The interpreted ^1H NMR spectrum of ligand **2.17** is shown in figure 2.16. The CTG *endo* and *exo* doublets (i and j) are once again well preserved. The ether CH_2 protons (e) appear as a broad singlet at 4.37ppm. ESI mass spectrometry for compound **2.17** gave peaks at m/z $[542.7216]^{2+}$ and $[1084.433]^+$ (assigned as the $\{\text{M} + 2\text{H}\}^{2+}$ and $\{\text{M} + \text{H}\}^+$ peaks respectively). Mass spectrometry of compound **2.18** gave a similar scenario with peaks observed at $[362.1050]^{3+}$, $[542.7086]^{2+}$ and $[1084.4405]^+$ (which are assigned as the $\{\text{M} + 3\text{H}\}^{3+}$, $\{\text{M} + 2\text{H}\}^{2+}$ and $\{\text{M} + \text{H}\}^+$ respectively).

Both compounds gave consistent $^{13}\text{C}\{^1\text{H}\}$ NMR, infrared spectra and microanalytical data for the proposed structures. The infrared spectra of both of these ligands are largely unremarkable given the absence of defining functional groups but a strong band between $1135\text{-}1140\text{cm}^{-1}$ can be assigned as the C-O stretches of the ether groups. The azo N=N bond is once again IR inactive. Combustion analysis gave consistent data for each of these ligands with a molecule of DCM solvent.

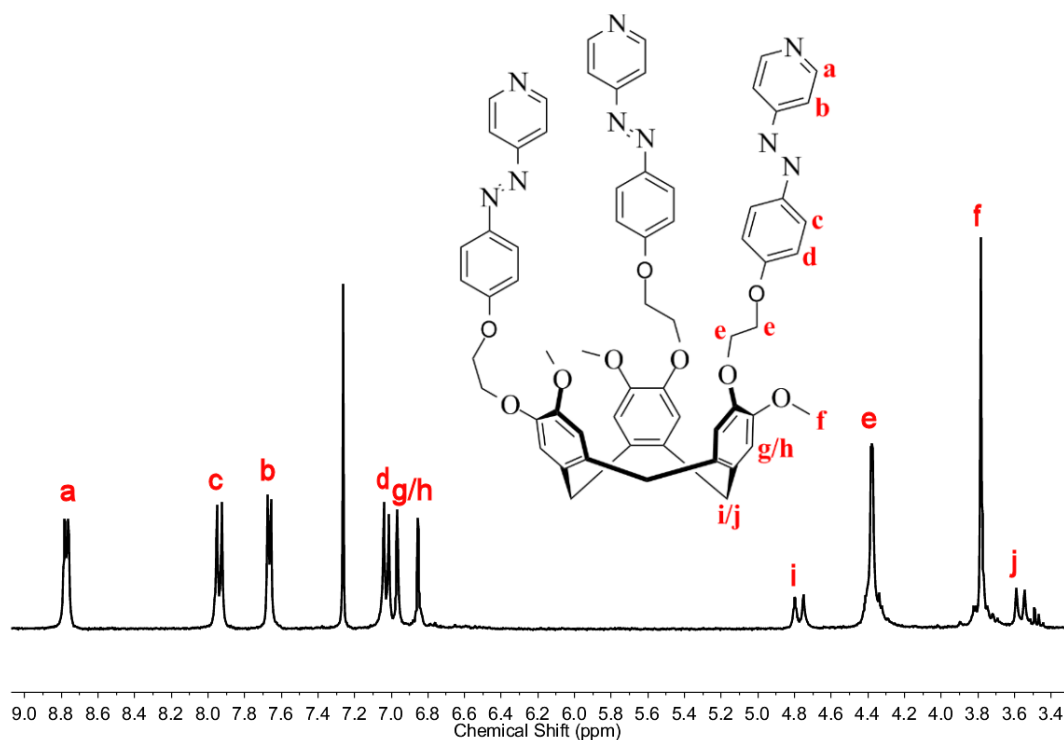


Figure 2.16: Interpreted ^1H NMR spectrum of compound **2.17** in CDCl_3 . A small amount of residual diethyl ether is present at 3.48 ppm.

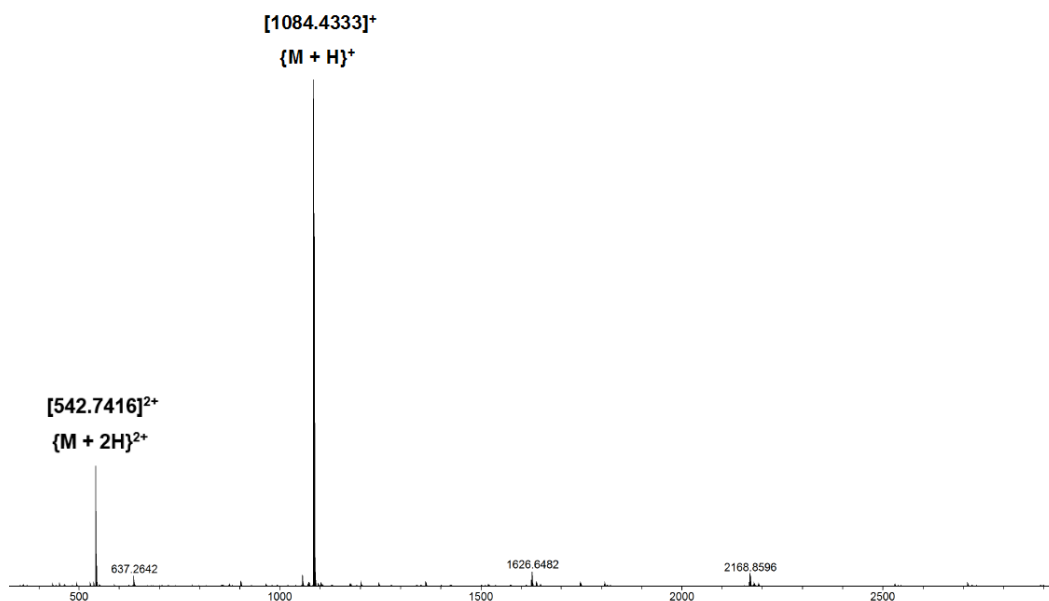


Figure 2.17: Interpreted HRMS of ligand **2.17**.

The structure of ligand **2.17** was confirmed by X-ray diffraction. Single crystals of **2.17**.3MeNO₂ were obtained from the slow diffusion of diethyl ether into a saturated solution of the ligand in nitromethane and isolated as orange needles. The structure was solved in the *I2/a* space group with a monoclinic unit cell. The asymmetric unit contains one molecule of **2.17** along with three molecules of nitromethane solvent (figure 2.18a). The symmetry expanded structure (figure 2.18b) reveals the presence of neatly ordered bowl-in-bowl stacks of compound **2.17** which are heavily interpenetrated *via* the azobenzene units of neighbouring stacks. Such interpenetration is again likely to result from stabilising π - π stacking interactions, with distances between layers 3.782Å. Void space is greatly reduced in this arrangement compared to compound **2.12**; this is manifested in the greatly superior diffraction of crystals of **2.17** versus those of **2.12**.

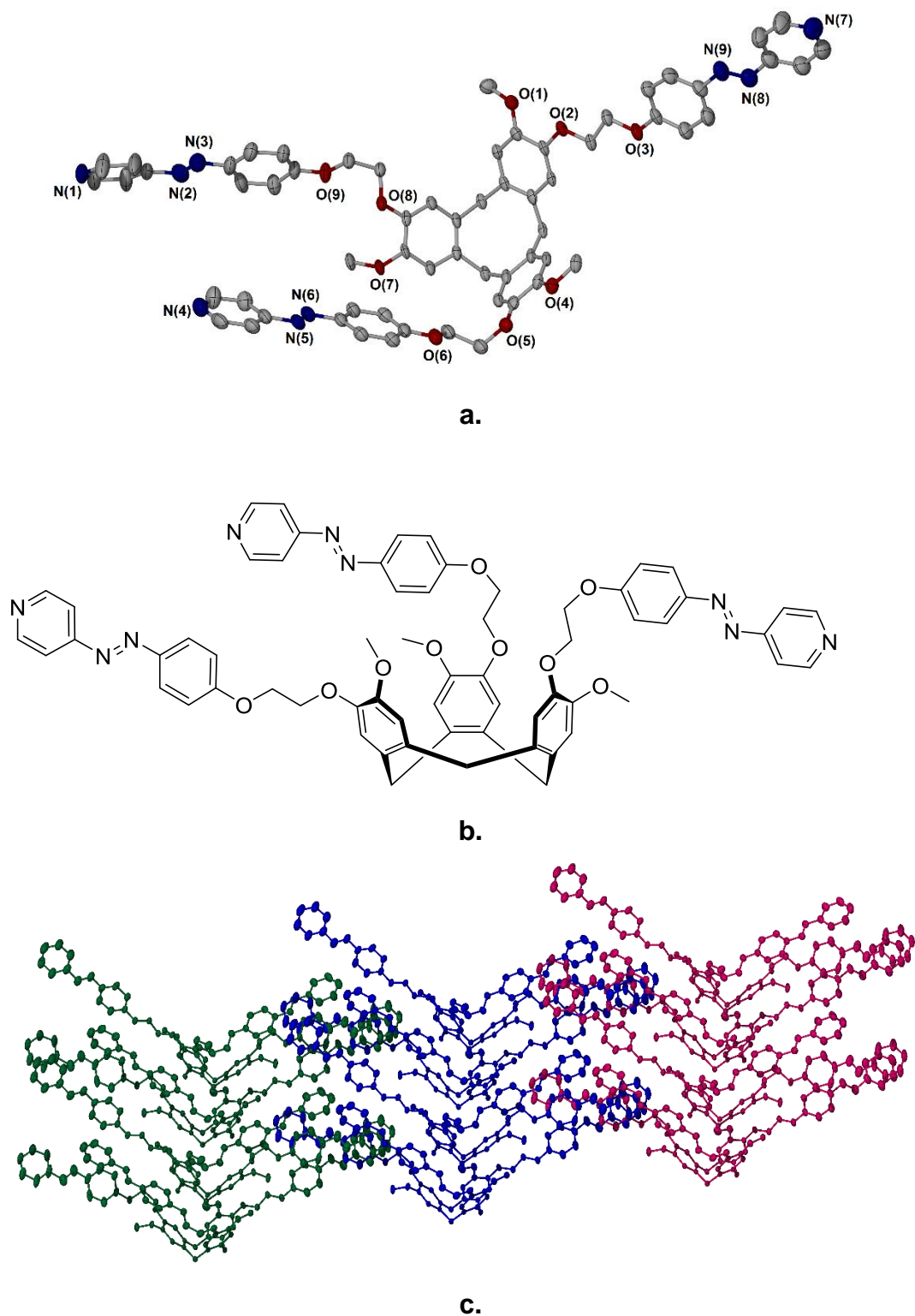
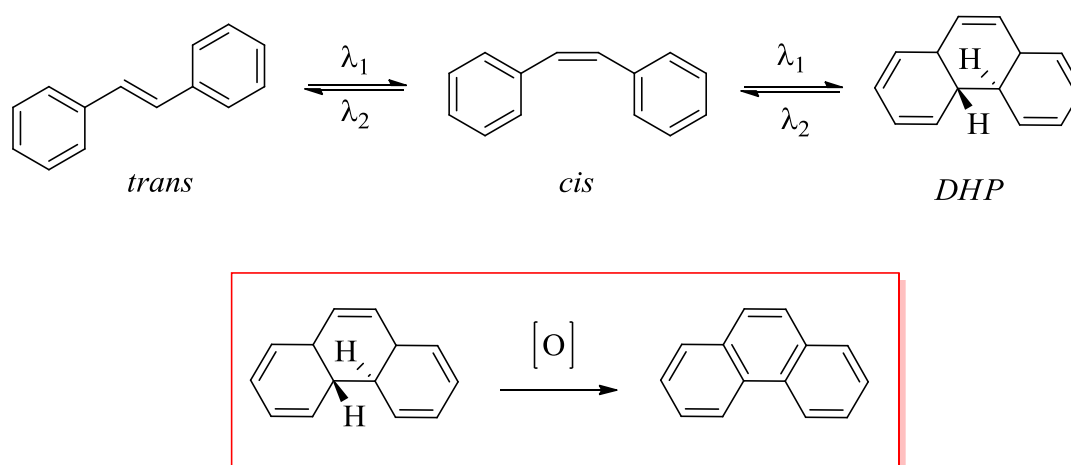


Figure 2.18: From the X-ray structure of compound **2.17** showing **a.** Asymmetric unit of **2.17**; **b.** Chemical representation of ligand **2.17**; **c.** Interpenetrating bowl-in-bowl stacks of **2.17** with individual stacks shown in a different colour. Ellipsoids are shown at 50% probability with solvents and hydrogen atoms omitted for clarity.

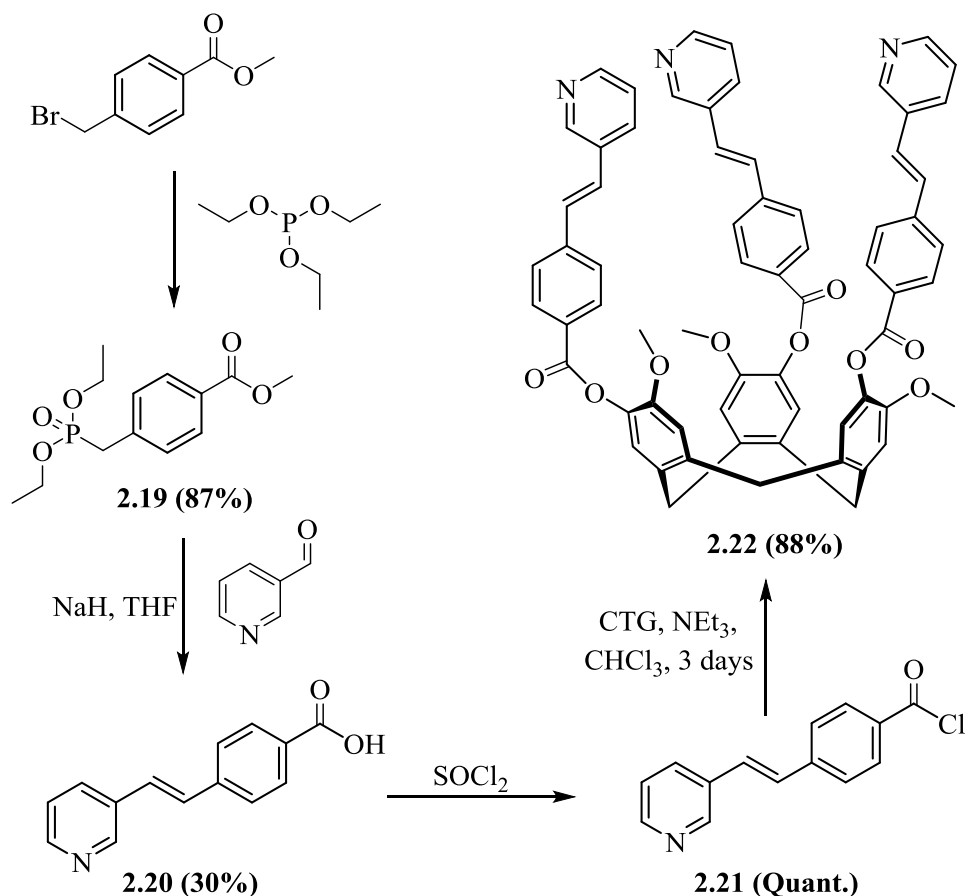
2.5 Stilbene (SBN) appended CTG ligands

With the successful preparation of AZB containing ligands the investigation was extended to the preparation of the analogous stilbene (SBN) compounds. Structurally these systems are highly similar to AZB with the N=N double bond replaced by a C=C double bond. Stilbenes are able to undergo *cis/trans* photoisomerisation in the same manner as azobenzenes. However stilbenes also have an additional possible photoproduct, the cyclised phenanthrenes as shown in scheme 2.9 below.⁴⁹ Unlike azobenzenes, where the mechanism of isomerisation is still hotly debated, stilbenes are known to undergo isomerisation exclusively by rotation-based mechanisms.²¹



Scheme 2.9: Photoisomerisation of stilbene.

The preparation of the ester-linked stilbene analogue of **2.12** was conducted on a small scale initially by the author. Subsequent scaleup and reaction optimisation was then conducted by MChem student Benjamin Swift under the supervision of the author. The synthetic route of the stilbene arm **2.20** was achieved in two steps starting from commercially available methyl 4-bromomethyl benzoate. Treatment of the starting material with triethyl phosphite gave the phosphonate ester **2.19** as a yellow oil in excellent yields following Kugelrohr distillation.⁵⁰ This oil was then treated with sodium hydride and 3-pyridinecarboxaldehyde in dry THF (Horner-Wadsworth Emmons reaction) to afford the target stilbene ‘arm’ **2.20** in modest yields in accordance with the procedure described by Anthony and coworkers.⁵¹ Treatment of this compound with SOCl_2 gave the acid chloride **2.21** in a quantitative yield; the reaction of this compound with CTG and NEt_3 in THF led to an incomplete reaction owing to the insolubility of the acid chloride. The use of chloroform as reaction solvent successfully circumvents this problem and the novel stilbene appended ligand **2.22** was isolated as a tan solid in good yields (scheme 2.10).



Scheme 2.10: Synthetic route to stilbene appended ligand **2.22**.

Single crystals of compound **2.22** could be reliably grown *via* the diffusion of diethyl ether into a chloroform solution of the ligand but were found to be extremely poorly diffracting, even using synchrotron radiation; presumably this is due to similar void spaces present in the AZB analogue **2.12**. Attempts to slow crystal growth and grow better quality crystals were all unsuccessful and thus a crystal structure of ligand **2.22** could not be obtained.

The ^1H NMR spectrum of compound **2.22** is shown in figure 2.19. The spectrum is very similar to that of the AZB analogue, with the main contrast being a sharp singlet at 7.23 ppm which is assigned as the vinyl protons of the double bond. This may be assigned as the all *trans* isomer of the compound as the *cis* isomer protons typically appear further downfield (*ca* 6.5ppm);⁵² no resonances are observed in this region. Compound **2.22** gives consistent data for ^{13}C NMR, infrared spectroscopy, combustion analysis and ESI mass spectrometry (with peaks at m/z 344.12 $\{\text{M} + 3\text{H}\}^{3+}$, 515.68 $\{\text{M} + 2\text{H}\}^{2+}$, and 1030.37 $\{\text{M} + \text{H}\}^+$). Synthesis of the 4-pyridyl analogue of **2.22** has been conducted previously in the Hardie group by postdoctoral researcher Tanya Ronson and upon isolation (in a low yield) was observed to degrade; as such this analogue was not pursued further.

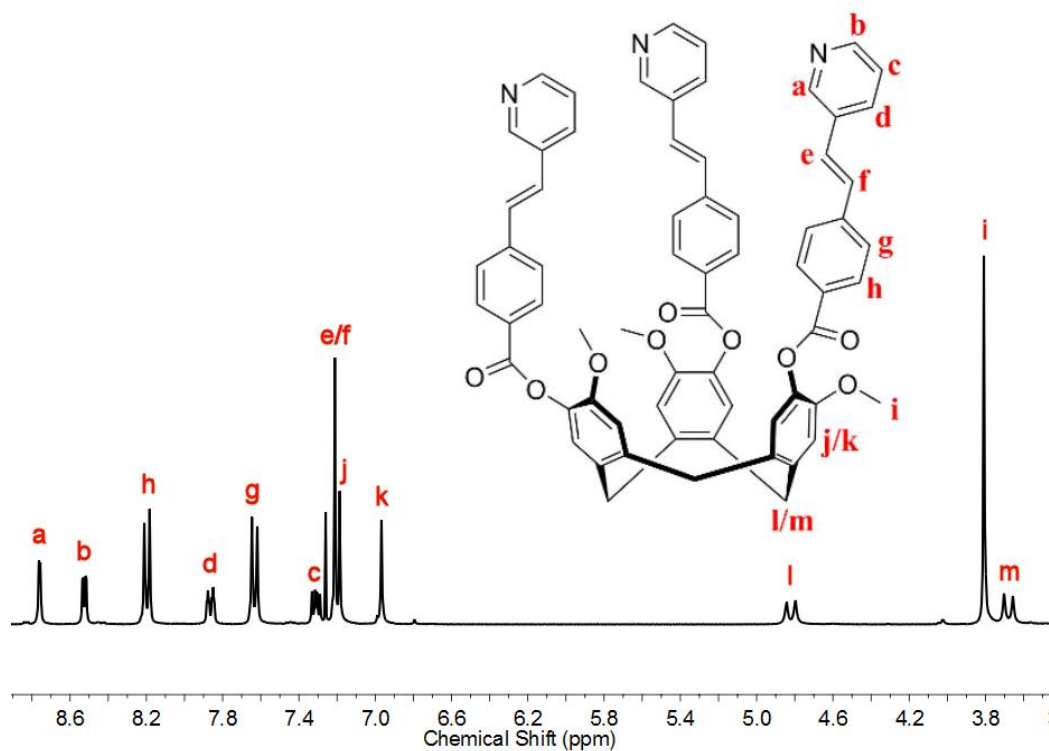


Figure 2.19: Interpreted ^1H NMR spectrum of compound **2.22** in CDCl_3 (singlet at 7.26 ppm)

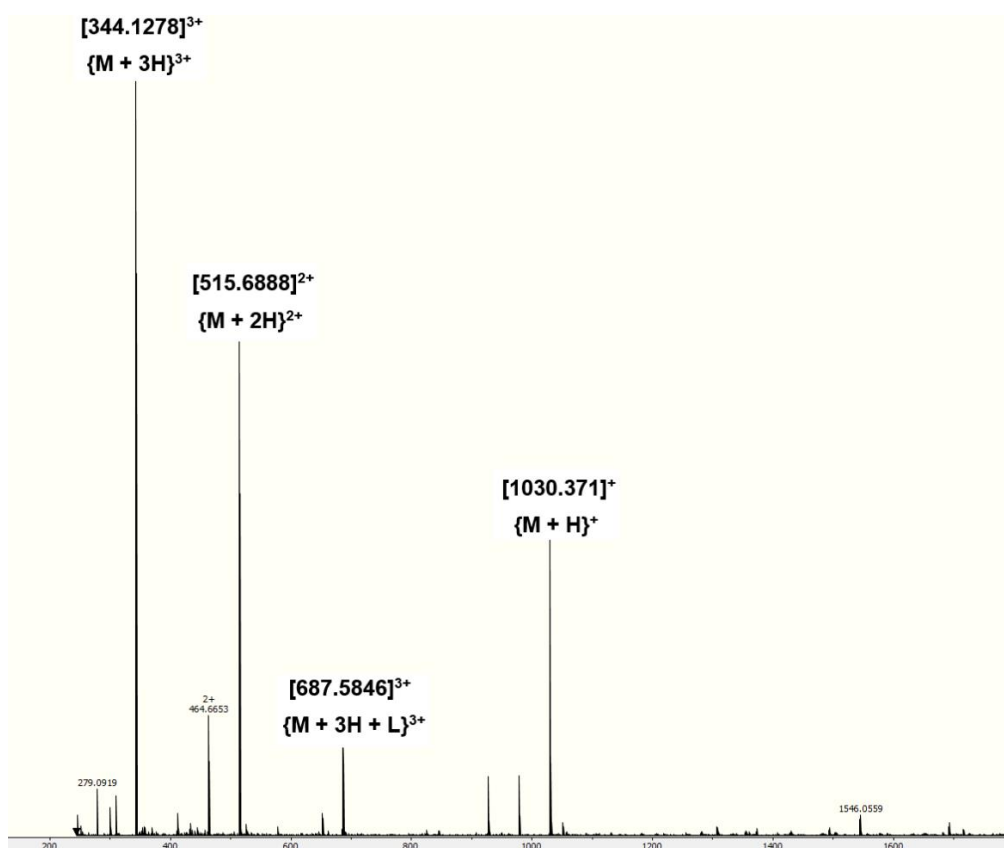
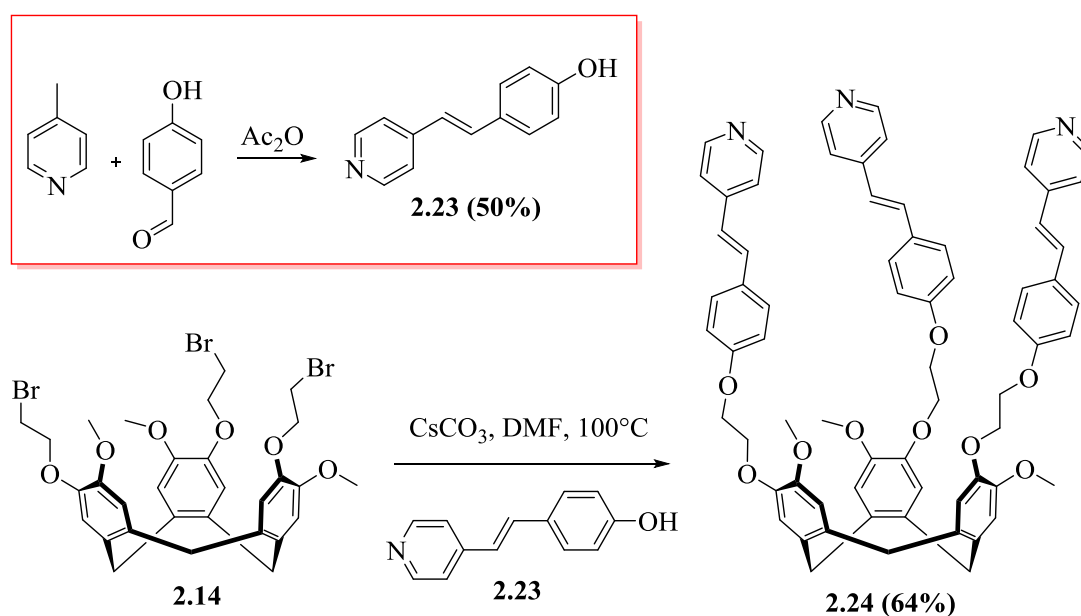


Figure 2.20: Interpreted HRMS of ligand **2.22**.

The analogous ether linked ligand **2.24** was prepared in a two-step procedure as shown in scheme 2.11; 4-methylpyridine was reacted with 4-hydroxybenzaldehyde using acetic anhydride as the solvent according to the procedure of Koopmans and coworkers (scheme 2.11, red box).⁵³ Using the same methodology as in the preparation of ligands **2.17** and **2.18**, the combination of an excess of stilbene arm **2.23** and Cs₂CO₃ with compound **2.14** in DMF led to the formation of ligand **2.24** as a pale yellow solid in good yields.

The ¹H NMR spectrum of ligand **2.24** is shown in figure 2.21. A significant degree of overlap of peaks occur in the aromatic region regardless of the solvent employed, making unambiguous assignment difficult. In this compound, the vinyl protons are observed as a broad doublet with a large coupling constant ($J = 16.3\text{Hz}$) but chemical shifts once again indicate a *trans* configuration of the stilbene bond. The ESI mass spectrum is far clearer with peaks observed at m/z 360.1587 $\{M + 3H\}^{3+}$, 539.7357 $\{M + 2H\}^{2+}$ and 1078.4607 $\{M + H\}^+$. Consistent data was also obtained for ¹³C NMR and IR analysis. The stilbene analogues displayed an improved solubility in non-polar solvents compared to their azobenzene counterparts but were significantly less soluble in more polar solvents such as nitromethane.



Scheme 2.11: Synthesis of ether linked stilbene **2.24**.

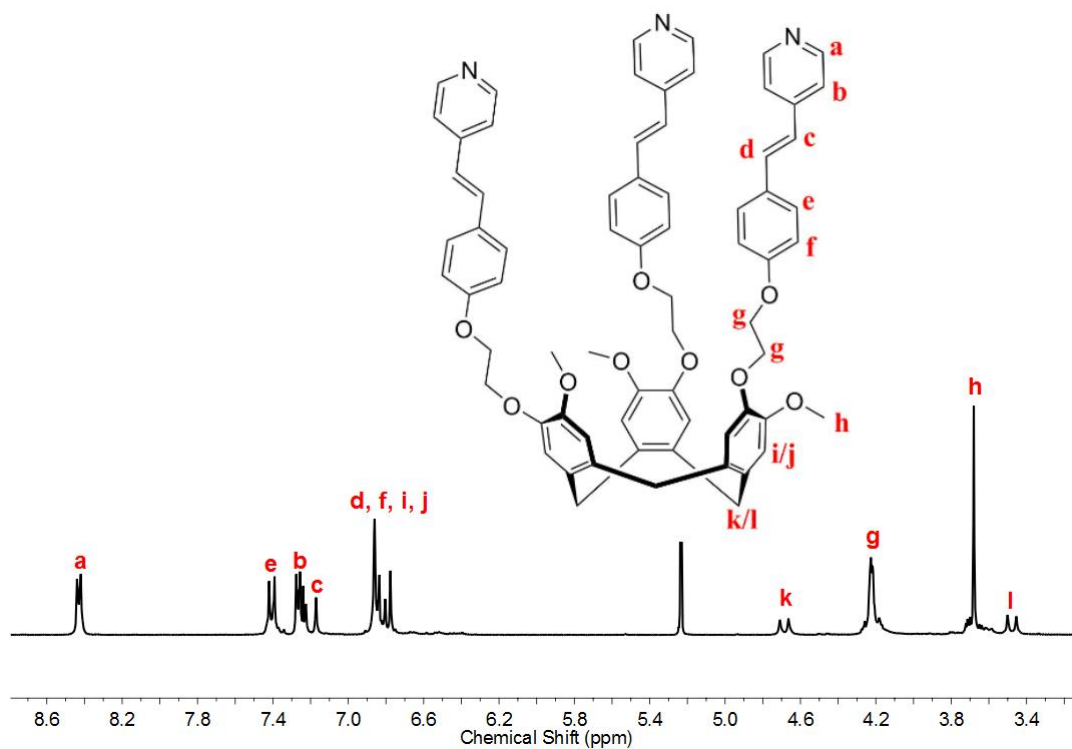


Figure 2.21: Interpreted ^1H NMR spectrum of ligand **2.24** in d^2 -DCM.

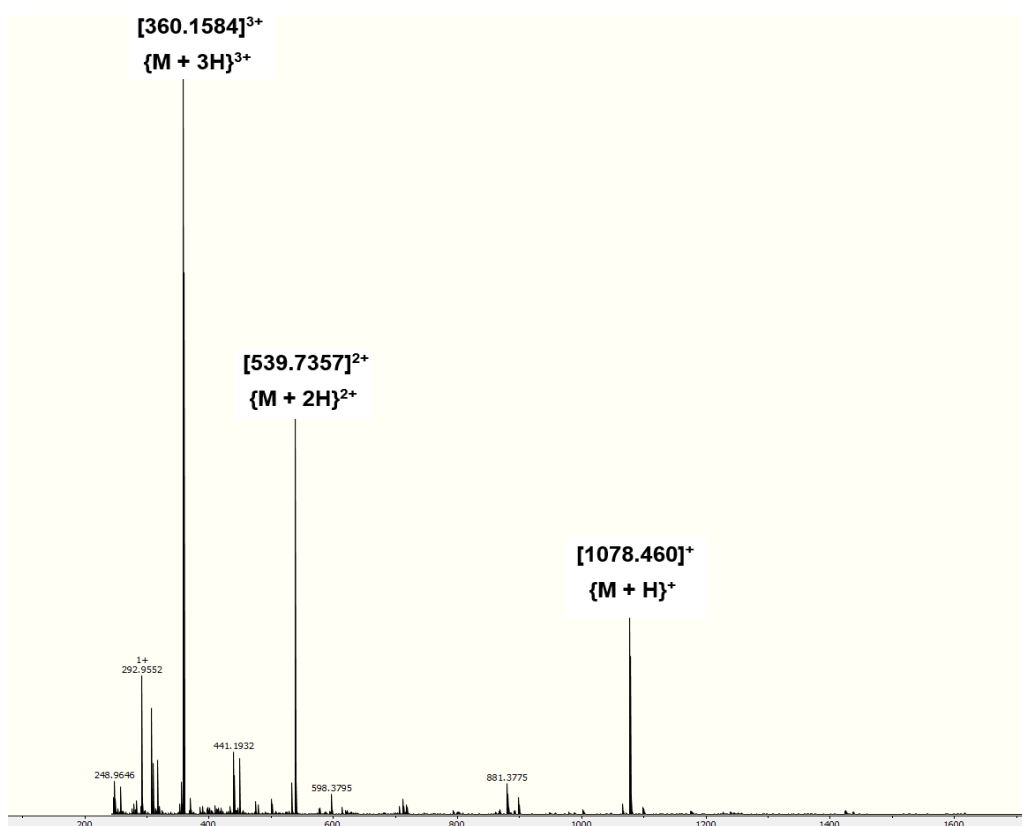


Figure 2.22: Interpreted HRMS of ligand **2.24**.

2.6 Conclusions and further direction

Novel synthetic methodology has been employed to synthesise a new class of azopyridines utilising base-catalysed coupling of aromatic nitroso compounds with aminopyridines. The scope of this reaction is unexplored and may possibly be useful for the synthesis of other previously inaccessible asymmetric azobenzenes. The reaction of these compounds with CTG has led to the first examples of CTG-based ligands appended with photoisomerisable azobenzene groups, **2.11** and **2.12**. The solubilised ethyl linked derivatives **2.17** and **2.18** have also been prepared utilising bromoethyl-appended CTG. The coordination chemistry and photoresponsive properties of these compounds are discussed in chapters 3 and 4 respectively.

The first examples of stable stilbene-appended CTG ligands, compounds **2.22** and **2.24** have also been successfully prepared. Whilst these ligands require varied synthetic strategies to prepare, the final products can be isolated in respectable yields. The coordination chemistry and photoresponsive properties of these compounds is discussed in chapter 4.

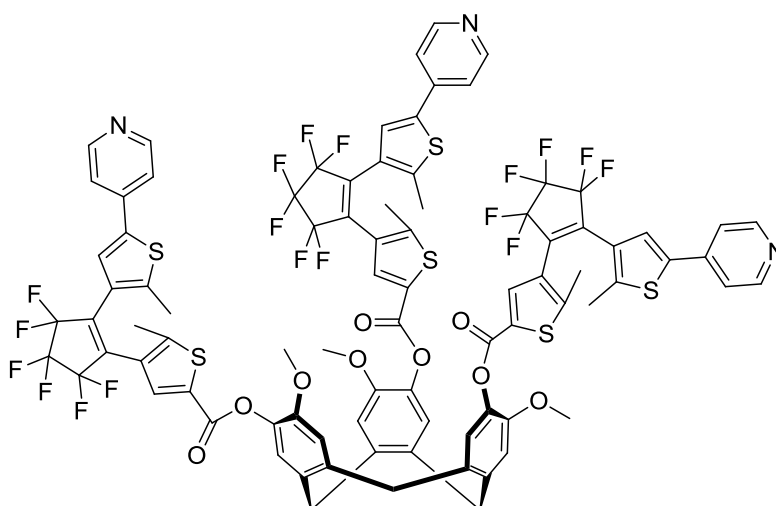
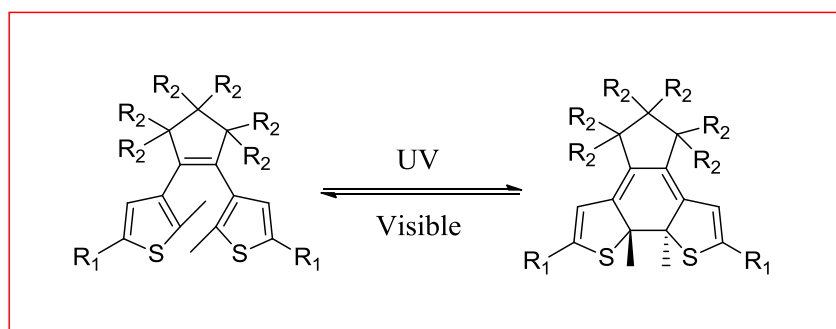


Figure 2.23: Potential DTE appended CTG ligand.

In addition to the ligands prepared in this chapter, there remain other molecular switches that have not been investigated; these include the more synthetically complex

but well-defined dithienylethenes (DTEs, figure 2.23) and the photochromic spiropyrans. Irradiation of the DTE unit with UV light induces a cyclisation reaction from the 'open' form (depicted in figure 2.23) to a 'closed' form. Due to the increased conjugation throughout the system, the closed form is often coloured whilst the open form is colourless. This could potentially allow for the preparation of photochromic CTG-based assemblies.

Connection of these units to CTG, whilst likely to prove challenging, would enable the creation of new libraries of ligands bearing photoresponsive units. DTE units in particular have proven highly effective photoisomerisable units and Clever has shown the concept can be incorporated into cage systems and used to switch between a self-assembled molecular triangle and a rhombicuboctahedral sphere.⁵⁴ The DTE photoswitch has been implicated in other structural transformations as well.⁵⁵ Owing to their synthetic challenge, investigations into such compounds are not presented here but remain an attractive concept for future investigations; the stilbene ligands prepared may be viewed as the simplest analogue of the diarylethenes.

In addition to this, further development of the 4-pyridyl analogues of this ligand would be a highly attractive proposition. 4-pyridyl appended ligands remain the most popular choice for CTG-based assemblies and have been employed in the past in the Hardie group to form a variety of different metallo-supramolecular systems. Solubilising the 4-pyridyl azo ligand **2.11** would likely require the substitution of the methoxy substituents on the CTG bowl with an ethyloxy or propyloxy analogue. This strategy has been employed in the solubilisation of M_3L_2 metallocages in the past¹² to great success. The development of both DTE appended CTG ligands and of solubilised CTG precursors remain a research focus in the Hardie group with current PhD researcher Edward Britton.

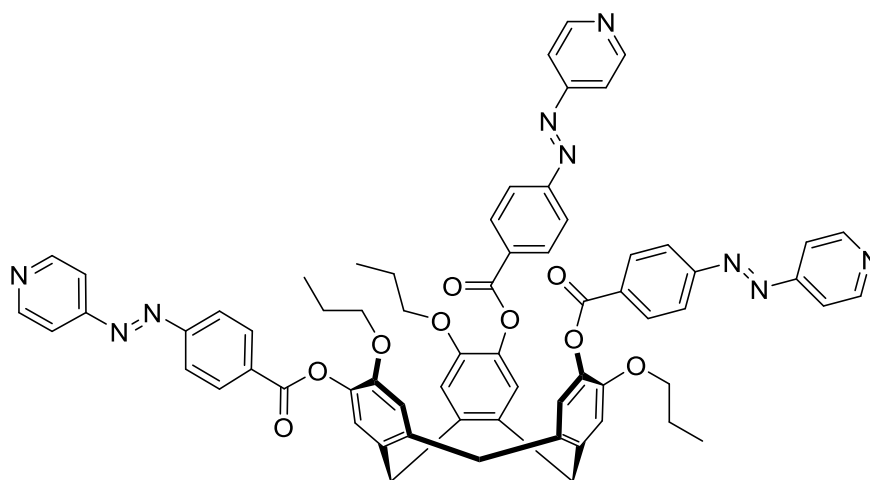


Figure 2.24: Potential solubilised analogue of ligand 2.11 utilising propylated CTG.

2.7 Experimental

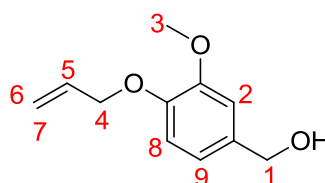
2.7.1 Instrumentation

^1H and $^{13}\text{C}\{^1\text{H}\}$ NMR spectra were recorded on a Bruker DPX 300MHz and a Bruker AscendTM 400MHz NMR spectrometer. Where appropriate, routine NMR assignments were confirmed by 2D ^1H - ^1H coupling experiments (COSY, HMQC, HMBC) which were all recorded on a Bruker AscendTM 400MHz NMR spectrometer. High-resolution electrospray mass spectra (ESI-MS) were recorded on a Bruker micro-TOF-Q mass spectrometer and FT-IR spectra were recorded as solid phase samples using a Perkin Elmer Spectrum One spectrometer. Melting points were recorded on a Stuart SMP3 melting point apparatus. Samples for microanalysis were dried under vacuum before analysis and determined by either Ms Tanya Marinko-Covell of the University of Leeds or Mr Stephen Boyer of London Metropolitan University. UV-Visible spectra were recorded on a Lambda 900 UV/Vis spectrophotometer and an Agilent Cary 100 UV/Vis spectrophotometer.

2.7.2 Chemical Syntheses

Where stated, reactions were carried out under an inert atmosphere of argon using an argon/vacuum dual manifold and standard Schlenk techniques. All chemicals and solvents were purchased from commercial suppliers (Sigma, Fluka) and were used as received. Dry solvents were obtained by passing through a column of activated alumina. Argon and nitrogen gas were pre-dried by passing through a small column of P_2O_5 before use.

3-Methoxy-4-(propenyloxy) benzyl alcohol (2.1)

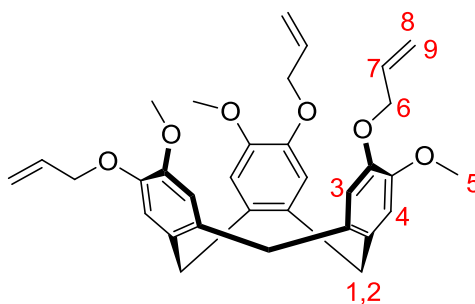


4-Hydroxy-3-methoxybenzyl alcohol (25.0 g, 158 mmol) was suspended in acetone (125 mL) along with potassium carbonate (21.8 g, 176 mmol). Allyl bromide (15.1 mL, 158 mmol) was added and the mixture heated to reflux for 24 hours under an argon atmosphere. The suspension was allowed to cool to room temperature before the solvent and any remaining allyl bromide were removed *in vacuo*. The resulting

solid was extracted with DCM (3 x 200 mL) and the combined organics were washed with water (2 x 200 mL) and dried over MgSO₄. The solvent was then removed *in vacuo* to give the product (28.1 g, 145 mmol, 91%) as a white solid.

¹H NMR (300 MHz, CDCl₃) δ_H; 6.94-6.80 (3H, m, Ar-H(2), Ar-H (8), Ar-H (9)), 6.18 – 5.98 (1H, m, C=CH (5)), 5.40 (1H, m, 1H, trans C=CH₂ (6)), 5.28 (1H, m, cis C=CH₂ (7)), 4.66 – 4.54 (4H, m, Ar-CH₂ (1), Ar-OCH₂ (4)), 3.89 (3H, s, OCH₃ (3)); ¹³C {¹H} NMR (75 MHz, CDCl₃) δ_C; 149.6, 147.5, 134.0, 133.3, 119.3, 118.0, 113.4, 110.9, 70.0, 65.2, 55.9; HR-MS (ES⁺): m/z 177.0909 {M+OH}⁺ (calculated for {C₁₁H₁₃O₂}⁺ 177.0916). All data is consistent with the literature.⁵⁶

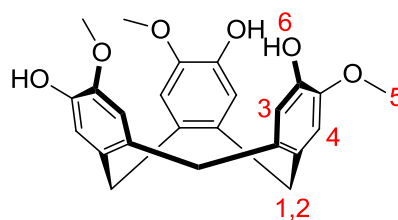
(±)-2,7,12-Trimethoxy-3,8,13-tris(propenyloxy)-10,15-dihydro-5H-tribenzo[a,d,g] cyclononatriene (2.2)



3-Methoxy-4-(propenyloxy) benzyl alcohol (24.6 g, 126 mmol) was heated and stirred at 75°C until all the material melted. A catalytic amount of phosphoric acid (spatula tip) was added and the reaction stirred overnight until the all the mixture solidified. The solid was triturated in methanol (300 mL) and sonicated to obtain a fine white suspension. The solid was filtered, washed with more methanol and dried *in vacuo* to obtain the product (17.24g, 33 mmol, 79%) as a fine white solid.

¹H NMR (300 MHz, CDCl₃) δ_H; 6.85 (3H, s, Ar-H (3)), 6.79 (3H, s, Ar-H (4)), 6.16 – 5.96 (m, 3H, C=CH (7)), 5.37 (3H, dq, J 17.3, 1.6, trans C=CH₂ (8)), 5.24 (3H, dq, J 10.5, 1.4, cis C=CH₂ (9)), 4.74 (3H, d, J 13.8, CTG endo-H (1)), 4.68 – 4.49 (6H, m, Ar-OCH₂ (6)), 3.83 (9H, s, OCH₃ (5)), 3.51 (3H, d, J 13.7, CTG exo-H (2)); ¹³C NMR (75 MHz, CDCl₃) δ 148.2, 146.8, 133.7, 132.3, 131.8, 117.5, 115.6, 113.6, 70.2, 56.1, 36.5; HR-MS (ES⁺): m/z 546.28 {M + H₂O}⁺ (calculated for {C₃₃H₃₈O₇}⁺ 546.2618). All data is consistent with the literature.⁵⁷

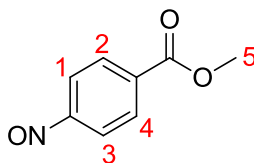
(±)-2,7,12-Trimethoxy-3,8,13-tris(hydroxy)-10,15-dihydro-5H-tribenzo[*a,d,g*] cyclononatriene (CTG, 2.3)



(±)-2,7,12-Trimethoxy-3,8,13-tris(propenyloxy)-10,15-dihydro-5H-tribenzo[*a,d,g*] cyclononatriene (3.00 g, 5.67 mmol) was dissolved in a mixture of dry THF (150 mL), diethylamine (27 mL) and water (23 mL) under an argon atmosphere. The resulting pale yellow solution was stirred at reflux for two hours. Palladium (II) acetate (0.09 g, 0.39 mmol) and triphenylphosphine (0.28 g, 1.07 mmol) were added as solids and the resulting orange solution was stirred at reflux overnight under an argon atmosphere. The black solution was then cooled to room temperature and filtered through a plug of celite. The solvent was removed *in vacuo* to give a light brown residue which was triturated in methanol (150 mL) before being filtered to yield the product (1.64g, 4.01 mmol, 71%) as a fine off-white solid. ²⁶

¹H NMR (300 MHz, CDCl₃) δ_H: 6.88 (3H, s, Ar-H (3)), 6.79 (3H, s, Ar-H (4)), 5.39 (3H, s, OH (6)), 4.71 (3H, d, J 13.7, CTG endo-H (1)), 3.85 (9H, s, OCH₃ (5)), 3.50 (3H, d, J 14.1 CTG exo-H (2)); ¹³C NMR (75 MHz, CDCl₃) δ_C 145.2, 144.1, 132.5, 131.2, 115.4, 112.3, 56.1, 36.3; HR-MS (ES⁺): m/z 426.19 {M + H₂O}⁺ (calculated for {C₂₄H₂₆O₇}⁺ 426.1679). All data is consistent with the literature.

4-Nitroso methyl benzoate (2.4)

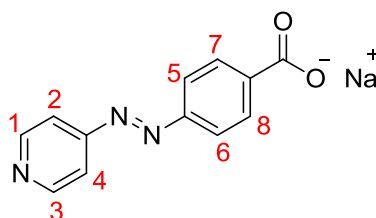


Methyl 4-aminobenzoate (2.50 g, 16.6 mmol) was dissolved in DCM (100 mL). A solution of Oxone (20.3 g, 33.1 mmol) in 200 mL of water was added. The resulting green mixture was stirred vigorously at room temperature under a nitrogen

atmosphere for 2 hours. The mixture was then allowed to separate before the aqueous layer was extracted with further DCM (3 x 150 mL). The combined organic layers were then washed with 1M HCl, saturated NaHCO₃, water and brine. The organic layers were dried over magnesium sulphate and the solvent removed *in vacuo* to give a bright yellow solid. This crude product was recrystallised from DCM to give the desired product (2.41 g, 14.7 mmol, 89%) as a bright yellow solid.

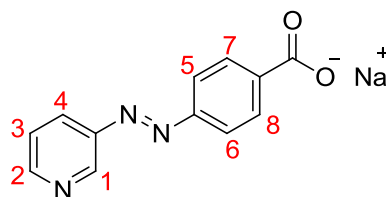
¹H NMR (300 MHz, CDCl₃) δ_H 8.30 (2H, dt, J 9.0 Ar-H (1), Ar-H (3)), 7.94 (2H, dt, J 9.0 Ar-H (2), Ar-H (4)), 3.98 (3H, s, OCH₃ (5)); ¹³C NMR (75 MHz, CDCl₃) δ_C 165.7, 164.4, 135.2, 131.0, 125.3, 120.4, 52.8; HR-MS (ES⁺): m/z 166.04 {M + H}⁺ (calculated for {C₈H₈NO₃}⁺ 166.0499) All data is consistent with the literature.³⁵

4,4'-Pyridyl-azo-sodium benzoate (2.5)



Solid sodium hydroxide (3.00 g, 75 mmol) was dissolved in 100 mL of water to form a 3% NaOH solution. 4-Aminopyridine (0.52 g, 5.6 mmol) and 4-nitroso methylbenzoate (0.5 g, 3.0 mmol) were added and the mixture was heated to reflux overnight. The resulting deep red solution was then cooled to room temperature resulting in the formation of a bright orange precipitate. The solid was filtered and dried *in vacuo* to give the product (0.53g, 2.19 mmol, 73%) as an orange solid.

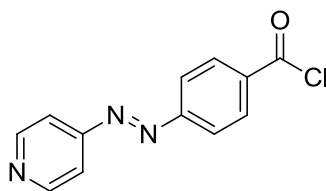
M.pt >300°C; ¹H NMR (300 MHz, DMSO-d₆) δ_H 8.83 (2H, dd, J 6.0, 1.8, Ar-H (1), Ar-H (3)), 8.04 (2H, dt, J 9.0, 1.8, Ar-H (7), Ar-H (8)), 7.85 (2H, dt, J 9.0, 1.8, Ar-H (5), Ar-H (6)), 7.76 (2H, d, J 6.0, 1.8, Ar-H (2), Ar-H (4)); ¹³C NMR (75 MHz, MeOD-d₄) δ_C 159.26, 151.80, 131.24, 123.81, 117.76; HR-MS (ES⁺) m/z 228.0766 {M + H}⁺ (calculated for {C₁₂H₁₀N₃O₂}⁺ 228.0768); FT-IR (cm⁻¹) = 3241, 1676, 1591, 1536, 1381, 1306, 1224, 1095, 830, 792, 691, 598, 588. 506; Analysis calculated for sodium bridged dimer **2.8**.(Na₂(H₂O)₈ (from crystal structure) (% calculated; found) C (44.80, 44.52), H (4.90, 4.67), N (13.00, 12.98); UV-Vis (DMSO) λ_{max} (nm) 315 (π → π*), 445 (n → π*).

4,3'-Pyridyl-azo-sodium benzoate (2.6)

Solid sodium hydroxide (3.00 g, 75 mmol) was dissolved in 100 mL of water to form a 3% NaOH solution. 3-Aminopyridine (1.48 g, 15.7 mmol) and 4-nitroso methylbenzoate (1.40 g, 8.47 mmol) were added and the mixture was heated to reflux overnight. The resulting red solution was then cooled to room temperature resulting in the formation of orange-red crystals. The crystals were filtered and washed with acetone and diethyl ether to give the product (2.07 g, 8.31 mmol, 98%) as a bright orange solid.

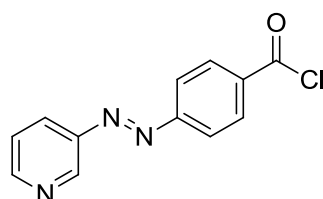
M.pt >300°C; ^1H NMR (300 MHz, D_2O) δ_{H} 9.07 (1H, dd, J 2.4, 0.7, Ar-H (1)), 8.70 (1H, dd, J 4.9, 1.5, Ar-H (2)), 8.26-8.22 (1H, m, Ar-H (4)), 8.05 (2H, dt, J 8.7, 1.8, Ar-H (7), Ar-H (8)), 7.95 (2H, dt, J 8.7, 2.1, Ar-H (5), Ar-H (6)), 7.71-7.66 (1H, m, J 8.3, Ar- (3)); Over time in solution also observe new peaks in *cis* isomer: ^1H NMR (300 MHz, D_2O) δ_{H} 8.30 (1H, dd, J 4.2, 2.3), 8.21 (1H, dd, J 2.1, 1.2), 7.73 (2H, dt, J 8.4, 1.8), 7.34 – 7.31 (2H, m), 6.92 (2H, dt, J 8.4, 2.1); ^{13}C NMR (75 MHz, D_2O) δ_{C} 156.19, 153.30, 151.13, 147.83, 145.08, 139.45, 129.88, 128.63, 124.95, 122.43; HR-MS (ES^+) m/z 228.0780 $\{\text{M} + \text{H}\}^+$ (calculated for $\{\text{C}_{12}\text{H}_{10}\text{N}_3\text{O}_2\}^+$ 228.0768); FT-IR (cm^{-1}) = 1593, 1539, 1385, 1310, 1220, 1099, 1014, 810, 786, 700, 622, 591; Analysis calculated for **2.9**.0.5 H_2O (% calculated; found) C (55.82, 56.20), H (3.51, 3.20), N (16.27, 16.50); UV-Vis (DMSO) λ_{max} (nm) 326 ($\pi \rightarrow \pi^*$), 440 ($n \rightarrow \pi^*$).

4,4'-Pyridyl-azo-benzoyl chloride (2.9)



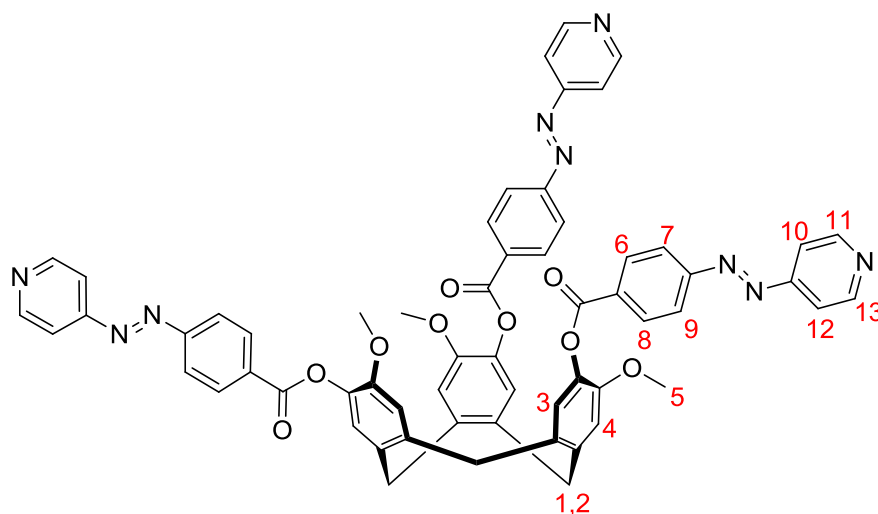
4,4'-Pyridyl-azo-sodium benzoate (0.5 g, 2.20 mmol) was suspended in thionyl chloride (15 mL) under an argon atmosphere. The resulting red suspension was heated to reflux overnight. The flask was allowed to cool to room temperature before the thionyl chloride was removed *in vacuo* to give the product as a pale red solid in a quantitative yield that was used in the next reaction immediately without further purification.

4,3'-Pyridyl-azo-benzoyl chloride (2.10)



4,3'-Pyridyl-azo-sodium benzoate (1.75 g, 7.03 mmol) was suspended in thionyl chloride (15 mL) under an argon atmosphere. The resulting red suspension was heated to reflux overnight. The flask was allowed to cool to room temperature before the thionyl chloride was removed *in vacuo* to give the product as a dark pink solid in a quantitative yield that was used in the next reaction immediately without further purification.

(±)-2,7,12-Trimethoxy-3,8,13-tris(4,4'-Pyridyl-azophenylcarboxy)-10,15-dihydro-5H-tribenzo[*a,d,g*] cyclononatriene (2.11)

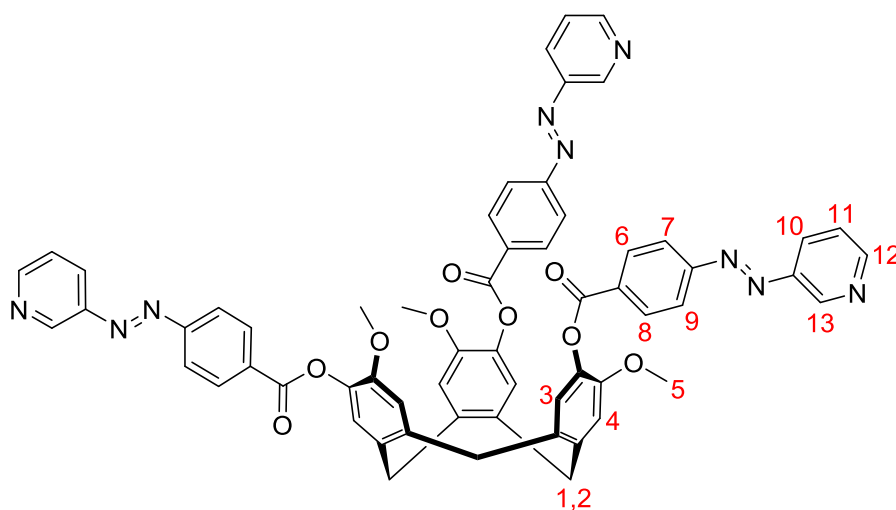


CTG (0.11 g, 0.27 mmol) was dissolved in dry THF (100 mL) under argon. The flask was cooled to 0°C in an ice bath and triethylamine (15 mL) was added. The resulting yellow solution was stirred at 0°C for 1 hour before being added dropwise via cannula to solid 4,4'-pyridyl-azo-benzoyl chloride (0.49 g, 2.20 mmol) under argon. The resulting red-orange suspension was allowed to stir at room temperature for 3 days. The solids were filtered off and triturated in methanol (100 mL) and then THF (100 mL) to give the product (0.22 g, 0.21 mmol, 79%) as a yellow-orange solid.

M.pt 259-261°C; ¹H NMR (300 MHz, DMSO-*d*⁶) δ_H 8.89 (6H, d, J 5.4, Ar-H (11), Ar-H (13)), 8.36 (6H, d, J 8.7, Ar-H (6), Ar-H (8)), 8.13 (6H, d, J 8.7, Ar-H (7), Ar-H (9)), 7.83 (6H, d, J 6.0, Ar-H (10), Ar-H (12)), 7.61 (3H, s, Ar-H (3)), 7.37 (3H, s, Ar-H (4)), 4.93 (3H, d, J 13.7, CTG endo-H (1)), 3.79 – 3.71 (12H, m, O-CH₃ (5) overlapped with CTG exo-H (2)); ¹³C NMR (75 MHz, CDCl₃) δ_C 163.92, 156.91, 154.92, 151.54, 151.46, 149.89, 138.54, 138.18, 132.36, 131.79, 131.53, 131.46, 124.03, 123.26, 116.32, 114.30, 77.44, 77.22, 77.02, 76.59, 56.31, 36.56; HR-MS (ES⁺) *m/z* 2072.6807 {2M + H}⁺ (calculated for {C₁₂₀H₉₁N₁₈O₁₈}⁺ 2072.6787), 1555.0155 {3M + 2H}²⁺ (calculated for {C₁₈₀H₁₃₇N₂₇O₂₇}²⁺ 1555.0117) 1053.3935 {M + H₂O}⁺ (calculated for {C₆₀H₄₇N₉O₁₀}⁺ 1053.3446) 1036.3418 {M + H}⁺ (calculated for {C₆₀H₄₆N₉O₉}⁺ 1036.3413); FT-IR (cm⁻¹) = 3030, 2931, 1721, 1584,

1505, 1476, 1461, 1405, 1258, 1060, 1005, 941, 924, 893, 860, 825, 683, 555; Analysis calculated for **2.11**.CHCl₃.H₂O (% calculated; found) C (62.44, 62.40), H (4.12, 4.33), N (10.74, 10.84); UV-Vis (DMSO) λ_{max} (nm) 312 ($\pi \rightarrow \pi^*$), 465 ($n \rightarrow \pi^*$).

(±)-2,7,12-Trimethoxy-3,8,13-tris(4,3'-Pyridyl-azophenylcarboxy)-10,15-dihydro-5H-tribenzo[*a,d,g*] cyclonatriene (2.12)

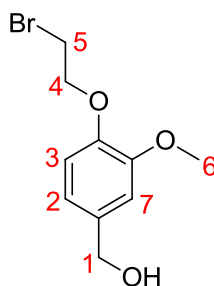


CTG (0.52 g, 1.27 mmol) was dissolved in dry THF (100 mL) under argon. The flask was cooled to 0°C in an ice bath and triethylamine (15 mL) was added. The resulting yellow solution was stirred at 0°C for 1 hour before being added dropwise via cannula to solid 4,3'-pyridyl-azo-benzoyl chloride (1.89 g, 7.70 mmol). The resulting red-orange suspension was allowed to stir at room temperature for 3 days. The solids were filtered off and the solvent removed *in vacuo* to yield a red-orange residue. This crude product was triturated in methanol (2 x 100 mL) to give the product (1.16 g, 1.12 mmol, 88%) as a fine orange solid.

M.pt 250-252°C; ¹H NMR (300 MHz, CDCl₃) δ_{H} 9.26 (3H, d, J 1.8, Ar-H (13)), 8.76 (3H, dd, J 4.6, 1.7, Ar-H (12)), 8.38 (6H, dt, J 8.7, 2.1, Ar-H (6), Ar-H (8)), 8.21 (3H, dt, J 8.3, 1.9, Ar-H (10)), 8.05 (6H, dt, J 8.7, 1.8, Ar-H (7), Ar-H (9)), 7.48 (3H, dd, J 8.2, 4.7, Ar-H (11)), 7.22 (3H, s, Ar-H (3)), 7.00 (3H, s, Ar-H (4)), 4.87 (3H, d, J 13.7, CTG endo-H (1)), 3.82 (9H, s, OCH₃ (5)), 3.72, d, J 13.9, CTG exo-H (2)); ¹³C

NMR (75 MHz, CDCl₃) δ 164.19, 155.30, 152.52, 150.07, 147.91, 147.85, 138.73, 138.31, 131.95, 131.68, 131.59, 127.23, 124.22, 123.12, 114.45, 56.46, 36.68; HR-MS (ES⁺) m/z 1036.3463{M + H}⁺ (calculated for {C₆₀H₄₆N₉O₉}⁺ 1036.3413), 518.6194 {M + 2H}²⁺ (calculated for {C₆₀H₄₆N₉O₉}²⁺ 518.6743); FT-IR (cm⁻¹) = 3066, 2933, 2833, 1786, 1724, 1601, 1583, 1506, 1323, 1260, 1177, 1061, 1006, 859, 764, 697; Analysis calculated for **2.12**. H₂O (% calculated; found) C (68.37, 68.10), H (4.49, 4.30), N (11.96, 11.90); UV-Vis (DMSO) λ_{max} (nm) 326 ($\pi \rightarrow \pi^*$), 411 ($n \rightarrow \pi^*$).

[4-(2-Bromoethoxy)-3-methoxyphenyl] methanol⁵⁶ (**2.13**)

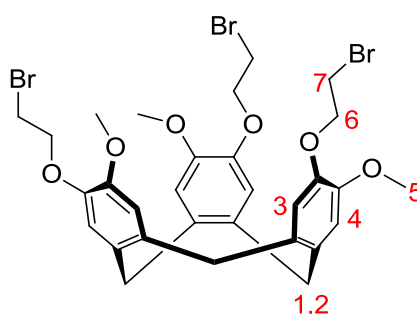


4-Hydroxy-3-methoxybenzyl alcohol (8.02 g, 50.7 mmol) and potassium carbonate (35.0 g, 253 mmol) were suspended in anhydrous DMF (75 mL) under an argon atmosphere. The white suspension was stirred for 40 minutes at room temperature before 1,2 dibromoethane (43.5 mL, 507 mmol) was added via syringe. The reaction was heated overnight at 55°C. The resulting white suspension was then poured into water (400 mL) and extracted with ethyl acetate (3 x 200 mL). The organic layers were concentrated *in vacuo* to approximately 100 mL and then washed with 1M NaOH (100 mL), water (2 x 100 mL) and brine (100 mL). The organic layers were dried (MgSO₄), filtered and the solvent removed *in vacuo* to give a yellow oil. Excess hexane (150 mL) was added resulting in the rapid crystallization of a white solid. The solid was filtered and washed thoroughly with more hexane to give the product (8.55 g, 32.7 mmol, 65%) as a white crystalline solid.

¹H NMR (300 MHz, CDCl₃) δ_{H} 6.96 – 6.83 (3H, m, Ar-H (2), Ar-H (3), Ar-H (7)), 4.61 (2H, d, J 4.5, CH₂OH (1)), 4.31 (2H, t, J 6.7, OCH₂CH₂Br (4)), 3.86 (3H, s, OCH₃ (6)), 3.64 (2H, t, J 6.6, OCH₂CH₂Br (5)); ¹³C NMR (75 MHz, CDCl₃) δ 150.12,

147.05, 135.33, 119.49, 115.00, 111.40, 77.16, 69.52, 65.24, 56.12, 29.02. All data is consistent with the literature.⁴⁶

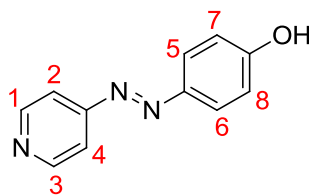
2,7,12-Tris-(2-bromoethoxy)-3,8,13-trimethoxy-10,15-dihydro-2H tribenzo [a,d,g]cyclononene (2.14)



[4-(2-Bromoethoxy)-3-methoxyphenyl] methanol (3.20 g, 12.3 mmol) and Sc(OTf)₃ (0.18g, 0.37 mmol) were dissolved in dry acetonitrile (80 mL) under an argon atmosphere. The reaction was heated to 80°C for two days under an argon atmosphere. The solids were filtered off and the solvent removed to give a pale yellow oil. This crude product was purified with successive column chromatography, eluting with DCM→5% Et₂O/DCM to give the product (1.17 g, 1.60 mmol, 39%) as a white crystalline solid.⁴⁶

¹H NMR (300 MHz, CDCl₃) δ 6.92 (3H, s, Ar-H (3)), 6.84 (3H, s, Ar-H (4)), 4.74 (3H, d, J 13.8, CTG endo-H (1)), 4.31 – 4.26 (6H, t, J 7.2, OCH₂CH₂Br (6)), 3.84 (9H, s, OCH₃ (5)), 3.60 – 3.52 (9H, m, OCH₂CH₂Br (7) overlapped with CTG exo-H (2)); ¹³C NMR (75 MHz, CDCl₃) δ 149.10, 146.04, 133.94, 131.90, 117.95, 113.99, 77.16, 70.02, 56.34, 36.52, 29.29; HR-MS (ES⁺) m/z 748.0117 {M + H₂O}⁺ (calculated for C₃₀H₃₆Br₃O₇)⁺ 748.3225), 1475.9932 {2M + H₂O}⁺ (calculated for C₆₀H₆₈Br₆O₁₃)⁺ 1475.9699), 2205.9751 {3M + H₂O}⁺ (calculated for {C₉₀H₁₀₁Br₉O₁₉)⁺ 2205.9150). All data is consistent with the literature.

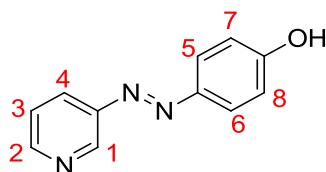
(4-Pyridylazo)phenol (2.15)



Phenol (5.00 g, 53.1 mmol) and sodium nitrite (4.00 g, 57.9 mmol) were dissolved in a 10% w/w NaOH solution (20 mL). The solution was cooled to 0°C and added dropwise to a solution of 4-aminopyridine (6.00 g, 63.7 mmol) in aqueous HCl (25 mL of 11M HCl diluted with 20 mL of water) at 0°C. The reaction was stirred at 0°C for 40 minutes during which time the solution turned deep orange. The pH was adjusted to 7 with the addition of 60 mL of a 10% NaOH solution. The resulting red-brown precipitate was filtered and washed thoroughly with water. Trituration in acetone (75 mL) gave the desired product (4.06 g, 20.2 mmol, 38%) as a yellow solid.

^1H NMR (300 MHz, MeOD) δ_{H} 8.72 (2H, dd, J 6.3, 1.5, Ar-H (1), Ar-H (3)), 7.93 (2H, dt, J 9.0, 2.1, Ar-H (5), Ar-H (6)), 7.78 (2H, dd, J 6.3, 1.8, Ar-H (2), Ar-H (4)), 6.97 (2H, dt, J 9.0, 2.1, Ar-H (7), Ar-H (8)); ^{13}C NMR (75 MHz, DMSO) δ_{C} 162.30, 156.80, 151.30, 145.23, 125.75, 116.17, 115.75, 39.52; HR-MS (ES⁺) m/z 200.0832 $\{M + H\}^+$ (calculated for $\{C_{11}H_{10}N_3O\}^+$ 200.2205). All data is consistent with the literature.⁴⁷

(3-Pyridylazo)phenol (2.16)

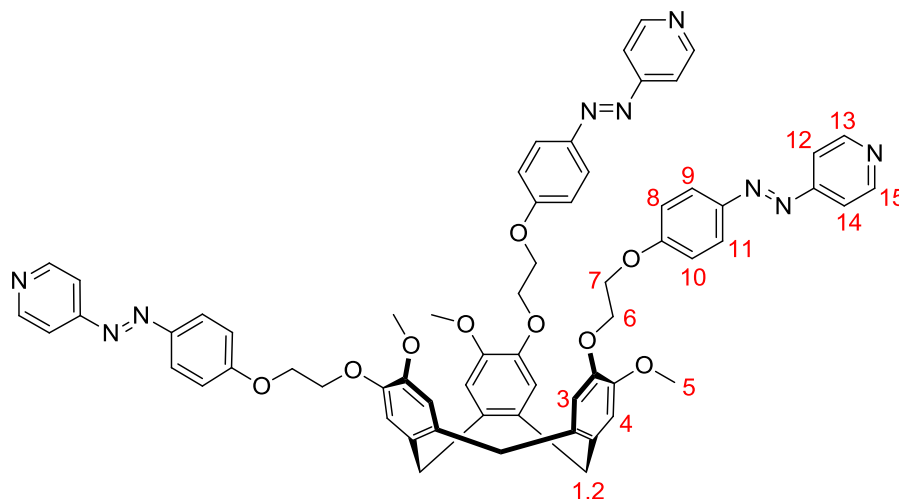


Phenol (5.00 g, 53.1 mmol) and sodium nitrite (4.00 g, 57.9 mmol) were dissolved in a 10% w/w NaOH solution (45 mL). The solution was cooled to 0°C and added dropwise to a solution of 3-aminopyridine (6.00 g, 63.7 mmol) in aqueous HCl (25 mL of 11M HCl diluted with 20 mL of water) at 0°C. The reaction was stirred at 0°C for 20 minutes during which time the solution turned deep orange. The pH was adjusted to 6 with the addition of 100 mL of a 10% NaOH solution. The resulting yellow-orange precipitate was filtered and washed thoroughly with water. Trituration

in diethyl ether (75 mL) gave the desired product (8.16 g, 0.04 mmol, 77%) as a pale orange solid.

^1H NMR (300 MHz, MeOD) δ_{H} 9.03 (1H, d, J 2.4, Ar-H (1)), 8.62 (1H, dd, J 4.9, 1.5, Ar-H (2)), 8.28 (1H, dt, J 8.2, 1.9, Ar-H (4)), 7.93 (2H, dt, J 9.0, 3.0, Ar-H (5), Ar-H (6)), 7.63 (1H, dd, J 8.3, 4.9, Ar-H (3)), 6.98 (2H, dt, J 9.0, 3.0, Ar-H (7), Ar-H (8)); ^{13}C NMR (101 MHz, MeOD) δ 163.20, 150.64, 149.96, 147.49, 146.09, 129.59, 126.57, 126.08, 116.90, 49.00; HR-MS (ES⁺) m/z 200.0934 {M + H}⁺ (calculated for {C₁₁H₁₀N₃O}⁺ 200.2205). All data is consistent with the literature.⁴⁸

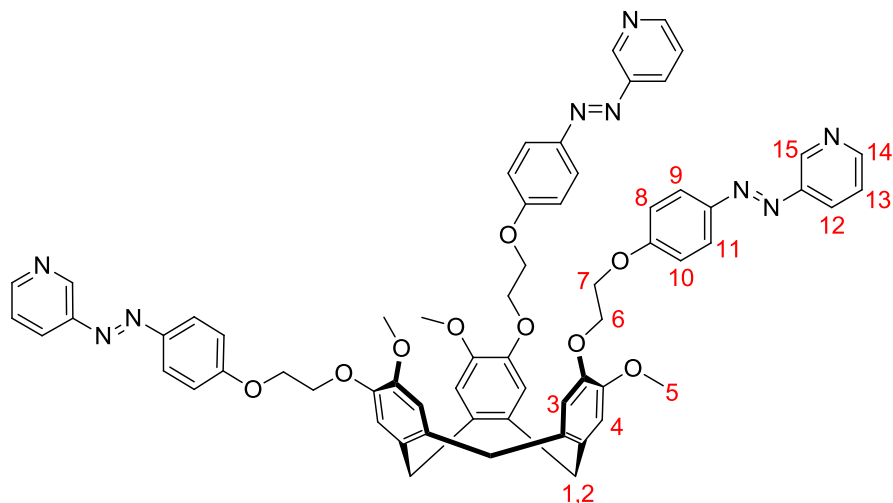
2,7,12-Tris-(2-(4-pyridylazo)ethoxy)-3,8,13-trimethoxy-10,15-dihydro-2H tribenzo [a,d,g]cyclononene (2.17)



p-(4-Pyridylazo)phenol (1.11 g, 5.55 mmol), 2,7,12-Tris-(2-bromoethoxy)-3,8,13-trimethoxy-10,15-dihydro-2H tribenzo [a,d,g]cyclononene (0.45 g, 0.62 mmol) and caesium carbonate (2.65 g, 8.16 mmol) were dissolved in anhydrous DMF (10 mL) under an argon atmosphere. The resulting bright red solution was heated to 100°C for 3 days. The reaction was cooled to room temperature and water (90 mL) was added slowly. The resulting reddy-brown precipitate was filtered off and washed with methanol (50 mL) and diethyl ether (50 mL) to give a crude yellow-orange solid. This crude product was triturated in DCM (100 mL), filtered and the solvent removed under reduced pressure to give the product (0.58 g, 5.38 mmol, 85%) as an orange crystalline powder.

M.pt 232-234°C; ^1H NMR (300 MHz, CDCl_3) δ 8.77 (6H, d, J 6.0, Ar-H (13), Ar-H (15)), 7.93 (6H, d, J 9.0, Ar-H (9), Ar-H (11)), 7.66 (6H d, J 6.0, Ar-H (12), Ar-H (14)), 7.02 (6H, d, J 9.0, Ar-H (8), Ar-H (10)), 6.97 (3H, s, Ar-H (3)), 6.85 (3H, s, Ar-H (4)), 4.76 (3H, d, J 13.9, CTG endo-H (1)), 4.43 – 4.32 (12 H, m, OCH_2CH_2 (6,7)), 3.78 (9H, s, OCH_3 (5)), 3.56 (3H, d, J 13.8, CTG exo-H (2)); ^{13}C NMR (75 MHz, CDCl_3) δ 162.19, 157.35, 151.23, 148.84, 147.01, 146.71, 133.48, 131.95, 125.54, 117.32, 116.15, 115.03, 114.14, 68.32, 66.96, 56.28, 36.49; HR-MS (ES^+) m/z 1084.4333 $\{\text{M} + \text{H}\}^+$ (calculated for $\{\text{C}_{63}\text{H}_{58}\text{N}_9\text{O}_9\}^+$ 1084.4352), 542.7416 $\{\text{M} + 2\text{H}\}^{2+}$ (calculated for $\{\text{C}_{63}\text{H}_{58}\text{N}_9\text{O}_9\}^{2+}$ 542.7212); FT-IR (cm^{-1}) = 3348, 2930, 1598, 1582, 1497, 1452, 1417, 1402, 1250, 1214, 1137, 1089, 1058, 1042, 1001, 989, 922, 834, 743, 623, 559, 518; Analysis calculated for **2.17**. DCM (% calculated; found) C (65.75, 65.80), H (5.09, 5.05), N (10.78, 10.40); UV-Vis (DMSO) λ_{max} (nm) 354 ($\pi \rightarrow \pi^*$, trans isomer), 445 ($n \rightarrow \pi^*$, cis isomer).

2,7,12-Tris-(2-(3-pyridylazo)ethoxy)-3,8,13-trimethoxy-10,15-dihydro-2H tribenzo [a,d,g]cyclononene (2.18)

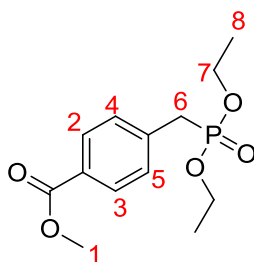


p-(3-Pyridylazo)phenol (0.98 g, 4.93 mmol), 2,7,12-Tris-(2-bromoethoxy)-3,8,13-trimethoxy-10,15-dihydro-2H tribenzo [a,d,g]cyclononene (0.40 g, 0.54 mmol) and caesium carbonate (2.32 g, 7.14 mmol) were dissolved in anhydrous DMF (10 mL) under an argon atmosphere. The resulting bright red solution was heated to 100°C for 3 days. The reaction was cooled to room temperature and water (90 mL) was added slowly. The resulting reddy-brown precipitate was filtered off and washed with

methanol (50 mL) and diethyl ether (50 mL) to give a crude yellow-orange solid. This crude product was triturated in DCM (100 mL), filtered and the solvent removed under reduced pressure to give the product (0.32 g, 0.29 mmol, 55%) as a yellow solid.

M.pt 159-161 °C; ¹H NMR (400 MHz, CDCl₃) δ 9.14 (3H, d, J 2.1, Ar-H (15)), 8.66 (3H, dd, J 4.7, 1.7, Ar-H (14)), 8.10 (3H, dt, J 8.2, 2.1, Ar-H (12)), 7.92 (6H, dt, J 6.7, 2.7, Ar-H (9), Ar-H (11)), 7.42 (3H, dd, J 8.1, 4.7, Ar-H (13)), 7.01 (6H, dt, J 6.9, 1.5, Ar-H (8), Ar-H (10)), 6.97 (3H, s, Ar-H (3)), 6.85 (3H, s, Ar-H (4)), 4.77 (3H, d, J 13.7, CTG endo-H (1)), 4.43 – 4.32 (12H, m, OCH₂CH₂ (6,7)), 3.78 (9H, s, OCH₃ (5)), 3.57 (3H, d, J 13.8, CTG exo-H (2)); ¹³C NMR (101 MHz, CDCl₃) δ 161.76, 151.25, 148.98, 148.09, 147.27, 147.18, 146.86, 133.60, 132.08, 126.89, 125.19, 124.03, 117.46, 115.10, 114.25, 77.16, 68.48, 67.04, 56.41, 36.63; HR-MS (ES⁺) m/z. 1084.4359 {M + H}⁺ (calculated for {C₆₃H₅₈N₉O₉}⁺ 1084.4352), 542.7206 {M + 2H}²⁺ calculated for {C₆₃H₅₉N₉O₉}²⁺ 542.7212); FT-IR (cm⁻¹) = 3432, 2924, 1598, 1582, 1498, 1452, 1398, 1313, 1250, 1217, 1140, 1061, 1019, 1000, 918, 836, 809, 743, 723, 701, 616, 552, 518; Analysis calculated for **2.18**. 0.5 DCM (% calculated; found) C (67.75, 67.60), H (5.33, 5.15), N (11.11, 10.73); UV-Vis (DMSO) λ_{max} (nm) 354 (π→π* trans isomer), 448 (n→π* cis isomer).

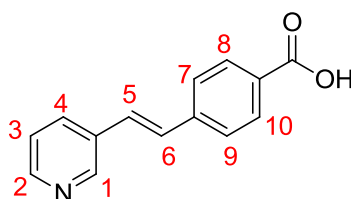
Diethyl (4-(methoxycarbonyl)benzyl)phosphonate (2.19)



Methyl 4-bromomethyl benzoate (5.00 g, 21.8 mmol) was suspended in triethyl phosphite (7.5 mL, 43.6 mmol). The reaction was heated to 120 °C for five hours during which time all of the starting material dissolved to give a yellow oil. The flask was cooled to room temperature and the excess triethyl phosphite was removed by Kugelrohr distillation (boiling point 110 °C under high vacuum) to give the pure product (5.01 g, 18.4 mmol, 87%) as a pale yellow oil.

^1H NMR (300 MHz, CDCl_3) δ 7.98 (2H, dd, J 7.5, 0.9, Ar-H (2), Ar-H(3)), 7.37 (2H, dd, J 8.6, 2.2, Ar-H (4), Ar-H(5)), 4.06 – 3.96 (4H, m, POCH_2 (7)), 3.90 (3H, s, COOCH_3 (1)), 3.19 (2H, d, J 22.2, ArCH_2 (6)), 1.23 (6H, t, J 7.1, POCH_2CH_3 (8)); ^{13}C NMR (75 MHz, CDCl_3) δ 166.81, 137.23, 129.84, 128.76, 77.16, 62.29, 52.03, 34.88, 33.06, 16.37; HR-MS (ES^+) m/z 287.1052 $\{\text{M} + \text{H}\}^+$ (calculated for $\{\text{C}_{13}\text{H}_{20}\text{O}_5\text{P}\}^+$ 287.1043). All data is consistent with the literature.⁵⁰

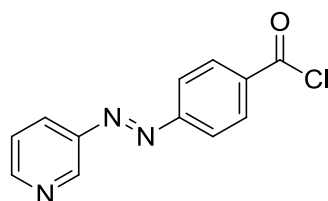
4-[(E)-2-(3-Pyridinyl)ethenyl]benzoic acid (2.20)



Diethyl (4-(methoxycarbonyl)benzyl)phosphonate (1.02 g, 3.5 mmol) was dissolved in dry THF (15 mL) under a nitrogen atmosphere. The flask was cooled to 0°C and sodium hydride (0.28 g, 60% dispersion in mineral oil, 11.7 mmol) was added in portions. The resulting suspension was stirred for 1 hour at 0°C. A solution of 3-pyridinecarboxaldehyde (0.37 g, 3.5 mmol) in dry THF (15 mL) was added via cannula. The reaction was stirred overnight at room temperature. The reaction was cooled to 0°C and water (5 mL) was added slowly. The reaction was acidified to pH 1 *via* the addition of a 1M HCl solution leading to the formation of a white precipitate which was filtered, washed with water and diethyl ether and dried *in vacuo* to give the product (0.24 g, 10.6 mmol, 30%) as a white solid.

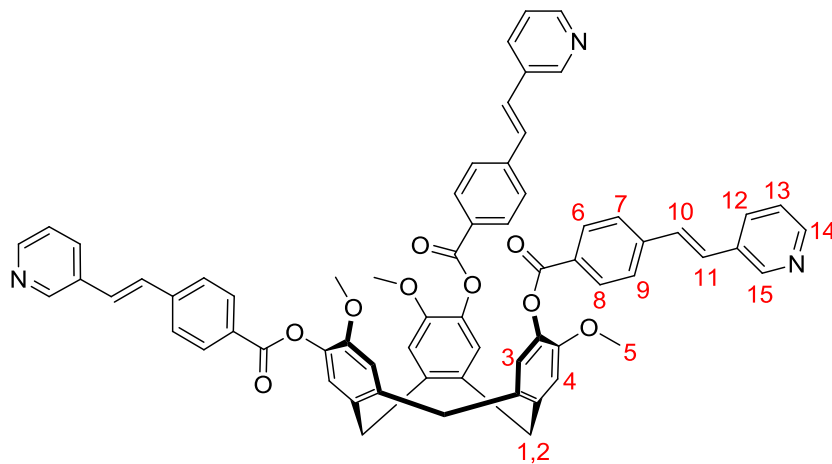
^1H NMR (300 MHz, DMSO-d_6) δ 9.08 (1H, d, J 1.9, Ar-H (1)), 8.77 (1H, dd, J 5.5, 1.3, Ar-H(2)), 8.71 (1H, dt, J 8.3, 1.7, Ar-H(3)), 8.04 – 7.95 (3H, m, Ar-H(4) overlapped with Ar-H(7) and Ar-H(9)), 7.82 – 7.69 (3H, m, Stilbene H(5) overlapped with Ar-H(8) and Ar-H(10)), 7.57 (1H, d, J 16.6, Stilbene H(6)); ^{13}C NMR (75 MHz, DMSO) δ 166.90, 143.20, 142.94, 140.30, 138.86, 134.89, 132.12, 130.47, 129.87, 126.98, 125.99, 125.47; HR-MS (ES^+) m/z 226.0874 $\{\text{M} + \text{H}\}^+$ (calculated for $\{\text{C}_{14}\text{H}_{12}\text{NO}_2\}^+$ 226.0863). All data is consistent with the literature.⁵¹

4,3'-Pyridyl-ethynyl-benzoyl chloride (2.21)



4-[(E)-2-(3-pyridinyl)ethenyl]benzoic acid (0.2g, 8.84 mmol) was suspended in thionyl chloride (15 mL) under an argon atmosphere. The resulting pale yellow suspension was heated to reflux overnight during which time all the material dissolved. The flask was allowed to cool to room temperature before the thionyl chloride was removed *in vacuo* to give the product as a pale yellow solid in a quantitative yield that was used in the next reaction immediately without further purification.

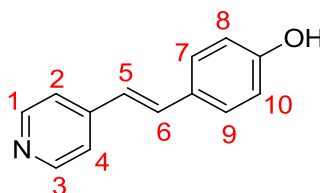
(±)-2,7,12-trimethoxy-3,8,13-tris(4,3'-Pyridyl-ethynylphenylcarboxy)-10,15-dihydro-5H-tribenzo[*a,d,g*] cyclononatriene (2.22)



CTG (0.52 g, 1.27 mmol) was dissolved in dry CHCl_3 (100 mL) under argon. The flask was cooled to 0°C in an ice bath and triethylamine (15 mL) was added. The resulting yellow solution was stirred at 0°C for 1 hour before being added dropwise via cannula to solid 4,3'-pyridyl-ethynylbenzoyl chloride (1.89 g, 7.70 mmol). The resulting yellow suspension was allowed to stir at room temperature for 3 days. The solids were filtered off and the solvent removed *in vacuo* to yield a brown residue. This crude product was triturated in methanol (2 x 100 mL) to give the product (1.16 g, 1.12 mmol, 88%) as a fine tan solid.

M.pt 222-224 °C; ¹H NMR (300 MHz, CDCl₃) δ 8.78 (3H, d, J 2.2, Ar-H (15)), 8.54 (3H, dd, J 4.8, 1.6, Ar-H (14)), 8.22 (6H, d, J 8.4, Ar-H (6), Ar-H(8)), 7.88 (3H, dt, J 8.1, 2.0, Ar-H(12)), 7.65 (6H, d, J 8.4, Ar-H (7), Ar-H (9)), 7.33 (3H, dd, J 7.8, 5.1, Ar-H (13)), 7.23 (6H, s, Stilbene H (10), Stilbene H (11)), 7.21 (3H, s, Ar-H (3)), 6.99 (3H, s, Ar-H (4)), 4.84 (3H, d, J 13.9, CTG endo H (1)), 3.83 (9H, s, O-CH₃ (5)), 3.70 (3H, d, J 13.8, CTG exo H (2)); ¹³C NMR (75 MHz, CDCl₃) δ 164.52, 150.09, 149.28, 148.89, 141.69, 138.78, 138.15, 133.11, 132.54, 131.68, 130.99, 129.76, 128.92, 127.84, 126.74, 124.26, 123.78, 114.44, 77.16, 56.45, 36.65; HR-MS (ES⁺) m/z 344.12 {M + 3H}³⁺ (calculated for {C₆₆H₅₄N₃O₉}³⁺ 344.1281), 515.68 {M + 2H}²⁺ (calculated for {C₆₆H₅₃N₃O₉}²⁺ 515.6885), 1030.37 {M + H}⁺ (calculated for {C₆₆H₅₂N₃O₉}⁺ 1030.3698); FT-IR (cm⁻¹) = 2933, 1727, 1604, 1506, 1419, 1260, 1205, 1174, 1138, 1090, 1060, 1013, 957, 835, 795, 756, 704, 646, 621; Analysis calculated for **2.22** (% calculated; found) C (76.95, 77.01), H (4.99, 5.10), N (4.08, 4.25); UV-Vis (DCM) λ_{max} (nm) 323 (π→π*).

4-[2-(4-Pyridinyl)ethynyl] phenol (**2.23**)

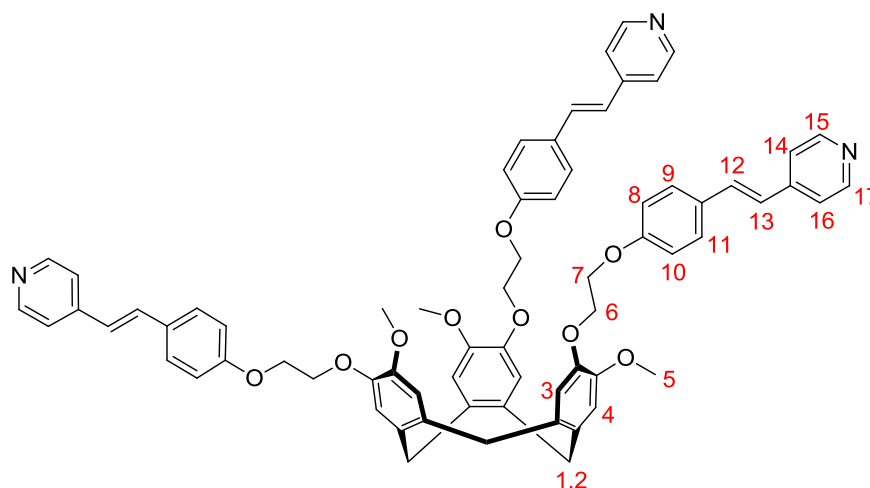


4-hydroxybenzaldehyde (15.3 g, 0.13 mmol) was suspended in acetic anhydride (19mL). 4-methylpyridine (9.73 mL, 0.1 mmol) was added and the mixture heated to reflux overnight. The mixture was poured in 300 mL of iced water and stirred for 1 h to hydrolyze the excess of acetic anhydride. The precipitate was filtered and then washed with water. The solid was redissolved in 180 mL of ethanol along with 7g of potassium hydroxide and refluxed for 90 minutes. The flask was cooled to room temperature and the resulting precipitate was filtered, and washed with ethanol and diethyl ether to give the product (10.1 g, 0.05 mmol, 50%) as a pale yellow solid.

¹H NMR (400 MHz, DMSO-d₆) δ 8.35 (2H, d, J 5.6, Ar-H (1), Ar-H (3)), 7.34 – 7.31 (2H, d, J 6.0, Ar-H (2), Ar-H (4)), 7.26 (1H, d, J 16.1, Stilbene H (5)) 7.19 – 7.14 (2H, d, J 8.8, Ar-H (7), Ar-H (9)), 6.54 (1H, d, J 16.1, Stilbene H (6)), 6.25 (2H, d, J 8.3,

Ar-H (8), Ar-H (10)); ^{13}C NMR (75 MHz, DMSO) δ 149.53, 140.75, 135.07, 129.16, 119.49, 118.57, 115.07, 109.53, 39.52; HR-MS (ES⁺) m/z 198.0913 {M + H}⁺ (calculated for {C₁₃H₁₂NO}⁺ 198.0913). All data is consistent with the literature.⁵³

2,7,12-Tris-(2-(4-pyridylethynyl)ethoxy)-3,8,13-trimethoxy-10,15-dihydro-2H tribenzo [a,d,g]cyclononene (2.24)



4-(4-Pyridylethynyl)phenol (0.48 g, 2.43 mmol), 2,7,12-Tris-(2-bromoethoxy)-3,8,13-trimethoxy-10,15-dihydro-2H tribenzo [a,d,g]cyclononene (0.20 g, 0.27 mmol) and caesium carbonate (1.16 g, 3.57 mmol) were dissolved in anhydrous DMF (10 mL) under an argon atmosphere. The resulting brown suspension was heated to 100°C for 3 days. The reaction was cooled to room temperature and water (90 mL) was added slowly. The resulting yellow precipitate was filtered off and washed with methanol (50 mL) and diethyl ether (50 mL) to give a crude yellow solid. This crude product was triturated in methanol (100 mL) to give the product (0.18 g, 0.17 mmol, 64%) as a pale yellow solid.

^1H NMR (300 MHz, CD₂Cl₂) δ 8.45 (6H, d, J 6.0, **Ar-H (15), Ar-H (17)**), 7.43 (6H, d, J 8.7, **Ar-H (9), Ar-H (11)**), 7.29 (6H, d, J 6.0, **Ar-H (14), Ar-H (16)**), 7.21 (d, J 16.3, **Stilbene H (13)**), 6.90 – 6.78 (15H, m, **Ar-H (3) overlapped with Ar-H (4), Ar-H (8), Ar-H (10) and Stilbene H (12)**) 4.70 (3H, d, J 13.8, **CTG endo H (1)**), 4.37 – 4.25 (12H, m, **OCH₂CH₂ (6,7)**), 3.77 (9H, s, **OCH₃**), 3.56 (3H, d, J 13.7, **CTG exo H (2)**); ^{13}C NMR (75 MHz, DMSO) δ 158.76, 149.92, 147.56, 146.19, 144.59, 132.60, 132.06, 128.96, 128.54, 123.64, 120.59, 115.32, 114.86, 114.02, 67.27, 66.51, 55.86, 39.52, 35.05; HR-MS (ES⁺) m/z 360.1587 {M + 3H}³⁺ (calculated for

{C₆₉H₆₆N₃O₉}³⁺ 360.1594), 539.7357 {M + 2H}²⁺ (calculated for {C₆₉H₆₅N₃O₉}²⁺ 539.7355), 1078.4607 {M + H}⁺ (calculated for {C₆₉H₆₄N₃O₉}⁺ 1078.4637); Analysis calculated for **2.24**. DCM (% calculated; found) C (72.28, 72.74), H (5.63, 5.57), N (3.61, 3.81) UV-Vis (DCM) λ_{max} (nm) 262 (π→π*).

2.7.3 X-ray crystallography

Crystals were mounted under inert oil on a MiTeGen tip and flash frozen using an Oxford Cryosystems low temperature device. X-ray diffraction data were collected using graphite monochromated Mo-K radiation (λ = 0.71073, compounds **2.5** and **2.6**); or CuKα radiation (λ = 1.54184 Å, compound **2.17**) on a Agilent Supernova dual-source diffractometer with Atlas S2 CCD detector and fine-focus sealed tube generator. Data for compounds **2.8** and **2.12** were collected using synchrotron radiation (λ = 0.6889 Å) using a Crystal Logic 4-circle Kappa goniometer and Rigaku Saturn 724 CCD diffractometer at station I19 of Diamond Light Source. Data were corrected for Lorentzian and polarization effects and absorption corrections were applied using multi-scan methods. The structures were solved by direct methods using SHELXS-97 and refined by full-matrix on F² using SHELXL-97.⁵⁸

Crystals of compound **2.12** were poorly diffracting and collected using synchrotron radiation at station I19 of Diamond Light Source. The azobenzene ligand arms were heavily disordered, hence the whole structure was refined isotropically. One phenyl ring was refined at 35% occupancy and another azopyridyl unit was refined at 50% occupancy. Eight phenyl rings were restrained so as to be chemically reasonable. Additionally the bond distances of two of the N=N azo bonds were restrained to be chemically reasonable. The structure contained residual electron density that could not be meaningfully refined as solvent hence the SQUEEZE⁴⁵ routine of PLATON was employed.

The residual electron density present in the structure of compound **2.17** was modelled as three molecules of nitromethane solvent, one at 100% occupancy with the remaining two disordered at 75% and 50% occupancy respectively. Thermal parameters were restrained with a rigid bond restraint. Additionally, the N-O bonds in these solvent molecules were restrained to be chemically reasonable.

	2.5	2.6	2.8	2.12	2.17
Empirical Formula	C ₁₂ H ₁₆ N ₃ NaO ₆	C ₁₂ H ₁₈ N ₃ NaO ₇	C ₂₄ H ₁₆ Cl ₂ N ₆ O ₄	C ₁₂₀ H ₉₀ N ₁₈ O ₁₈	C ₆₃ H ₅₇ N ₉ O ₉
Mr	333.56	353.25	531.23	2072.36	1084.34
Crystal Appearance	Orange Needle	Orange Needle	Yellow Block	Orange Needle	Orange Plates
Crystal Size (mm)	0.04 x 0.05 x 0.19	0.09 x 0.16 x 0.35	0.20 x 0.20 x 0.20	0.10 x 0.17 x 0.33	0.13 x 0.14 x 0.29
Crystal system	Triclinic	Monoclinic	Orthorhombic	Triclinic	Monoclinic
Space group	P $\bar{1}$	P2 ₁ /n	P ca2 ₁	P $\bar{1}$	I2/a
a (Å)	6.1765 (4)	6.5197 (6)	6.525 (16)	9.6864 (5)	35.503 (7)
b (Å)	7.0883 (4)	35.222 (3)	14.281 (3)	29.786 (2)	9.6091 (19)
c (Å)	17.593 (6)	7.2310 (7)	23.149 (6)	34.468 (4)	37.339 (8)
α (°)	88.175 (4)	90	90	71.898 (8)	90
β (°)	83.629 (5)	102.838 (10)	90	88.532 (6)	103.589 (2)
γ (°)	69.716 (6)	90	90	34.468 (5)	90
V (Å ³)	717.98	1619	2157	9448.9	12384.3
Z	1	1	2	2	1
Pcalc (g.cm ⁻³)	1.379	1.392	1.215	0.718	1.31
μ (mm ⁻¹)	0.118	0.136	0.105	0.05	0.772
F (000)	298	712	788	2100	5136
Radiation (λ)	Mo (0.71073)	Mo (0.71073)	Synchrotron (0.6889)	Synchrotron (0.6889)	Cu (1.54184)
2 θ range	4.66 to 52.6	6.22 to 56.56	3.42 to 53.18	3.06 to 40.3	6.182 to 127.652
Reflections collected	13191	11758	19611	62098	41057
Independent reflections	2761	4026	4791	19726	10085
Data/restraints/parameters	2761/0/263	4026/0/248	4791/1/327	19726/2/375	10085/40/844
Goof on F2	0.58	1.259	1.061	1.713	1.037
Final R indexes [$I \geq 2\sigma(I)$]	R1 = 0.0341	R1 = 0.0911	R1 = 0.0547	R1 = 0.2948	R1 = 0.0917
Final R indexes (all data)	wR2 = 0.0970	wR2 = 0.1714	wR2 = 0.1438	wR2 = 0.4929	wR2 = 0.2944

Table 2.3: Details of crystal collection and analyses for X-ray datasets of compounds 2.5, 2.6, 2.8, 2.12 and 2.17.

2.8 References

1. C. Carruthers, T. K. Ronson, C. J. Sumby, A. Westcott, L. P. Harding, T. J. Prior, P. Rizkallah and M. J. Hardie, *Chemistry – A European Journal*, 2008, **14**, 10286-10296.
2. J. J. Henkelis, T. K. Ronson and M. J. Hardie, *CrystEngComm*, 2014, **16**, 3688-3693.
3. J. J. Henkelis, S. A. Barnett, L. P. Harding and M. J. Hardie, *Inorganic Chemistry*, 2012, **51**, 10657-10674.
4. A. Westcott, J. Fisher, L. P. Harding, P. Rizkallah and M. J. Hardie, *Journal of the American Chemical Society*, 2008, **130**, 2950-2951.
5. J. M. Fowler, F. L. Thorp-Greenwood, S. L. Warriner, C. E. Willans and M. J. Hardie, *Chemical Communications*, 2016, **52**, 8699-8702.
6. M. J. Hardie, R. M. Mills and C. J. Sumby, *Organic & Biomolecular Chemistry*, 2004, **2**, 2958-2964.
7. C. J. Sumby, K. C. Gordon, T. J. Walsh and M. J. Hardie, *Chemistry – A European Journal*, 2008, **14**, 4415-4425.
8. C. J. Sumby and M. J. Hardie, *Angewandte Chemie International Edition*, 2005, **44**, 6395-6399.
9. N. J. Cookson, J. J. Henkelis, R. J. Ansell, C. W. G. Fishwick, M. J. Hardie and J. Fisher, *Dalton Transactions*, 2014, **43**, 5657-5661.
10. C. Carruthers, J. Fisher, L. P. Harding and M. J. Hardie, *Dalton Transactions*, 2010, **39**, 355-357.
11. J. J. Henkelis, T. K. Ronson, L. P. Harding and M. J. Hardie, *Chemical Communications*, 2011, **47**, 6560-6562.
12. J. J. Henkelis, C. J. Carruthers, S. E. Chambers, R. Clowes, A. I. Cooper, J. Fisher and M. J. Hardie, *Journal of the American Chemical Society*, 2014, **136**, 14393-14396.
13. M. J. Hardie, *Chemical Society Reviews*, 2010, **39**, 516-527.
14. M. J. Hardie, *Israel Journal of Chemistry*, 2011, **51**, 807-816.
15. J. J. Henkelis, J. Fisher, S. L. Warriner and M. J. Hardie, *Chemistry – A European Journal*, 2014, **20**, 4117-4125.
16. T. K. Ronson, J. Fisher, L. P. Harding and M. J. Hardie, *Angewandte Chemie International Edition*, 2007, **46**, 9086-9088.
17. T. K. Ronson, C. Carruthers, J. Fisher, T. Brotin, L. P. Harding, P. J. Rizkallah and M. J. Hardie, *Inorganic Chemistry*, 2009, **49**, 675-685.
18. F. L. Thorp-Greenwood, V. E. Pritchard, M. P. Coogan and M. J. Hardie, *Organometallics*, 2016, **35**, 1632-1642.
19. V. E. Pritchard, D. Rota Martir, S. Oldknow, S. Kai, S. Hiraoka, N. J. Cookson, E. Zysman-Colman and M. J. Hardie, *Chemistry – A European Journal*, 2017, **23**, 6290-6294.
20. E. Merino and M. Ribagorda, *Beilstein Journal of Organic Chemistry*, 2012, **8**, 1071-1090.

21. H. M. D. Bandara and S. C. Burdette, *Chemical Society Reviews*, 2012, **41**, 1809-1825.
22. G. H. Clever, S. Tashiro and M. Shionoya, *Journal of the American Chemical Society*, 2010, **132**, 9973-9975.
23. Nuriman, B. Kuswandi and W. Verboom, *Analytica Chimica Acta*, 2009, **655**, 75-79.
24. E. Busseron, J. Lux, M. Degardin and J. Rebek, *Chemical Communications*, 2013, **49**, 4842-4844.
25. A. Asadi, D. Ajami and J. Rebek, *Chemical Communications*, 2014, **50**, 533-535.
26. J. Canceill, J. Gabard and A. Collet, *Journal of the Chemical Society, Chemical Communications*, 1983, 122-123.
27. H. Zimmermann, P. Tolstoy, H.-H. Limbach, R. Poupko and Z. Luz, *The Journal of Physical Chemistry B*, 2004, **108**, 18772-18778.
28. J. W. Steed, P. C. Junk, J. L. Atwood, M. J. Barnes, C. L. Raston and R. S. Burkhalter, *Journal of the American Chemical Society*, 1994, **116**, 10346-10347.
29. E. Huerta, S. A. Serapian, E. Santos, E. Cequier, C. Bo and J. de Mendoza, *Chemistry – A European Journal*, 2016, **22**, 13496-13505.
30. F. L. Thorp-Greenwood, A. N. Kulak and M. J. Hardie, *Nature Chemistry*, 2015, **7**, 526-531.
31. E. Merino, *Chemical Society Reviews*, 2011, **40**, 3835-3853.
32. K. Takumi, F. Jun-ichi, N. Jotaro, U. Satoshi, K. Takaya and S. Hiroshi, *Japanese Journal of Applied Physics*, 2012, **51**, 10NE02.
33. B. Priewisch and K. Rück-Braun, *The Journal of Organic Chemistry*, 2005, **70**, 2350-2352.
34. R. Zhao, C. Tan, Y. Xie, C. Gao, H. Liu and Y. Jiang, *Tetrahedron Letters*, 2011, **52**, 3805-3809.
35. D. Takamatsu, K.-i. Fukui, S. Aroua and Y. Yamakoshi, *Organic & Biomolecular Chemistry*, 2010, **8**, 3655-3664.
36. E. Elacqua, P. Kaushik, R. H. Groeneman, J. C. Sumrak, D.-K. Bučar and L. R. MacGillivray, *Angewandte Chemie International Edition*, 2012, **51**, 1037-1041.
37. H.-X. Chen, F. Zhou, Y. Ma, X.-P. Xu, J.-F. Ge, Y. Zhang, Q.-F. Xu and J.-M. Lu, *Dalton Transactions*, 2013, **42**, 4831-4839.
38. A. N. Pearce, E. W. Chia, M. V. Berridge, G. R. Clark, J. L. Harper, L. Larsen, E. W. Maas, M. J. Page, N. B. Perry, V. L. Webb and B. R. Copp, *Journal of Natural Products*, 2007, **70**, 936-940.
39. H. D. Ansporn, *Organic Syntheses*, 1945, 86.
40. M. M. J. Tecklenburg, D. J. Kosnak, A. Bhatnagar and D. K. Mohanty, *Journal of Raman Spectroscopy*, 1997, **28**, 755-763.
41. U. Funke and H.-F. Grützmacher, *Tetrahedron*, 1987, **43**, 3787-3795.
42. Y. Norikane, R. Katoh and N. Tamaoki, *Chemical Communications*, 2008, **0**, 1898-1900.

43. S. A. Nagamani, Y. Norikane and N. Tamaoki, *The Journal of Organic Chemistry*, 2005, **70**, 9304-9313.
44. M. Sinan, M. Panda, A. Ghosh, K. Dhara, P. E. Fanwick, D. J. Chattopadhyay and S. Goswami, *Journal of the American Chemical Society*, 2008, **130**, 5185-5193.
45. P. van der Sluis and A. L. Spek, *Acta Crystallographica Section A*, 1990, **46**, 194-201.
46. O. Taratula, P. A. Hill, Y. Bai, N. S. Khan and I. J. Dmochowski, *Organic Letters*, 2011, **13**, 1414-1417.
47. H. Zhang, R. Hao, J. K. Jackson, M. Chiao and H. Yu, *Chemical Communications*, 2014, **50**, 14843-14846.
48. M. M. Naoum, A. A. Fahmi, A. A. Refaie and M. A. Alaasar, *Liquid Crystals*, 2012, **39**, 47-61.
49. D. H. Waldeck, *Chemical Reviews*, 1991, **91**, 415-436.
50. A. Batra, P. Darancet, Q. Chen, J. S. Meisner, J. R. Widawsky, J. B. Neaton, C. Nuckolls and L. Venkataraman, *Nano Letters*, 2013, **13**, 6233-6237.
51. N. G. Anthony, D. Breen, J. Clarke, G. Donoghue, A. J. Drummond, E. M. Ellis, C. G. Gemmell, J.-J. Helesbeux, I. S. Hunter, A. I. Khalaf, S. P. Mackay, J. A. Parkinson, C. J. Suckling and R. D. Waigh, *Journal of Medicinal Chemistry*, 2007, **50**, 6116-6125.
52. V. Vicinelli, P. Ceroni, M. Maestri, M. Lazzari, V. Balzani, S.-K. Lee, J. v. Heyst and F. Vogtle, *Organic & Biomolecular Chemistry*, 2004, **2**, 2207-2213.
53. C. Koopmans and H. Ritter, *Journal of the American Chemical Society*, 2007, **129**, 3502-3503.
54. M. Han, Y. Luo, B. Damaschke, L. Gómez, X. Ribas, A. Jose, P. Peretzki, M. Seibt and G. H. Clever, *Angewandte Chemie International Edition*, 2016, **55**, 445-449.
55. S. Chen, L.-J. Chen, H.-B. Yang, H. Tian and W. Zhu, *Journal of the American Chemical Society*, 2012, **134**, 13596-13599.
56. J. Canceill, A. Collet and G. Gottarelli, *Journal of the American Chemical Society*, 1984, **106**, 5997-6003.
57. Q. Wei, G. K. Seward, P. A. Hill, B. Patton, I. E. Dimitrov, N. N. Kuzma and I. J. Dmochowski, *Journal of the American Chemical Society*, 2006, **128**, 13274-13283.
58. G. Sheldrick, *Acta Crystallographica Section A*, 2008, **64**, 112-122.

Chapter 3

Synthesis and characterisation of Ir(III) metallocryptophanes with photoresponsive functionality

3.1 Introduction

Coordination cages have been a subject of great interest in supramolecular chemistry for a number of years owing to their structural variability, tunability and host-guest chemistry. A wealth of examples and design strategies are present in the literature with some particular highlights coming from the groups of Fujita,¹⁻⁴ Nitschke,⁵⁻⁸ Raymond⁹⁻¹¹ and Lusby.¹²⁻¹⁵ These cages displayed a diverse array of chemical properties and applications including the stabilisation of white phosphorus,⁸ catalysis,¹⁶ protein encapsulation¹⁷ and as nanoscale reaction vessels.^{16,18} A major component of the success of these systems is the ability to tune the ligand and cage design to favour particular cage sizes and architectures. A particularly effective method of achieving this is to employ metallotectons; these are metals that bear auxiliary ligands which serve to occupy some of the coordination sites on the metal. In this manner, incoming ligands are restricted to occupying certain positions around the metal centre, thus enabling control over the geometry and direction of incoming ligands.

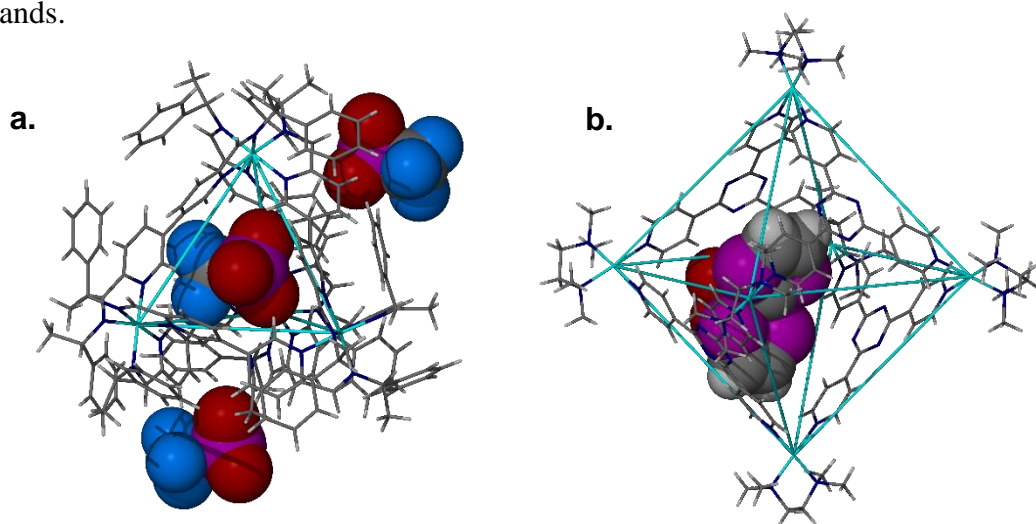


Figure 3.1: SCXRD structures of a. Tetrahedral cage prepared by Nitschke with anionic triflate guest;⁷ b. Octahedral cage prepared by Fujita² with tetrafulvalene guest. Guest molecules are shown in spacefilling mode and all counterions have been omitted for clarity.

Shinkai and coworkers were the first to show this strategy could be applied to CTG based systems.¹⁹ They employed a pyridyl-appended CTG ligand along with the *cis*-protected metallocryptand [Pd(P[^]P)(OTf)₂] (where P[^]P = bis(diphenylphosphino)ethane (dppe) or bis(diphenylphosphino)propane (dppp)) in order to template the formation of the first example of a ‘metallocryptophane’ (figure 3.2a). Cryptophanes were first prepared by Collet in 1981.²⁰ They are capsule-like molecules consisting of two CTG derived ligands linked *via* an organic bridging unit (figure 3.2b).²¹

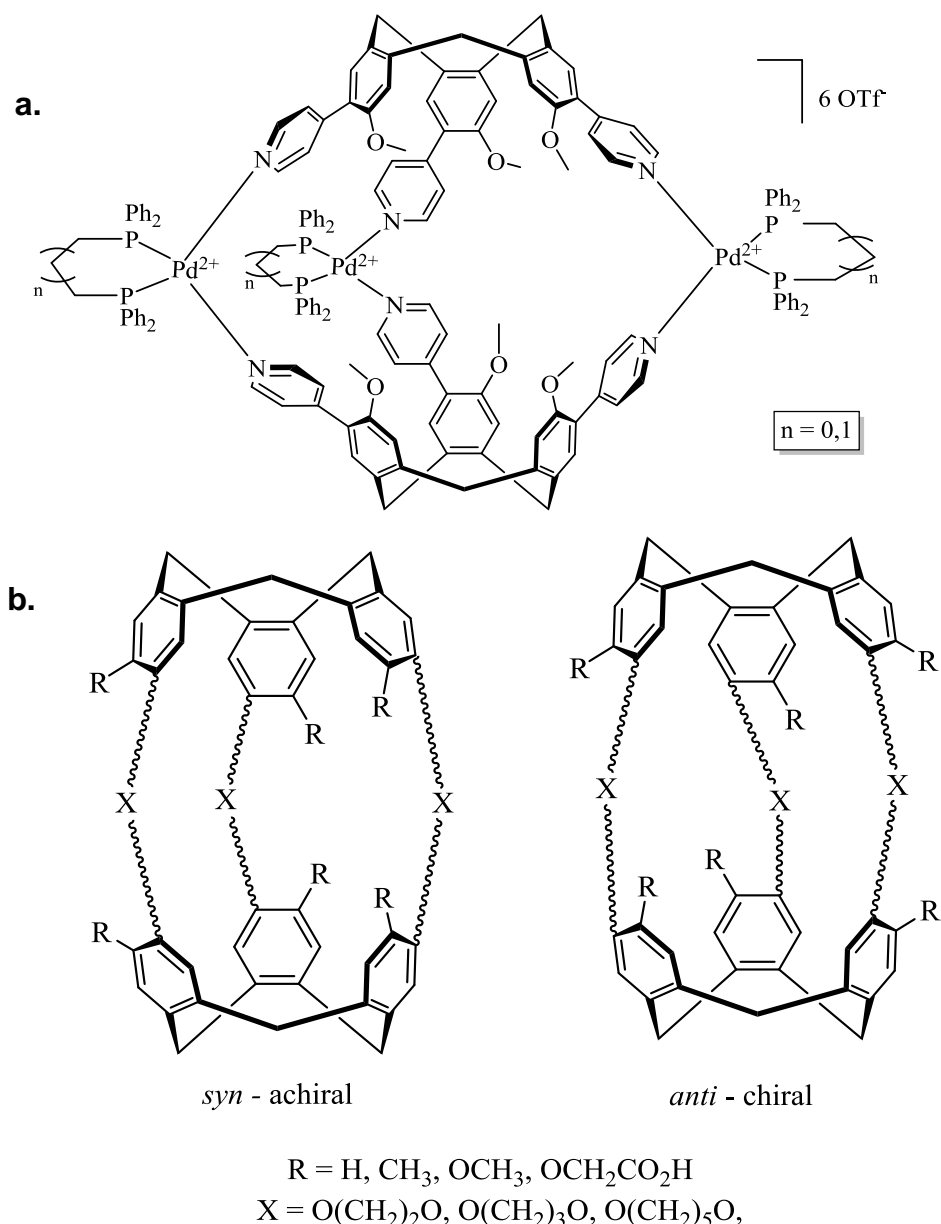


Figure 3.2: **a.** Palladium M_3L_2 metallocryptophane prepared by Shinkai and coworkers;¹⁹ **b.** *Syn* and *anti* forms of cryptophanes.

Owing to the chirality of CTG and its derived ligands, cryptophanes can form as either the *syn* (achiral) or *anti* (chiral) isomers.²¹ The internal cavity has proven to be an effective host for a variety of guest molecules, most notably Xenon gas.^{22, 23} Thus both organic cryptophanes as well as their metallated analogues^{19, 24-26} have been of interest for a variety of applications in host-guest chemistry.^{21, 27-30} The same protected phosphino metallotecton has been employed for a similar purpose more recently by Chambron and coworkers.³¹ In this example, the CTV component has been appended with a linear nitrile ligand. Under ambient conditions, the *anti* form of the metallocryptophane predominates but the *syn* isomer can be observed at low temperatures. The high degree of stereoselection observed for the system was proposed to originate from alleviation of strain by mutual twisting of the nitrile units which is not possible in the *syn* conformation.

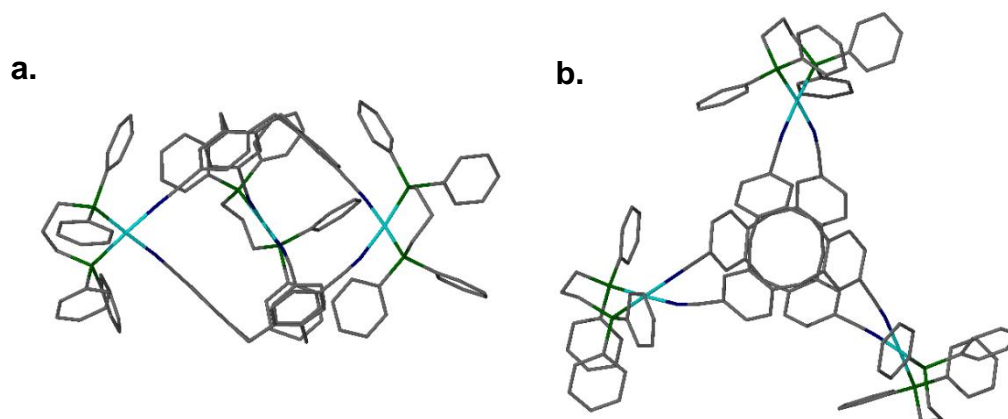


Figure 3.3: SCXRD structure of the metallocryptophane prepared by Chambron and coworkers³¹ showing **a.** Side view; **b.** Top view. All hydrogen atoms, counterions and solvents of crystallisation have been removed for clarity.

Earlier work from the Hardie group from Henkelis showed that employing a *cis*-protected palladium(II) metallotecton, $[\text{Pd}(\text{MeCN})_2(\text{bis-NHC-nap})].2\text{BF}_4$, where ‘bis-NHC-nap’ is a 2-naphthalene derived *N*-heterocyclic carbene (NHC), in combination with the pyridyl-appended CTG ligand (\pm)-2,7,12-Trimethoxy-3,8,13-tris(isonicotinoyl)-10,15-dihydro-5H-tribenzo[*a,d,g*] cyclononatriene, favours the formation of the $[\text{Pd}(\text{NHC})_3\text{L}_2]$ assembly over larger polymeric structures as the system is geometrically directed towards this arrangement (figure 3.4a).³² The use of NHC auxiliary ligands stabilises the M_3L_2 stoichiometry; use of ethylenediamine (en) as the *cis*-protecting ligand results in the M_3L_2 architecture being metastable over time and rearranging to a larger M_6L_8 coordination cage.

More recent work from the Hardie group has demonstrated that the same ligand could be assembled in the same manner with a *cis*-protected iridium(III) metallotecton,

$[\text{Ir}(\text{ppy})_2(\text{MeCN})_2]\cdot\text{X}^-$, where ‘ppy’ is 2-phenylpyridine and ‘X’ is the PF_6^- or BF_4^- counterion, to give the same $[\text{Ir}(\text{ppy})_2]_3\text{L}_2$ stoichiometry (figure 3.4b). Owing to the photophysical properties of the iridium unit and its ancillary ligands, these cages now had a luminescence output which could be tuned between yellow and cyan depending on the ligand structure.³³ Lusby has also demonstrated the assembly of this same $[\text{Ir}(\text{ppy})_2]$ unit with 1,3,5-tricyanobenzene (tcb) ligands into $[\text{Ir}(\text{ppy})_2]_6(\text{tcb})_4$ octahedra with appreciable orange luminescence.¹² Whilst examples exist where no geometrically directing metallotectons have been employed,²⁴⁻²⁶ this approach remains a highly effective strategy for the synthesis of metallocryptophanes with a recent review published by Hardie and coworkers.³⁴

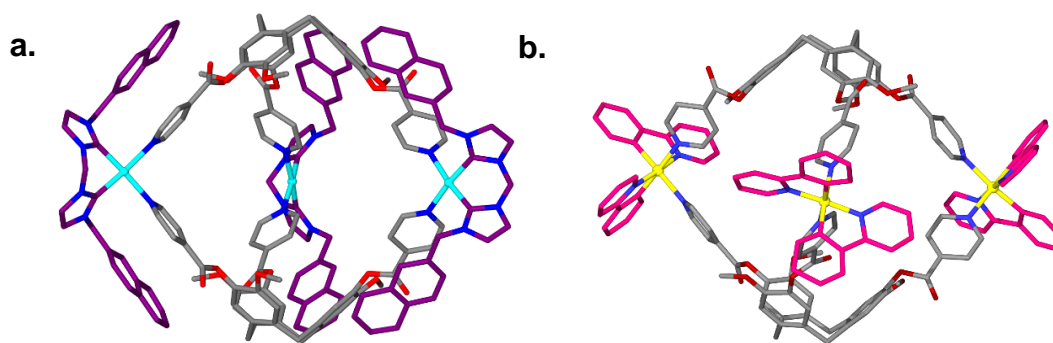


Figure 3.4: CTG-based M_3L_2 assemblies from the Hardie group favoured by geometrically directing metallotectons: **a.** $[\text{Pd}(\text{NHC})]_3\text{L}_2$ cage prepared by Henkeli;³² **b.** $[\text{Ir}(\text{ppy})_2]_3\text{L}_2$ cage prepared by Pritchard containing luminescent functionality.³³

An attractive concept is the introduction of stimuli-responsive elements into coordination cages. Many examples of metal-ligand assemblies that are responsive to a variety of stimuli, including chemical, pH, electrical, solvent and via guest uptake.³⁵ Light-responsive elements, such as azobenzene, are a particularly attractive class of stimuli-responsive functional groups. The azobenzene unit undergoes a significant conformational change from its *trans* isomer to the *cis* isomer upon irradiation with UV light.³⁶ This unit has been employed extensively in supramolecular systems for a variety of applications³⁷⁻⁴⁰ including guest uptake and release.⁴¹⁻⁴³ However most of these examples feature systems bearing pendant photoresponsive units, with reports of systems constructed from bridging ligands that are responsive to light remaining relatively rare. To the best of the author’s knowledge, there are currently no examples of coordination cages constructed from bridging ligands that contain the azobenzene group although metallocages with pendant endohedral⁴⁴ and exohedral⁴⁵ azobenzene groups are known.

The concept of photoswitchable bridging ligands has been demonstrated by Clever and coworkers utilising the dithienylethene photoswitchable moiety. In this example, a $[Pd_2L_4]$ metallocage, where L is a pyridyl-appended dithienylethene ligand was shown to be able to switch between the 'open' and 'closed' forms of the photoswitch *via* irradiation with light (figure 3.5). These altered forms of the cage were demonstrated to be capable of modifying the binding constant of $[B_{12}F_{12}]^{2-}$ guest molecules.⁴⁶ Work from the same group has demonstrated that similar ligands can also be used to assemble $[Pd_3L_6]$ metallotriangles when the ligand is in its 'open' conformation. If the ligand is converted to the 'closed' isomer prior to self-assembly however, a different product is obtained, a giant $[Pd_{24}L_{48}]$ rhombicuboctahedral sphere.⁴⁷ Slow light-mediated conversion can be observed between the triangle and sphere assemblies upon irradiation. DFT calculations indicated a huge discrepancy in the size of these systems with the triangle having a diameter of 2.6Å and the sphere a diameter of 6.4Å.⁴⁷ Such a discrepancy would undoubtedly offer selective uptake of guest molecules depending on the conformation. These two examples represent the most sophisticated current attempts at incorporating photoresponsive elements into the structural framework of coordination cages.

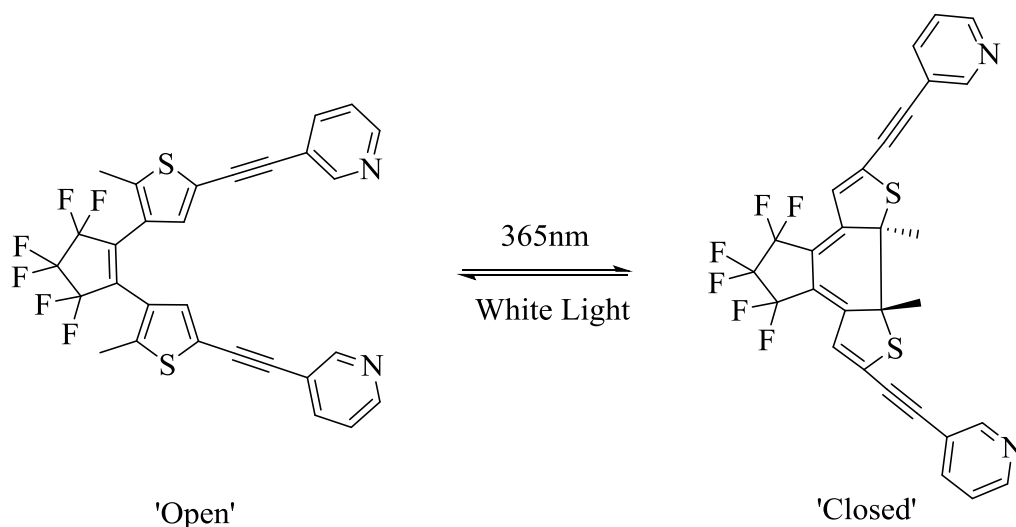


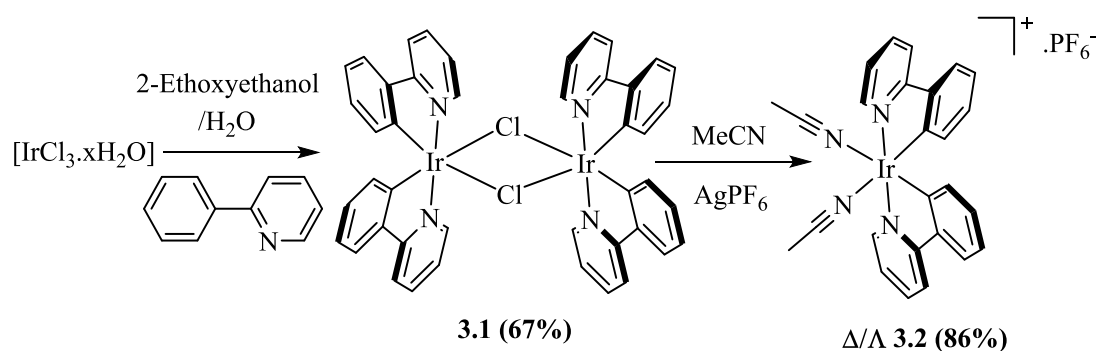
Figure 3.5: Clever's photoswitchable ligand that can be incorporated into $[Pd_2L_4]$ coordination cages.⁴⁶

This chapter discusses the assembly of CTG-derived iridium(III) metallocryptophanes incorporating the photoresponsive azobenzene moiety. This represents the first efforts towards light-responsive architectures based on the CTG framework as well as a demonstration that rational design strategies can be employed to incorporate a desired functionality into CTG based systems. The ability to introduce this functionality at will, in combination with the huge variability of different assemblies possible with

CTG-derived compounds, could provide a formidable tool kit for the synthesis of supramolecular systems with targeted applications.

3.2 Cis-protected Ir(III) metallotectons

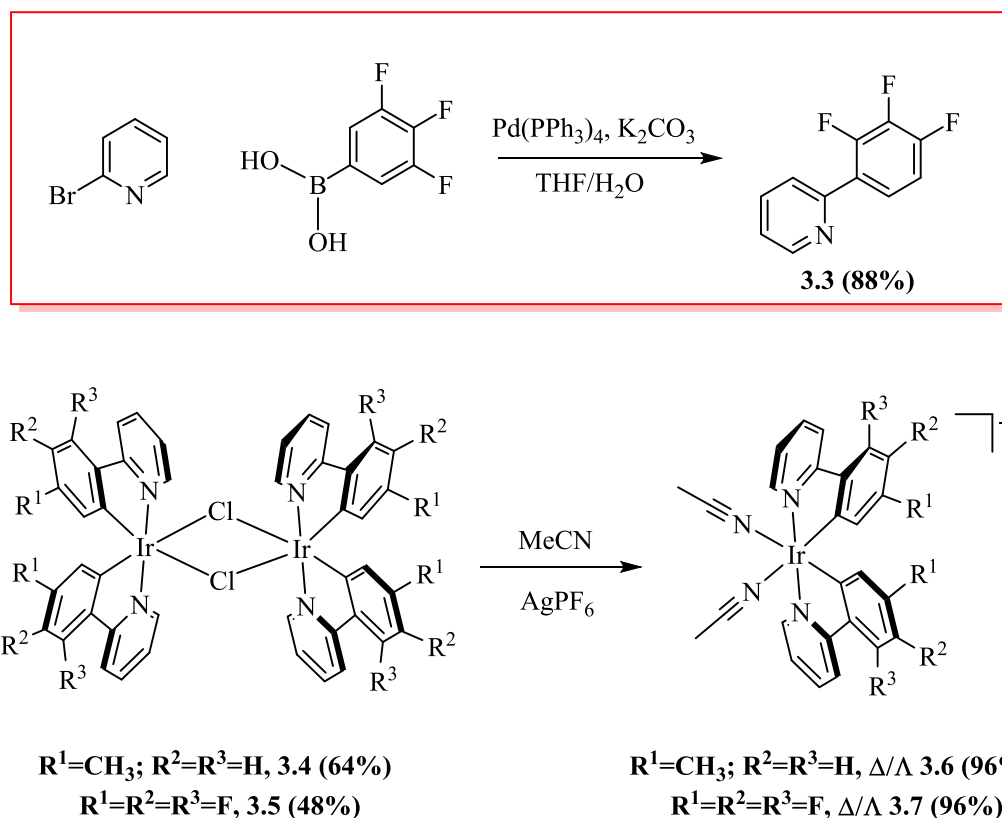
The success of *cis*-protected metallotectons in exclusively targeting the M_3L_2 stoichiometry made these precursors ideal for efforts towards discrete coordination cages with photoresponsive functionality. Synthesis of the *cis*-protected Ir(III) metallotecton is facile and well characterised in the literature owing to the considerable interest in these compounds for luminescence applications. It was hoped that the combination of this tecton with the azobenzene appended ligands discussed in chapter 2 could lead to systems with dual photoresponsive/luminescent functionality. The parent compound $[Ir^+(ppy)_2(MeCN)_2].X^-$ (where ppy is 2-phenylpyridine and X^- is the hexafluorophosphate anion) is synthesised in two steps from iridium trichloride as illustrated in scheme 3.1. Reaction of iridium trichloride with 2-phenylpyridine in a mixed solvent system of 2-ethoxyethanol and water gave the chloride bridged iridium dimer **3.1** as a bright yellow solid in good yields.⁴⁸ This compound can then be converted to the desired *cis*-protected **3.2** in acetonitrile using silver hexafluorophosphate.⁴⁹ The target product is obtained as a racemic mixture of Δ/Λ optical isomers.



Scheme 3.1: Synthesis of cis-protected metallotecton 3.2.

The metallotecton can be readily functionalised by derivatising the phenylpyridine precursor used in the synthesis of the dimer. In this manner, two more metallotectons **3.6** and **3.7** incorporating solubilising methyl⁵⁰ and fluorine⁵¹ components respectively were synthesised in the same manner from their parent dimers **3.4** and **3.5** (scheme 3.2). Trifluorophenylpyridine **3.3** can be synthesised from 2-bromopyridine and 3,4,5 trifluorophenyl boronic acid using a Suzuki coupling reaction (red box, scheme 3.2).⁵¹ These compounds were noticeably more soluble than

the unfunctionalised tecton with the aim of transferring this increased solubility to any resulting complexes.

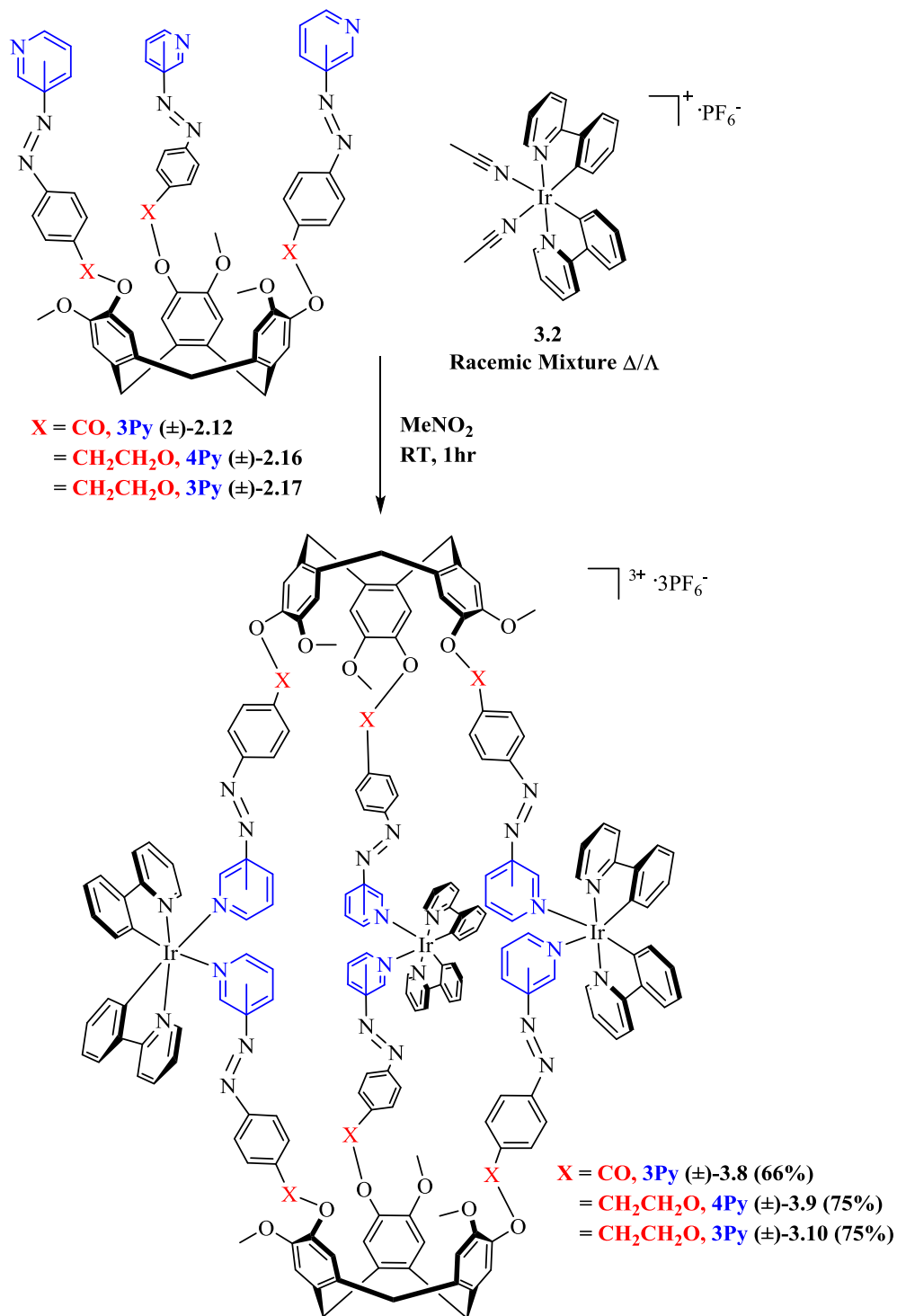


Scheme 3.2: Synthesis of substituted metallotectons **3.6** and **3.7**; Red box: synthesis of 3,4,5 trifluorophenylpyridine **3.3** via a Suzuki coupling reaction.

3.3 Self-assembly of M₃L₂ metallocryptophanes bearing azobenzene units

The self-assembly of the photoresponsive ligands **2.12**, **2.16** or **2.17** (section 2.4, chapter 2) with the iridium precursor **3.2** were investigated *via* ¹H NMR and ESI-mass spectrometry. The appropriate ligand (2 equivalents) was combined with 3 equivalents of **3.2** in non-coordinating nitromethane solvent. The free ligand is poorly soluble at room temperature in nitromethane but upon addition of **3.2** does not precipitate from solution. Over time, spectroscopic analysis showed the conversion of the reactants to the desired metallocages **3.7**, **3.8** and **3.9** (scheme 3.3) of composition [Ir(ppy)₂]₃(L)₂³⁺·3PF₆⁻ where ‘ppy’ is 2-phenylpyridine and ‘L’ is the appropriate ligand. The self-assembly process is swift with detailed studies indicating a complete reaction after only one hour in solution (discussed in section 3.4) with cages been left for 24 hours in solution to ensure completion. Upon completion of the reaction (as monitored by ESI-MS), the cages can be precipitated from solution *via* addition of

diethyl ether and isolated as orange powders in good yields. The cages do not undergo any noticeable degradation in the solid phase and can be redissolved to give identical spectroscopic data after many weeks.



Scheme 3.3: Preparation of $[\{\text{Ir}(\text{ppy})_2\}_3(\text{L})_2]^{3+} \cdot 3\text{PF}_6^-$ metallocryptophanes **3.8**, **3.9** and **3.10**.

No attempt was made to chirally resolve either the ligands or the metallotectons. As such, the cages in solution likely exist as a mixture of isomers. Assuming all of the azobenzene units remain in their thermodynamically favoured *trans* states, there is still the helical *P/M* chirality of the ligand and the octahedral Δ/Λ chirality of each of the metal centres to consider. Hardie's analogous Ir₃L₂ metallocryptophanes with pyridyl appended CTG ligands chirally self-sort in solution into the enantiomeric *PP*- $\Delta\Delta\Delta$ and *MM*- $\Lambda\Lambda\Lambda$ cages but such chiral self-sorting is relatively rare.³³ Other examples of chiral self-sorting in solution include Boer's helicates,⁵² Yan's tetrahedra⁵³ and Gutz's M₂L₄ cages⁵⁴ and several examples of chiral discrimination from the Lutzen group.⁵⁵⁻⁵⁸ Complexation of the ligands in the head-to-head fashion depicted in scheme 3.3 can theoretically lead to cages containing the same enantiomer of ligand (termed *anti-(PP)* or *anti-(MM)*) or to cages with one of each enantiomer (termed the *syn-(MP)* cage). Combined with Δ/Λ chirality of the metal leads to 12 possible stereoisomers in solution. This leads to noticeably broad ¹H NMR spectra (discussed further in section 3.4).

[{Ir(ppy)₂}₃(L)₂]³⁺.3PF₆⁻ metallocages can also be formed with the substituted iridium metallotectons **3.6** and **3.7**. The reaction of 3 equivalents of the methylated tecton **3.6** with ligand **2.12** affords the methyl substituted metallocryptophane **3.11** in a virtually identical reaction procedure (figure 3.6). The fluorinated analogue requires a noticeably lengthier reaction time of 48 hours for reaction with ligand **2.12**. This is possibly due to a steric effect during self-assembly. Alternatively, this observation can be rationalised by the electron-withdrawing fluorine groups which lead to a weaker *trans* effect on the bound acetonitrile ligands and thus a longer reaction time. In reality, a subtle blend of steric and electronic effects are likely to play a role. After 48 hours in solution, spectroscopic analysis indicates a pure product, compound **3.12**. Both of these systems are distinctly more soluble in organic solvents than their unsubstituted counterparts.

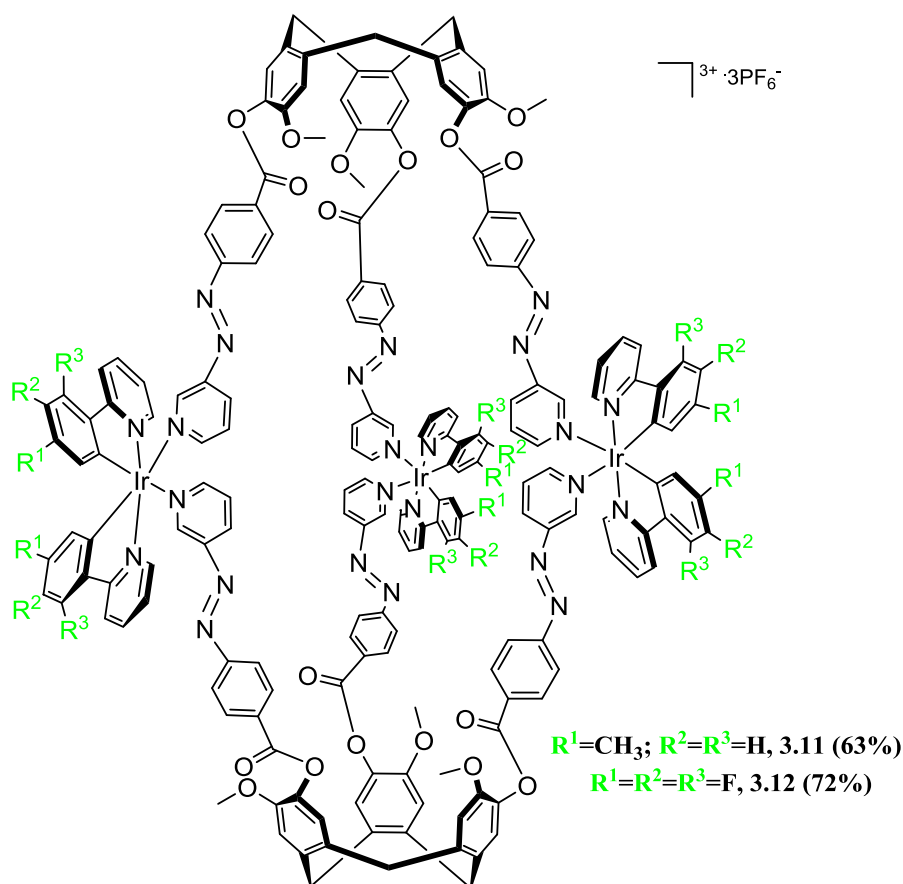


Figure 3.6: Structure of substituted $[\{Ir(ppy)_2\}_3(L)_2]^{3+} \cdot 3PF_6^-$ metallocryptophanes **3.11** and **3.12**.

3.4 Spectroscopic analysis of metallocryptophanes

High resolution ESI mass spectrometry proved to be a critical tool for analysis of all cage complexes. For the reaction of ligand **2.12** with $[Ir^+(ppy)_2(MeCN)_2] \cdot PF_6^-$, clear evidence of cage formation is observed in the gas phase with the main peak observed at $[1191.3190]^{3+}$ assigned as the intact cage $[\mathbf{3.8-3PF}_6]^{3+}$ where the intact cage is observed with no associated PF_6^- counterions (figure 3.7, calculated m/z for $\{C_{186}H_{140}Ir_3N_{24}O_{18}\}^{3+}$ $[1191.3179]^{3+}$). A small amount of gas phase fragmentation is often observed with the most common fragment of $[1536.4288]^{2+}$ assigned as the $[M_2L_2-2PF_6]^{2+}$ fragment, where $M = [Ir(ppy)_2]$ and $L =$ ligand **2.12**, also observed without PF_6^- counterions (calculated m/z for $\{C_{164}H_{124}Ir_2N_{22}O_{18}\}^{2+}$ $[1536.9361]^{2+}$). The isotope pattern of the intact cage is a perfect match to the simulated pattern, confirming the assignment. Similar results are observed for cages **3.9**, **3.10**, **3.11** and **3.12** with the $[M_3L_2]$ peaks observed at $[1223.3784]^{3+}$ (figure 3.8, calculated m/z for $\{C_{192}H_{164}Ir_3N_{24}O_{18}\}^{3+}$ 1223.3805), $[1223.3820]^{3+}$ (figure 3.9, calculated m/z for $\{C_{192}H_{164}Ir_3N_{24}O_{18}\}^{3+}$ 1223.3805), $[1219.3517]^{3+}$ (figure 3.10, calculated m/z for

{C₁₉₂H₁₅₂Ir₃N₂₄O₁₈}³⁺ 1219.3492) and [1299.2626]³⁺ (figure 3.11, calculated m/z for {C₁₈₆H₁₂₂F₁₈Ir₃N₂₄O₁₈}³⁺ 1299.2613) respectively.

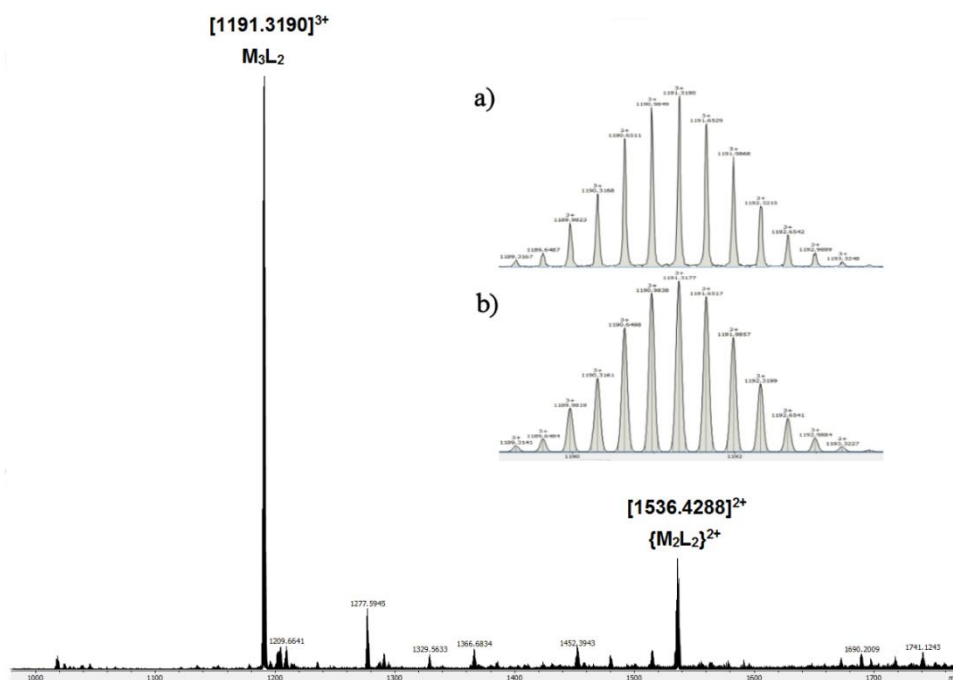


Figure 3.7: Interpreted high resolution mass spectrum of complex 3.8; inset **a**. Experimental isotope pattern; **b**. Calculated isotope pattern for the M₃L₂ peak of cage 3.8 (where M = [Ir(ppy)₂] and L = ligand 2.12).

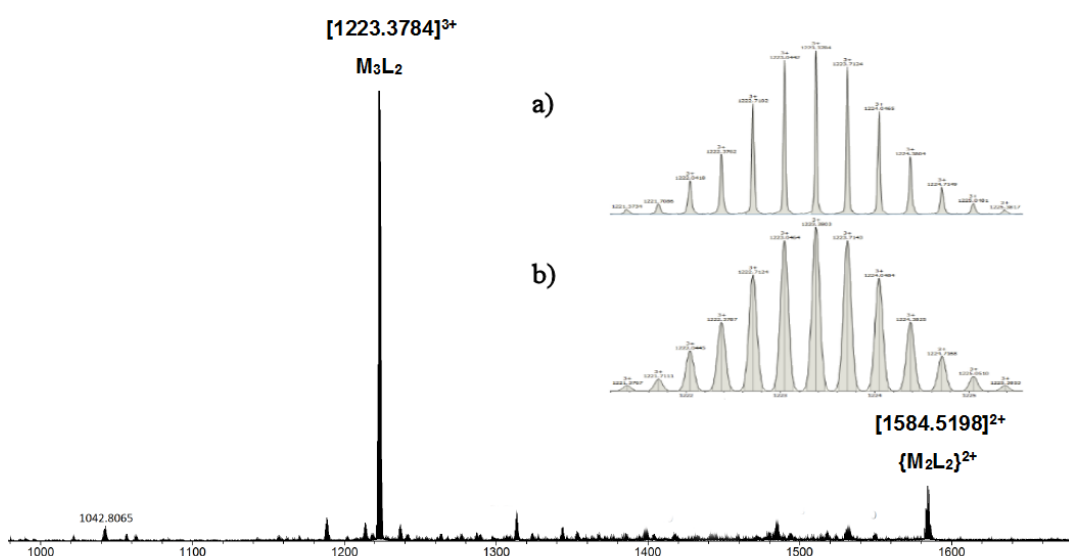


Figure 3.8: Interpreted high resolution mass spectrum of complex 3.9; inset **a**. Experimental isotope pattern; **b**. Calculated isotope pattern for the M₃L₂ peak of cage 3.9 (where M = [Ir(ppy)₂] and L = ligand 2.17).

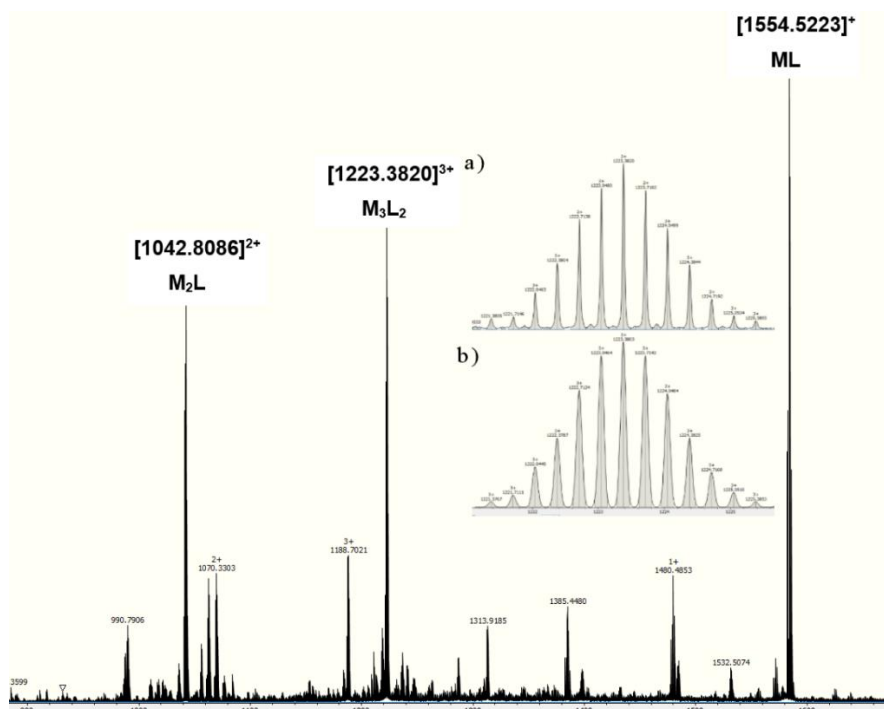


Figure 3.9: Interpreted high resolution mass spectrum of complex **3.10**; inset **a**. Experimental isotope pattern; **b**. Calculated isotope pattern for the M_3L_2 peak of cage **3.10** (where $M = [Ir(ppy)_2]$ and $L = \text{ligand } 2.18$).

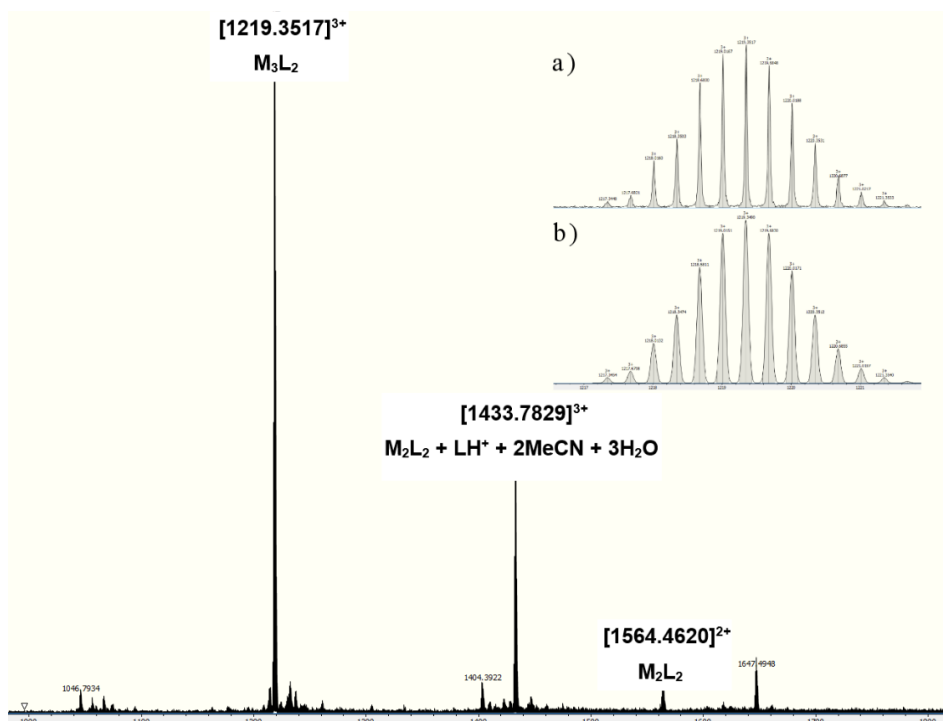


Figure 3.10: Interpreted high resolution mass spectrum of complex **3.11**; inset **a**. Experimental isotope pattern; **b**. Calculated isotope pattern for the M_3L_2 peak of cage **3.10** (where $M = [Ir(ppy)_2]$ and $L = \text{ligand } 2.12$).

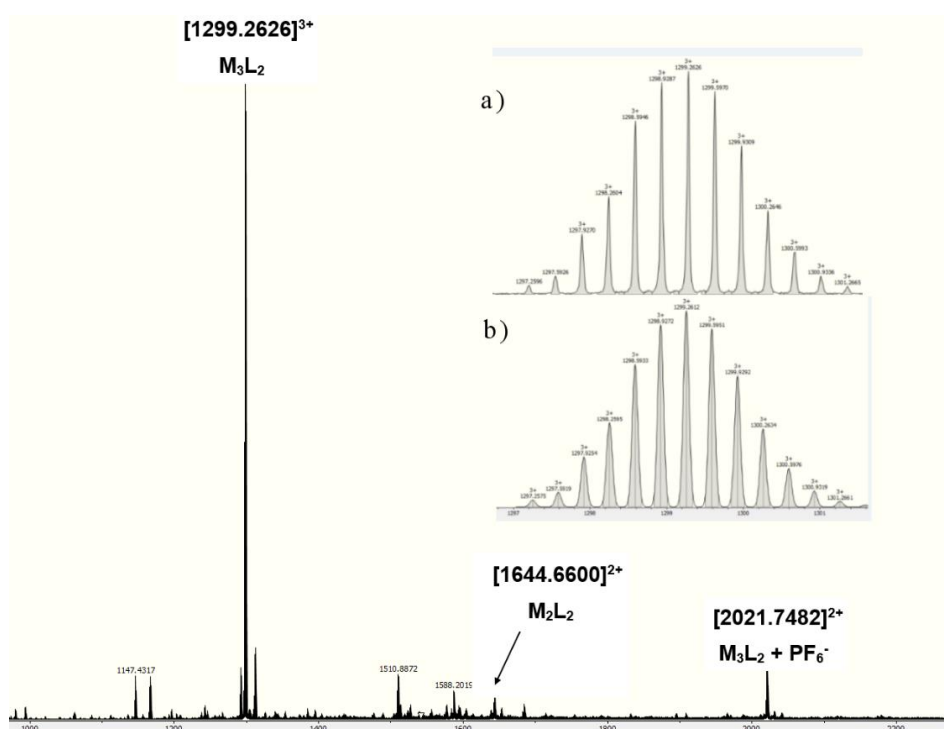


Figure 3.11: Interpreted high resolution mass spectrum of complex **3.12**; inset **a**. Experimental isotope pattern; **b**. Calculated isotope pattern for the M_3L_2 peak of cage **3.12** (where $M = [Ir(ppy)_2]$ and $L = \text{ligand } \mathbf{2.12}$).

As illustrated in figures 3.7-3.11, despite the intact cages often being the most intense ions observed, gas phase fragmentation is commonplace for these complexes. The 3-pyridyl ether linked cage **3.10** (figure 3.9) appears particularly sensitive to gas-phase fragmentation which raises potential issues of impurities in the sample. However, diffusion ordered NMR (DOSY) studies confirm the presence of a single species in solution in each sample (the DOSY results are discussed later in this section) indicating that the additional ions observed here are a consequence of gas-phase fragmentation and not of sample impurity.

The relative ease at which self-assembly takes place in complexes **3.8-3.11** is somewhat surprising given that low-spin d^6 electron configurations such as Ir(III) are typically kinetically inert compounds. Moreover, the process occurs at room temperature with the M_3L_2 assembly the thermodynamic product although other intermediates of the process (ML , M_2L , M_2L_2 amongst others) are often observed in the mass spectrum before reaction completion. To probe the self-assembly process, comprehensive 1H NMR studies were undertaken with the ester-linked metallocryptophane, compound **3.8**. Figure 3.12 shows the timecourse 1H NMR spectrum following the formation of **3.8** in $d\text{-MeNO}_2$.

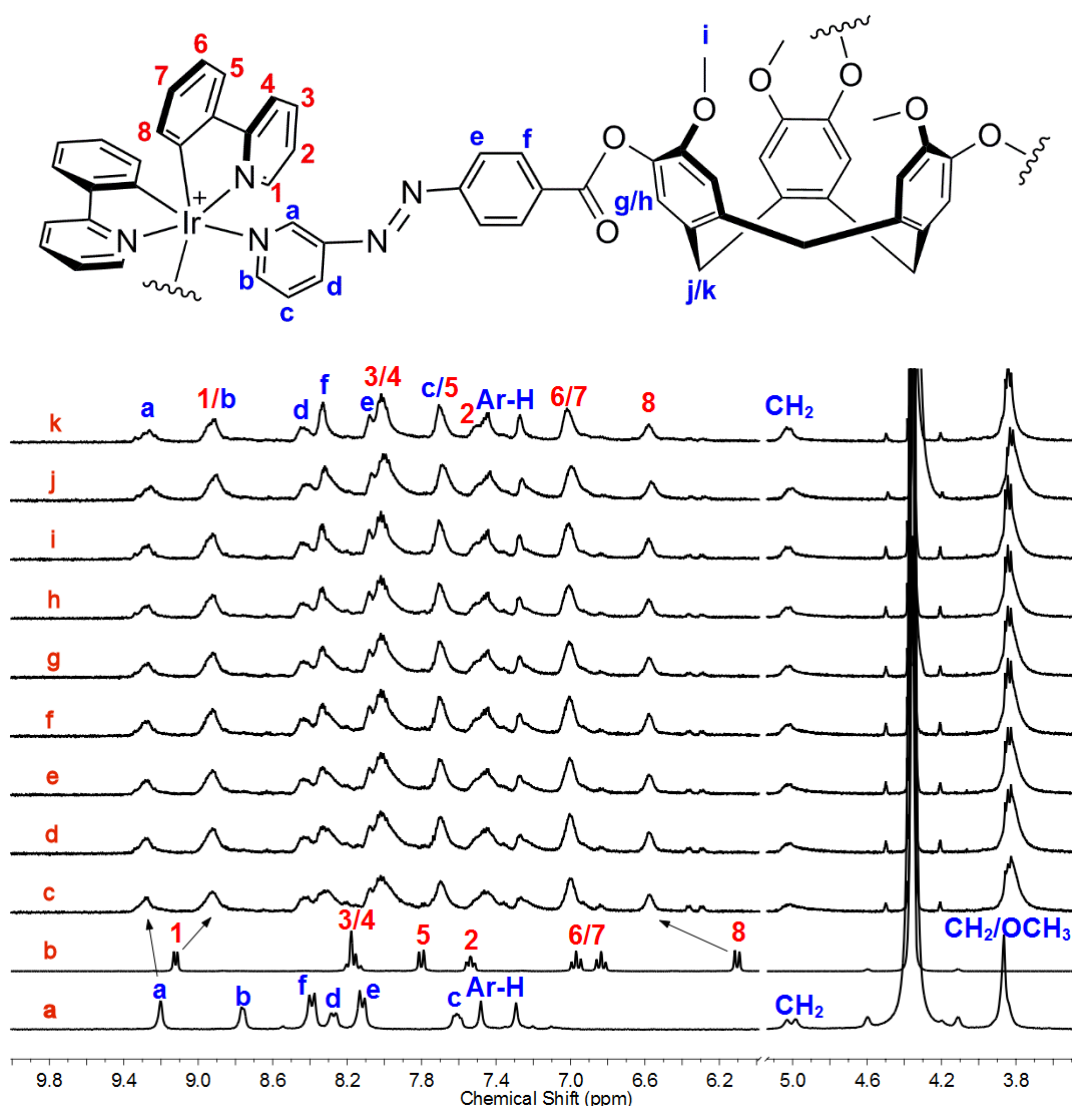


Figure 3.12: Interpreted timecourse ^1H NMR showing the formation of **3.8** over time in *d*-MeNO₂ with key shifts indicated by arrows; **a**. Ligand **2.12**; **b**. Metallotecton **3.2**; **c**. 15 minutes rt; **d**. 30 minutes rt; **e**. 45 minutes rt; **f**. 60 minutes rt; **g**. 75 minutes rt; **h**. 90 minutes rt; **i**. 105 minutes rt; **j**. 120 minutes rt; **k**. 48 hours rt. The region 6.1–5.1 ppm has been omitted for clarity.

Significant shifts are observed for the protons closest to the iridium centre on the phenylpyridine ancillary ligand with H₁ shifted upfield (from 9.12 to 8.92 ppm) and H₈ shifted downfield (from 6.10 to 6.58 ppm). The ligand protons H_a are shifted downfield from 9.20 to 9.29 ppm. These shifts are all indicative of coordination between the two units. The initial spectrum upon mixing of the components is broad but does sharpen up to a degree over time.

The ^1H NMR spectrum collected immediately upon mixing the two components is dramatically broadened and contains a significant portion of assembled product (spectrum **c**). A number of intermediates of self-assembly can be identified by HRMS

at this stage including $[1536.4288]^{2+}$ (M_2L_2) $^{2+}$, $[1018.9508]^{3+}$ ($M_2L_2 + H$) $^{3+}$ along with significant amounts of free metal ($[501.1877]^+$). The reaction is essentially complete after 60 minutes (spectrum f) upon which the main peak in the HRMS is the target product with a small amount of fragmentation present. No further changes are observed in the 1H NMR spectrum after this point with aside from some sharpening to the product peaks which is associated with chiral self-sorting of cage enantiomers (discussed in detail in section 3.5). Figures 3.13-3.16 show the interpreted 1H NMR spectra of each of the cages **3.9-3.12** upon completion of self-assembly:

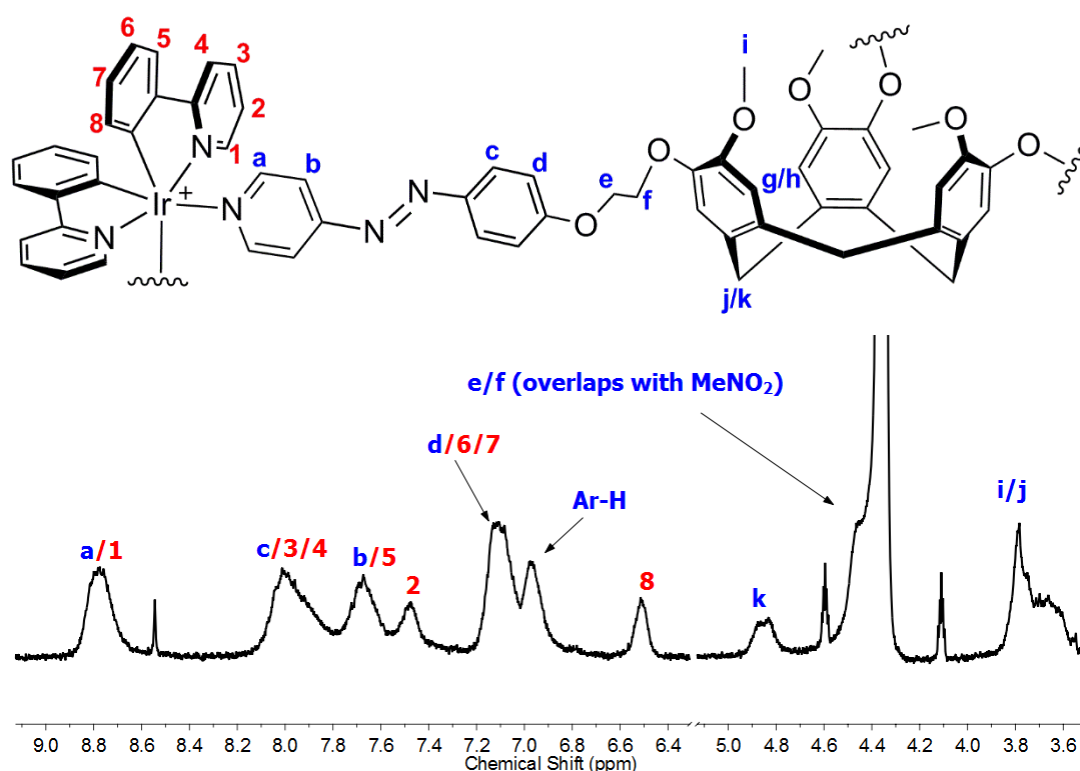


Figure 3.13: Interpreted 1H NMR spectrum of complex **3.9** in d -MeNO $_2$. The region 6.3-5.1 ppm has been omitted for clarity.

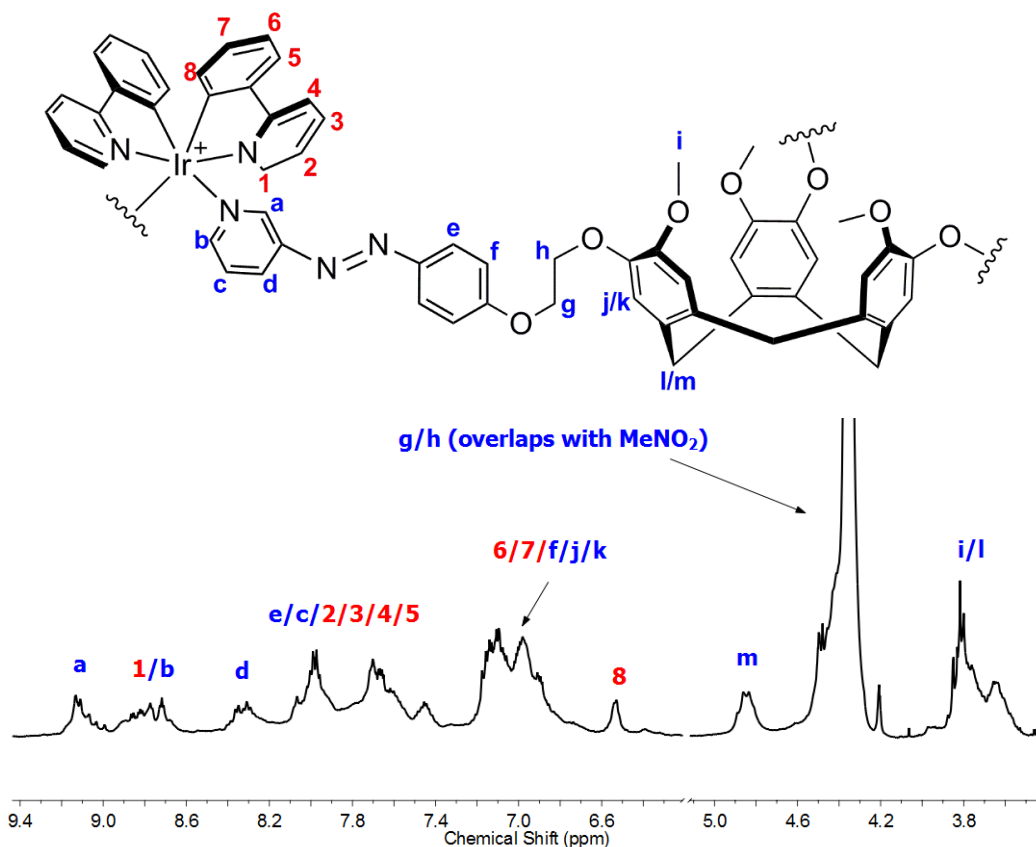


Figure 3.14: Interpreted ^1H NMR spectrum of complex **3.10** in $d\text{-MeNO}_2$. The region 6.3-5.1 ppm has been omitted for clarity.

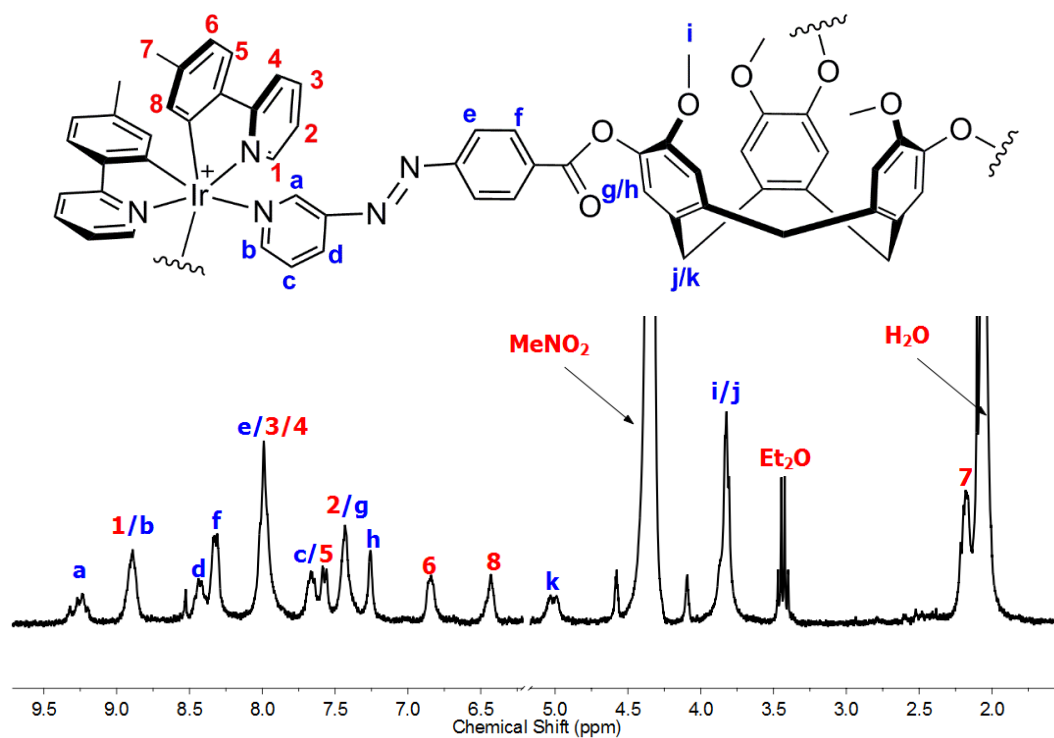


Figure 3.15: Interpreted ^1H NMR spectrum of complex **3.11** in $d\text{-MeNO}_2$. The region 6.3-5.1 ppm has been omitted for clarity.

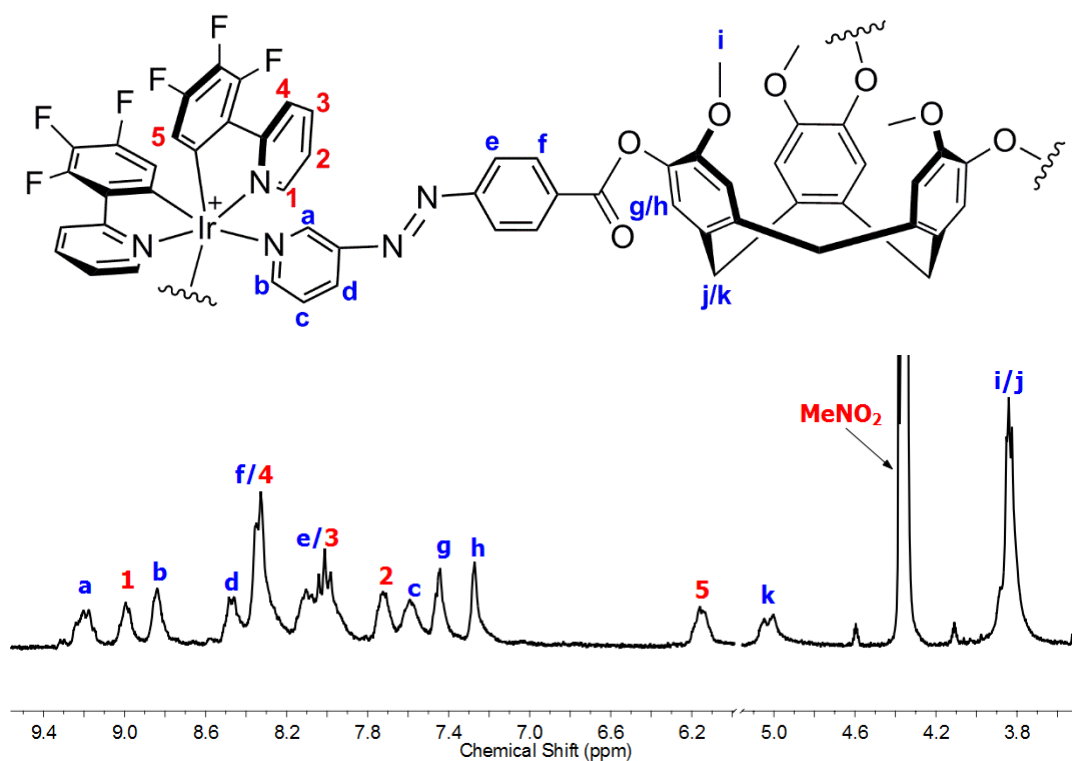


Figure 3.16: Interpreted ^1H NMR spectrum of complex **3.12** in $d\text{-MeNO}_2$. The region 6.1–5.1 ppm has been omitted for clarity.

Comprehensive 2D NMR spectroscopy was employed to ensure accurate assignment of all resonances observed in the ^1H NMR spectra of all metallocryptophanes. The cages were insufficiently soluble to enable the collection of $^{13}\text{C}\{^1\text{H}\}$ NMR but accurate assignments could be confirmed by 2D ^1H NMR techniques. A selection of 2D NMR data is discussed here for complex **3.8**; analogous analyses for all other complexes is detailed in the appendices. The ^1H - ^1H COSY spectrum of cage **3.8** is shown in figure 3.17. Despite the significant amount of overlap of peaks in the ^1H NMR spectrum, the COSY spectrum, along with integration allows assignment of the spectra.

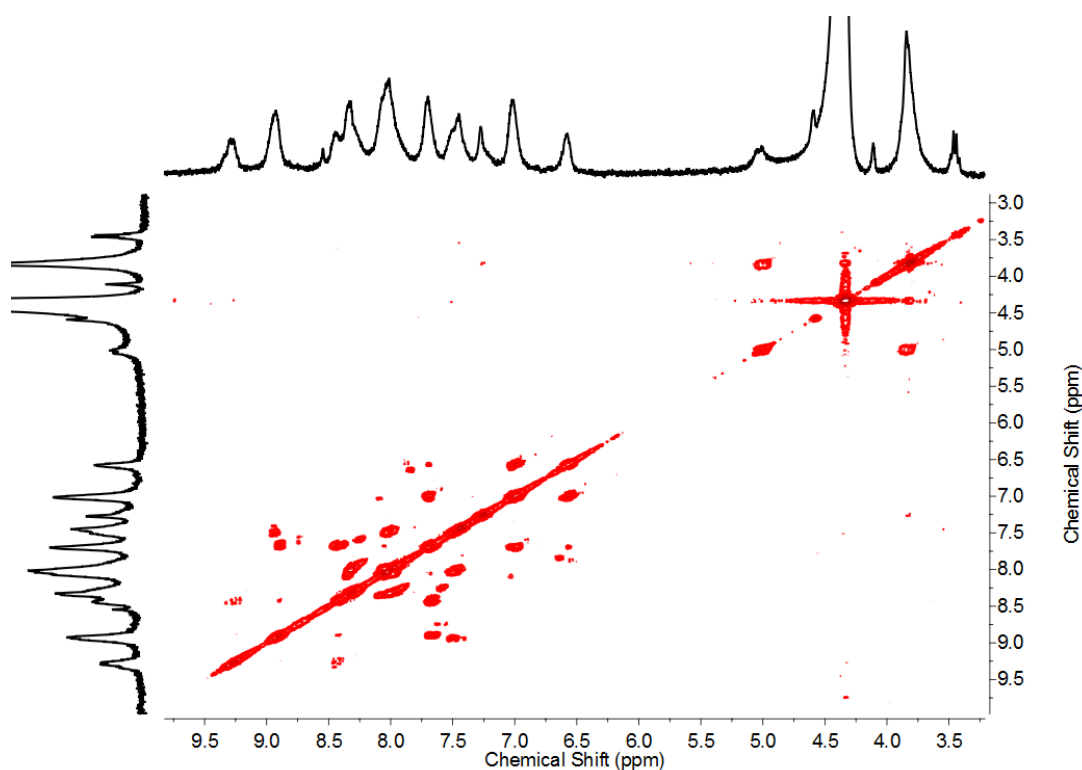


Figure 3.17: ^1H - ^1H COSY NMR of metallocryptophane **3.8** in $d\text{-MeNO}_2$.

Further evidence of complexation was provided from the ROESY NMR of complex **3.8**. A detailed discussion of the ROESY couplings observed is provided in conjunction with the molecular model of complex **3.8** (section 3.6); however an unambiguous through-space coupling is observed between the ortho protons on the ligand and the protons adjacent to the cyclometalated carbon on the phenylpyridine ancillary ligand. Molecular modelling indicates these two protons are separated by a distance of 5.14\AA which is at the threshold distance detectable in ROESY owing to the distance dependence of $1/r^6$ (where r is internuclear separation). This explains the weak nature of the interaction; indeed this interaction is observed in the ROESY NMR of some complexes (**3.8**, **3.9**, **3.11**) but not all (**3.10** and **3.12**).

The intermediates of self-assembly (M_2L_2 , M_2L , ML_2) would be expected to have a dramatically different size from the intact M_3L_2 cage and thus a different diffusion constant to the intact cage. Diffusion ordered spectroscopy (DOSY) was therefore employed to confirm the presence of only the target M_3L_2 cage in solution and eliminate the possibility of any impurities. Figure 3.18 shows the DOSY spectrum of compound **3.8** illustrating the cage peaks which all have the same diffusion constant and thus can be assigned as being present as a single species, with the only other species present being residual solvents. This technique was also applied to cages **3.9**, **3.10**, **3.11** and **3.12** all of which show a single large species in solution (figures 3.19-3.22).

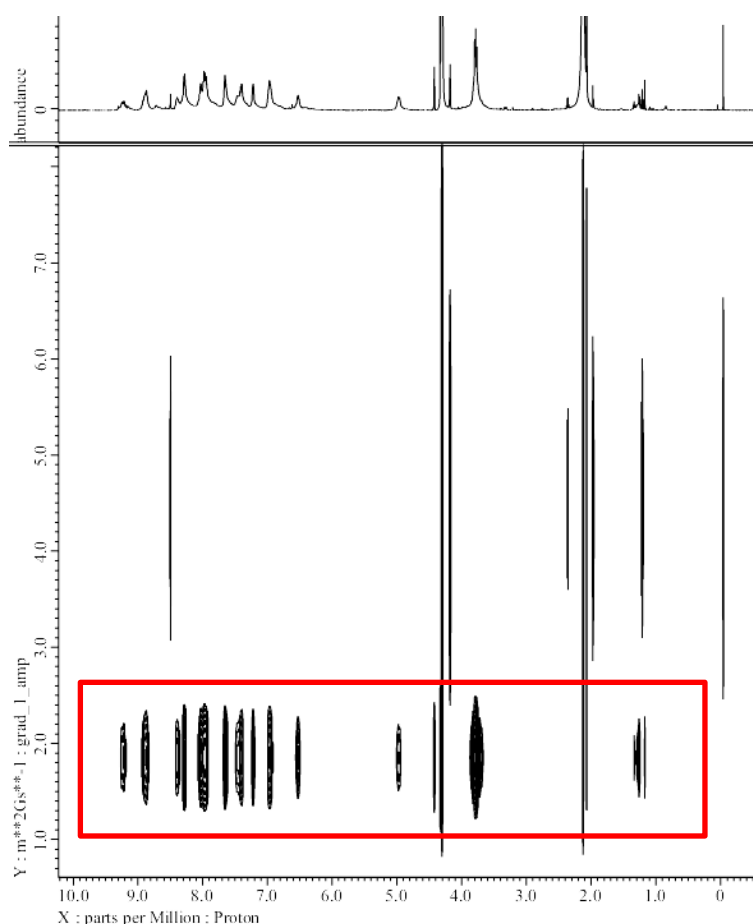


Figure 3.18: The DOSY spectrum of cage **3.8** in *d*-MeNO₂ showing the aromatic cage peaks diffusing with a D of $1.86 \times 10^{-10} \text{ m}^2 \text{ s}^{-1}$ (red box). The additional signals diffusing with a D of $5.00 \times 10^{-10} \text{ m}^2 \text{ s}^{-1}$ arise from various solvents (MeNO₂, H₂O, Et₂O).

The diffusion constant of cage **3.8** was found to be $1.86 \times 10^{-10} \text{ m}^2 \text{ s}^{-1}$ in nitromethane solvent (figure 3.11). Diffusion constants can be used to generate a rough approximation of the hydrodynamic radius using the Stokes-Einstein equation (equation 3.1) and has previously been employed in estimation of the sizes of M₃L₂ metallocryptophanes.^{32, 33} Inputting the values for cage **3.8** results in a hydrodynamic radius of 17.32 Å. This is larger than the previously reported values for CTG metallocryptophanes which gave values of 14.4 Å (Pd₃L₂ cage)³² and 9.73 Å (Ir₃L₂ cage)³³ which is to be expected given the longer azobenzene units in cage **3.8**. These values should be regarded as approximations however as the Stokes-Einstein equation becomes less valid as the system deviates from a perfect sphere; whilst the metallocryptophanes are symmetrical, they cannot be considered spherical. Unfortunately a comparison diffusion constant of the free ligand in nitromethane could not be obtained due to the poor solubility of ligand **2.12** in nitromethane which leads to rapid crystallisation of the ligand.

$$r = \frac{k_B T}{6\pi\eta D}$$

Equation 3.1: Stokes-Einstein equation for rationalisation of diffusion constants where r = hydrodynamic radius (m), k_B = Boltzmann constant ($J K^{-1}$), T = temperature (K), η = solvent viscosity ($Pa s^{-1}$), D = diffusion constant ($m^2 s^{-1}$).

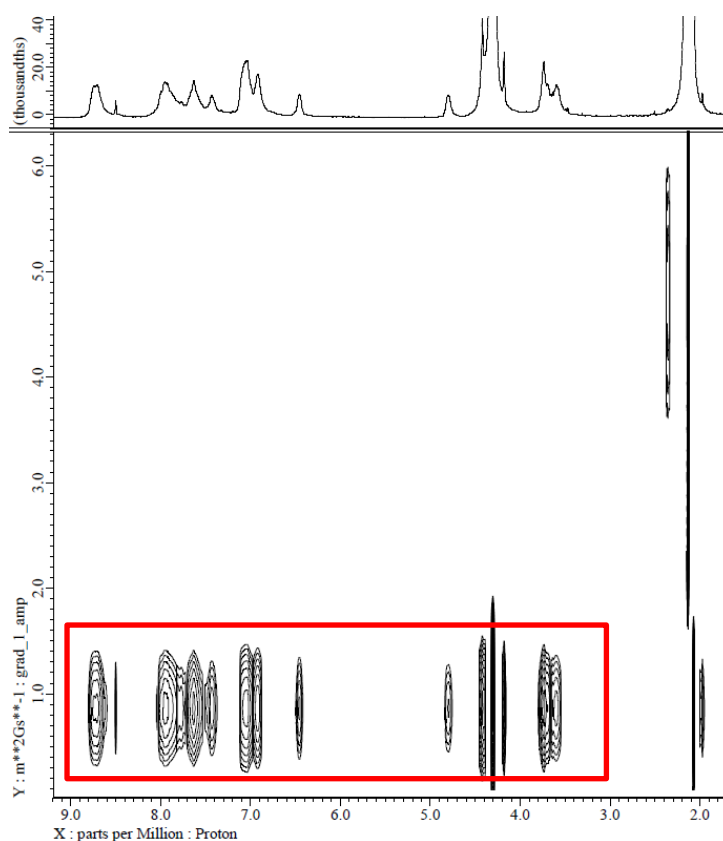


Figure 3.19: The DOSY spectrum of cage **3.9** in $d\text{-MeNO}_2$ showing a single large species in solution.

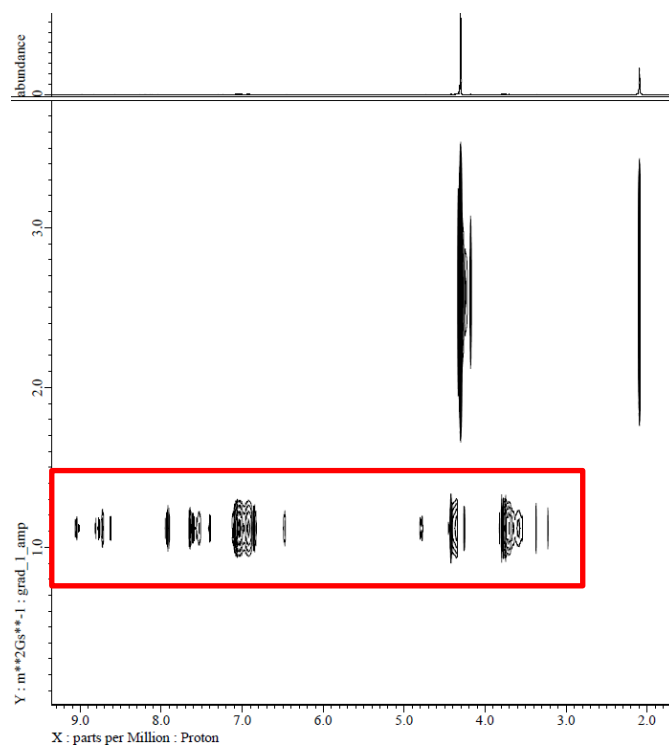


Figure 3.20: The DOSY spectrum of cage 3.10 in $d\text{-MeNO}_2$ showing a single large species in solution.

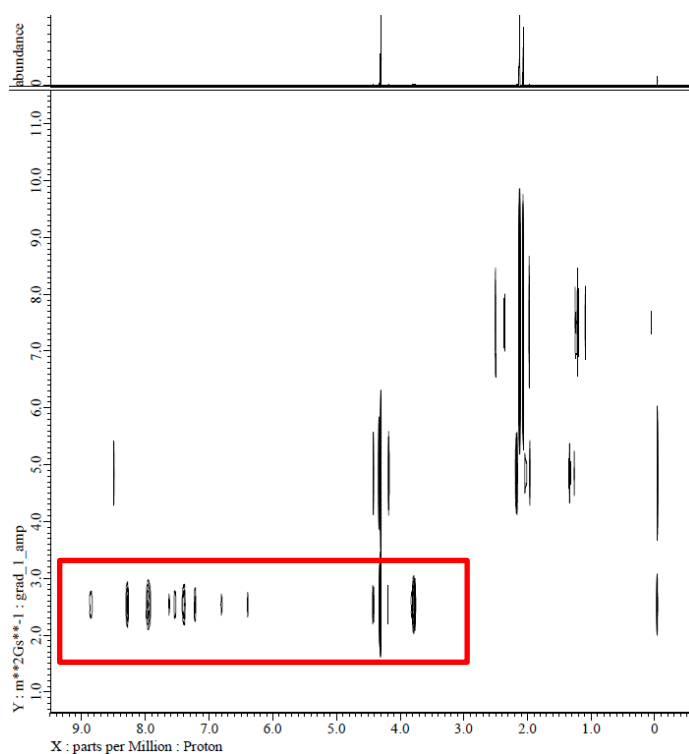


Figure 3.21: The DOSY spectrum of cage 3.11 in $d\text{-MeNO}_2$ showing a single large species in solution.

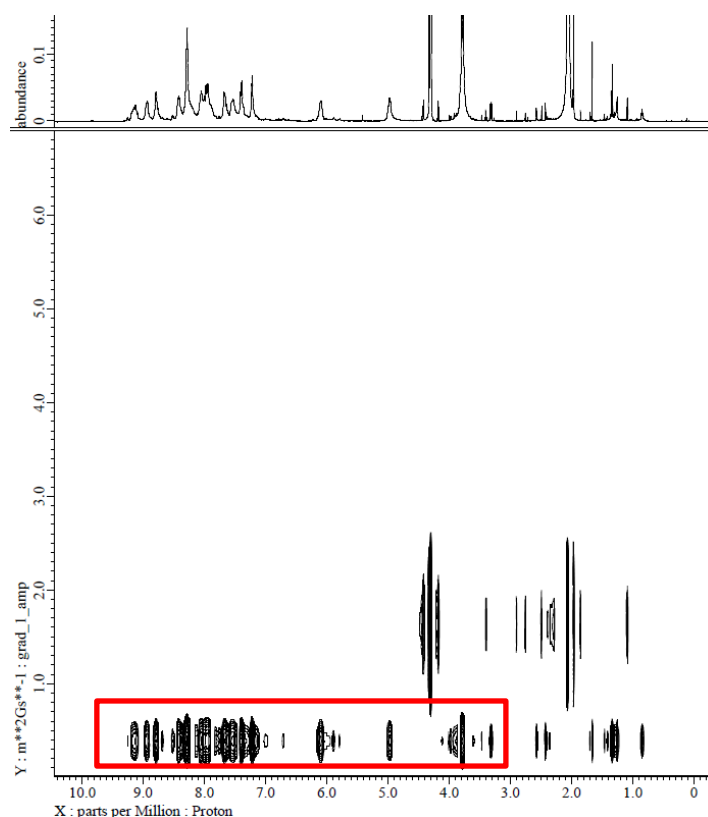


Figure 3.22: The DOSY spectrum of cage **3.12** in *d*-MeNO₂ showing a single large species in solution.

Infrared spectroscopy was consistent with the proposed structures. All of the cages show an intense P-F stretch between 831-836 cm⁻¹ originating from the hexafluorophosphate counterion. The ester linked cages display an intense C=O stretch between 1732-1734 cm⁻¹ which is absent in the ether linked assemblies. Microanalysis of the cage systems proved challenging however; despite extensive drying on the cages on a vacuum line, satisfactory microanalytical data could only be obtained for cages **3.8** and **3.12**. ¹H NMR spectroscopy revealed this is likely to be due to persistent levels of solvation that occur even after prolonged drying of samples.

3.5 Chiral self-sorting of metallocryptophanes in solution

The elucidation of the solid state SCXRD structure of the metallocryptophane of formula [$\{\text{Ir}(\text{ppy})_2\}_3(\text{L})_2\]^{3+} \cdot 3\text{BF}_4^-$ (where ppy is 2-phenylpyridine and L is an isonicotinic acid appended CTG ligand) as reported previously by Hardie and coworkers³³ indicated an interesting phenomena: the metallocryptophanes were only present in their homochiral enantiomeric forms. With the presence of both Δ and Λ isomers of the metallotecton, as well as *M/P* isomers of the ligands, there are 12

possible stereoisomers of the M_3L_2 cages, yet only the $MM-\Delta\Delta\Delta$ and $PP-\Delta\Delta\Delta$ enantiomeric pairs are observed in the X-ray crystal structure.³³ Such self-sorting is relatively uncommon when racemic ligands are present in solution.^{52-54, 59} Lusby and coworkers circumvented the issue of enantiomers in solution by employing enantiopure iridium(III) metallotectons in their synthesis of luminescent M_6L_4 coordination capsules.¹² More recently Zysman-Colman and coworkers employed the same strategy to prepare enantiopure luminescent Ir_8Pd_4 metallosupramolecular cages.⁶⁰ Whilst effective for the resolution of the iridium Δ/Λ isomers, this strategy cannot be employed here on account of the racemisation of the CTV framework in solution *via* its saddle conformation.

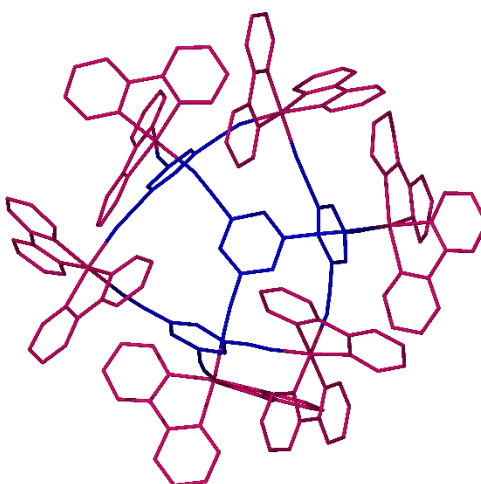
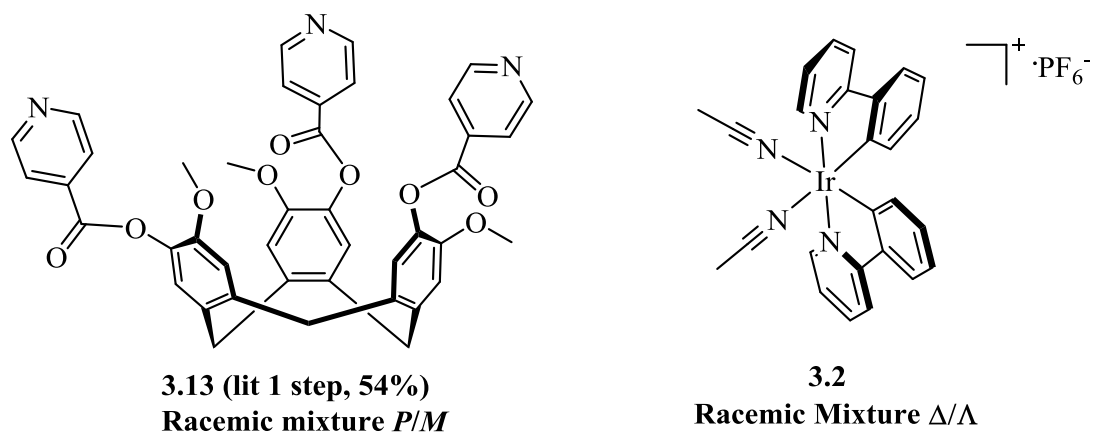
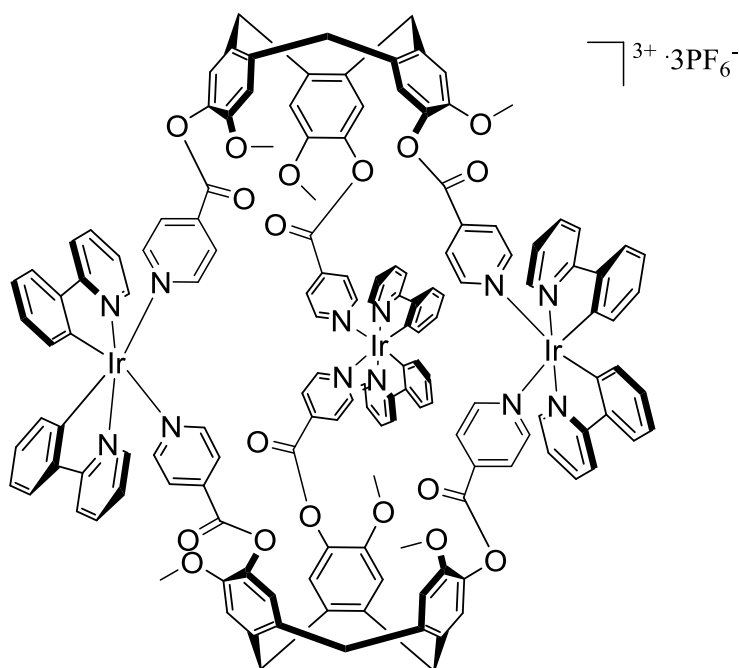


Figure 3.23: SCXRD structure of the enantiopure $M_6L_4 \Delta\Delta\Delta$ metallocage prepared by Lusby.¹² Iridium units and tricyanobenzene ligand units are shown in pink and blue respectively. All hydrogen atoms, counterions and solvents of crystallisation have been omitted for clarity.

It was of interest to investigate this self-sorting phenomena in solution by 1H NMR spectroscopy. The required ligand **3.13** (scheme 3.4) was prepared according to literature methods.⁶¹ Reaction of two equivalents of ligand **3.13** with three equivalents of the iridium metallotecton $[Ir^+(ppy)_2(MeCN)_2].PF_6^-$ in $d\text{-MeNO}_2$ leads to the formation of the $[{\{Ir(ppy)_2\}_3(L)_2}]^{3+}.3PF_6^-$ metallocage **3.14** (where ‘ppy’ is 2-phenylpyridine and ‘L’ is ligand **3.13**) as illustrated in scheme 3.4:



MeNO₂
RT, Time
Self-Sorting



Scheme 3.4: Self-assembly of the metallocryptophane 3.14.

The reaction was followed by timecourse ¹H NMR spectroscopy and mass spectrometry. Figure 3.24 shows the timecourse ¹H NMR spectra following this assembly. Initial mixing of the two components yields a broad NMR spectrum (spectrum c) which gradually begins to sharpen over time. Mass spectrometry analysis shows that the assembled product is present in significant quantities after 60 minutes (spectrum g) with a large peak at [982.6447]³⁺ which is assigned as the intact cage

$[\mathbf{3.14}\cdot 3\text{PF}_6]^{3+}$ where the intact cage is observed with no associated PF_6^- counterions (calculated m/z for $\{\text{C}_{150}\text{H}_{114}\text{Ir}_3\text{N}_{12}\text{O}_{18}\}^{3+}$ [982.9085] $^{3+}$). Gas phase fragmentation is often observed with the most common fragment of $[1223.9857]^{2+}$ assigned as the $[\text{M}_2\text{L}_2\cdot 2\text{PF}_6]^{2+}$ fragment, where $\text{M} = [\text{Ir}(\text{ppy})_2]$ and $\text{L} =$ ligand **3.13**, also observed without PF_6^- counterions (calculated m/z for $\{\text{C}_{128}\text{H}_{98}\text{Ir}_2\text{N}_{10}\text{O}_{18}\}^{2+}$ [1223.8159] $^{2+}$).

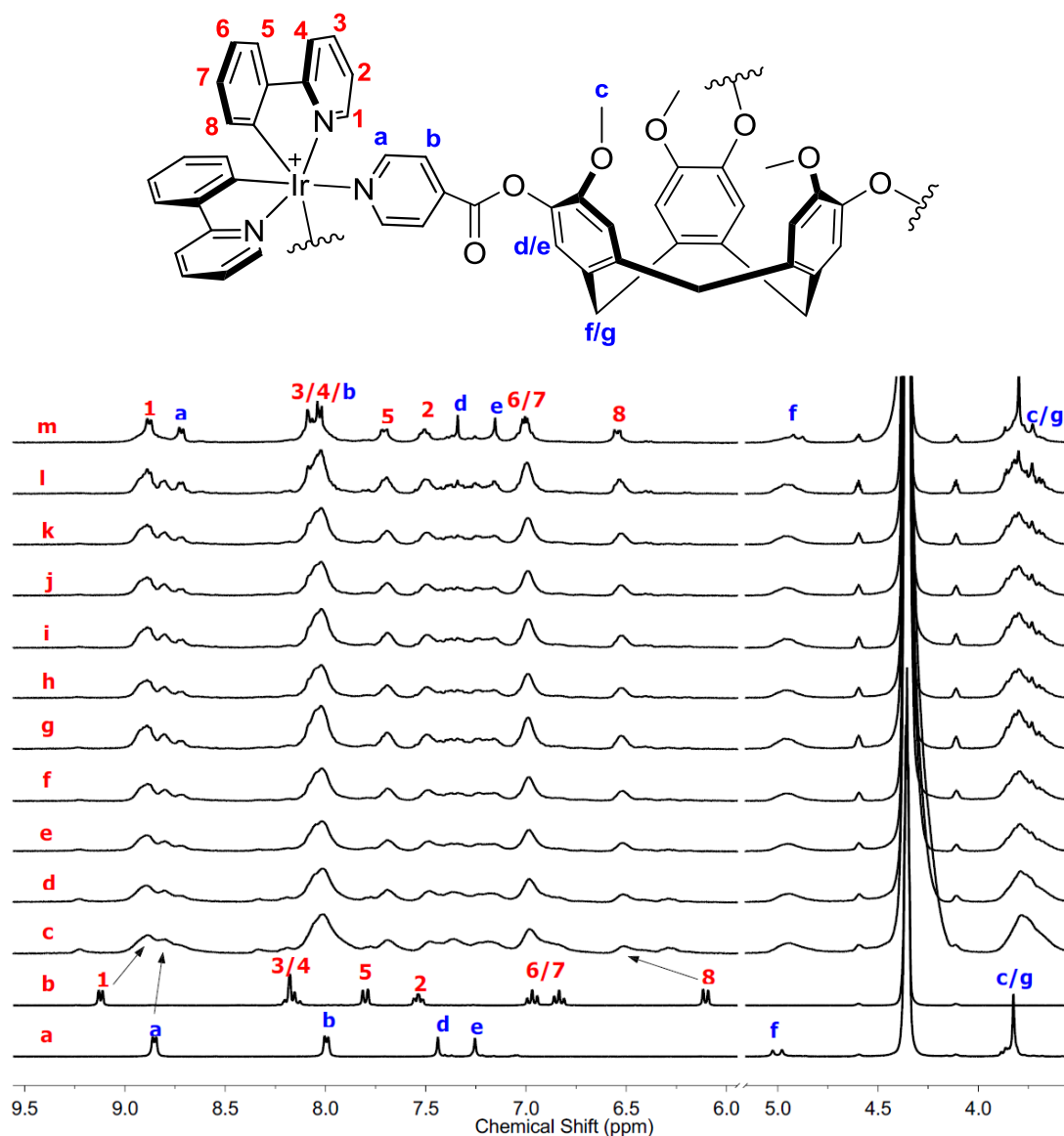
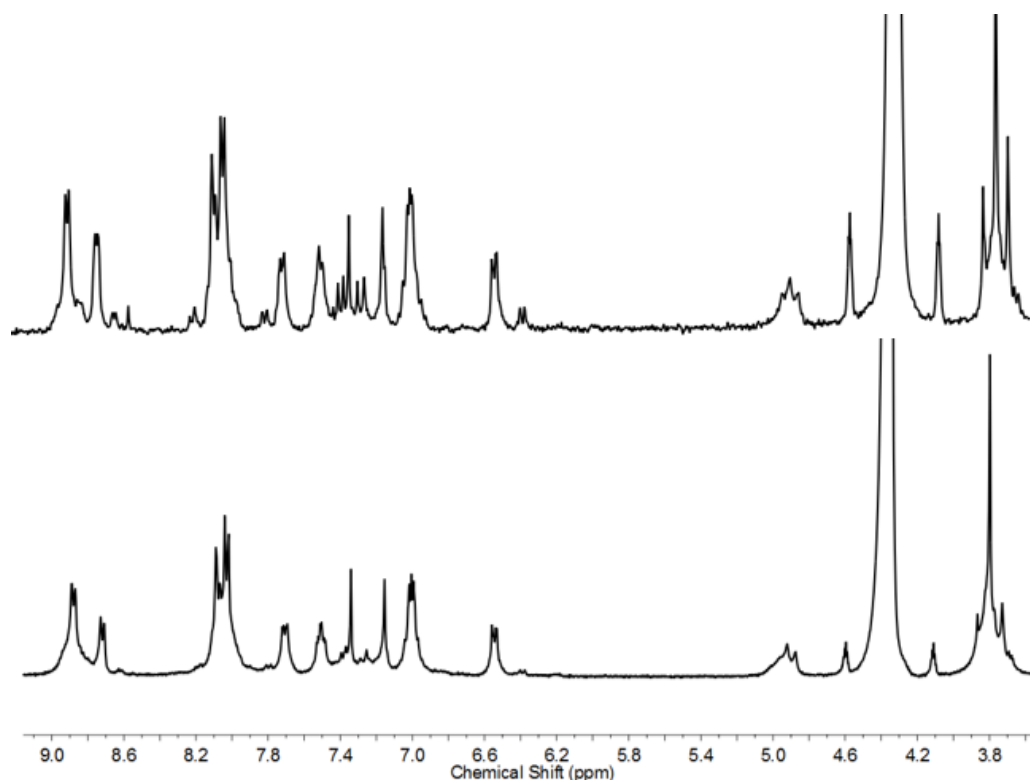


Figure 3.24: Interpreted timecourse ^1H NMR showing the formation of **3.14** over time in $d\text{-MeNO}_2$ with key shifts indicated by arrows; **a**. Ligand **2.12**; **b**. Metallotecton **3.2**; **c**. Immediately upon mixing; **d**. 15 minutes rt; **e**. 30 minutes rt; **f**. 45 minutes rt; **g**. 60 minutes rt; **h**. 75 minutes rt; **i**. 90 minutes rt; **j**. 105 minutes rt; **k**. 120 minutes rt; **l**. 48 hours rt; **m**. 3 months rt. The region 6.1-5.1 ppm has been omitted for clarity.

Interestingly, it can be seen that although self-assembly of the intact product is completed reasonably quickly, the spectra continue to sharpen for a long time after mass spectrometry has revealed a complete reaction. This is indicated in the spectrum m (taken after 3 months in solution) which is noticeably sharper than the spectrum taken after 48 hours (spectrum l). Collaborative work from Hiraoka indicated that the ^1H NMR spectral sharpening of this system is likely a consequence of chiral self-sorting.³³ This suggests that the chiral self-sorting observed in the SCXRD structure of complex **3.14** likely occurs in solution before crystallisation (approx. 2 weeks) and is not necessarily a phenomena of the crystallisation process itself. The ^1H NMR spectrum of the redissolved, self-sorted single crystals of complex **3.14** bears a strong resemblance to the self-sorted solution shown in spectrum l providing further evidence this phenomena is occurring in solution.



*Figure 3.25: Comparison of ^1H NMR spectra of the self-sorted solution (after 3 months, bottom) against self-sorted single crystals (top) of complex **3.15**.*

It was of interest to see whether this self-sorting process could be influenced by the presence of spherical chiral additives.⁶² Five such additives were investigated – chiral guests *R*-Camphor, *S*-Camphor, *R*-Camphorsulfonic acid, *S*-Camphorsulfonic acid and achiral adamantane. An aliquot of each additive (3 milligrams) was added to the reaction components upon mixing and the assembly process was once again followed by ^1H NMR spectroscopy and mass spectrometry. Figure 3.26 shows the comparison

of the ^1H NMR spectra of complex **3.15** conducted with or without guest molecules present after 24 hours in solution:

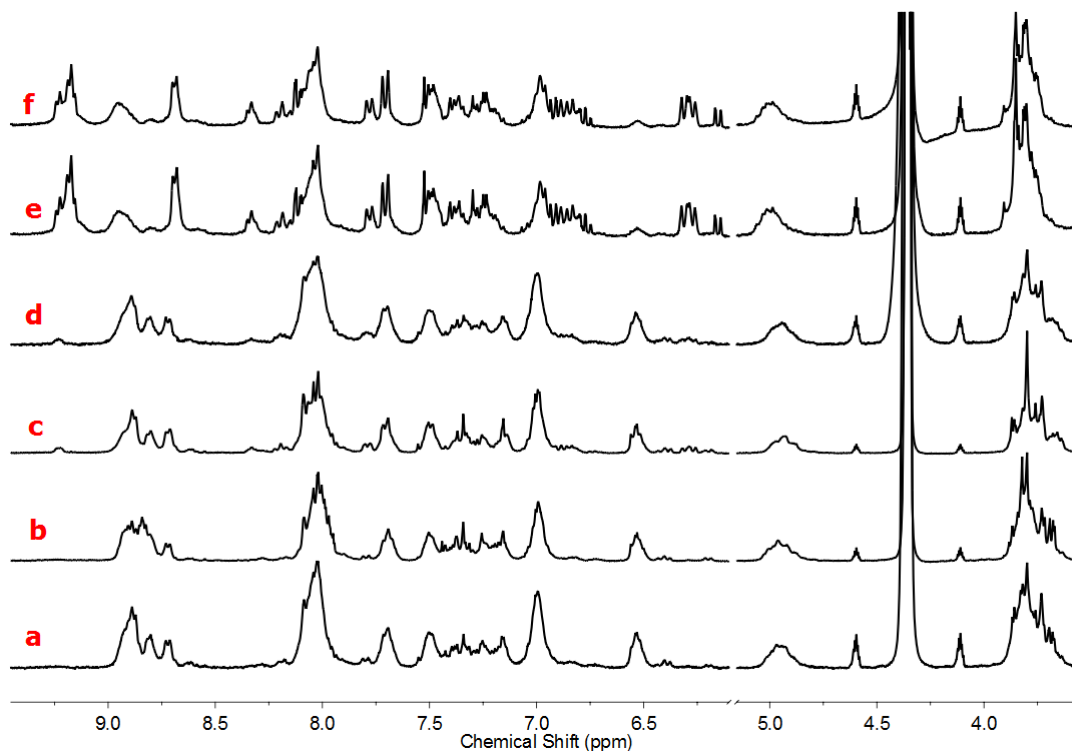


*Figure 3.26: Timecourse ^1H NMR spectra of complex **3.15** after 24 hours containing: a. no added guest; b. *R*-Camphor added guest; c. *S*-Camphor added guest; d. Adamantane added guest; e. *R*-camphor sulfonic acid added guest; f. *S*-camphor sulfonic acid added guest. The region between 6.1 and 5.1ppm has been omitted for clarity.*

The addition of *R*-camphor (spectrum b) or *S*-Camphor (spectrum c) to the system led to faster sharpening of the NMR spectra than in their absence (spectrum a) but the effect is not overly dramatic. Addition of achiral adamantane (spectrum d) had no observed effect on the rate of sharpening whereas addition of either of the sulfonic acids (spectra e and f) led to an inhibition of cage formation entirely. Presumably this is due to the presence of a competing ligand in the acid functional group.

This investigation was then extended to the azobenzene cage **3.8** (figure 3.15). Interestingly, the formation of the azobenzene cage **3.8** appears indifferent to the presence of these guest molecules with no noticeable increased rate of sharpening observed. Addition of the chiral *R*- and *S*-Camphorsulphonic acids to the reaction inhibited cage formation entirely in concurrence with observations made for complex **3.15**. After 60 minutes in solution, there is no increased degree of sharpening in the solutions containing additional guest when compared against the solution containing

no guest. Since the degree of sharpening is indicative of chiral self-sorting, there appears to be no acceleration of this process upon addition of chiral guest molecules in contrast to complex **3.15**.

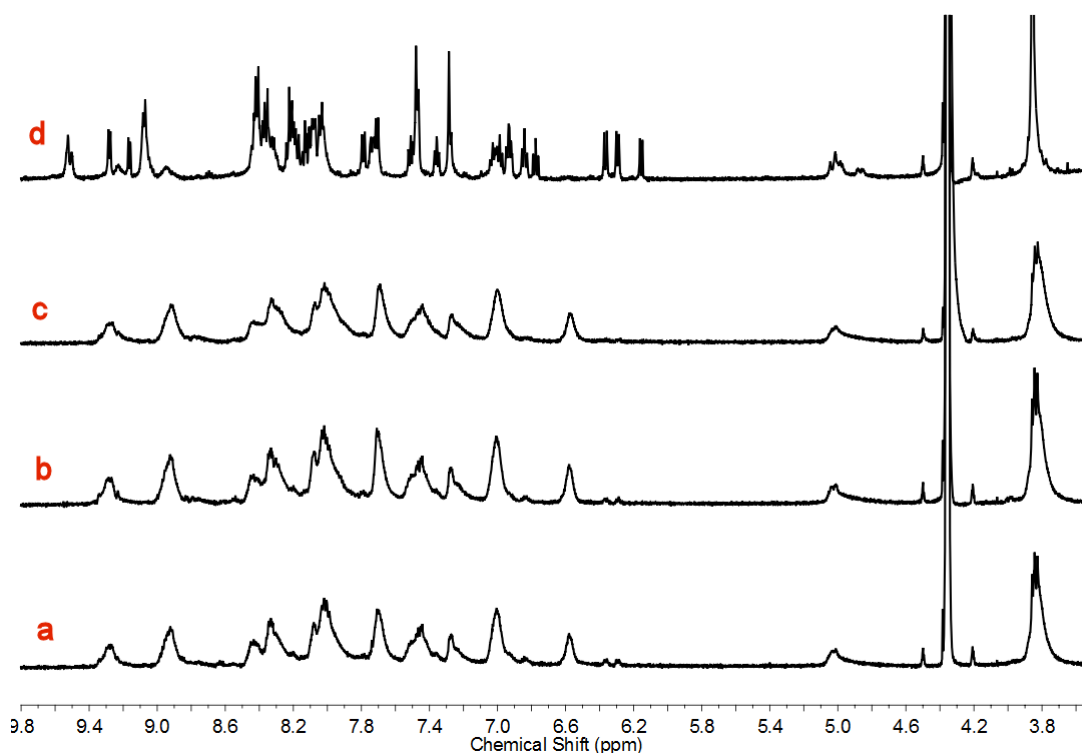


*Figure 3.27: ^1H NMR spectra of the formation of cage **3.8** after 60 minutes in $d\text{-MeNO}_2$ in the presence of: **a.** No added guest; **b.** 4 mgs *R*-Camphor; **c.** 4 mgs *S*-Camphor; **d.** 4 mgs *S*-camphorsulfonic acid (no cage formation evident). The presence of chiral guests appears to have no noticeable effect on the self-sorting process of cage **3.8**.*

Cage formation is sensitive to both solvent choice and exact 3:2 stoichiometry of metal:ligand. No cage formation is observed in coordinating solvents such as acetonitrile or DMSO; additionally redissolution of the pure powder of complex **3.5** in either of these solvents leads to cage degradation with peaks assigned to free ligand and metal observed after several hours in solution. Henkelis and co-workers reported a metastable metallocryptophane prepared using a CTG derived ligand and $[\text{Pd}(\text{en})(\text{NO}_3)_2]$ where ‘en’ is 1,2-ethylenediamine. Although this system initially forms an Pd_3L_2 architecture, over time it spontaneously rearranges to larger Pd_6L_8 metallocages.⁶³ The azobenzene cages in nitromethane solvent however, appear to be stable indefinitely as no degradation is observed by ^1H NMR even after several months in solution (figure 3.28). These re-dissolved samples continue to sharpen over time indicating self-sorting of cage enantiomers. Mass spectrometry of these solutions show the intact cages as the main species present even after several months.

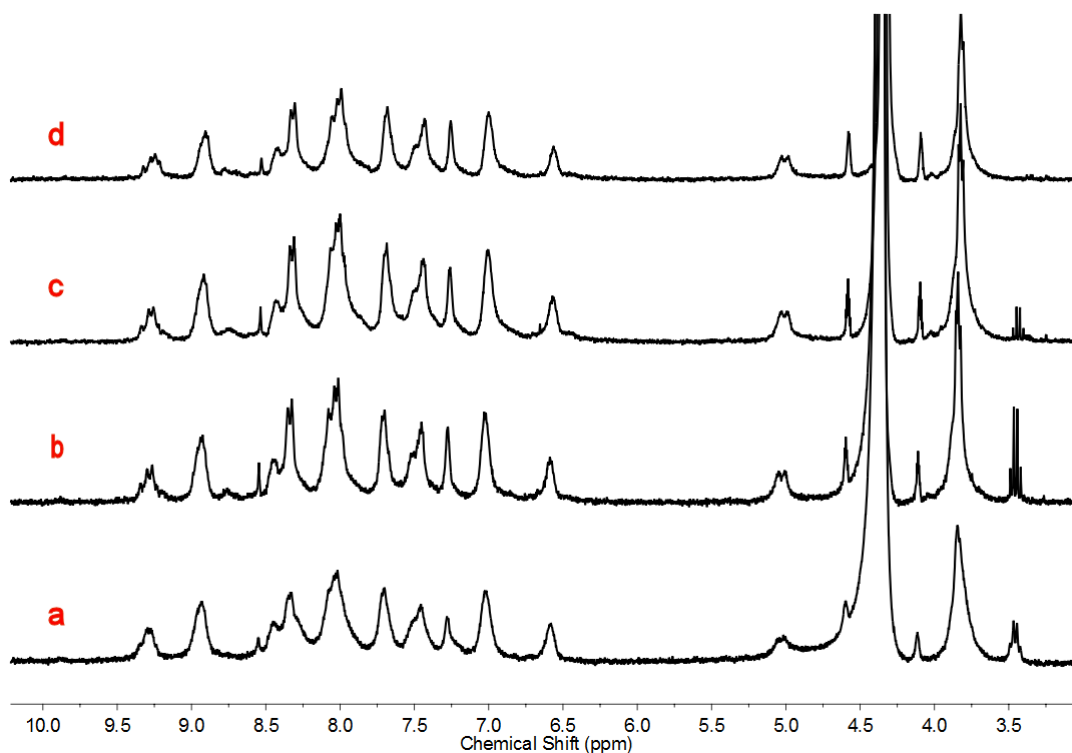


Figure 3.28: Stability of complex **3.8** in *d*-MeNO₂ solution over time; **a**. redissolved powder; **b**. 1 month in solution; **c**. 4 months in solution; **d**. 9 months in solution.

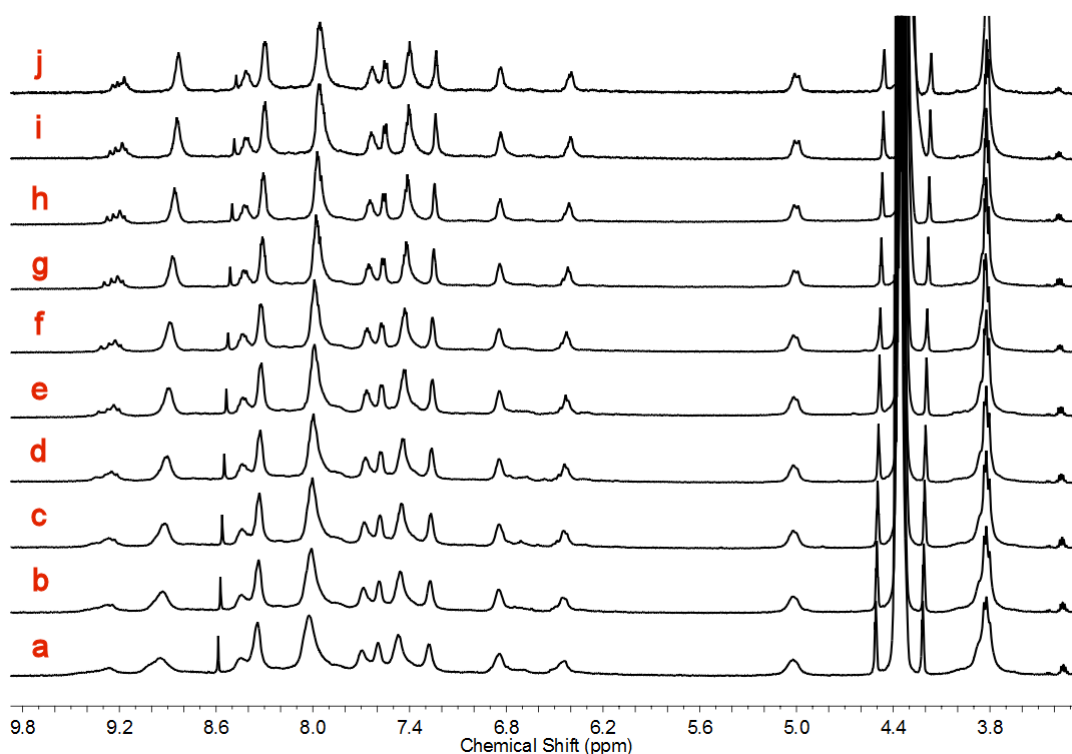


Figure 3.29: Variable temperature (VT) NMR spectrum of cage **3.11** in *d*-MeNO₂; **a**. 253K; **b**. 263K; **c**. 273K; **d**. 283K; **e**. 293K; **f**. 303K; **g**. 313K; **h**. 323 K; **i**. 333 K; **j**. 343K.

A degree of sharpening can also be seen in the variable temperature (VT) NMR spectrum of complex **3.11** as shown in figure 3.29. Upon cooling a sample of cage **3.11** to 253K, a broad spectrum is observed, figure 3.17a). Upon increasing the temperature in increments of 10K, it can be seen that all of the peaks begin to sharpen, a phenomena that persists above ambient temperature all the way through to 343K (figure 3.17j).

An interesting point of note is the formation of complexes **3.5**, **3.7**, **3.11** and **3.12**, all of which contain ligands that coordinate to the iridium centre *via* a 3-pyridyl motif. Whilst 4-pyridyl ligand motifs are among the most popular building blocks for metallo-supramolecular assemblies, the 3-pyridyl motif is far less common. Severin has reported the formation of $[\text{Pd}_6\text{L}_{12}]^{12+}$ coordination cages (where 'L' is a clathrochelate based bipyridyl ligand) where the ligands coordinate to the metal *via* a 3-pyridyl moiety.⁶⁴ A handful of other examples of 3-pyridyl coordination in metallo-supramolecular architectures have also been described⁶⁵⁻⁷³ with many of these examples coming from the Clever group. A recent review from Clever covers most of these examples.⁷⁴ The penchant for 4-pyridyl derived ligands over their 3-pyridyl analogues is attributed to restricted bonding vectors in the 4-pyridyl systems when rotating about the adjacent bond as illustrated in figure 3.30:

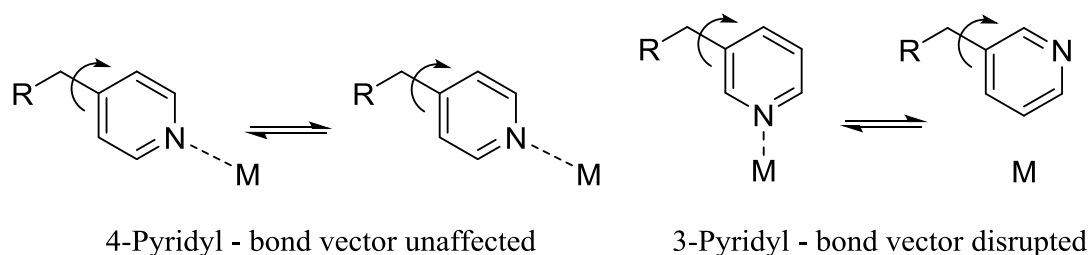


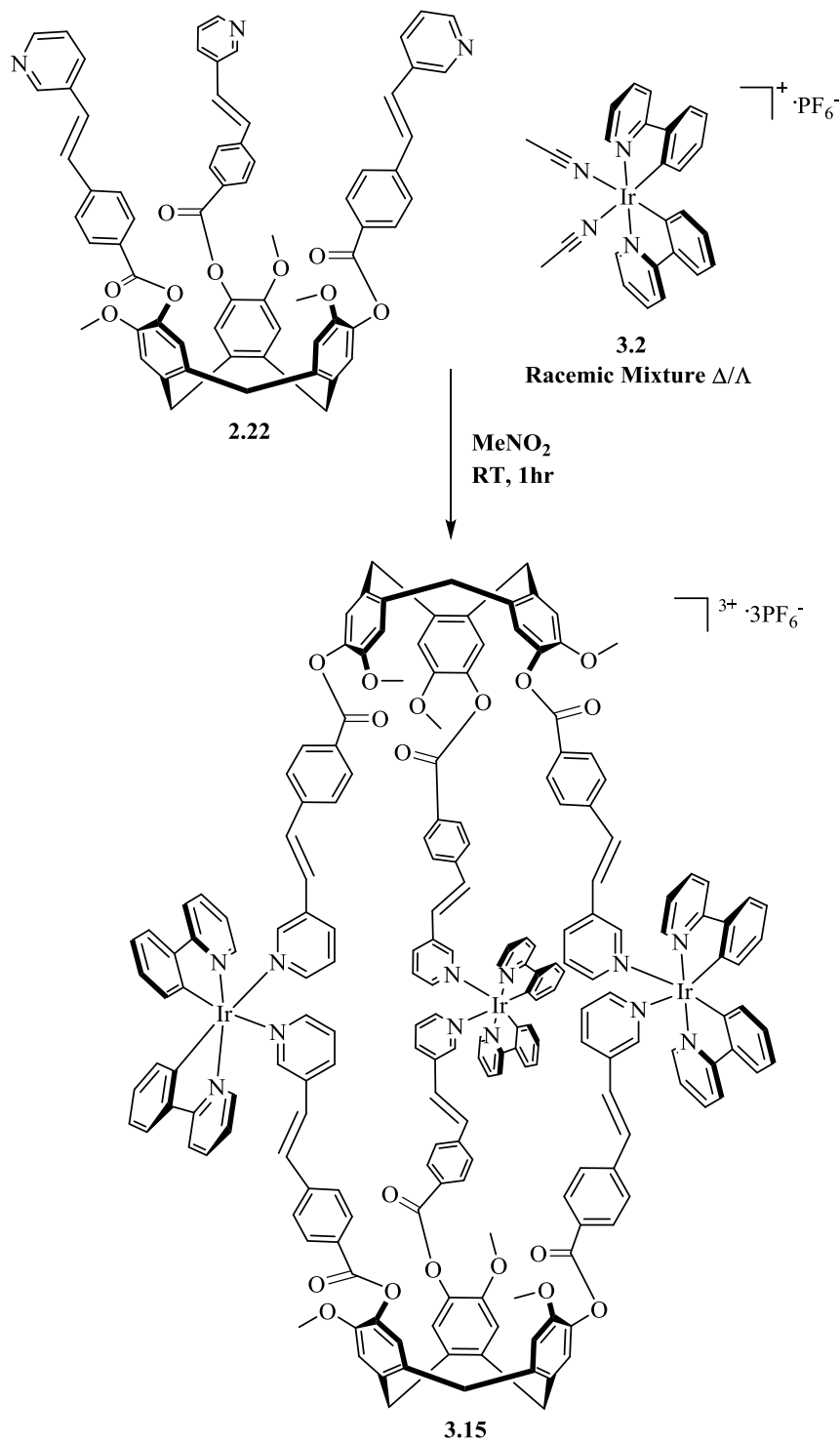
Figure 3.30: Comparison of 4-pyridyl and 3-pyridyl bond vectors.

The formation of metallogages **3.5**, **3.7**, **3.11** and **3.12** are in particular contrast to the systems reported by Hardie where the 3-pyridyl isonicotinic acid ligands were shown to be incapable of self-assembly into M_3L_2 metallogages.³³ The ability of ligands **2.12** and **2.17** to overcome this limitation is likely to be due to the more flexible, lengthier azobenzene side-arms which are able to twist to accommodate the necessary binding angle.

3.6 Self-assembly of a M_3L_2 metallocryptophane bearing stilbene units

In the same fashion as the azobenzene metallogages, the stilbene analogue of complex **3.8** was investigated in collaboration with MChem student Ben Swift. The reaction of two equivalents of ligand **2.22** with three equivalents of metallotecton **3.2** in

nitromethane solvent led to the self-assembly of the target metallocryptophane of composition $[\{\text{Ir}(\text{ppy})_2\}_3(\text{L})_2]$ where 'ppy' is 2-phenylpyridine and 'L' is ligand 2.22, compound **3.15**, as illustrated in scheme 3.5.



*Scheme 3.5: Self-assembly of metallocryptophane **3.15** bearing stilbene units.*

^1H NMR studies of this assembly process (figure 3.31) initially showed a spectrum similar to the analogous azobenzene cage **3.8** (spectrum c). However, over time, the spectrum continues to broaden until a more complex ^1H NMR spectrum (e) is acquired as shown in figure 3.31. Initially it was thought that some form of degradation had taken place or mixture of products had been obtained. However, the HRMS of the solution after 120 hours in solution (spectrum e) shows no evidence of side products or degradation with the predominant peak at m/z $[1187.5441]^{3+}$ which is assigned as the intact $[\{\text{Ir}(\text{ppy})_2\}_3(\text{L})_2]^{3+}$ metallocryptophane (figure 3.31) observed without the PF_6^- counterions. The DOSY NMR spectrum of complex **3.15** is also indicative of a single species in solution, ruling out the possibility of an incomplete reaction. The broad nature of this spectrum could be due to a complete disorder of chiral sites present in the system. The preparation of this analogue has only been conducted on an NMR scale to this date.

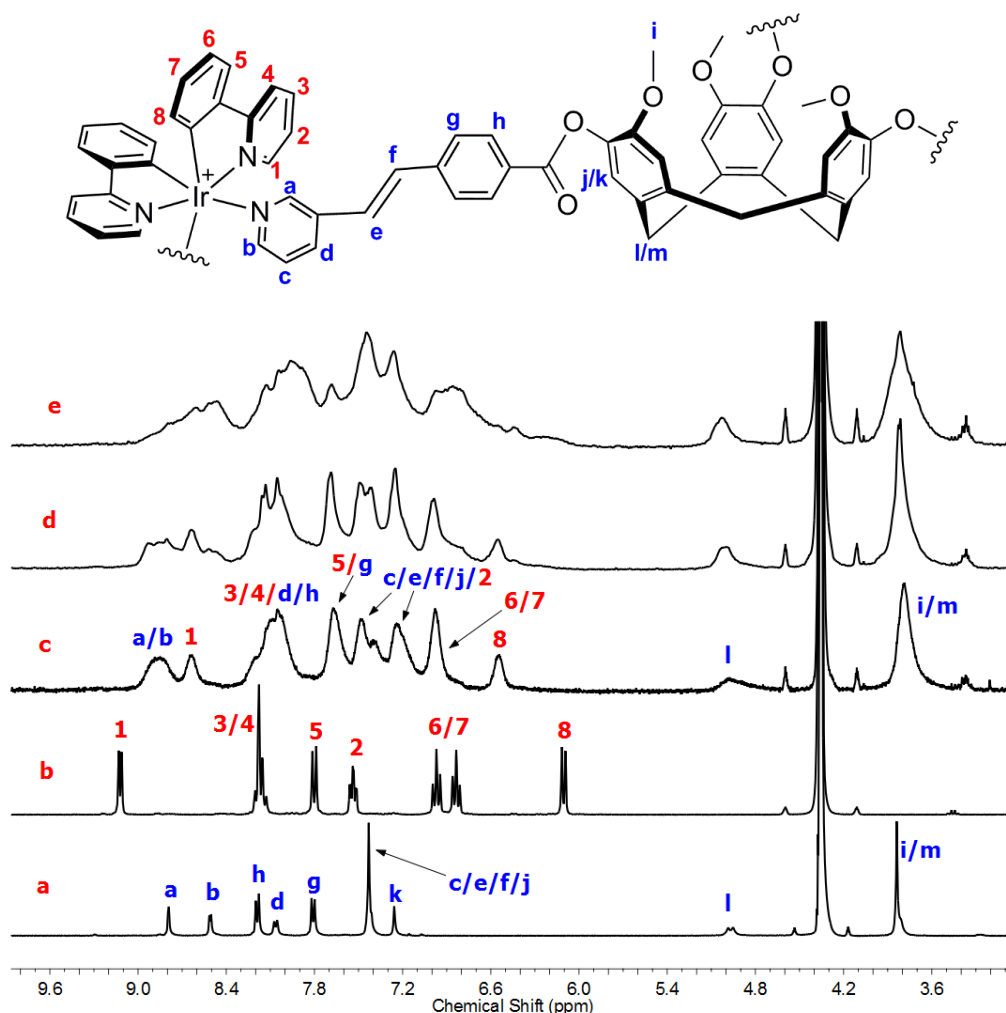


Figure 3.31: Timecourse ^1H NMR spectra following the formation of metallocryptophane **3.15** in $d\text{-MeNO}_2$; **a**. Ligand **2.22**; **b**. Metallotecton **3.2**; **c**. Initial spectrum upon mixing; **d**. 24 hours in solution; **e**. 120 hours in solution.

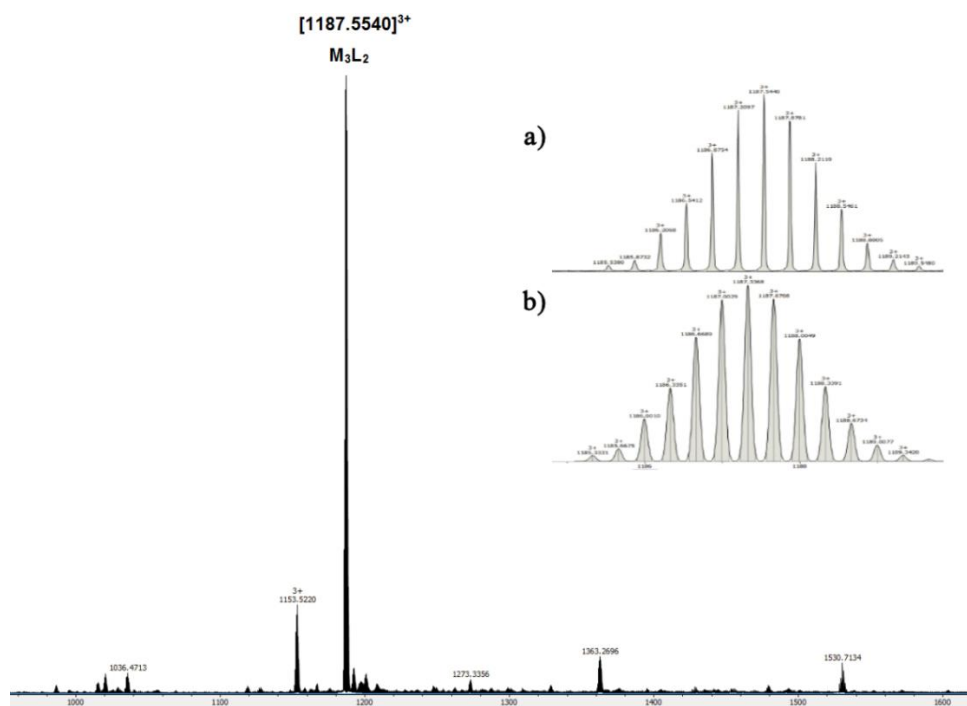


Figure 3.32: Interpreted high resolution mass spectrum of cage 3.15 taken after 120 hours in solution; inset a. experimental isotope pattern; b. calculated isotope pattern for cage 3.15.

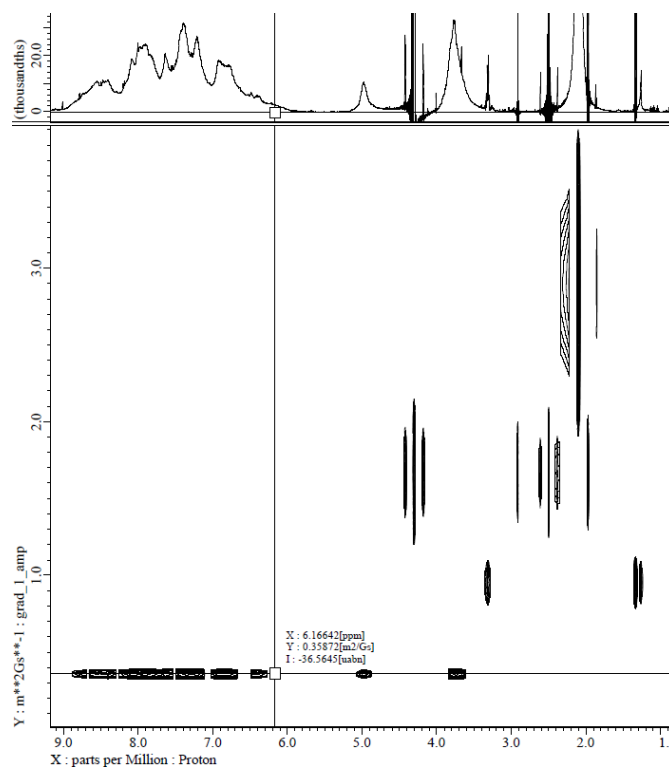


Figure 3.33: The DOSY spectrum of cage 3.15 in d -MeNO₂ showing a single large species in solution.

The DOSY spectrum of complex **3.15** (figure 3.33) has particularly ‘stretched’ resonances in the aromatic region. Although all of the aromatic peaks belong to species of the same size, this is a possible indication of a multitude of isomers present in the sample suggesting that chiral self-sorting of this cage may be slower or not in effect for the stilbene cage. However all of these isomers are the same size, implying the broadness of the ^1H NMR spectrum is a consequence of isomers and not of an incomplete self-assembly. This also explains why the mass spectrum is so clear as different M_3L_2 isomers would all still be observed as the same mass.

3.7 Computational modelling of cage **3.8**

A single crystal X-ray structure could not be obtained of any of the complexes owing to the failure to grow suitable crystals for X-ray diffraction. Despite a wealth of conditions employed and the addition of potential guest molecules (o-carborane, fullerenes, iodine amongst others), vapour diffusion experiments yielded only precipitate. Altering the concentration of cage, the solvents employed, cage counterions (*via* the iridium salt prepared) and methods of crystallisation fared no better. With the absence of single crystal data, molecular modelling of cage **3.8** was performed in collaboration with Professor Colin Fishwick of the University of Leeds in an effort to gain insights into the likely molecular structure.

As similar spectral sharpening was observed in the ^1H NMR spectra of both complex **3.8** and the previously reported complex **3.14**, complex **3.8** was believed to be undergoing a similar chiral self-sorting process, hence an enantiopure *MM*- $\Lambda\Lambda\Lambda$ cage was used for modelling. The starting model was derived from the SCXRD structures of complex **3.14** (as reported by Hardie) and of ligand **2.12**. The models were constructed using the Maestro molecular modelling package from Schrödinger Inc. The procedure involved ‘by eye’ grafting of the [Ir(ppy)] units onto the crystal structure of ligand **2.12**. The resulting hybrid structure was then minimised using the molecular mechanics force field (MMFF) feature within Maestro, with all atoms free to move during this process until an energy minima was reached. The results of this process are shown in figure 3.34 for the all *trans* metallocage. Additional models were prepared illustrating the coordination cage containing 1, 3 or 6 *cis* azobenzene units.

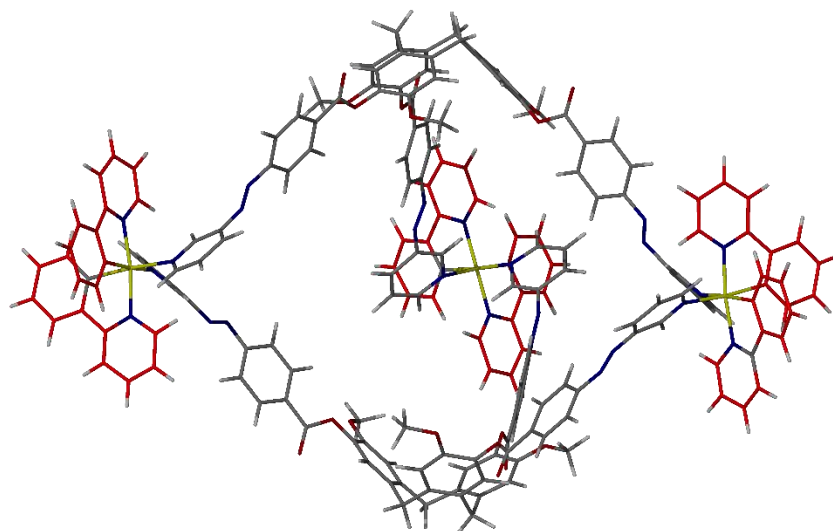


Figure 3.34: Energy-minimised (MMFF) molecular structure of all *trans* cage **3.8**. Phenylpyridine units are shown in red for clarity.

A degree of twisting of the azobenzene unit is necessary in order to accommodate the coordination to the iridium(III) centre *via* a 3-pyridyl motif. However, this twist is not necessarily implausible; several copper coordination polymers have been prepared bearing the rigid ester ligand **2.12** and depending upon the metal coordination environment, twists of this nature were found to be occurring in experimental X-ray diffraction studies (discussed in more detail in chapter 5). The degree of twisting in the model was calculated by defining the pyridyl and phenyl units adjacent to each N=N bond as a plane and then measuring the angles between planes for each of the six azo units. The calculated values for these angles are measured at 54.03°, 54.85°, 54.51°, 44.07°, 61.80° and 43.50°. This equates to an average of 52.12°, a reasonably significant degree of twisting. Isolated *trans*-azobenzene has been demonstrated by electron diffraction measurements to be twisted by up to 30° in the gas phase.⁷⁵ Furthermore, similar twisting has been demonstrated by Maity in coordination polymers containing azobenzene-appended bipyridyl ligands.⁷⁶ As expected, the degree of twisting is far more significant in the model of the all *cis* metallocage with the average degree of twisting 75.16°.

The energy-minimised *trans* metallocage has a structure consistent with experimental observations from the 2D ROESY studies. The ROE is a consequence of the mutual dipolar relaxation of protons close in space which falls away rapidly with internuclear distance at a rate of $1/r^6$ where r is the distance between protons.⁷⁷ The practical consequence of this is a limit to the distance in which ROEs can be observed, typically around 5-6Å. The distance between H_a on the ligand and the cyclometallated proton H₈ is 5.143Å which leads, as expected to a weak ROE (figure 3.35). However this

interaction is the only unambiguous evidence of through space coupling between the ancillary phenylpyridine unit and the azobenzene ligand.

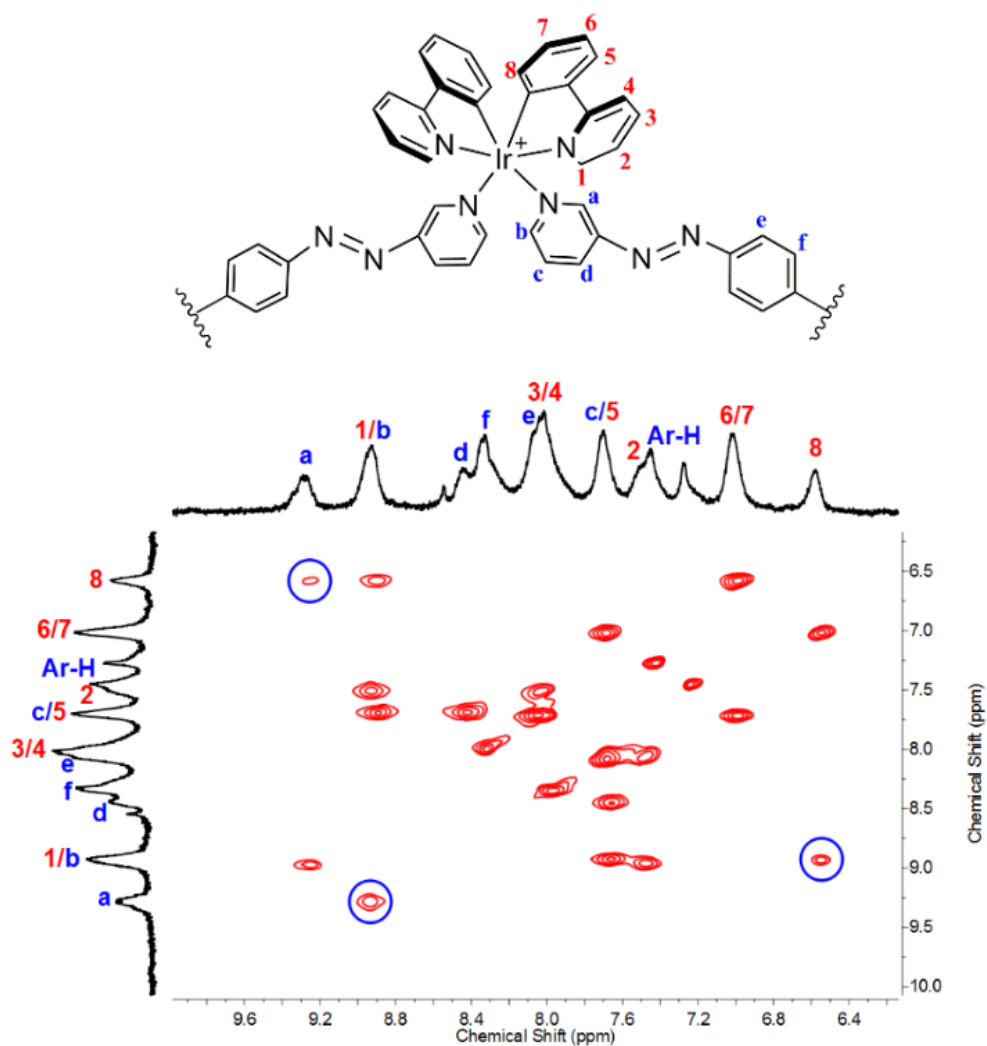


Figure 3.35: Interpreted ROESY spectrum of complex 3.8 with important through-space correlations indicated in blue circles.

A much stronger coupling is observed between H_a (ligand pyridyl) and an overlapped peak of H₁ (phenylpyridine based) and H_b (ligand pyridyl). This coupling could be arising as a result of H_a---H₁ or H_a---H_b through space interactions. As this coupling is very intense, it is likely to arise from the interaction that is closer in space which is indicated by the model to be the H_a---H₁ interaction (2.317Å). The intraligand coupling would be expected to be far weaker as the H_a---H_b protons are reasonably spaced apart (4.181Å). This provides another indicator of complexation.

A similar analysis can be applied to the ROE observed between H₈ (phenylpyridine based) and the signal assigned as H_b (ligand) overlapped with H₁ (phenylpyridine based). Two couplings are again possible – H₈---H_b or H₈---H₁. Molecular distances

predicted by the model suggest this is more likely to be the former case (2.652Å separation versus 3.503Å) which would indicate another indicator of complexation. However this is not without ambiguity. A full assignment of all the observed ROE's and their likely origin is detailed in table 3.1; all the observed ROE's are consistent with the structure proposed by the model.

Table 3.1: Assignments of through space coupling interactions observed in the ROESY NMR spectrum of cage 3.8.

ROE interaction	Assignment (NMR)	Distance (Å) ^a	Origin ^b
6.546---7.018	H ₈ ---H ₆ + H ₇	2.487/4.311	Ppy---Ppy
6.548---8.931 ^c	H ₈ ---H _b + H ₁	2.652/3.503	Ligand---Ppy
6.989---7.719	H ₆ + H ₇ ---H _c ^d + H ₅	2.472/4.304	Ppy---Ppy
7.242---7.465	H _h ---H _i	1.706	Ligand---Ligand
7.678---8.084	H _c ^d + H ₅ ---H _e ^d + H ₃	4.657	Ppy---Ppy
7.657---8.453	H _c + H ₅ ^d ---H _d + H _f ^d	2.450	Ligand---Ligand
7.657---8.926	H _c + H ₅ ^d --- H _b + H ₁ ^d	2.513	Ligand---Ligand
8.034---7.509	H _e ^d + H ₃ --- H _h ^d + H ₂	2.541	Ppy---Ppy
8.929---7.509	H _b + H ₁ --- H _h ^d + H ₂	4.504/2.586	Ppy---Ppy
8.939---9.279 ^c	H _b + H ₁ ---H _a	4.174/2.411	Ligand---Ppy
9.233---6.584 ^c	H _a ---H ₈	5.143	Ligand---Ppy

^a Distances calculated from model; ^b Likely origin selected from closest interaction where overlapping peaks occur. ^c Key coupling - interaction likely to originate from couplings between protons on phenylpyridine ancillary unit and ligand; ^d Proton likely too distant to make a significant contribution to the observed ROE.

Comparison to the all *cis* cage was also carried out through molecular modelling. The twist of the *cis* azobenzene units brings the H_a protons into closer proximity (4-5Å) with several protons on the phenylpyridine auxiliary ligand (H₄, H₅ H₆ and H₇) than in the *trans* isomer (6-7Å). This proximity should manifest itself in weak through space interactions. However no such interactions are observed with any of these protons in the experimental ROESY spectrum (figure 3.35) which supports the conclusion that the resting state of the metallocages is the all *trans* isomer. ROESY spectra were acquired for all of the other cage complexes **3.9-3.12**, with all observed couplings similar to the example discussed here.

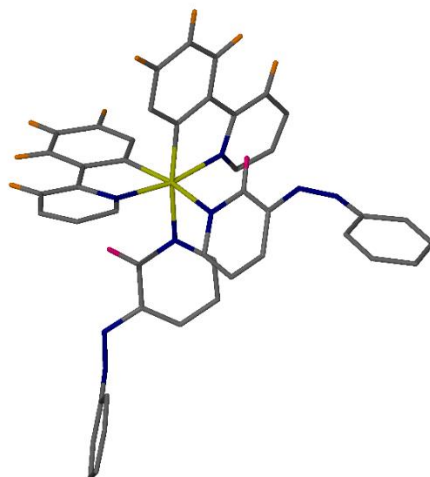


Figure 3.36: From the model of the all cis cage; the ortho pyridyl protons (shown in pink) should have four through space interactions to the phenylpyridine protons shown in orange as internuclear distances are between 4-5Å. Yet none of these interactions are observed in experimental ROESY NMR data.

The model can also be used to calculate an estimated hydrodynamic radius by measuring the distances between the centre of the cage and the periphery. Using the CTG bowls and phenylpyridine auxiliary ligands to define the periphery, a hydrodynamic radius of 11-19Å is obtained. This is also consistent with experimental data obtained from the DOSY spectrum of complex **3.8** which gave a calculated hydrodynamic radius of 17.32Å. However these values should be regarded as approximations only due to the lack of an X-ray crystal structure and the spherical assumptions needed for the Stokes-Einstein equation.

3.8 Other azobenzene containing metallocryptophanes

This chapter has focussed exclusively on the preparation of a single architecture (M_3L_2) using only one metal source, iridium(III). Owing to the wealth of supramolecular chemistry CTG and its derivatives have access to, this leaves plenty of scope for further investigations. Many other architectures have been synthesised using CTG based derivatives and the flexibility of the azobenzene ligand arms could give rise to an array of different photoresponsive systems (some examples of non-discrete coordination polymers utilising these ligands are discussed in chapter 5). Recent work in the group with current PhD researcher Edward Britton has utilised the 3-pyridyl ester ligand **2.12** in the self-assembly of a rhodium(III) metallocryptophane of formula $[\{Rh(ppy)_2\}_3(L)_2]^{3+} \cdot 3PF_6^-$, the rhodium (III) analogue of complex **3.8** via the reaction of ligand **2.12** with the monometallic rhodium tecton

$[\text{Rh}(\text{ppy})_2(\text{MeCN})_2]^+\text{PF}_6^-$. The initial ^1H NMR spectrum of this complex is virtually indistinguishable from that of complex **3.8**, providing strong evidence of metallocryptophane formation.

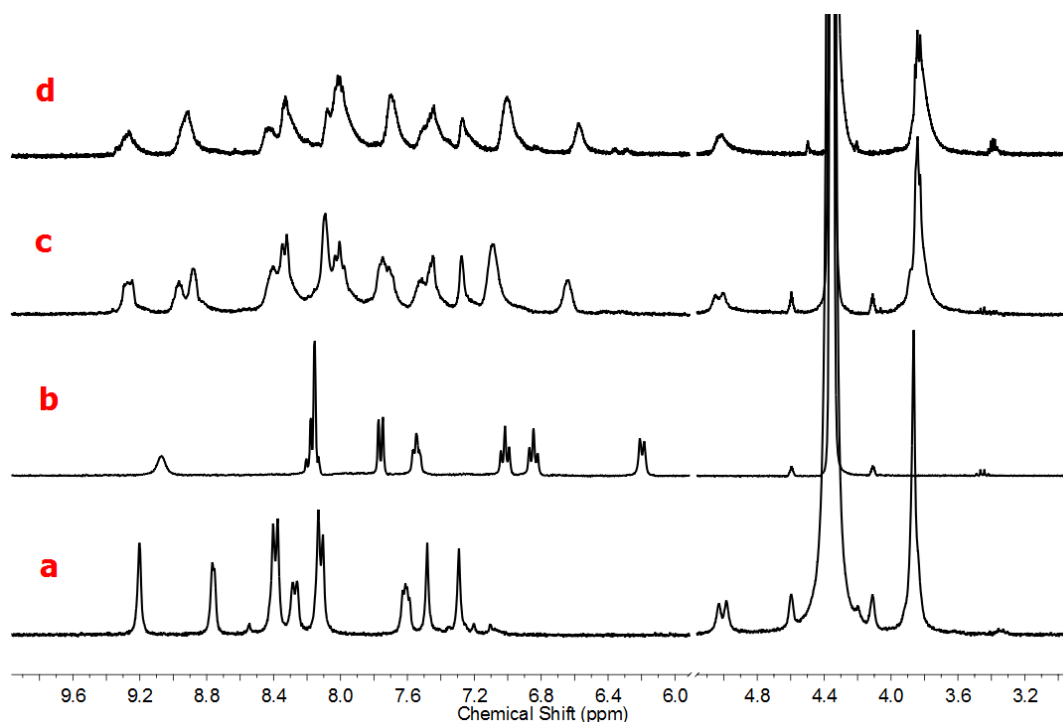


Figure 3.37: ^1H NMR spectrum evidencing the formation of the rhodium analogue of complex **3.8** showing: **a.** Ligand **2.12**; **b.** $[\text{Rh}(\text{ppy})_2(\text{MeCN})_2]^+\text{PF}_6^-$ metallotecton; **c.** Initial spectrum of $[\{\text{Rh}(\text{ppy})_2\}_3(\text{L})_2]^{3+} \cdot 3\text{PF}_6^-$; **d.** Complex **3.8**, $[\{\text{Ir}(\text{ppy})_2\}_3(\text{L})_2]^{3+} \cdot 3\text{PF}_6^-$ (shown for comparative purposes).

Use of rhodium in place of iridium may well constitute an alteration in the photoswitching ability of the azobenzene units owing to subtle differences in the absorption spectra of these classes of complexes (further consideration of this point is discussed in more depth in chapter 4). In addition to this system, efforts have also commenced towards the preparation of metallocryptophanes containing the palladium(II) tecton prepared previously in the Hardie group, $[\text{Pd}(\text{MeCN})_2(\text{bis-NHC-nap})] \cdot 2\text{BF}_4$ where ‘bis-NHC-nap’ is a 2-naphthalene derived *N*-heterocyclic carbene (NHC).³² The flexibility of the azobenzene ligands presented here could lead to other families of metallocryptophanes which are due to be investigated by current PhD student Edward Britton.

3.9 Conclusions and further direction

A reliable route to M_3L_2 metallocryptophanes utilising the *cis*-protected metallotecton $[\text{Ir}(\text{ppy})_2(\text{MeCN})_2]^+\text{PF}_6^-$ has been achieved, successfully incorporating the

azobenzene or stilbene functionality into the target product. The flexible ligand arms employed circumvents the need for a 4-pyridyl binding motif observed in examples with more rigid cavitands as demonstrated previously in the Hardie group. The analogous 2-pyridyl ligand could not be prepared for comparison in self-assembly. The metallocryptophanes self-assemble spontaneously under ambient conditions with remarkably short reaction times (with the exception of the fluorinated derivative **3.12**). These systems can be isolated in good yields and purity and have been shown to be stable when monitored over several months in nitromethane solvent. Switching between an ester and ether moieties as the linker units appears to have no impact on the readiness of self-assembly.

¹H NMR studies have shown that the chiral self-sorting of the metallocages prepared by Hardie can be influenced by the presence of globular chiral guests, whilst the presence of competing ligands prevents cage formation entirely. This is not the case for the azobenzene cage **3.8** which undergoes self-assembly whilst remaining indifferent to the presence of chiral guests. Whilst no crystal structure could be obtained for any of the cage complexes, a molecular model suggests the system is organised in the same manner as those previously prepared by Hardie, with the model supported by experimental ¹H NMR data.

The route allows for tuning of cage properties *via* modification of either the ligand design or the metallotecton, offering the opportunity to insert a desirable property into these systems and prepare a library of derivatives based on ester and ether linkages. Simple substitutions on the metallotecton are also tolerated. The photoresponsive and photophysical properties of these systems are explored in chapter 4.

The host-guest properties of these systems are also still unexplored. Molecular modelling has revealed the fullerenes and their derivatives as potential guest molecules (figure 3.38). The cages are well defined in solution and guest uptake could potentially be characterised by a variety of methods (¹H NMR, ESI-MS, UV-visible spectroscopy). Guest incarceration in the solid state by CTV derivatives as reported by Chiu and coworkers⁷⁸ is also a potential option. Purification of fullerenes remains a difficult challenge and contributes to the high cost of these materials. Their sequestration inside molecular hosts and subsequent release under the influence of UV light could potentially lead to sophisticated purification methods for these systems. The molecular hosting properties of the metallocages discussed here, is a future research goal in collaboration with Dr. Thomas Chamberlain of the University of Leeds.

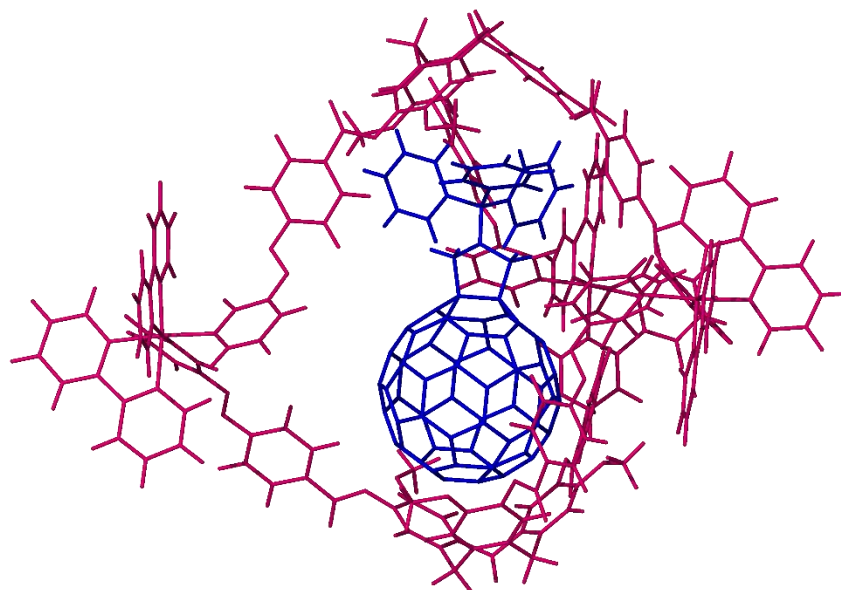


Figure 3.38: Model of a substituted fullerene derivative (blue) encapsulated in the azobenzene metallocryptophane 3.8.

3.10 Experimental

3.10.1 Instrumentation

^1H and $^{13}\text{C}\{^1\text{H}\}$ NMR spectra were recorded on a Bruker DPX 300MHz or a Bruker AscendTM 400MHz NMR spectrometer. Where appropriate, routine NMR assignments were confirmed by 2D ^1H - ^1H coupling experiments (COSY, HMQC, HMBC) which were all recorded on a Bruker AscendTM 400MHz NMR spectrometer. 2-D ROESY ^1H -NMR experiments were performed using a Varian Unity Inova 500 spectrometer (Varian Inc., Palo Alto, California, USA) operating at 499.97 MHz proton frequency. Data were recorded at 298K using a 5 mm $^1\text{H}\{^{13}\text{C}, ^{15}\text{N}, ^{31}\text{P}\}$ ID/PFG VT probe. Phase-sensitive 2D ROESY experiments were performed with a mixing time of 300 ms, 64 transients, a relaxation delay of 4.0 s, 256 increments (states phase cycling, so 512 increments in total) and a spectral width of 6000 Hz and 2K data points. Data were processed using ACD Spectrus Processor 2015 of the ACD labs 2015 software package from Advanced Chemistry Development, (Toronto, Canada). DOSY measurements were made on a Jeol ECA 600ii 600 MHz spectrometer operating under regulated temperature conditions (20°C), with a 5mm probe. The pulse sequence is a bipolar pulse pair simulated echo (BPPSTE) operating

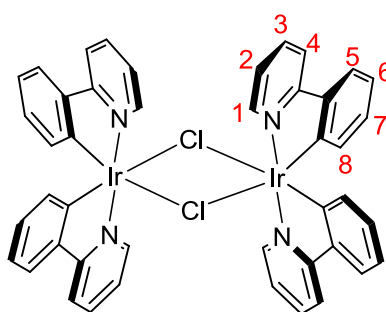
in the ONESHOT experiment. Spectra were processed using the DOSY toolbox⁷⁹. Data was zero-filled twice (from 16384 to 65536 points) and a Lorentzian window function of 0.5 was used. The DOSY plot has a digitisation of 64 points (number of data points calculated in the diffusion dimension)

High-resolution electrospray mass spectra (ESI-MS) were recorded on a Bruker micro-TOF-Q mass spectrometer and FT-IR spectra were recorded as solid phase samples using a Perkin Elmer Spectrum One spectrometer. Samples for microanalysis were dried under vacuum before analysis and determined by either Ms Tanya Marinko-Covell of the University of Leeds or Mr Stephen Boyer of London Metropolitan University. UV-Visible spectra were recorded on a Lambda 900 UV/Vis spectrophotometer and an Agilent Cary 100 UV/Vis spectrophotometer.

3.10.2 Chemical Syntheses

Where stated, reactions were carried out under an inert atmosphere of argon using an argon/vacuum dual manifold and standard Schlenk techniques. All chemicals and solvents were purchased from commercial suppliers (Sigma, Fluka) and were used as received. Dry solvents were obtained by passing through a column of activated alumina. Argon and nitrogen gas were pre-dried by passing through a small column of P₂O₅ before use.

Bis-[Ir(ppy)₂Cl₂] dimer (3.1)

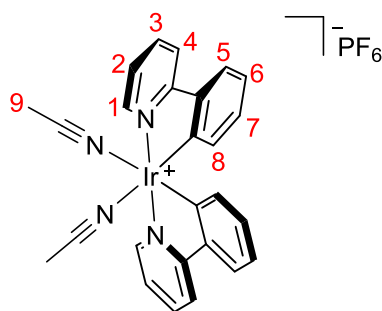


Iridium trichloride (0.40 g, 1.33 mmol) and 2-phenylpyridine (0.48 mL, 3.34 mmol) were suspended in a 3:1 mixture of 2-ethoxyethanol and water (12 mL). The reaction was heated to reflux overnight resulting in the formation of a bright yellow precipitate.

The precipitate was filtered and washed thoroughly with water and diethyl ether and dried *in vacuo* to give the product (0.48g, 0.45 mmol, 67%) as a bright yellow solid.

^1H NMR (300 MHz, CDCl_3), δ (ppm) 9.24 (2H, ddd, J 5.8, 1.6, 0.7, **Ar-H (1)**), 7.91 – 7.84 (2H, m, **Ar-H (4)**), 7.73 (2H, ddd, J 8.1, 7.3, 1.6, **Ar-H (3)**), 7.48 (2H, dd, J 7.8, 1.4, **Ar-H (5)**), 6.82 – 6.70 (4H, m, **Ar-H (2)**, **Ar-H (7)**), 6.56 (2H, td, J 7.5, 1.4, **Ar-H (6)**), 5.93 (2H, dd, J 7.7, 1.1, **Ar-H (8)**); ^{13}C NMR, compound too insoluble. All data is consistent with the literature.⁴⁸

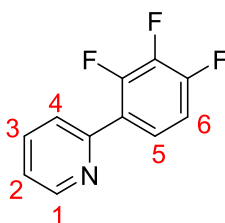
***cis*-[Ir(ppy)₂(CH₃CN)₂]⁺PF₆⁻ (3.2)**



Bis-[Ir(ppy)₂Cl₂] dimer (0.10 g, 0.09 mmol) was suspended in 10 mL of acetonitrile. Silver hexafluorophosphate (58.8 mg, 0.23 mmol) was added and the reaction shielded from light. The reaction was heated to reflux overnight during which time a yellow solution with a white precipitate was formed. The mixture was filtered through celite and the filtrate concentrated *in vacuo* to a volume of 1 mL. This was allowed to evaporate slowly in a beaker overnight to give a yellow glass which was filtered and washed thoroughly with diethyl ether to give the product (0.12g, 0.16 mmol, 86%) as a yellow crystalline powder.

^1H NMR (300 MHz, CD_3NO_2) δ (ppm) 9.12 (2H, d, J 5.8, **Ar-H (1)**), 8.20-8.12 (4H, m, **Ar-H (3)**, **Ar-H (4)**), 7.80 (1H, d, J 7.6, **Ar-H (5)**), 7.54 (2H, td, J 6.3, 2.2, **Ar-H (2)**), 6.97 (2H, t, J 7.5, **Ar-H (6)**), 6.84 (2H, t, J 7.5, **Ar-H (7)**), 6.10 (2H, d, J 7.4, **Ar-H (8)**), 2.09 (2H, s, **MeCN (9)**); ^{13}C NMR (101 MHz, CD_3NO_2) δ 167.89, 152.22, 146.63, 143.59, 140.42, 131.38, 130.91, 126.02, 125.14, 124.49, 121.26, 120.98, 62.80, 3.23, 1.43; HR-MS (ES^+) m/z 501.0929 $\{\text{M}(-2\text{MeCN})\}^+$ (calculated for $\{\text{C}_{22}\text{H}_{16}\text{IrN}_2\}^+$ 501.0937). All data is consistent with the literature.⁴⁹

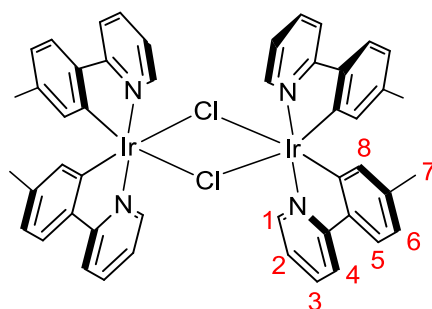
2-(4,5,6-Trifluoro)phenylpyridine (3.3)



2-Bromopyridine (0.79 mL, 8.3 mmol), trifluorophenyl boronic acid (1.76 g, 10 mmol), K_2CO_3 (5.52 g, 40 mmol), and tetrakis(tri-phenylphosphine)palladium(0) (0.12 g, 0.1 mmol) were dissolved in a mixture of dry THF and water (40/30 mL) under a nitrogen atmosphere. The solution was heated to reflux overnight during which time the mixture turned black. The solution was cooled to room temperature and then filtered through a plug of celite. The solvents were removed *in vacuo* and the resulting residue was extracted with DCM (3 x 30 mL). The DCM layer was washed with water (3 x 30 mL), dried ($MgSO_4$), filtered and the solvent removed to give an orange residue. This crude product was purified using column chromatography (10:1 Petroleum ether: ethyl acetate) to give the product (1.52 g, 7.27 mmol, 88%) as a white crystalline powder.

1H NMR (300 MHz, Acetone- d_6) δ (ppm) 8.73 (1H, m, Ar-H(1)), 7.97 – 7.81 (3H, m, Ar-H(3), Ar-H(4), Ar-H(5)), 7.42 (1H, ddd, J 7.4, 4.8, 1.2, Ar-H(2)), 7.38 – 7.27 (2H, ddd, J 9.6, 5.1, 2.1 Ar-H(6)); ^{19}F NMR (282 MHz, Acetone- d_6) δ 41.27 (dd), 37.19 (dd), 14.31 (t); ^{13}C NMR (75 MHz, Acetone- d_6) δ 150.92, 137.77, 125.87, 124.93, 124.81, 124.12, 113.45, 113.27, 29.84; HR-MS (ES^+) m/z 210.0523{M + H} $^+$ (calculated for $\{C_{11}H_7F_3N\}^+$ 210.0525). All data is consistent with the literature.⁵¹

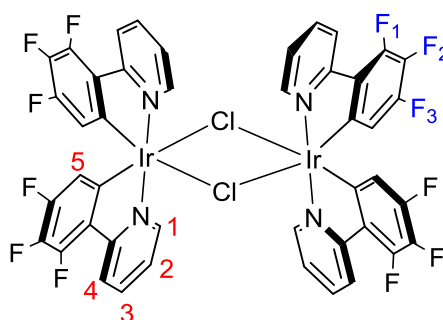
Bis-[Ir(ptppy) $_2$ Cl $_2$] dimer (3.4)



Iridium trichloride (0.15 g, 0.50 mmol) and 2-(p-tolyl) pyridine (0.21 mL, 1.25 mmol) were suspended in 12 mL of a 3:1 mixture of 2-ethoxyethanol and water. The reaction was heated to reflux overnight resulting in the formation of a bright yellow precipitate. The precipitate was filtered and washed thoroughly with water and diethyl ether and dried *in vacuo* to give the product (0.2g, 0.16 mmol, 64%) as a bright yellow solid.

^1H NMR (300 MHz, $\text{MeNO}_2\text{-d}_3$) δ (ppm) 9.25 (4H, d, J 5.9, Ar-H (1)), 8.06 (4H, d, J 8.3, Ar-H (4)), 7.95 (4H, td, J 7.8, 1.6, Ar-H (3)), 7.54 (4H, d, J 7.9, Ar-H (5)), 7.01 (4H, td, J 6.3, 1.5, Ar-H (2)), 6.64 (4H, dd, J 7.9, 1.7, Ar-H (6)), 5.74 (4H, s, Ar-H (8)), 2.12 (12H, s, Ar- CH_3 (7)); ^{13}C NMR (101 MHz, CD_3NO_2) δ 169.06, 152.75, 146.22, 143.32, 140.56, 138.60, 132.49, 124.94, 124.19, 123.85, 119.73, 62.80, 21.49. All data is consistent with the literature.⁵⁰

Bis-[Ir(4,5,6 tFppy) $_2$ Cl $_2$] dimer (3.5)

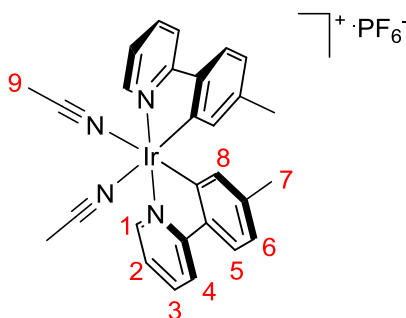


Iridium trichloride (0.15 g, 0.50 mmol) and 2-(4,5,6-trifluorophenyl) pyridine (0.26 g, 1.25 mmol) were suspended a 3:1 mixture of 2-ethoxyethanol and water (12mL). The reaction was heated to reflux overnight resulting in the formation of a yellow solution. Upon cooling to room temperature, a yellow solid precipitated. The precipitate was filtered and washed thoroughly with water and diethyl ether and dried *in vacuo* to give the product (0.16 g, 0.12 mmol, 48%) as a bright yellow solid.

^1H NMR (300 MHz, CDCl_3) δ (ppm) 9.10 (4H, dd, J 6.9, 1.2, Ar-H (1)), 8.32 (4H, d, J 8.3, Ar-H (4)), 7.88 (4H, td, J 7.8, 1.6, Ar-H (3)), 6.88 (4H, td, J 8.4, 1.5 Ar-H (2)), 5.27 (4H, ddd, J 8.4, Ar-H (5)); ^{19}F NMR (282 MHz, CDCl_3) δ -131.37 (dd, Ar- F_1), -136.56 (dd, Ar- F_3), -168.81 (t, Ar- F_2); ^{13}C NMR (75 MHz, CDCl_3) δ 165.26, 151.46,

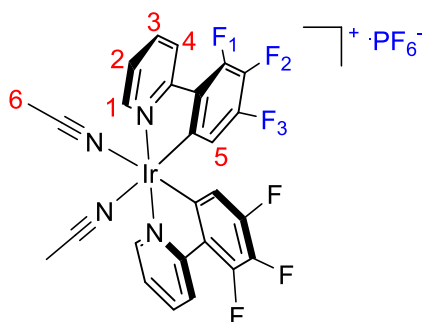
138.06, 136.92, 128.19, 123.34, 123.07, 112.75; HR-MS (ES⁺) m/z 609.0324 {M-[Ir(2ppy)₂Cl₂]}⁺ (calculated for {C₂₂H₁₀F₆IrN₂}⁺ 609.0372); All data is consistent with the literature.⁵¹

***cis*-[Ir(ptppy)₂(CH₃CN)₂]⁺PF₆⁻ (3.6)**



Bis-[Ir(ptppy)₂Cl₂] dimer (0.10 g, 0.09 mmol) was suspended in 15 mL of acetonitrile. Silver hexafluorophosphate (56.3 mgs, 0.22 mmol) was added and the reaction shielded from light. The reaction was heated to reflux overnight during which time a yellow solution with a white precipitate was formed. The mixture was filtered through celite and the filtrate concentrated *in vacuo* to a volume of 1 mL. This was allowed to evaporate slowly in a beaker overnight to give a yellow glass which was filtered and washed thoroughly with diethyl ether to give the product (78.2 mgs, 0.08 mmol, 96%) as a crystalline yellow solid.

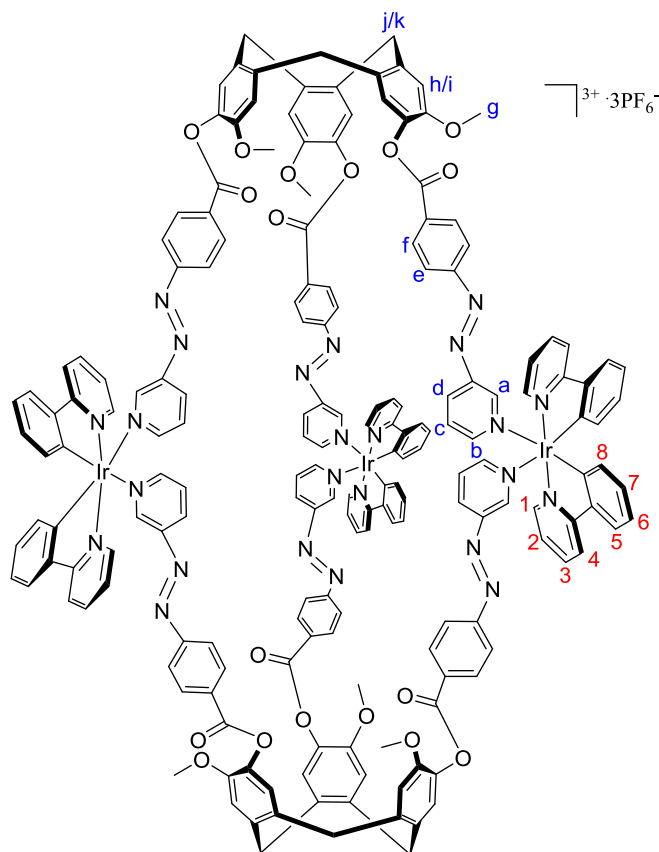
¹H NMR (300 MHz, MeNO₂) δ (ppm) 9.11 (2H, dt, J 5.8, 1.2, Ar-H (1)), 8.09 – 8.06 (4H, m, Ar-H⁴, Ar-H (3)), 7.59 (2H, d, J 7.9, Ar-H (4)), 7.45 (2H, dt, J 5.8, 4.4, Ar-H (5)), 6.77 (2H, dd, J 7.9, 1.7, Ar-H (6)), 6.01 (2H,s, Ar-H (8)), 2.38 (6H, s, Ar-CH₃ (7)), 2.02 (6H, s, Ir-MeCN (9)); ¹³C NMR (75 MHz, MeNO₂) δ 168.53, 151.95, 145.32, 143.46, 141.37, 140.00, 133.25, 125.41, 124.99, 124.26, 120.78, 120.55, 62.80, 21.56, 3.26; HR-MS (ES⁺) m/z 529.12 {M (-2MeCN)}⁺ (calculated for {C₂₄H₂₀IrN₂}⁺ 529.1250); All data is consistent with the literature.⁵⁰

***cis*-[Ir(4,5,6 tFppy)₂(CH₃CN)₂]⁺PF₆⁻ (3.7)**

Bis-[Ir(4,5,6 tFppy)₂Cl₂] dimer (0.10 g, 0.09 mmol) was dissolved in 15 mL of acetonitrile. Silver hexafluorophosphate (48.8 mgs, 0.22 mmol) was added and the reaction shielded from light. The reaction was heated to reflux overnight during which time a yellow solution with a white precipitate was formed. The mixture was filtered through celite and the filtrate concentrated *in vacuo* to a volume of 1 mL. This was allowed to evaporate slowly in a beaker overnight to give a yellow glass which was filtered and washed thoroughly with diethyl ether to give the product (125.1 mgs, 1.49 mmol, 96%) as a crystalline yellow solid.

¹H NMR (300 MHz, MeNO₂) δ (ppm) 9.18 (2H, m, Ar-H(1)), 8.40 (2H, d, *J* 8.1, 1H Ar-H(4)), 8.20 (2H, m, Ar-H(3)), 7.61 (2H, td, *J* 6.6, 5.8, 1.5, Ar-H(2)), 5.72 (ddd, *J* 10.1, 7.2, 2.1, Ar-H(5)), 2.20 (6H, s, MeCN (6)); ¹⁹F NMR (282 MHz, CD₃CN) δ -71.72 to -74.22 (d, PF₆⁻), -133.88 (dd, Ar-F₁), -137.84 (dd, Ar-F₃), -170.26 (t, Ar-F₂); HR-MS (ES⁺) *m/z* 609.0374 {M-2MeCN}⁺ (calculated for {C₂₂H₁₀F₆IrN₂}⁺ 609.0372), 650.0633 {M-MeCN}⁺ (calculated for {C₂₄H₁₃F₆IrN₃} 650.0637).

$[\{\text{Ir}(\text{2-ppy})_2\}_3(\text{2.12})_2]^{3+} \cdot 3\text{PF}_6^- \text{ M}_3\text{L}_2 \text{ Cage (3.8)}$

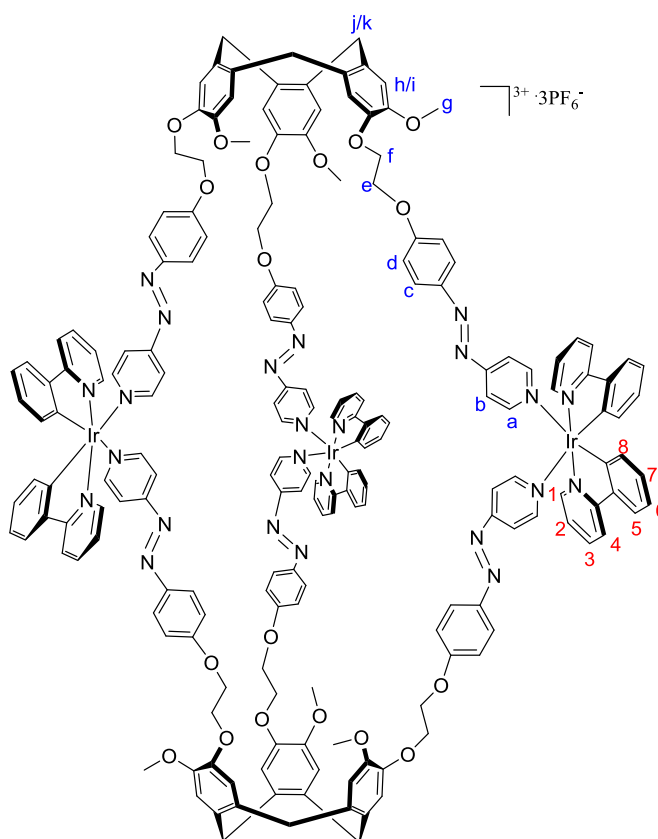


$[\text{Ir}(\text{ppy})_2(\text{MeCN})_2]^+ \text{PF}_6^-$ (26.3 mgs, 0.037 mmol) and ligand **2.12** (25.0 mgs, 0.024 mmol) were suspended in nitromethane (5 mL). The orange suspension was stirred at room temperature overnight during which time all of the material dissolved. Diethyl ether was added slowly to the solution which resulted in the precipitation of a fine orange powder. The solid was filtered and washed with more diethyl ether to give the product (32.1 mgs, 0.008 mmol, 66%) as an orange powder.

^1H NMR (300 MHz, $\text{MeNO}_2\text{-d}_3$) δ (ppm) 9.36-9.22 (6H, br m, Ar-H (a)), 9.00-8.86 (12 H, br m, Ar-H (b) overlapped with Ar-H (1)), 8.48-8.20 (18H, br m, Ar-H (d) overlapped with Ar-H (f)), 8.12-7.88 (24H, br m, Ar-H (e) overlapped with Ar-H (3) and Ar-H (4)), 7.76-7.62 (12H, br m, Ar-H (c) overlapped with Ar-H (5)), 7.58-7.36 (12H, br m, CTG Ar-H (h) overlapped with Ar-H (2)), 7.30-7.22 (6H, br m, CTG Ar-H (i)), 7.08-6.94 (12H, br m, Ar-H⁶ overlapped with Ar-H⁷), 6.64-6.52 (6H, br m, Ar-H⁸), 5.08-4.96 (6H, br m, CTG endo-H (j)), 3.91-3.74 (24H, br m, CTG exo-H (k) overlapped with OCH_3 (g)); HR-MS (ES^+) m/z 1536.4289 $\{\text{M}_2\text{L}_2\}^{2+}$ (calculated for

$\{C_{164}H_{124}Ir_2N_{22}O_{18}\}^{2+}$ 1536.9361), 1191.3193 $\{M_3L_2\}^{3+}$ (calculated for $\{C_{186}H_{140}Ir_3N_{24}O_{18}\}^{3+}$ 1191.3179); FT-IR (cm^{-1}) = 3061, 1732, 1582, 1505, 1478, 1420, 1256, 1176, 1086, 1057, 1009, 835, 756, 735, 697, 586; Analysis calculated for **3.8** (% calculated; found) C (55.73, 51.01), H (3.47, 3.39), N (8.39, 8.15); UV-Vis λ_{max} (nm) 280 (Intraligand $\pi \rightarrow \pi^*$ transitions), 320 ($\pi \rightarrow \pi^*$ trans isomer), 425 ($n \rightarrow \pi^*$ cis isomer).

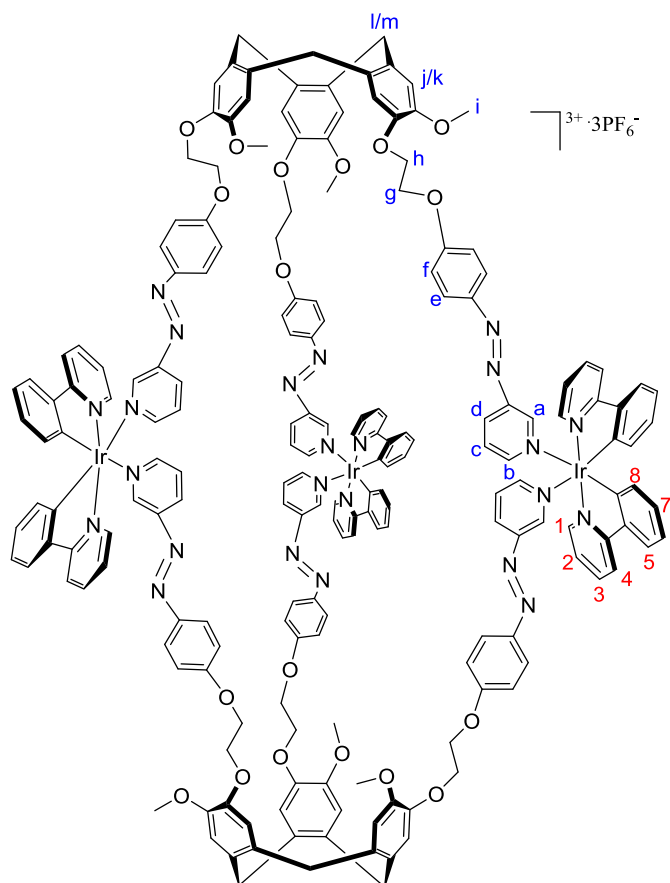
[{Ir(ppy)₂]₃(2.17)₂]³⁺·3PF₆⁻ M₃L₂ Cage (3.9)



$[Ir(ppy)_2(MeCN)_2]^+PF_6^-$ (26.3 mgs, 0.037 mmol) and ligand **2.17** (25.0 mgs, 0.024 mmol) were suspended in nitromethane (5 mL). The orange suspension was stirred at room temperature overnight during which time all of the material dissolved. Diethyl ether was added slowly to the solution which resulted in the precipitation of a fine orange powder. The solid was filtered and washed with more diethyl ether to give the product (35.3 mgs, 0.009 mmol, 75%) as an orange powder.

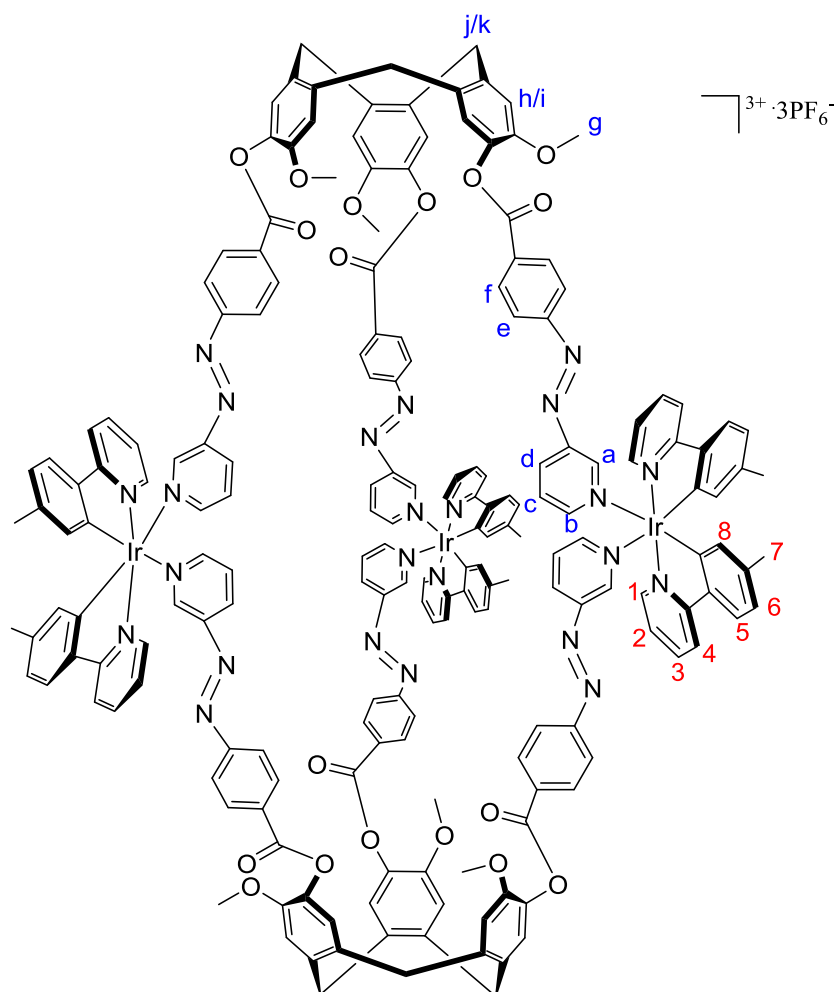
^1H NMR (300 MHz, $\text{MeNO}_2\text{-d}^3$) δ (ppm) 8.86-8.68 (18H, br m, *Ar-H* (a)) overlapped with *Ar-H* (1)), 8.08-7.86 (24H, br m, *Ar-H* (c)) overlapped with *Ar-H* (3) and *Ar-H* (4)), 7.75-7.61 (18H, br m, *Ar-H* (b)) overlapped with *Ar-H* (5)), 7.52-7.44 (6H, br m, *Ar-H* (2)), 7.18-7.03 (24H, br m, *Ar-H* (d)) overlapped with *Ar-H* (6) and *Ar-H* (7)), 7.01-6.91 (12H, br m, CTG *Ar-H* (h)) overlapped with CTG *Ar-H* (i)), 6.55-6.47 (6H, br m, *Ar-H* (8)), 4.91-4.80 (6H, br m, CTG *endo-H* (j)), 4.52-4.30 (24H, br m, OCH_2CH_2 (e,f – overlaps with MeNO_2 signal)), 3.85-3.74 (18H, br m, OCH_3 (g)), 3.72-3.58 (6H, br m, CTG *exo-H* (k)); HR-MS (ES $^+$) m/z 1584.5199 $\{\text{M}_2\text{L}_2\}^{2+}$ (calculated for $\{\text{C}_{170}\text{H}_{148}\text{Ir}_2\text{N}_{22}\text{O}_{18}\}^{2+}$ 1584.0222) 1223.3784 $\{\text{M}_3\text{L}_2\}^{3+}$ (calculated for $\{\text{C}_{192}\text{H}_{164}\text{Ir}_3\text{N}_{24}\text{O}_{18}\}^{3+}$ 1223.3805); FT-IR (cm^{-1}) = 3041, 2929, 1594, 1582, 1497, 1477, 1446, 1405, 1252, 1135, 1089, 926, 831, 755, 732, 628, 555; Analysis calculated for **3.9** (% calculated; found) C (54.20, 54.50), H (3.80, 4.19), N (7.60, 7.94); UV-Vis λ_{max} (nm) 263 (Intraligand $\pi \rightarrow \pi^*$ transitions), 323 ($\pi \rightarrow \pi^*$ *trans* isomer), 436 ($n \rightarrow \pi^*$ *cis* isomer);

$[\{\text{Ir}(\text{ppy})_2\}_3(\mathbf{2.18})_2]^{3+} \cdot 3\text{PF}_6^- \cdot \text{M}_3\text{L}_2$ Cage (3.10**)**



[Ir(ppy)₂(MeCN)₂]⁺PF₆⁻ (26.3 mgs, 0.037 mmol) and ligand **2.18** (25.0 mgs, 0.024 mmol) were suspended in nitromethane (5 mL). The orange suspension was stirred at room temperature overnight during which time all of the material dissolved. Diethyl ether was added slowly to the solution which resulted in the precipitation of a fine orange powder. The solid was filtered and washed with more diethyl ether to give the product (35.3 mgs, 0.009 mmol, 75%) as a yellow-orange powder.

¹H NMR (300 MHz, MeNO₂) δ (ppm) 9.22-8.98 (6H, br m, Ar-H (a)), 8.93-8.72 (12H, br m, Ar-H (b) overlapped with Ar-H (1)), 8.38-8.18 (6H, br m, Ar-H (d)), 8.10 – 7.37 (42H, br m, Ar-H (e) and Ar-H(c) overlapped with with Ar-H (3), Ar-H (4), Ar-H (5) and Ar-H (2)), 7.18-6.82 (36H, br m, Ar-H (f), CTG-H (j) and CTG-H (k) overlapped with Ar-H (6) and Ar-H (7)), 6.60-6.48 (6H, br m, Ar-H (8)), 4.89-4.76 (6H, br m, CTG endo-H (m)), 3.86-3.58 (24H, br m, CTG exo-H (l) overlapped with OCH₃ (i)); HR-MS (ES⁺) m/z 1584.5232 {ML}⁺ (calculated for C₈₅H₇₃IrN₁₁O₉)⁺ 1584.0222) 1223.7167 {M₃L₂}³⁺ (calculated for {C₁₉₂H₁₆₄Ir₃N₂₄O₁₈}³⁺ 1223.3805); 1042.8080 {M₂L}²⁺ (calculated for {C₁₀₇H₉₁Ir₂N₁₃O₉}²⁺ 1042.8143); FT-IR (cm⁻¹) = 3049, 2926, 1597, 1582, 1499, 1478, 1449, 1415, 1253, 1226, 1188, 1141, 1090, 1048, 1032, 932, 836, 757, 737, 670, 623, 556, 468; UV-Vis λ_{max} (nm) 251 (Intraligand π→π* transitions), 276 (Intraligand π→π* transitions), 295 (Intraligand π→π* transitions), 358 (π→π* *trans* isomer), 463 (n→π* *cis* isomer).

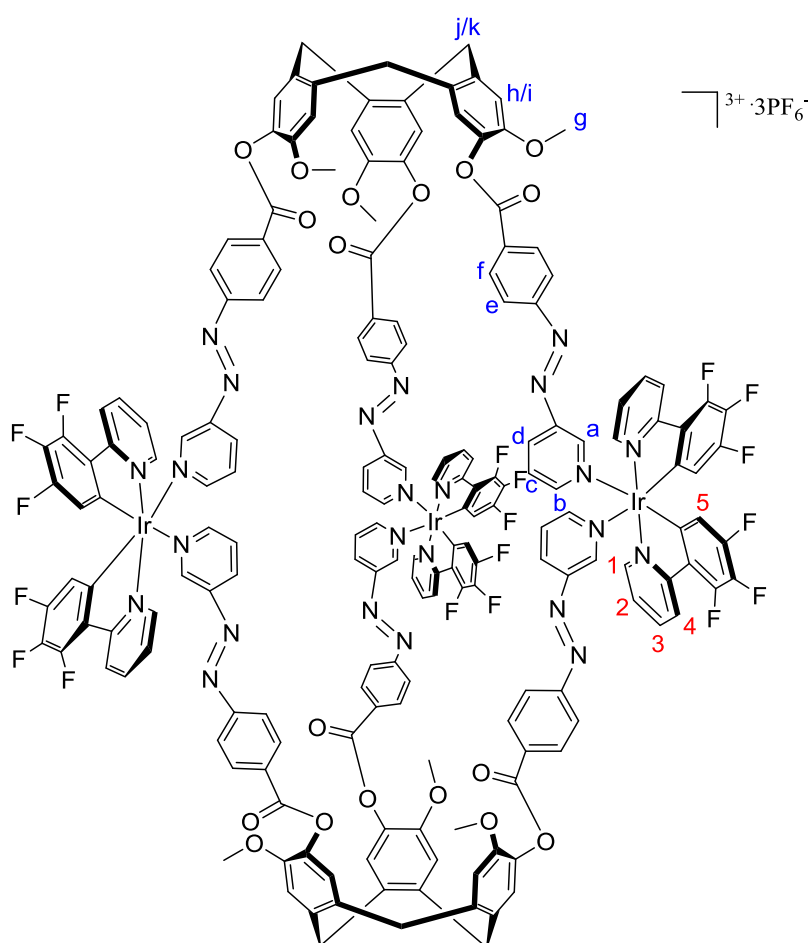
$$[\{\text{Ir}(\text{ptppy})_2\}_3(\mathbf{2.12})_2]^{3+} \cdot 3\text{PF}_6^- \text{ M}_3\text{L}_2 \text{ Cage } (\mathbf{3.11})$$


$[\text{Ir}(\text{ptppy})_2(\text{MeCN})_2]^+ \text{PF}_6^-$ (26.3 mgs, 0.037 mmol) and ligand **2.12** (25.0 mgs, 0.024 mmol) were suspended in nitromethane (5 mL). The orange suspension was stirred at room temperature overnight during which time all of the material dissolved. Diethyl ether was added slowly to the solution which resulted in the precipitation of a fine orange powder. The solid was filtered and washed with more diethyl ether to give the product (30.5 mgs, 0.007 mmol, 63%) as an orange powder.

^1H NMR (300 MHz, $\text{MeNO}_2\text{-d}_3$) δ (ppm) 9.36-9.20 (6H, br m, **Ar-H(a)**), 8.98-8.86 (12 H, br m, **Ar-H(b)** overlapped with **Ar-H(1)**), 8.50-8.42 (6H, br m, **Ar-H(d)**) 8.38-8.28 (18H, br m, **Ar-H(f)**), 8.08-7.92 (24H, br m, **Ar-H(e)** overlapped with **Ar-H(3)** and **Ar-H(4)**), 7.74-7.64 (6H, br m, **Ar-H(c)**), 7.62-7.56 (6H, br m, **Ar-H(5)**), 7.50-7.38 (12H, br m, **CTG Ar-H(h)** overlapped with **Ar-H(2)**), 7.32-7.24 (6H, br m, **CTG**

Ar-H (i), 6.90-6.80 (6H, br m, Ar-H (6)), 6.50-6.40 (6H, br m, Ar-H (8)), 5.09-4.98 (6H, br m, CTG endo-H (j)), 3.94-3.78 (24H, br m, CTG exo-H (k)) overlapped with OCH₃ (g), 2.24-2.18 (18H, br m, Ar-CH₃ (7)); HR-MS (ES⁺) m/z 1219.3517{M₃L₂}³⁺ (calculated for {C₁₉₂H₁₅₂Ir₃N₂₄O₁₈}³⁺ 1219.3492); FT-IR (cm⁻¹) = 2918, 1734, 1605, 1587, 1563, 1464, 1257, 1205, 1176, 1087, 1058, 1009, 836, 768, 698, 555; Analysis calculated for **3.11** (% calculated; found) C (56.34, 57.83), H (3.69, 3.77), N (8.21, 7.83); UV-Vis λ_{max} (nm) 258 (Intraligand π→π* transitions), 312 (π→π* trans isomer), 426 (n→π* cis isomer);

[{Ir(4,5,6 tFppy)₂]₃(2.12)₂}³⁺·3PF₆⁻ M₃L₂ Cage (3.12)

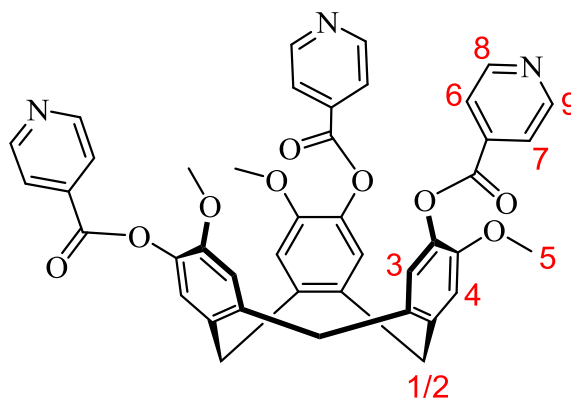


[Ir(4,5,6 tFppy)₂(MeCN)₂]⁺·PF₆⁻ (30.2 mgs, 0.036 mmol) and ligand **2.12** (25.0 mgs, 0.024 mmol) were suspended in nitromethane (5 mL). The orange suspension was stirred at room temperature overnight during which time all of the material dissolved. Diethyl ether was added slowly to the solution which resulted in the precipitation of

a fine orange powder. The solid was filtered and washed with more diethyl ether to give the product (47.6mgs, 0.012mmol, 50%) as an orange crystalline powder.

^1H NMR (300 MHz, MeNO_2) δ (ppm) 9.26-9.14 (6H, br m, Ar-H (a)), 9.03-8.96 (6H br m, Ar-H (1)), 8.88-8.80 (6H br m, Ar-H (b)), 8.51-8.43 (6H, br m, Ar-H (d)), 8.40 – 8.25 (18H, br m, Ar-H (f) overlapped with Ar-H (4)), 8.16 -7.90 (18H, br m, Ar-H (e) overlapped with Ar-H (3)), 7.77-7.67 (6H br m, Ar-H (2)), 7.63-7.53 (6H, br m, Ar-H (c)), 7.49-7.40 (6H, br m, CTG Ar-H (h)), 7.31-7.23 (6H, br m, CTG Ar-H (i)), 6.21-6.10 (6H br m, Ar-H (5)), 5.09-4.97 (6H br m, J 4.5, CTG *exo*-H (j)); 3.92-3.75 (24H, br m, CTG *endo*-H (k) overlapped with OCH_3 (g); HR-MS (ES^+) m/z 1299.5033 $\{\text{M}_3\text{L}_2\}^{3+}$ (calculated for $\{\text{C}_{186}\text{H}_{122}\text{F}_{18}\text{Ir}_3\text{N}_{24}\text{O}_{18}\}^{3+}$ 1299.2613); FT-IR (cm^{-1}) = 2932, 1733, 1667, 1603, 1587, 1555, 1507, 1486, 1431, 1400, 1375, 1318, 1257, 1204, 1176, 1137, 1087, 1060, 1042, 914, 804, 758, 699, 653, 623, 574, 447; Analysis calculated for **3.12** (% calculated; found) C (51.56, 51.49), H (2.79, 2.90), N (7.76, 7.80) UV-Vis λ_{max} (nm) 262 (Intraligand $\pi \rightarrow \pi^*$ transitions), 290 (Intraligand $\pi \rightarrow \pi^*$ transitions), 324 ($\pi \rightarrow \pi^*$ *trans* isomer), 432 ($n \rightarrow \pi^*$ *cis* isomer).

(±)-2,7,12-Trimethoxy-3,8,13-tris(isonicotinoyl)-10,15-dihydro-5H-tribenzo[a,d,g] cyclonatriene (3.13)

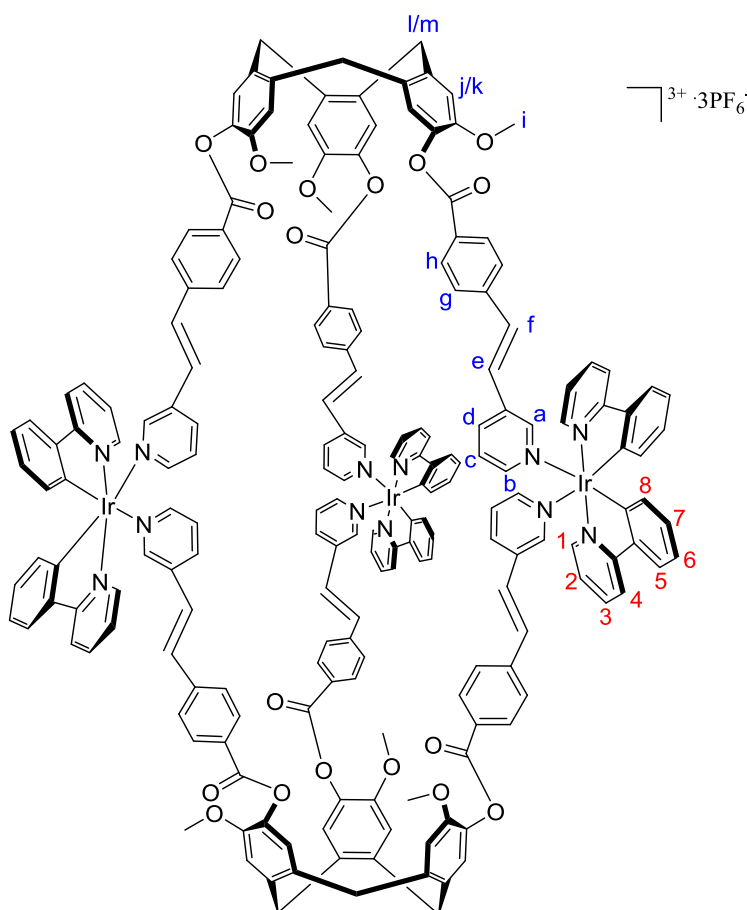


CTG (0.10 g, 0.24 mmol) was dissolved in dry THF (30 mL) under a nitrogen atmosphere. The flask was cooled to 0°C in an ice bath and triethylamine (0.53 mL) was added and the reaction stirred for 15 minutes. Isonicotinoyl chloride hydrochloride (0.23 g, 1.27 mmol) was added in portions. The resulting white suspension was allowed to stir at 0°C for three hours before being warmed to room temperature and stirred for three days. The solvent was removed *in vacuo* to give a

cream residue. This crude product was triturated in ethanol (50 mL), filtered, washed with more ethanol and diethyl ether before drying *in vacuo* to give the product (92 mgs, 0.13 mmol, 54%) as a white powder.

^1H NMR (300 MHz, CDCl_3) δ 8.84 (6H, d, J 5.8, Ar-H(8), Ar-H(9)), 7.99 (6H, d, J 5.8, Ar-H(6), Ar-H(7)), 7.17 (3H, s, Ar-H(3)), 6.96 (3H, s, Ar-H(4)), 4.84 (3H, d, J 13.8, CTG *endo*-H (1)), 3.80 (9H, s, OCH_3 (5)), 3.69 (3H, d, J 13.9, CTG *exo*-H (2)); HR-MS (ES^+) m/z 724.2296 $\{\text{M} + \text{H}\}^+$ (calculated for $\{\text{C}_{42}\text{H}_{34}\text{N}_3\text{O}_9\}^+$ 724.2290). All data is consistent with the literature.⁶¹

NMR scale preparation of $[\{\text{Ir}(\text{ppy})_2\}_3(\mathbf{2.22})_2]^{3+} \cdot 3\text{PF}_6^-$ M₃L₂ Cage (3.14)



$[\text{Ir}(\text{ppy})_2(\text{MeCN})_2]^+ \cdot \text{PF}_6^-$ (4.24 mgs, 5.82×10^{-3} mmol) and **2.22** (4.0 mgs, 3.88×10^{-3} mmol) were suspended in deuterated MeNO_2 (0.5 mL). An initial ^1H NMR spectrum

was recorded. The yellow suspension was allowed to stand at room temperature with additional ^1H NMR spectra being recorded after 24 hours and 120 hours.

^1H NMR (300 MHz, MeNO_2 after 24 hours) δ 8.85 (12H, br m, Ar-H(a) overlapped with Ar-H(b)), 8.63 (6H, br m, Ar-H(1)), 8.05 (30H, br m, Ar-H(3), Ar-H(4), Ar-H(d) and Ar-H(h)), 7.67 (18H, br m, Ar-H(5) overlapped with Ar-H(g)), 7.55-7.09 (36H br m, Ar-H(2), Ar-H(c), Ar-H(e), Ar-H(f), Ar-H(j) and Ar-H(k)), 6.98 (12H, br m, Ar-H(6) and Ar-H(7)), 6.54 (6H, br m, Ar-H(8)), 4.98 (6H, br m, CTG endo-H (l)), 3.79 (24H, br m, OCH_3 (i) overlapped with CTG exo-H (m)); HR-MS (ES^+), after 24 hours m/z 1187.5540 $\{\text{M}_3\text{L}_2\}^{3+}$ (calculated for $\{\text{C}_{198}\text{H}_{150}\text{Ir}_3\text{N}_{12}\text{O}_{18}\}^{3+}$ 1187.3369).

3.10.3 Chiral guest experiments with metallocryptophane 3.14

3.13 (4.0 mgs, 5.53×10^{-3} mmol, 2 eq) was suspended in deuterated MeNO_2 (0.4ml) in an NMR tube. The tube was sonicated for ten minutes and heated (heat gun) until all the material dissolved. A solution of $[\text{Ir}(\text{ppy})_2(\text{MeCN})_2]^+\text{PF}_6^-$ (6.03 mgs, 8.29×10^{-3} mmol, 3 eq) and appropriate guest (3 mgs, 19.7×10^{-3} mmol, 7.13 equivalents for R/S camphor; 3 mgs, 22.0×10^{-3} mmol, 7.95 equivalents for adamantane; 3 mgs, 12.9×10^{-3} mmol, 4.66 equivalents for R/S Camphor sulfonic acid) in 0.3 mL deuterated MeNO_2 was added. An initial spectrum was immediately recorded followed by a subsequent spectrum every 15 minutes up until 2 hours, then at longer intervals.

3.10.4 Chiral guest experiments with metallocryptophane 3.8

3.8 (4.8 mgs, 4.63×10^{-3} mmol, 2 eq) was suspended in deuterated MeNO_2 (0.4ml) in an NMR tube. The tube was sonicated for ten minutes and heated (heat gun) until all the material dissolved. A solution of $[\text{Ir}(\text{ppy})_2(\text{MeCN})_2]^+\text{PF}_6^-$ (5.00 mgs, 6.94×10^{-3} mmol, 3 eq) and appropriate guest (4 mgs, 26.3×10^{-3} mmol, 11.36 equivalents for R/S camphor; 4 mgs, 29.3×10^{-3} mmol, 12.6 equivalents for adamantane; 4 mgs, 17.2×10^{-3} mmol, 7.42 equivalents for R/S Camphor sulfonic acid) in 0.3 mL deuterated MeNO_2 was added. An initial spectrum was immediately recorded followed by a subsequent spectrum every 15 minutes up until 2 hours, then at longer intervals.

3.11 References

1. M. Yoshizawa, J. K. Klosterman and M. Fujita, *Angewandte Chemie International Edition*, 2009, **48**, 3418-3438.
2. Y. Inokuma, T. Arai and M. Fujita, *Nature Chemistry*, 2010, **2**, 780-783.
3. H. Takezawa, T. Murase, G. Resnati, P. Metrangolo and M. Fujita, *Journal of the American Chemical Society*, 2014, **136**, 1786-1788.
4. Y. Inokuma, M. Kawano and M. Fujita, *Nature Chemistry*, 2011, **3**, 349-358.
5. P. Mal, D. Schultz, K. Beyeh, K. Rissanen and J. R. Nitschke, *Angewandte Chemie International Edition*, 2008, **47**, 8297-8301.
6. A. Jiménez, R. A. Bilbeisi, T. K. Ronson, S. Zarra, C. Woodhead and J. R. Nitschke, *Angewandte Chemie International Edition*, 2014, **53**, 4556-4560.
7. J. L. Bolliger, T. K. Ronson, M. Ogawa and J. R. Nitschke, *Journal of the American Chemical Society*, 2014, **136**, 14545-14553.
8. P. Mal, B. Breiner, K. Rissanen and J. R. Nitschke, *Science*, 2009, **324**, 1697-1699.
9. D. L. Caulder, C. Brückner, R. E. Powers, S. König, T. N. Parac, J. A. Leary and K. N. Raymond, *Journal of the American Chemical Society*, 2001, **123**, 8923-8938.
10. T. N. Parac, D. L. Caulder and K. N. Raymond, *Journal of the American Chemical Society*, 1998, **120**, 8003-8004.
11. M. Scherer, D. L. Caulder, D. W. Johnson and K. N. Raymond, *Angewandte Chemie International Edition*, 1999, **38**, 1587-1592.
12. O. Chepelin, J. Ujma, X. Wu, A. M. Z. Slawin, M. B. Pitak, S. J. Coles, J. Michel, A. C. Jones, P. E. Barran and P. J. Lusby, *Journal of the American Chemical Society*, 2012, **134**, 19334-19337.
13. P. R. Symmers, M. J. Burke, D. P. August, P. I. T. Thomson, G. S. Nichol, M. R. Warren, C. J. Campbell and P. J. Lusby, *Chemical Science*, 2015, **6**, 756-760.
14. H. M. O'Connor, S. Sanz, M. B. Pitak, S. J. Coles, G. S. Nichol, S. Piligkos, P. J. Lusby and E. K. Brechin, *CrystEngComm*, 2016, **18**, 4914-4920.
15. J. M. Frost, S. Sanz, T. Rajeshkumar, M. B. Pitak, S. J. Coles, G. Rajaraman, W. Wernsdorfer, J. Schnack, P. J. Lusby and E. K. Brechin, *Dalton Transactions*, 2014, **43**, 10690-10694.
16. D. Fiedler, H. van Halbeek, R. G. Bergman and K. N. Raymond, *Journal of the American Chemical Society*, 2006, **128**, 10240-10252.
17. D. Fujita, K. Suzuki, S. Sato, M. Yagi-Utsumi, Y. Yamaguchi, N. Mizuno, T. Kumasaka, M. Takata, M. Noda, S. Uchiyama, K. Kato and M. Fujita, *Nature Communications*, 2012, **3**, 1093.
18. C. J. Hastings, M. D. Pluth, R. G. Bergman and K. N. Raymond, *Journal of the American Chemical Society*, 2010, **132**, 6938-6940.
19. Z. Zhong, A. Ikeda, S. Shinkai, S. Sakamoto and K. Yamaguchi, *Organic Letters*, 2001, **3**, 1085-1087.

20. J. Gabard and A. Collet, *Journal of the Chemical Society, Chemical Communications*, 1981, **0**, 1137-1139.
21. T. Brotin and J.-P. Dutasta, *Chemical Reviews*, 2008, **109**, 88-130.
22. K. Bartik, M. Luhmer, J.-P. Dutasta, A. Collet and J. Reisse, *Journal of the American Chemical Society*, 1998, **120**, 784-791.
23. H. A. Fogarty, P. Berthault, T. Brotin, G. Huber, H. Desvaux and J.-P. Dutasta, *Journal of the American Chemical Society*, 2007, **129**, 10332-10333.
24. T. K. Ronson, H. Nowell, A. Westcott and M. J. Hardie, *Chemical Communications*, 2011, **47**, 176-178.
25. J. J. Henkelis, T. K. Ronson, L. P. Harding and M. J. Hardie, *Chemical Communications*, 2011, **47**, 6560-6562.
26. A. Westcott, J. Fisher, L. P. Harding, P. Rizkallah and M. J. Hardie, *Journal of the American Chemical Society*, 2008, **130**, 2950-2951.
27. B. Chatelet, E. Payet, O. Perraud, P. Dimitrov-Raytchev, L.-L. Chapellet, V. r. Dufaud, A. Martinez and J.-P. Dutasta, *Organic Letters*, 2011, **13**, 3706-3709.
28. A. Collet, J.-P. Dutasta, B. Lozach and J. Canceill, in *Supramolecular Chemistry I — Directed Synthesis and Molecular Recognition*, Springer Berlin Heidelberg, 1993, vol. 165, ch. 3, pp. 103-129.
29. O. Perraud, J.-B. Tommasino, V. Robert, B. Albela, L. Khrouz, L. Bonneviot, J.-P. Dutasta and A. Martinez, *Dalton Transactions*, 2013, **42**, 1530-1535.
30. G. Vériot, J.-P. Dutasta, G. Matouzenko and A. Collet, *Tetrahedron*, 1995, **51**, 389-400.
31. A. Schaly, Y. Rousselin, J.-C. Chambron, E. Aubert and E. Espinosa, *European Journal of Inorganic Chemistry*, 2016, **2016**, 832-843.
32. J. J. Henkelis, C. J. Carruthers, S. E. Chambers, R. Clowes, A. I. Cooper, J. Fisher and M. J. Hardie, *Journal of the American Chemical Society*, 2014, **136**, 14393-14396.
33. V. E. Pritchard, D. Rota Martir, S. Oldknow, S. Kai, S. Hiraoka, N. J. Cookson, E. Zysman-Colman and M. J. Hardie, *Chemistry – A European Journal*, 2017, **23**, 6290-6294.
34. N. J. Cookson, J. M. Fowler, D. P. Martin, J. Fisher, J. J. Henkelis, T. K. Ronson, F. L. Thorp-Greenwood, C. E. Willans and M. J. Hardie, *Supramolecular Chemistry*, 2017, 1-12.
35. A. J. McConnell, C. S. Wood, P. P. Neelakandan and J. R. Nitschke, *Chemical Reviews*, 2015, **115**, 7729-7793.
36. E. Merino and M. Ribagorda, *Beilstein Journal of Organic Chemistry*, 2012, **8**, 1071-1090.
37. O. B. Berryman, A. C. Sather, A. Lledó and J. Rebek, *Angewandte Chemie International Edition*, 2011, **50**, 9400-9403.
38. H. Shinmori, M. Takeuchi and S. Shinkai, *Journal of the Chemical Society, Perkin Transactions 2*, 1998, **0**, 847-852.

39. F. Hamon, F. Djedaini-Pilard, F. Barbot and C. Len, *Tetrahedron*, 2009, **65**, 10105-10123.
40. M. Han, D. Ishikawa, E. Muto and M. Hara, *Journal of Luminescence*, 2009, **129**, 1163-1168.
41. E. Busseron, J. Lux, M. Degardin and J. Rebek, *Chemical Communications*, 2013, **49**, 4842-4844.
42. O. B. Berryman, A. C. Sather and J. Rebek Jr, *Chemical Communications*, 2011, **47**, 656-658.
43. H. Dube and J. Rebek, *Angewandte Chemie International Edition*, 2012, **51**, 3207-3210.
44. J. Park, D. Yuan, K. T. Pham, J.-R. Li, A. Yakovenko and H.-C. Zhou, *Journal of the American Chemical Society*, 2012, **134**, 99-102.
45. J. Park, L.-B. Sun, Y.-P. Chen, Z. Perry and H.-C. Zhou, *Angewandte Chemie International Edition*, 2014, **53**, 5842-5846.
46. M. Han, R. Michel, B. He, Y.-S. Chen, D. Stalke, M. John and G. H. Clever, *Angewandte Chemie International Edition*, 2013, **52**, 1319-1323.
47. M. Han, Y. Luo, B. Damaschke, L. Gómez, X. Ribas, A. Jose, P. Peretzki, M. Seibt and G. H. Clever, *Angewandte Chemie International Edition*, 2016, **55**, 445-449.
48. J. Zhang, Y. Li, F. Zhang, C. Hu and Y. Chen, *Angewandte Chemie International Edition*, 2016, **55**, 1872-1875.
49. K. A. McGee and K. R. Mann, *Inorganic Chemistry*, 2007, **46**, 7800-7809.
50. C. Li, Y. Liu, Y. Wu, Y. Sun and F. Li, *Biomaterials*, 2013, **34**, 1223-1234.
51. C.-C. Wang, Y.-M. Jing, T.-Y. Li, Q.-L. Xu, S. Zhang, W.-N. Li, Y.-X. Zheng, J.-L. Zuo, X.-Z. You and X.-Q. Wang, *European Journal of Inorganic Chemistry*, 2013, **2013**, 5683-5693.
52. S. A. Boer and D. R. Turner, *Chemical Communications*, 2015, **51**, 17375-17378.
53. L.-L. Yan, C.-H. Tan, G.-L. Zhang, L.-P. Zhou, J.-C. Bünzli and Q.-F. Sun, *Journal of the American Chemical Society*, 2015, **137**, 8550-8555.
54. C. Gütz, R. Hovorka, G. Schnakenburg and A. Lützen, *Chemistry – A European Journal*, 2013, **19**, 10890-10894.
55. T. Weilandt, U. Kiehne, G. Schnakenburg and A. Lützen, *Chemical Communications*, 2009, **0**, 2320-2322.
56. T. Weilandt, U. Kiehne, J. Bunzen, G. Schnakenburg and A. Lützen, *Chemistry – A European Journal*, 2010, **16**, 2418-2426.
57. G. Meyer-Eppler, F. Topić, G. Schnakenburg, K. Rissanen and A. Lützen, *European Journal of Inorganic Chemistry*, 2014, **2014**, 2495-2501.
58. J. Bunzen, T. Bruhn, G. Bringmann and A. Lützen, *Journal of the American Chemical Society*, 2009, **131**, 3621-3630.

59. C. Maeda, T. Kamada, N. Aratani and A. Osuka, *Coordination Chemistry Reviews*, 2007, **251**, 2743-2752.
60. D. Rota Martir, D. Escudero, D. Jacquemin, D. Cordes, A. Slawin, H. Fruchtl, S. Warriner and E. Zysman-Colman, *Chemistry – A European Journal*, 2017, **23**, 14358-14366.
61. M. J. Hardie and C. J. Sumby, *Inorganic Chemistry*, 2004, **43**, 6872-6874.
62. H. Jędrzejewska and A. Szumna, *Chemical Reviews*, 2017, **117**, 4863-4899.
63. J. J. Henkelis, J. Fisher, S. L. Warriner and M. J. Hardie, *Chemistry – A European Journal*, 2014, **20**, 4117-4125.
64. M. D. Wise, J. J. Holstein, P. Pattison, C. Besnard, E. Solari, R. Scopelliti, G. Bricogne and K. Severin, *Chemical Science*, 2015, **6**, 1004-1010.
65. D. K. Chand, K. Biradha, M. Kawano, S. Sakamoto, K. Yamaguchi and M. Fujita, *Chemistry – An Asian Journal*, 2006, **1**, 82-90.
66. J. E. M. Lewis, A. B. S. Elliott, C. J. McAdam, K. C. Gordon and J. D. Crowley, *Chemical Science*, 2014, **5**, 1833-1843.
67. G. H. Clever, W. Kawamura, S. Tashiro, M. Shiro and M. Shionoya, *Angewandte Chemie International Edition*, 2012, **51**, 2606-2609.
68. J. E. M. Lewis, E. L. Gavey, S. A. Cameron and J. D. Crowley, *Chemical Science*, 2012, **3**, 778-784.
69. M. Han, J. Hey, W. Kawamura, D. Stalke, M. Shionoya and G. H. Clever, *Inorganic Chemistry*, 2012, **51**, 9574-9576.
70. N. Kishi, Z. Li, K. Yoza, M. Akita and M. Yoshizawa, *Journal of the American Chemical Society*, 2011, **133**, 11438-11441.
71. P. Liao, B. W. Langloss, A. M. Johnson, E. R. Knudsen, F. S. Tham, R. R. Julian and R. J. Hooley, *Chemical Communications*, 2010, **46**, 4932-4934.
72. G. H. Clever, S. Tashiro and M. Shionoya, *Angewandte Chemie International Edition*, 2009, **48**, 7010-7012.
73. H. S. Sahoo and D. K. Chand, *Dalton Transactions*, 2010, **39**, 7223-7225.
74. M. Han, D. M. Engelhard and G. H. Clever, *Chemical Society Reviews*, 2014, **43**, 1848-1860.
75. M. Traetteberg, I. Hillmo and K. Hagen, *Journal of Molecular Structure*, 1977, **39**, 231-239.
76. D. K. Maity, A. Halder, S. Ghosh and D. Ghoshal, *Crystal Growth & Design*, 2016, **16**, 4793-4804.
77. D. Braun and O. Steinhauser, *Physical Chemistry Chemical Physics*, 2015, **17**, 8509-8517.
78. T.-H. Wong, J.-C. Chang, C.-C. Lai, Y.-H. Liu, S.-M. Peng and S.-H. Chiu, *The Journal of Organic Chemistry*, 2014, **79**, 3581-3586.
79. M. Nilsson, *Journal of Magnetic Resonance*, 2009, **200**, 296-302.

Chapter 4

Photoisomerisation and photophysical studies of CTG-based Ir(III) metallocryptophanes

4.1 Introduction

The azobenzene (AZB) moiety has been employed in a wide range of systems ranging from discrete complexes to polymers¹⁻⁵ with polymers generally experiencing more interest from the scientific community. Their use for biological applications are also numerous,⁶⁻⁹ with considerable focus on ion sensing,¹⁰⁻¹² along with copious reports for applications in catalysis.¹³⁻¹⁶ The range of applications for these compounds all exploit the photoswitching ability of AZB. AZB is by far the most common choice of photoisomerisable unit owing to its robust nature and easily tunable photoswitching properties.^{17, 18} Chapter 2 of this thesis has demonstrated a strategy to append this unit into the ligand design of the molecular host CTG; subsequently chapter 3 discussed the incorporation of the AZB unit into discrete M_3L_2 metallocryptophanes.

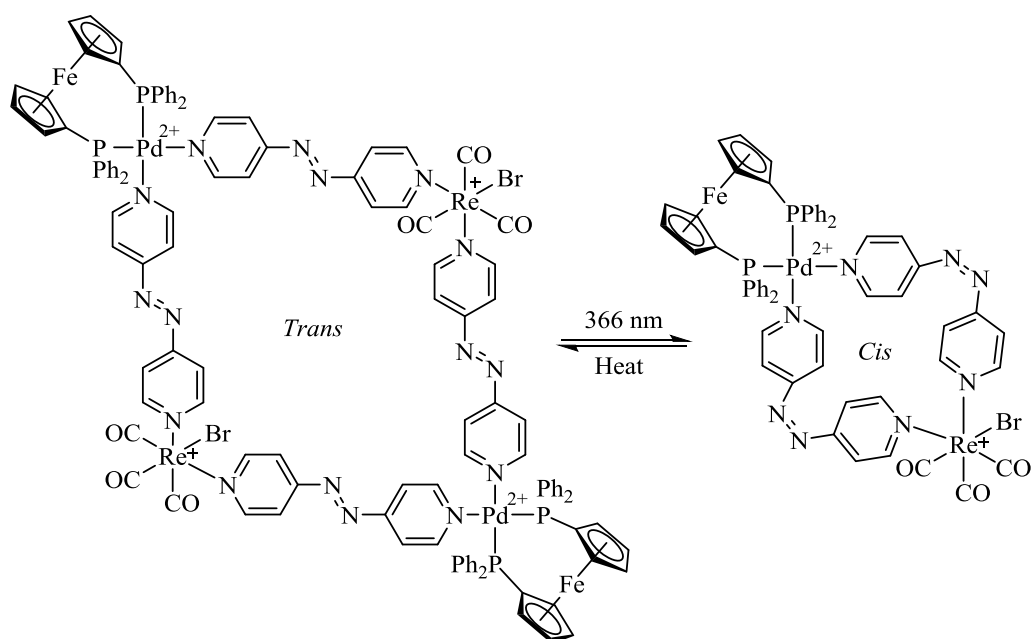


Figure 4.1: Light controlled interconversion between tetranuclear and dinuclear squares as prepared by Lees.¹⁹

Although many examples exist of AZB units in supramolecular systems^{13, 20-23}, to the best of the author's knowledge, no examples exist of the AZB unit incorporated into the physical structure of discrete metallo-cages with the closest examples being Clever's dithienylethene M_2L_4 cages²⁴ and Rebek's organic AZB capsules.^{21, 25} Lees has reported the light-controlled interconversion between tetranuclear and dinuclear metallocages (figure 4.1) but these systems do not possess an internal cavity for guest binding.¹⁹ Fujita has reported the functionalisation of giant $Pd_{12}L_{24}$ coordination cages²⁶ with pendant AZB units which project into the interior of the cage.²⁷ The photoisomerisation of these units allow the switching of the hydrophobicity of the interior of the cage and thus control over the binding of pyrene guest molecules. Conversely, Park and coworkers have reported AZB functionalised Cu metal-organic polyhedra (MOPs) where the pendant AZB units are now located on the exterior of the assembly.²⁸ These examples are uncommon in that they utilise the presence of multiple photoresponsive units in discrete complexes; this is also the case with the metallocages discussed in this chapter. A far more common approach is to utilise just the one AZB unit to provide a 'hinge-like'²³ or 'scissoring'^{22, 29, 30} range of molecular motion.

Many of the examples of larger systems bearing AZB units are polymeric architectures. Several examples of dendrimers bearing multiple AZB units have been reported,^{5, 31-35} along with examples of dendrimers with only one azo unit.^{36, 37} Kitagawa has recently prepared star coordination polymers bearing AZB units but has not yet remarked on their photoswitching behaviour.³⁸ Ballester has recently reported a series of hydrogen bonded dimeric capsules based on tetraureacalix [4] arenes bearing four terminal AZB groups (figure 4.2).³⁹ The all *trans* resting state was observed to encapsulate the Me_4P^+ cation but upon light driven isomerisation to a *cis*-rich photostationary state, changes in the capsule volume render it unsuitable for this guest, which is expelled into the bulk solution. The same group has also reported the photo-induced degradation of a hydrogen bonded dimeric resorcinarene capsule by invoking *trans* to *cis* AZB isomerisation.⁴⁰ Pendant AZB units have also been fused onto calix[4]resorcinarenes by Sakano⁴¹ and utilised to move liquid droplets across a photoresponsive surface.⁴²

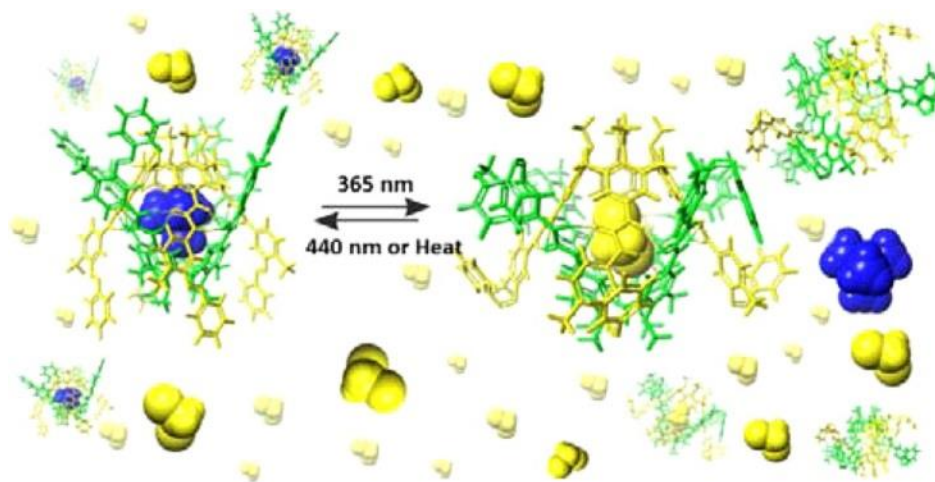


Figure 4.2: Representation of uptake and release of guest molecules in Ballester's hydrogen bonded capsules.³⁹ Reprinted with permission from 'F.A. Arroyave and P. Ballester, *The Journal of Organic Chemistry*, 2015, **80**, 10866-10873.' Copyright 2015 American Chemical Society.

The metallocages discussed here have the AZB unit embedded into the ligand design and thus the cage framework rather than being attached as pendant chains. The rationale for this design strategy is the combination of the dramatic conformational change of the AZB unit with multiple units per cage with the aim of invoking a more powerful response to light. This chapter focusses on the photoswitching of the embedded AZB units within these cages as well as the efficiency and reversibility of this process. Further to this, the Ir(III) centre could potentially lead to a luminescent output for these systems which is explored in section 4.8.

4.2 General considerations – photoisomerisation of azobenzene

UV-visible spectroscopy is an excellent tool for monitoring the isomerisation process of AZB units due to dramatic changes in the symmetry allowed $\pi \rightarrow \pi^*$ transition (typically between 300-350 nm) upon isomerisation. This transition is intense in the *trans* isomer but upon conversion to the *cis* isomer, experiences a significant decrease in intensity proportional to the amount of the compound isomerising.⁴³ A much smaller change is observed in the $n \rightarrow \pi^*$ transition (typically between 400-450 nm) which becomes symmetry-allowed in the *cis* isomer and thus increases in intensity compared to the *trans* isomer, but throughout this chapter, conversion between isomers is monitored predominantly by examining the changes in the $\pi \rightarrow \pi^*$ transition.

These electronic transitions excite AZB units into the S_1 ($n \rightarrow \pi^*$) and S_2 ($\pi \rightarrow \pi^*$) excited states respectively⁴⁴ where isomerisation takes place. Figure 4.3 shows a simplified Jablonski diagram illustrating this process. Excitation to these excited

states give transition states which can relax to either give the *trans* or *cis* isomer. As a result, a photostationary state is reached which consists of a mixture of *trans* and *cis* isomers; the position of this equilibrium is determined by a number of factors including solvent polarity, pH and temperature; a comprehensive review of the factors affecting this process has been published by Burdette.⁴⁴ AZB is often a popular choice for molecular switching applications owing to a lack of overlap of the UV spectra of the *trans* and *cis* isomers, enabling selective irradiation and typically high photoisomerisation quantum yields.

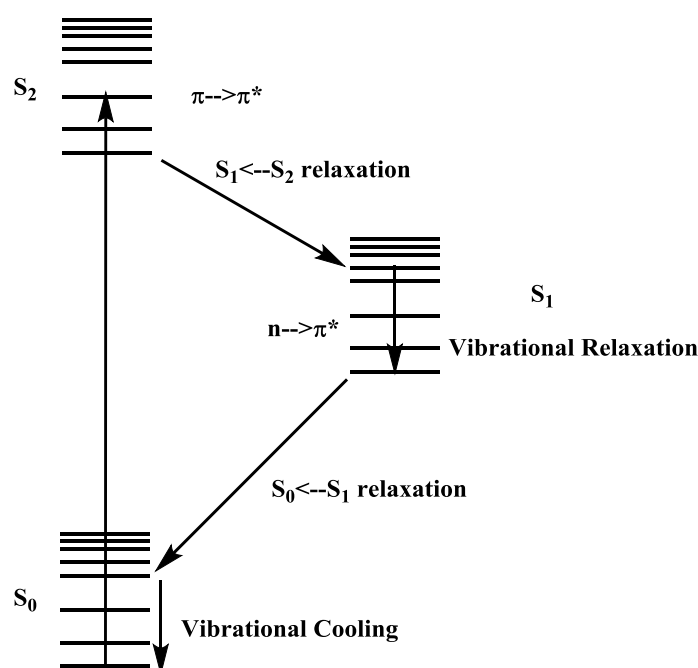


Figure 4.3: Simplified Jablonski diagram showing the excitation of AZB. Adapted and redrawn from reference 44.

The mechanism of isomerisation for AZB derivatives is hotly debated (compared to the stilbene analogue which is known to isomerise exclusively by rotation).⁴⁴ Four main classes of isomerisation mechanism – rotation, inversion, concerted inversion, and inversion assisted rotation have been invoked to explain experimental results with an assortment of evidence for each mechanism. A full investigation and discussion of the mechanistic aspects of the systems discussed here is beyond the scope of this work; some brief discussion is provided where appropriate experimental evidence offers some insight.

The systems examined here are more complex than those typically found in the literature owing to the presence of three photoresponsive AZB units per CTG ligand rather than just one. This complexity is compounded further in the M₃L₂

metallocryptophanes which bear six AZB units per cage. Conversion to a *cis*-rich photostationary state is the far more challenging process and requires UV light between 300-350 nm whereas regeneration of the starting *trans* isomer can be accomplished by either visible light (390-700 nm) or thermally *via* heating. Hecht and co-workers have also demonstrated that this reverse process can also be achieved through electrochemical stimulus.⁴⁵

For consistency, all ligand isomerisations were carried out in DMSO solvent whereas all cage isomerisations were conducted in non-coordinating CH₂Cl₂ to suppress the possibility of cage degradation. Nitromethane (the best solvent for solubilising the metallocages) is not a suitable solvent for irradiation studies owing to its high UV cutoff (~400 nm) below which the solvent itself absorbs light and also due to the safety concerns associated with nitromethane decomposition. The reverse *cis*→*trans* reaction for all compounds discussed in this chapter were performed using visible light irradiation rather than heating due to the comparatively slower thermal relaxation pathways of *cis* AZB.

The complexity of the systems discussed here coupled with the presence of multiple isomers at the photostationary state means that an accurate determination of the quantum yields Φ of isomerisation, are impractical either *via* the method of Rau⁴⁶ (which relies on the isolation of stable *cis* isomers) or *via* chemical actinometry. Therefore throughout this chapter, the efficiency of isomerisation between *trans* and *cis* isomers is quoted as a conversion which is calculated according to the equation:

$$\text{Conversion} = \frac{A_{0(\text{max})} - A_{\text{PSS}(\text{max})}}{A_{0(\text{max})}}$$

Equation 4.1: Calculation of conversion for isomerisation processes discussed in this chapter where $A_{0(\text{max})}$ is the initial absorbance at the maxima of interest and $A_{\text{PSS}(\text{max})}$ is the absorbance of the maxima at the photostationary state after irradiation.

Two conversion values have been determined for each system discussed herein, the *trans*→*cis* conversion and the reverse *cis*→*trans* conversion each with an associated band maxima in the UV spectrum. It should be noted that this calculation is a rough measurement of the efficiency of the isomerisations and assumes that the *cis* isomers of the azo unit have negligible absorbance between 300-350 nm and the *trans* isomers have negligible absorbance between 400-450 nm.

4.3 Photoisomerisation of free ligands

Photoisomerisation studies were first conducted on the free ligands to ensure the photoswitching properties of the AZB unit were maintained upon connection to CTG. The symmetry of the ^1H NMR spectra of these ligands (see chapter 2, section 2.4) indicated that, as expected, all three AZB units were present in their thermodynamically favoured *trans* configuration in the absence of an irradiation source. This is further observed in the solid state from the X-ray structures of ligands **2.12** and **2.17** (chapter 2, section 2.4) which also show a *trans* arrangement. There is no evidence to indicate that any *cis* isomer is present prior to irradiation.

All samples were prepared as a $30\mu\text{M}$ solution in DMSO. The photoisomerisations on a UV scale were performed using a 75W Xenon lamp equipped with a tunable power arc monochromator in collaboration with Dr Mark Blitz of the University of Leeds. An initial UV spectrum of the sample was recorded and the optimal wavelengths for *trans* \rightarrow *cis* (λ_1) and *cis* \rightarrow *trans* (λ_2) irradiation were determined from the absorption maxima of the $\pi\rightarrow\pi^*$ transition and the $n\rightarrow\pi^*$ transition respectively. The sample was then irradiated at λ_1 (UV) for 45 minutes to induce *trans* \rightarrow *cis* isomerisation and another UV spectrum recorded. Figure 4.4 shows the observed changes in the UV spectrum of ligand **2.12** after 45 minutes of irradiation with light of λ_1 :

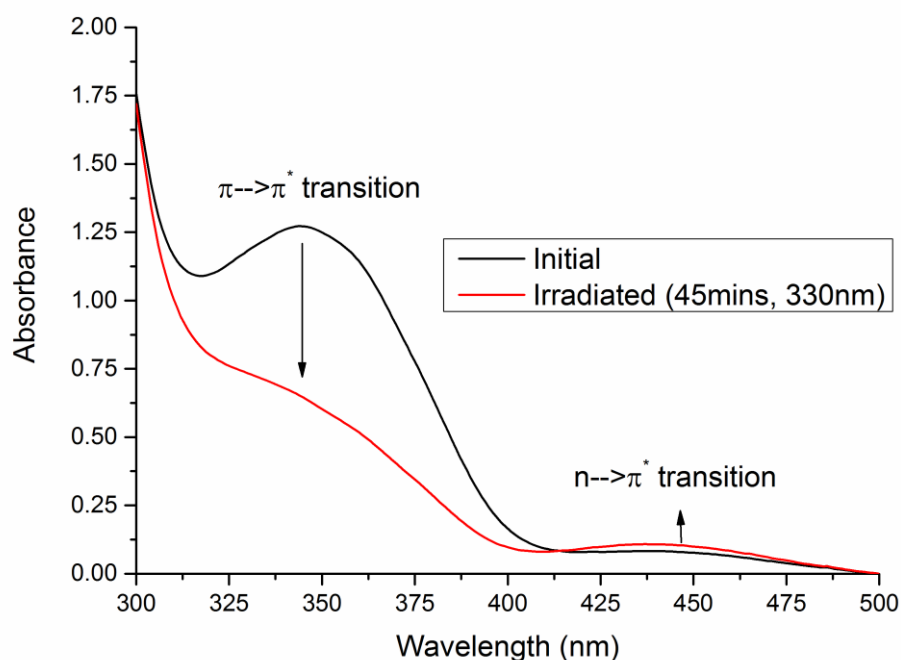


Figure 4.4: Changes in the UV spectrum of ligand **2.12** upon irradiation at 330 nm (λ_1) for 45 minutes in DMSO solvent.

A significant decrease in the $\pi \rightarrow \pi^*$ transition is observed as irradiation proceeds, an observation consistent with the formation of *cis* isomers of the AZB unit in solution. A small increase is also observed in the symmetry forbidden $n \rightarrow \pi^*$ transition; also consistent with the formation of *cis* isomers of AZB in solution. This solution was then irradiated at λ_2 (visible light) for 15 minutes to induce the reverse *trans* \rightarrow *cis* reaction. Figure 4.5 shows the changes to the UV spectrum after 15 minutes of irradiation of light of λ_2 :

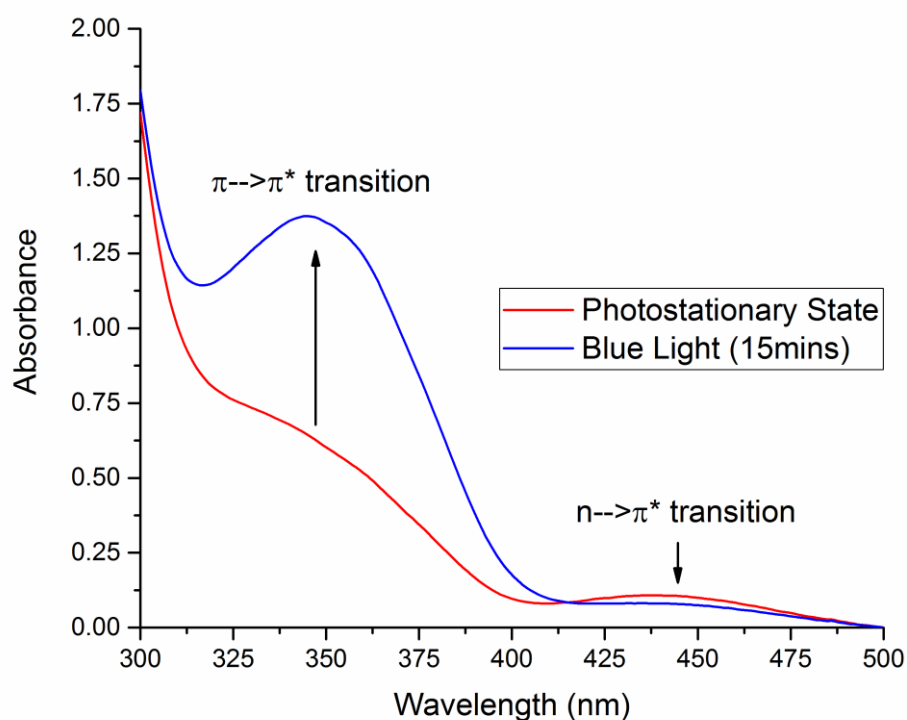


Figure 4.5: Changes in the UV spectrum of the photostationary state of ligand **2.12** upon irradiation at 450 nm (λ_2) for 15 minutes in DMSO solvent.

After irradiation with 450 nm blue light, the reverse procedure occurs with the regeneration of the starting intense $\pi \rightarrow \pi^*$ transition and the weaker $n \rightarrow \pi^*$ transition; both of these observations are consistent with successful *cis* \rightarrow *trans* isomerisation of AZB in solution. The absorbance maxima of the $\pi \rightarrow \pi^*$ transition is fully regenerated which shows a 100% successful reversion to the starting *trans* isomer. It should be noted the *cis* \rightarrow *trans* isomerisation, in addition to having a quantitative photochemical yield, also proceeds much more quickly, being complete after just 15 minutes. This is attributed to the resting *trans* state being more thermodynamically stable. All of these observations can also be seen using the other CTG ligands, compounds **2.17** and **2.18**, figures 4.6-4.9:

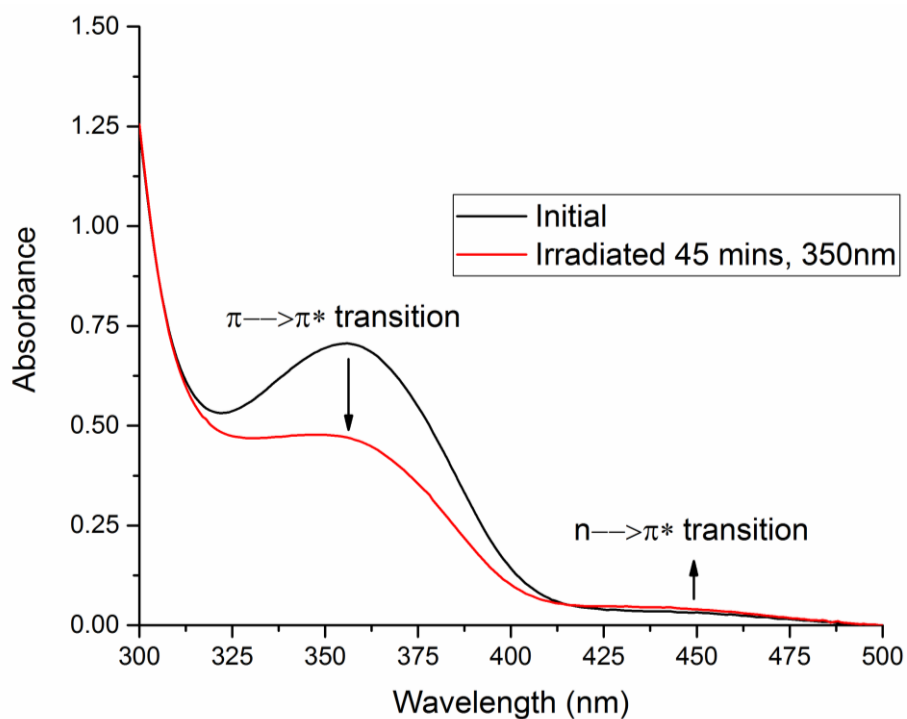


Figure 4.6: Changes in the UV spectrum of ligand 2.17 upon irradiation at 350 nm (λ_1) for 45 minutes in DMSO solvent.

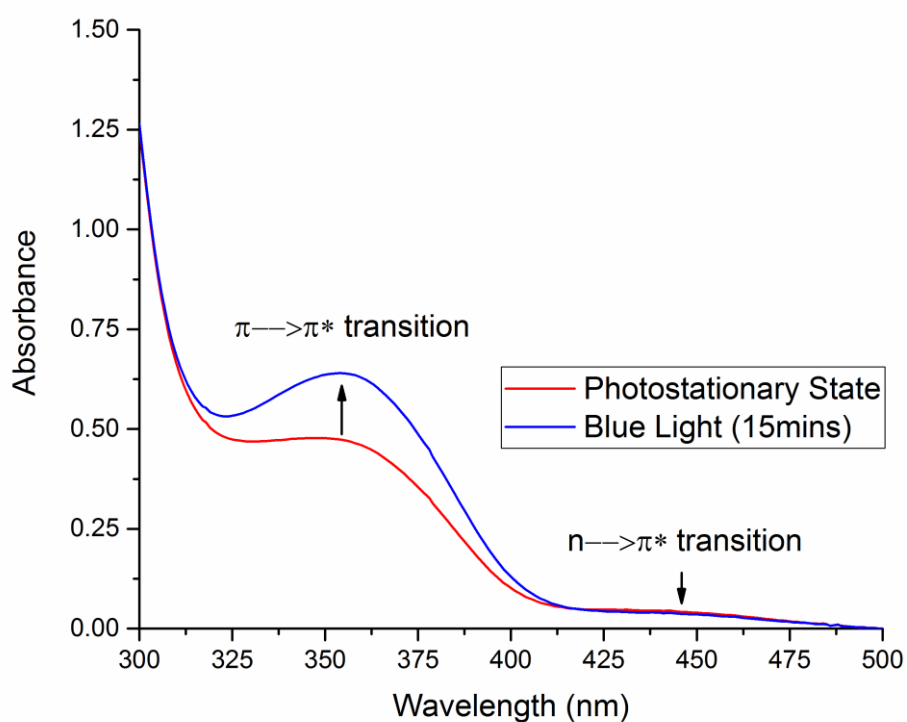


Figure 4.7: Changes in the UV spectrum of the photostationary state of ligand 2.17 upon irradiation at 450 nm (λ_2) for 15 minutes in DMSO solvent.

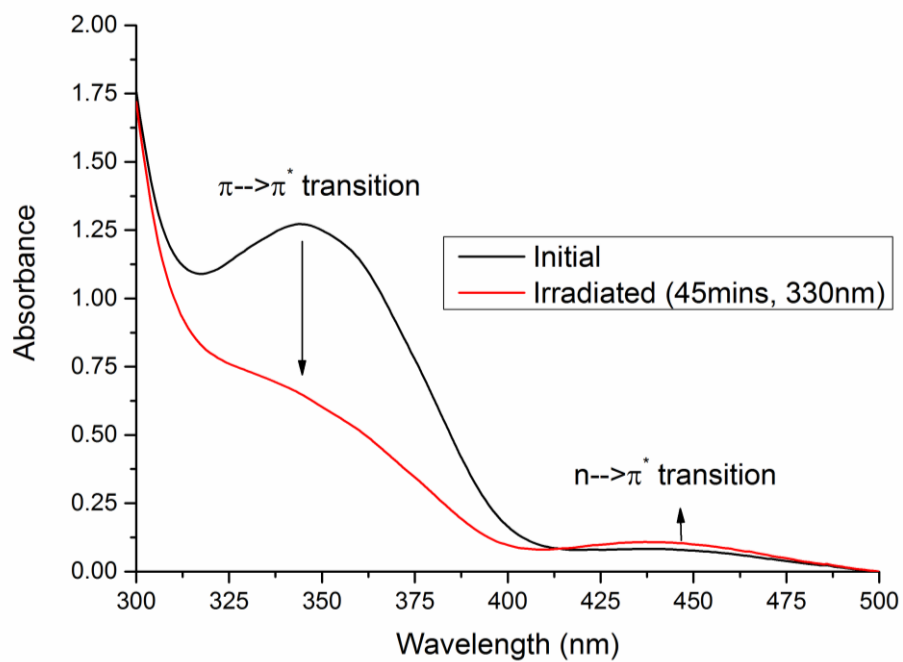


Figure 4.8: Changes in the UV spectrum of ligand **2.18** upon irradiation at 330 nm (λ_1) for 45 minutes in DMSO solvent.

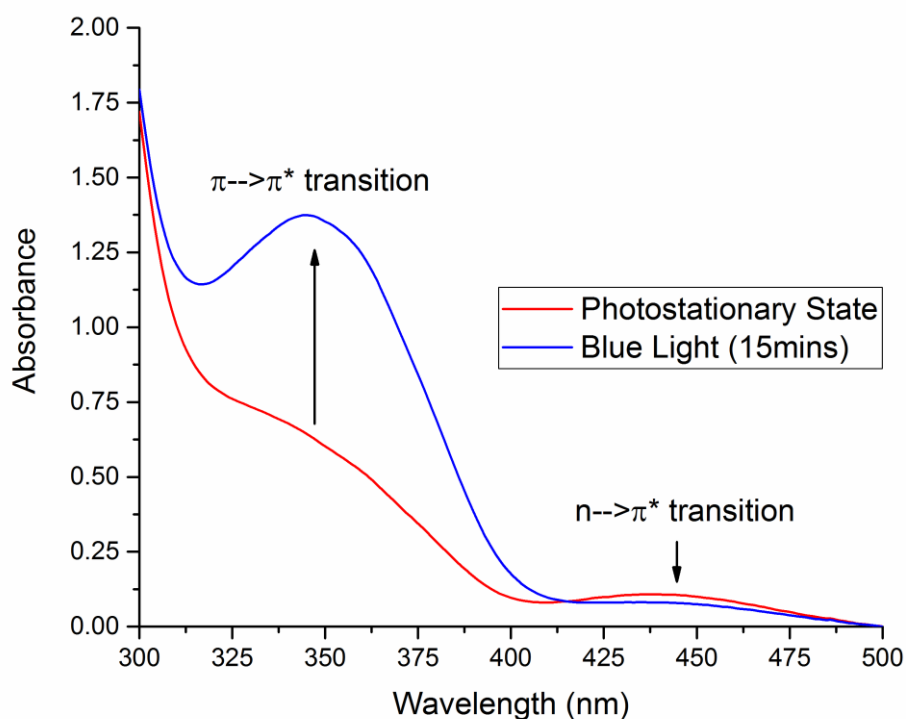


Figure 4.9: Changes in the UV spectrum of the photostationary state of ligand **2.18** upon irradiation at 450 nm (λ_2) for 15 minutes in DMSO solvent.

As all of these systems were studied under the same conditions, it is possible to compare the efficiency of the isomerisation process between *trans* and *cis* isomers of different ligands. Table 4.1 shows the conversion between these isomers; these values have been generated based on the changes to the $\pi \rightarrow \pi^*$ transition in the UV spectra. As expected, the reverse reaction from *cis* \rightarrow *trans* is more favourable and so despite reduced reaction times, proceeds with high efficiency. The forward reaction also generates a respectable amount of *cis* isomer and is likely to proceed further with longer irradiation periods. Interestingly, after 45 minutes the 4-pyridyl isomer has performed poorly compared to both of the 3-pyridyl analogues:

Table 4.1: Conversion efficiency between isomers of free ligands; *a* = after 45 minutes irradiation at λ_1 ; *b* = after 15 minutes irradiation at λ_2 .

Compound	$\lambda_{1 \text{ max}}$ (nm)	Conversion (<i>trans</i> \rightarrow <i>cis</i>) ^{<i>a</i>}	$\lambda_{2 \text{ max}}$ (nm)	Conversion (<i>cis</i> \rightarrow <i>trans</i>) ^{<i>b</i>}
2.12 (3py ester)	330	50%	450	100%
2.17 (4py ether)	350	36%	450	91%
2.18 (3py ether)	340	56%	450	100%

As the reaction between *trans* and *cis* isomers is reversible, the system should eventually reach an equilibrium of *trans* and *cis* isomers, the photostationary state. The nature of the photostationary state is dependent upon the quantum yield (Φ) of the reaction the irradiation wavelength λ and the absorption spectra of the species involved.⁴⁴ As three AZB units are present in the system, it is possible for a mixture of isomers to be generated with compounds bearing one, two or three *cis* ligand arms. In fact a total of four isomers are possible – *trans trans trans* (*EEE*), *trans trans cis* (*EEZ*), *trans cis cis* (*EZZ*), or *cis cis cis* (*ZZZ*). It would be expected that each individual isomerisation of the three AZB units would have its own quantum yield and that the photostationary state would lie somewhere between the two extremes, *EEE* and *ZZZ* isomers.

To probe the nature of the photostationary state, a further study was undertaken on ligand **2.12** using ¹H NMR spectroscopy. A solution of **2.12** in CD₂Cl₂ was irradiated using a 355 nm Nd:Yttrium Aluminium Garnet (YAG) laser, a far more powerful irradiation source. The protons adjacent to the azo group typically experience significantly higher shielding in the *cis* isomer due to their orientation towards the

other ring (figure 4.10); this change is strikingly apparent in the ^1H NMR spectrum as the change in chemical shift, $\Delta\delta$, can often be up to 1.0 ppm.^{47, 48} Figure 4.11 shows the timecourse NMR spectrum of ligand **2.12** after undergoing laser irradiation at various intervals.

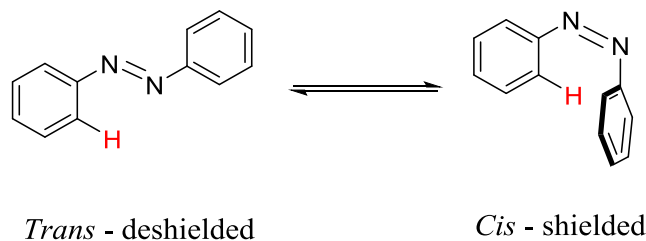


Figure 4.10: Shielding of aromatic protons in the *cis* isomer of AZB leading to pronounced chemical shift differences between isomers.

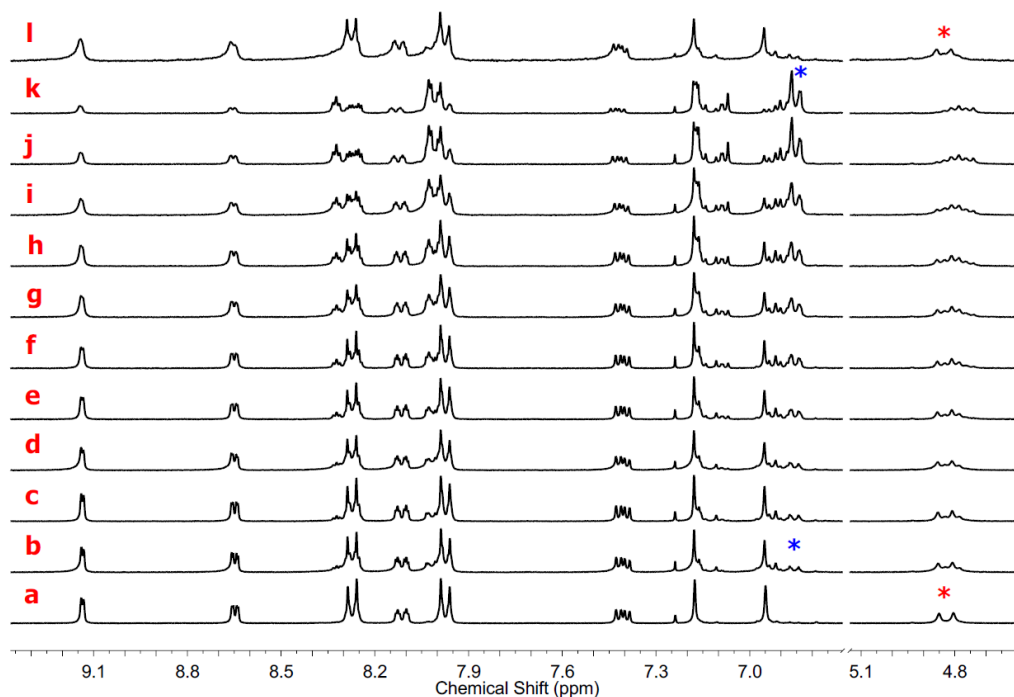


Figure 4.11: Timecourse ^1H NMR spectra of ligand **2.12** in CD_2Cl_2 showing spectrum after irradiating with 355 nm laser for: **a.** 0 seconds; **b.** 10 seconds; **c.** 20 seconds; **d.** 60 seconds; **e.** 120 seconds; **f.** 180 seconds; **g.** 240 seconds; **h.** 300 seconds; **i.** 450 seconds; **j.** 750 seconds; **k.** 900 seconds; **l.** Re-irradiated with blue light (60 minutes). The region 6.7-5.2ppm has been omitted for clarity.

An instantly obvious change is the CTG doublet at 4.8 ppm characteristic of a single CTG species in solution (*) which broadens and collapses to a complex multiplet as more *cis* species are generated. The fact that a clean doublet does not re-form over time (spectrum k) as the irradiation proceeds is a good indication that the photostationary state contains (as expected) a mixture of a number of different isomers

and that full conversion to entirely one species does not occur; no further changes to the spectrum are observed after 900 seconds of irradiation. The aromatic region of the spectra between 7.2 and 6.8 ppm becomes more complicated; whilst it is difficult to draw any concrete conclusions, the new doublet at 6.9 ppm (*) is likely to be the shielded protons in the *cis* isomers. Integration of this peak against the analogous peak in the *trans* isomer (8.21 ppm) reveals a photostationary state that contains approximately 76% *cis* isomers. This composition can be corroborated with UV spectroscopy (figure 4.12). Upon irradiation with blue light (spectrum 1) for 60 minutes, the majority of the new resonances disappear and the spectrum now strongly resembles the resting *trans* configuration (spectrum a). Interestingly, it can be seen that a small proportion of the sample remains in the *cis* configuration as several small resonances are present in the ^1H NMR spectrum even after an hour of irradiation with blue light. The HRMS of this solution reveals no evidence of any degradation products indicating a reasonably stable *cis* isomer.

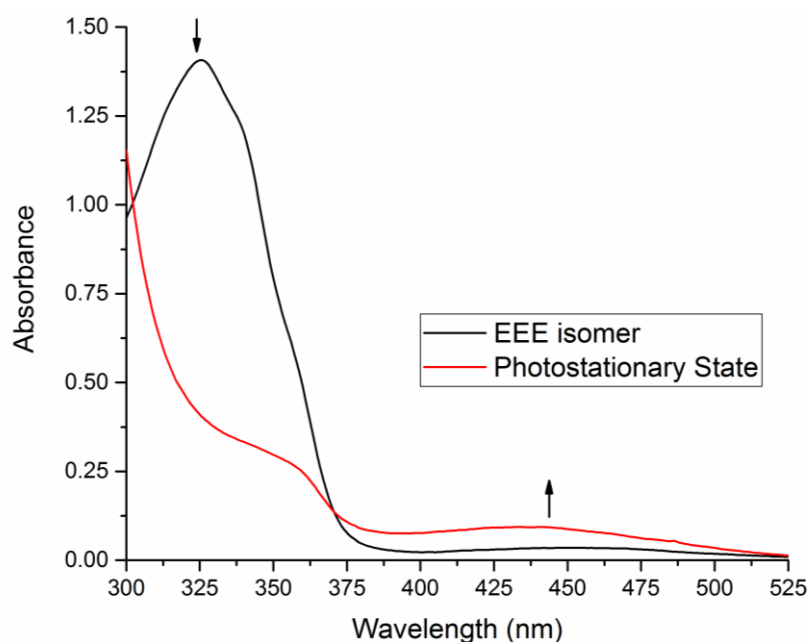


Figure 4.12: UV spectrum of the photostationary state (red line) compared to the initial *trans* isomer (black line) of ligand **2.12**; the calculated conversion is 78% from the UV spectrum, in agreement with that calculated from NMR studies.

The stability of the *cis* isomers of AZB is dependent on the local electronic environment about the azo group; considerable research interest focuses on the stabilisation of *cis* derivatives in order to have a more finite control over the configuration of the photoswitch.⁴⁹ Depending on the electronic arrangement of substituents on the aryl rings along with the separation of the $\pi \rightarrow \pi^*$ and $n \rightarrow \pi^*$

transitions, azo compounds may be classified (based on their $\pi \rightarrow \pi^*$ transitions) into one of three classes⁴⁴ – AZBs (ABn), aminoazobenzenes (aABn) and pseudostilbenes (pSbn) as illustrated in figure 4.13.

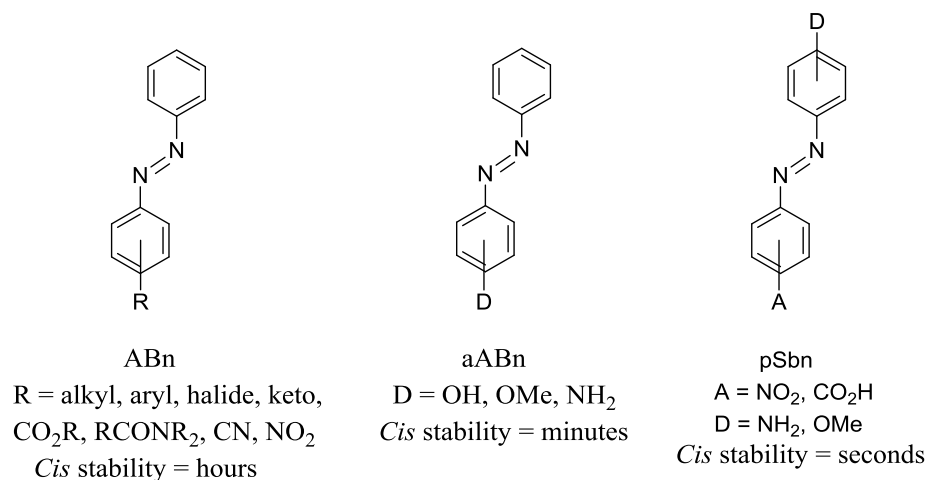


Figure 4.13: Electronic classification and characteristics of azo derivatives.

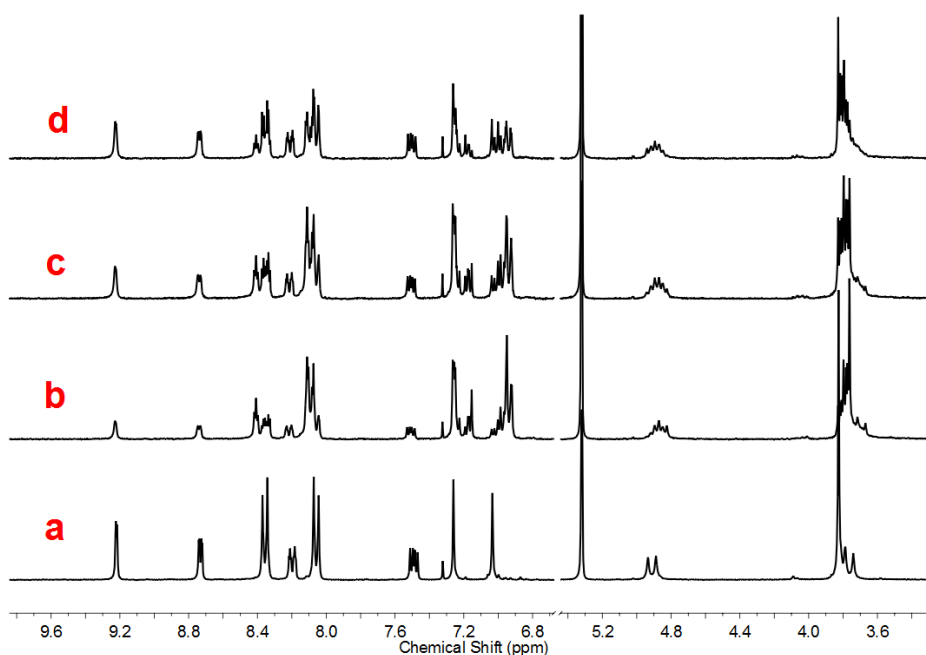


Figure 4.14: Stability of *cis*-rich photostationary state of ligand **2.12** in CD₂Cl₂ showing: **a**. Initial all *trans* isomer; **b**. After irradiation for 900s with 355 nm Nd:YAG laser; **c**. Photostationary state after 24 hours in the dark; **d**. Photostationary state after 48 hours in the dark. The region between 6.7 and 5.3 ppm has been omitted for clarity.

The ester linked ligand **2.12** may be classified as an ABn derivative based on substituent effects and the position of the $\pi \rightarrow \pi^*$ transition in the UV spectra; as such, a *cis* lifetime of several hours is expected. Solutions of the photostationary state of

ligand **2.12** show negligible changes to their ^1H NMR spectra over 24 hours when stored in the dark (figure 4.14, spectrum c). After 48 hours in the dark, conversion to the starting *trans* isomer has begun but still proceeds far more slowly than expected indicating a highly stable *cis*-rich photostationary state.

This analysis can also be obtained for the ether linked CTG ligand **2.18**. Figure 4.15 shows the changes to the ^1H NMR spectra of ligand **2.18** upon irradiating at 355 nm for 900 seconds. Once again a new large multiplet at 6.9 ppm evidences the formation of *cis* isomers. The CTG doublets remain reasonably well resolved with only a small amount of desymmetrisation observed. This implies fewer species in solution compared to the photostationary state of the ester ligand **2.12**. This in turn suggests a particular *cis* isomer may be more stable and is formed preferentially over a mixture of different isomers. The photostationary state for this ligand contains approximately 73% *cis* isomers.

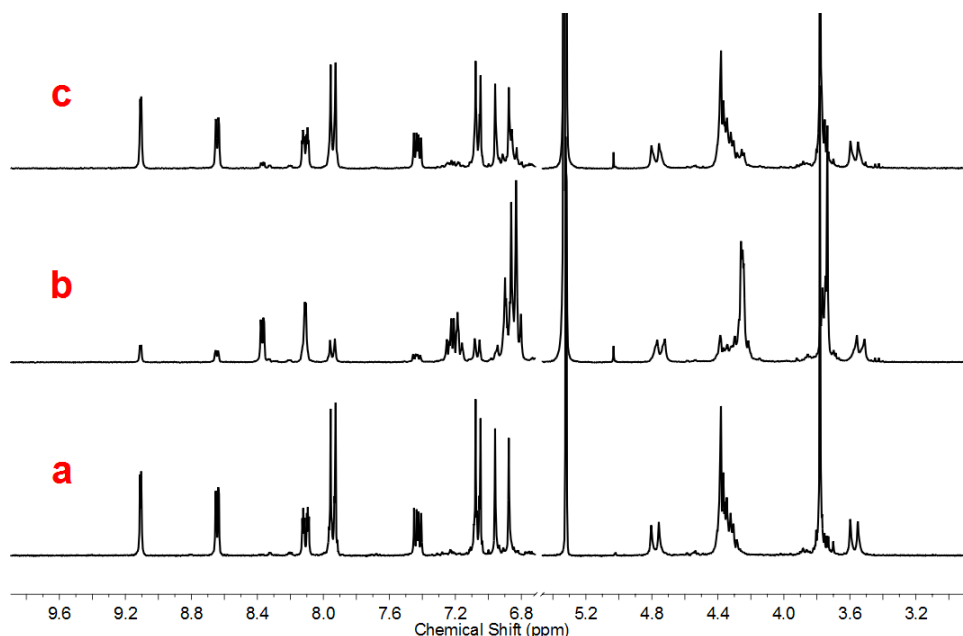


Fig 4.15. Thermal relaxation of ligand **2.18** in CD_2Cl_2 showing; **a**. Initial all *trans* isomer; **b**. After irradiation for 900s with 355 nm Nd:YAG laser; **c**. Photostationary state after 24 hours in the dark. The region between 6.8 and 5.3 ppm has been omitted for clarity.

Interestingly, upon storing the photostationary state of the ether linked analogue **2.18** in the dark for 24 hours, significant relaxation to the starting *trans* isomer is observed with the *trans* isomer the main species present after 24 hours (figure 4.15c). This indicates a far less stable population of *cis* isomers with thermal relaxation taking place rapidly in the dark. For such a simple change in the ligand design (C=O to $\text{CH}_2\text{CH}_2\text{O}$ linker) to have such a dramatic effect in the stability of the *cis* rich

photostationary state may seem initially surprising. However this phenomena is likely due to the altered electronic configuration with the electron-withdrawing ester group leading to stabilisation of the *cis*-isomers. Replacement of this with the more electron-donating alkoxy substituent leads to a more aABn-like configuration. Electron-donating substituents on the aryl rings decrease the thermal isomerisation energy barrier *via* the donation of electrons into the π^* orbital.^{50, 51} Attempts to crystallise *cis* isomers from the *cis*-rich photostationary state to try and elucidate their solid state structures were unfortunately unsuccessful. The crystallisation process is likely to be hindered by thermal isomerisation to the *trans* isomer and a mixture of species in solution. An interesting point raised by the stability of these *cis* isomers is the potential formation of the metallocryptophanes from the mixture of *trans* and *cis* isomers at the photostationary state. This strategy has not yet been attempted due to the complex mixture of *cis* isomers present.

4.4 UV studies of M_3L_2 ester cage isomerisation

The photoisomerisation studies of the M_3L_2 metallocages were carried out in non-coordinating DCM to prevent any cage breakdown during the switching studies. A solution of isolated $[Ir(2ppy)_2(MeCN)_2]^+.PF_6^-$ was irradiated at 355nm using a Xe lamp for 60 minutes; no changes were observed in the UV spectra, confirming there is no interference from the Ir(III) centre when measuring the changes in the UV region associated with AZB isomerisation.

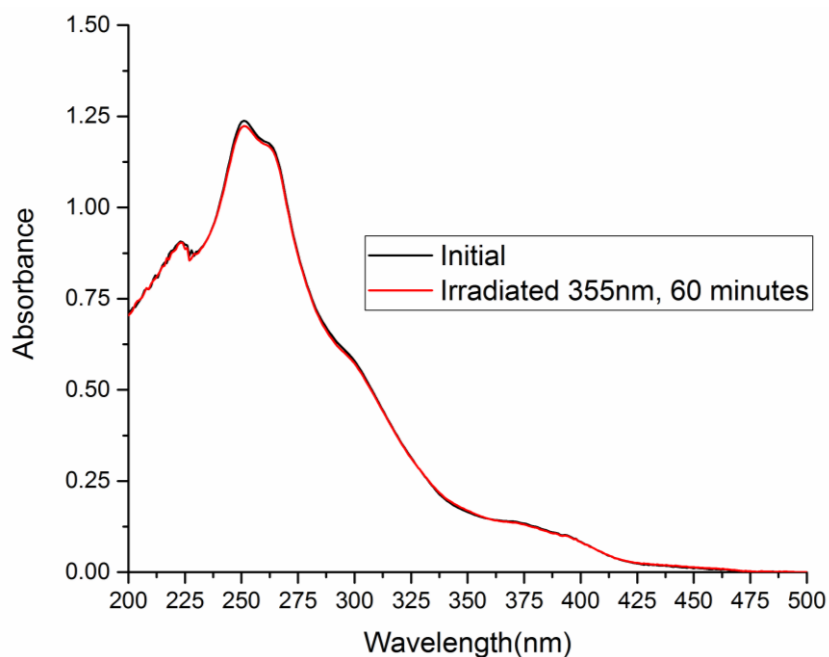


Figure 4.16: UV spectra of $[Ir(ppy)_2(MeCN)_2]^+.PF_6^-$ in CH_2Cl_2 solvent showing the lack of spectral changes after irradiating at 355 nm for 1 hour.

Unfortunately, studies of all cages apart from cage **3.12** were restricted to UV studies due to insufficient solubility in DCM for ^1H NMR experiments to be performed. The UV spectra of the metallocages are somewhat more complicated than that of the free ligands. Figure 4.17 shows the UV spectrum of cage **3.8**. Two ligand centred transitions (^1LCs) are observed at λ_{max} 274 nm and 293 nm localised on the phenylpyridine ancillary ligands. The AZB $\pi \rightarrow \pi^*$ transition dominates the region from 300-390 nm although there are likely to be contributions from spin-allowed and spin-forbidden mixed metal-to-ligand and ligand to-ligand charge transfer ($^1\text{MLCT}/^1\text{LLCT}$ and $^3\text{MLCT}/^3\text{LLCT}$) transitions in this region as well. The weak band at 400 nm is likely to arise as a result of spin-forbidden $n \rightarrow \pi^*$ AZB centred transitions.

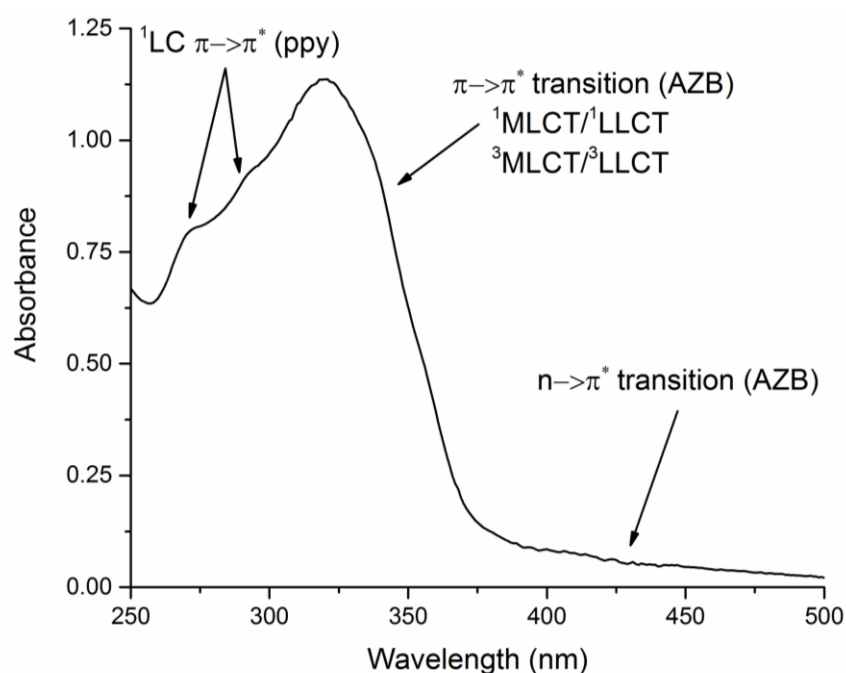


Figure 4.17: Interpreted UV spectrum of ester linked metallocage **3.8**.

Photoisomerisations of the cage compounds were initially conducted using the Xe lamp to select optimal wavelengths for isomerisation. However it transpired that prolonged irradiation times (several hours) were necessary in order to achieve only small changes in the UV spectrum. The difficulty in switching the cage compounds compared to the free ligands is likely a consequence of having tethered the AZB unit to the iridium centre thus restricting its ability to undergo rotation. This in turn, provides some indirect evidence that the mechanism of isomerisation of these metallocages has a rotational component.

As a result of this, experiments were therefore undertaken using a Nd:YAG laser in collaboration with Dr Mark Blitz of the University of Leeds. Although this provides

a fixed wavelength of 355 nm, this apparatus is able to deliver a much higher level of energy to induce photoisomerisation in the system. The laser can be set to a frequency of 1Hz which delivers one laser pulse or ‘shot’ per second to the sample (additional details of this procedure are given in the experimental, section 4.10). As the energy per shot can also be altered, this allows a high level of control and power for photoisomerisation experiments. The drawback to this approach is the wavelength of light is fixed at 355 nm and cannot be tuned for optimal isomerisation wavelength. This phenomena of high energy laser irradiation being necessary for photoswitching of the AZB unit has also been observed by Uchida and coworkers, who found that their AZB gels were unresponsive to a 500W Xe arc lamp but readily undergo photoswitching in response to laser irradiation.⁵² All UV experiments discussed herein were carried out with each shot providing 15 mJ of energy to the system. Figures 4.18-4.20 show the UV changes upon irradiation of the ester linked cages **3.8**, **3.11** and **3.12** respectively:

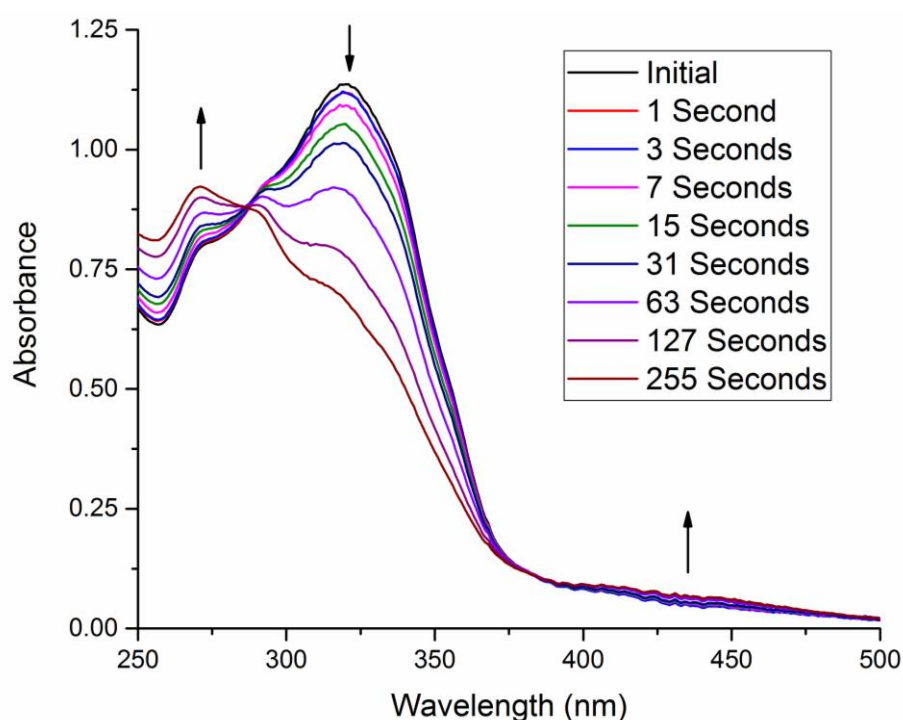


Figure 4.18: changes to the UV spectrum of cage 3.8 upon irradiating at 355 nm using Nd:YAG laser.

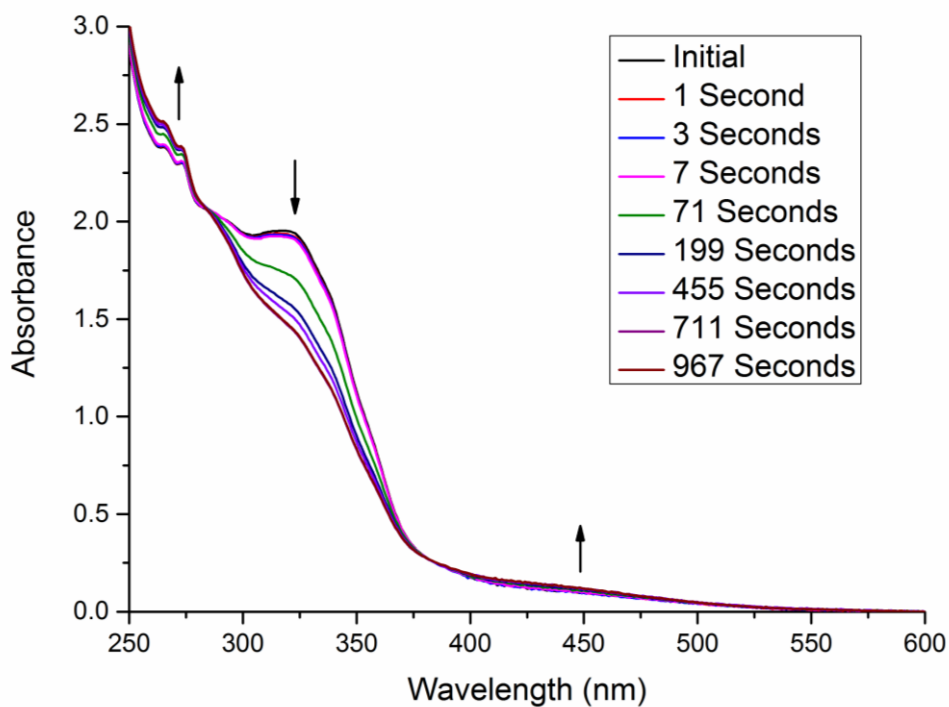


Figure 4.19: Changes to the UV spectrum of cage **3.11** upon irradiating at 355 nm using Nd:YAG laser.

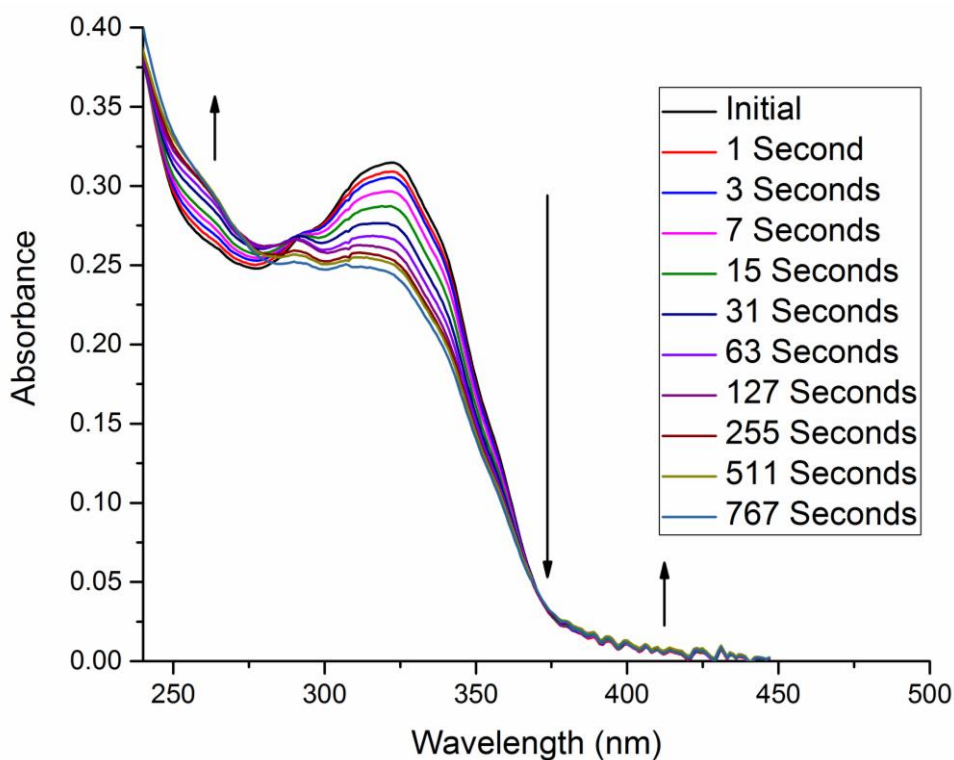


Figure 4.20: Changes to the UV spectrum of cage **3.12** upon irradiating at 355 nm using Nd:YAG laser.

Using laser irradiation, it can be seen that now isomerisation does proceed in the cage compounds although with reduced efficiency (discussed further in section 4.6). Once again, the characteristic $\pi \rightarrow \pi^*$ absorption decreases as *trans* to *cis* isomerisation is induced. A small increase in the intensity of the $n \rightarrow \pi^*$ transition is also observed. The reverse reaction from *cis* to *trans* remains easy to promote and once again can be achieved by irradiation with blue light (450 nm) for 15 minutes using a Xe lamp (figures 4.21-4.23). This is unsurprising as the difficulty experienced in inducing *trans* \rightarrow *cis* isomerisation indicates a much higher energy barrier to form *cis* isomers; the reverse reaction to regenerate the *trans* isomer would therefore be expected to be energetically favourable. A key observation is the presence of multiple isosbestic points in each spectrum, once again indicating that the spectral changes are caused by photoisomerisation rather than a concentration gradient.

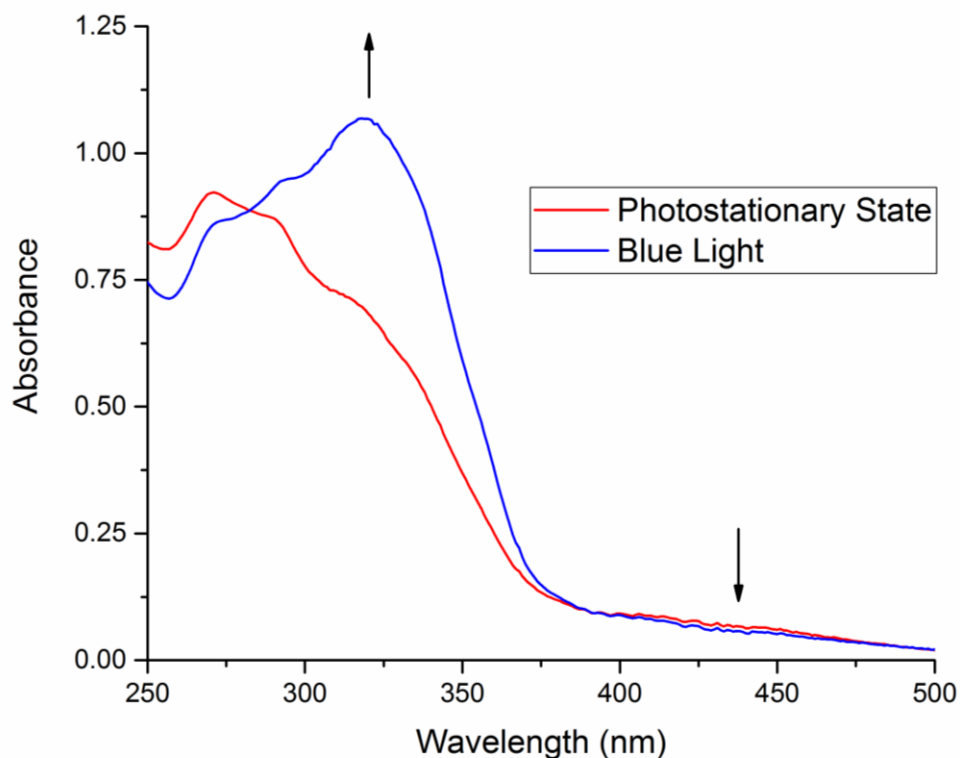


Figure 4.21: Regeneration of starting cage 3.8 configuration using irradiation with blue light for 15 minutes.

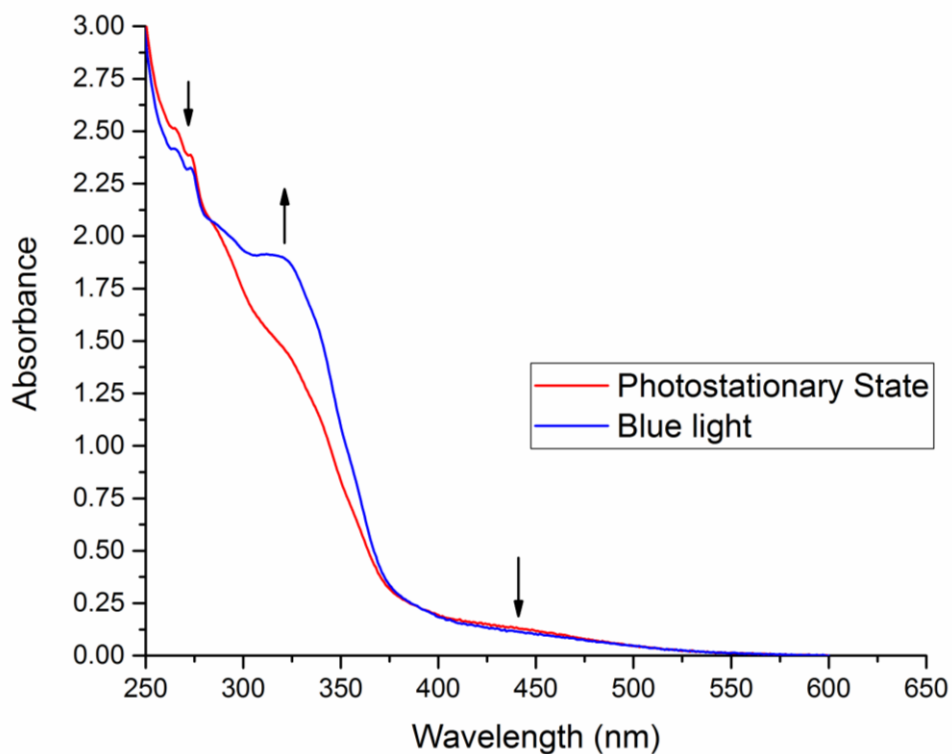


Figure 4.22: Regeneration of starting cage 3.11 configuration using irradiation with blue light for 15 minutes.

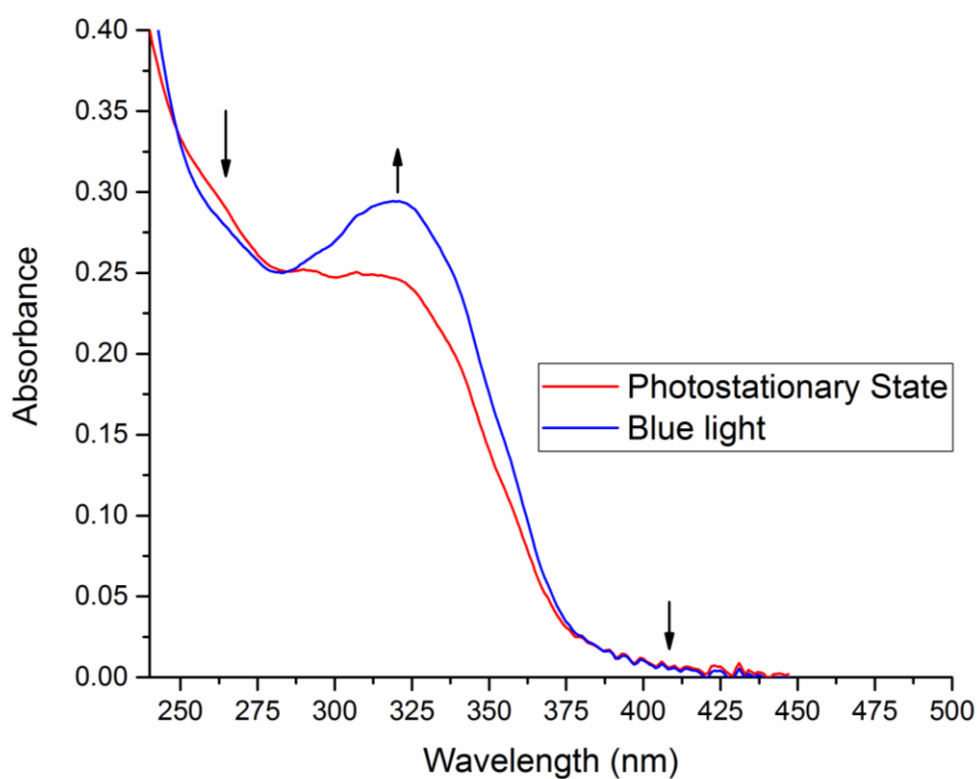


Figure 4.23: Regeneration of starting cage 3.12 configuration using irradiation with blue light for 15 minutes.

4.5 UV studies of M₃L₂ ether cage isomerisation

The isomerisation studies were also conducted on the ether linked cages **3.9** and **3.10**. Once again applying a series of laser pulses to solutions of the cages in CH₂Cl₂ resulted in successful alterations to the UV spectra consistent with the formation of *cis* isomers. The UV spectral changes for these compounds are displayed in figures 4.24 and 4.25.

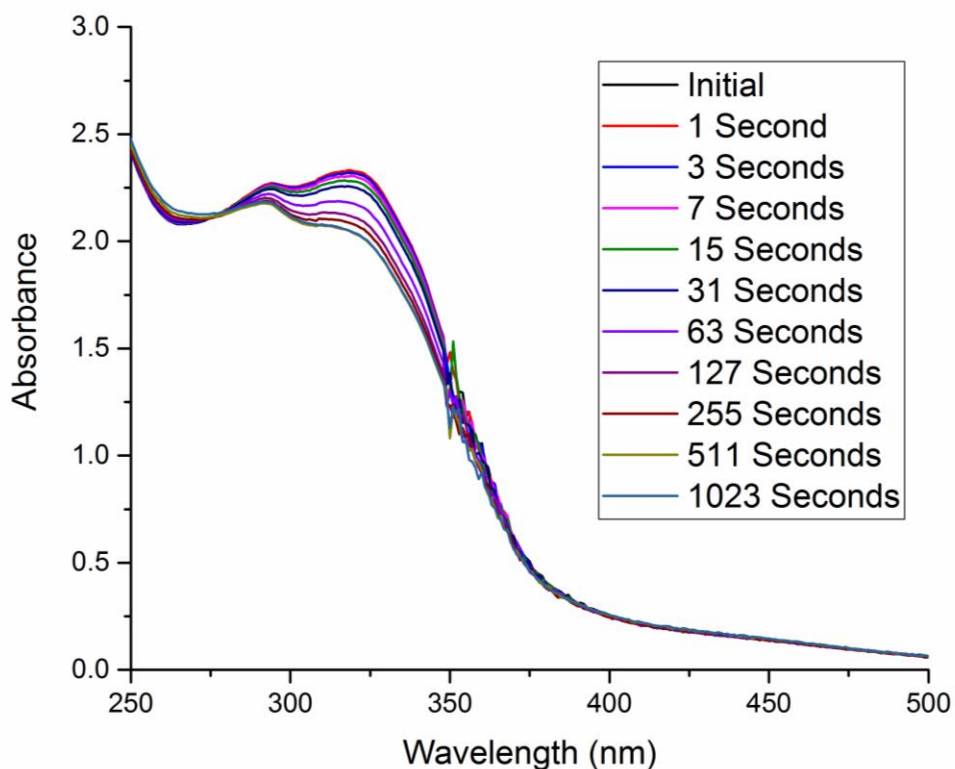


Figure 4.24: changes to the UV spectrum of cage 3.9 upon irradiating at 355 nm using Nd:YAG laser. The jagged portion of the spectrum at ca. 360 nm is an artefact of the UV source changeover in the instrument.

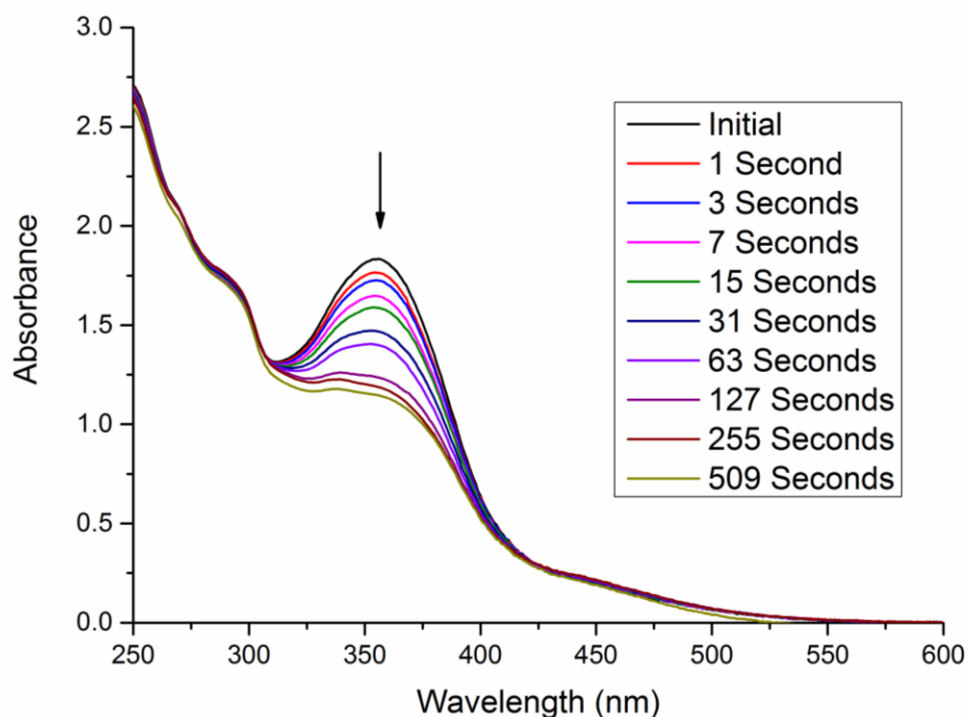


Figure 4.25: changes to the UV spectrum of cage **3.10** upon irradiating at 355 nm using Nd:YAG laser.

Once again the reverse reaction $cis \rightarrow trans$ proved easier to accomplish than the $trans \rightarrow cis$ conversion. The UV spectra after reirradiation with blue light for 15 minutes are shown in figures 4.26 and 4.27. Spectral observations remain consistent once more with $trans \rightarrow cis$ isomerisation, including an increase in the AZB $\pi \rightarrow \pi^*$ transition and a small decrease in the $n \rightarrow \pi^*$ transition. All of the cage compounds (whether ester linked or ether linked) show a high reversion to the resting $trans$ state, a point which is discussed further in section 4.6. The presence of isosbestic points and a general lack of any photochromic shifts in any of the spectra imply these spectral changes are due to a photoisomerisation process and are unlikely to be arising as a result of cage decomposition.

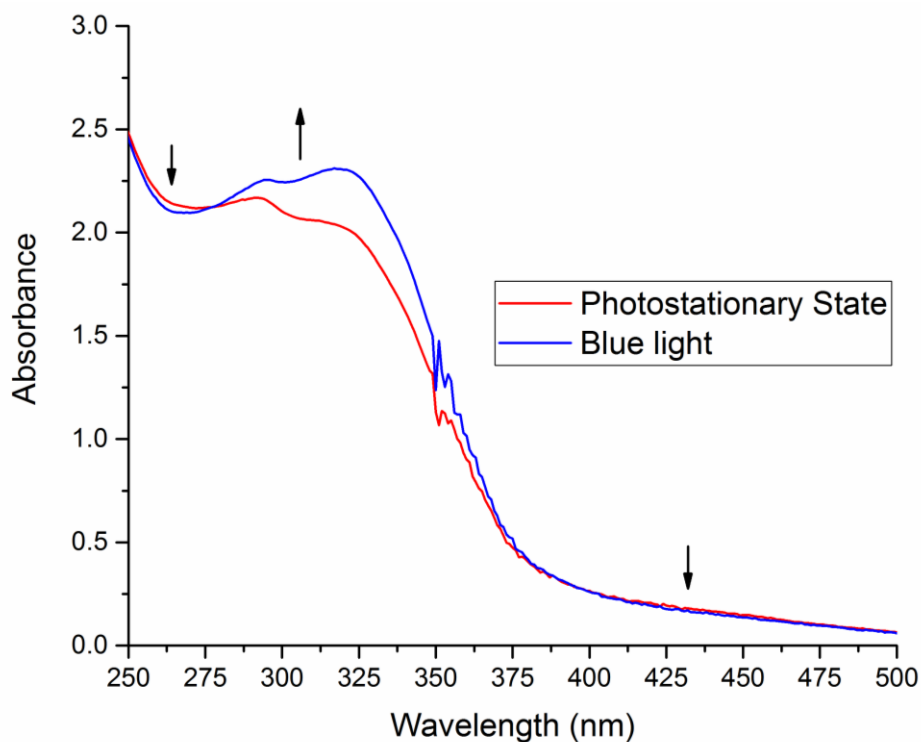


Figure 4.26: Regeneration of starting cage 3.9 configuration using irradiation with blue light for 15 minutes. The jagged portion of the spectrum at ca. 360 nm is an artefact of the UV source changeover in the instrument.

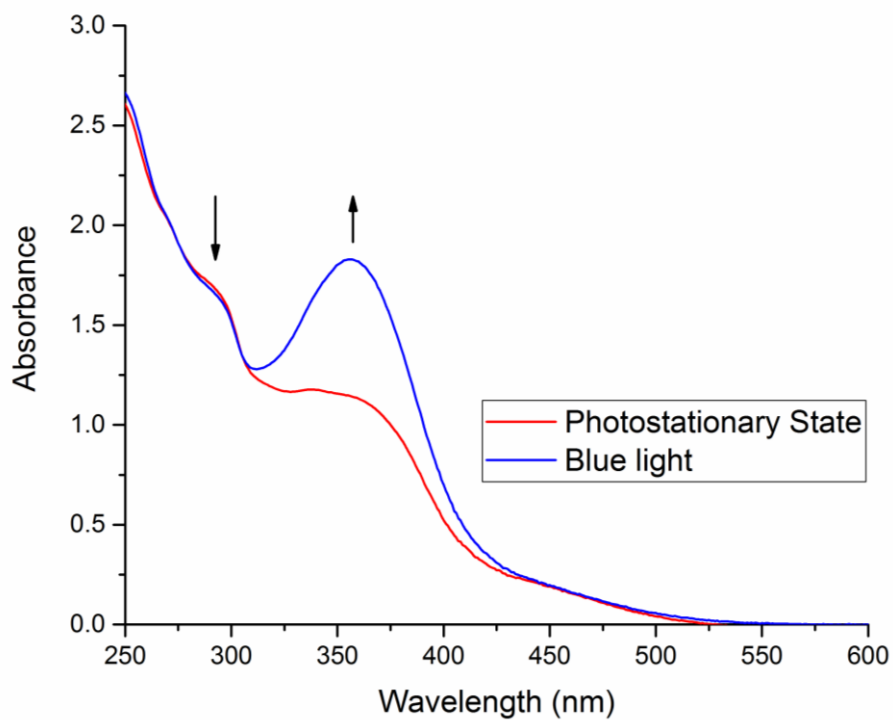


Figure 4.27: Regeneration of starting cage 3.10 configuration using irradiation with blue light for 15 minutes.

4.6 Stilbene analogue

The photoisomerisation of the stilbene analogue of ligand **2.12** was also investigated in collaboration with MChem student Ben Swift. The stilbene absorption band is slightly blue-shifted compared to the AZB analogue with a λ_{max} of 320 nm in CH_2Cl_2 solvent. This is still an uncommonly high wavelength for a stilbene absorption⁵³ but is likely to be a consequence of significant levels of conjugation present in ligand **2.22**.⁵⁴ A 30 μM solution of the compound in CH_2Cl_2 was irradiated with UV light at 320 nm for 80 minutes with a UV spectrum being recorded at 10 minute intervals (figure 4.28). With time, the absorption band at 320nm decreases in intensity as more *cis* isomer is generated.⁵⁵ This is accompanied by the appearance of a new band at 270nm which is assigned as the *cis* stilbene.^{56, 57}

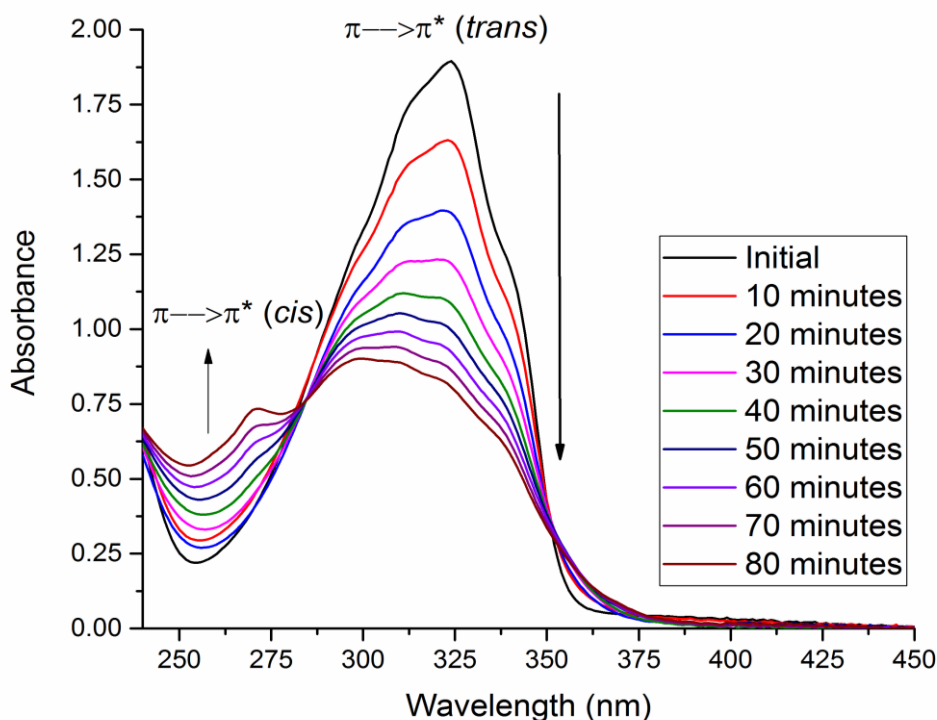


Figure 4.28: Timecourse UV experiment showing photoisomerisation to the *cis* form of ligand **2.22** upon irradiation at 320 nm.

The *cis*-band for the stilbene ligand grows in at approx. 270 nm. The sample was therefore irradiated at 270 nm for 30 minutes to induce *cis*→*trans* isomerisation. Surprisingly, minimal changes were observed in the UV spectrum indicating that UV light cannot influence the *cis*→*trans* isomerisation. Irradiation with blue light also produced no observable changes. A photocyclisation reaction to form the

dihydrophenanthrene derivative⁵⁸ is unlikely given the lack of emergence of any phenanthrene absorption bands.

The M₃L₂ metallogage containing this ligand has also been prepared by MChem student Ben Swift (see chapter 2 for synthetic details) but only on an NMR scale at this point. As such, the scaleup of this metallogage needs to be completed before any photoswitching studies can be performed. Since stilbenes are known to undergo isomerisation exclusively *via* a rotation based mechanism, comparison of the efficiency of this process may give interesting insights into the possible mechanism of the AZB containing metallogages.

4.7 Conversion limits and photochemical fatigue

The ability of the cage compounds to undergo photoisomerisation is the key property in their ability to function as responsive host molecules. Therefore the efficiency of this process is also of great importance. Unfortunately, the incorporation of the ligands into the cage design resulted in the *trans*→*cis* isomerisation becoming more difficult compared to the free ligands which is likely a consequence of restraining the AZB rotation by coordinating it to a metal centre. This phenomena has been observed in the literature with additional strain resulting in less conversion between isomers; this was demonstrated in the extreme case by Wegner and co-workers who prepared a series of cyclotrisazobenzenes that were so rigid they did not undergo any isomerisation at all.⁵⁹

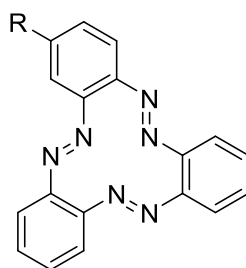


Figure 4.29: Cyclotrisazobenzene prepared by Wegner and coworkers incapable of photoisomerisation.⁵⁹

Rigidity and functional group manipulation has also been exploited to design systems where the *cis* isomer of the AZB unit is the more stable component.^{49, 60-62} Rau and coworkers have synthesised a series of rotation-restricted AZB derivatives^{63, 64} where the isomerisation process is independent of the irradiating wavelength. Yam and coworkers prepared M₄L₂ macrocycles bearing AZB units in close proximity to alkyne units. Upon addition of Ag⁺ ions to the system, π -coordination of the alkyne

units to the silver ions occurs which prevents *trans*→*cis* isomerisation by restricting rotation of the azo bond.⁶⁵ Several metal-organic frameworks (MOFs) have also been reported where the azo unit has been incorporated into the framework rather than as a pendant moiety;⁶⁶⁻⁷⁰ however none of these examples successfully demonstrated photoisomerisation.

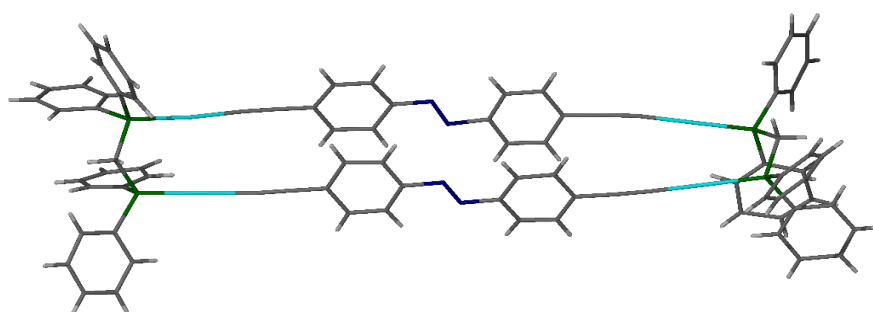


Figure 4.30: The M_4L_2 macrocycle prepared by Yam and coworkers that can modulate the efficiency of its photoisomerisation using Ag^+ ions.⁶⁵

Owing to the rotational restrictions present in the metallocages, a study into the limits of the *trans*→*cis* isomerisation was undertaken with UV spectroscopy. A sample of cage **3.8** in DCM was irradiated with 355 nm light using a Nd:YAG laser and the changes to the absorption at 320 nm were monitored over time; these results are summarised in figure 4.31:

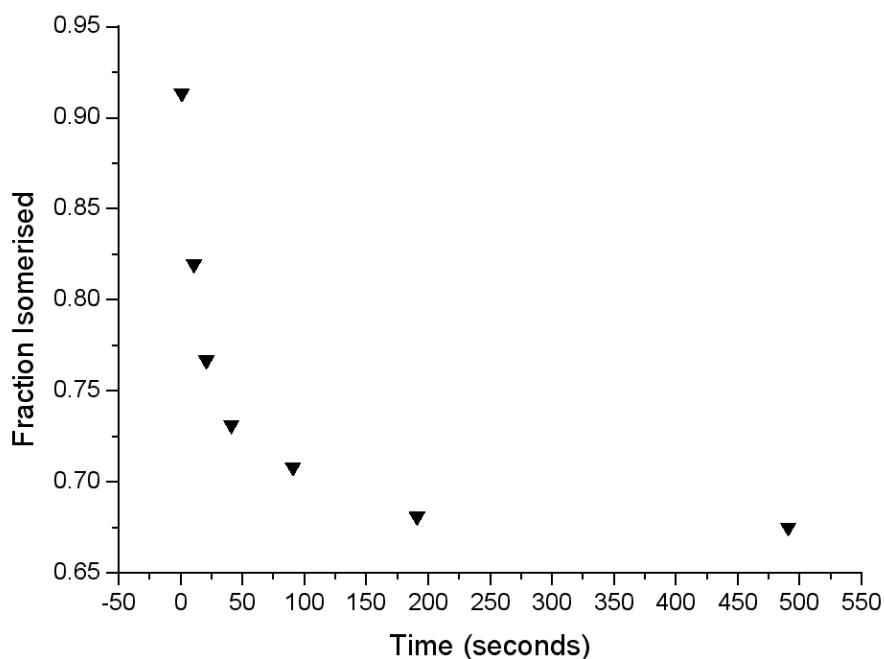


Figure 4.31: *Trans*→*cis* conversion of cage **3.8** over time.

As can be seen in figure 4.31, a significant amount of conversion is observed initially before the conversion rate decreases, eventually stopping after 200 seconds of irradiation. Further prolonged irradiation has no effect on the sample at this stage. Thus the reaction has a defined maximum yield or conversion beyond which no further *cis* product can be generated. This is likely due to increasing strain in the *cis* intermediates as the compound undergoes demanding conformational changes. These observations are similar to those made by Fujita and coworkers who found that a Pd₁₂L₂₄ cage assembly appended with AZB units was able to achieve a photostationary state comprised of 17% *cis* isomers but further irradiation time yielded no further isomerisation.²⁷ The free ligand by comparison, achieved a photostationary state with 67% *cis* isomers. Curiously, visible light was ineffective in encouraging the *cis*→*trans* isomerisation of Fujita's cage which proceeds by heating. This contrasts with the examples presented here which exhibit highly efficient visible light promoted *cis*→*trans* isomerisation. It has also been shown in a series of azo-containing polymers that rotational restrictions can restrict or even fully prevent isomerisation.⁷¹

The difficulty in switching Fujita's Pd₁₂L₂₄ cage was ascribed to the dominant absorption of a Pd-Py MLCT band in the same region as the azo π → π^* band.²⁷ This could also be a contributing factor for the metallocages discussed here as the azo π → π^* band overlaps with Ir(III) MLCT and LMCT bands. The preparation of organic analogues of these coordination cages could potentially overcome such a limitation but would present a significant synthetic challenge. Moreno and coworkers have recently shown that careful substitution of the AZB unit at the ortho position causes a significant red shift of the absorption wavelength enabling selective irradiation of the azo π → π^* band even in the presence of [Ir(ppy)] units.⁷²

Energy transfer between the two chromophores *via* mechanisms such as Förster resonance energy transfer (FRET) is also a possible concern as this could result in the transfer of energy away from the AZB unit to the iridium(III) centre, thus providing a quenching mechanism for the isomerisation. The reverse process – transfer of energy *via* FRET from an iridium(III) complex to an AZB unit has been demonstrated by Shiu and coworkers who exploited this phenomena to develop a sensing system for cysteine and homocysteine.⁷³ This is a possible explanation for the poor quantum yields of luminescence observed in these complexes (discussed further in section 4.9).

Additionally, several reports have noted that confinement of the AZB chromophore within the framework of different dendrimers appears to yield poorer conversion of the *trans*→*cis* isomerisation than when the azo units were located on the dendrimer periphery.^{31,32,37} Freixa and coworkers have prepared a series of AZB appended Ir(III)

complexes where the azo unit is attached to a bipyridine auxiliary ligand.⁷⁴ The authors experienced considerable difficulty in achieving an efficient *trans*→*cis* isomerisation compared to the free ligands which isomerise with high efficiency; this discrepancy was once again ascribed to the overlap of the azo π → π^* transition with the ³MLCT transition of the iridium (III) centre. A simplified schematic is shown in figure 4.32. Photoirradiation of isolated AZB leads to isomerisation in the excited state (figure 4.32a) whereas the excited state in the iridium complexes can also undergo S_1 → T_1 crossing promoted by the large spin-orbit coupling of the Ir(III) centre, thus providing a competing pathway to isomerisation.

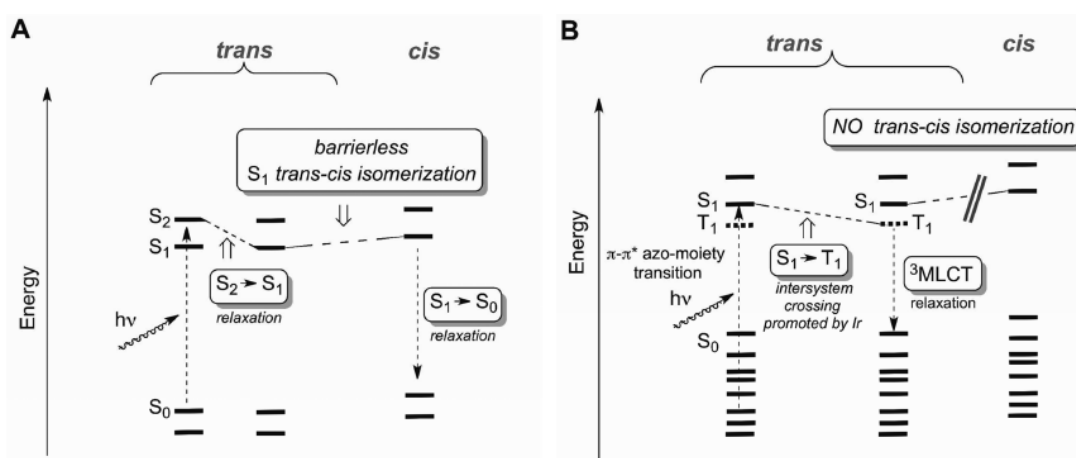


Figure 4.32: Schematic representation of the energy levels involved in the photoisomerisation of **a.** isolated azobenzene; **b.** A model azobenzene-iridium (III) complex, showing the competing pathway provided by excitation of the Ir (III) centre. Reprinted with permission from 'A. Telleria, J.P Miqueo, A. Altube, E. G. Lecina, A. Cozar and Z. Freixa, *Organometallics* 2015, **34**, 5513-5529.' Copyright 2015 American Chemical Society.

The conversion between isomers can be monitored for all of the cage compounds for both their *trans*→*cis* and *cis*→*trans* isomerisations and is summarised in table 4.2. Typical conversion (*trans*→*cis*) is between 30-40% with the reverse reaction (*cis*→*trans*) giving practically quantitative conversion after just 15 minutes. This is superior to the conversion achieved by Fujita's Pd₁₂L₂₄ cage (*trans*→*cis* of 20%) which was capable of regulating guest uptake and release.²⁷ These conversions also compare favourably with several other supramolecular examples of AZB photoswitching.^{21, 29, 30} Intriguingly, the only cage bearing a 4-pyridyl substituent (cage **3.9**) once again performs poorly with only 16% conversion from *trans*→*cis*.

Given that all the cages bearing 3-pyridyl substituents isomerise with reasonable consistency, this may hint at a potential angular strain present in the 4-pyridyl cage that makes the photoisomerisation more difficult.

Table 4.2: Conversion efficiency between isomers of metallocages; a = after irradiating at λ_1 until a photostationary state is generated; b = after 15 minutes irradiation at λ_2 .

Compound	$\lambda_{1 \text{ max}}$ (nm)	Conversion (% <i>trans</i> → <i>cis</i>) ^a	$\lambda_{2 \text{ max}}$ (nm)	Conversion (% <i>cis</i> → <i>trans</i>) ^b
3.8 (3py ester; unsubstituted Ir tecton)	355	39	450	94
3.9 (4py ether, unsubstituted Ir tecton)	355	16	450	99
3.10 (3py ether, unsubstituted Ir tecton)	355	40	450	100
3.11 (3py ester, methylated Ir tecton)	355	30	450	95
3.12 (3py ester, fluorinated Ir tecton)	355	26	450	94

The formation of the 3-pyridyl cages was somewhat unexpected given the preference for the 4-pyridyl isomer observed previously by Hardie.⁷⁵ A possible explanation for the increased isomerisation efficiency of the 3-pyridyl cages is that they are somewhat distorted which may make photoswitching easier to accommodate; obtaining a crystal structure could provide evidence for this hypothesis.

The photochemical fatigue of the isomerisation process was also measured using UV visible spectroscopy. Although a single isomerisation between *trans* and *cis* is enough to probe the uptake and release of guest molecules, many cycles with no fatigue is a valuable property in the use of photochromic compounds in molecular electronics.⁷⁶ Repeated cycles of *trans*→*cis* photoisomerisations were therefore conducted on metallocage **3.9**, as summarised in figure 4.33.

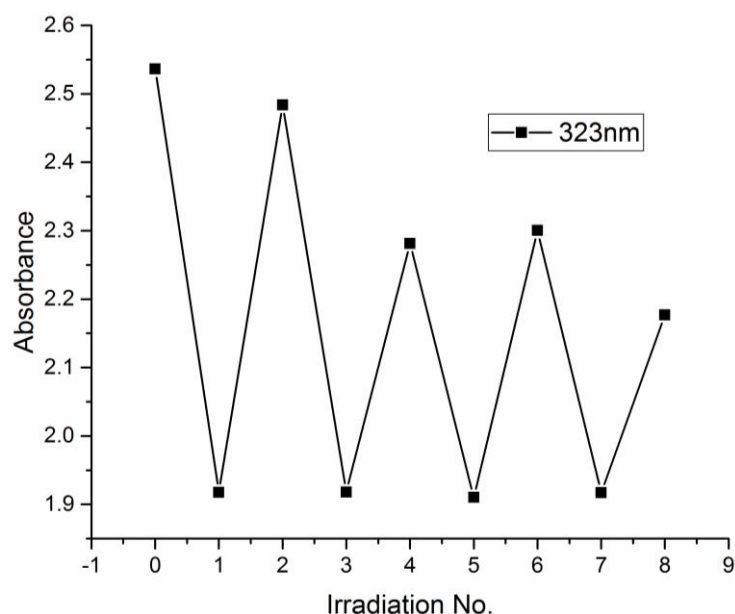


Figure 4.33: Cycles of *trans-cis* irradiation of compound **3.9** showing the changes to the absorbance at 320 nm.

As can be seen, as the cycle number increases, the cages begin to experience a reasonable degree of photochemical fatigue. Interestingly this seems to be localised on the *cis*→*trans* reaction which would have been expected to be the more reliable isomerisation. This indicates that some form of stable *cis* isomer is accumulating which is resistant to reversion to the *trans* isomer. This is in concurrence with observations made during the ^1H NMR study of the analogous free ligand **2.12** which showed high levels of thermal *cis*-stability along with a small proportion of *cis*-isomers resisting photochemical reversion to the *trans* state (as discussed in section 4.3). These levels of fatigue unfortunately preclude the use of these systems in any kind of molecular electronic applications which require a resistance to photochemical fatigue but they may well retain enough photoswitching properties to enable control of guest uptake and release.

4.8 ^1H NMR study of cage **3.12** photoisomerisation

The addition of fluorine groups into the cage design *via* the fluorinated metallotecton **3.7** rendered the resulting cage compound **3.12** sufficiently soluble in CH_2Cl_2 for ^1H NMR studies to be undertaken. Metallocage **3.12** was dissolved in d_2 -DCM and an initial ^1H NMR spectrum recorded (figure 4.34a). The sample was then transferred to a quartz cuvette and exposed to laser irradiation using a 355 nm Nd:YAG laser (10Hz, 15mJ/shot) for 200 seconds to rapidly generate the photostationary state by inducing *trans*→*cis* isomerisation. The ^1H NMR spectrum was then recorded (figure 4.34b) along with the mass spectrum (figure 4.35). The sample was then irradiated once more

with blue light (figure 4.34c) for 40 minutes using a Xe lamp to promote the *cis*→*trans* reaction.

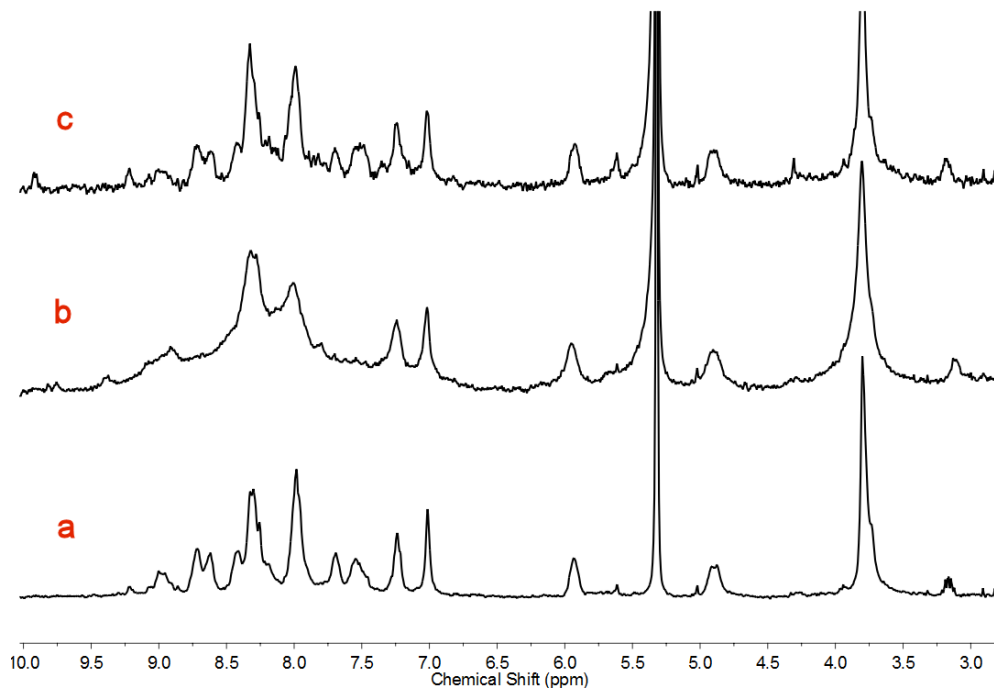


Figure 4.34: Photoisomerisation of metallocage **3.12** in d_2 -DCM; **a**. Initial spectrum of cage **3.12**; **b**. After irradiation for 200 seconds with Nd:YAG laser (355 nm, 10Hz); **c**. Re-irradiation for 40 minutes with Xe lamp (450nm).

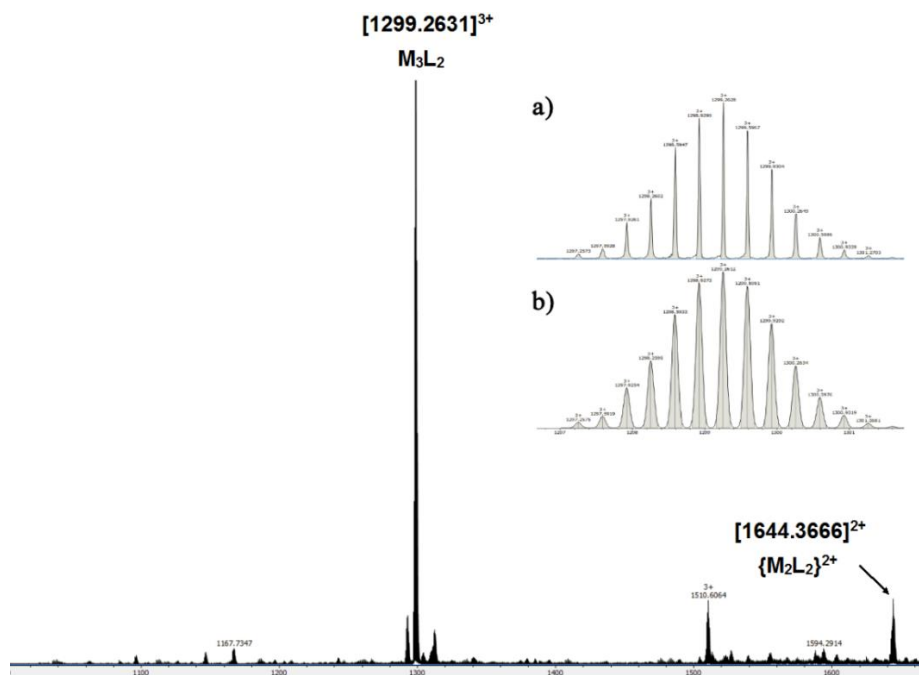


Figure 4.35: ESI-Mass spectrum of cage **3.12** taken after 200 seconds of irradiation with 355nm Nd:YAG laser in CH_2Cl_2 .

The ^1H NMR spectrum taken after irradiation of the sample is extremely broad and unfortunately no meaningful information about the composition of the photostationary state can be extracted from it. A full comparison with the UV spectra is therefore not possible. Resolution of optically pure iridium precursors (as demonstrated by Lusby)⁷⁷ could potentially help to reduce the mixture of isomers present at the photostationary state. Encouragingly, the mass spectrum taken at this time is extremely clear with the main peak corresponding to the intact M_3L_2 metallocryptophane despite very harsh irradiation conditions (due to the faster pulse sequence of 10Hz, this experiment delivers far more energy to the system than in any of the UV experiments). This suggests that the cage does not degrade when irradiated and the changes observed in the ^1H NMR spectrum can be ascribed to photoisomerisation. It is however plausible that individual ligand arms could be detaching from the Ir(III) centres and undergoing photoisomerisation without the cage collapsing (this would still result in the M_3L_2 ion in the mass spectrum).

Upon irradiation with blue light for 40 minutes, pleasingly the spectrum regains much of its former structure (figure 4.33c). The broad mass between 9.3 and 7.0ppm is replaced with assignable peaks which indicates the successful reformation of the starting all *trans* cage. Mass spectrometry of this solution confirms the M_3L_2 arrangement as the main species still in solution thus ruling out a structural rearrangement such as those observed by Lees¹⁹ or Clever.⁷⁸ Again similarities to the free ligand behaviour are observed with residual peaks appearing in the aromatic region which may be due to unusually stable residual *cis* isomers. Further irradiation of the sample, even up to periods of an hour, do not result in any further changes to the spectrum. These observations are consistent with the UV study which also indicated an incomplete conversion to the resting *trans* state (approx. 94% reconversion) and may be responsible for the photochemical fatigue observed for cage **3.11**.

The composition of this photostationary state, as was found for the isolated free ligand (section 4.3), is complex and likely to consist of a mixture of different isomers rather than any one isomer in particular; this is further complicated by the presence of six AZB units per cage. This is likely to be the cause of the extremely broad ^1H NMR spectrum observed. Although the process does not appear to be as smooth as the photoisomerisations performed by Clever,²⁴ a significant perturbation of the resting *trans* state is obtained after irradiation which mass spectrometry suggests is not due to the formation of any decomposition products. The structural perturbation involved in AZB *trans/cis* isomerisation is also much greater than that of dithienylethene ring opening/closing so it is to be expected that these systems suffer in terms of efficiency

compared to those reported by Clever; this is reflected in the molecular models of metallo cage **3.8** which are discussed in chapter 3. Unfortunately, attempts to try and elucidate any further information about the composition of the photostationary state using DOSY NMR were unsuccessful due to a rapidly changing equilibrium of isomers during the timescale of the experiment (several hours).

Although few literature examples exist of systems bearing six AZB units, a few parallels can be drawn with the dendrimer prepared by McGrath and coworkers prepared bearing six AZB units which presented a similar conundrum of a complex photostationary state.³³ Owing to the greater polarity of the *cis* azo units, they were able to show *via* thin-layer chromatography (TLC) that all six possible isomers (EEEEEE, EEEEEZ, EEEEEZ, EEEZZZ, EEZZZZ, EZZZZZ and ZZZZZZ) were present at the photostationary state, which is likely also the case with the species studied here. GPC traces indicated the hydrodynamic volume of the dendrimer altered by up to 30% upon irradiation.

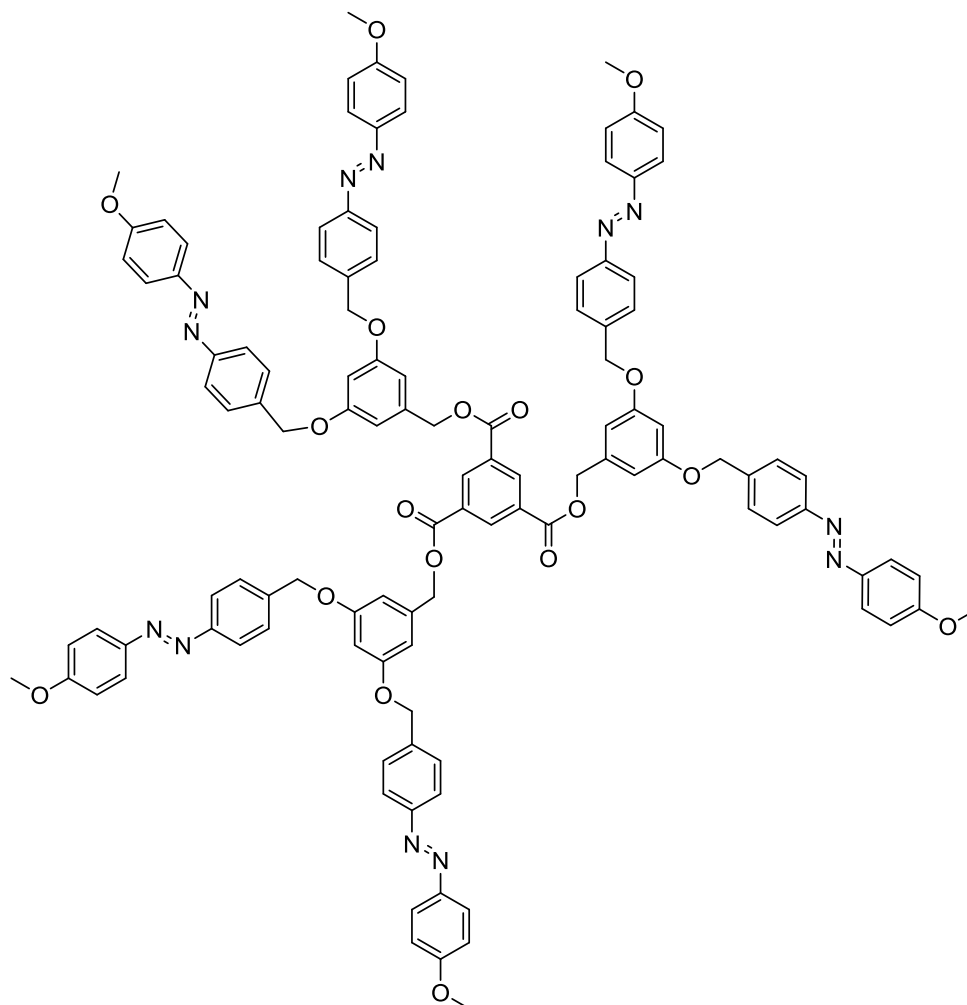


Figure 4.36: Dendrimeric species prepared by McGrath containing six AZB units.³³

Similarly, Norikane and coworkers prepared a series of organic macrocycles containing two, three or four AZB units.⁷⁹ Upon photoirradiation, high-performance liquid chromatography (HPLC) techniques could be used to detect and quantify the proportions of isomers present at the photostationary state with once again a mixture of isomers being generated. A reasonably significant perturbation of the resting *trans* state of the metallocages is observed here; whether this is significant enough for applications in molecular recognition remains an exciting outlook for further research.

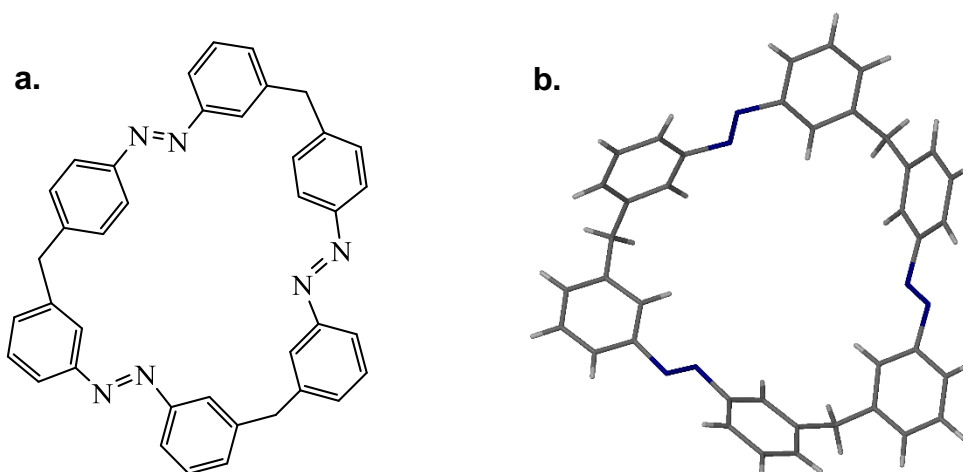


Figure 4.37: Macrocycle prepared by Norikane containing multiple azo units showing a. Chemical structure; b. SCXRD structure. Solvents of crystallisation have been omitted for clarity. The CH₂ spacers allow efficient photoisomerisation which generate a mixture of product isomers.

4.9 Photophysics of Metallocryptophanes

The presence of the iridium phenylpyridine moiety in these systems make them candidates for luminescent output akin to that observed in similar CTV based systems prepared by Hardie.^{75, 80, 81} Few examples of this moiety in metallocages exist in the literature.^{77, 82} Of particular interest was the impact of the AZB unit on the luminescence output. Freixa and coworkers have demonstrated that iridium (III) complexes bearing cyclometallated⁸³ or bipyridyl appended^{74, 84} AZB units have negligible luminescence output owing to the trapping of electrons in the MLCT excited state by the azo group.⁸⁵ Upon reduction of the azo bond, luminescence output was regenerated, enabling the application of these compounds as sensors for reducing agents such as sulphite.⁸⁶ Additional examples of photophysical properties being regulated by the azo group have been reported with ruthenium^{85, 87} and rhodium⁸⁸ complexes.

The photophysical studies of cages **3.8**, **3.9**, **3.10** and **3.11** were performed at the University of St. Andrews by Diego Rota Martir of the Zysman-Colman research group. All photophysical studies were performed in non-coordinating DCM solvent to prevent any potential cage degradation. In addition to this, cages were spin coated onto a polymethylmethacrylate (PMMA) inert matrix in order to inhibit vibrational quenching of luminescence. The photophysical data for all cages is summarised in table 4.3, below:

Table 4.3: Photophysical properties of metallocryptophanes.

	λ_{em} (nm) ^{a,b}		Φ_{PL} (%) ^c		τ_e ^a	
	DCM	Film ^d	DCM	Film ^{d,e}	DCM (ns) ^f	Film (ns) ^{d,f}
3.8	414 (0.8), 434 (1), 466 (0.7)	452	1.3	1.7	6.0 (69), 20.8 (13), 262.5 (18)	7.4 (49), 56.3 (10), 2922 (41)
3.9	410 (0.7), 432 (1), 464 (0.7)	430	0.8	0.9	1.5 (85), 4.5(10), 13.1 (5)	1.7 (24), 9.2 (54), 54.8 (22)
3.10	413 (0.7), 437 (1), 459 (0.8)	436	0.7	1.0	1.5 (82), 4.7 (12), 13.2 (6)	1.3 (41), 6.6 (48), 33 (11)
3.11	414 (0.8), 438 (1), 464 (0.9)	446	1.5	1.9	7.2 (70), 24.0 (11), 274.9 (19)	7.4 (47), 56.9 (10), 3002 (43)

^a Measurements in degassed DCM at 298 K. ^b Principal emission peaks listed with values in brackets indicating relative intensity. ^c Quinine sulfate employed as the external reference ($\Phi_{PL} = 54.6\%$ in 0.5 M H₂SO₄ at 298 K).⁸⁹ ^d PMMA doped films (5 wt % of complexes) formed by spin-coating deposition on quartz substrate. Photoluminescence quantum yield (PLQY) measurements were carried out under nitrogen. ^e Values obtained using an integrating sphere. ^f Values in parentheses are pre-exponential weighting factor, in relative % intensity, of the emission decay kinetics ($\lambda_{ex} = 378$ nm).

The cages are weakly emissive in both DCM solvent and in the PMMA matrix. Spin coating onto such a matrix can often serve to enhance Φ by mitigating non-radiative decay pathways that arise from vibrational modes. With the AZB cages, whilst Φ improves slightly in the PMMA matrix, this strategy does not have the same magnitude of effect as seen in the metallocryptophanes prepared by Hardie⁷⁵ which

showed a markedly improved Φ in the PMMA matrix (5.5%) compared to in DCM solvent (1%). The emission lifetime τ_e of the ester linked cages **3.8** and **3.11** was significantly enhanced by the matrix however (2922 and 3002 ns) than in DCM (265 and 272 ns). The ether linked cages **3.9** and **3.10** show minimal changes in either Φ or τ_e between DCM and PMMA matrix suggesting that their emission properties are ligand based, since ligand-based emission would be less affected by vibrational quenching. The short lifetimes of all the emissive bands in these ether-linked cages support this conclusion as they are indicative of short-lived organic based transitions. The longer-lived emission observed at 466 nm and 464 nm in complexes **3.8** and **3.11** respectively are more likely to be arising due to metal-based phosphorescence.

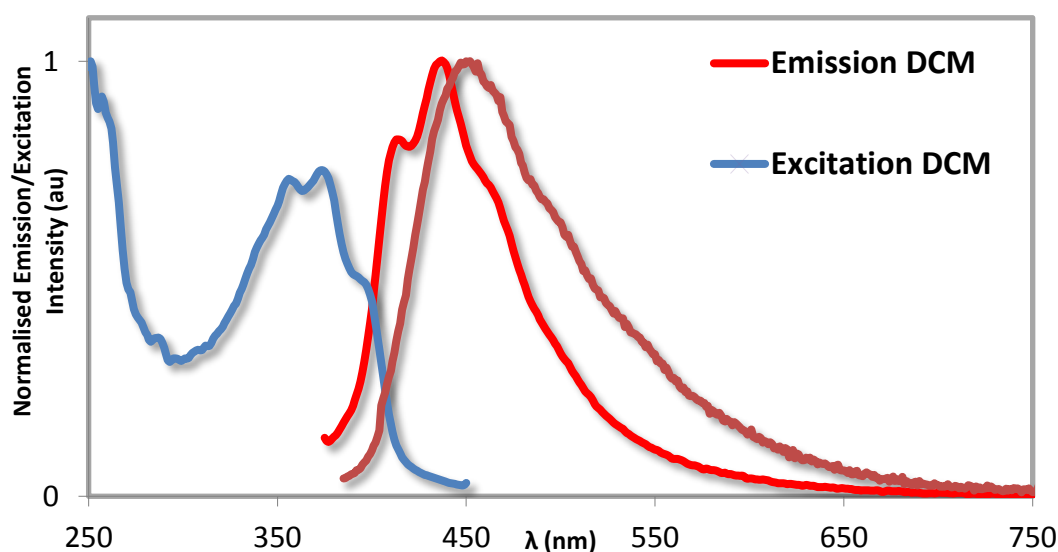


Figure 4.38: Emission profile of ester complex **3.8** in DCM solvent and doped film.

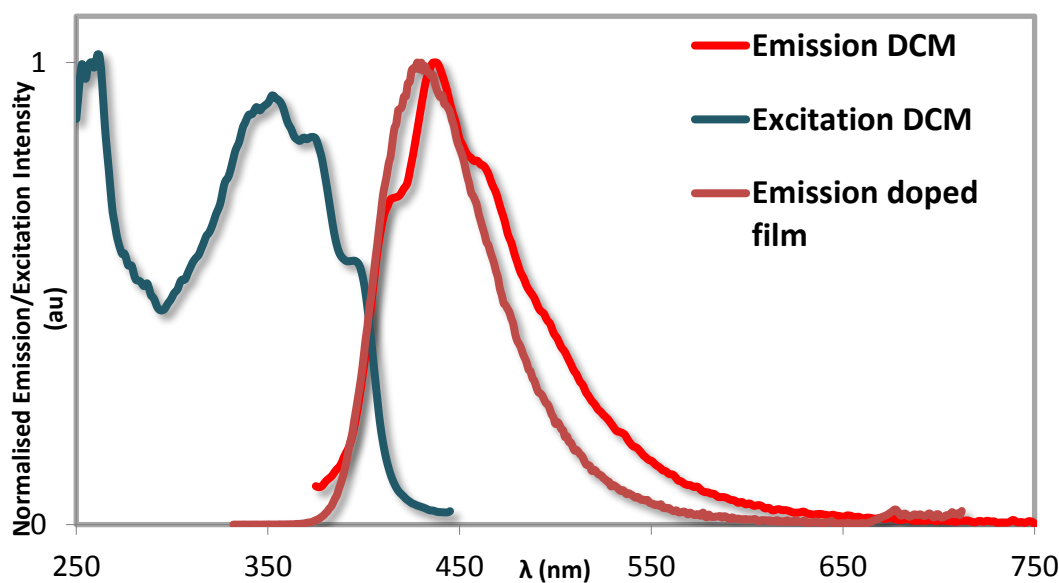


Figure 4.39: Emission profile of ether complex **3.9** in DCM solvent and doped film.

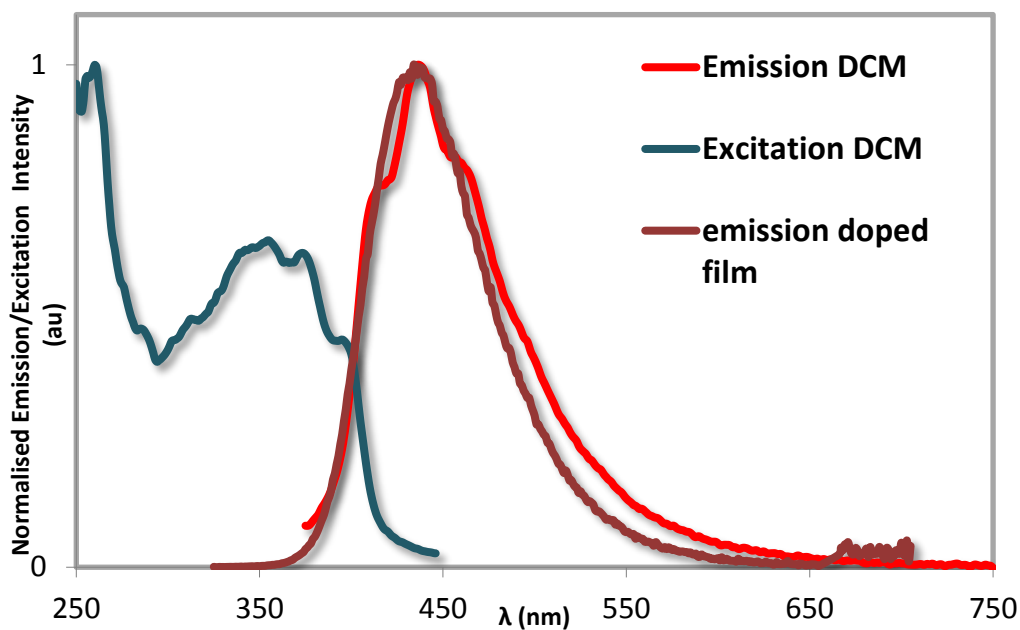


Figure 4.40: Emission profile of ether complex **3.10** in DCM solvent and doped film.

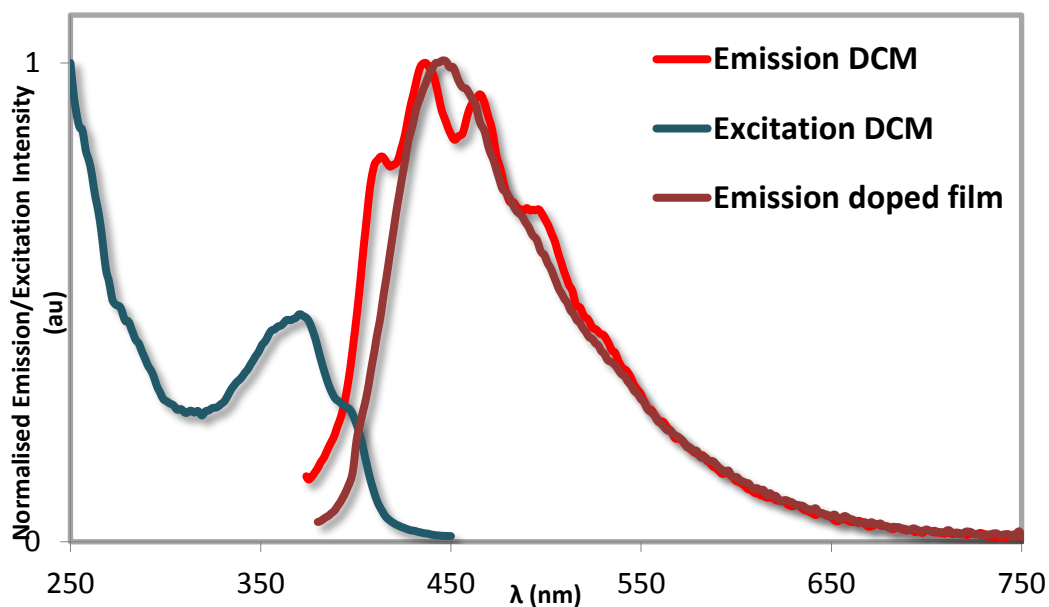


Figure 4.41: Emission profile of ester complex **3.11** in DCM solvent and doped film.

An interesting effect is the noticeably blue emission of all the metallocryptophanes. The emission of the metallocryptophanes prepared by Pritchard was tunable depending on the linkage to the CTG unit with an ester linkage giving rise to a yellow-orange emission (λ_{em} 604 nm in DCM) and an ether linkage giving a cyan emission (λ_{em} 485 nm in DCM).⁷⁵ The AZB metallocryptophanes are indifferent to the presence of different linkers to the CTV scaffold, with all cages giving rise to a deep blue emission (λ_{em} 410-414 nm in DCM). This indicates a large HOMO-LUMO gap which is likely a consequence of the electron-withdrawing nature of the azo group. This blue

emission is somewhat challenging for cationic Ir(III) complexes⁹⁰ owing to the population of non-emissive metal centred states as the HOMO-LUMO gap increases. Strategies to prepare blue Ir(III) emitters have been reported⁹¹⁻⁹⁴ (and also their encapsulation in molecular hosts)⁹⁵ due to their potential in organic light emitting diodes (OLEDs). The slightly red-shifted λ_{em} observed for the ester linked cages **3.8** and **3.11** can be ascribed to increased conjugation into the CTV scaffold that is not possible in the ether linked assemblies.

The emission profile is similar in both DCM and PMMA matrix; this implies that vibrational quenching is not necessarily an important factor in the quenching of emission for these systems. This is supported by the low Φ in the PMMA matrix as limiting the vibrational modes has not meaningfully altered the quantum yields. Both of these observations indicate the emission is likely to be ligand centred since this would be least affected by vibrational quenching. A ligand centred process is also more likely to be responsible for the blue colour of the emission. The poor Φ observed for these systems is not necessarily surprising as despite the indifference to vibrational quenching, there are certain to be other methods of non-radiative decay in such a complex system, the mechanisms of which are also likely to be complex.

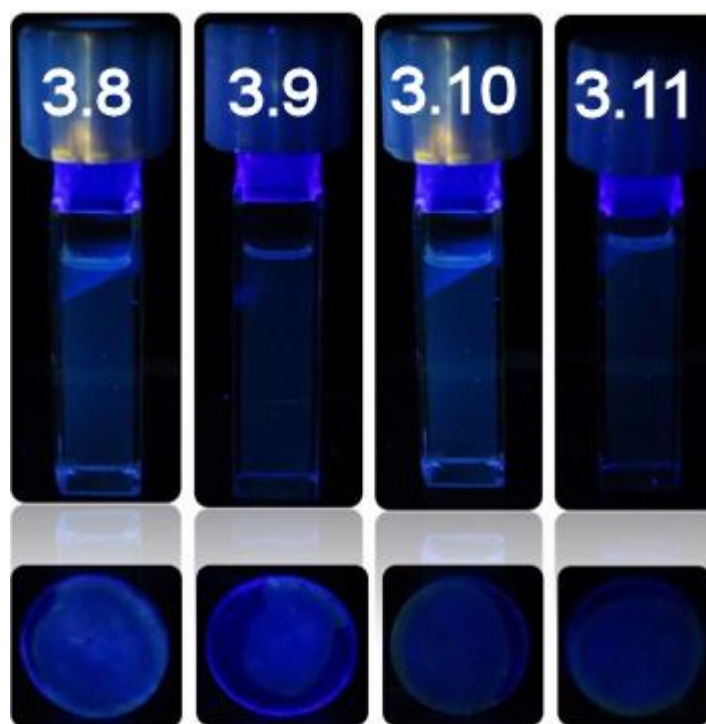


Figure 4.42: Dark-room images of cages 3.8, 3.9, 3.10 and 3.11 showing the blue emission after irradiation with 360 nm light; top: solution in DCM solvent; bottom: powder.

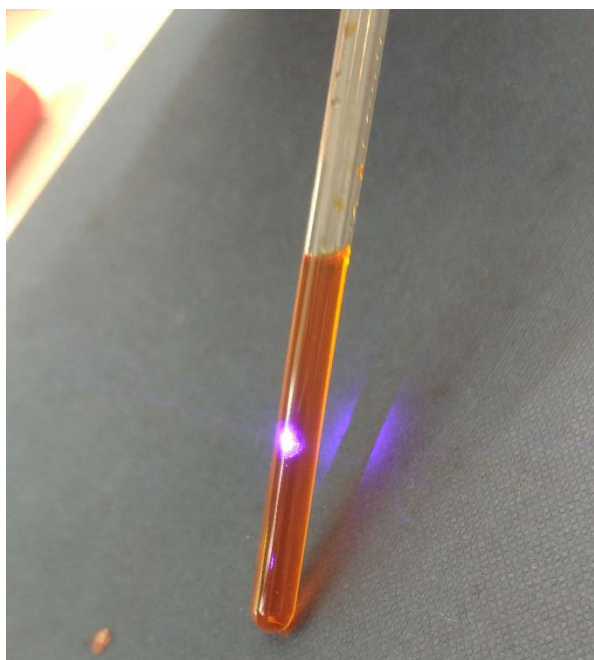


Figure 4.43: Solution phase emission of cage **3.9** in CD_3NO_2 upon excitation with a 405 nm laser pen.

4.10 Conclusions and further direction

The connection of the AZB unit to CTG does not impede the photoisomerisation of the AZB unit in the free ligands. Smooth conversion between the *trans* and *cis* isomers of the AZB units is observed by UV spectroscopy using UV light to induce *trans*→*cis* isomerisation and blue light to induce *cis*→*trans* isomerisation. The nature of the photostationary state was probed *via* 1H NMR and was revealed to be a complex mixture of isomers, with no particular species favoured over the others. Upon re-irradiation with blue light, a small amount of stable *cis* isomer remains present. Switching between an ester and ether linkage has a dramatic effect on the rate of thermal isomerisation from the *cis* to the *trans* isomer with the ester linked ligand being somewhat more resistant to thermal *cis*→*trans* isomerisation.

The photoswitching of the metallocryptophanes is much more challenging than the isolated ligands, likely a consequence of tethering the azo unit to the Ir(III) centre or absorption of Ir centred MLCT transitions in the same region as the azo π → π^* transition. Despite this, upon employing a powerful irradiation source (355nm Nd:YAG laser), the generation of *cis* isomers can be achieved, typically in a 30-40% conversion as studied by UV spectroscopy. All cages reach a photostationary state at this point where no further isomerisation is possible. This is presumably due to further isomerisation requiring a structural rearrangement that is not possible in the tethered metallocages and is observed in other metallocages.²⁷ The potential for non-radiative

decay processes is complicated further by processes such as FRET which could lead to energy transfer between the azobenzene and the Ir(III) chromophores. A full description of the photophysical behaviour of these systems is likely to be highly complex but could be studied using computational methods such as density functional theory (DFT).

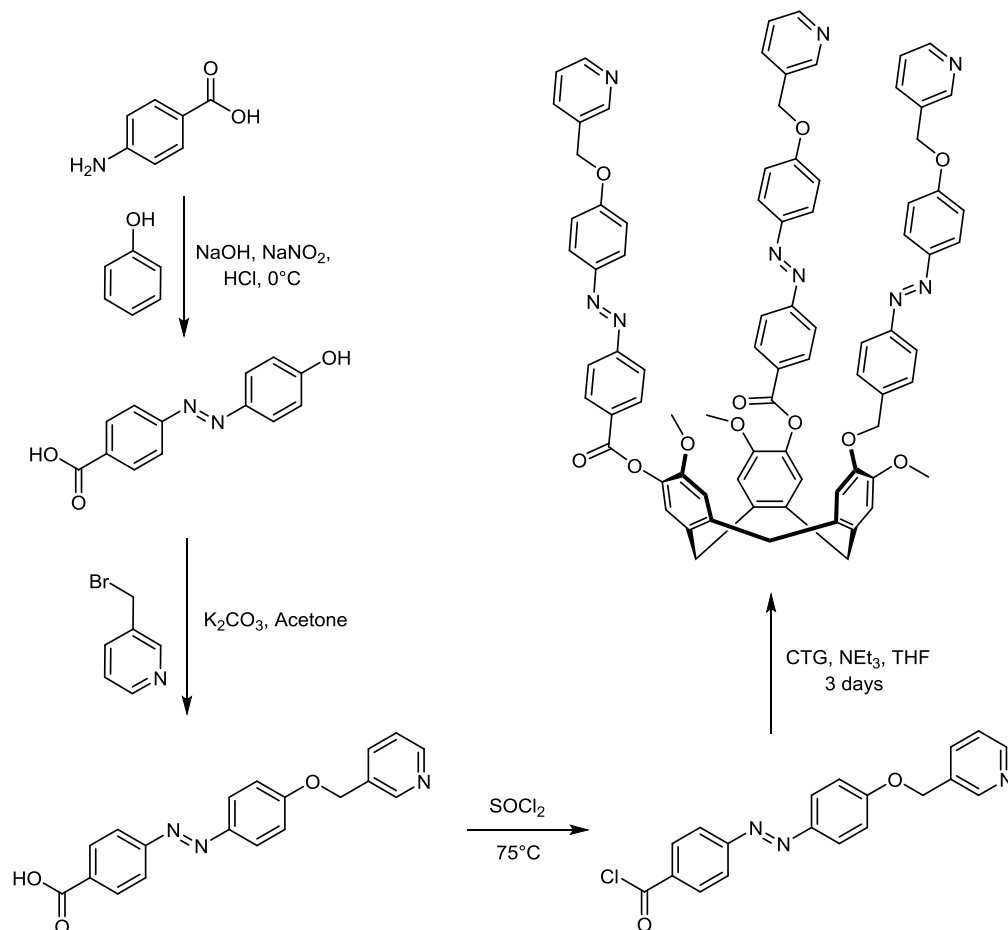
These systems represent a highly unusual class of coordination cages that have photoresponsive characteristics and, to the best of the author's knowledge, the very first examples of coordination cages with embedded AZB units that undergo photoisomerisation. Several studies of dendrimers embedded with AZB units have observed a decrease in *trans*→*cis* conversion efficiency with increasing dendrimer generation.^{5, 31, 32, 96} A fatigue study of the cages reveal that they also show some degree of photochemical fatigue.

The introduction of fluorine groups on the phenylpyridine ancillary ligands (see chapter 2 for synthetic details) successfully solubilised the fluorinated cage **3.12** in DCM to allow a ¹H NMR study to be performed. Upon irradiation of the sample, a significant loss of resolution was observed along with severe broadening of the spectrum. This is likely to be caused by a multitude of isomers in the photostationary state; the broad nature of the spectrum makes the extraction of any further information difficult. The mass spectrum of this solution showed intact cage species with no evidence of cage degradation. Upon re-irradiation with blue light, the spectrum regains much of its former structure, once again a small amount of *cis* isomer remains present however.

The photoswitching properties of the cages could allow control of the uptake and release of guest molecules, which is an obvious point for further study. Perhaps the greatest drawback of these metallocryptophanes is their poor solubility, with only the fluorinated example soluble in DCM; the use of more coordinating solvents compromises the cage integrity. In addition to this, the cages seem to have a limit to their conversion to a *cis*-rich state which is hypothesised to be due to their tethering to the Ir(III) centre.

A potential way to avoid this would be the incorporation of a ligand where the azo unit is completely isolated from the iridium unit which would allow uninhibited photoisomerisation. The design of such a ligand is indicated in scheme 4.1; the proposed synthesis can be tailored to have the same number of synthetic steps as the some of the current ligands. Diazotization of commercially available 4-aminobenzoic acid would furnish the N=N bond as reported by Palmer and coworkers.⁹⁷ The free hydroxyl group could then be appended with the metal-coordinating pyridyl unit

(commercially available) before connection of the full arm to CTG using methodology described in chapter 2. The presence of the OCH₂ unit should allow free rotation of the azo unit upon irradiation and thus may lead to cages with better conversion and fatigue efficiency; Norikane's azo macrocycles containing CH₂ spacers undergo photoisomerisation with a good quantum yield.⁷⁹



Scheme 4.1: Proposed synthetic route to ligands incorporating a spacer unit between the AZB unit and the Ir(III) centre.

Another method to overcome this limitation is the use of a photoswitching unit which has a mechanism of switching that is less likely to be impacted by the Ir(III) centre. Once again, the best candidate for such a purpose in the dithienylethene (DTE) photoswitch. This system is likely to be unaffected by the presence of metal-coordinated pyridyl units. Lehn has prepared a series of metal complexes bearing pyridyl-appended DTE ligands.^{98, 99} Upon irradiation with UV light, conversions of up to 90% between the open/closed isomeric forms was achieved. Tian has shown this photoswitch remains active even when the DTE unit is cyclometallated to the Ir(III) complexes.^{100, 101} Several other complexes bearing the DTE unit with Ir(III)^{100, 102-104} and other metals have also been reported.^{105, 106} The subtle nature of the

conformational switching in DTE derivatives gives them high efficiency and fatigue resistant properties⁷⁶ but would likely be less effective for inducing guest-uptake and release. Whether a higher conversion could be achieved with the DTE analogues of these metallocages, and whether this would enable efficient control over guest uptake and release, are interesting points for further investigation.

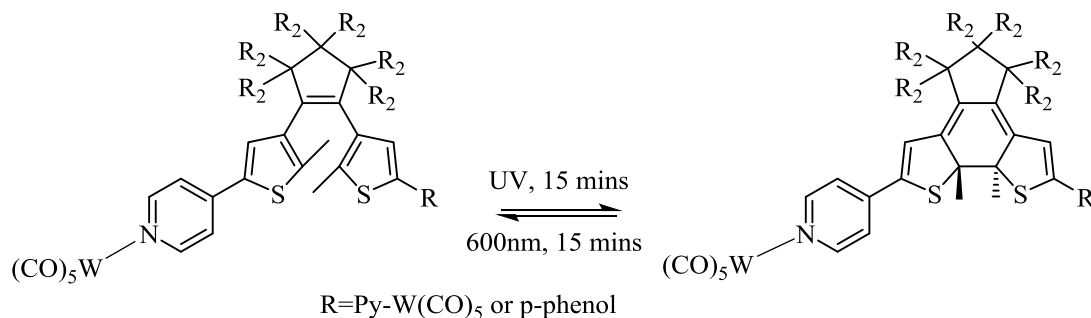


Figure 4.44: Metal coordinated dithienylethene photoswitches prepared by Lehn.⁹⁸

Despite the metal-coordinated pyridyl unit, these systems show impressive conversions of 90% between isomers with short irradiation times.

Preliminary studies have also been conducted on the stilbene analogue of ligand **2.12**. The ligand undergoes efficient photoreaction to form a new species which is assigned as the *cis* isomer; however currently all attempts to induce the reverse reaction and regenerate the resting *trans* isomer have been unsuccessful. As such, the nature of the photostationary state is currently unclear. Further study of this ligand and the stilbene metallocage could offer interesting mechanistic insights in comparison to the AZB system since stilbenes are known to undergo isomerisation exclusively by rotation.

The photophysical properties of the systems have been explored and all complexes display a deep blue emission which is uncommon for cationic Ir(III) complexes. However the quantum yield Φ and lifetime τ_e of the emission are low in all cases which unfortunately precludes their use in luminescent devices. The exact mechanism of emission quenching remains unclear without further investigation but is likely to be a consequence of the large HOMO-LUMO gap typical of blue emitters which leads to non-radiative decay from non-emissive metal centred states.

4.11 Experimental

4.11.1 General considerations

¹H NMR spectra were recorded on a Bruker DPX 300MHz and a Bruker AscendTM 400MHz NMR spectrometer. High-resolution electrospray mass spectra (ESI-MS) were recorded on a Bruker micro-TOF-Q mass spectrometer UV-Visible spectra were

recorded on a Lambda 900 UV/Vis spectrophotometer and an Agilent Cary 100 UV/Vis spectrophotometer.

Photoisomerisation studies of free ligands were performed using a 75W Xenon lamp equipped with a tunable PowerArc monochromator. Use of the monochromatic wavelength selector results in much of this energy being filtered out. Experimental energy levels were found to be <1mW of energy being supplied to the sample. This is likely to be a contributing factor for the slow rate of isomerisation observed for the metallocages.

Photoisomerisation studies of the metallocages and NMR studies of the free ligands were conducted using a Continuum Powerlite 8010 355 nm Nd:YAG laser. For experiments requiring a frequency of 10Hz, the natural frequency of the laser (10Hz) was employed without interference. For experiments requiring a frequency of 1Hz, the excited population was split after 200 μ s using a Q-switch in pulse divide mode set at a frequency of 1Hz.

4.11.2 UV studies of free ligands

Trans→*cis* isomerisation: A 30 μ M solution of the appropriate ligand in DMSO was prepared and the UV spectrum recorded. The sample was irradiated at λ_1 for 45 minutes using a 75W Xenon lamp equipped with a tunable power arc monochromator to induce *trans*→*cis* isomerisation. The UV spectrum of this solution was then recorded for comparison.

Cis→*trans* isomerisation: The solution was irradiated at λ_2 for 15 minutes using a 75W Xenon lamp equipped with a tunable power arc monochromator to induce *cis*→*trans* isomerisation. The UV spectrum of this solution was then recorded for comparison.

4.11.3 ¹H NMR studies of free ligands

Generation of photostationary state (*Trans*→*cis* isomerisation): An NMR sample of the appropriate ligand in CD₂Cl₂ was prepared and the ¹H NMR spectrum recorded. The sample was irradiated at 355 nm using a Nd:YAG laser (10Hz, 15mJ/laser pulse) and ¹H NMR spectra were recorded at various intervals.

Cis→*trans* isomerisation: The solution was irradiated at 450 nm for 15 minutes using a 75W Xenon lamp equipped with a tunable power arc monochromator to induce *cis*→*trans* isomerisation. The ¹H NMR spectrum of this solution was then recorded for comparison.

4.11.4 UV studies of metallocryptophanes

Trans→*cis* isomerisation: A 30 μM solution of the appropriate metallocage in DCM was prepared and the UV spectrum recorded. The sample was irradiated at 355 nm using a Nd:YAG laser (1Hz, 15mJ/laser pulse) and UV spectra were recorded at various intervals.

Cis→*trans* isomerisation: The solution was irradiated at λ_2 for 15 minutes using a 75W Xenon lamp equipped with a tunable power arc monochromator to induce *cis*→*trans* isomerisation. The UV spectrum of this solution was then recorded for comparison.

4.11.5 ¹H NMR study of metallocryptophane 3.12

Generation of photostationary state (*Trans*→*cis* isomerisation): An NMR sample of metallocage **3.12** in CD₂Cl₂ was prepared and the ¹H NMR spectrum recorded. The sample was irradiated at 355 nm using a Nd:YAG laser (10Hz, 15mJ/laser pulse) for 900 seconds. The ¹H NMR spectrum of this solution was recorded for comparison.

Cis→*trans* isomerisation: The solution was irradiated at λ_2 for 15 minutes using a 75W Xenon lamp equipped with a tunable power arc monochromator to induce *cis*→*trans* isomerisation. The ¹H NMR spectrum of this solution was recorded for comparison.

4.11.6 Photophysical Studies

All samples were prepared at the University of St Andrews by Diego Rota Martir, in HPLC grade DCM with varying concentrations in the order of 10⁻⁴-10⁻⁶ M. Absorption spectra were recorded at room temperature using a Shimadzu UV-1800 double beam spectrophotometer. Molar absorptivity determination was verified by linear least-squares fit of values obtained from at least four independent solutions at varying concentrations with absorbance ranging from 6.05 × 10⁻⁵ to 2.07 × 10⁻⁵ M.

The sample solutions for the emission spectra were prepared in HPLC-grade DCM and degassed via freeze-pump-thaw cycles using a quartz cuvette designed in-house. Steady-state emission and excitation spectra and time-resolved emission spectra were recorded at 298 K using an Edinburgh Instruments F980. All samples for steady-state measurements were excited at 360 nm, while samples for time-resolved measurements were excited at 378 nm using a PDL 800-D pulsed diode laser. Emission quantum yields were determined using the optically dilute method.⁶⁴ A stock solution with

absorbance of *ca.* 0.5 was prepared and then four dilutions were prepared with dilution factors between 2 and 20 to obtain solutions with absorbances of *ca.* 0.095, 0.065, 0.05 and 0.018, respectively. The Beer-Lambert law was found to be linear at the concentrations of these solutions. The emission spectra were then measured after the solutions were rigorously degassed via three freeze-pump-thaw cycles prior to spectrum acquisition. For each sample, linearity between absorption and emission intensity was verified through linear regression analysis and additional measurements were acquired until the Pearson regression factor (R^2) for the linear fit of the data set surpassed 0.9. Individual relative quantum yield values were calculated for each solution and the values reported represent the slope value. The equation $\Phi_s = \Phi_r (A_r/A_s)(I_s/I_r)(n_s/n_r)^2$ was used to calculate the relative quantum yield of each of the sample, where Φ_r is the absolute quantum yield of the reference, n is the refractive index of the solvent, A is the absorbance at the excitation wavelength, and I is the integrated area under the corrected emission curve. The subscripts s and r refer to the sample and reference, respectively. A solution of quinine sulfate in 0.5 M H_2SO_4 ($\Phi_r = 54.6\%$) was used as external references.

PMMA doped films were prepared by spin coating the samples from a solution of 2-methoxyethanol (HPLC grade) containing 5 % w/w of the desired sample. Steady-state emission and excitation spectra and time-resolved emission spectra of both powders and doped films were recorded at 298 K using an Edinburgh Instruments F980. Solid-state PLQY measurements of thin films were performed in an integrating sphere under a nitrogen purge in a Hamamatsu C9920-02 luminescence measurement system.

4.12 References

1. C.-U. Bang, A. Shishido and T. Ikeda, *Macromolecular Rapid Communications*, 2007, **28**, 1040-1044.
2. F. Puntoriero, P. Ceroni, V. Balzani, G. Bergamini and F. Vögtle, *Journal of the American Chemical Society*, 2007, **129**, 10714-10719.
3. R. M. Parker, J. C. Gates, H. L. Rogers, P. G. R. Smith and M. C. Grossel, *Journal of Materials Chemistry*, 2010, **20**, 9118-9125.
4. G. S. Kumar and D. C. Neckers, *Chemical Reviews*, 1989, **89**, 1915-1925.
5. S. Yokoyama, T. Nakahama, A. Otomo and S. Mashiko, *Journal of the American Chemical Society*, 2000, **122**, 3174-3181.
6. M. R. Banghart, A. Mourot, D. L. Fortin, J. Z. Yao, R. H. Kramer and D. Trauner, *Angewandte Chemie International Edition*, 2009, **48**, 9097-9101.
7. L. Guerrero, O. S. Smart, G. A. Woolley and R. K. Allemann, *Journal of the American Chemical Society*, 2005, **127**, 15624-15629.
8. J. A. Phillips, H. Liu, M. B. O'Donoghue, X. Xiong, R. Wang, M. You, K. Sefah and W. Tan, *Bioconjugate Chemistry*, 2011, **22**, 282-288.
9. M. Volgraf, P. Gorostiza, S. Szobota, M. R. Helix, E. Y. Isacoff and D. Trauner, *Journal of the American Chemical Society*, 2007, **129**, 260-261.
10. C. A. Hunter, M. Togrul and S. Tomas, *Chemical Communications*, 2004, **0**, 108-109.
11. S. Shinkai, T. Minami, Y. Kusano and O. Manabe, *Journal of the American Chemical Society*, 1983, **105**, 1851-1856.
12. M. Irie and M. Kato, *Journal of the American Chemical Society*, 1985, **107**, 1024-1028.
13. O. B. Berryman, A. C. Sather, A. Lledó and J. Rebek, *Angewandte Chemie International Edition*, 2011, **50**, 9400-9403.
14. R. S. Stoll and S. Hecht, *Angewandte Chemie International Edition*, 2010, **49**, 5054-5075.
15. F. Würthner and J. Rebek, *Journal of the Chemical Society, Perkin Transactions 2*, 1995, **0**, 1727-1734.
16. F. Würthner and J. Rebek, *Angewandte Chemie International Edition in English*, 1995, **34**, 446-448.
17. A. A. Beharry, O. Sadovski and G. A. Woolley, *Journal of the American Chemical Society*, 2011, **133**, 19684-19687.
18. D. Bléger, J. Schwarz, A. M. Brouwer and S. Hecht, *Journal of the American Chemical Society*, 2012, **134**, 20597-20600.
19. S.-S. Sun, J. A. Anspach and A. J. Lees, *Inorganic Chemistry*, 2002, **41**, 1862-1869.
20. M. Liu, X. Yan, M. Hu, X. Chen, M. Zhang, B. Zheng, X. Hu, S. Shao and F. Huang, *Organic Letters*, 2010, **12**, 2558-2561.

21. A. Asadi, D. Ajami and J. Rebek, *Chemical Communications*, 2014, **50**, 533-535.
22. O. B. Berryman, A. C. Sather and J. Rebek Jr, *Chemical Communications*, 2011, **47**, 656-658.
23. E. Busseron, J. Lux, M. Degardin and J. Rebek, *Chemical Communications*, 2013, **49**, 4842-4844.
24. M. Han, R. Michel, B. He, Y.-S. Chen, D. Stalke, M. John and G. H. Clever, *Angewandte Chemie International Edition*, 2013, **52**, 1319-1323.
25. O. B. Berryman, H. Dube and J. Rebek, *Israel Journal of Chemistry*, 2011, **51**, 700-709.
26. M. Tominaga, K. Suzuki, M. Kawano, T. Kusukawa, T. Ozeki, S. Sakamoto, K. Yamaguchi and M. Fujita, *Angewandte Chemie International Edition*, 2004, **43**, 5621-5625.
27. T. Murase, S. Sato and M. Fujita, *Angewandte Chemie International Edition* 2007, **46**, 5133-5136.
28. J. Park, L.-B. Sun, Y.-P. Chen, Z. Perry and H.-C. Zhou, *Angewandte Chemie International Edition*, 2014, **53**, 5842-5846.
29. T. Muraoka, K. Kinbara, Y. Kobayashi and T. Aida, *Journal of the American Chemical Society*, 2003, **125**, 5612-5613.
30. T. Muraoka, K. Kinbara and T. Aida, *Nature*, 2006, **440**, 512-515.
31. S. Wang, X. Wang, L. Li and R. C. Advincula, *The Journal of Organic Chemistry*, 2004, **69**, 9073-9084.
32. R.-M. Sebastián, J.-C. Blais, A.-M. Caminade and J.-P. Majoral, *Chemistry – A European Journal*, 2002, **8**, 2172-2183.
33. L.-X. Liao, D. M. Junge and D. V. McGrath, *Macromolecules*, 2002, **35**, 319-322.
34. S. Li and D. V. McGrath, *Journal of the American Chemical Society*, 2000, **122**, 6795-6796.
35. D. M. Junge and D. V. McGrath, *Journal of the American Chemical Society*, 1999, **121**, 4912-4913.
36. D.-L. Jiang and T. Aida, *Nature*, 1997, **388**, 454-456.
37. D. Grebel-Koehler, D. Liu, S. De Feyter, V. Enkelmann, T. Weil, C. Engels, C. Samyn, K. Müllen and F. C. De Schryver, *Macromolecules*, 2003, **36**, 578-590.
38. N. Hosono, K. Omoto and S. Kitagawa, *Chemical Communications*, 2017, **53**, 8180-8183.
39. F. A. Arroyave and P. Ballester, *The Journal of Organic Chemistry*, 2015, **80**, 10866-10873.
40. L. Osorio-Planes, M. Espelt, M. A. Pericas and P. Ballester, *Chemical Science*, 2014, **5**, 4260-4264.
41. T. Sakano, T. Ohashi, M. Yamanaka and K. Kobayashi, *Organic & Biomolecular Chemistry*, 2015, **13**, 8359-8364.
42. K. Ichimura, S.-K. Oh and M. Nakagawa, *Science*, 2000, **288**, 1624-1626.

43. E. Merino and M. Ribagorda, *Beilstein Journal of Organic Chemistry*, 2012, **8**, 1071-1090.
44. H. M. D. Bandara and S. C. Burdette, *Chemical Society Reviews*, 2012, **41**, 1809-1825.
45. A. Goulet-Hanssens, M. Utecht, D. Mutruc, E. Titov, J. Schwarz, L. Grubert, D. Bléger, P. Saalfrank and S. Hecht, *Journal of the American Chemical Society*, 2017, **139**, 335-341.
46. H. Rau, *Angewandte Chemie International Edition in English*, 1973, **12**, 224-235.
47. K. M. Tait, J. A. Parkinson, S. P. Bates, W. J. Ebenezer and A. C. Jones, *Journal of Photochemistry and Photobiology A: Chemistry*, 2003, **154**, 179-188.
48. N. A. Wazzan, P. R. Richardson and A. C. Jones, *Photochemical & Photobiological Sciences*, 2010, **9**, 968-974.
49. Y. Norikane, R. Katoh and N. Tamaoki, *Chemical Communications*, 2008, **0**, 1898-1900.
50. D. G. Whitten, P. D. Wildes, J. G. Pacifici and G. Irick, *Journal of the American Chemical Society*, 1971, **93**, 2004-2008.
51. A. A. Blevins and G. J. Blanchard, *The Journal of Physical Chemistry B*, 2004, **108**, 4962-4968.
52. K. Uchida, S. Yamaguchi, H. Yamada, M. Akazawa, T. Katayama, Y. Ishibashi and H. Miyasaka, *Chemical Communications*, 2009, **0**, 4420-4422.
53. F. Bejarano, I. Alcon, N. Crivillers, M. Mas-Torrent, S. T. Bromley, J. Veciana and C. Rovira, *RSC Advances*, 2017, **7**, 15278-15283.
54. D. I. Schuster, B. Nuber, S. A. Vail, S. MacMahon, C. Lin, S. R. Wilson and A. Khong, *Photochemical & Photobiological Sciences*, 2003, **2**, 315-321.
55. V. Vicinelli, P. Ceroni, M. Maestri, M. Lazzari, V. Balzani, S.-K. Lee, J. v. Heyst and F. Vogtle, *Organic & Biomolecular Chemistry*, 2004, **2**, 2207-2213.
56. R. H. Dyck and D. S. McClure, *The Journal of Chemical Physics*, 1962, **36**, 2326-2345.
57. J. M. Rodier and A. B. Myers, *Journal of the American Chemical Society*, 1993, **115**, 10791-10795.
58. K. A. Muszkat and E. Fischer, *Journal of the Chemical Society B: Physical Organic*, 1967, **0**, 662-678.
59. R. Reuter, N. Hostettler, M. Neuburger and H. A. Wegner, *European Journal of Organic Chemistry*, 2009, **2009**, 5647-5652.
60. E. Bassotti, P. Carbone, A. Credi, M. Di Stefano, S. Masiero, F. Negri, G. Orlandi and G. P. Spada, *The Journal of Physical Chemistry A*, 2006, **110**, 12385-12394.
61. S. A. Nagamani, Y. Norikane and N. Tamaoki, *The Journal of Organic Chemistry*, 2005, **70**, 9304-9313.

62. Z. Ahmed, A. Siiskonen, M. Virkki and A. Priimagi, *Chemical Communications*, 2017, **53**, 12520-12523.
63. Y.-C. Lu, E. W.-G. Diao and H. Rau, *The Journal of Physical Chemistry A*, 2005, **109**, 2090-2099.
64. H. Rau, *Journal of Photochemistry*, 1984, **26**, 221-225.
65. H.-S. Tang, N. Zhu and V. W.-W. Yam, *Organometallics*, 2006, **26**, 22-25.
66. Y. Liu, J. F. Eubank, A. J. Cairns, J. Eckert, V. C. Kravtsov, R. Luebke and M. Eddaoudi, *Angewandte Chemie International Edition*, 2007, **46**, 3278-3283.
67. T. M. Reineke, M. Eddaoudi, D. Moler, M. O'Keeffe and O. M. Yaghi, *Journal of the American Chemical Society*, 2000, **122**, 4843-4844.
68. Z.-F. Chen, R.-G. Xiong, B. F. Abrahams, X.-Z. You and C.-M. Che, *Journal of the Chemical Society, Dalton Transactions*, 2001, **0**, 2453-2455.
69. V. Zeleňák, Z. Vargová, M. Almáši, A. Zeleňáková and J. Kuchár, *Microporous and Mesoporous Materials*, 2010, **129**, 354-359.
70. C.-M. Jin, Z. Zhu, Z.-F. Chen, Y.-J. Hu and X.-G. Meng, *Crystal Growth & Design*, 2010, **10**, 2054-2056.
71. X. Meng, A. Natansohn and P. Rochon, *Journal of Polymer Science Part B: Polymer Physics*, 1996, **34**, 1461-1466.
72. J. Moreno, L. Grubert, J. Schwarz, D. Bléger and S. Hecht, *Chemistry – A European Journal*, 2017, **23**, 14090-14095.
73. H.-Y. Shiu, M.-K. Wong and C.-M. Che, *Chemical Communications*, 2011, **47**, 4367-4369.
74. A. Telleria, J. Pérez-Miqueo, A. Altube, E. García-Lecina, A. de Cózar and Z. Freixa, *Organometallics*, 2015, **34**, 5513-5529.
75. V. E. Pritchard, D. Rota Martir, S. Oldknow, S. Kai, S. Hiraoka, N. J. Cookson, E. Zysman-Colman and M. J. Hardie, *Chemistry – A European Journal*, 2017, **23**, 6290-6294.
76. M. Irie, *Chemical Reviews*, 2000, **100**, 1685-1716.
77. O. Chepelin, J. Ujma, X. Wu, A. M. Z. Slawin, M. B. Pitak, S. J. Coles, J. Michel, A. C. Jones, P. E. Barran and P. J. Lusby, *Journal of the American Chemical Society*, 2012, **134**, 19334-19337.
78. M. Han, Y. Luo, B. Damaschke, L. Gómez, X. Ribas, A. Jose, P. Peretzki, M. Seibt and G. H. Clever, *Angewandte Chemie International Edition*, 2016, **55**, 445-449.
79. Y. Norikane, K. Kitamoto and N. Tamaoki, *The Journal of Organic Chemistry*, 2003, **68**, 8291-8304.
80. V. E. Pritchard, D. Rota Martir, E. Zysman-Colman and M. J. Hardie, *Chemistry – A European Journal*, 2017, **23**, 8839-8849.
81. F. L. Thorp-Greenwood, V. E. Pritchard, M. P. Coogan and M. J. Hardie, *Organometallics*, 2016, **35**, 1632-1642.

82. E. Baranoff, E. Orselli, L. Allouche, D. Di Censo, R. Scopelliti, M. Gratzel and M. K. Nazeeruddin, *Chemical Communications*, 2011, **47**, 2799-2801.
83. J. Perez-Miqueo, A. Telleria, M. Munoz-Olasagasti, A. Altube, E. Garcia-Lecina, A. de Cozar and Z. Freixa, *Dalton Transactions*, 2015, **44**, 2075-2091.
84. J. Perez-Miqueo, A. Altube, E. Garcia-Lecina, A. Tron, N. D. McClenaghan and Z. Freixa, *Dalton Transactions*, 2016, **45**, 13726-13741.
85. J. Otsuki, M. Tsujino, T. Iizaki, K. Araki, M. Seno, K. Takatera and T. Watanabe, *Journal of the American Chemical Society*, 1997, **119**, 7895-7896.
86. G. Li, Y. Chen, J. Wang, Q. Lin, J. Zhao, L. Ji and H. Chao, *Chemical Science*, 2013, **4**, 4426-4433.
87. J. Otsuki, K. Sato, M. Tsujino, N. Okuda, K. Araki and M. Seno, *Chemistry Letters*, 1996, **25**, 847-848.
88. T. Yutaka, M. Kurihara, K. Kubo and H. Nishihara, *Inorganic Chemistry*, 2000, **39**, 3438-3439.
89. W. H. Melhuish, *J. Phys. Chem.*, 1961, **65**, 229-235.
90. X. Yang, X. Xu and G. Zhou, *Journal of Materials Chemistry C*, 2015, **3**, 913-944.
91. A. F. Henwood, A. K. Pal, D. B. Cordes, A. Slawin, T. W. Rees, C. Momblona, A. Babaei, A. Pertegas, E. Orti, H. J. Bolink, E. D. Baranoff and E. Zysman-Colman, *Journal of Materials Chemistry C*, 2017, **5**, 9638-9650.
92. A. F. Henwood, A. K. Bansal, D. B. Cordes, A. M. Z. Slawin, I. D. W. Samuel and E. Zysman-Colman, *Journal of Materials Chemistry C*, 2016, **4**, 3726-3737.
93. J. Lee, H.-F. Chen, T. Batagoda, C. Coburn, P. I. Djurovich, M. E. Thompson and S. R. Forrest, *Nature Materials*, 2016, **15**, 92-98.
94. J.-H. Lee, G. Sarada, C.-K. Moon, W. Cho, K.-H. Kim, Y. G. Park, J. Y. Lee, S.-H. Jin and J.-J. Kim, *Advanced Optical Materials*, 2015, **3**, 211-220.
95. D. Rota Martir, D. Escudero, D. Jacquemin, D. Cordes, A. Slawin, H. Fruchtl, S. Warriner and E. Zysman-Colman, *Chemistry – A European Journal*, 2017, **23**, 14358-14366.
96. A. Archut, F. Vögtle, L. De Cola, G. C. Azzellini, V. Balzani, P. S. Ramanujam and R. H. Berg, *Chemistry – A European Journal*, 1998, **4**, 699-706.
97. L. C. Palmer, C.-Y. Leung, S. Kewalramani, R. Kumthekar, C. J. Newcomb, M. Olvera de la Cruz, M. J. Bedzyk and S. I. Stupp, *Journal of the American Chemical Society*, 2014, **136**, 14377-14380.
98. A. Fernández-Acebes and J.-M. Lehn, *Advanced Materials*, 1998, **10**, 1519-1522.

99. A. Fernández-Acebes and J.-M. Lehn, *Chemistry – A European Journal*, 1999, **5**, 3285-3292.
100. S. Monaco, M. Semeraro, W. Tan, H. Tian, P. Ceroni and A. Credi, *Chemical Communications*, 2012, **48**, 8652-8654.
101. W. Tan, Q. Zhang, J. Zhang and H. Tian, *Organic Letters*, 2009, **11**, 161-164.
102. L. Insuk, Y. Youngmin, L. Seon-Jeong and P. S. Young, *Chemistry Letters*, 2007, **36**, 888-889.
103. V. Aubert, L. Ordronneau, M. Escadeillas, J. A. G. Williams, A. Boucekkine, E. Coulaud, C. Dragonetti, S. Righetto, D. Roberto, R. Ugo, A. Valore, A. Singh, J. Zyss, I. Ledoux-Rak, H. Le Bozec and V. Guerschais, *Inorganic Chemistry*, 2011, **50**, 5027-5038.
104. D.-K. Cao, R.-H. Wei, X.-X. Li, J.-F. Chen and M. D. Ward, *Dalton Transactions*, 2015, **44**, 4289-4296.
105. C.-C. Ko, W.-M. Kwok, V. W.-W. Yam and D. L. Phillips, *Chemistry – A European Journal*, 2006, **12**, 5840-5848.
106. J. K.-W. Lee, C.-C. Ko, K. M.-C. Wong, N. Zhu and V. W.-W. Yam, *Organometallics*, 2007, **26**, 12-15.

Chapter 5

Coordination polymers featuring azobenzene functionalised molecular hosts

5.1 Introduction

In addition to efficient preparation of discrete cage and capsule-like assemblies, the cyclotrimeratrylene family of molecular hosts has also been shown to assemble into a diverse range of coordination polymers.¹ Coordination polymers (first prepared in 1964 by Bailar)² are the result of the combination of multidentate organic ligands and bridging metal cations to create infinite polymeric networks.³ These can be one, two or multi-dimensional systems. Depending on the ligand-metal combination, such networks often possess significant internal pores or void space⁴ and the most significant interest in these materials comes in their potential for storing a variety of gases (such as hydrogen). Hydrogen gas (H₂) has attracted much interest as a potential fuel source but due to its flammable properties, it is difficult to store safely.⁵

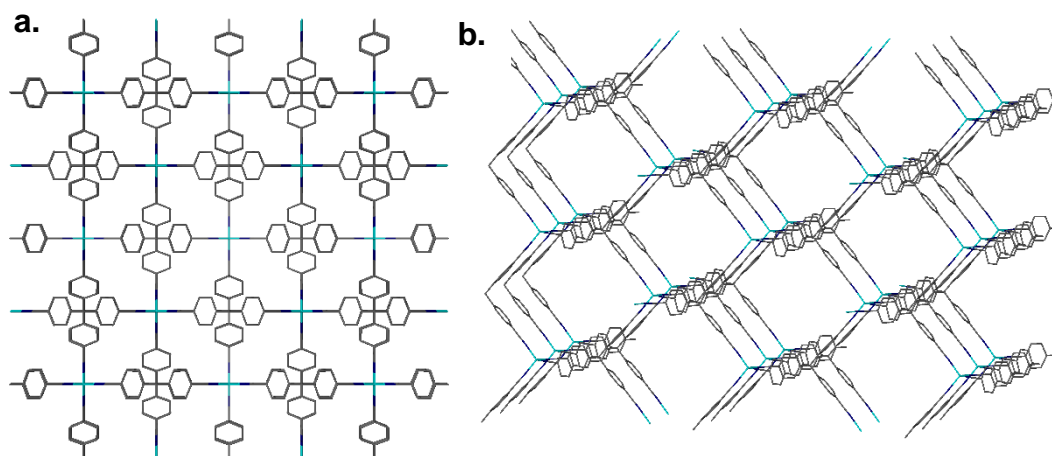


*Figure 5.1: SCXRD structure of the 3D network prepared by Robson and coworkers⁶ illustrating **a.** View down the crystallographic *c*-axis showing the repeating ligand and metal units; **b.** Offset view of the 3D network highlighting the tetragonal cavities. Hydrogen atoms have been omitted for clarity.*

The first 3D coordination polymer was prepared in 1989 by Robson and coworkers (figure 5.1).⁶ This represented the first efforts to deliberately design a 3D coordination network and outline their potential applications. This prototypical network was assembled from the reaction of [Cu(MeCN)₄].BF₄⁻ with 4,4',4'',4'''-tetracyanotetraphenylmethane. Structural analysis by SCXRD revealed that the

resulting network possessed tetragonally elongated adamantane-like cavities with significant levels of internal void space. The authors proposed that the potential applications for these systems were widespread, including ion recognition, catalysis and as molecular sieves.

Subsequently, Yaghi and coworkers coined the term ‘metal organic framework’ (MOF) to describe 3D coordination polymers of this ilk in the synthesis of a 3D network based on $\text{Cu}(\text{NO}_3)_2$ and 4,4'-bipyridine using hydrothermal synthesis techniques.⁷ Yaghi noted the existence of large pores within the resulting network and subsequently developed ‘MOF-5’ a highly porous structure based on $\text{Zn}(\text{NO}_3)_2$ and benzene 1,4-dicarboxylic acid (figure 5.2). MOF-5 and related materials demonstrated impressive hydrogen uptake properties owing to the isoreticular structure providing easy access for gas adsorption.⁸

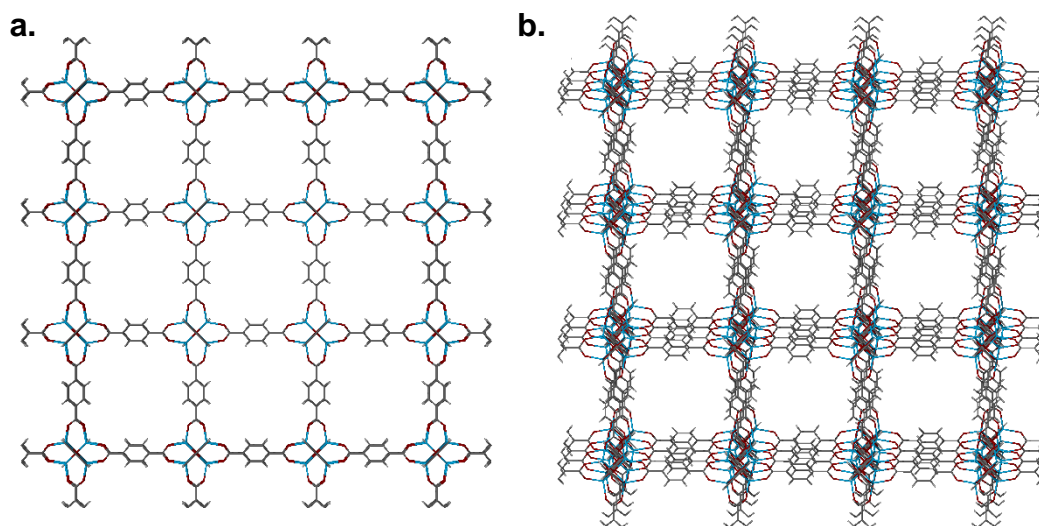


*Figure 5.2: SCXRD structures of MOF-5 as prepared by Yaghi and coworkers⁸ assembled from $\text{Zn}(\text{NO}_3)_2$ and benzene 1,4-dicarboxylic acid showing: **a.** View down the crystallographic *c*-axis; **b.** Offset view of the cubic network illustrating the 3D system. The Zn atoms have been displayed in blue for clarity.*

A number of coordination polymers have been prepared utilising the cyclotrimeratrylene family of ligands. Research within the Hardie group alone has seen the preparation of diverse ligand sets which in turn lead to a diverse range of coordination polymers. Appendage of CTG with hard pyridyl N-oxide or carboxylate donors led to a series of coordination polymers incorporating transition metal⁹ or lanthanide¹⁰ cations. Pyridyl donors also feature heavily in these systems¹¹⁻¹⁷ but other donors such as allyl,¹⁸ bipyridyl,¹⁹ carboxylates¹⁰ and pyridine N-oxides^{9, 10} have been used to prepare a diverse array of coordination networks. The incorporation of

cryptophane units into polymeric assemblies of these ligands is also known.^{16, 20, 21} Highly unusual and rare topologies are also accessible.

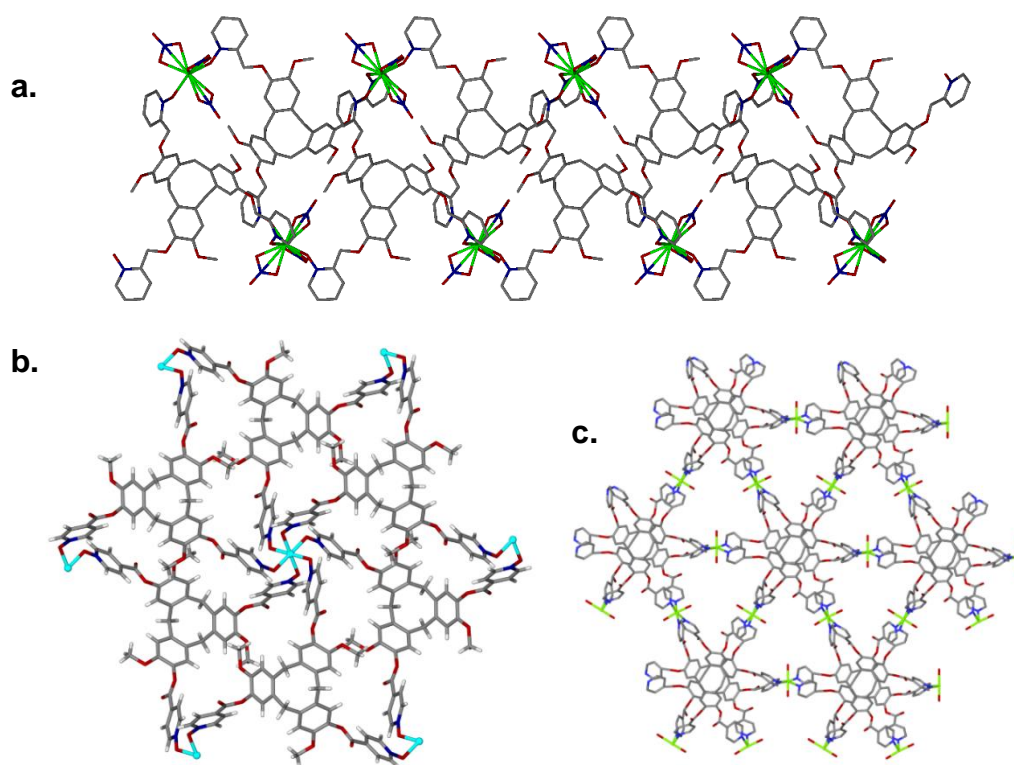


Figure 5.3: SCXRD structures of some examples of coordination polymer networks prepared by Hardie and coworkers showing: a. Ladder-like coordination polymer prepared by Hardie consisting of a pyridyl-appended CTG derivative and $Gd(NO_3)_2$;¹⁰ b. Pyridyl N-Oxide appended CTG ligand coordinating to $Zn(BF_4)_2$ forming a 3,6 network;⁹ c. Network of linked M_3L_2 metallocryptophanes formed from the assembly of a hexapodal cyclotricatechylene (CTC) derivative with $Ni(NO_3)_2$.²²

Holman and coworkers have reported the polymerisation of a carboxylic acid decorated CTG cryptophane upon reaction with $Cu(NO_3)_2$ ²⁰ (figure 5.4). The size of the channels within the material can be altered by the removal of the crystals from the mother liquor. These crystal can then be resolvated to regenerate the original channel sizes. Hard-oxygen functionalised CTV derivatives have also been used by Robson^{23,24} to form tetrahedral coordination cages. Purely organic covalent organic frameworks (COFs) constructed from CTV and its derivatives have also been demonstrated on a number of occasions.²⁵⁻²⁷

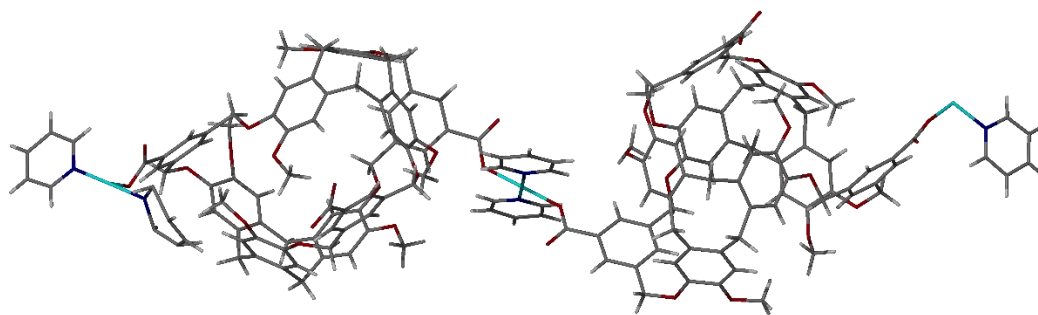


Figure 5.4: From the SCXRD structure of the coordination polymer prepared by Holman and coworkers.²⁰

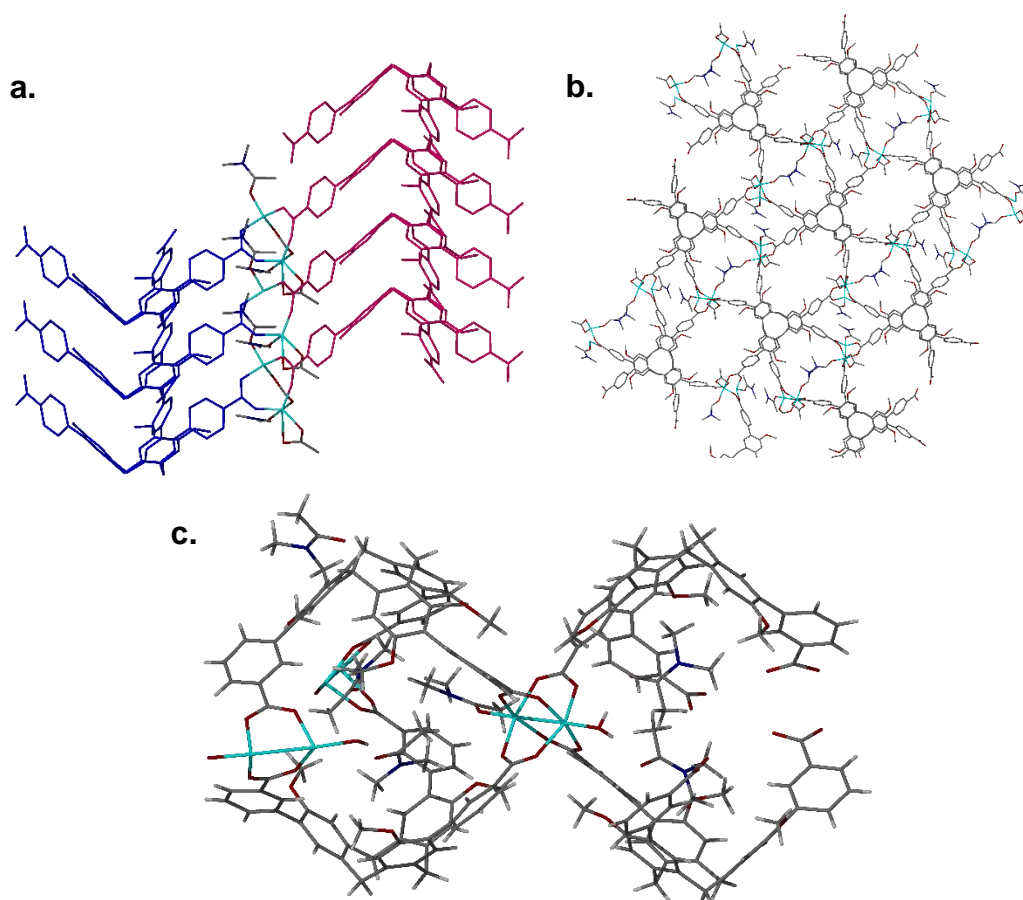


Figure 5.5: SCXRD structures of the metal-organic frameworks prepared by Schröder and coworkers illustrating **a.** π - π stacking in a para-substituted CTV ligand with individual ligand stacks shown in pink and blue ; **b.** The resulting hexagonal network; **c.** Lack of π - π stacking in the meta-substituted analogue leading to a completely different four-bladed zinc(II) paddlewheel.²⁸

More recently, Schröder and co-workers have shown that the appending a CTV ligand with carboxylate units can result in the formation of different metal-organic frameworks with zinc(II) nitrate depending on whether the carboxylate units are in

the *meta* or *para* position (figure 5.5) despite the reaction conditions being identical, once again illustrating the diverse range of structures accessible to CTV derivatives.²⁸ In the *para*-substituted system, the dominant factor is π - π stacking between CTV ligands whereas the meta-substituted system does not benefit from this stacking and formation of a different four-blade zinc(II) paddlewheel is facilitated instead.

Whilst many reports have documented the introduction of azobenzene (AZB) units into dendrimers,²⁹⁻³¹ polymers³²⁻³⁶ and gels,³⁷⁻⁴² reports of coordination polymers utilising the AZB unit are less common, with the majority of examples coming from metal-organic framework (MOF) chemistry.⁴³⁻⁴⁷ Zhao and coworkers have recently reported the preparation of a self-catenated MOF from the assembly of zinc(II) nitrate with a mixture of 4,4'-oxybisbenzoic acid and an dual azo/stilbene ligand.⁴⁸ Remarkably, photoisomerisation of the AZB unit could be achieved in the solid state *via* single crystal to single crystal transformations (SCTSC) under the influence of UV light. This is extremely rare in the solid state for AZB and stilbene derivatives⁴⁹⁻⁵¹ and was demonstrated to be able to control the uptake of CO₂ according to the conformation adopted. The work of Zhou⁵² and Yaghi⁵³ has demonstrated similar control of gaseous guest uptake using pendant azobenzene units.

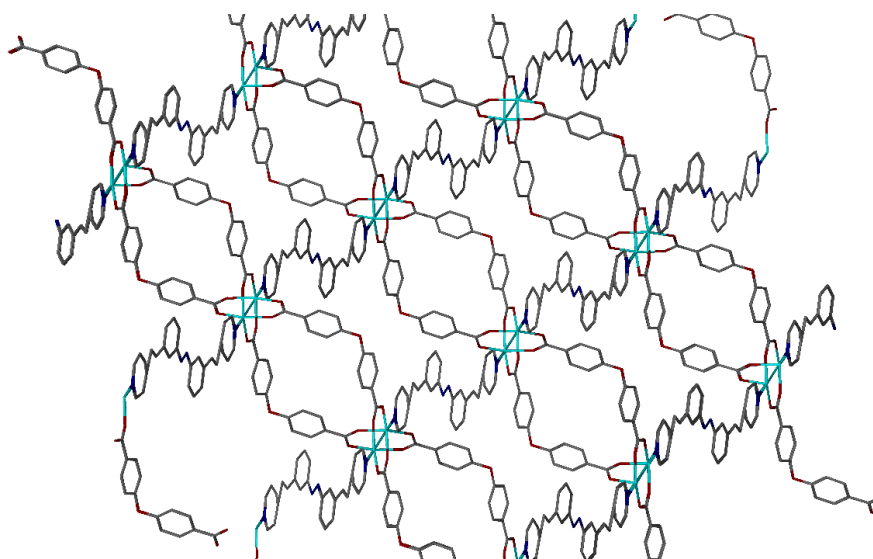


Figure 5.6: SCXRD structure of Zhao's zinc(II) metal-organic framework containing both AZB and stilbene units.⁴⁸

This chapter examines the incorporation of the photoresponsive AZB ligand **2.12** into coordination polymers with a series of transition metal salts. The complexes discussed herein represent the first examples of their kind combining the photoresponsive AZB unit with the cyclotrimeratrylene host. Initial investigations into the host-guest

properties of one of these systems is presented with the potential applications of these systems in molecular recognition also a main focus of the chapter.

5.2 General Remarks

All coordination polymers discussed henceforth were prepared by vapor-diffusion methods using the ligand (\pm)-2,7,12-trimethoxy-3,8,13-*tris*(4,3'-Pyridyl-azophenylcarboxy)-10,15-dihydro-5*H*-tribenzo[*a,d,g*] cyclononatriene (**2.12**) (figure 5.7, synthesis of this ligand is discussed in chapter 2). Complexation reactions with all additional ligands failed to grow suitable quality crystals for single crystal X-ray diffraction (SCXRD) measurements to be performed.

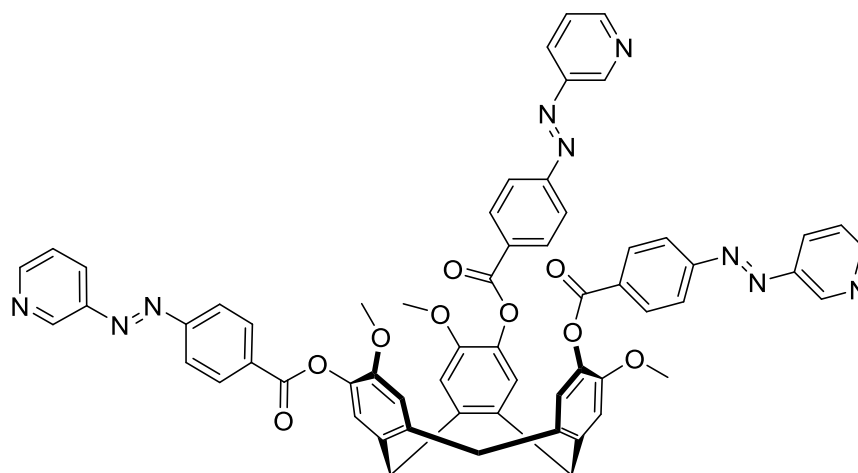


Figure 5.7: Structure of ligand **2.12** employed in this chapter.

In all cases crystallography of these systems proved challenging with crystals being characterised by poor diffraction and in particular poor resolution and disordered components. The specific issues with each complex are indicated in the main text with a full discussion of the refinements given in the experimental section. Although it is difficult to reason exactly why these systems are so intractable, a likely explanation involves a high degree of flexibility in ligand **2.12** (leading to disorder and poor thermal ellipsoids) in combination with excessive void spaces in the complexes (leading to poor resolution). In addition to this, crystals appeared to suffer in the absence of bulk solvent, as all attempts to obtain powder X-ray spectra on these samples revealed the presence of significant levels of amorphous material in all cases. Void space calculations have been performed on all complexes and with the possible exception of complex **5.5**, all complexes were found to possess significant levels of internal void space which is likely to have contributed heavily to the poor quality of the datasets obtained.

5.3 $\{[\text{Cu}_3(\text{H}_2\text{O})_6(\mathbf{2.12})_4] \cdot 6\text{BF}_4 \cdot 9\text{NMP} \cdot 4\text{H}_2\text{O}\}_n$ 2D Network

The reaction of ligand **2.12** and Cu(II) tetrafluoroborate (BF_4^-) in N-methylpyrrolidone (NMP) solvent led to the formation of a 2D network of formula $\{[\text{Cu}_3(\text{H}_2\text{O})_6(\mathbf{2.12})_4] \cdot 6\text{BF}_4 \cdot 9\text{NMP} \cdot 4\text{H}_2\text{O}\}_n$, complex **5.1**. Single crystals suitable for X-ray diffraction were grown from the slow vapour diffusion of diethyl ether into a solution of complex **5.1** in NMP and isolated as orange plates. The complex crystallised with a trigonal unit cell and was solved in the $R\bar{3}$ space group. Similar crystals can also be grown from a solution of the complex in dimethylacetamide (DMAC) which give an identical structure.

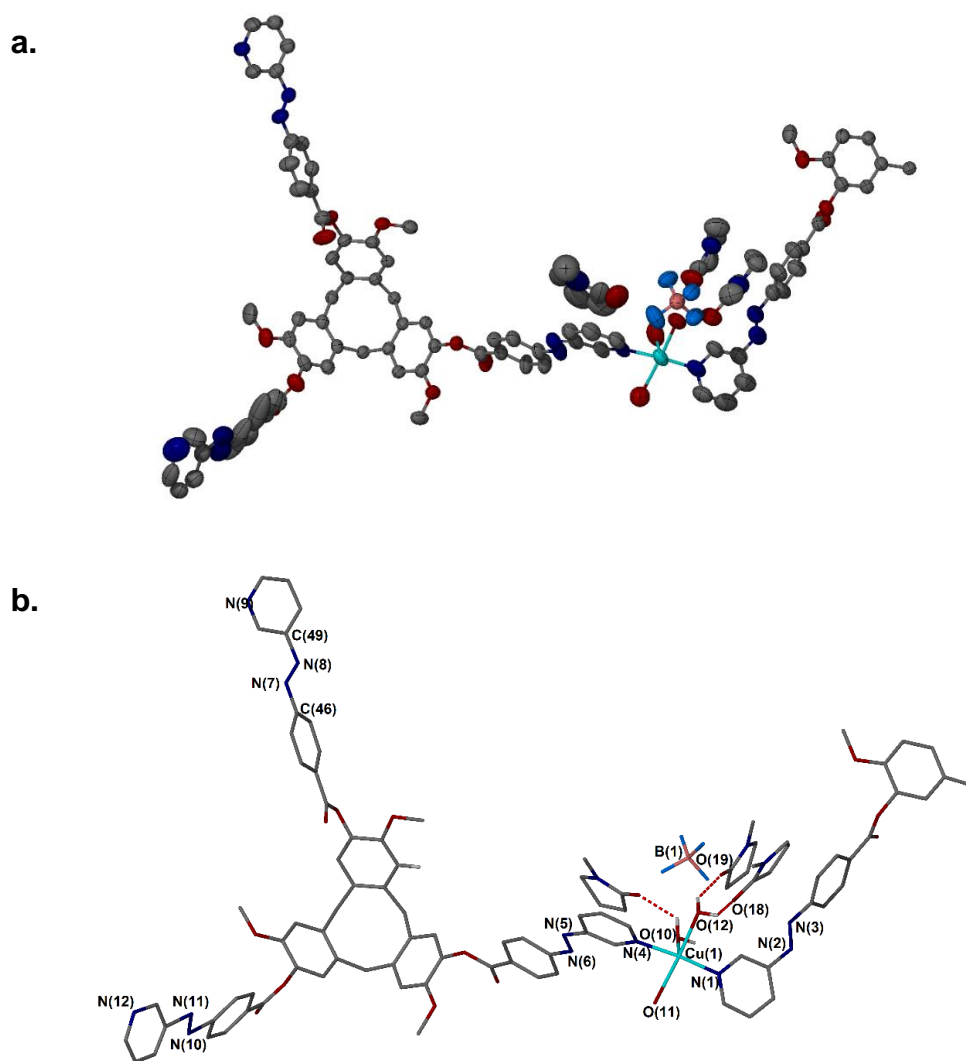


Figure 5.8: The asymmetric unit of complex 5.1 showing: a. Anisotropic displacement ellipsoids (displayed at 50% probability); b. Stick diagram illustrating hydrogen bonding to NMP solvent molecules (dashed lines). Hydrogen atoms (aside from those participating in hydrogen bonding) have been omitted for clarity in both cases.

Crystals of complex **5.1** were poorly diffracting and so were collected using synchrotron radiation at Diamond Light Source. The asymmetric unit contains one Cu(II) centre and one full molecule of ligand **2.12**, figure 5.8. A further one third of another ligand unit is present, with both ligands coordinating to the Cu(II) centre. The remaining coordination sites are filled with two molecules of water and a further weaker interaction to a third water molecule. The asymmetric unit is completed by three NMP solvent molecules (which display hydrogen bonding interactions with the coordinated water molecules) and a tetrafluoroborate counterion. The second tetrafluoroborate could not be located crystallographically. Both ligands in the asymmetric unit are the *M* isomers of the ligand.

The structure contained residual electron density that could not be meaningfully refined as solvent, hence the SQUEEZE routine of PLATON was applied⁵⁴ (additional details given in the experimental section). The geometry about the Cu(II) centre is best described as distorted square pyramidal. Upon symmetry expansion of the asymmetric unit, each Cu(II) centre is coordinated by three pyridyl units from separate **2.12** ligands in a T-shaped arrangement of ligands. The square pyramidal arrangement is completed by two coordinated water molecules; a further water molecule engages in a weak interaction with the metal (with an interatomic separation of 2.520 Å).

Table 5.1: Selected bond lengths (Å) and angles (°) from the crystal structure of complex 5.1.

Cu (1) – O(10) _{eq}	2.027(11)	N(1) – Cu(1) – N(4)	172.27(9)
Cu (1) – O(11) _{ax}	2.520	N(1) – Cu(1) – O(11)	87.11(6)
Cu (1) – O(12) _{ax}	2.282(14)	N(1) – Cu(1) – O(12)	95.79(8)
Cu (1) – N(1) _{eq}	1.988(3)	N(1) – Cu(1) – O(10)	86.39(7)
Cu (1) – N(4) _{eq}	2.014(2)		
Cu (1) – N(9) _{eq}	2.043(18)		
O (10) – O(17)	2.650		
O (12) – O(19)	2.789		
O (12) – O(18)	2.722		

Table 5.1 illustrates a selected portion of bond lengths and angles in complex **5.1**. It can be seen that the interatomic distance between the Cu(II) centre and the axial water

molecules, Cu(1)---O(11) and Cu(1)---O(12), are elongated compared to the equatorial bond distances. All AZB units are observed in their thermodynamically stable *trans* configuration.

The network assembles into large star-shaped macrocycles with each star consisting of an M_6L_6 stoichiometry of ligands (figure 5.9). The CTV units act as bridging ligands between two copper centres. The third pyridyl unit of each ligand points into the centre of the macrocycle and remains non-coordinating; this behaviour is observed again with Cu(OAc) in section 5.4. Each star is bordered by six further macrocycles of M_4L_4 stoichiometry.

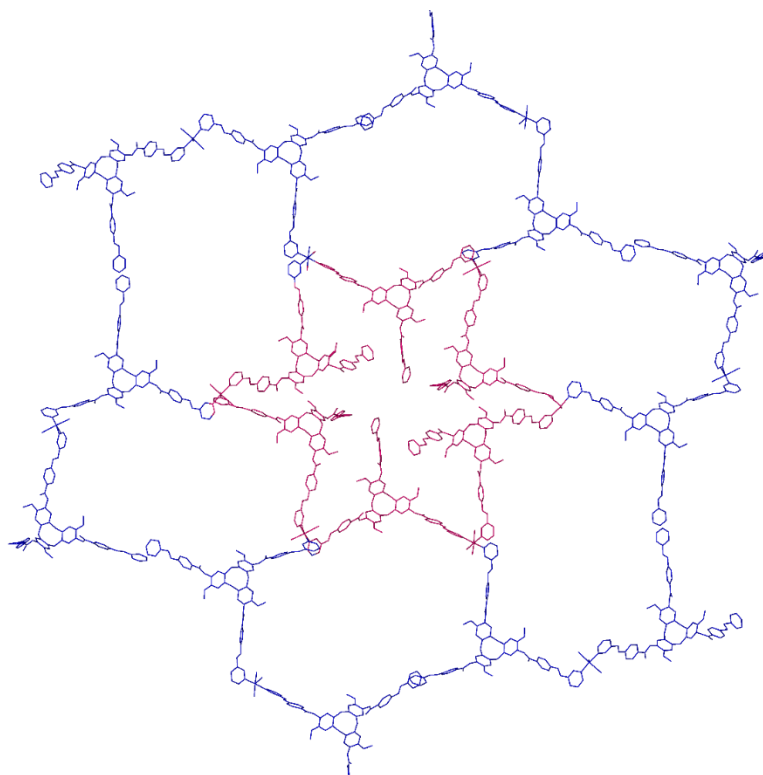
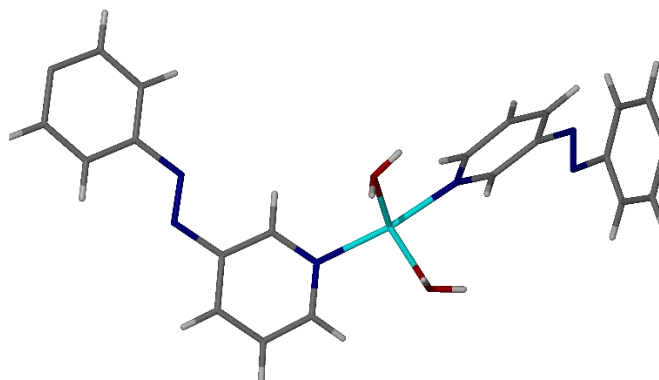


Figure 5.9: The star shaped M_6L_6 macrocyclic moiety in the crystal structure of complex 5.1. Hydrogen atoms, solvent molecules and counterions have all been omitted for clarity.

Significant twisting of some azobenzene units are observed which can be measured *via* defining the pyridyl and phenyl units adjacent to the N=N bond as separate planes and then measuring the angle between them (figure 5.10). Using this method, some twists in the structure of complex 5.1 are calculated as being up to 48.65° , which is comparable to the twisting observed during molecular modelling of the metallocryptophane 3.8 as discussed in chapter 3, section 3.7. This provides some indirect evidence that such twists are plausible with coordinated AZB units originating from ligand 2.12. Complex 5.1 provides a good illustration of the flexibility and

adaptability of the AZB units in ligand **2.12** as in addition to the heavily twisted AZB units, there are also several which are only subtly perturbed from being rigidly planar, with twists of only 8.32°.



*Figure 5.10: From the SCXRD structure of complex **5.1** showing a coordination environment around Cu(1). The different AZB twists are shown with the left AZB unit experiencing a mild twist of 8.32° and the right AZB unit a far more substantial 48.65°.*

In between layers, stabilising π - π stacking interactions can be observed between the AZB side arms in different layers. (figure 5.11a) This leads to the formation of a 2D \rightarrow 2D threefold interpenetrated network of 6³ topology (figure 5.11b). Host guest interactions are also observed between the AZB side arms and the cyclotrimeratrylene bowl on adjacent ligands. Thermogravimetric analysis (TGA) indicated a 25% net mass loss up to 100°C (water) and a further loss of 15% up to 200°C (NMP solvent). This level of solvation is higher than shown from the SCXRD structure which is to be expected. The infrared spectrum of complex **5.1** displays the characteristic B-F bond stretch at 1058 cm⁻¹ along with the expected ester C=O stretch (ligand **2.12**) at 1738 cm⁻¹.

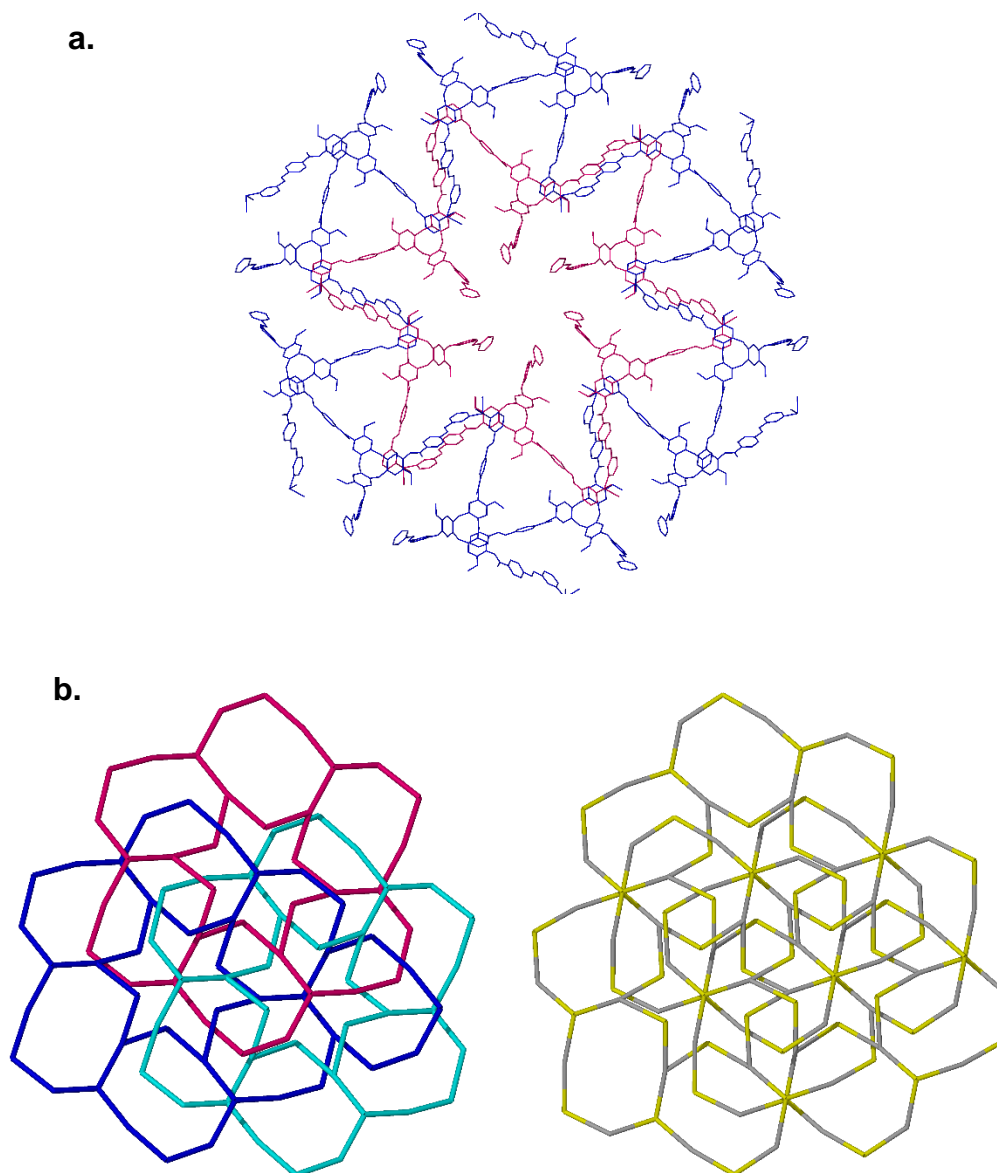


*Figure 5.11: From the crystal structure of complex 5.1 showing: **a.** Two of the three layers of interpenetration showing some of the interactions governing interpenetration (π stacking and host-guest bowl interactions); **b.** (left) View down the crystallographic c -axis showing the threefold interpenetration with each ligand colour coded for clarity (right) topological representation of complex 5.1 with the metal ions coloured grey and the ligand centroids coloured yellow. Hydrogen atoms have been omitted for clarity in all cases.*

Void space calculations revealed three internal channels of significant size, at 7822, 7806 and 7807 Å³ respectively. With respect to the total volume of the unit cell (63763 Å³), this accounts for 36.7% of the total crystal volume. This significant degree of void space is in reality likely occupied by solvent molecules that could not be elucidated crystallographically. Nevertheless, the significant degree of void space

present goes some way to explaining the poorly diffracting nature of the crystals. When viewed in spacefilling mode (figure 5.12) these void spaces are evident as a dominating feature of the polymer. This may yet hold potential in molecular recognition.

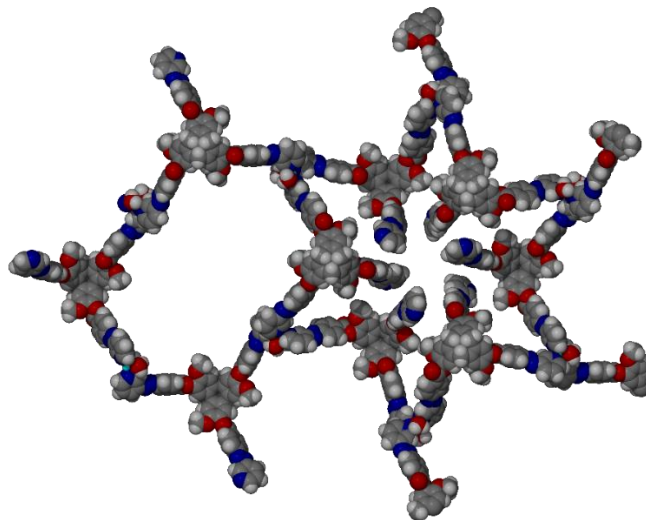


Figure 5.12: Spacefilling view of the pores in complex 5.1 showing one of each of the star-shaped pores and one of the M_4L_4 macrocycles.

From a topological standpoint, the smallest repeating unit in the system are hexagons (when treating the metal centres as nodes) with connections to three neighbouring nodes. Thus the topological descriptor for this system is a 6^3 network. This type of network has been observed previously by Hardie for CTG derivatives bearing quinoly¹² and pyridylphenyl²¹ ligands.

5.4 [Cu(2.12)₂(OAc)₂] discrete complex

The reaction of ligand **2.12** with Cu(II) acetate in dimethylacetamide (DMAC) solvent led to the formation of a discrete complex of formula [Cu(**2.12**)₂(OAc)₂], complex **5.2**. Single crystals suitable for X-ray diffraction analysis were grown *via* slow diffusion of diethyl ether into a solution of complex **5.2** and isolated as yellow needles. The complex crystallised in a triclinic unit cell and was solved in the $P\bar{1}$ space group. The asymmetric unit (figure 5.13) contains two molecules of ligand displaying the bowl in bowl stacking commonly observed with CTV derivatives.¹ One ligand arm is coordinated to the Cu(II) centre which also bears two coordinated acetate molecules. The asymmetric unit bears a strong resemblance to the crystal structure of the isolated ligand (discussed in chapter 2, section 2.4). One of each *P* and *M* enantiomers of ligand **2.12** are present in the asymmetric unit (also in concurrence with the crystal structure of the free ligand).

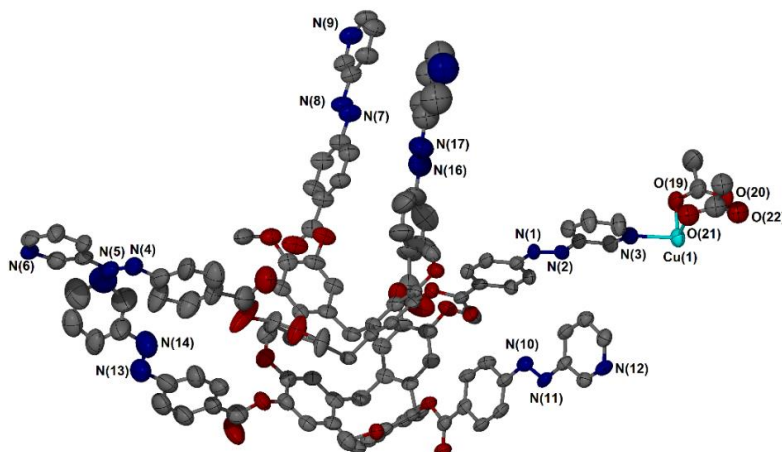


Figure 5.13: The asymmetric unit of complex 5.2. Anisotropic displacement ellipsoids are shown at a 50% probability level and hydrogen atoms have been omitted for clarity.

Symmetry expansion reveals the system adopts a paddlewheel structure that is somewhat typical of metal acetates (figure 5.14).⁵⁵ This results in two five coordinate Cu(II) centres separated by a distance of 2.63(17) Å. Four of the coordination sites on each metal are occupied by acetate ligands with the axial water molecule being replaced by a pyridyl unit from ligand **2.12**. The ligands are oriented in antiparallel bowl-in bowl stacks with alternating ligands coordinating to the Cu(II) centre. Only one of the ligand arms coordinate to the Cu(II) centre, leaving the remaining two ligand arms free to participate in stabilising π - π stacking interactions with typical interatomic distances around 3.8Å. No polymeric network is formed, resulting in a discrete complex as depicted in figure 5.14.

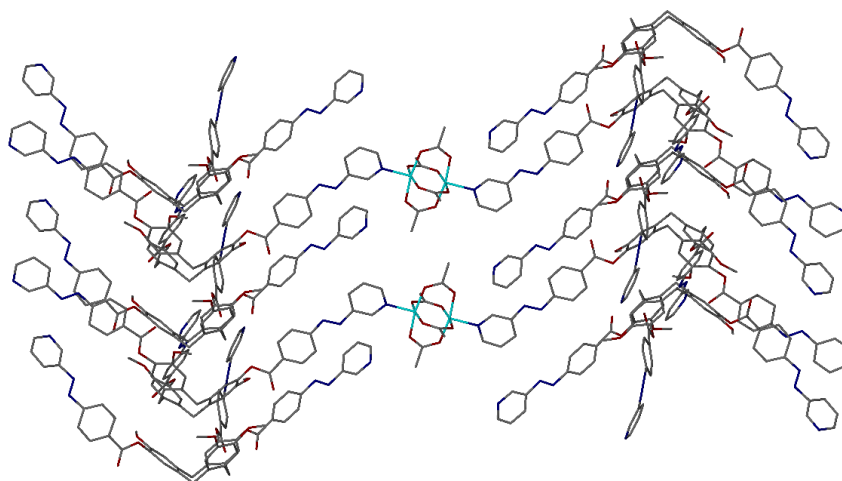


Figure 5.14: The columnar bowl-in-bowl stacks of ligand 2.12 in the crystal structure of complex 5.2. Alternating ligands bridge the antiparallel stacks via a Cu(II) paddlewheel centre to give the discrete complex.

Table 5.2: Selected bond lengths (Å) and angles (°) from the crystal structure of complex **5.2**.

Cu (1) – O(21)	1.965(6)	N(3) – Cu(1) – O(20)	100.79(2)
Cu (1) – O(22)	1.988(6)	N(3) – Cu(1) – O(22)	97.45(2)
Cu (1) – O(19)	1.948(5)	N(3) – Cu(1) – O(19)	91.15(2)
Cu (1) – O(20)	1.955(5)	N(3) – Cu(1) – O(21)	93.48(2)
Cu (1) – N(3)	2.161(5)		
Cu-Cu separation	2.630(17)		

Selected bond lengths and angles for complex **5.2** are displayed in table 5.2. The coordinating AZB side arms are rigidly planar in contrast to the twisted arrangement found in complex **5.1**, with twist angles of just 3.87°. In contrast, the non-coordinating ligand arms have sharp twists of up to 48.89°. This arrangement does offer π stacking with neighbouring ligand arms in a similar manner observed in the crystal structure of the isolated ligand **2.12** which does not exhibit twists of this magnitude. Ligand-ligand interactions still play a significant role in governing the arrangement of complex **5.2** as illustrated in figures 5.15a and 5.15b.

The structure still contained residual electron density that could not be meaningfully refined as solvent, hence the SQUEEZE routine of PLATON was applied⁵⁴ (additional details given in the experimental section). This is the consequence of large void spaces in the crystal lattice though these are not as prominent as those observed for ligand **2.12**. Void space calculations revealed one internal void spaces of significant size, at 1639 Å³ in size. With respect to the total volume of the unit cell (7036 Å³), this accounts for 23.3% of the total crystal volume in comparison to a void space of 48% in the isolated free ligand **2.12**. Some of these voids are filled by the Cu(II) paddlewheel units (figure 5.15a); the diffraction observed for complex **5.2** is far superior to that of the isolated ligand which may be due to these discrepancies in void spaces and the presence of electron-rich Cu(II) centres. The large pores are most evident when viewed in spacefilling mode as shown in figure 5.15c.

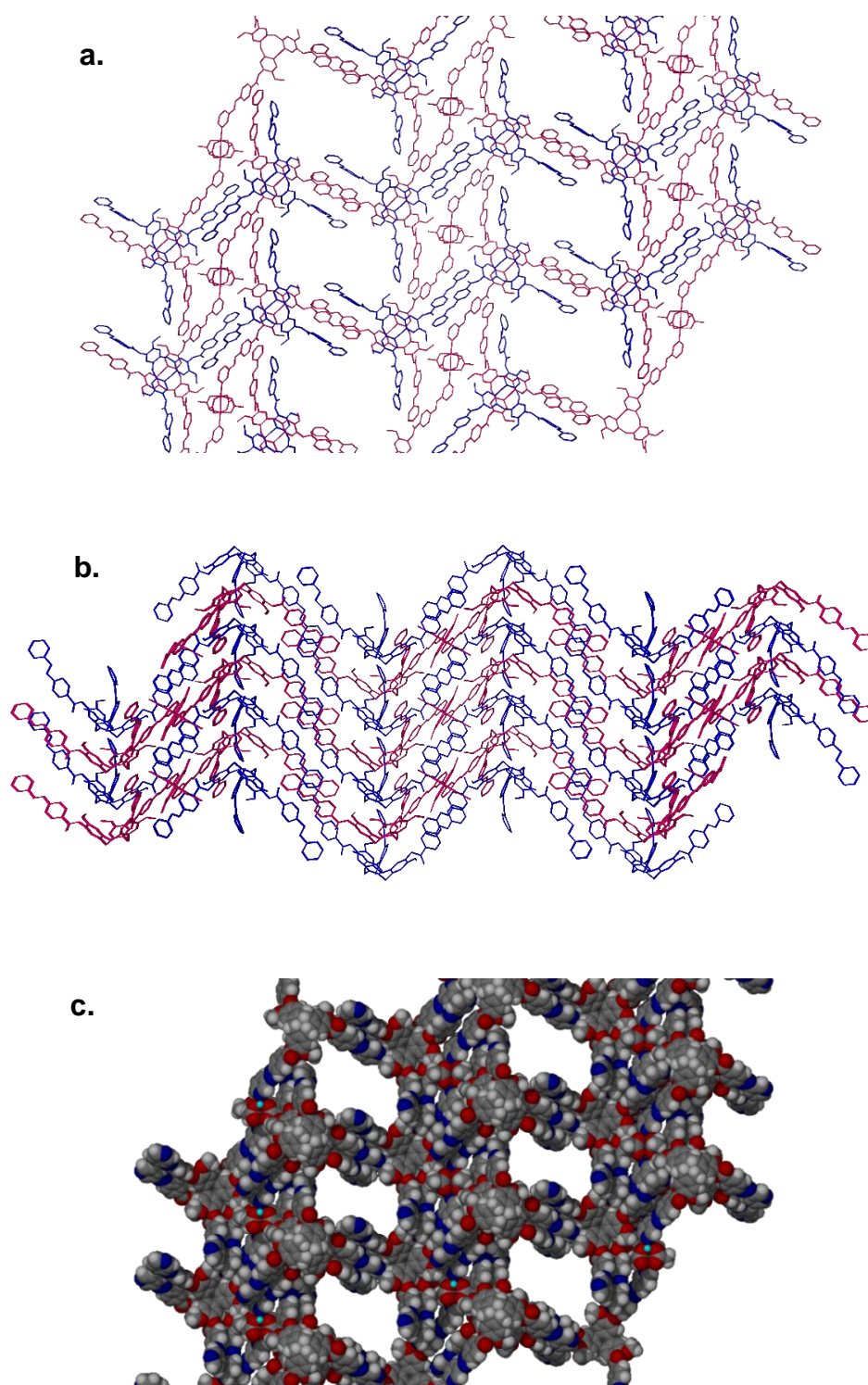


Figure 5.15: From the crystal structure of complex 5.2 as viewed down: a. crystallographic a-axis; b. crystallographic-b axis; c. spacefilling mode showing the pores of complex 5.2. Metal coordinating ligands are shown in pink and non-coordinating ligands are shown in blue, highlighting the alternating layers of ligands. All hydrogen atoms have been omitted for clarity.

The relative stability of the bidentate acetylacetonate ligands is one potential explanation for the selective coordination observed in complex **5.2**, with the axial water ligands far likelier to be replaced. The author notes that the crystals of complex **5.2** were very few in number and accompanied in the crystallisation vials by significant amounts of precipitate. The author believes that this precipitate is likely to be composed of higher order coordination polymers (where more of the acetate ligands have been replaced by ligand **2.12**) which are insoluble and so precipitate from the crystallisation vessel before crystal growth can occur. Alteration of the solvent system and crystallisation conditions fared no better at crystallising any species other than complex **5.2**. However in a DMAC/Et₂O solvent system, the formation and crystallisation of complex **5.2** (alongside significant levels of precipitate) can be demonstrated many times indicating that it is a stable enough intermediate in solution to allow the growth of crystals.

5.5 [Ag(**2.12**)]_nX 1D coordination polymer (X = BF₄⁻, PF₆⁻, OTf⁻)

The reaction of ligand **2.12** with Ag(I) trifluoromethanesulfonate in DMF led to the formation of a 1D coordination polymer of formula [Ag(**2.12**)]_n.OTf, complex **5.3**. Single crystals suitable for X-ray diffraction analysis were grown *via* slow diffusion of diethyl ether into a solution of complex **5.3** and isolated as red blocks. Crystals of complex **5.3** were well diffracting but gave consistently poor resolution regardless of the counterion employed (PF₆⁻, BF₄⁻ and OTf⁻ salts of complex **5.3** were all obtained and gave consistent unit cells). Therefore, data collection on the triflate salt of complex **5.3** was obtained using synchrotron radiation at Diamond Light Source. Complex **5.3** crystallised in a trigonal unit cell and the structure was solved in the $R\bar{3}$ space group. All salts of this complex suffered from heavy disorder; as illustrated in figure 5.16, the silver atom is disordered over three positions with two of the AZB arms also disordered. An EDX analysis of the crystals confirms the presence of silver but it is unusual for a metal to be disordered in this manner.

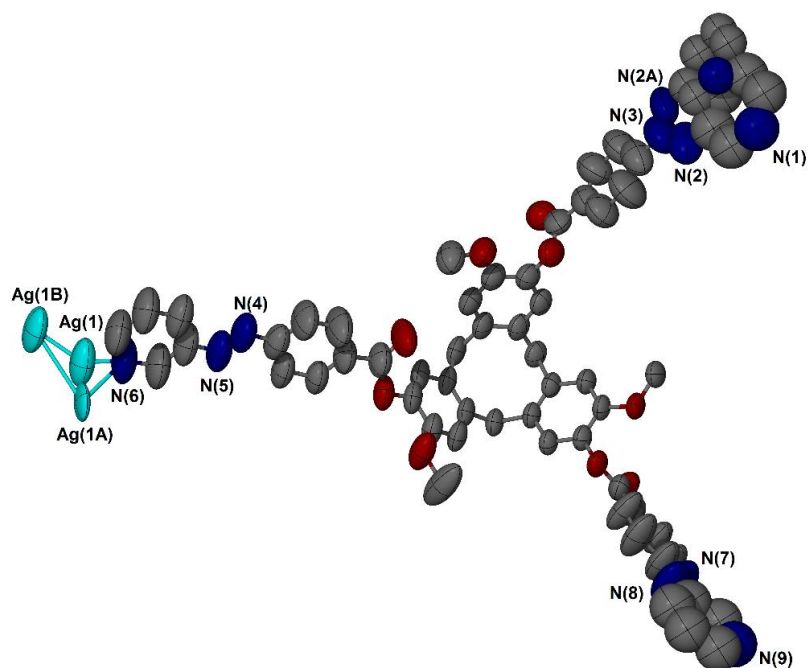


Figure 5.16: The asymmetric unit of complex **5.3** showing the disorder of the AZB arm and the silver ion. Anisotropic displacement ellipsoids are shown at the 50% probability level and hydrogen atoms have been omitted for clarity

Table 5.3: Selected bond lengths (Å) and angles (°) from the crystal structure of complex **5.3**.

N (6) – Ag (1)	1.740	N(6) – Ag (1) – N(6)	172.23(10)
N (6) – Ag (1a)	2.311(10)		
N (6) – Ag (1b)	3.836		
N (4) – N (5)	1.210(9)		
N (7) – N (8)	1.197(10)		
N (2) – N (3)	1.211(10)		

Selected bond lengths and angles for complex **5.3** are displayed in table 5.3 above. The AZB units are relatively planar compared to complex **5.1**. The coordinating ligands and Ag(I) centre adopt a linear coordination mode that is typical of Ag(I) complexes. Similar to in complex **5.1**, one AZB arm is left free and does not coordinate, with the two coordinating AZB arms forming a 1D polymeric chain.

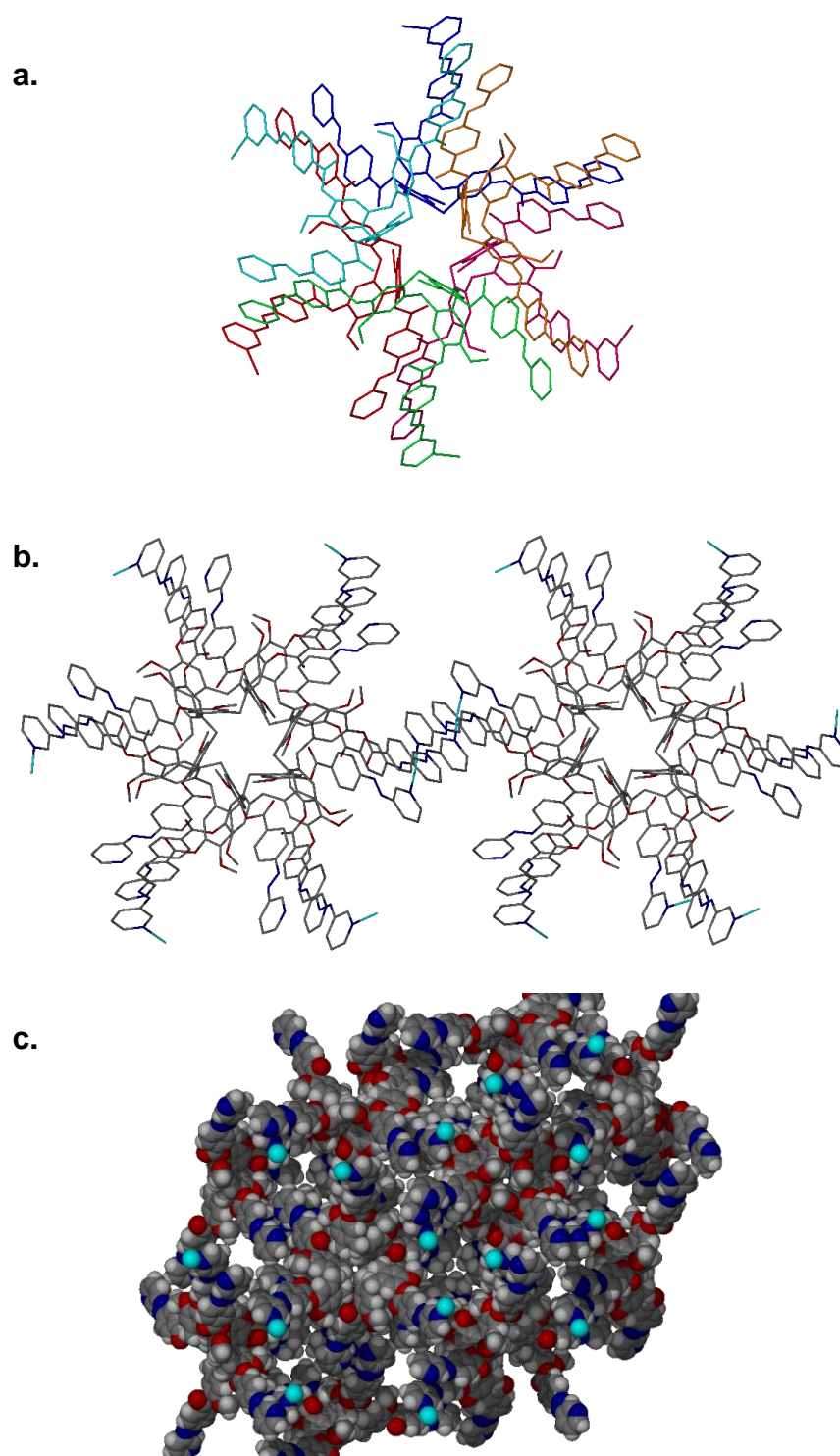


Figure 5.17: From the SCXRD structure of complex 5.3 showing: a. The star-shaped pore motif formed from six individual 2.12 ligand units. Each ligand is shown in a different colour for clarity; b. π -stacking interactions forming connections between star-shaped pores; c. Spacefilling view of the channels in complex 5.3 showing the lack of internal space for host-guest chemistry.

Symmetry expansion reveals that six individual ligand **2.12** units pack back-to-back to form an enclosed star-shaped pore (figure 5.17a). These pores are connected to neighbouring pores by the ligand arms which undertake extensive π -stacking interactions (figure 5.17b). In the PF_6^- analogue, these star-shaped pores are occupied by the PF_6^- counterions. Void space calculations (calculated using a 1.2\AA probe in Olex) revealed one internal void spaces of significant size, at 13657\AA^3 . With respect to the total volume of the unit cell (35102\AA^3), this accounts for 39.4% of the total crystal volume, a significant level of void space. Potential applications in molecular recognition however, are likely to be challenging owing to the lack of accessible channels as depicted in figure 5.17c. The AZB ligand arms are relatively planar in this structure with all AZB units exhibiting a modest twist angle of *ca* 17.4° . The infrared spectrum of the BF_4^- salt of complex **5.3** displays the strong ester absorbance at 1728 cm^{-1} and a strong band at 813 cm^{-1} characteristic of the tetrafluoroborate counterion.

5.6 $\{[\text{Cu}_5(\mathbf{2.12})_4(\text{H}_2\text{O})_{12}]\cdot 2\text{H}_2\text{O}\cdot 4\text{NMP}\cdot 10\text{OTf}\}_n$ 2D polymer

The reaction of ligand **2.12** with Cu(II) trifluoromethanesulfonate in NMP led to the formation of a coordination polymer of formula $\{[\text{Cu}_5(\mathbf{2.12})_4(\text{H}_2\text{O})_{12}]\cdot 2\text{H}_2\text{O}\cdot 4\text{NMP}\cdot 10\text{OTf}\}_n$, complex **5.4**. Single crystals suitable for X-ray diffraction analysis were grown *via* slow diffusion of diethyl ether into a solution of complex **5.4** and isolated as orange plates. Crystals of complex **5.4** were very difficult to separate owing to the stacking of very thin plates on top of one another. Complex **5.4** crystallised in a triclinic unit cell and was solved in the $P\bar{1}$ space group. The asymmetric unit contains two full molecules of ligand **2.12** that are connected by a bridging Cu(II) centre in a similar manner to complex **5.1**. The central copper atom is also coordinated by two molecules of NMP solvent and two molecules of water to give an octahedral coordination geometry. The ligands also coordinate to an additional Cu(II) centre each (figure 5.18). A single trifluoromethanesulfonate counterion can be observed with the second counter-ion unable to be located crystallographically. The reaction of ligand **2.12** with Cu(II) trifluoroacetate in NMP solvent gives crystals that upon analysis are revealed to be the same structure as complex **5.4**.

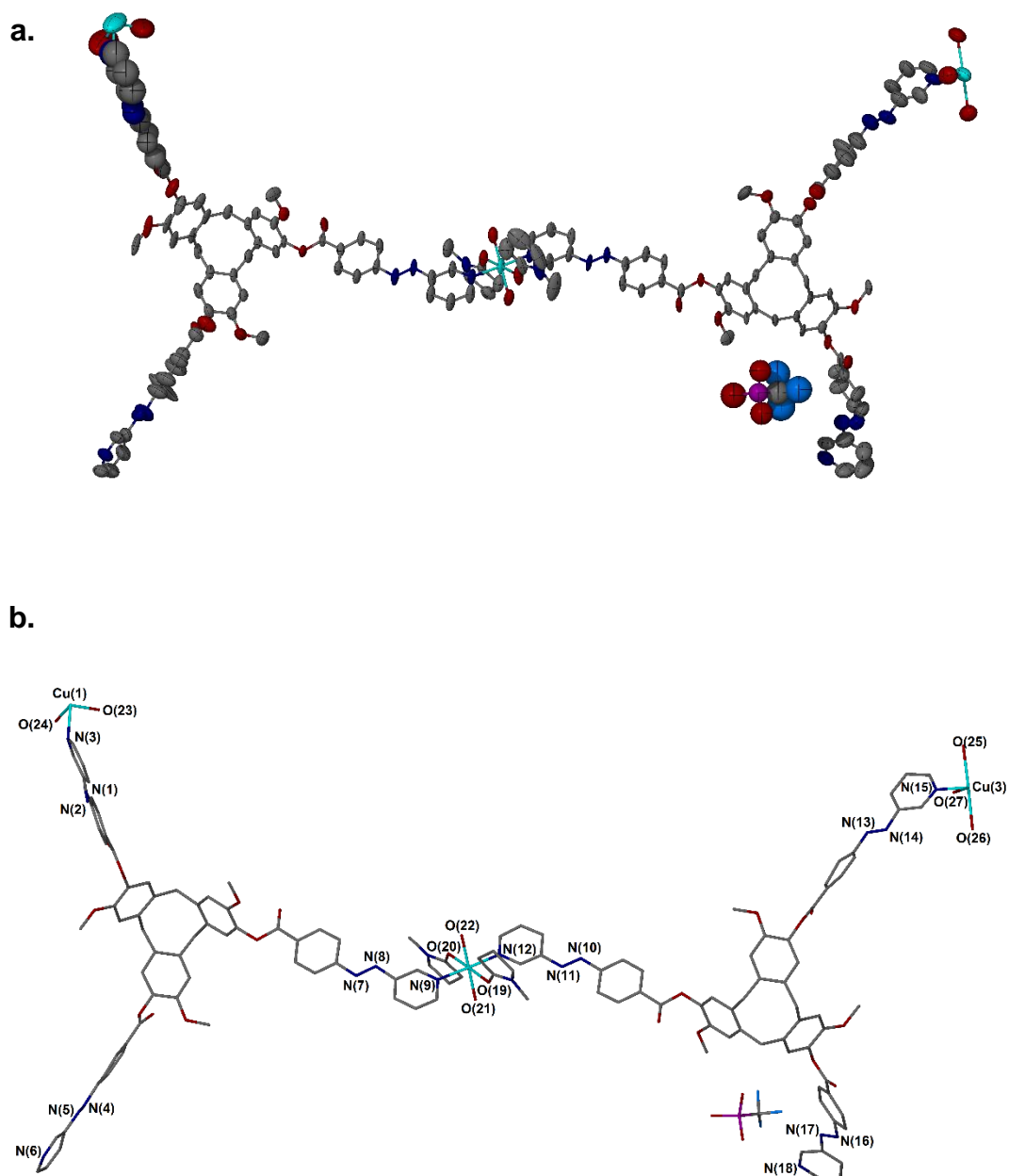


Figure 5.18: The asymmetric unit of complex **5.4** showing: **a.** Anisotropic displacement ellipsoids (displayed at 50% probability); **b.** Stick diagram. Hydrogen atoms have been omitted for clarity in both cases.

Selected bond lengths and angles for complex **5.4** are shown in table 5.4. AZB units that are coordinated are planar when coordinating to Cu(2) but twisted when coordinating to Cu(3) highlighting the flexibility of ligand **2.12**. Cu(1) is sited on an inversion centre. The central Cu(2) displays distorted octahedral geometry with the axial NMP solvent molecules displaying typical Jahn-Teller elongation⁵⁶ (Cu(2)---O(20) = 2.347(8)Å and Cu(2)---O(19) = 2.350(10)Å compared to typical values of

2.0Å for the equatorial ligands) in a similar manner to complex **5.1**. The other copper centres, Cu(1) and Cu(3) are also distorted octahedral geometry but with a different composition of ligands. The asymmetric unit contains one of each *P* and *M* enantiomers of the ligand **2.12** leading to their being oriented with the bowls facing in opposite directions.

Table 5.4: Selected bond lengths (Å) and angles (°) from the crystal structure of complex 5.4.

Cu (1) – N(3)	2.049(2)	N(3) – Cu(1) – O(24)	85.55(15)
Cu (1) – O(23)	1.854(3)	N(3) – Cu(1) – O(23)	95.66(12)
Cu (1) – O(24)	2.358(2)	N(9) – Cu(2) – O(21)	90.38(4)
Cu (2) – N(9)	2.012(10)	N(9) – Cu(2) – O(22)	89.35(4)
Cu (2) – O(20)	2.347(8)	N(9) – Cu(2) – N(12)	178.27(4)
Cu (2) – O(19)	2.350(10)	N(9) – Cu(2) – O(19)	89.75(3)
Cu (2) – O(21)	2.019(10)	N(9) – Cu(2) – O(20)	89.78(3)
Cu (2) – O(22)	1.999(10)	N(15) – Cu(3) – O(25)	88.94(6)
Cu (2) – N(12)	2.007(10)	N(15) – Cu(3) – O(26)	90.38(5)
Cu (3) – N(15)	2.010(18)	N(15) – Cu(3) – O(27)	91.08(7)
Cu (3) – O(25)	2.378(12)		
Cu (3) – O(26)	2.343(13)		
Cu (3) – O(27)	2.033(12)		

Upon symmetry expansion, the structure forms an 2D network (figure 5.19). The principal motif may be viewed as a series of puckered M_8L_8 rings (figure 5.19a). When viewed down the crystallographic *b*-axis, these rings take up a conformation not dissimilar to the chair conformation adopted by cyclohexane (figure 5.19b). All the ligand **2.12** units connect to three metals with no free AZB arms as observed in complexes **5.1** and **5.2**.

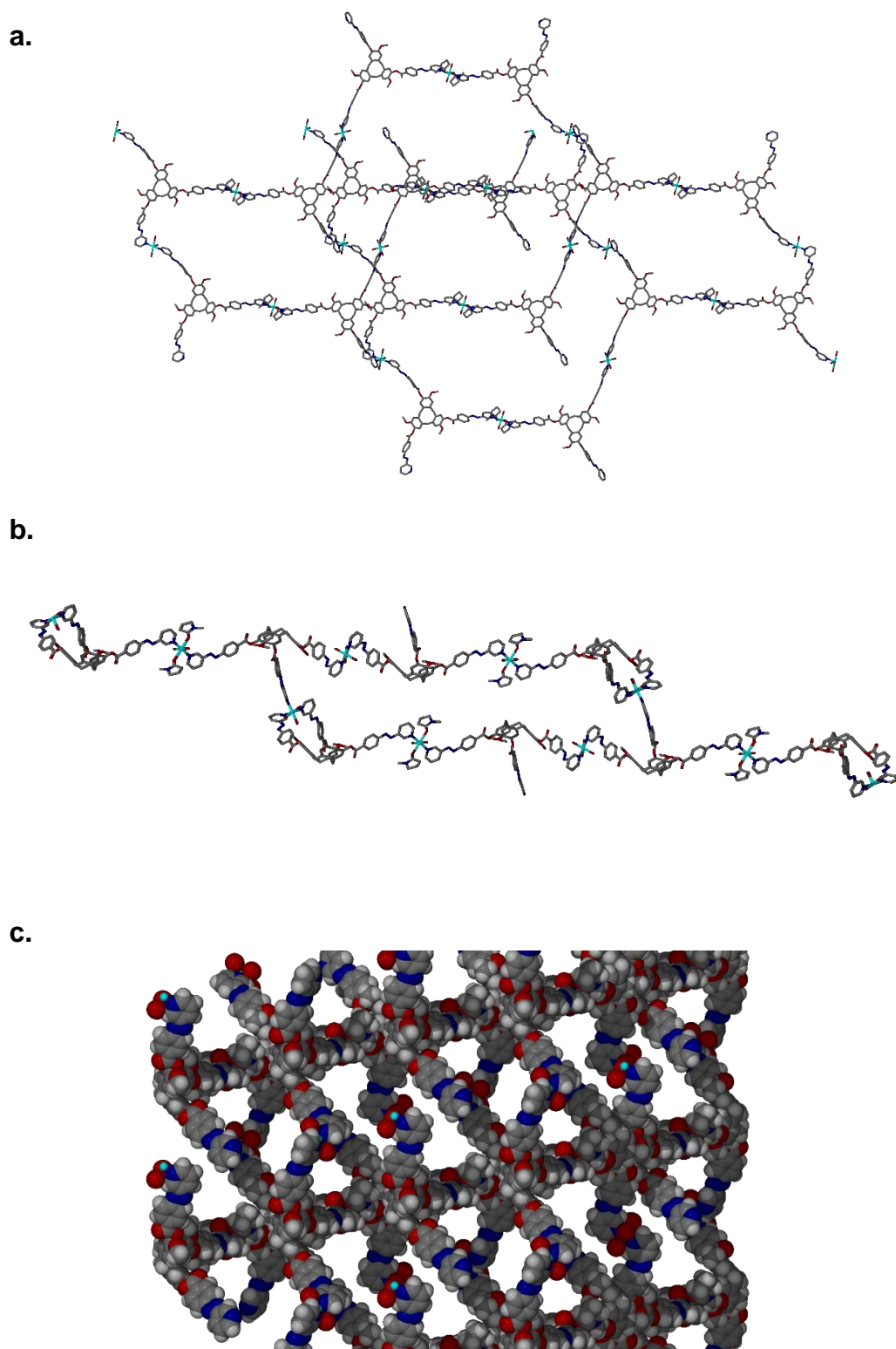


Figure 5.19: Motifs from the symmetry expansion of complex 5.4 showing: a. View down the crystallographic c-axis showing the interpenetration of ligand 2.12; b. View down the crystallographic b-axis showing the 'chair-like' motif in complex 5.4; c. View down the crystallographic a-axis with atoms displayed in spacefilling mode to illustrate the pores in complex 5.4.

Void space calculations (calculated using a 1.2Å probe in Olex) revealed one internal void spaces of significant size, at 8763Å³. With respect to the total volume of the unit cell (13805Å³), this accounts for a substantial 63.5% of the total crystal volume, going a long way to explaining the weakly diffracting nature of the crystals. The coordinating AZB units in this system exhibit modest twist angles of 14.26° whereas the non-coordinating AZB units once again show more dramatic twists, with angles of up to 38.84° observed. The vast majority of the crystals are in fact void space which lends plenty of potential for the hosting of guest molecules within the polymer network, a point which is explored further in section 5.7. Topologically, the system is once again arranged in a 6³ network as illustrated by figure 5.20b.

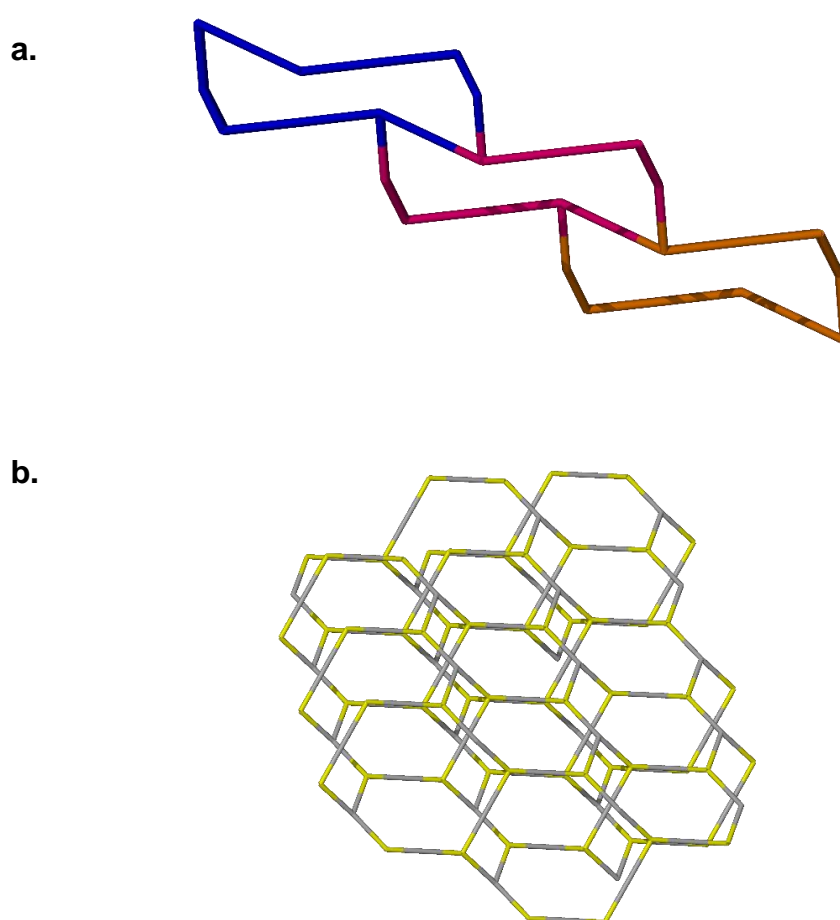


Figure 5.20: Topological depiction of the connectivity in complex 5.4, showing: a. View down the crystallographic b-axis showing the ‘chair-like’ layering of complex 5.4; b. View down the crystallographic c-axis showing the interpenetration of the 2.12 ligands in complex 5.4. Copper atoms are shown as grey spheres and ligand centroids shown as yellow spheres.

5.7 $\{[\text{Cu}_2(\mathbf{2.12})_2(\text{CF}_3\text{CO}_2^-)_2(\text{NMP})_2].7(\text{o-C}_6\text{H}_4\text{Cl}_2)\}_n$ 2D coordination polymer

The growth of single crystals of all the complexes discussed thus far was difficult to achieve, with crystals growing slowly and often sporadically. The crystals obtained upon reaction with CuOTf (complex **5.4**) and with AgBF₄ (complex **5.3**) were notable exceptions to this with crystals growing reliably within 2 weeks. Unfortunately all attempts to introduce small globular guests into the crystal lattice of complex **5.3** have proven unsuccessful with only starting polymer obtained after several days of soaking of crystals in a solution of guest molecules. This may be due to insufficient space in the crystal lattice for the binding of guest molecules.

Complex **5.4** however, possesses significant levels of internal void space, with the void spanning 8763 Å³ accounting for over 60% of the total crystal volume. Therefore complex **5.4** was identified as the best candidate for host guest experiments to try and introduce a guest molecule into the void space of the crystal lattice. Fullerene, C₆₀, was selected as a guest candidate of interest due to the propensity of cyclotrimeratrylene derivatives to act as a molecular host for fullerenes.⁵⁷⁻⁵⁹ The NMP solvent was decanted from the reaction vessel and replaced with a solution of C₆₀ in dichlorobenzene, and the vial allowed to stand for two weeks.

Pleasingly, the crystals did not appear to visually suffer in the absence of NMP. Initial screenings of the crystals revealed an alteration in the unit cell lengths (from 14.46, 27.38, 34.44 to 14.60, 18.89, 21.20) but no obvious colour change to the crystal (solutions of C₆₀ are deep purple). Elucidation of the structure revealed a new coordination polymer of formula $\{[\text{Cu}_2(\mathbf{2.12})_2(\text{CF}_3\text{CO}_2^-)_2(\text{NMP})_2].7(\text{o-C}_6\text{H}_4\text{Cl}_2)\}_n$ complex **5.5**. The new system exhibits a (4².6²)(4.6²)₂ topology that has been reported previously in a series of CTV coordination polymers prepared by Hardie.⁶⁰ No evidence of C₆₀ could be located crystallographically but five molecules of dichlorobenzene solvent were identified in the asymmetric unit. The structure was solved in the $P\bar{1}$ space group with a triclinic unit cell. The asymmetric unit consists of one molecule of ligand **2.12** coordinated to two Cu(II) centres. A coordinated NMP solvent molecule has survived the solvent switch and remains coordinated to one of the Cu(II) centres. Each copper centre is also coordinated by one triflate ion *via* the SO₃⁻ unit. One AZB arm is disordered over two positions as shown in figure 5.21. Further to this one of the chlorine atoms on one of the dichlorobenzene units is disordered about the aryl ring.

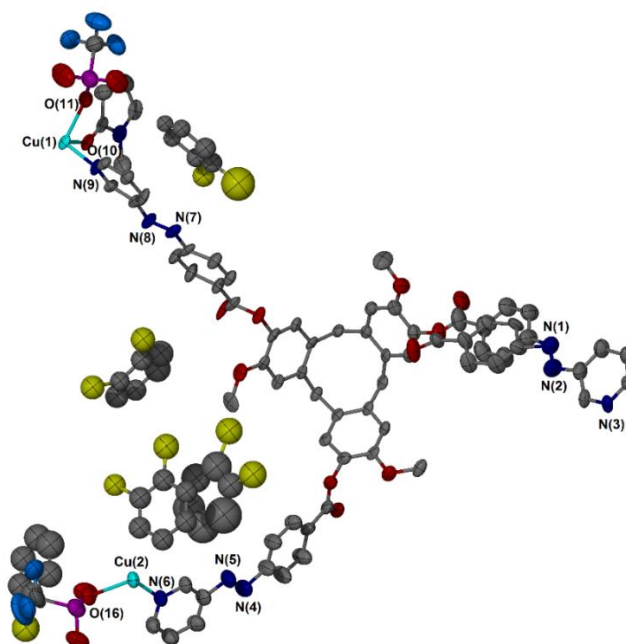


Figure 5.21: The asymmetric unit of complex **5.5**. Anisotropic displacement ellipsoids are shown at a 50% probability level and hydrogen atoms have been omitted for clarity.

Table 5.5: Selected bond lengths (Å) and angles (°) from the crystal structure of complex **5.4**.

Cu(1) – N(3)	2.008(11)	N(6) – Cu(2) – O(16)	93.49(4)
Cu(1) – O(10)	1.996(8)	N(9) – Cu(1) – O(11)	90.86(4)
Cu(1) – O(11)	2.344(10)	N(9) – Cu(1) – O(10)	88.56(4)
Cu(2) – N(6)	2.039(12)		
Cu(2) – O(16)	2.406(9)		

Selected bond lengths and angles are displayed in table 5.4. Interestingly, after two weeks the transformation appears to be a complete process. Screenings of multiple crystals revealed no trace of the unit cell of complex **5.4** after two weeks in dichlorobenzene. Conversely, no evidence of the new polymer could be detected in vials of crystals where no dichlorobenzene was added. Control experiments where just dichlorobenzene (and no C₆₀) was added show the same transformation indicating the C₆₀ does not play a role. The transformation can be repeated on many different vials of crystals, illustrating the reproducibility of the process.

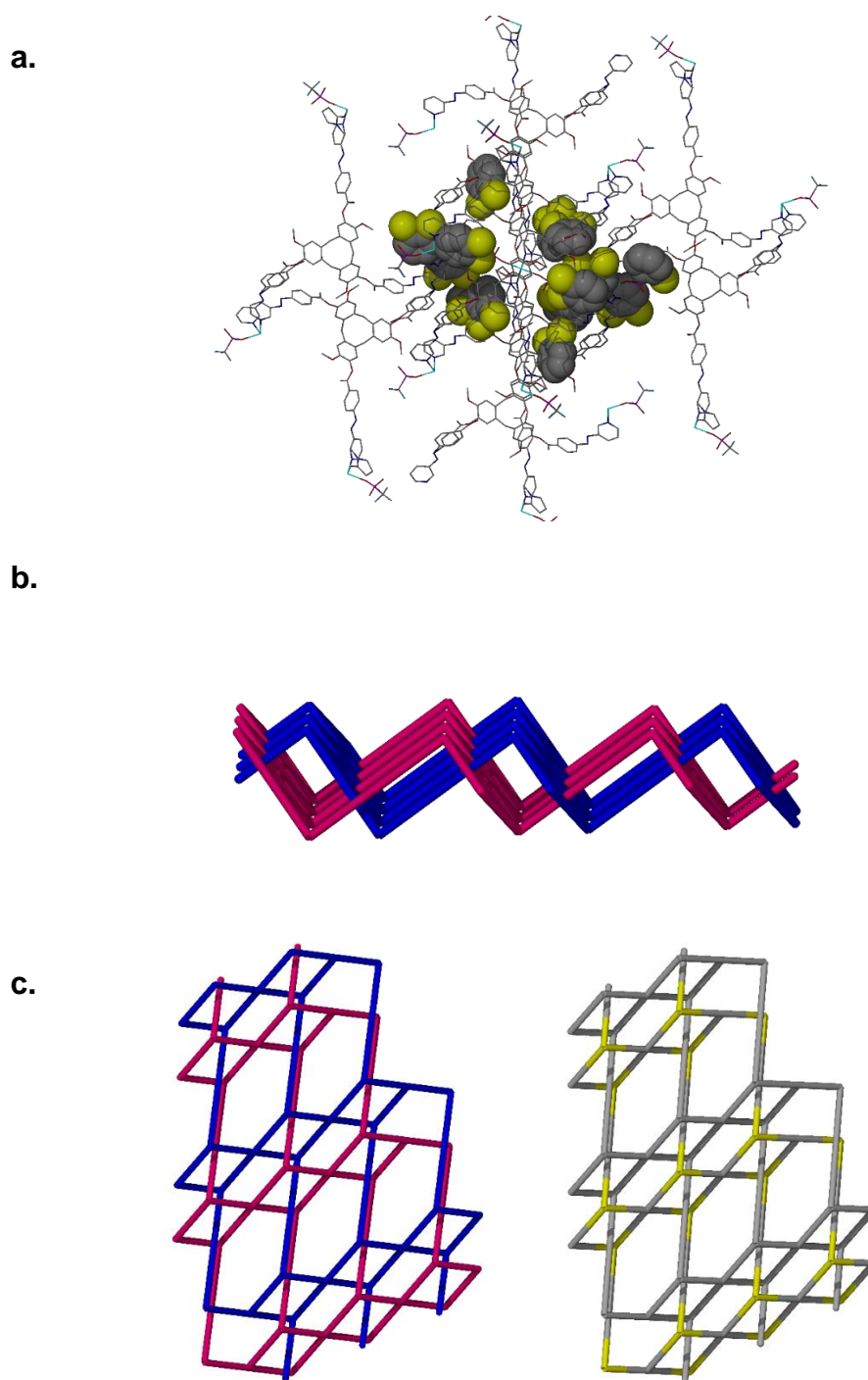


Figure 5.22: From the SCXRD structure of complex 5.5 showing a. Symmetry expanded view of one layer of the complex 5.5 with dichlorobenzene guest shown in spacefilling mode; b. The 2-fold interpenetration of crystal layers with individual layers in pink and blue respectively; c. View down the crystallographic b-axis showing the interpenetrated layers. Individual layers are shown in pink and blue respectively (left); Copper atoms and ligand centroids are shown in grey and yellow respectively (right).

Void space calculations (calculated using a 1.2Å probe in Olex) revealed very little internal void space with the two largest voids of 264 and 379 Å³ accounting for only 12% of the total crystal volume. It is immediately apparent that this is substantially different from the original complex **5.4** which possesses the largest solvent-accessible void space of any of the complexes discussed in this chapter. The structure consists of octahedral coordinated Cu(II) centres. The Cu(2) units are coordinated by four molecules of ligand **2.12** with the remaining two sites occupied by two triflate ions. Jahn-Teller distortion can be observed in this moiety with the bonds to the triflate oxygens, Cu(2)—O(16), significantly longer (2.406(9)Å) than those to the equatorial ligand **2.12** (2.039Å). The Cu(1) units are coordinated by two molecules of ligand **2.12** with octahedral geometry completed by two molecules of NMP solvent and two triflate ions. Once again the axial triflate ligands experience Jahn-Teller distortion. One dichlorobenzene exhibits offset π - π stacking interactions with the AZB arm of ligand **2.12** (centroid-centroid distance of 3.719Å).

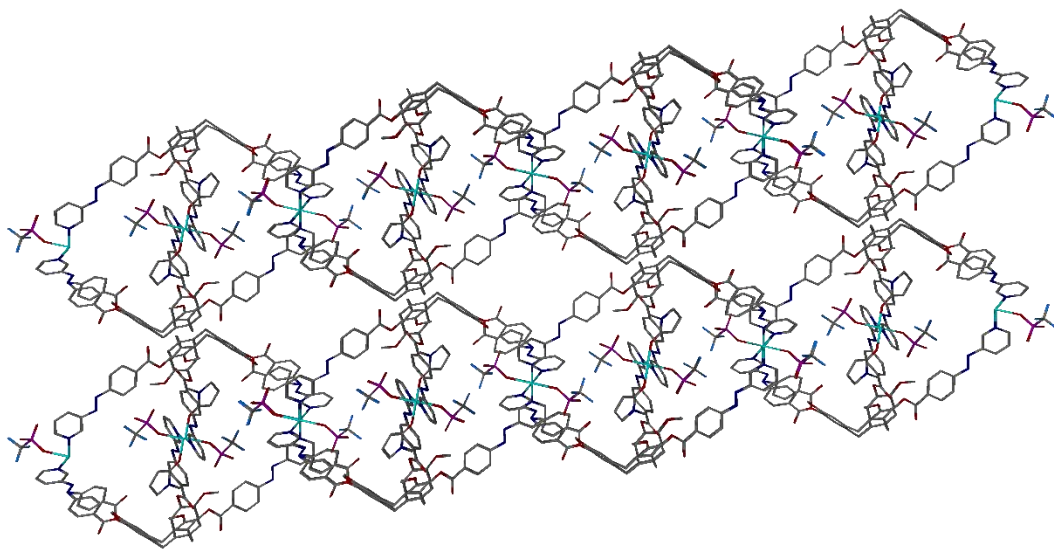


Figure 5.23: Symmetry expanded view of complex 5.5 as viewed down the crystallographic a-axis. Hydrogen atoms and dichlorobenzene guests have been omitted for clarity.

Payne has recently reported the single crystal transformation of a CTV inclusion compound *via* alteration of the solvent composition.⁶¹ In the presence of acetonitrile, the crystal structure shows a dimeric structure with stacking between CTV layers into columnar assemblies. Upon desolvation *via* heating of the crystals, a new polymorph is formed due to rotation of the CTV methoxy units. Atwood has reported a single-crystal-to-single-crystal (SCTSC) transformation of p-tert-butylcalix[4]arene upon soaking of single crystals of the host in a solution of vinyl bromide guest molecule.⁶² The process occurs without any dissolution of the crystals. Guest uptake in a SCTSC

fashion in CTV derivatives has also been demonstrated before by Hardie's metallocryptophanes which can bind I_2 in both gaseous form and in solution, although not reversibly.⁶³ The same metallocryptophanes have also been shown to uptake 1,2 dichlorobenzene which exchanges positions with nitromethane solvents of crystallisation. Once bound, the iodine cannot be displaced by solvent nor removed *via* heating at 80°C under vacuum for 30 minutes.

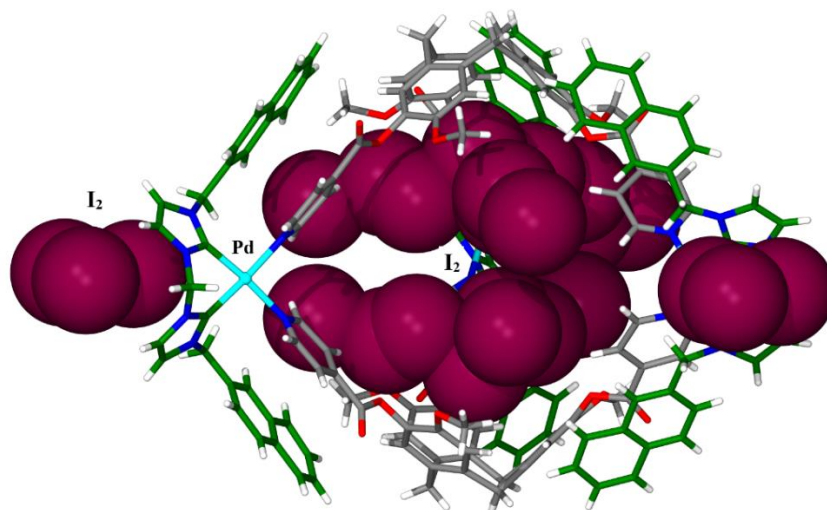


Figure 5.24: SCXRD structure showing the encapsulation of iodine guest that has been achieved in a SCTSC fashion by Hardie's M_3L_2 metallocryptophanes.⁶³

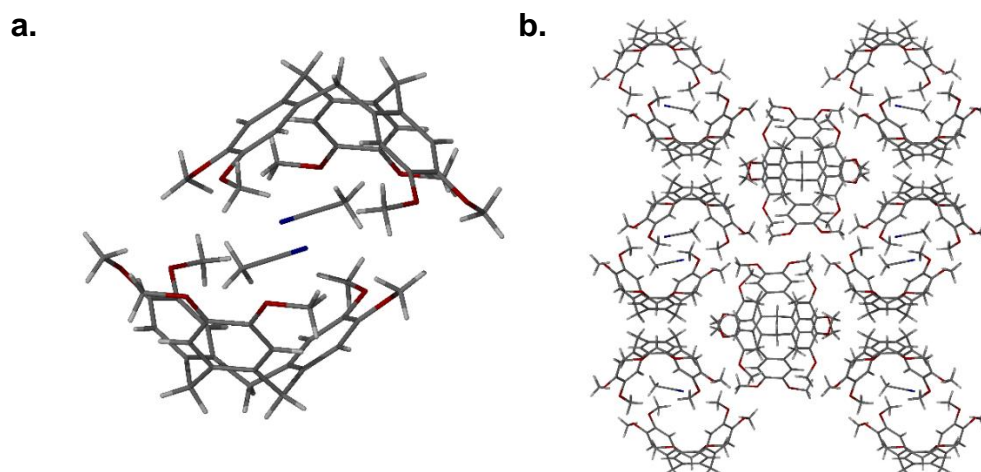


Figure 5.25: From the SCXRD structure of the CTV inclusion complex prepared by Payne⁶¹ showing **a.** Individual CTV inclusion dimer with acetonitrile; **b.** Packed structure shown down the crystallographic c-axis. Removal of the acetonitrile solvent results in a single crystal-to-single crystal transformation to an alternate polymorph of the inclusion complex.

The structural rearrangement observed in complex **5.4** was proposed to be taking place *via* one of two mechanisms; a solid state rearrangement or a microdissolution of the crystals and recrystallization as the new system. To probe this process, SEM imaging studies were conducted on samples of complex **5.4** (original polymer) and complex **5.5** (rearranged polymer) in collaboration with Alex Kulak at the university of Leeds. Images were first recorded using an optical microscope, figure 5.26:

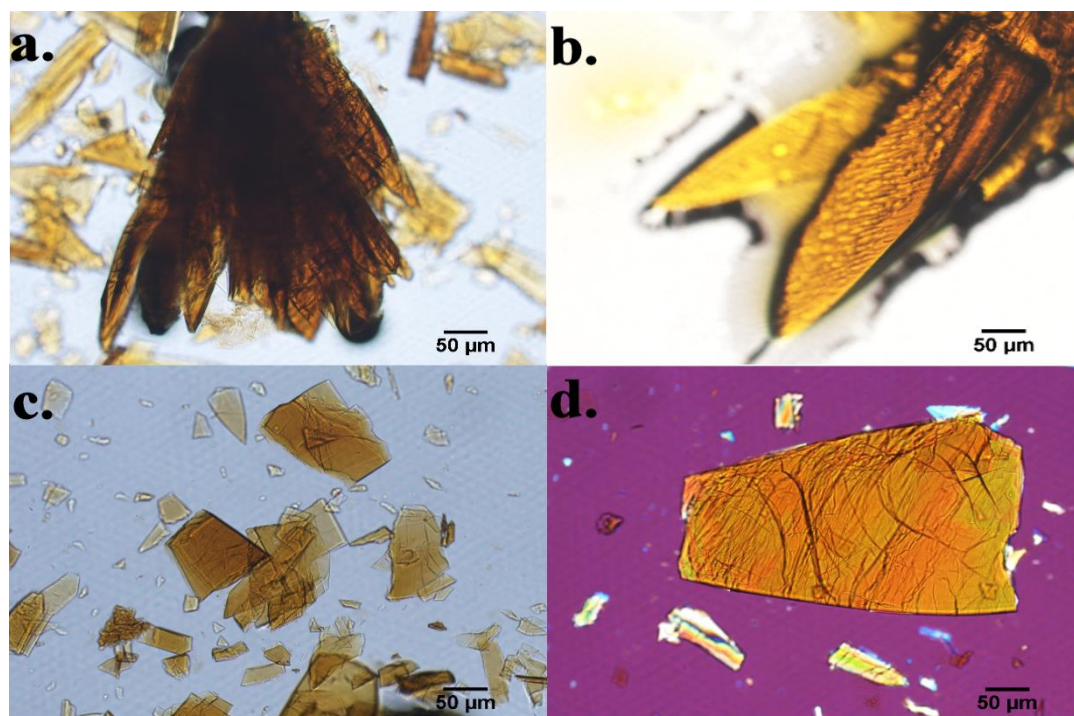


Figure 5.26: Optical microscope images of crystals of complexes 5.4 and 5.5 showing: a. Clustered crystals of complex 5.4; b. Close view of an individual cluster of complex 5.4; c. Plates of complex 5.5; d. Plate of complex 5.5 viewed under polarizer.

Samples were coated with a thin layer of iridium using a sputter coater prior to analysis to improve electrical conductivity. Pleasingly the crystals were stable to solvent loss under vacuum as well as under exposure to the electron beam enabling high resolution SEM imaging to be conducted. Figure 5.27 below shows the SEM images of both complexes **5.4** and **5.5**:

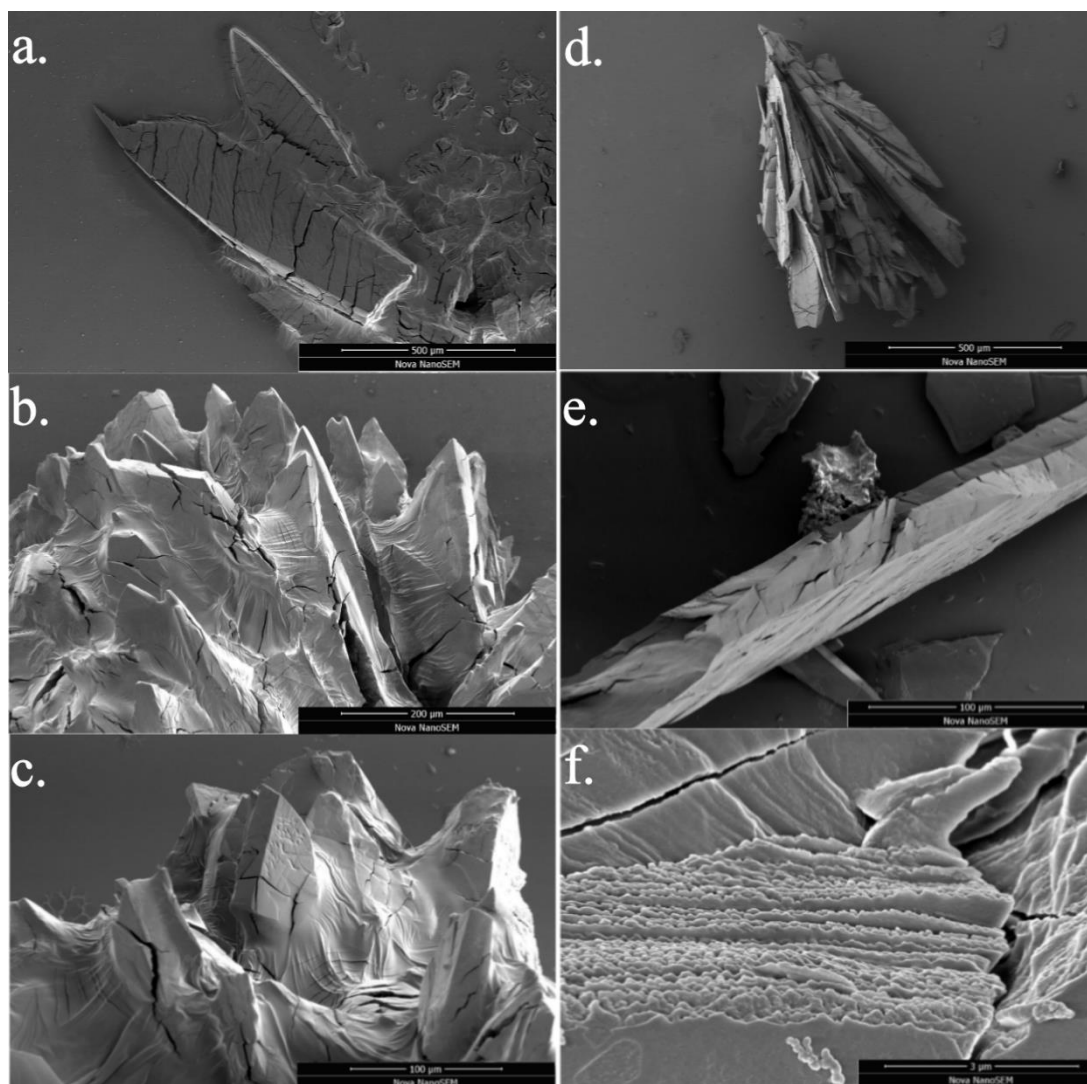


Figure 5.27 : SEM images of complex 5.4 (a-c) and complex 5.5 (d-f) showing: a. 500 μm scale of complex 5.4; b. 200 μm scale of crystal stack of complex 5.4; c. 100 μm scale of crystal stack of complex 5.4; d. 500 μm scale of complex 5.5; e. 100 μm scale of complex 5.5; f. 3 μm scale of complex 5.5 showing layered structure.

SEM images revealed the new system, complex 5.5, possesses a series of crystal layers throughout the structure (figure 5.27f) which explains the difficulty experienced in isolating a single crystal of the material. These layers are new, with no evidence of their appearance in the original complex 5.4. The likely origin for the formation of these layers is crystal stacking upon crystallisation which indicates the rearrangement observed is due to a dissolution and recrystallization mechanism of complex 5.4 to generate complex 5.5.

Similar techniques such as transmission electron microscopy (TEM) and AFM (atomic force microscopy) have been previously employed by Schröder and co-workers to elucidate the mechanism of anion-induced structural rearrangement of a series of silver(I) coordination polymers bearing 4,4'-bipyridine ligands.⁶⁴ Changes to the crystal surface during dynamic AFM studies revealed that the surface profile undergoes significant changes with holes and peaks becoming more pronounced, indicative of a solvent-mediated rearrangement.

5.8 Additional Coordination Complexes

In addition to the fully refinable, obtainable datasets discussed in this chapter, a further example of a coordination polymer with ligand **2.12** has been observed. The purpose of this section is to illustrate a general overview of the gross structural features of this complex without detailed analysis as despite repeated attempts, crystals were plagued by consistently poor resolution, making structural elucidation extremely challenging. Consequently, the structural discussion that follows should be regarded as an approximation rather than an absolute proof of molecular structure.

The reaction of ligand **2.12** with copper(II) nitrate in NMP led to the formation of a 2D coordination polymer of formula $[\{\text{Cu}_3(\text{2.12})_2(\text{H}_2\text{O})_8\} \cdot \text{H}_2\text{O}]_n$, complex **5.6**. Single crystals of complex **5.6** were obtained by the vapour-diffusion of diethyl ether into a solution of the complex in NMP and isolated as orange plates. Crystals of complex **5.6** diffracted well and were reliably regrown several times but yielded consistently poor resolution. Complex **5.6** crystallised with a trigonal unit cell and was solved in the $R\bar{3}$ space group.

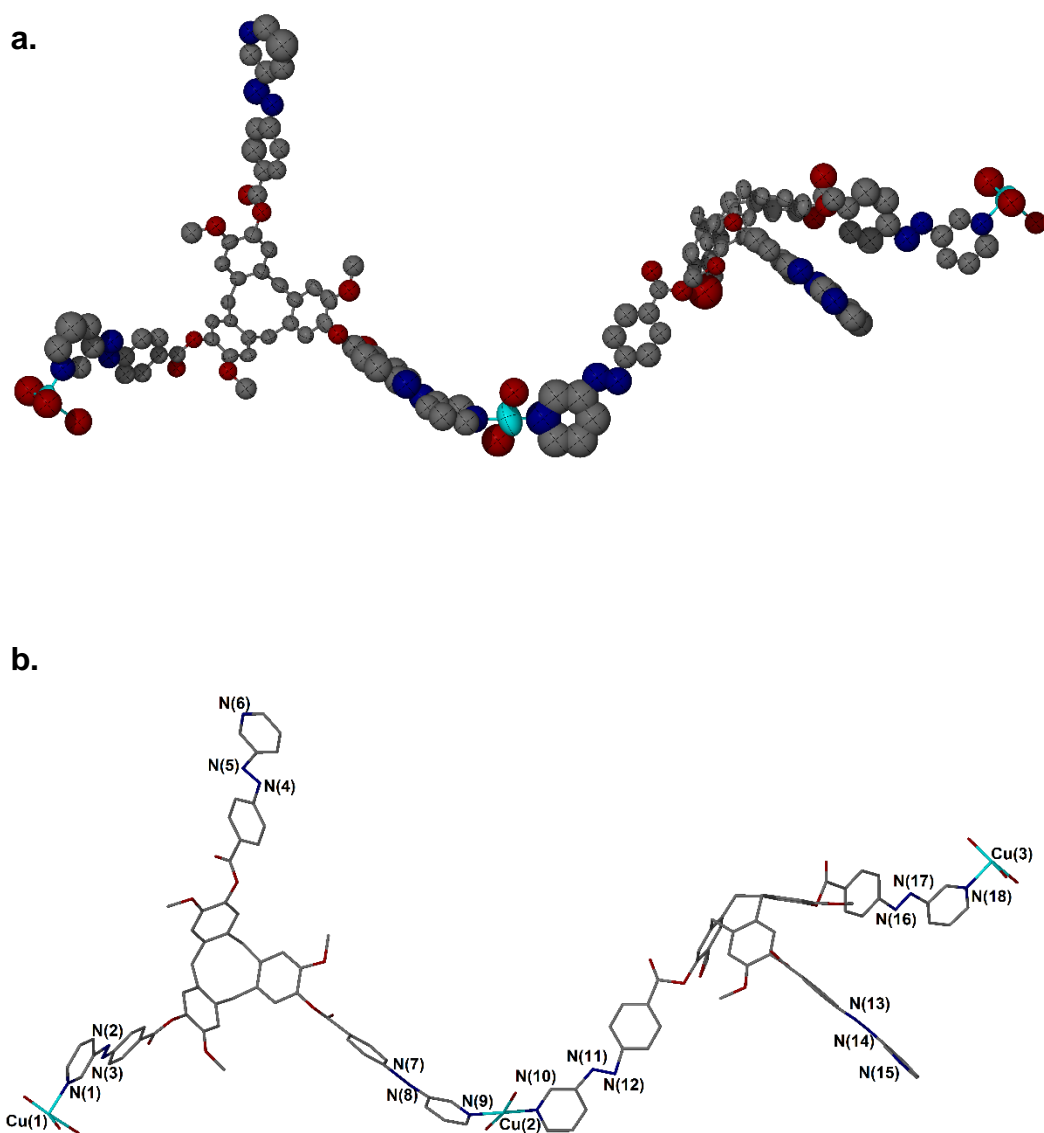
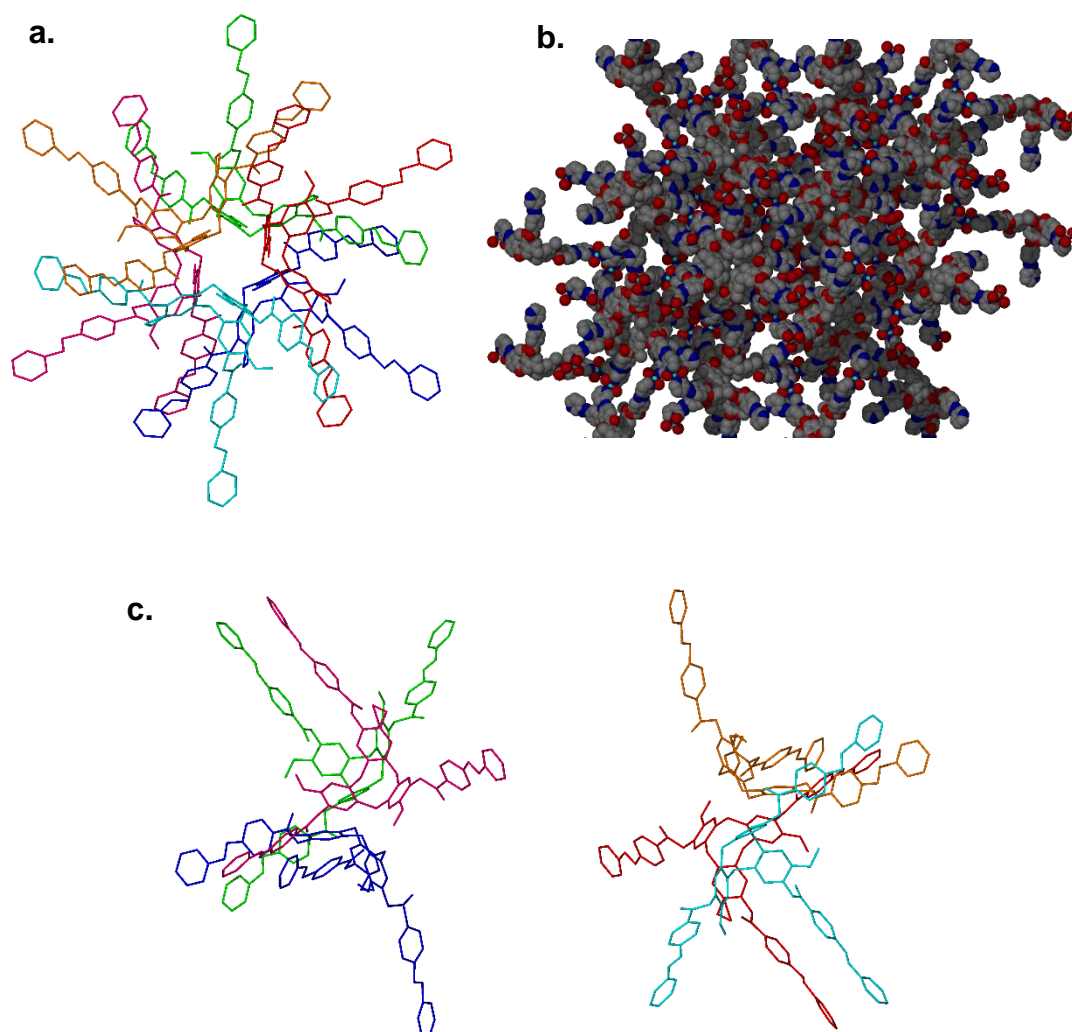


Figure 5.28: The asymmetric unit of complex 5.6 showing a. Thermal ellipsoids, shown at 50% probability; b. Stick representation of complex 5.6. All hydrogen atoms have been omitted for clarity.

The asymmetric unit of complex **5.6** is illustrated in figure 5.28. The structure is poorly resolved but is seen to be similar to complex **5.4**, with a central copper(II) ion coordinated by two ligands, each of which also coordinates another copper(II) centre. The copper centres are further coordinated by aqua ligands which could not be meaningfully refined and significant levels of disorder were observed for the AZB arms. Symmetry expansion reveals that the remaining AZB arm on each ligand also coordinates in contrast to the free ligand arms observed in complexes **5.2** and **5.3**. Void space calculations reveal a significant level of internal space of 67% of the total

cell volume which is likely to be responsible for the particularly poor quality of the datasets obtained for complex **5.6**. A star shaped motif, similar to that observed in complex **5.3** is once again apparent when viewed down the crystallographic *c*-axis. However in this case, the star is formed from the back-to-back stacking of three ligand **2.12** molecules rather than six (figure 5.29c). Despite the large degree of internal void space, solvent accessible voids are minimal upon viewing the system in spacefilling mode (figure 5.29a).



*Figure 5.29: From the SCXRD structure of complex **5.6** illustrating **a**. View down the crystallographic *c*-axis showing the star shaped formation; **b**. View of complex **5.6** in spacefilling mode highlighting the lack of solvent accessible void space; **c**. View down the crystallographic *b*-axis showing three ligands back-to-back which forms the star shaped formation when viewed down the *c*-axis.*

The author believes it probable that other coordination polymers featuring ligand **2.12** have been successfully prepared but have resisted structural elucidation due to poor quality X-ray data. The reaction of ligand **2.12** with cobalt(II) chloride in DMF and subsequent diffusion of diethyl ether into this solution led to the growth of green needles. Resolution was extremely poor, even using synchrotron radiation. Crude structure solution reveals the coordination of ligand **2.12** to the metal centres but the data was too poor to allow for a full structural elucidation. A similar outcome was also obtained for the reaction of ligand **2.12** with copper(II) chloride in DMAC solvent. Diffusion of diethyl ether resulted in the growth of small yellow needles which again showed a large unit cell and crude refinements indicating complex formation. Unless a strategy can be developed to circumvent the poor resolution of these systems however, their structural elucidation is likely to remain a challenge.

5.9 Conclusions and further direction

Ligand **2.12** displays versatile coordination chemistry with a variety of copper(II) and silver(I) cations with the first five examples of AZB appended CTG coordination polymers being fully isolated and studied *via* single crystal X-ray crystallography. The change of counterion appears to have a dramatic effect on the complex formed with only two copper salts (CF_3CO_2^- and CF_3SO_2^-) giving the same structure. This variability depending on the counterion suggests that some form of templation effect may be taking place during the formation of the copper coordination polymers, as only the two most similar counterions were observed to yield the same structure. This is not an uncommon phenomenon in the literature with several reported examples of coordination polymers that vary in structure when the counterion is altered.⁶⁵⁻⁶⁷

The silver coordination polymer, complex **5.3** was observed to be the same structure with a variety of different counterions, suggesting anion templation is not as important. The AZB units are observed to be highly conformationally flexible, with some examples being virtually planar and not twisting at all and others exhibiting significant twisting both when coordinating to a metal or not. This flexibility is thought to be important for the successful assembly of the iridium(III) metallocryptophanes discussed in chapter 3 which molecular modelling has revealed likely require high degrees of twisting to self-assemble and undergo photoisomerisation.

The flexibility of the azo unit does leads to the structural elucidation of such complexes being significantly challenging with problems such as poor diffraction/resolution and heavily disordered moieties becoming a recurring theme

throughout analysis. Crystal growth also proved challenging in many instances with many crystallisations of ligand **2.12** and of the other azo appended ligands **2.17** and **2.18** failing to grow suitable crystals. For these reasons, the author believes it highly probable that other coordination complexes of these ligands exist that have resisted characterisation by these means. Seeing as these problems are due to the nature of the complexes under study, it is difficult to propose how these limitations may be overcome.

The majority of the complexes prepared here do not possess significant internal space for undertaking host-guest chemistry with exceptions being complexes **5.2** and **5.4**. Complex **5.4** has already displayed an affinity for the binding of dichlorobenzene solvent molecules. This coincides with the rearrangement of complex **5.4** into complex **5.5** in dichlorobenzene solvent. SEM studies of this process revealed that the likely mechanism for the process is the dissolution and micro-recrystallisation at the surface of the crystals rather than a solid state rearrangement. Potential for photoisomerisation in the solid state also remains a possible option for further investigation in accordance with the systems reported by Zhao.⁴⁸

5.10 Experimental

5.10.1 Instrumentation

FT-IR spectra were recorded as solid phase samples using a Perkin Elmer Spectrum One spectrometer. Samples for microanalysis were dried under vacuum before analysis and determined by Mr Stephen Boyer of London Metropolitan University. Samples for TGA and EDX analyses were dried under vacuum and determined by Dr Algy Kazlauciusas of the University of Leeds. Optical images were taken on a Nikon Eclipse LV100 microscope and a Nikon SMZ 1500 microscope.

Samples for SEM were coated with a thin layer of iridium (2 nm) using a sputter coater Cressington 208HR. Samples were then imaged using an FEI Nova NanoSEM 450 operating at 3 kV. Elemental analyses were made by an EDAX (AMTEK) operating at 18keV.

5.10.2 Chemical Synthesis

Synthesis of $\{[\text{Cu}_3(\text{H}_2\text{O})_6(2.12)_4] \cdot 6\text{BF}_4 \cdot 9\text{NMP} \cdot 4\text{H}_2\text{O}\}_n$ (complex 5.1)

Copper tetrakis acetonitrile tetrafluoroborate (5.00 mgs, 0.016 mmol) was dissolved in NMP (0.5 mL). A solution of **2.12** (10.0 mgs, 0.0096 mmol) in NMP (1 mL) was added to give an orange solution. Diethyl ether vapours were diffused into the solution, where orange shards of complex **5.1** formed after 14 days that were analysed by single crystal X-ray diffraction.

FT-IR (cm^{-1}) = 3179, 2958, 2879, 1738, 1655, 1507, 1473, 1423, 1301, 1262, 1208, 1089, 749, 651, 470; Analysis calculated for $\text{C}_{285}\text{H}_{281}\text{Cu}_3\text{F}_{24}\text{N}_{45}\text{O}_{55}$ (% calculated; found) C (57.44, 61.06), H (4.78, 6.76), N (10.63, 11.08); TGA (single crystals, dried under vacuum for 5 hours).

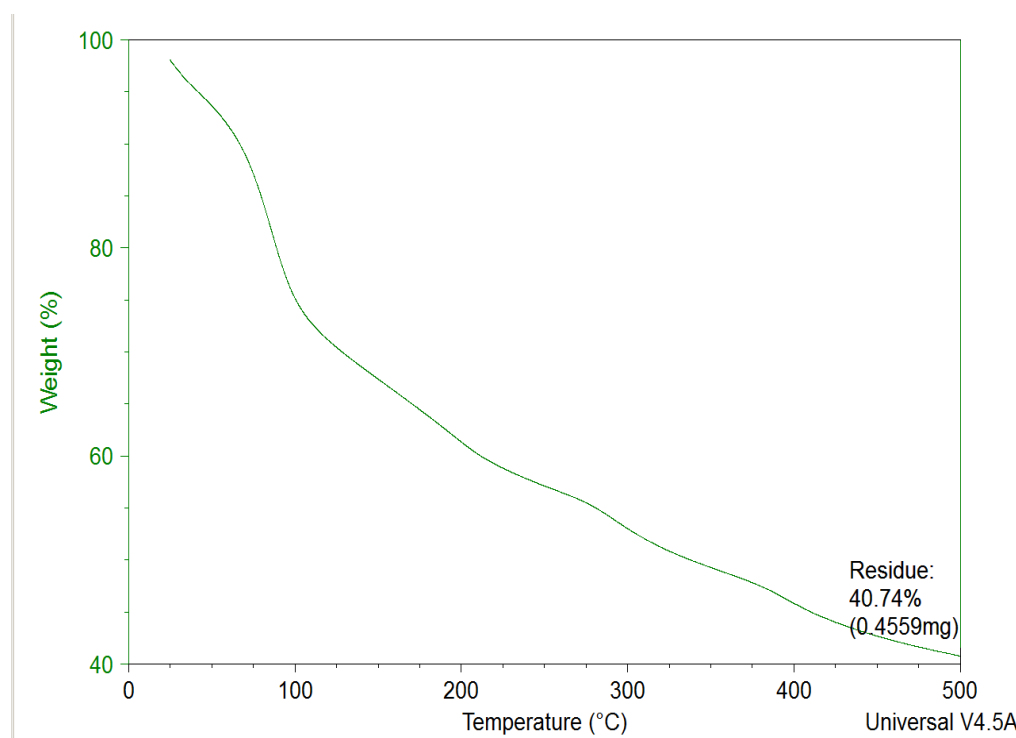


Figure 5.30: TGA spectrum of complex 5.1.

Synthesis of $[\text{Cu}(2.12)_2(\text{OAc})_2]_n$ (complex 5.2)

Copper (II) acetate (5.00 mgs, 0.016 mmol) was dissolved in DMAC (0.5 mL). A solution of **2.12** (10.0 mgs, 0.0096 mmol) in DMAC (1 mL) was added to give a

yellow solution. Diethyl ether vapours were diffused into the solution, where yellow needles of complex **5.2** formed after 14 days that were analysed by single crystal X-ray diffraction.

Analysis calculated for $C_{124}H_96Cu_2N_{18}O_{22}$ (% calculated; found) C (64.27, 53.88), H (4.18, 4.85), N (10.88, 9.79).

Synthesis of $[Ag(L^1).X]_n$ ($X = OTf_2, PF_6, BF_4$, complex **5.3**)

Silver tetrakis acetonitrile tetrafluoroborate (5.00 mgs, 0.014 mmol) was dissolved in DMF (0.5 mL). A solution of **2.12** (10.0 mgs, 0.0096 mmol) in DMF (1 mL) was added to give an orange solution. Diethyl ether vapours were diffused into the solution, where pale red blocks of complex **5.3** formed after 7 days that were analysed by single crystal X-ray diffraction.

(Analysis presented is for the BF_4^- counterion) FT-IR (cm^{-1}) = 2929, 1728, 1652, 1602, 1507, 1446, 1387, 1323, 1258, 1205, 1139, 1087, 1056, 1005, 861, 813, 766, 695, 658, 624, 517; Analysis calculated for $C_{60}H_{45}AgBF_4N_9O_9$ (% calculated; found) C (58.55, 53.61), H (3.69, 4.15), N (10.24, 9.37); TGA (single crystals, dried under vacuum for 5 hours):

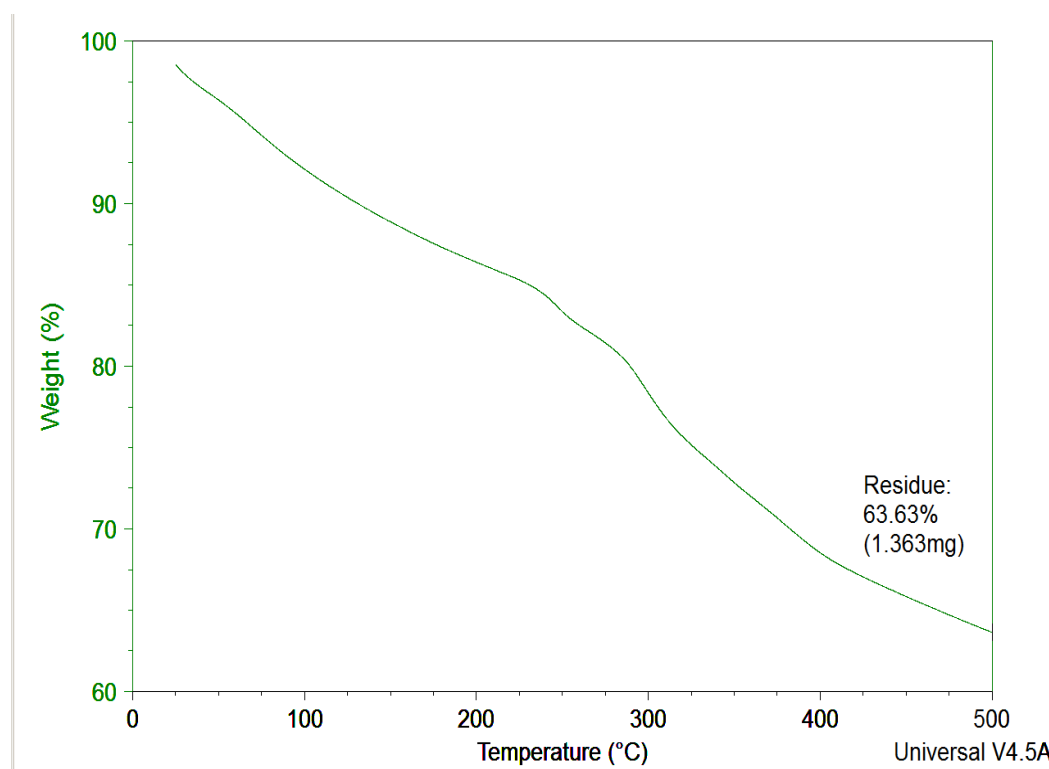


Figure 5.31: TGA spectrum of complex **5.3**.

Synthesis of $\{[\text{Cu}_5(\mathbf{2.12})_4(\text{H}_2\text{O})_{12}]\cdot 2\text{H}_2\text{O} \cdot 4\text{NMP} \cdot 10\text{OTf}\}_n$ (complex **5.4)**

Copper triflate (5.00 mgs, 0.017 mmol) was dissolved in NMP (0.5 mL). A solution of **2.12** (10.0 mgs, 0.0096 mmol) in NMP (1 mL) was added to give an orange solution. Diethyl ether vapours were diffused into the solution, where orange plates of complex **5.4** formed after 28 days that were analysed by single crystal X-ray diffraction.

FT-IR (cm^{-1}) = 2953, 2879 1737, 1644, 1583, 1403, 1255, 1223, 1155, 1089, 1061, 1029, 927, 865, 766, 701, 636; Analysis calculated for $\text{C}_{270}\text{H}_{244}\text{Cu}_5\text{F}_{30}\text{N}_{40}\text{O}_{74}$ (% calculated; found) C (50.35, 51.65), H (3.82, 5.38), N (8.70, 10.21).

Synthesis of $\{[\text{Cu}(\text{L}^1)_2(\text{NMP})_2\cdot\text{CF}_3\text{SO}_3\text{ DCB}]\}_n$ (complex **5.5)**

Crystals of complex **5.4** were drained of NMP solvent. 1,2 dichlorobenzene (0.5 mL) was added and the vial allowed to stand for 14 days after which crystals were analyzed by single crystal X-ray diffraction and SEM.

5.10.3 X-ray crystallography

Crystals were mounted under inert oil on a MiTeGen tip and flash frozen using an Oxford Cryosystems low temperature device. X-ray diffraction data for complexes **5.2**, **5.4** and **5.5** were collected using $\text{CuK}\alpha$ radiation ($\lambda = 1.54184 \text{ \AA}$) on a Agilent Supernova dual-source diffractometer with Atlas S2 CCD detector and fine-focus sealed tube generator. Data for complexes **5.1** and **5.3** were collected using synchrotron radiation ($\lambda = 0.6889 \text{ \AA}$) using a Crystal Logic 4-circle Kappa goniometer and Rigaku Saturn 724 CCD diffractometer at station I19 of Diamond Light Source. Data were corrected for Lorentzian and polarization effects and absorption corrections were applied using multi-scan methods. The structures were solved by direct methods using SHELXS-97 and refined by full-matrix on F^2 using SHELXL-97.⁶⁸

For complex **5.1**, the AZB arms show significant levels of disorder with all eight of the rings being restrained to idealized geometry using the AFIX command in ShelX. The BF_4^- counterion and the NMP solvent molecules were restrained to idealized geometry using the AFIX command in ShelX. The structure contained residual

electron density which could not be meaningfully refined as solvent, hence the SQUEEZE⁵⁴ routine of PLATON⁵⁴ was employed.

For complex **5.2**, one pyridyl ring showed persistent disorder and so was restrained to idealised geometry using the AFIX command in ShelX and refined isotropically. One of the acetate units was refined with restraints on the bond lengths, was restrained to be planar and refined isotropically. Finally restraints were applied to the displacement parameters of one of the phenyl ester moieties which was refined as a group. The structure contained residual electron density which could not be meaningfully refined as solvent, hence the SQUEEZE⁵⁴ routine of PLATON⁵⁴ was employed.

For complex **5.3** the AZB arms show significant levels of disorder with all six of the rings being restrained to idealized geometry using the AFIX command in ShelX. One ring was refined at 50% occupancy. This disordered AZB arm was also refined with group isotropic displacement parameters. The silver ion was heavily disordered and was refined at 33% occupancy over three positions.

For complex **5.4** the AZB arms showed significant levels of disorder; the CF₃SO₃⁻ counterion along with one of these arms was refined isotropically. The two N-C bonds from this azo unit were restrained to be chemically reasonable and the rings on this arm were refined with group U_{iso} values using the EADP command in ShelX and were also refined with rigid body constraints using the AFIX command in ShelX. Anisotropic displacement parameters were constrained to be similar using the DELU command in ShelX.

For complex **5.5** much of the high angle data was weak and was excluded from the refinement. The phenyl unit of one of the AZB sidearms was heavily disordered and was refined with rigid body restraints and disordered at 60%/40% occupancies. The five dichlorobenzene solvent molecules were all refined isotropically and with rigid body restraints. Three of the dichlorobenzene molecules were refined at 50% occupancy. One of the Cl atoms of one of these dichlorobenzene molecules could not be crystallographically located. Additionally, one dichlorobenzene molecule was

restrained to be planar. Anisotropic displacement parameters were constrained to be similar using the DELU and SIMU commands in ShelX.

For complex **5.6**, the copper(II) centres were refined anisotropically. The bowls of the CTG ligands were refined anisotropically but with anisotropic displacement parameters restrained using the RIGU command in ShelX. The rest of the structure was refined isotropically to ensure a stable refinement. All phenyl and pyridyl rings of the ligand arms were heavily disordered and were therefore restrained to idealized geometry using the AFIX command in ShelX. The thermal parameters of three of the phenyl rings have been constrained using the EADP command in ShelX. The C-N and N=N bonds of the azo ligand arms have been restrained to 1.45(1) and 1.23(1) Å respectively. The exact nature of the additional ligands coordinating to the copper(II) centers could not be determined and have been assigned as oxygen. Therefore no comment on the exact coordination environment of the copper(II) center has been discussed in the main text and should not be inferred from this dataset.

	5.1	5.2	5.3	5.4	5.5
Empirical Formula	$C_{285}H_{381}B_6Cu_3F_{24}N_{45}O_{55}$	$C_{124}H_{96}CuN_{18}O_{22}$	$C_{60}H_{45}AgN_9O_9$	$C_{270}H_{264}Cu_3F_{30}N_{40}O_{94}S_{10}$	$C_{180}H_{140}Cu_2F_{12}N_{20}O_{38}Cl_{14}$
Mr	5928.1	2253.78	1142.23	6781.55	3882.58
Crystal Appearance	Orange Plates	Yellow Needles	Red Blocks	Orange Plates	Orange Plates
Crystal Size (mm)	0.18 x 0.17 x 0.11	0.051 x 0.073 x 0.087	0.11 x 0.10 x 0.08	0.20 x 0.26 x 0.31	0.11 x 0.17 x 0.23
Crystal system	Trigonal	Triclinic	Trigonal	Triclinic	Triclinic
Space group	$R\bar{3}$	$P\bar{1}$	$R\bar{3}$	$P\bar{1}$	$P\bar{1}$
a (Å)	41.380 (6)	9.7265 (2)	45.2053 (7)	14.4606 (2)	14.6028 (4)
b (Å)	41.380 (6)	20.1403 (6)	45.2053 (7)	27.3879 (6)	18.9001 (6)
c (Å)	42.999 (6)	36.7167 (9)	19.8346 (3)	37.4413 (7)	21.2164 (6)
α (°)	90	79.541 (2)	90	75.797 (2)	78.027 (3)
β (°)	90	89.201 (2)	90	80.544 (1)	75.498 (3)
γ (°)	120	84.157 (2)	120	75.017 (2)	76.125 (3)
V (Å ³)	63762	7036.3	35102.1	13805.7	5435.5 (3)
Z	1	1	1	1	1
P_{calc} (g cm ⁻³)	0.926	1.064	0.974	0.651	1.209
μ (mm ⁻¹)	0.216	0.753	0.301	0.65	2.593
F (000)	18474	2342	10566	2795	2024
Radiation (λ)	Synchrotron (0.6889)	Cu (1.54184)	Synchrotron (0.6889)	Cu (1.54184)	Cu (1.54184)
2 θ range	1.9 to 72.26	6.02 to 102.48	1.746 to 40.296	6.36 to 103.1	6.38 to 102.88
Reflections collected	482144	33596	96032	74577	25963
Independent reflections	71597	14813	8164	29368	11531
Data/restraints/parameters	71597/0/1181	14813/27/1423	8164/566/607	29368/2/1558	11531/1122/1090
Goof on F ²	0.921	1.088	2.301	2.944	2.344
Final R indexes [$I \geq 2\sigma(I)$]	R1 = 0.1025	R1 = 0.0904	R1 = 0.1856	R1 = 0.2921	R1 = 0.211

Table 5.6: Details of crystal collection and analyses for X-ray datasets of compounds 5.1, 5.2, 5.3, 5.4 and 5.5.

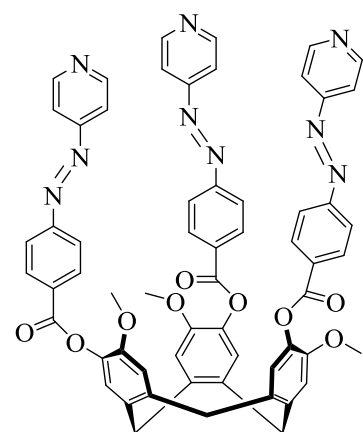
5.11 References

1. M. J. Hardie, *Chemical Society Reviews*, 2010, **39**, 516-527.
2. J.C.Bailar, *Prep.Inorg.React.*, 1964, **1**, 1-57.
3. R. Robson, *Journal of the Chemical Society, Dalton Transactions*, 2000, **0**, 3735-3744.
4. S. Kitagawa, R. Kitaura and S.-i. Noro, *Angewandte Chemie International Edition*, 2004, **43**, 2334-2375.
5. J. L. C. Rowsell and O. M. Yaghi, *Angewandte Chemie International Edition*, 2005, **44**, 4670-4679.
6. B. F. Hoskins and R. Robson, *Journal of the American Chemical Society*, 1989, **111**, 5962-5964.
7. O. M. Yaghi and H. Li, *Journal of the American Chemical Society*, 1995, **117**, 10401-10402.
8. N. L. Rosi, J. Eckert, M. Eddaoudi, D. T. Vodak, J. Kim, M. O'Keeffe and O. M. Yaghi, *Science*, 2003, **300**, 1127-1129.
9. J. J. Henkelis, S. A. Barnett, L. P. Harding and M. J. Hardie, *Inorganic Chemistry*, 2012, **51**, 10657-10674.
10. J. J. Henkelis, T. K. Ronson and M. J. Hardie, *CrystEngComm*, 2014, **16**, 3688-3693.
11. C. Carruthers, J. Fisher, L. P. Harding and M. J. Hardie, *Dalton Transactions*, 2010, **39**, 355-357.
12. M. J. Hardie, R. Ahmad and C. J. Sumby, *New Journal of Chemistry*, 2005, **29**, 1231-1240.
13. C. J. Sumby and M. J. Hardie, *Crystal Growth & Design*, 2005, **5**, 1321-1324.
14. M. J. Hardie and C. J. Sumby, *Inorganic Chemistry*, 2004, **43**, 6872-6874.
15. C. J. Sumby, K. C. Gordon, T. J. Walsh and M. J. Hardie, *Chemistry – A European Journal*, 2008, **14**, 4415-4425.
16. F. L. Thorp-Greenwood, T. K. Ronson and M. J. Hardie, *Chemical Science*, 2015, **6**, 5779-5792.
17. F. L. Thorp-Greenwood, A. N. Kulak and M. J. Hardie, *Nature Chemistry*, 2015, **7**, 526-531.
18. M. A. Little, M. A. Halcrow, L. P. Harding and M. J. Hardie, *Inorganic Chemistry*, 2010, **49**, 9486-9496.
19. M. J. Hardie, R. M. Mills and C. J. Sumby, *Organic & Biomolecular Chemistry*, 2004, **2**, 2958-2964.
20. S. T. Mough and K. T. Holman, *Chemical Communications*, 2008, **0**, 1407-1409.
21. T. K. Ronson and M. J. Hardie, *CrystEngComm*, 2008, **10**, 1731-1734.
22. F. L. Thorp-Greenwood, G. T. Berry, S. S. Boyadjieva, S. Oldknow and M. J. Hardie, *Inorganic Chemistry*, 2018, **Submitted**.

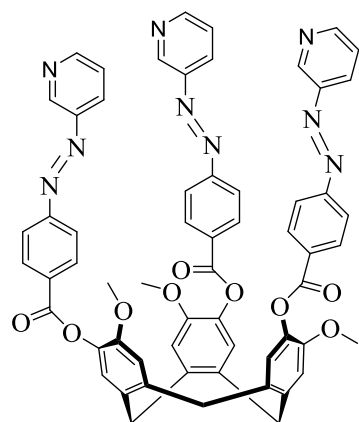
23. B. F. Abrahams, N. J. FitzGerald and R. Robson, *Angewandte Chemie International Edition*, 2010, **49**, 2896-2899.
24. B. F. Abrahams, B. A. Boughton, N. J. FitzGerald, J. L. Holmes and R. Robson, *Chemical Communications*, 2011, **47**, 7404-7406.
25. J.-R. Song, J. Sun, J. Liu, Z.-T. Huang and Q.-Y. Zheng, *Chemical Communications*, 2014, **50**, 788-791.
26. N. B. McKeown, B. Gahnem, K. J. Msayib, P. M. Budd, C. E. Tattershall, K. Mahmood, S. Tan, D. Book, H. W. Langmi and A. Walton, *Angewandte Chemie International Edition*, 2006, **45**, 1804-1807.
27. J.-T. Yu, Z. Chen, J. Sun, Z.-T. Huang and Q.-Y. Zheng, *Journal of Materials Chemistry*, 2012, **22**, 5369-5373.
28. A. D. Martin, T. L. Easun, S. P. Argent, W. Lewis, A. J. Blake and M. Schroder, *CrystEngComm*, 2017, **19**, 603-607.
29. S. Li and D. V. McGrath, *Journal of the American Chemical Society*, 2000, **122**, 6795-6796.
30. L.-X. Liao, D. M. Junge and D. V. McGrath, *Macromolecules*, 2002, **35**, 319-322.
31. D. M. Junge and D. V. McGrath, *Journal of the American Chemical Society*, 1999, **121**, 4912-4913.
32. C. Appiah, K. R. Siefermann, M. Jorewitz, H. Barqawi and W. H. Binder, *RSC Advances*, 2016, **6**, 6358-6367.
33. X. Li, R. Wen, Y. Zhang, L. Zhu, B. Zhang and H. Zhang, *Journal of Materials Chemistry*, 2009, **19**, 236-245.
34. C. Weber, T. Liebig, M. Gensler, L. Pithan, S. Bommel, D. Bléger, J. P. Rabe, S. Hecht and S. Kowarik, *Macromolecules*, 2015, **48**, 1531-1537.
35. S. Dong, L. Gao, J. Li, D. Xu and Q. Zhou, *Polymer Chemistry*, 2013, **4**, 3968-3973.
36. H. Chen, X. Ma, S. Wu and H. Tian, *Angewandte Chemie International Edition*, 2014, **53**, 14149-14152.
37. C. D. Jones and J. W. Steed, *Chemical Society Reviews*, 2016, **45**, 6546-6596.
38. S. Lee, S. Oh, J. Lee, Y. Malpani, Y.-S. Jung, B. Kang, J. Y. Lee, K. Ozasa, T. Isoshima, S. Y. Lee, M. Hara, D. Hashizume and J.-M. Kim, *Langmuir*, 2013, **29**, 5869-5877.
39. Z. L. Pianowski, J. Karcher and K. Schneider, *Chemical Communications*, 2016, **52**, 3143-3146.
40. F. Xie, L. Qin and M. Liu, *Chemical Communications*, 2016, **52**, 930-933.
41. K. Uchida, S. Yamaguchi, H. Yamada, M. Akazawa, T. Katayama, Y. Ishibashi and H. Miyasaka, *Chemical Communications*, 2009, **0**, 4420-4422.
42. M. Moriyama, N. Mizoshita, T. Yokota, K. Kishimoto and T. Kato, *Advanced Materials*, 2003, **15**, 1335-1338.

43. A. Karmakar, A. Paul and A. J. L. Pombeiro, *CrystEngComm*, 2017, **19**, 4666-4695.
44. Y. Liu, J. F. Eubank, A. J. Cairns, J. Eckert, V. C. Kravtsov, R. Luebke and M. Eddaoudi, *Angewandte Chemie International Edition*, 2007, **46**, 3278-3283.
45. T. M. Reineke, M. Eddaoudi, D. Moler, M. O'Keeffe and O. M. Yaghi, *Journal of the American Chemical Society*, 2000, **122**, 4843-4844.
46. C.-M. Jin, Z. Zhu, Z.-F. Chen, Y.-J. Hu and X.-G. Meng, *Crystal Growth & Design*, 2010, **10**, 2054-2056.
47. V. Zeleňák, Z. Vargová, M. Almáši, A. Zeleňáková and J. Kuchár, *Microporous and Mesoporous Materials*, 2010, **129**, 354-359.
48. W.-C. Song, X.-Z. Cui, Z.-Y. Liu, E.-C. Yang and X.-J. Zhao, *Scientific Reports*, 2016, **6**, 34870.
49. A. Chanthapally, W. T. Oh and J. J. Vittal, *Chemical Communications*, 2014, **50**, 451-453.
50. S.-Y. Yang, X.-L. Deng, R.-F. Jin, P. Naumov, M. K. Panda, R.-B. Huang, L.-S. Zheng and B. K. Teo, *Journal of the American Chemical Society*, 2014, **136**, 558-561.
51. F.-L. Hu, S.-L. Wang, B. F. Abrahams and J.-P. Lang, *CrystEngComm*, 2015, **17**, 4903-4911.
52. J. Park, D. Yuan, K. T. Pham, J.-R. Li, A. Yakovenko and H.-C. Zhou, *Journal of the American Chemical Society*, 2012, **134**, 99-102.
53. J. W. Brown, B. L. Henderson, M. D. Kiesz, A. C. Whalley, W. Morris, S. Grunder, H. Deng, H. Furukawa, J. I. Zink, J. F. Stoddart and O. M. Yaghi, *Chemical Science*, 2013, **4**, 2858-2864.
54. P. van der Sluis and A. L. Spek, *Acta Crystallographica Section A*, 1990, **46**, 194-201.
55. J. N. Van Niekerk and F. R. L. Schoening, *Nature*, 1953, **171**, 36-37.
56. R. J. Deeth and M. A. Hitchman, *Inorganic Chemistry*, 1986, **25**, 1225-1233.
57. E. Huerta, S. A. Serapian, E. Santos, E. Cequier, C. Bo and J. de Mendoza, *Chemistry – A European Journal*, 2016, **22**, 13496-13505.
58. E. Huerta, E. Cequier and J. d. Mendoza, *Chemical Communications*, 2007, **0**, 5016-5018.
59. E. Huerta, G. A. Metselaar, A. Fragoso, E. Santos, C. Bo and J. de Mendoza, *Angewandte Chemie*, 2007, **119**, 206-209.
60. M. A. Little, T. K. Ronson and M. J. Hardie, *Dalton Transactions*, 2011, **40**, 12217-12227.
61. R. M. Payne and C. L. Oliver, *CrystEngComm*, 2016, **18**, 7965-7971.
62. J. L. Atwood, L. J. Barbour, A. Jerga and B. L. Schottel, *Science*, 2002, **298**, 1000-1002.
63. J. J. Henkelis, C. J. Carruthers, S. E. Chambers, R. Clowes, A. I. Cooper, J. Fisher and M. J. Hardie, *Journal of the American Chemical Society*, 2014, **136**, 14393-14396.

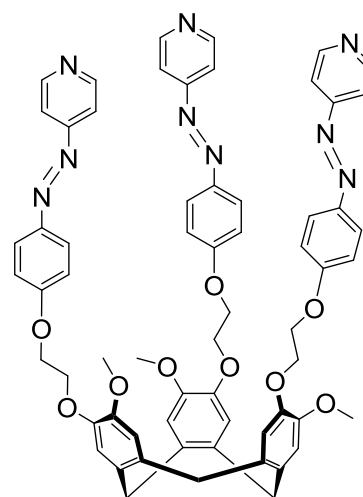
64. A. N. Khlobystov, N. R. Champness, C. J. Roberts, S. J. B. Tandler, C. Thompson and M. Schroder, *CrystEngComm*, 2002, **4**, 426-431.
65. Y.-B. Dong, J.-Y. Cheng, R.-Q. Huang, M. D. Smith and H.-C. zur Loye, *Inorganic Chemistry*, 2003, **42**, 5699-5706.
66. L. Yi, X. Yang, T. Lu and P. Cheng, *Crystal Growth & Design*, 2005, **5**, 1215-1219.
67. T. L. Hennigar, D. C. MacQuarrie, P. Losier, R. D. Rogers and M. J. Zaworotko, *Angewandte Chemie International Edition in English*, 1997, **36**, 972-973.
68. G. Sheldrick, *Acta Crystallographica Section A*, 2008, **64**, 112-122.



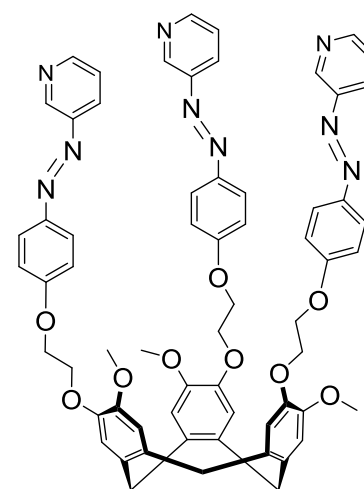
2.11



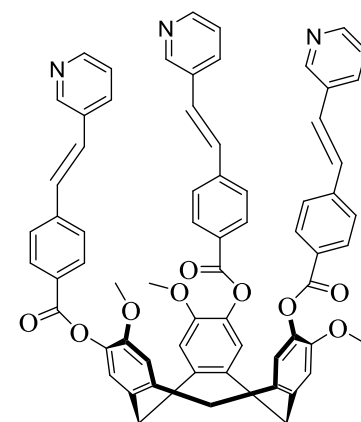
2.12



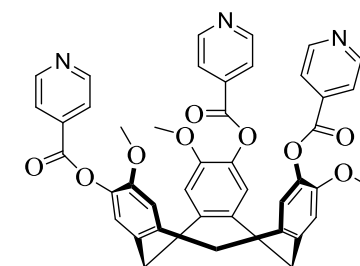
2.17



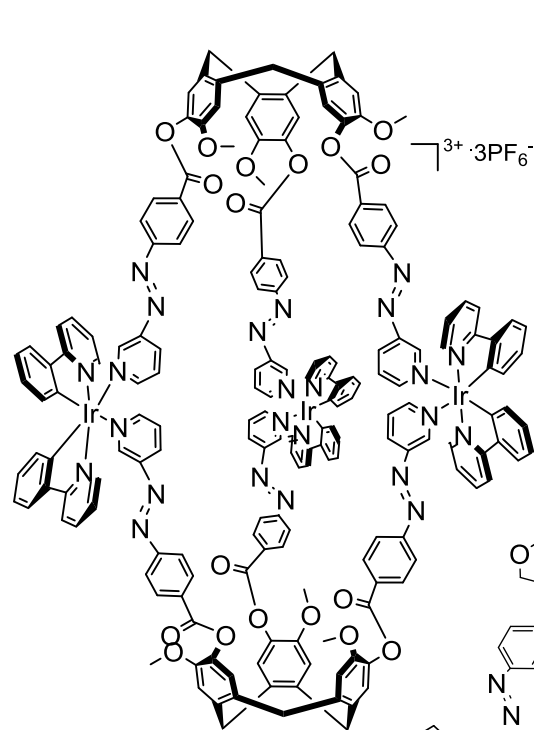
2.18



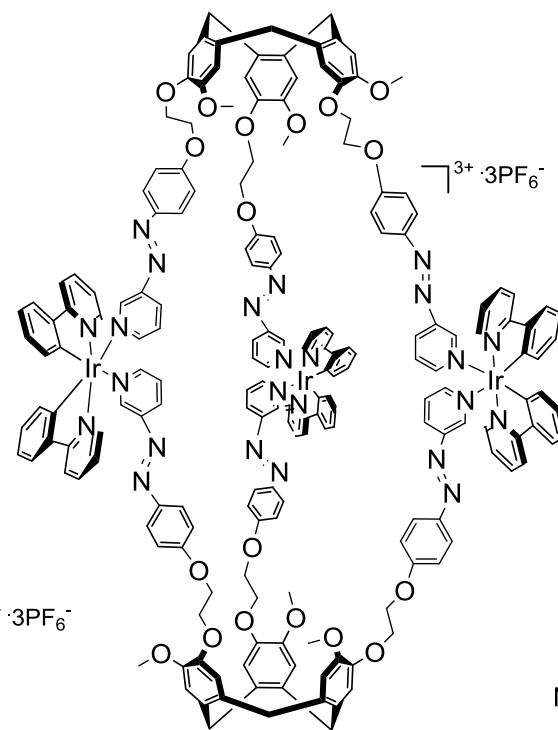
2.22



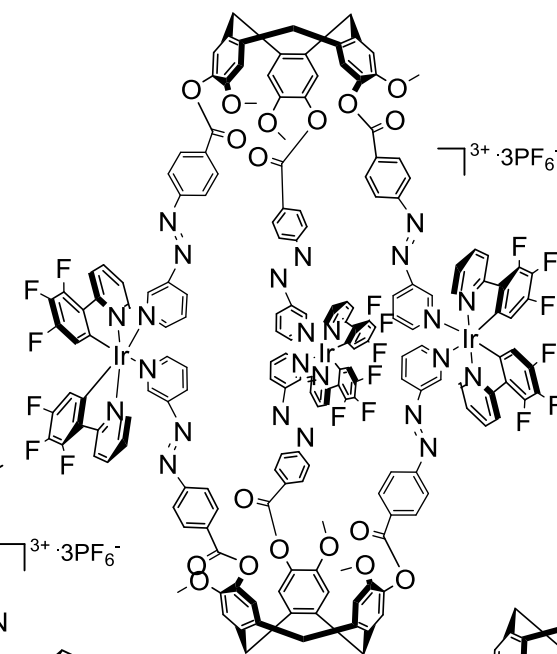
3.13



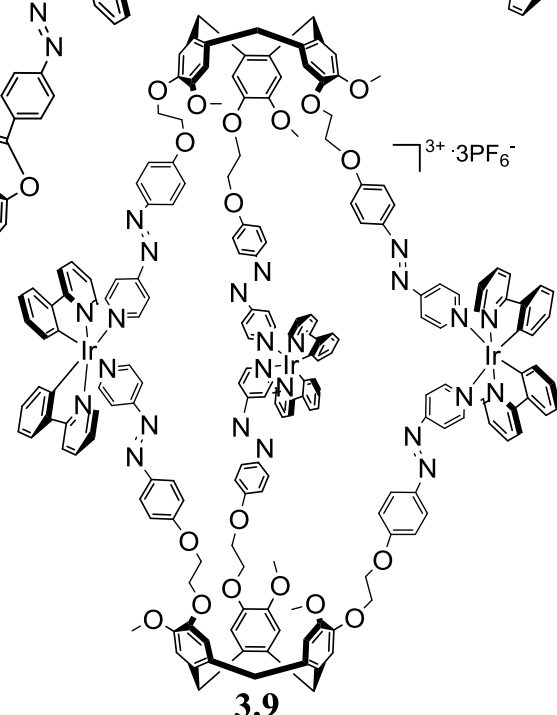
3.8



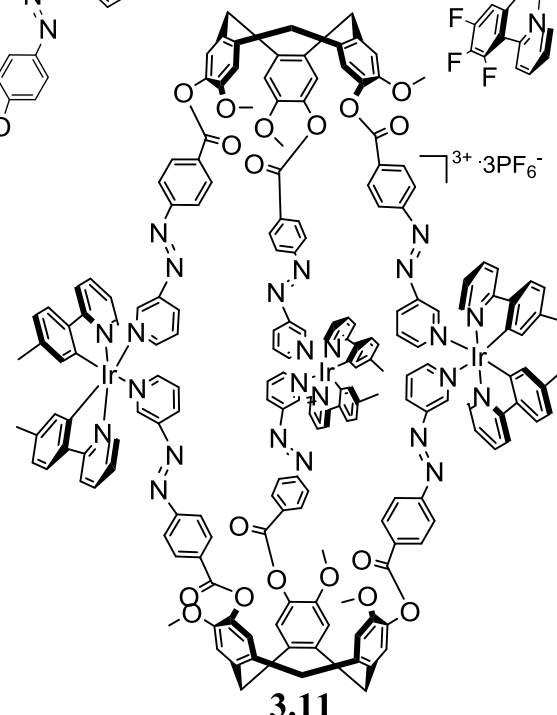
3.10



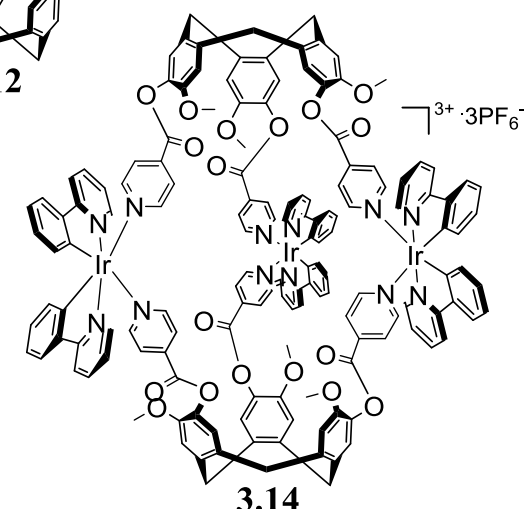
3.12



3.9



3.11



3.14